REACTOR

CHAPTER 4

TABLE OF CONTENTS

CHAPTER 4

TABLE OF CONTENTS (Cont'd)

CHAPTER 4

LIST OF TABLES

CHAPTER 4

LIST OF TABLES

CHAPTER 4

LIST OF FIGURES

LIST OF FIGURES (Cont'd)

LIST OF FIGURES (Cont'd)

LIST OF FIGURES (Cont'd)

LIST OF FIGURES (Cont'd)

LIST OF FIGURES (Cont'd)

UPDATE REFERENCE LIST

Chapter 4

Section	Cross References
Revision 12-B	
Section 4.3A.6	ER-W3-2000-1027/DRN 03-270
Revision 13	
Section 4.2.1.2.1	ER-W3-2003-0678/DRN 03-1821
TOC Page 4-i TOC Page 4-iv TOC Page 4-ix Section 4.2.4.2.3.2 Table 4.2-1 Sht 3 Section 4.3A.1 Section 4.3A.2 Section 4.3A.3 Table 4.3A-1 Table 4.3A-5 Sht 1 Table 4.3A-5 Sht 2 Figure 4.3A-2 Figure 4.3A-3 Figure 4.3A-7 Figure 4.3A-8 Figure 4.3A-9 Figure 4.3A-10	ER-W3-2003-0654/DRN 04-502
Revision 13-A	
Section 4.4.6.1	ER-W3-2003-0418-000/DRN 03-1689
Revision 14	
Section 4.2.1 Section 4.2.1.2.2.1 Section 4.2.1.2.5 Section 4.2.1.3.3 Section 4.2.1.3.3.1 Section 4.2.1.3.3.3 Section 4.2.3.1.2.3 Section 4.2.3.1.3 Section 4.3A.4.1 Section 4.3A.4.2 Section 4.4.1.1 Section 4.4.2.6.3 Section 4.5.2.4.2.3 Table 4.3A-5 Table 4.6-1	ER-W3-2001-1149-000/DRN 03-2058

Section	Cross References
Revision 14 Cont'd	
Section 4.2.1.2.4.4 Section 4.2.1.2.7 Section 4.3.2.2.1 Section 4.4.1.3 Reference 4.4	ER-W3-2002-0110-001/DRN 04-1096
Section 4.4.6.1	ER-W3-2003-0418-001/DRN 04-1780
Table Of Contents Section 4.3A Section 4.3A.1 Section 4.3A.2.1.1 Section 4.3A.2.3 Section 4.3A.2.5 Section 4.3A.3.1.1 Section 4.3A.3.1.2 Section 4.3A.3.1.3	ER-W3-2004-0116-003/DRN 05-508
Table 4.3A-1 Table 4.3A-2 Table 4.3A-3 Table 4.3A-4 Table 4.3A-5	
Figure 4.3A-2 Figure 4.3A-3 Figure 4.3A-8 Figure 4.3A-9 Figure 4.3A-10	
Revision 15	
Section 4.3.3.1.1 Section 4.4.4.2.1 Section 4.4.6.1 Section 4.6.5	ER-W3-2006-0281-000/DRN 06-871
Section 4.2.1.1.5 Section 4.2.1.4.4 Section 4.2.4.1.2 Section 4.3.2.3.2 Section 4.3.3.1.2.1 Figure 4.3-57 Table 4.3-1 Sh. 1	ER-W3-2001-1023-000/DRN 06-895
Section 4.3.2.7.2	ER-W3-2006-0223-000/DRN 06-914

Section	Cross References
Revision 15 Cont'd	
Section 4.2.1.2.2.1 Table 4.2-1 Sh. 3	ER-W3-2004-0116-018/DRN 06-992
Table of Contents Section 4.2.1.1.2 Section 4.2.1.2.1 Section 4.2.1.2.2.1 Section 4.2.1.2.2.2 Section 4.2.1.2.5 Section 4.2.1.2.5.1 Section 4.2.1.2.8 Section 4.2.1.3 Section 4.2.2.2 Section 4.2.2.3 Section 4.2.3.1.3 Section 4.2.3.1.4 Section 4.2.3.3.1 Section 4.2: References Table 4.2-1 Sh. 2 Figure 4.2-11A Section 4.3A Section 4.3A.1 Section 4.3A.2.1.1 Section 4.3A.2.1.2 Section 4.3A.2.3 Section 4.3A.2.5 Section 4.3A.3.1.1 Section 4.3A.3.1.2 Section 4.3A.3.1.3 Section 4.3A.3.3.3 Section 4.3: References Table 4.3A-1 thru Table 4.3A-5 Figure 4.3A-1 thru Figure 4.3A-3 Figure 4.3A-8 thru Figure 4.3A-10 Figure 4.3A-19a	ER-W3-2005-0447-004/DRN 06-1059
Section 4.2.3.2.3	ER-W3-2004-0094-003/DRN 06-1141
Revision 302	
Section 4.1 Figure 4.1.2a Section 4.2.1.1.2 Section 4.2.1.1.5 Section 4.2.1.1.7	EC-9533

Section	Cross References
Revision 302 Cont'd	
Section 4.2.1.1.8	
Section 4.2.1.1.9	
Section 4.2.1.2.1	
Section 4.2.1.2.2.1	
Section 4.2.1.2.2.2	
Section 4.2.1.2.5	
Section 4.2.1.2.6	
Section 4.2.1.2.8	
Section 4.2.2.1	
Section 4.2.2.2	
Section 4.2.2.3	
Section 4.2.3.1.1	
Section 4.2.3.1.3	
Section 4.2.3.1.4	
Section 4.2.3.2.3	
Section 4.2.3.2.4.2	
Section 4.2.3.2.7	
Section 4.2.3.2.12	
Section 4.2.4.1.1	
Section 4.2.4.1.2	
Section 4.2: References	
Table 4.2-1 Sh. 1	
Table 4.2-1 Sh. 2	
Table 4.2-1 Sh. 3	
Figure 4.2-8a	
Figure 4.2-10B	
Figure 4.2-11B	
Section 4.3: References	
Section 4.3A	
Section 4.3A.1	
Section 4.3A.2.1.1	
Section 4.3A.2.1.2	
Section 4.3A.2.3	
Section 4.3A.2.4	
Section 4.3A.2.5	
Section 4.3A.3.1.1	
Section 4.3A.3.1.2	
Section 4.3A.3.1.3	
Section 4.3A.3.3.1	
Section 4.3A.3.3.2	
Section 4.3A.3.3.3	
Section 4.3A.4.1	
Section 4.3A.4.2	
Table 4.3A-1	
Table 4.3A-2	
Table 4.3A-3	

Section	Cross References
Revision 302 Cont'd	
Table 4.3A-4	
Table 4.3A-5	
Figure 4.3A-1	
Figure 4.3A-2	
Figure 4.3A-3a	
Figure 4.3A-3b	
Figure 4.3A-8	
Figure 4.3A-9	
Figure 4.3A-10	
Figure 4.3A-18b	
Figure 4.3A-19b	
Section 4.4.1.1	
Section 4.4.2.1	
Section 4.4.2.2.1	
Section 4.4.2.2.2	
Section 4.4.2.9.4	
Section 4.4.4.1	
Section 4.4: References	
Revision 304	
Section 4.5.2.1	EC-10453
Section 4.2.2.2	EC-13881
Section 4.3.2.2.2	
Section 4.3A	
Table 4.3A-1	
Table 4.3A-2	
Table 4.3A-3	
Table 4.3A-4	
Table 4.3A-5	
Figure 4.3A-1	
Figure 4.3A-2	
Figure 4.3A-3a	
Figure 4.3A-3b	
Figure 4.3A-8	
Figure 4.3A-9	
Figure 4.3A-10	
Figure 4.3A-19b	
Section 4.4.2.1	
Section 4.4.2.2.1	
Section 4.4.2.2.2	
Section 4.4.2.2.2.2	
Section 4.4.2.4	
Section 4.4.2.6.3	
Section 4.4.2.8	

Section	Cross References
Revision 304 Cont'd	
Section 4.4.2.9.4 Section 4.4.4.1 Section 4.4.4.2.3 Section 4.4.4.5.2 Section 4.4: References	EC-13881 (Continued)
Figure 4.3A-5	EC-18688
Revision 305	
Table 4.4-6 Sheet 2 of 3	EC-14765
Section 4.4.6.1	EC-26965
Revision 307	
Section 4.1 Table 4.1-1 Sh. 1 of 3	EC-1020
Section 4.1 Table 4.1-1 Sh. 1 of 3 Table 4.3-1 Sh. 1 of 2 Section 4.5.1.1 Section 4.5.1.3 Section 4.5.1.3.2 Section 4.5.1.3.3 Section 4.5.1.4 Section 4.5.2.4.2.2 Section 4.5.2.4.2.4 Section 4.5.2.4.3 Figure 4.6-1	EC-2800
Table of Contents Section 4.2.1.1.7 Section 4.2.2.1 Section 4.3A Table 4.3A-1 Table 4.3A-2 Table 4.3A-3 Table 4.3A-4 Table 4.3A-5 Section 4.4.1.1 Section 4.4.2.2.1 Section 4.4.2.2.2 Section 4.4.2.9.4 Section 4.4.4.1	EC-30663

Section	Cross References
Revision 307 (Continued)	
Figure 4.3A-1	EC-30663 (Continued)
Figure 4.3A-2	
Figure 4.3A-3a	
Figure 4.3A-3b	
Figure 4.3A-8	
Figure 4.3A-9	
Figure 4.3A-10	
Revision 308	
Table of Contents	LBDCR 14-008
Section 4.3A	
Section 4.3A.1	
Section 4.3A.2	
Section 4.3A.2.3	
Section 4.3A.2.4	
Section 4.3A.2.5	
Section 4.3A3.1.1	
Section 4.3A.3.1.2	
Section 4.3A.3.1.3	
Section 4.3A.6	
Table 4.3A-1	
Table 4.3A-2	
Table 4.3A-3	
Table 4.3A-4	
Table 4.3A-5	
Figure 4.3A-1	
Figure 4.3A-2	
Figure 4.3A-3a	
Figure 4.3A-3b	
Figure 4.3A-8	
Figure 4.3A-9	
Figure 4.3A-10	
Revision 309	
	LBDCR 13-014
Section 4.2.1.2.5.3	
Section 4.3.2	
Section 4.3.2.4	
Section 4.3.2.4.4.3	
Section 4.4.5	
Section 4.4.6	
Table of Contents	LBDCR 15-035
4-i	
4-iv	

Section	Cross-References
Revision 309 (con't)	
4-ix TOC	LBDCR 15-035 (con't)
Section 4.2.1.2.2.1	
Section 4.2.2.1	
Section 4.2.2.2	
Section 4.2.3.2.3	
Section 4.2.3.2.12	
Reference 4.2	
Section 4.3A	
Section 4.3A.2.2	
Section 4.3A.3.1.1	
Section 4.3A.3.1.3	
Table 4.3A-1	
Table 4.3A-2	
Table 4.3A-3	
Table 4.3A-4	
Table 4.3A-5	
Figure 4.3A-1	
Figure 4.3A-2	
Figure 4.3A-3a	
Figure 4.3A-3b	
Figure 4.3A-8	
Figure 4.3A-9	
Figure 4.3A-10	
Section 4.2.4.4	LBDCR 15-039
Section 4.2.1.1.2	LBDCR 15-025
Section 4.2.1.1.6	
Section 4.2.2.1	
Section 4.2.2.3	
Section 4.2.2.3	
Section 4.2.4.1.1	
Revision 310	
TOC Chapter 4	LBDCR 17-015
Table 4.1-1 Sh 3 of 3	LBDCR 17-020
Section 4.2.4.4	LBDCR 16-063
Section 4.3.2.8	LBDCR 16-060/17-020
Section 4.3.3.3	LBDCR 16-060/17-020
Section 4.3 Reference	LBDCR 17-020
Section 4.3A	LBDCR 17-015
Section 4.3A1	
Section 4.3A.2.1.1	
Section 4.3A.2.3	
Section 4.3A.2.4	
Section 4.3A.2.5	
Section 4.3A.3.1.1	
Section 4.3A.3.1.2	
Section 4.3A.3.1.3	
Table 4.3A-1	

Section	Cross References
Revision 310 (Con't)	
Table 4.3A-2	
Table 4.3A-3	
Table 4.3A-4	
Table 4.3A-5	
Figure 4.3A-1	
Figure 4.3A-2	
Figure 4.3A-3a	
Figure 4.3A-3b	
Figure 4.3A-8	
Figure 4.3A-9	
Figure 4.3A-10	
Section 4.6.*5*	LBDCR 16-012

4.0 REACTOR

4.1 SUMMARY DESCRIPTION

→(DRN 01-1103, R12; 02-1477, R12; EC-9533, R302)
The reactor is of the pressurized water (PWR) type using two reactor coolant loops. A vertical cross-section of the reactor is shown in Figure 4.1-1. The reactor core is composed of 217 fuel assemblies and 87 control element assemblies, which provides for 236 fuel rod positions, consists of five guide tubes welded or bulged to spacer grids, and is closed at the top and bottom by end fittings. The guide tubes each displace four fuel rod positions and provide channels that guide the CEAs over their entire length of travel. In selected fuel assemblies, the central guide tube houses incore instrumentation.
←(DRN 01-1103, R12; 02-1477, R12)

The fuel is low enriched UO_2, in the form of ceramic pellets and is encapsulated in pre-pressurized Zircaloy, ZIRLO™, or Optimized ZIRLO™ tubes that form a hermetic enclosure.
←(EC-9533, R302)

The reactor coolant enters the upper section of the reactor vessel, flows downward between the reactor vessel wall and the core barrel, passes through the flow skirt where the flow distribution is equalized, and into the lower plenum. The coolant then flows upward through the core, removing heat from the fuel rods, exits from the reactor vessel and passes through the tube side of the vertical U-tube steam generators where heat is transferred to the secondary system. The reactor coolant pumps return the coolant to the reactor vessel.

→(EC-9533, R302)
Figure 4.1-2 shows the reactor core cross section and certain dimensional relationships between fuel assemblies, fuel rods, and CEA guide tubes.

→(EC-1020, R307)
The original reactor vessel closure head (ORVCH) was replaced. The replacement reactor vessel closure head (RRVCH) is identical in design to the ORVCH in all its major dimensions and functions. The main differences are the elimination of four unused control element drive mechanism (CEDM) penetrations and the replacement of Alloy 600 nozzle material (Ni-Cr-Fe) with a material that is less susceptible to primary water stress corrosion cracking (PWSCC). The use of stainless steel or Alloy 690 in place of Alloy 600 reduces the likelihood of PWSCC. The head nozzles are Alloy 690 construction, and the ICI Quickloc II flange adaptor is stainless steel.
←(EC-1020, R307)

The reactor internals support and orient the fuel assemblies, control element assemblies, and in-core instrumentation, and guide the reactor coolant through the reactor vessel. The reactor internals also absorb static and dynamic loads and transmit the loads to the reactor vessel flange. They will safely perform their functions during normal operating, upset, emergency, and faulted conditions. The internals are designed to safely withstand forces due to dead weight, handling, temperature and pressure differentials, flow impingement, vibration, and seismic acceleration. All reactor components are considered Category I for seismic design. The design of the reactor internals limits deflection where required by function. The stress values of all structural members under normal operating and expected transient conditions are not greater than those established by Section III, Subsection NG, of the ASME Pressure Vessel Code. The effect of neutron irradiation on the materials concerned is included in the design evaluation. The effect of accident loads on the internals is included in the design analysis.
←(EC-9533, R302)

Reactivity control is provided by two independent systems - the control element drive system and the Chemical and Volume Control System (CVCS).

The control element drive system controls short term reactivity changes and is used for rapid shutdown. The CVCS compensates for long term reactivity changes and can make the reactor sub critical without the benefit of the control element drive system. Design of the core and the Reactor Protect System prevents fuel design limits from being exceeded for any single malfunction in either of the reactivity control systems.

➔(DRN 01-1103, R12; 02-1477, R12)
The standard control element assemblies consist of five poison rods assembled in a square array, with one rod in the center. The rods are connected to a spider structure that couples to the control element drive mechanism (CEDM) shafting.

The Waterford 3 core originally contained 91 CEAs, of which 83 were full length and eight contained only a part length poison column. Of the 83 full length CEAs, 79 were standard five element design and 4 were four element CEAs (did not have a center poison rod). The four element CEAs each spanned two fuel assemblies at the core periphery's major axes.

At the end of Cycle 11, the 4 four element CEAs were removed from the core internals and the 8 part length CEAs were replaced with standard five element design CEAs.

Commencing with Cycle 12, the Waterford 3 core will have a total of 87 CEAs, all of the standard five element design.
←(DRN 02-1477, R12)

➔(EC-2800, R307)
The CEAs are positioned by magnetic jack control element drive mechanisms mounted on the reactor vessel head. Beginning with Cycle 19, a replacement reactor vessel closure head will be installed equipped with 87 CEDM nozzles and 87 replacement CEDMs. The replacement CEDMS are of similar construction as compared to the original CEDMs. The replacement CEDMs have fewer welded/assembled parts (3 versus 4) and incorporate other design improvements such as the use of improved electrical wiring and pressure boundary materials that are more resistant to stress corrosion cracking.
←(DRN 01-1103, R12; EC-2800, R307)

The maximum reactivity worth of the CEAs and the associated reactivity addition rate are limited by system design to prevent sudden large reactivity increases. The design restraints are such that reactivity increases do not result in violation of the fueled limits, rupture of the reactor coolant pressure boundary, or disruption of the core or other internals sufficient to impair the effectiveness of emergency cooling.
➔(EC-9533, R302)
Boric acid dissolved in the coolant is used as a neutron absorber to provide long term reactivity control. In order to reduce the boric acid concentration required at beginning-of-operating conditions, and thus the moderator temperature coefficient, burnable poison rods are provided in certain fuel assemblies. The poison is boron carbide dispersed in aluminum pellets; the pellets are clad in Zircaloy, ZIRLO^{TM}, or Optimized ZIRLO^{TM} to form rods that are similar to the fuel rods.
←(EC-9533, R302)
A three batch fuel management scheme is employed, where 40-50 percent of the core assemblies are replaced at each refueling. The batch average burnup will be about 45,000 MWD/MTU over the three cycle life of the fuel. Sufficient margin is provided to ensure that peak burnups are within acceptable limits.

➔(EC-9533, R302)
The nuclear design of the core ensures that the combined response of all reactivity coefficients in the power operating range to an increase in reactor thermal power yields a net decrease in reactivity.
←(EC-9533, R302)
Control element assemblies are moved in groups to satisfy the requirements of shutdown, power level changes, and operational maneuvering. The control system is designed to produce power distributions that are within the acceptable limits of overall nuclear heat flux factor (F_Q) and departure from nucleate boiling ratio (DNBR). The Reactor Protection System and administrative controls ensure that these limits are not exceeded.

➔(DRN 01-1103, R12)
Axial xenon oscillations, should they occur, can be manually controlled by CEAs, using information provided by the nuclear instrumentation.
←(DRN 01-1103, R12)
The core originally contained two plutonium 238-beryllium neutron sources for initial and subsequent start-ups. The neutron sources were removed prior to cycle 7 startup. However, the core design has startup and operational capability without the sources.

→
Design of the reactor internals is discussed in Subsections 3.9.5 and 4.5.2; fuel assembly design is discussed in Section 4.2; nuclear design of the core is discussed in Section 4.3; and the thermal and hydraulic design is discussed in Section 4.4. Summary lists of significant core parameters are presented in Tables 4.2-1, 4.3-1, and 4.4-1. A tabulation of the analysis techniques, load conditions, and computer codes utilized in the analyses of various reactor internal components is presented in Table 4.1-1. Appendix 4.3A provides an update of the information above with respect to the current fuel cycle.
←

SECTION 4.1: REFERENCES

1. Ghosh, S. and Wilson E., "Dynamic Stress Analysis of Axisymmetric Structures under Arbitrary Loading," Dept. No. EERC 69-10, University of California, Berkeley, September 1969.

2. Gabrielson, V. K., "SHOCK - A Computer Code for Solving Lumped-Mass Dynamic Systems, "SCL-DR-65-34, January 1966.

3. MRI/STARDYNE - Static and Dynamic Structural Analysis Systems; "User Information Manual," Control Data Corporation, June 1, 1970.

4. MRI/STARDYNE User Manual, Computer Methods Department, Mechanics Research, Inc., Los Angeles, California, January 1, 1970.

5. Tillerson, J. R. and Haisler, W. E., "SAMMSOR II - A Finite Element Program to Determine Stiffness and Mass Matrices of Shells-of-Revolution," TEES-RPT-70-18, Texas A&M 'University, October 1970. "DYNASOR II - A Finite Element Program for the Dynamic Non-Linear Analysis of Shells-of-Revolution," TEES-RPT-70-19, Texas A&M University, October 1970.

6. Nieh, L. C., "SAAS - Finite Element Stress Analysis of Axisymmetric Solids with Orthotropic Temperature Dependent Material Properties, AVCO Digital Computer Program 2663 User's Manual," AVCO Missiles, Space and Electronics Group, Missile Systems Division, April 1968.

7. Dunham, R. S., et al., "NAOS - Finite Element Analysis of Axisymmetric Solids with Arbitrary Loadings," Structural Engineering Laboratory, University of California, Berkeley, California, June 1967.

8. ICES STRUDL II, "The Structural Design Language: Engineering User's Manual, Volume I," Structures Division and Civil Engineering Systems Laboratory, Department of Civil Engineering, MIT, Second Edition, June 1970.

9. De Salvo, G. J. and Swanson, J.A., ANSYS - Engineering Analysis System User's Manual, Swanson Analysis Systems, Inc., March 8, 1975.

10. McCormack, T. R., "Heat Transfer by Relaxation," Computer Program No. WIN 12100, Combustion Engineering, Windsor, Connecticut, 1968.

section 4.1: REFERENCES (Cont'd)

11. SHELL, "Analysis of Thin Shells of Revolution," General Electric Mark II Time-Sharing Service User's Guide No. 91036.9.

12. Rowe, D. S., "COBRA-III, A Digital Computer Program to Steady State and Transient Thermal-Hydraulic Analysis of Rod Bundle Nuclear Fuel Elements," BNWL-B-82, 1971.

→(EC-9533, R302)

13. Rowe D.S., "COBRA-IIIC: A Digital Computer Program for Steady State and Transient Thermal-Hydraulic Analysis of Rod Bundle Nuclear Fuel Elements," BNWL-1695, March 1973.

←(EC-9533, R302)

14. CENPD-161 P, (Proprietary) TORC CODE - A Computer Code for Determining the Thermal Margin of a Reactor Core, July 1975. CENPD-161 (Non-Proprietary), July 1975.

15. See subsection 4.3.3, Analytical Methods.

16. "C-E Fuel Evaluation Model Topical Report," CENPD-139 (Proprietary), CENPD-139 Rev. 01 (Non-Proprietary), CENPD - 139 Supplement 1, Rev. 01 (Non-Proprietary), July 1974.

TABLE 4.1-1 (Sheet 1 of 3) Revision 307 (07/13)

ANALYSIS TECHNIQUES

Internal Components	Description	Analysis Technique	Computer Code
Core Support Barrel	Axial and Lateral Loads	Shell Analysis Beam Analysis	ASHSD[1] SHOCK[2] STARDYNE[3,4]
	Dynamic Buckling	Shell Analysis	SAMMSOR[5] - DYNASOR
Upper and Lower Core Support Barrel Flanges	Lateral Loads Axial Loads & Bending Moments	Finite Element Analysis	SAAS[6] NAOS[7]
Lower Support Structure Beams	Lateral Loads	Plane Grid Structure Analysis Simply Supported Beams	STRUDL II[8]
Columns	Axial Loads Bending Loads	Column Analysis	SHOCK[2] STARDYNE[3,4]
Upper Guide Structure	Lateral Loads	Beam Analysis	SHOCK[2]
CEAs	Axial Loads	Column Analysis	STARDYNE[3,4]
Beam Structure	Uniform Lateral Loading	Plane Grid Structure	STRUDL II[8]
Support Plate Flange	Axial Loads	Finite Element Analysis	SAAS[6]
	Bending Moments	NAOS(7)	
Core Shroud	Thermal & Pressure Loading	Finite Element Analysis	ANSYS[9]
CEDM →(EC-2800, R307)	Pressure, Fatigue and Thermal Loads	Finite Element Analysis	SAAS[6]
←(EC-2800, R307)	Seismic Loading	Framed Structure	ANSYS[9]
→(EC-1020, R307) CEDM and R.V. Nozzles ←(EC-1020, R307)	Thermal Loading	Relaxation Analysis	ANSYS[9]
→(EC-2800, R307) CEDM Omega Seals ←(EC-2800, R307)	Pressure, Thermal Rotational and Displacement Loadings	Finite Element Analysis	ANSYS[9]

TABLE 4.1-1 (Sheet 2 of 3)

ANALYSIS TECHNIQUES

Internal Components	Description	Analysis Technique	Computer Code
Fuel Assembly	Seismic	Lumped Mass-Spring-Damper	SHOCK[2]
	Lateral Vertical	(Direct numerical Integration, Non-Linear/Linear Capability)	
	Loss-of-Coolant Accident Lateral Vertical	(Springs From Beam Stiffness Coefficients)	
Fuel Rod	Thermal-Mechanical	Generalized plane strain analysis including thermal, mechanical and creep effects solved by finite difference techniques	FATES[16]
Fuel Assembly	DNB Calculation	Open core	TORC[12,13,14]
Fuel Assembly, Structure, Reflector	Few-group cross-section generation for diffusion codes		CEPAK[15]
CEA Control Rod Fingers	Effective diffusion theory constants for diffusion codes	Match extrapolation lengths on outer surface to those based on tabulated capture probabilities	CERES[15]
Burnable Poison Rod	Effective diffusion theory constants for diffusion codes	Sequences of HAMMER, DTF-IV and M0807 based on relative reaction rates	HADTMO[15]
Fuel Assemblies and Reactor Core	Static and depletion dependent reactivities, flux, nuclides, power distributions in one, two, and three dimensions	Diffusion-depletion using PDQ-7 and HARMONY programs but with modifications to allow various feedback options	PDQX[15]

ANALYSIS TECHNIQUES

→(LBDCR 17-020, R310)

Internal Components	Description	Analysis Technique	Computer Code
Reactor Core	Static and time dependent one dimensional (axial) studies, with control rod motion	Diffusion code using up to 140 distinct regions with variable mesh intervals. Feed-back, Eigenvalue searches and power shaping searches	QUIX[15]
Reactor Vessel and Vessel Internals	Fast neutron flux and fluence	Combination of discrete ordinate transport and point kernel codes using core power distributions from PDQ-X	ANISN-SHADRAC[15]*
Reactor Core	Xenon stability analysis	Linear modal analysis employing the funda-mental and first harmonic modes	HILLAMA[15]

*ANISN-SHADRAC was used for initial vessel radiation calculations. The most recent radiation calculations were performed when surveillance capsule W-263 was analyzed using the DORT[15] code

←LBDCR 17-020, R310)

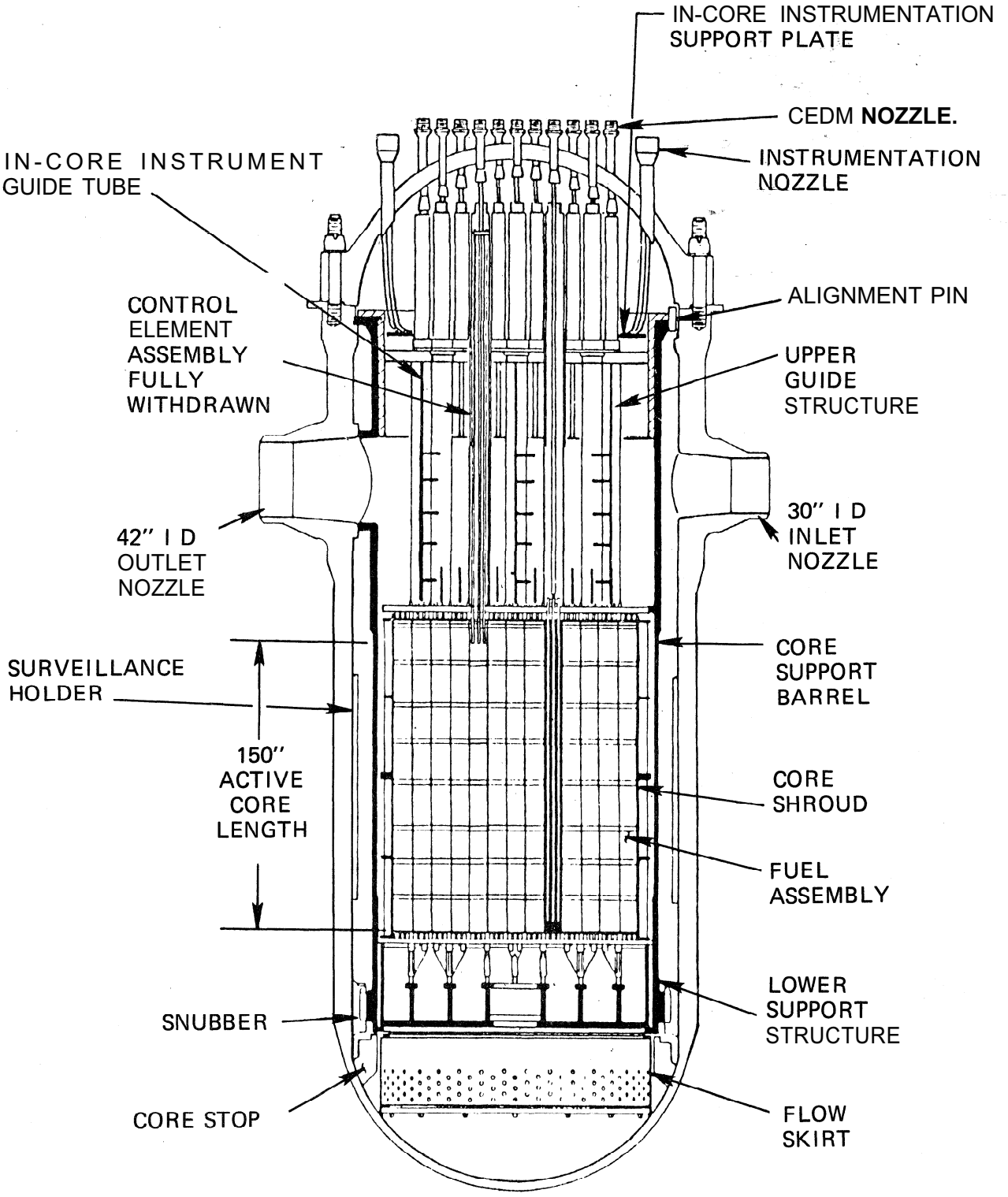

LOUISIANA **POWER & LIGHT CO.** **Waterford Steam Electric Station**	REACTOR VERTICAL ARRANGEMENT	**Figure** 4.1–1

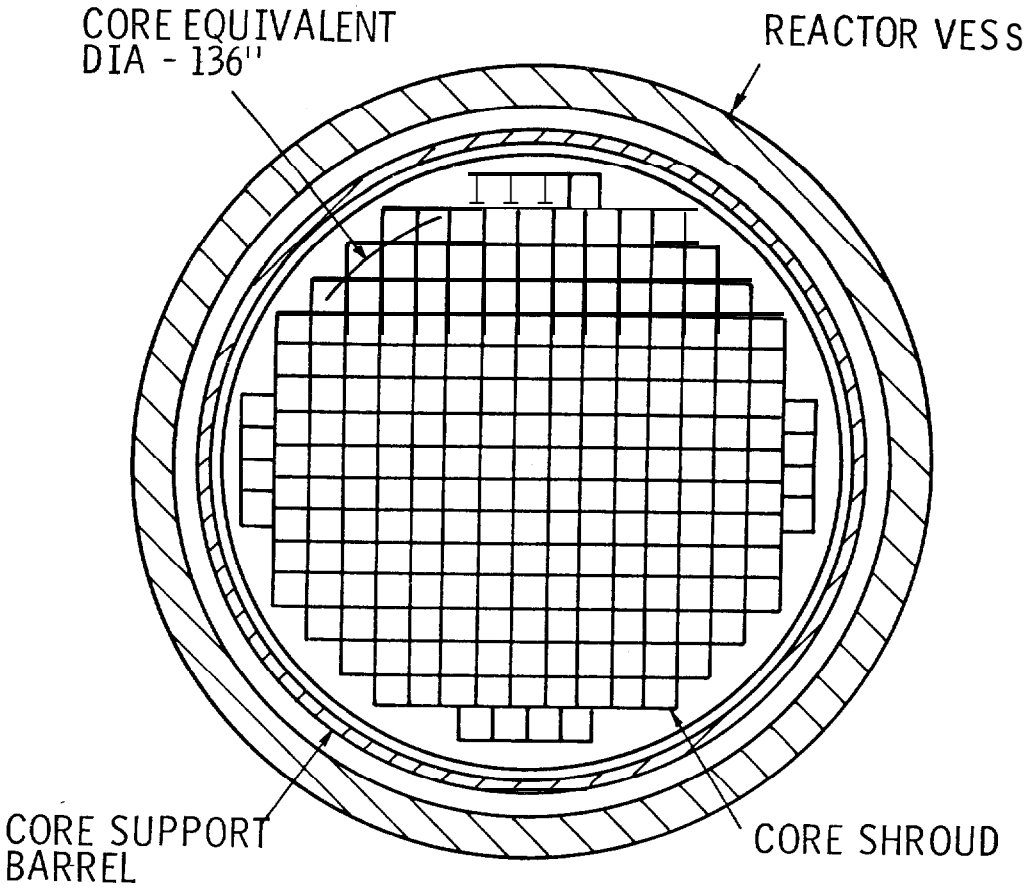

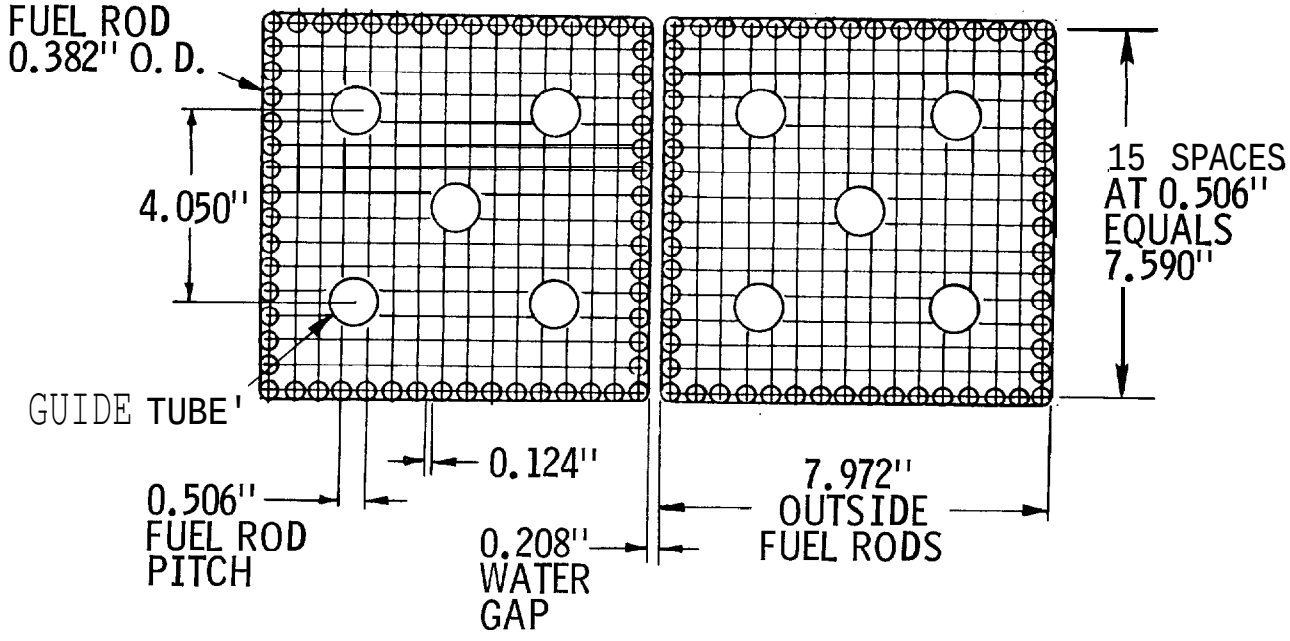

LOUISIANA
POWER & LIGHT CO.
Waterford Steam
Electric Station I

REACTOR CORE CROSS-SECTION

Figure
4.1-2

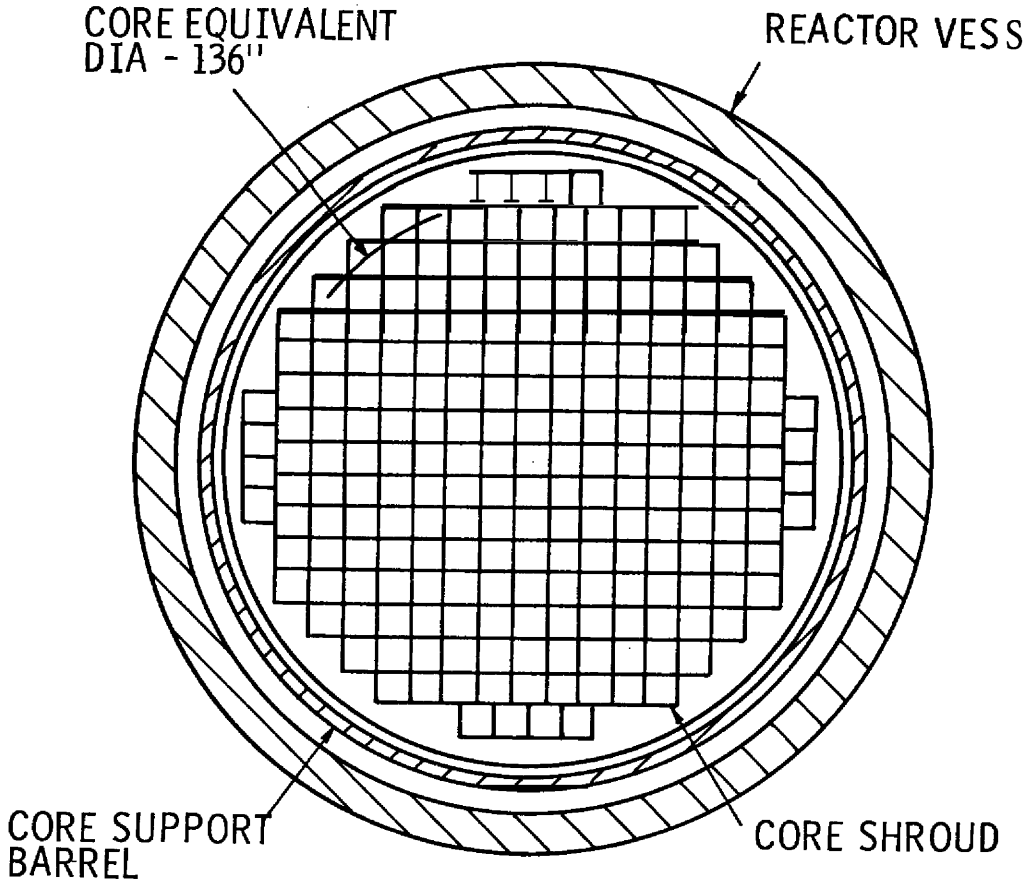

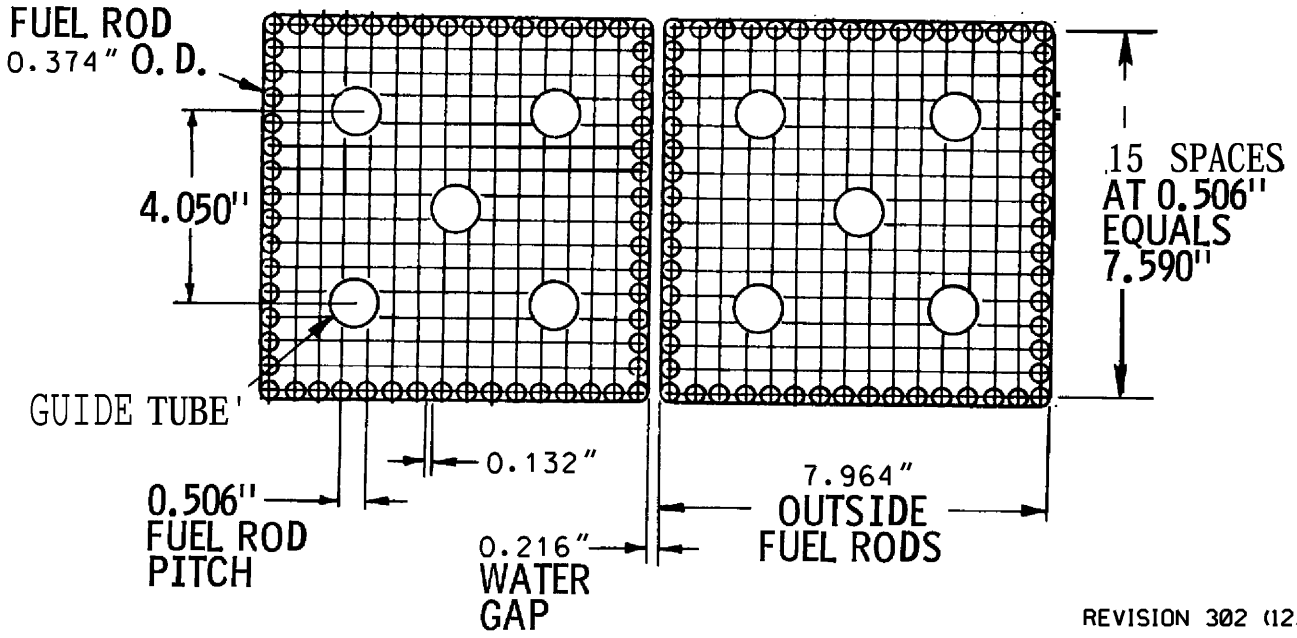

REVISION 302 (12/08)

LOUISIANA POWER & LIGHT CO. Waterford Steam Electric Station	REACTOR CORE CROSS-SECTION (NGF)	Figure 4.1-2a

4.2 FUEL SYSTEM DESIGN

4.2.1 DESIGN BASES

The bases for fuel system design are discussed in the following subsections. Additional information for the current fuel cycle is discussed in Appendix 4.3A.

4.2.1.1 Fuel Assembly

The fuel assemblies are required to meet design criteria for each design condition listed below to assure that the functional requirements are met. Except where specifically noted, the design bases presented in this section are consistent with those used for previous designs.

a) Condition I: Non-operation and Normal Operation

Condition I situations are those which are planned or expected to occur in the course of handling, initial shipping, storage, reactor servicing and power operation (including maneuvering of the plant). Condition I situations must be accommodated without fuel assembly failure and without any effect which would lead to a restriction on subsequent operation of the fuel assembly. The guidelines stated below are used to determine loads during Condition I situations:

1) Handling and Fresh Fuel Shipping

Loads correspond to the maximum possible axial and lateral loads and accelerations imposed on the fuel assembly by shipping and handling equipment during these periods, assuming that there are no abnormal contact between the fuel assembly and any surface, nor any equipment malfunction. Irradiation effects on material properties are considered when analyzing the effects of handling loads which occur during refueling. Additional information regarding shipping and handling loads is contained in Subsection 4.2.3.1.5.

2) Storage

Loads on both new and irradiated fuel assemblies reflect storage conditions of temperature, chemistry, means of support, and duration of storage.

3) Reactor Servicing

Loads on the fuel assembly reflect those encountered during refueling and reconstitution.

4) Power Operation

Loads are derived from conditions encountered during transient and steady-state operation in the design power range. (Hot operational testing, system startup, hot standby, operator controlled transients within specified rate limits and system shutdown are included in this category.)

5) Reactor Trip

Loads correspond to those produced in the fuel assembly by control element assembly (CEA) motion and deceleration.

b) Condition II: Upset Condition

Condition II situations are unplanned events which may occur with moderate frequency during the life of the plant. The fuel assembly design should have the capability to withstand any upset condition with margin to mechanical failure and with no permanent effects which would prevent continued normal operation. Incidents classified as upset conditions are listed below:

1) Operating basis earthquake (OBE)

2) Uncontrolled CEA withdrawal

3) Uncontrolled boron dilution

4) Partial loss-of-coolant flow

5) Idle loop startup (in violation of established operating procedures)

6) Loss of load (reactor-turbine load mismatch)

7) Loss of normal feedwater

8) Loss of offsite power

9) Excessive heat removal (feedwater system malfunction)

10) CEA drop

11) Accidental depressurization of the Reactor Coolant System (RCS)

c) Condition III: Emergency Conditions

Condition III events are unplanned incidents which might occur very infrequently during plant life. Fuel rod mechanical failure must be prevented for any Condition III event in any area not subject to extreme local conditions (e.g., in any fuel rod not immediately adjacent to the impact surface during fuel handling accident).

The Condition III incidents listed below are included as a category to provide assurance that under the occurrence of a Condition III event, rod damage is minimal.

1) Complete loss or interruption of primary coolant flow at 100% power, excluding reactor coolant pump locked rotor

2) Steam bypass malfunction

3) Minor fuel handling accident (fuel assembly and grapple remain connected)

4) Inadvertent loading of fuel assembly into improper position

d) Condition IV: Faulted Conditions

Condition IV incidents are postulated events whose consequences are such that the integrity and operability of the nuclear energy system may be impaired. Mechanical fuel failures are permitted, but they must not impair the operation of the Engineered Safety Features (ESF) systems to mitigate the consequences of the postulated event. Condition IV incidents are listed below:

1) Safe shutdown earthquake (SSE)

2) Loss-of-coolant accident (LOCA)

3) Locked coolant pump rotor

4) Major secondary system pipe rupture

5) CEA ejection

6) Major fuel handling accident (fuel assembly and grapple are disengaged)

→(DRN 03-2058, R14)

See Sections 3.6.2.1.1.1(d) and 3.6.3 for discussions on pipe break criteria and leak-before-break.

←(DRN 03-2058, R14)

4.2.1.1.1 Fuel Assembly Structural Integrity Criteria

For each of the design conditions, there are criteria which apply to the fuel assembly and components with the exception of fuel rods. These criteria are listed below and give the allowable stresses and functional requirements for each design condition.

a) Design Conditions I and II

$$P_m \leq S_m$$

$$P_m + P_b \leq F_s S_m$$

Under cyclic loading conditions, stresses must be such that the cumulative fatigue damage factor does not exceed 0.8. Cumulative damage factor is defined as the sum of the ratios of the number of cycles at a given cyclic stress (or strain) condition to the maximum number permitted for that condition. The selected limit of 0.8 is used in place of 1.0 (which would correspond to the absolute maximum damage factor permitted) to provide additional margin in the design.

Deflections must be such that the allowable trip time of the control element assemblies is not exceeded.

b) Design Condition III

$P_m \leq 1.5\ S_m$

$P_m + P_b \leq 1.5\ F_S S_m$

Deflections are limited to a value allowing the CEAS to trip, but not necessarily within the prescribed time.

c) Design Condition IV

$P_m \leq S'_m$

$P_m + P_b \leq F_S\ S'_m$

where S'_m = smaller value of 2.4 S_m or 0.7 S_u.

1) If the equivalent diameter pipe break in the LOCA does not exceed the largest line connected to the main reactor coolant lines, the fuel assembly deformation shall be limited to a value not exceeding the deformation which would preclude satisfactory insertion of the CEAS.

2) For pipe breaks larger in equivalent diameter than the largest lines connected to the main reactor coolant lines, deformation of structural components is limited to maintain the fuel in a coolable array. CEA insertion is not required for these events as the appropriate safety analyses do not take credit for CEA insertion.

d) Nomenclature

The symbols used in defining the allowable stress levels are as follows:

P_m = Calculated general primary membrane stress (a)

P_b = Calculated primary bending stress

S_m = Design stress intensity value as defined by Section III, ASME Boiler and Pressure Vessel Code (b)

S_u = Minimum unirradiated ultimate tensile strength

→ (DRN 00-644)

F_s = Shape factor corresponding to the particular cross section being analyzed(c)

← (DRN 00-644)

S'_m = Design stress intensity value for faulted conditions

The definitions of S' as the lesser value of 2.4 S_m and 0.7 S_u is contained in the ASME Boiler and Pressure Vessel Code (19/4) Section III, Appendix F-1323.1.

(a) P_m and P_b are defined by Article NB-3000, Section III, ASME Boiler and Pressure Vessel Code, 1971.

(b) With the exception of zirconium base alloys, the design stress intensity values, S_m, of materials not tabulated by the Code are determined in the same manner as the Code. The design stress intensity of zirconium base alloys shall not exceed two-thirds of the unirradiated minimum yield strength at temperature. Basing the design stress intensity on the unirradiated yield strength is conservative because the yield strength of zircaloy increases with irradiation. The use of the two-thirds factor ensures 50% to component yielding in response to primary stresses. This 50% margin together with its application to the minimum unirradiated properties and the general conservatism applied in the establishment of design conditions is sufficient to ensure an adequate design.

(c) The shape factor, F_s, is defined as the ratio of the "plastic" moment (all fibers just at the yield stress) to the initial yield amount (extreme fiber at the yield stress and all other fibers stressed in proportion to their distance from the neutral axis). The capability of cross sections loaded in bending to sustain moments considerably in excess of that required to yield the outermost fibers is discussed in Timoshenko.(1)

4.2.1.1.2 Material Selection

→(DRN 02-1538, R12)

The fuel assembly grid cage structure consists of 10 Zircaloy-4 spacer grids, 1 Inconel 625 spacer grid (at the lower end), 5 Zircaloy-4 CEA guide tubes, 2 stainless steel end fittings, and 5 Inconel X-750 coil springs. Beginning with Batch U, some grid cages will have 9 Zircaloy-4 grids and 2 Inconel 625 grids (at the upper and lower ends) Zircaloy-4, selected for fuel rod cladding, guide tubes and spacer grids, has a low neutron absorption cross section, high corrosion resistance to reactor water environment and there is little reaction between the cladding and fuel or fission products. As described in Subsection 4.2.3, Zircaloy-4 has demonstrated its ability as a cladding, CEA guide tube, and spacer grid material.

→(DRN 06-1059, R15)

Beginning with the Region Y fuel assemblies in Cycle 15, ZIRLO™ is introduced as a fuel rod cladding material to provide added corrosion resistance and fuel reliability. ZIRLO™ is a zirconium-based alloy that improves fuel assembly corrosion resistance and dimensional stability under irradiation.

←(DRN 06-1059, R15)

The bottom spacer grid is of Inconel 625 and is welded to the lower end fitting. For the assembly designs with the Inconel 625 top grids, the grid is retained by 10 Zircaloy-4 sleeves that are welded to the Zircaloy-4 guide tubes. In these regions of higher turbulence, Inconel 625 was selected rather than Zircaloy-4 to provide additional strength and relaxation resistance. Inconel 625 is a very strong material with good ductility, corrosion resistance and stability under irradiation at temperatures below 1000°F.

←(DRN 02-1538, R12)

→(DRN 02-1538, R12, LBDCR 15-025, R309)
The fuel assembly lower end fitting is of cast stainless steel (Grade CF-3) and the upper end fitting assembly consists of two cast stainless steel plates and five Type 304 stainless steel machined alignment posts. This material was selected based on considerations of adequate strength and high-corrosion resistance. Also, Type 304 stainless steel has been used successfully in almost all pressurized water reactor environments, including all currently operating C-E reactors.
←(DRN 02-1538, R12, LBDCR 15-025, R309)
→(EC-9533, R302; LBDCR 13-014, R309)
With the introduction of the Next Generation Fuel (NGF) design in Region Z (Cycle 16), the fuel assembly grid cage structure consists of 13 spacer grids (an Inconel-718 top grid, six vaned Optimized ZIRLO™ mid grids, three unvaned Optimized ZIRLO™ mid grids, two vaned Optimized ZIRLO™ Intermediate Flow Mixing grids (IFMs), and one Inconel-625 bottom grid), five Stress-Relief Annealed (SRA) ZIRLO™ CEA guide tubes, two stainless steel end fittings, and five Inconel X-750 coil springs. Instead of welds, the NGF grid cage structure utilizes bulges to secure the spacer grids to the CEA guide tubes. Similarly, the CEA guide tube flange-to-tube connection is bulged for NGF instead of welded.
←(LBDCR 13-014, R309)
The use of Optimized ZIRLO for the mid grid and IFMs improves the corrosion resistance dimensional stability of the grids, thereby reducing grid growth and improving fretting resistance. Similarly, the use of ZIRLO for the CEA guide tubes improves the corrosion resistance and dimensional stability of the guide tubes.
→(LBDCR 13-014, R309)
The use of Inconel-718 for the top grid maintains the ductility, strength, and stability benefits of the prior Inconel-625 top grid while utilizing a design that is compatible with the NGF rod diameter and basically the same as used in Westinghouse reactors for many years with excellent performance results.
←(LBDCR 13-014, R309)
The NGF fuel rod design utilizes Optimized ZIRLO™ for the cladding and includes several geometric changes (see Section 4.2.2.2 for description of the NGF fuel rod geometry). The use of Optimized ZIRLO™ improves the corrosion resistance of the cladding.
←(EC-9533, R302)

4.2.1.1.3 Control Element Assembly Guide Tubes

All CEA guide tubes are manufactured in accordance with Grade RA-2, ASTM B353, Wrought Zirconium and Zirconium Alloy Seamless and Welded Tubes for Nuclear Service, with the following exceptions and/or additions:

a) Chemical Properties
→(EC-9533, R302)

Chemical analyses are performed for the alloying elements. For Zircaloy-4 guide tubes, the analyses check for tin, iron, chromium, oxygen, and zirconium. For ZIRLO™ guide tubes, the analyses check for tin, iron, niobium, oxygen, and zirconium.

←(EC-9533, R302)
b) Mechanical Properties
→(EC-9533, R302)

The guide tubes are fabricated from Zircaloy-4 or, starting with NGF, ZIRLO™ in the stress-relief annealed (SRA) condition and are tested for yield strength, ultimate strength, and elongation at room temperature and elevated temperature conditions.

←(EC-9533. R302)
c) Dimensional Requirements

Dimension	Permissible Tolerance (in.)
OD	± 0.003
ID	± 0.005 (thru Batch y) ± 0.002 (Batch Z and beyond)

→(EC-9533, R302)
←(EC-9533, R302)

4.2.1.1.4 Zircaloy-4 Bar Stock

→(DRN 00-644)

All Zircaloy-4 bar stock is fabricated in accordance with Grade RA-2, ASTM B351, Hot-Rolled and Cold-Finished Zirconium and Zirconium Alloy Bars, Rod and Wire for Nuclear Application, with the following exceptions or additions:

←(DRN 00-644)

a) Chemical Properties

Additional limits are placed on oxygen and silicon content.

b) Metallurgical Properties

1) Grain Size

The maximum average grain size is restricted.

→(EC-9533, R302)

4.2.1.1.5 Zirconium-Based Alloy Strip Stock

←(EC-9533, R302)

→(DRN 00-644)

All Zircaloy-4 strip stock is fabricated in accordance with Grade RA-2, ASTM B352, Zirconium Alloy Sheet, Strip and Plate for Nuclear Application, with the following exceptions or additions:

←(DRN 00-644)

a) Chemical Properties

→(EC-9533, R302)

Chemical analyses are performed for the alloying elements. For Zircaloy-4 strip stock, the analyses check for tin, iron, chromium, oxygen, and zirconium. For Optimized ZIRLO™ strip stock, the analyses check for tin, iron, niobium, oxygen, and zirconium.

←(EC-9533, R302)

b) Metallurgical Properties

(1) Grain Size

The maximum average grain size is restricted.

c) Mechanical Properties

1) Bend

→(DRN 06-895, R15)

Spacer and perimeter strips for spacer grids are to be free of cracks. Strips from each material lot are penetrant inspected in accordance with a quality control plan that ensures, with 95% confidence, that at least 95% of the strips are free of cracks. The method used is capable of detecting known cracks in a standard specimen grid strip. All strips found to have cracks shall be rejected.

←(DRN 06-895, R15)

d) Coefficient of Thermal Expansion

Axial direction - See Reference 2

e) Irradiation Properties:

The yield and tensile strengths are enhanced by irradiation. The stress relaxation with irradiation at operating temperatures proceeds at a rapid rate until nearly complete. The irradiation induced growth is documented.

4.2.1.1.6 Stainless Steel Castings

→(DRN 02-1538, R12, LBDCR 15-025, R309)

Stainless steel castings are fabricated in accordance with Grade CF-3, ASTM A744/A744M, with the following addition:

←(DRN 02-1538, R12)

a) Chemical Properties

Cobalt content is limited.

Starting in 2015, stainless steel end fitting castings are fabricated in accordance with Westinghouse Specification MACASS01. MACASS01 duplicates the requirements of ASTM A744 except for two changes. The required heat treatment (i.e., solution anneal) is not necessary for this application and is not specified. The specification to control delta ferrite level is removed given the relatively low carbon content of the CF-3 cast stainless steel. Casting soundness and casting mechanical properties and other properties affected by the ferrite level are controlled by non-destructive examination and mechanical property measurements of representative samples.

←(LBDCR 15-025, R309)

4.2.1.1.7 Stainless Steel Tubing

→(EC-9533, R302; EC-30663, R307)

Stainless steel tubing is fabricated in accordance with ASTM A269 (with additional requirements) for wear sleeves and the Guardian[TM1] grid inserts, and in accordance with either ASTM A213 or A249 (both with additional requirements) for the top Inconel grid sleeve.

←(EC-9533, R302; EC-30663, R307)

a) Chemical Properties

Carbon content is limited on tubing to be welded. Cobalt content is limited.

4.2.1.1.8 Inconel X-750 Compression Springs

→(DRN 02-1538, R12; EC-9533, R302)

All Inconel springs are fabricated in accordance with AMS 5699, with the following addition:

←(DRN 02-1538, R12; EC-9533, R302)

a) Chemical Properties

Cobalt content is limited.

→(DRN 02-1538, R12)

4.2.1.1.9 Inconel 625 Spacer Grid Strip Material

→(EC-9533, R302)

Inconel spacer grid strip material is procured in accordance with the specification for nickel-chromium-molybdenum-columbium alloy plate, sheet, and strip (ASTM B443) for Inconel 625 strip and age-hardenable nickel-chromium-iron alloy sheet, strip, and plate (ASTM B670) for Inconel 718, both with the following additional requirements:

←(DRN 02-1538, R12; EC-9533, R302)

a) Chemical Properties

Cobalt content is limited.

b) Special Tests

A check analysis and a bend test are required.

4.2.1.2 Fuel Rod

4.2.1.2.1 Fuel Cladding Design Limits

The fuel cladding is designed to sustain the effects of steady-state and expected transient operating conditions without exceeding acceptable level of stress and strain. Except where specifically noted, the design bases presented in this section are consistent with those used for previous core designs. The fuel rod design accounts for cladding irradiation growth, external pressure, differential expansion of fuel and clad, fuel swelling, clad

[1] **Guardian** is a trademark or registered trademark of Westinghouse Electric Company LLC, its affiliates and/or its subsidiaries in the United States of America and may be registered in other countries throughout the world. All rights reserved. Unauthorized use is strictly prohibited. Other names may be trademarks of their respective owners.

creep, fission and other gas releases, initial internal helium pressure, thermal stress, pressure and temperature cycling, and flow-induced vibrations. The structural criteria discussed below are based on the following for the normal, upset, and emergency loading combinations identified in Subsection 4.2.1.1. For a discussion of the thermal/hydraulic criteria, see Subsection 4.4.1.

→(DRN 06-1059, R15; EC-9533, R302)

a) During normal operating and upset conditions, the maximum primary tensile stress in the Zircaloy, ZIRLO™, or Optimized ZIRLO™ clad shall not exceed two-thirds of the minimum unirradiated yield strength of the material at the applicable temperature. The corresponding limit under emergency conditions is the material yield strength. The use of the unirradiated material yield strength as the basis for allowable stress is conservative because the yield strength of zircaloy increases with irradiation. The use of the two-thirds factor ensures 50 percent margin to component yielding in response to primary stresses. The 50 percent margin, together with its application to the minimum unirradiated properties and the general conservatism applied in the establishment of design conditions, is sufficient to ensure an adequate design.

←(DRN 06-1059, R15)

b) Net unrecoverable circumferential strain shall not exceed one percent as predicted by computations considering clad creep and fuel clad interaction effects. In addition, the incremental total strain induced during a transient is also limited to one percent, as described in Reference 82 for Zircaloy-4 cladding, Reference 80 for ZIRLO™ cladding, and Reference 84 for the NGF design with Optimized ZIRLO™ cladding.

←(EC-9533, R302)

Data from O'Donnell and Weber were used to determine the present one percent strain limit. (See References 4 & 5.) O'Donnell developed an analytical failure curve for Zircaloy cladding based upon the maximum strain of the material at its point of plastic instability. O'Donnell compared his analytical curve to circumferential strain data obtained on irradiated coextruded Zr-U metal fuel rods tested by Weber. The correlation was good, thus substantiating O'Donnell's instability theory. Since O'Donnell performed his analysis, additional data have been derived at Bettis and AECL. (See References 6, 7, 8, 9 & 10.)

These new data are shown in Figure 4.2-1, along with O'Donnell's curve and Weber's data. This curve was then adjusted because of differences in anisotropy, stress and strain rates; and the design limit was set at one percent.

→(DRN 06-1059, R15; EC-9533, R302)

The conservatism of the clad strain calculations is provided by the selection of adverse initial conditions and material behavior assumptions, and by the assumed operating history. The acceptability of the 1.0 percent unrecoverable circumferential strain limits is demonstrated by data from irradiated Zircaloy-clad fuel rods which show no cladding failures (due to strain) at or below this level, as illustrated in Figure 4.2-1.

←(DRN 06-1059, R15)

The ductility of ZIRLO™ is expected to be at least equivalent to Zircaloy-4 (Reference 80, Section 5.3.5). Section B.7 of Reference 83 documents that the ductility of Optimized ZIRLO™ and ZIRLO™ are indistinguishable from each other at temperatures above room temperature, so the ductility of Optimized ZIRLO™ is also at least equivalent to that of Zircaloy-4. Ductility is a function of irradiation and hydride formation in the cladding. Since the corrosion rates of ZIRLO™ and Optimized ZIRLO™ are significantly less than that of Zircaloy-4, fewer hydrides will be formed at high burnup levels. Therefore the 1% strain capability limit criterion will continue to be applied and satisfied in Westinghouse fuel mechanical design analysis.

c) The clad will be initially pressurized with helium to an amount sufficient to prevent gross clad deformation under the combined effects of external pressure and long-term creep. The clad design can rely on the support of fuel pellets (Reference 82) or the holddown spring (Reference 81) to prevent gross deformation.

←(EC-9533, R302)

d) Cumulative strain cycling usage, defined as the sum of the ratios of the number of cycles in a given effective strain range ($\Delta\varepsilon$) to the permitted number (N) at that range, as taken from Figure 4.2-2, will not exceed 0.8.

→(EC-9533, R302)

The cyclic strain limit design curve shown on Figure 4.2-2, is based upon the Method of Universal Slopes developed by S.S. Manson and has been adjusted to provide a strain cycle margin for the effects of uncertainty and irradiation. The resulting curve has been compared with known data on the cyclic loading of Zircaloy and has been shown to be conservative. (See Reference 11.) Specifically, it encompasses all the data of O'Donnell and Langer. (See Reference 12). The application of the curve to ZIRLO™ is documented in Reference 80 and Appendix B.10 of Reference 83 documents that there is no distinguishable difference in the fatigue characteristics of ZIRLO™ and Optimized ZIRLO™.

←(EC-9533, R302)

As discussed in Subsection 4.2.3.2.5, the fatigue calculation method includes the effect of clad creep to reduce the pellet to clad diametral gap during that portion of operation when the pellet and clad are not in contact. The same model is used for predicting clad fatigue as is used for predicting clad strain. Therefore, the effects of creep and fatigue loadings are considered together in determining end-of-life cumulative fatigue damage factor and the end-of-life cumulative fatigue damage factor and the end-of-life clad strain. Moreover, the current fatigue damage calculation method includes a factor of two which is applied to the calculated strain before determining the allowable number of cycles associated with that strain. This, in combination with the allowable fatigue usage factor of 0.8 ensures a considerable degree of conservatism (see Figure 4.2-2).

e) There is no specific limit on lateral fuel rod deflection for structural integrity considerations except that which is brought about through application of cladding stress criteria. The absence of a specific limit on rod deflection is justified because it is the fuel assembly structure, and not the individual fuel rod, that is the limiting factor for fuel assembly lateral deflection.

f) Fuel rod internal pressure increases with increasing burnup and toward end-of-life the total internal pressure, due to the combined effects of the initial helium fill gas and the released fission gas, can approach values comparable to the external coolant pressure. The maximum predicted fuel rod internal pressure will be consistent with the following criteria.

1) The primary stress in the cladding resulting from differential pressure will not exceed the stress limits specified earlier in this section.

→(DRN 02-1538, R12)

2) The internal pressure will not cause the clad to creep outward from the fuel pellet surface while operating at the design peak linear heat rate for normal operation. In determining compliance with this criterion, internal pressure is calculated for the peak power rod in the reactor, including accounting for the maximum computed fission gas release. In addition, the pellet swelling rate (to which the calculated clad creep rate is compared) is based on the observed swelling rate of "restrained" pellets (i.e., pellets in contact with clad), rather than on the greater observed swelling behavior of pellets which are free to expand.

←(DRN 02-1538, R12)

→(DRN 03-1821, R13)

The criteria discussed above do not limit fuel rod internal pressure to values less than the primary coolant pressure, and the occurrence of positive differential pressures would not adversely affect normal operation so long as appropriate criteria for cladding stress, strain, and strain rate were satisfied. The fuel rod maximum pressure criterion for allowing fuel rods to operate in reactors with internal hot gas pressure in excess of reactor coolant system pressure is provided in Reference 79.

←(DRN 03-1821, R13)

g) The design limits of the fuel rod cladding, with respect to vibration considerations, are incorporated within the fuel assembly design. It is a requirement that the spacer grid intervals, in conjunction with the fuel rod stiffness, be such that fuel rod vibration, as a result of mechanical or flow induced excitation, does not result in excessive wear of the fuel rod cladding at the spacer grid contact areas.

4.2.1.2.2 Fuel Rod Cladding Properties

4.2.1.2.2.1 Mechanical Properties

a) Modulus of Elasticity

→(DRN 06-1059, R15; EC-9533, R302)

Young's Modulus x 10^6 = value specified in Reference 13 for Zircaloy-4, in Reference 80 for ZIRLO™, and in Reference 83 for Optimized ZIRLO™.

←(DRN 06-1059, R15; EC-9533, R302)

b) Poisson's Ratio

→(DRN 06-1059, R15; EC-9533, R302)

n = value specified in Reference 13 for Zircaloy-4, in Reference 80 for ZIRLO™, and in Reference 83 for Optimized ZIRLO™.

←(DRN 06-1059, R15; EC-9533, R302)

c) Thermal Coefficient of Expansion

→(DRN 06-1059, R15; EC-9533, R302)

diametral direction = value specified in Reference 13 for Zircaloy-4, in Reference 80 for ZIRLO™, and in Reference 83 for Optimized ZIRLO™.

←(DRN 06-1059, R15; EC-9533, R302)

d) Yield Strength

→(DRN 06-1059, R15; EC-9533, R302)

Yield strength in the non-irradiated condition is shown in Figure 4.2-20 of Reference 13 for Zircaloy-4, in Section 5.3.7.1 of Reference 80 for ZIRLO™, and in Figure B.7-6 of Reference 83 for Optimized ZIRLO™.

←(DRN 06-1059, R15; EC-9533, R302)

The cladding stress limits identified in Subsection 4.2.1.2.1 are based on values taken from the minimum yield strength curve at the appropriate temperatures. The limits are applied over the entire fuel lifetime, during conditions of reactor heatup and cooldown, steady state operation, and normal power cycling. Under these conditions, cladding temperatures and fast fluences can range from 70° to 750°F and from 0 to 1 x 10^{22} nvt, respectively.

e) Ultimate Strength

→(DRN 06-1059, R15; EC-9533, R302)

Ultimate tensile strength in the non-irradiated condition is shown in Figure 4.2-21 of Reference 13 for Zircaloy-4, in Section 5.3.7.2 of Reference 80 for ZIRLO™, and in Figure B7-7 of Reference 83 for Optimized ZIRLO™.

←(DRN 06-1059, R15; EC-9533, R302)

f) Uniform Tensile Strain

→(DRN 02-1538, R12)

Uniform tensile strain in the irradiated condition approaches one percent and remains relatively constant (Subsection 4.2.1.2.1).

→(DRN 06-1059, R15; EC-9533, R302)

Ductility is a function of irradiation and hydride formation in the cladding wall. The ductility of ZIRLO™ and Optimized ZIRLO is expected to be at least equivalent to Zircaloy-4 because the waterside corrosion is significantly lower for ZIRLO™ and Optimized ZIRLO and will result in less hydrogen uptake and less hydride formation. Total strain capability of ZIRLO™ and Optimized ZIRLO is projected to be in excess of 1% at burnup levels of 60 MWd/kgU.

←(DRN 02-1538, R12; 06-1059, R15)

Note: No flare test currently done on production cladding.

g) Hydrostatic Burst Test

Hydrostatic burst tests are conducted on Zircaloy-4 cladding to verify that burst pressure and circumferential elongation exceed prescribed minimum values.

←(EC-9533, R302)

The procedures originally used by CE for the hydrostatic tests were described by D.G. Hardy, J.R. Stewart and A.L. Lowe, Jr., "Development of a Closed End Burst Test Procedure for Zircaloy Cladding," Zirconium in Nuclear Applications, STP-551, ASTM, 1974, pp. 14-30. This information was incorporated into ASTM B353-77. The present procedure for CE cladding is essentially the same procedure as described in B353-77. Typical burst pressures of 35 samples from three lots ranged from 16.6 to 18.8 ksi.

→(EC-9533, R302)

h) Corrosion

→(DRN 03-2058, R14; 06-1059, R15, LBDCR 15-035, R309)

The Zircaloy-water reaction rate correlation used for non-LOCA applications is given in Reference 74. Note that for current analyses, the cladding corrosion rates are described in Reference 82 for Zircaloy-4 and in Reference 85 for ZIRLO™ and in Optimized ZIRLO™.

←(DRN 03-2058, R14; 06-1059, R15; EC-9533, R302, LBDCR 15-035, R309)

→(DRN 06-992, R15)

The maximum allowed fuel rod cladding corrosion will be limited to 100 microns. The corrosion thickness will be calculated using the best estimate models and methods described in CENPD-404-P.

←(DRN 06-992, R15)

4.2.1.2.2.2 Dimensional Requirements

a) Tube straightness is limited to 0.010 in./ft, and inside diameter and wall thickness are tightly controlled.

→(DRN 06-1059, R15; EC-9533, R302)

b) Ovality is measured as the difference between maximum and minimum inside diameters and is acceptable if within the diameter tolerances. Outside diameter is specified as 0.382 ± 0.002 in. Inside diameter is specified as 0.332 ± 0.0015 in. NGF valves are 0.374 ± .0015 in. for the outside diameter and 0.329 ± .0015 in. for the inside diameter.

←(DRN 06-1059, R15; EC-9533, R302)

c) Eccentricity is defined as the difference between maximum and minimum wall thickness at a cross section and is specified as 0.004 inches maximum.

→(EC-9533, R302)

d) Wall thickness is specified as 0.023 in. minimum (the nominal value reported elsewhere is based on the nominal O.D. and I.D.). Minimum wall thickness specified in NGF is 0.0207 in.

←(EC-9533, R302)

4.2.1.2.2.3 Metallurgical Properties

a) Hydride Orientation

A restriction is placed on the hydride orientation factor for any third of the tube cross-section (inside, middle, or outside). The hydride orientation factor, defined as the ratio of the number radially oriented hydride platelets to the total number of hydride platelets shall not exceed 0.3. The independent evaluation of three portions of the cross section is included to allow for the possibility that hydride orientation may not be uniform across the entire cross section.

4.2.1.2.2.4 Chemical Properties

→(DRN 02-1538, R12)

All fuel rod cladding is manufactured in accordance with Grade RA-2, ASTM B811, Wrought Zirconium and Zirconium Alloy Seamless and Welded Tubes for Nuclear Service, except additional limits are placed on oxygen, silicon, and iron content.

←(DRN 02-1538, R12)

4.2.1.2.3 Fuel Rod Component Properties

4.2.1.2.3.1 Zircaloy-4 Bar Stock

→(DRN 02-1538, R12)

All Zircaloy-4 bar stock is fabricated in accordance with Grade RA-2, ASTM B351, Hot-Rolled and Cold-Finished Zirconium and Zirconium Alloy Bars, Rod and Wire for Nuclear Application, with the following exceptions and/or additions:

←(DRN 02-1538, R12)

a) Chemical Properties

Additional limits are placed on oxygen and silicon content.

b) Metallurgical Properties

1) Grain Size

The maximum average grain size is restricted.

4.2.1.2.3.2 Stainless Steel Compression Springs

→(DRN 02-1538, R12)

All stainless steel springs are fabricated in accordance with AMS 5688.

←(DRN 02-1538, R12)

→(DRN 02-1538, R12)

←(DRN 02-1538, R12)

4.2.1.2.4 UO_2 Fuel Pellet Properties

4.2.1.2.4.1 Chemical Composition

Salient points regarding the structure, composition, and properties of the UO_2 fuel pellets are discussed in the following subsections. Where the effect of irradiation on a specific item is considered to be of sufficient importance to warrant reflection in the design or analyses, that effect is also discussed.

a) Chemical analyses are performed for the following constituents:

1) Total Uranium

2) Carbon

3) Nitrogen

4) Fluorine

5) Chlorine and Fluorine

6) Iron

7) Thorium

8) Nickel

→(DRN 02-1538)

9) Aluminum

10) Chromium

11) Silicon

12) Calcium

13) Magnesium

14) Erbium

←(DRN 02-1538)

b) Limits are placed on the oxygen-to-uranium ratio.

c) The sum of the calcium + aluminum + silicon contents shall not exceed 300 ppm by weight.

d) The sum of the thermal neutron capture cross-sections of the following impurities shall not exceed a specified equivalent thermal-neutron capture cross-section of natural boron:

1) Boron

2) Silver

3) Cadmium

4) Gadolinium

5) Europium

6) Samarium

7) Dysprosium

→(DRN 02-1538)

8) Erbium

←(DRN 02-1538)

e) The total hydrogen content of finished ground pellets is restricted.

f) The nominal enrichment of the fuel pellet will be specified and shall be held within ± 0.05 wt percent U_{235}.

4.2.1.2.4.2 Microstructure

→(DRN 02-1538)

a) Acceptable porosity distribution will be determined by comparison of approved visual standards with photo-micrographs from each pellet lot.

←(DRN 02-1538)

b) The average grain size shall exceed a specified minimum size.

4.2.1.2.4.3 Density

→(DRN 02-1538)

a) The density of the sintered pellet after grinding shall be between 94.0 and 96.5 percent of theoretical density (TD), based on a UO_2 theoretical density of 10.96 g/cm^3.

b) The in-pile stability of the fuel is ensured by the use of an NRC-approved out-of-pile test during production.

←(DRN 02-1538)

c) The effects of irradiation on the density of sintered UO_2 pellets are discussed in Reference 14.

4.2.1.2.4.4 Thermal Properties

a) Thermal Expansion

The thermal expansion of UO_2 is described by the following temperature dependent equations:[15][16]

$$\% \text{ Linear Expansion} = (-1.723 \times 10^{-2}) + (6.797 \times 10^{-4}T) + (2.896 \times 10^{-7}T^2)$$

$$(25 \leq T \leq 2200)$$

$$\% \text{ Linear Expansion} = 0.204 + (3 \times 10^{-4}T) + (2 \times 10^{-7}T^2) (10^{-10}T^3)$$

$$(T > 2200)$$

where T = fuel temperature, degrees Celsius.

b) Thermal Emissivity

A value of 0.85 is used for the thermal emissivity of UO_2 pellets over the temperature range 800 to 2600K. (See References 17, 18 and 19.)

c) Melting Point and Thermal Conductivity

The fuel temperature required to incur melting is linearly dependent on local burnup as given by:

$$T_{melt} = 5080 - 290 \times \frac{(\text{Burnup})}{50,000}$$

→(DRN 04-1096, R14)

where, T_{melt} is in °F and burnup is in MWD/MTU. This equation T_{melt} is based on UO_2 melt data given by Reference 76. In addition, the fuel melting temperature may be reduced depending on the amount and type of burnable poison in the fuel as described in Reference 78.

←(DRN 04-1096, R14)

The variation of the thermal conductivity of UO_2 with burnup is not explicitly treated, but is implicitly taken from the porosity relationship discussed in Subsection 2.2.5 of Reference 14.

d) Specific Heat of UO_2

The specific heat of UO_2 is described by the following temperature dependent equations.[20]

→(DRN 04-1096, R14)

$$T \leq 2240° F$$

$$C_p = 49.67 + 2.2784 \times 10^{-3} T - \left(\frac{3.2432 \times 10^6}{(T + 460)^2} \right)$$

←(DRN 04-1096, R14)

$$T \geq 2240° F$$

$$C_p = -126.07 + (0.2621 T) - (1.399 \times 10^{-4} T^2) + (3.1786 \times 10^{-8} T^3) - (2.483 \times 10^{-12} T^4)$$

where:

Cp = specific heat, BTU/lbm-°F

T = fuel temperature, °F

4.2.1.2.4.5 Mechanical Properties

a) Young's Modulus of Elasticity

The Young's modulus of elasticity for UO_2 is used in the analytical model for prediction of the effects of pellet clad interaction. Its value may be found in Reference 21.

Subsection 4.2.3.2.11 discusses the pellet clad interaction model.

b) Poisson's Ratio

→(DRN 02-1538, R12)

Poisson's ratio = 0.32 - (1.8×10^{-5} (T-25)) for the range of temperature between 25°C to 1800°C, Poisson's ratio is assumed constant at 0.29 where T = fuel temperature, °C.

←(DRN 02-1538, R12)

c) Yield Stress (not applicable)

d) Ultimate Stress (not applicable)

e) Uniform Ultimate Strain (not applicable)

4.2.1.2.5 Fuel Rod Pressurization

Fuel rods are initially pressurized with helium for two reasons:

a) Preclude clad collapse during the design life of the fuel. The internal pressurization, by reducing stresses from differential pressure, extends the time required to produce creep collapse beyond the required service life of the fuel.

b) Improve thermal conductivity of the pellet-to-clad gap within the fuel rod. Helium has a higher coefficient of conductivity than the gaseous fission products.

In unpressurized fuel, the initially good helium conductivity is eventually degraded through the addition of the fission product gases released from the pellets. The initial helium pressurization results in a high helium to fission products ratio over the design life of the fuel with a corresponding increase in the gap conductivity and heat transfer.

The effect of fuel rod power level and pin burnup on fuel rod internal pressure has been studied parametrically. Figures 4.2-3 and 4.2-4 show predicted variation of fuel rod internal pressure with pin burnup and pin peaking factor for minimum pressure rods and maximum pressure rods, respectively, for a full power core.

→(DRN 03-2058, R14; 06-1059, R15; EC-9533, R302)

The initial helium fill pressure will be 395 $\pm$ 15 psia for UO_2 and Erbia rods. Due to the design changes associated with the NGF rods, the initial helium fill pressure for UO_2 rods of the NGF design is specified as 275 ± 15 psig at 75F. This initial fill pressure will be sufficient to prevent clad collapse as discussed in Subsection 4.2.3.2.8. The calculational methods employed to generate internal pressure histories are discussed in Reference 14.

←(DRN 03-2058, R14)

The ZrB_2 IFBA rod for both non-NGF and NGF designs is pre-pressurized at a lower helium fill pressure (approximately 150 psig) to prevent an unacceptable maximum pressure due to an increased helium release.

←(DRN 06-1059, R15; EC-9533, R302)

4.2.1.2.5.1 Capacity for Fission Gas Inventory

The greater portion of the gaseous fission products remain either within the lattice or the microporosity of the UO_2 fuel pellets and do not contribute to the fuel rod internal pressure. However, a fraction of the fission gas is released from the pellets by diffusion and pore migration and thereafter contributes to the internal pressure.

→(DRN 06-1059, R15)

The annular pellets provide additional void volume to help control the rod pressure increases due to release of Helium from the thin IFBA coating during the lifetime of such rod.

←(DRN 06-1059, R15)

The determination of the effect of fission gas generated in and released from the pellet column is discussed in Subsection 4.2.3.2.2. The rod pressure increase which results from the release of a given quantity of gas from the fuel pellets depends upon the amount of open void volume available within the fuel rod and the temperatures associated with the various void volumes. In the fuel rod design, the void volumes considered in computing internal pressure are:

Fuel rod upper end plenum

Fuel-clad annulus

Fuel pellet-end dishes and chamfers

Fuel pellet open porosity

→(DRN 06-1059, R15)
Hollow center of annular pellets
←(DRN 06-1059, R15)

These volumes are not constant during the life of the fuel. The model used for computing the available volume is a function of burnup and power level and accounts for the effects of fuel and clad thermal expansion fuel pellet densification, clad creep, and irradiation induced swelling of the fuel pellets.

4.2.1.2.5.2 Fuel Rod Plenum Design

The fuel rod upper end plenum is required to serve the following functions:

a) Provide space for axial thermal expansion and burnup swelling of the pellet column.

b) Contain the pellet column holddown spring.

c) Act as a plenum region to ensure an acceptable range of fuel rod internal pressures.
→(DRN 02-1538, R12)
Of these functions, listing c is expected to be the most limiting constraint on plenum length selection, since the range of temperatures in fuel rod, together with the effects of swelling, thermal expansion, and fission gas release, can produce a wide range of internal pressure during the life of the fuel. The fuel rod plenum pressure will be consistent with the pressurization and clad collapse criteria specified in Subsection 4.2.1.2.1.
←(DRN 02-1538, R12)

4.2.1.2.5.3 Outline of Procedure Used to Size the Fuel Rod Plenum

a) A parametric study of the effects of plenum length on maximum and minimum rod internal pressure is performed. Because the criteria pertaining to maximum and minimum rod internal pressure differ, the study is divided into two sections:

1) Maximum Internal Pressure Calculation

Maximum rod pressure is limited by the stress criteria. Maximum end-of-life pressure is determined for each plenum length by including the fission gas released, selecting conservative values for components dimensions and properties, and accounting for burnup effects on component dimensions. The primary cladding stress produced by each maximum pressure is then compared to the stress limits to find the margin available with each plenum length. Stress limits are listed in Subsection 4.2.1.2.1.

2) Minimum Internal Pressure/Collapse Calculation

Minimum rod pressure is limited by the criterion that no rod will be subject to collapse during the design lifetime. The minimum pressure history for each plenum length is determined by neglecting fission gas release, selecting a conservative combination of component dimensions and properties, and accounting for dimension changes during irradiation. Each minimum pressure history is input to the cladding collapse model to establish the acceptability of the associated plenum length (see Reference 22).

b) For each plenum length, there is a resultant range of acceptable initial fill pressures. The optimum plenum length is generally considered to be the shortest which satisfies all criteria related to maximum and minimum rod internal pressure including a range sufficient to accommodate a reasonable manufacturing tolerance on initial fill pressure.

→(LBDCR 13-014, R309)

c) Additional information on those factors which have a bearing on determination of the plenum length are discussed below:

1) Creep and dimensional stability of the fuel rod assembly influence the fission gas release model and internal pressure calculations, and are accounted for in the procedure of sizing the fuel rod plenum length. Creep in the cladding is accounted for in a change in clad inside diameter, which in turn influences the fuel/clad gap. The gap change varies the gap conductance in the FATES computer code with resulting change in annulus temperature, internal pressure, and fission gas release (see Reference 14). In addition, the change in clad inside diameter causes a change in the internal volume, with its resulting effect on temperature and pressure. Dimensional stability considerations affect the internal volume of the fuel rod, causing changes in internal pressure and temperature. Fuel pellet densification reduces the stack height and pellet diameter. Irradiation-induced radial and axial swelling of the fuel pellets decreases the internal volume within the fuel rod. In-pile growth of the fuel rod cladding contributes to the internal volume. Axial and radial elastic deformation calculations for the cladding are based on the differential pressure the cladding is exposed to, resulting in internal volume changes. Thermal relocation, as well as differential thermal expansion of the fuel rod materials also affect the internal volume of the fuel rods.

←(LBDCR 13-014, R309)

→(DRN 02-1538, R12; 04-1096, R14)

2) The maximum expected fission gas release in the peak power rod is calculated using the FATES computer code. Rod power history input to the code is consistent with the design limit for peak linear heat rate set by LOCA considerations, and therefore the gas release used to size the plenum represents an upper limit. Because of time-varying gap conductance, fuel depletion, and expected fuel management, the release rate varies as a function of burnup.

←(DRN 02-1538, R12; 04-1096, R14)

4.2.1.2.6 Fuel Rod Performance

Steady state fuel temperatures are determined by the FATES computer program. The calculational procedure considers the effect of linear heat rate, fuel relocation, fuel swelling, densification, thermal expansion, fission gas release, and clad deformations. The model for predicting fuel thermal performance including the specific effects of fuel densification on increased linear heat generation rate (LHGR) and stored energy is discussed in detail in Reference 14.

→(DRN 02-1538, R12)

Significant parameters such as cold pellet and clad diameters, gas pressure and composition, burnup and void volumes are calculated and used as initial conditions for subsequent calculations for stored energy during the ECCS analysis. The coupling mechanism between FATES calculations and the ECCS analysis is described in detail in Reference 23.

←(DRN 02-1538, R12)

Discussions of uncertainties associated with the model, and of comparative analytical and experimental results, are also included in Reference 14.

→(DRN 02-1538, R12; EC-9533, R302)

The methodology for modeling the NGF design is described in the CE 16x16 Next Generation Fuel Topical Report, Reference 84.

←(EC-9533, R302)

4.2.1.2.7 Fuel Rod with Erbia (Er_2O_3) Addition

Some fuel rods in the fuel assembly may contain pellets which incorporate erbia (Er_2O_3) as a burnable absorber into the central portion of the pellet column. These fuel rods are analyzed by the same methods and subject to the same design criteria as fuel rods containing only urania pellets.

The urania-erbia pellets are fabricated by mechanically blending erbia powder with urania powder to produce a homogenous mixture, followed by pressing and sintering. These fuel pellets may contain up to 2.5 weight percent erbia.

←(DRN 02-1538, R12)

→(DRN 04-1096, R14)

The addition of erbia to urania fuel pellets may influence the thermal properties of the fuel. Of particular importance are the properties that are used in fuel performance analyses. These properties are: 1) solidus temperature, 2) specific heat, 3) density, 4) thermal expansion, and 5) thermal conductivity. The effect of erbia addition on these properties of urania is discussed in detail in Section 2.2 of Reference 78.

←(DRN 04-1096, R14)

→(DRN 06-1059, R15)

4.2.1.2.8 Fuel Rod with IFBA (ZrB_2 coated) Pellets

The Zirconium Diboride (ZrB_2) integral fuel burnable absorber (IFBA) fuel design commences with Batch Y for Cycle 15. The ZrB_2 is applied as a very thin uniform coating on the outer surface only of the solid UO_2 pellet stack prior to loading into the fuel rod cladding tube. The coating is applied over the center of the UO_2 pellet stack length, consistent with positioning of the Erbia (Er_2O_3 - UO_2) burnable absorber pellets in the prior batches present in Cycle 15 (T, U, W and X) and does not extend to either end of the fuel rod (see Figure 4.2-11A). Pellets at the ends of the pellet stack (cutback zones) are of an annular design.

→(EC-9533, R302)

The annular pellets have the same pellet outside diameter (.3250 inch for pre-NGF batches and .3225 inch for NGF batches) and pellet edge chamfer as the corresponding enriched solid fuel pellets, but have no dish on the pellet ends. The annular pellets are also longer

←(DRN 06-1059, R15; EC-9533, R302)

→(DRN 06-1059, R15; EC-9533, R302)
than the solid fuel pellets (.500 inch versus .390 inch for pre-NGF batches and 0.387 inch for NGF batches). The diameter of the annulus is 0.1625 inches (pre-NGF) or 0.1550 inches (NGF) which results in about 25% annular volume to accommodate gas release in the IFBA rods. The fully-enriched annular pellets in the IFBA rods increase the void volume for gas accommodation within the fuel rod compared to the previous burnable absorber fuel rod design (Erbia), thereby providing sufficient margin to meet the rod internal pressure criterion. Also, to compensate for the additional helium released from the ZrB_2 coating, the initial fill gas pressure, designed to reduce pressure differences across the cladding, is reduced as compared to non-IFBA rods.
←(EC-9533, R302)
Introduction of the ZrB_2 IFBA fuel rod design has influenced fuel rod pressurization as discussed in the Topical Report, Reference 81. During irradiation, the B-10 isotope absorbs a neutron and fissions into Helium and Lithium. Much of the Helium may be released from the thin coating into the fuel rod void by the time complete burnout is attained, thus additionally increasing the rod internal pressure at end of life. The released Helium compensates for the initial reduction in helium fill gas and mitigates the potential impact of less helium fill gas on the thermal heat transfer from the fuel pellets to the cladding and into the coolant. Thus, the IFBA coating and corresponding Helium release have no significant impact on the heat transfer characteristic of the fuel rod.
←(DRN 06-1059, R15)

4.2.1.3 Burnable Poison Rod

→(DRN 06-1059, R15)
The earlier cycles poison rods containing the Al_2O_3 burnable poison pellets were replaced by fuel rods with Erbia (Er_2O_3 - UO_2) burnable absorber pellets (Section 4.2.1.2.7) during the late 1990's. Most recently, the ZrB_2 IFBA fuel rod design (Section 4.2.1.2.8) is being introduced beginning with Batch Y in Cycle 15, such that the current core design uses only Erbia or IFBA burnable absorbers rods as poison rods. Hence, the previous design of the poison rods containing the Al_2O_3 burnable poison pellets, as presented in subsections 4.2.1.3.1 through .2.1.3.3.3, is only relevant to those poison rods, if any, that are being kept in long term storage outside of the current core.
←(DRN 06-1059, R15)

4.2.1.3.1 Burnable Poison Rod Cladding Design Limits

The burnable poison rod design accounts for external pressure, differential expansion of pellets and clad, pellet swelling, clad creep, helium gas release, initial internal helium pressure, thermal stress, and flow-induced vibrations. Except where specifically noted, the design bases presented in this section are consistent with those used for previous designs. The structural criteria for the normal, upset and emergency loading combinations identified in Subsection 4.2.1.1. are as follows:

a) During normal operating and upset conditions, the maximum primary tensile stress in the Zircaloy clad shall not exceed two-thirds of the minimum unirradiated yield strength of the material at the applicable temperature. The corresponding limit under emergency conditions is the material yield strength.b) Net unrecoverable circumferential strain shall not exceed one percent as predicted by computations considering clad creep and poison pellet swelling effects.

c) The clad will be initially pressurized with helium to an amount sufficient to prevent gross clad deformation under the combined effects of external pressure and long-term creep. The clad design will not rely on the support of pellets or the holddown spring to prevent gross deformation.

4.2.1.3.2 Burnable Poison Rod Cladding Properties

Cladding tubes for burnable poison rods are purchased under the specification for fuel rod cladding tubes. Therefore, the mechanical metallurgical chemical, and dimensional properties of the cladding are as discussed in Subsection 4.2.1.2.2.

→(DRN 03-2058, R14)

4.2.1.3.3 Al_2O_3-B_4C Burnable Poison Pellet Properties

→(DRN 02-1538, R12)

The Al_2O_3-B_4C burnable poison pellets used in C-E designed reactors consist of a relatively small volume fraction of fine B_4C particles dispersed in a continuous Al_2O_3 matrix. The boron loading is varied by adjusting the B_4C concentration in the range from 0.7 to 4.0 w/o (1 to 6.0 v/o). Typical pellets have a bulk density of about 90 percent of theoretical. Many properties of the two-phase Al_2O_3-B_4C mixture, such as thermal expansion, thermal conductivity, and specific heat are very similar to the properties of the Al_2O_3 major constituent. In contrast, properties such as swelling, helium release, melting point and corrosion are dependent on the presence of B_4C. The operating centerline temperature of burnable poison is less than 1100°F, with maximum surface temperatures close to 750°F.

←(DRN 02-1538, R12)

4.2.1.3.3.1 Thermal-Physical Properties

a) Thermal Expansion

The mean thermal expansion coefficients of Al_2O_3 and B_4C from 0 to 1850°F are 4.9 and 2.5 in/in.-°F x 10^{-6}, respectively (see References 24 and 25). The thermal expansion of the Al_2O_3-B_4C two-phase mixture can be considered to be essentially the same as the value for the continuous Al_2O_3 matrix, as the dispersed B_4C phase has a lower expansion coefficient and occupies no more than 6 v/o of the available volume. The low temperature (80 to 250°F) thermal expansion coefficient of Al_2O_3 irradiated at 480, 900, and 1300°F does not change as a result of irradiation (see Reference 26). The expansion of a similar material, beryllium oxide, up to 1900°F has also been reported to be relatively unchanged by irradiation (see Reference 27). It is therefore appropriate to use the values of thermal expansion measured for Al_2O_3 for the burnable poison pellets:

←(DRN 03-2058, R14)

Temperature Range (°F)	Linear Expansion (percent)
400	0.12
600	0.23
800	0.30
1000	0.40

b) Melting Point

→(DRN 03-2058, R14)

The melting points of Al_2O_3 (3710°F) and B_4C (4440°F) are higher than the melting point of the Zr-4 cladding (see References 28 and 29). No reactions have been reported between the component which would lower the melting point of the pellets to any significant extent. As the B_4C burns up, the lithium atoms formed occupy interstitial sites randomly distributed within the B_4C lattice, rather than forming a lithium-rich phase (see Reference 30). The solid solution of lithium in B_4C should not appreciably influence the melting point of the Al_2O_3-B_4C pellets, as only a small quantity of lithium compounds (0.5 w/o) forms during irradiation. It is concluded that the melting point of Al_2O_3-B_4C will remain considerably above the maximum 1100°F operating temperature.

←(DRN 03-2058, R14)

→(DRN 03-2058, R14)

c) Thermal Conductivity

The thermal conductivity of $A\ell_2O_3$-B_4C was calculated from the measured values for $A\ell_2O_3$ and B_4C using the Maxwell-Buckan relationship for a continuous matrix phase ($A\ell_2O_3$) with spherical dispersed phase (B_4C) particles (see Reference 31). Because of the high $A\ell_2O_3$ content of these mixtures and the similarity in thermal conductivity, the resultant values for $A\ell_2O_3$-B_4C were essentially the same as the values for $A\ell_2O_3$. The measured, unirradiated values of thermal conductivity at 750°F are 0.06 cal/sec-cm-°K for B_4C and 0.05 cal/sec-cm-°K for $A\ell_2O_3$.

The thermal conductivity of $A\ell_2O_3$ after irradiation decreases rapidly as a function of burnup to values of about one-third the unirradiated values (see Reference 26). The irradiated values of $A\ell_2O_3$-B_4C calculated from the above relationships are given below as a function of temperature (see References 26 and 32).

←(DRN 03-2058, R14)

Temperature (°F)	Thermal Conductivity (cal/sec-cm-°K)
400	0.015
600	0.013
800	0.010
1000	0.008

d) Specific Heat

→(DRN 03-2058, R14)

The specific heat of the $A\ell_2O_3$-B_4C mixture can be taken to be essentially the same as pure $A\ell_2O_3$ since the concentration of B_4C is low (6.0 v/o maximum). In addition, the effect of irradiation on specific heat is expected to be small based on experimental evidence from similar materials which do not sustain transmutations as a function of neutron exposure.

←(DRN 03-2058, R14)

→(DRN 03-2058, R14)

The values for $A\ell_2O_3$ measured on unirradiated samples [32][33] are given below:

Temperature (°F)	Specific Heat (cal/gm-°F)
250	0.12
450	0.13
800	0.14
1000 and above	0.15

←(DRN 03-2058, R14)

→(DRN 03-2058, R14)

4.2.1.3.3.2 Irradiation Properties

a) Swelling

$A\ell_2O_3$-B_4C consists of B_4C particles dispersed in a continuous $A\ell_2O_3$ matrix, which occupies more than 94 percent of the poison pellet. The swelling of $A\ell_2O_3$-B_4C depends primarily upon the neutron fluence on the continuous $A\ell_2O_3$ matrix and, secondarily, on the B^{10} burnup of the dispersed B_4C phase. Recent measurements performed on material containing about two w/o B_4C irradiated in a C-E PWR to 100 percent B^{10} burnup at a fluence of 2.4×10^{21} nvt (E>0.8 MeV) revealed a diametral swelling of about one percent. Pellets similar to the burnable poison used in C-E reactors with up to 3 w/o B_4C also sustained about 100 percent B^{10} burnup. Experimental data(34) on $A\ell_2O_3$ reveal a diametral swelling of about 0.7 percent at a fluence of 2.4×10^{21} nvt (E>0.8 MeV). Swelling of $A\ell_2O_3$ increases linearly with fluence to 1.8 percent diametral after an exposure of 6×10^{21} nvt (E>0.8 MeV).

These data show that $A\ell_2O_3$-B_4C swells somewhat more than $A\ell_2O_3$ up to a burnup of 100 percent B_4C (about 2×10^{21} nvt, E>0.8 MeV).

The C-E design value of $A\ell_2O_3$-B_4C swelling rate for fluences less than 2×10^{21} is greater than the swelling rate of $A\ell_2O_3$, while after 100 percent B^{10} burnup the swelling rate for $A\ell_2O_3$-B_4C is considered equal to that of $A\ell_2O_3$.

The data and considerations presented above result in best-estimate diametral swelling values at end-of-life (7×10^{21} nvt, E>0.8 MeV) of about two percent for $A\ell_2O_3$ and from two to three percent for $A\ell_2O_3$-B_4C depending on B_4C.

b) Helium Release

Experimental measurements reveal that less than five percent of the helium formed during irradiation will be released.(35) These measurements were performed on $A\ell_2O_3$-B_4C pellets irradiated at temperatures to 500°F and, subsequently, annealed at 1000°F for five days. The helium release in a burnable poison rod which operated for

←(DRN 03-2058, R14)

one cycle in a ABB CE PWR was calculated from internal pressure measurements to be less than five percent. The design is based on a release of three to ten percent of the helium generated. The design of the burnable poison rod will not be limited by helium pressure despite the conservative use of 10 percent release.

4.2.1.3.3.3 Chemical Properties

→(DRN 03-2058, R14)

a) $A\ell_2O_3$-B_4C Coolant Reactions

→(DRN 02-1538, R12)

The stability of $A\ell_2O_3$-B_4C in contact with reactor coolant has been investigated before and after irradiation. Prior to irradiation no significant boron loss was observed after testing for hundreds of hours at 650°F in borated water at 2250 psig. Visual and metallographic evaluations showed no erosion of the $A\ell_2O_3$ matrix. In addition, pellet measurements showed no change in diameter or length as a result of exposure to the borated water.

←(DRN 02-1538, R12; 03-2058, R14)

→(DRN 03-2058, R14)

A series of tests were performed to assess the compatibility of irradiated $A\ell_2O_3$-B_4C with reactor coolant. The results of these tests show that $A\ell_2O_3$-B_4C pellets irradiated to 100 percent B_{10} burnup retain their mechanical integrity after 350 hours in 650°F, 2250 psig water. Visual and metallographic observations indicate that the $A\ell_2O_3$ matrix does not sustain significant erosion of micro-cracking, although the B_4C particles are leached out of portions of the pellet. No diameter or length changes were noted in the pellets. The amount of B_4C loss is primarily dependent upon the accessibility of the B_4C particles to the reactor coolant, and the time of exposure. B_4C particles that are completely enclosed in the $A\ell_2O_3$ matrix do not corrode, as the $A\ell_2O_3$ matrix material has relatively good corrosion resistance.

Should irradiated B_4C particles be exposed to reactor coolant, the primary corrosion products that would be produced are H_3BO_3 and Li_2O, which are soluble in water, and free carbon. The presence of these products in the reactor coolant would not be detrimental to the operation of the plant.

b) Chemical Compatibility

Chemical compatibility between the $A\ell_2O_3$-B_4C pellets and the burnable poison rod cladding during long-term normal operations has been demonstrated by examinations of a burnable poison rod from the Maine Yankee Reactor. The rod had been exposed to an axial average fluence in excess of 2×10^{21} nvt (>0.821 MeV). No evidence of a chemical reaction was observed on the cladding I.D.

Short term chemical compatibility during upset and emergency conditions is demonstrated by the fact that conditions favorable to a chemical reaction between B_4C and $A\ell_2O_3$ are not present at temperatures below 1300°F[36] This temperature is higher than that which will occur at burnable poison pellet surfaces during Condition II and III occurrences (Subsection 4.2.1.1). The action between Zr-4 and $A\ell_2O_3$ described by Idaho Nuclear[37] was observed to occur rapidly only at temperatures in excess of 2500°F, well above the peak Condition IV Zr-4 temperatures in the higher energy fuel rods described in Chapter 15.

←(DRN 03-2058, R14)

4.2.1.4 Control Element Assembly

Except where specifically noted, the design bases presented in this section are consistent with those used for previous designs.

The mechanical design of the control element assemblies is based on compliance with the following functional requirements and criteria:

a) To provide for or initiate short term reactivity control under all normal and adverse conditions experienced during reactor start-up, normal operation, shutdown, and accident conditions.

b) Mechanical clearances of the CEA within the fuel and reactor internals are such that the requirements for CEA positioning and reactor trip are attained under the most adverse accumulation of tolerances.

c) Structural material characteristics are such that radiation induced changes to the CEA materials will not impair the functions of the reactivity control system.

4.2.1.4.1 Thermal-Physical Properties of Absorber Material

→ (DRN 00-644; 01-1103, R12)

The primary control rod absorber materials consist of boron carbide pellets (B_4C) and silver-indium-cadmium bars (Ag-In-Cd). Refer to Figures 4.2-5, 4.2-6, and 4.2-7 for the specific application and orientation of the absorber materials. The significant thermal and physical properties used in mechanical analysis of the absorber materials are listed below:

← (DRN 00-644; 01-1103, R12)

a) Boron Carbide (B_4C)

Configuration	Right cylinder
Outside diameter in.	0.737 ± 0.001
Pellet length, in. nominal	2
End chamber	0.03 in. by 45°
Density gm/cc	1.84
w/o boron, minimum	77.5
Percent open porosity in pellet	27
Ultimate tensile strength, psi	N/A
Yield strength, psi	N/A
Elongation, percent	N/A
Young's modulus, psi	N/A
Thermal conductivity (cal/sec-cm-°C):	Irradiated Unirradiated
800°F	8.3×10^{-3} 28×10^{-3}
1000°F	7.9×10^{-3} 24×10^{-3}
Melting point, °F	4400
Percent thermal linear expansion	0.23% @ 1000°F

b) Silver-Indium-Cadmium (Ag-In-Cd)

Configuration	Cylindrical bars with central hole
Outside diameter, in.	0.734 ± 0.003
Inside diameter, in.	1/4

Length of bar, in. nominal	12.5 (for 5 element CEAs), 5 (for 4 element CEAs)
Density, lb/in.3	0.367
Ultimate tensile strength, psi	N/A
Yield strength, psi	N/A
Elongation, percent	N/A
Young's modulus, psi	N/A

Thermal conductivity (cal/sec-cm-°C):

	Irradiated	Unirradiated
at 300°C	0.14	0.182
at 400°C	0.148	0.196

Melting point, °F	1,470
Linear thermal expansion (in./in.-°F0	12.5×10^{-6}

c) Inconel Alloy 625 (Ni-Cr-Fe)

Configuration (as absorber)	Cylindrical bar
Outside diameter, in.	0.816 ± 0.002
Inside diameter, in.	Solid
Length of cylinder, in.	See Figures 4.2-5, 4.2-6, 4.2-7
Density, lb/in.^{3}	0.305
Ultimate tensile Strength, psi	120-150
Specified minimum yield strength @ 650°F, ksi	65
Elongation in two in., percent	30

Young's modulus, psi

at 70°F	29.7×10^6
at 650°F	27.0×10^6

Thermal conductivity (Btu/hr-ft-°F):

70°F	5.7
600°F	8.2

→(DRN 00-644)

Linear thermal expansion (in./in.-°F)	7.4×10^{-6} (70 to 600°F)

←(DRN 00-644)

4.2.1.4.2 Compatibility of Absorber and Cladding Materials

The cladding material used for the control elements is Inconel Alloy 625. The selection of this material for use as cladding is based on considerations of strength, creep resistance, corrosion resistance, and dimensional stability under irradiation and also upon the acceptable performance of this material for this application in other ABB CE reactors currently in operation.

a) B_4C/Inconel 625 Compatibility

Studies have been conducted by HEDL(38) on the compatibility of Type 316 stainless steel with B_4C under irradiation for thousands of hours at temperatures between 1300 and 1600°F. Carbide formation to a depth of about 0.004 in. in the Type 316 stainless steel was measured after 4400 hours at 1300°F. Similar compound formation depths were observed after ex-reactor bench testing. After testing at 1000°F, only 0.0001 in/yr of penetration was measured. Since Inconel 625 is more resistant to carbide formation than 316 stainless steel, and the expected pellet/clad interfacial temperature in the Waterford 3 design is below 800°F, it is concluded that B_4C is compatible with Inconel.

4.2.1.4.3 Cladding Stress-Strain Limits

The stress limits for the Inconel Alloy 625 cladding are as follows:

Design Conditions I and II (Non Operation, Normal Operation, and Upset Conditions)

$$P_m \leq S_m$$

$$P_m + P_b \leq F_s S_m$$

Design Condition III (Emergency Conditions)

$$P_m \leq 1.5\, S_m$$

$$P_m + P_b \leq 1.5\, F_s S_m$$

Design Condition IV (Faulted Conditions)

$$P_m \leq S'_m$$

$$P_m + P_b \leq F_s S'_m$$

where S'_m is the smaller of $2.4S_m$ or $0.7S_u$

For definition of P_m, P_b, S_m, S'_m, S_u, and F_s see Subsection 4.2.1.1.1. For the Inconel 625 CEA cladding, the value of S_m is two-thirds of the minimum specified yield strength at temperature.

For Inconel 625, the specified minimum yield strength is 65,000 psi at 650°F.

F_S = Mp/My where Mp is the bending moment required to produce a fully plastic section and My is the bending moment which first produces yielding at the extreme fibers of the cross section. The capability of cross-sections loaded in bending to sustain moments considerably in excess of that required to yield the outermost fiber is discussed in Reference 1. For the CEA cladding dimensions, F_S = 1.33.

The strain of the cladding is limited to a value which will permit the CEAs to trip within the allowable time and which is less than the irradiated uniform elongation of the material.

The values of uniform and total elongation of Inconel Alloy 625 cladding are as follows:

Fluence (E>1 MeV), nvt	1 x 10^{22}	3 x 10^{22}
Uniform elongation, percent	3	1
Total elongation, percent	6	3

4.2.1.4.4 Irradiation Behavior of Absorber Materials

a) Boron Carbide Properties

1) Swelling. The linear swelling of B_4C increases with burnup according to the relationship:

$$\%\Delta L = (0.1)\, B_{10}\ \text{Burnup, a/o}$$

→(DRN 00-644; 06-895, R15)

This relationship was obtained from experimental irradiations on high density (90 percent theoretical density) wafers[39] and pellets with densities ranging between 71 and 98 percent TD.[38][40] Dimensional changes were measured as a function of burnup, after irradiating at temperatures expected in the Waterford 3 design.

←(DRN 00-644; 06-895, R15)

2) Thermal Conductivity. The thermal conductivity of unirradiated 73 percent dense B_4C decreases linearly with temperatures from 300 to 1600°F, according to the relationship:

$$\lambda = \frac{1\ cal\ /\ cm\text{-}°K\text{-}sec}{2.17(6.87 + 0.017\ T)}$$

This relationship was obtained from measurements performed on pellets ranging from 70 to 98 percent TD.[41]

The relationship between the thermal conductivity of irradiated 73 percent TD B_4C pellets and temperature given below was derived from measured values[41] on higher density pellets irradiated to fluences out to 3 x 10^{22} nvt (E > 1 MeV).

$$\lambda = \frac{1\ cal\ /\ cm\text{-}°K\text{-}sec}{2.17(38 + 0.025\ T)}$$

where T = temperature, °K

Thermal conductivity measurements of 17 B_4C specimens with densities ranging from 83 to 98 percent TD, irradiated at temperatures from 930 to 1600°F showed that thermal conductivity decreased significantly after irradiation. The rate of decrease is high at the lower irradiation temperatures, but saturates rapidly with exposure.

3) Helium Release. Helium is formed in B_4C as B_{10} burnup proceeds. The fraction of helium released from the pellets is important for determining rod internal gas pressure. The relationship between helium release and irradiation temperature given below was developed at ORNL[42] to fit experimental data obtained from thermal reactor irradiations.

→(DRN 00-644)

$$\%\,\text{He release} = e(A - 1.85D)e^{\frac{-Q}{RT}} + 5$$

←(DRN 00-644)

where:

A = Constant, 6.69 for ABB CE pellets

D = Fractional density, 0.73 for ABB CE pellets

Q = Activation energy constant, 3600 cal/mole

→(DRN 06-895, R15)

R = Gas constant, 1.98 cal/mole -°K

←(DRN 06-895, R15)

T = Pellet temperature, °K

This expression becomes

$$\%\,\text{He release} = 208e^{(-1820/T)} + 5$$

when the above parameters are substituted. In this form, design values for helium release as a function of temperature are generated. The five percent helium release allowance (the last term in the expression) was added to ensure that design values lie above all reported helium release data. Calculated values of helium release obtained from the recommended design expression lie above all experimental data points[38][43][44] obtained on B_4C pellet specimens irradiated in thermal reactors.

4) Pellet Porosity. Experimental evidence is available[45] which shows that for pellet densities below 90 percent, essentially all porosity is open at beginning-of-life. Irradiation induced swelling does not change the characteristics of the porosity, but only changes the bulk volume of the specimens. Therefore, the amount of porosity available at end-of-life is the same as that present at beginning-of-life.

b) Silver-Indium-Cadmium Properties

1) Swelling. Measurements performed on Ag-In-Cd rods irradiated at fluences up to 6.2 x 10^{21} nvt (E>0.6 eV) were employed to develop the following expression to predict the volumetric swelling for silver-indium-cadmium alloy:

$$\%\,\Delta V = \frac{0.3\phi}{10^{21}}$$

where ϕ = fluence, nvt (E>0.6 eV).

Linear swelling is approximately one-third of the volumetric swelling.

2) Thermal Conductivity. The increase in cadmium content from five to perhaps 10 w/o, and the formation of two to three w/o tin as a result of long-term exposures, is expected to decrease the thermal conductivity from the accepted[46] unirradiated values. Published data for unirradiated Ag-Cd binary alloys shows that thermal conductivity was decreasd by about 20 percent by increasing the cadmium content from 5.0 to 10.0 w/o.[46] Since irradiated Ag-In-Cd is expected to perform in much the same fashion, the unirradiated values of thermal conductivity are decreased by 25 percent to account for irradiation.

3) Linear Thermal Expansion. The coefficient of linear thermal expansion for unirradiated Ag-In-Cd material is 12.5×10^{-6} in./in.-°F over the temperature range of 70 to 930°F[47] Published data on unirradiated[46] Ag-Cd binary alloys reveal that a cadium increase of five percent will result in about a five percent increase in thermal expansion coefficient. The small changes in indium and tin content do not influence the thermal coefficient appreciably. For simplicity, the irradiated value of 13.1×10^{-6} in./in.-°F is used in all design calculations.

4) Melting Point. The melting point of unirradiated Ag-In-Cd has been measured as 1470 ± 30°F[46] (800 ± 17°C). The formation of three w/o tin due to the transmutation of indium and the increase in cadmium content to about 10 w/o due to the transmutation of silver may result in a small decrease in the melting point.

c) Inconel 625 Properties

1) Swelling. Available information indicates that Inconel 625 is highly resistant to radiation swelling. Exposure of Inconel 625 to a fluence of 3×10^{22} nvt (E>0.1 MeV) at a temperature of 400°C (752°F) showed no visible cavities in metallographic examinations[48] so that swelling, if any, would be very minor. Direct measurements made after exposure of Inconel 625 to fluence of 5×10^{22} nvt (E>0.1 MeV) at LMFBR conditions showed no evidence, of swelling.[49] Thus, Inconel 625 after fluences of 3×10^{22} nvt (>0.1 MeV) is not expected to swell.

2) Ductility. The ductility of Inconel 625 decreases after irradiation. Extrapolation of lower fluence data on Inconel 625 and 500 indicates that the values of uniform and total elongation of Inconel 625 after 1×10^{22} nvt (E>1 MeV) are three and six percent, respectively.

4.2.1.5 Surveillance Program

4.2.1.5.1 Requirements for Surveillance and Testing of Irradiated Fuel Rods

→(DRN 02-1538)

High burnup performance experience, as described in Subsection 4.2.2 has provided evidence that the fuel will perform satisfactorily under the design conditions. The current core design bases do not include a specific requirement for testing of irradiated fuel rods. However, the fuel assembly design allows disassembly and reassembly to facilitate such inspections, should the need arise.

←(DRN 02-1538)

A fuel rod irradiation program has been developed to evaluate the performance of the fuel rods designed for use in the 16 x 16 fuel assembly. The program includes the irradiation of six standard 16 x 16 assemblies, two each for one, two, and three cycles, respectively, in the Arkansas Nuclear One Unit 2 reactor (ANO-2). Each assembly will contain a minimum of 50 precharacterized, removable rods distributed within the assembly to obtain a spectrum of exposure levels for evaluation purposes in interim and terminal examinations. Interim examination of all six assemblies is planned during refueling shutdowns after each cycle.

→(DRN 02-1538)

The ANO-2 fuel rods and specific components of the fuel rods will receive detailed precharacterizations. The program calls for substantial cladding characterization to include mechanical properties, texture, hydride orientation and out-of-reactor low strain rate behavior. In addition to the ID and OD dimensional data normally obtained on the clad tubing material, a minimum of 300 fuel rods will be profiled to obtain as-loaded dimensions. Sufficient fuel rods will be profiled to obtain diameter and quality measurements such that changes in these parameters can be tracked by similar measurements during interim inspections. Also, a random selection of approximately 100 UO_2 pellets from each lot per batch used will be characterized dimensionally and the density distribution will be determined. About one-half of these pellets will be placed in known axial locations in selected fuel rods while the remainder will be set aside as archives.

A poolside non-destructive examination will be made during each of the first three refuelings at ANO-2. The six 16 x 16 assemblies with characterized rods will be removed from the reactor at each refueling and moved to the spent fuel pool for leak testing (if failed fuel is in the core) and for visual inspection. The length of the assembly and peripheral rods will be measured. During the shutdown, a target of 20 precharacterized rods per batch will be scheduled for examination and measurement. At some time after the refueling outage, pre-characterized rods retained in discharged assemblies will be measured. A target of 100 rods will be eddy current tested after each shutdown.

←(DRN 02-1538)

A post irradiation fuel surveillance program for Waterford 3 is planned. This program shall consist of a visual inspection of a minimum of six irradiated assemblies prior to replacement of the Reactor Vessel Head at each of the first three refueling outages. The six assemblies inspected shall consist of two assemblies of each fuel type and will be from core locations which are non-adjacent. Visual inspections shall consist of viewing the top and sides of each fuel assembly via an underwater TV camera or periscope.

The visual inspection will include observation with special attention to gross problems involving cladding defects, spacer grid damage and other major structural abnormalities. No special measurement devices for these effects are intended to be provided for this visual inspection.

If major abnormalities are detected during this visual inspection or if plant instrumentation indicates gross fuel failures, the fuel vendor will be informed and further inspections shall be performed. Depending on the nature of the observed condition, further examination could include fuel sipping, single rod examination and other examinations. The 16 x 16 fuel design enables reconstitution. Individual fuel rods and other structural components may be examined and replaced, if required. Under unusual circumstances, destructive examination of a fuel rod may be required but this would not be accomplished on site or during the refueling outage.

The NRC shall be contacted regarding gross fuel failure detected by plant instrumentation or major abnormalities observed during the post irradiation inspections described above.

→(DRN 02-1538)

The post fuel irradiation fuel surveillance program shall be continued following the first three cycles of operation of Waterford 3. Six assemblies shall be visually inspected during each refueling outage, not necessarily prior to replacement of the reactor vessel head. The visual inspection shall consist of viewing the tops and sides of each fuel assembly via an underwater TV camera or periscope. The visual inspection will include observation with special attention to gross problems involving cladding defects, spacer grid damage, and other major structural abnormalities. The NRC will be notified of major abnormalities noted as a result of these inspection activities.

←(DRN 02-1538)

4.2.2 DESCRIPTION AND DESIGN DRAWINGS

This subsection summarizes the mechanical design characteristics of the fuel system and discusses the design parameters which are of significance to the performance of the reactor. A summary of mechanical design parameters is presented in Table 4.2-1. These data are intended to be descriptive of the design; limiting values of these and other parameters will be discussed in the appropriate sections.

4.2.2.1 Fuel Assembly

The fuel assembly (Figure 4.2-8) consists of 236 fuel and poison rods, five control element assembly guide tubes, 11 fuel rod spacer grids, upper and lower end fittings, and a hold-down device. The outer guide tubes, spacer grids, and end fittings form the structural frame of the assembly.

→(DRN 02-1538)

The fuel spacer grids (Figure 4.2-9) maintain the fuel rod array by providing positive lateral restraint to the fuel rod but only frictional restraint to axial fuel rod motion. The grids are fabricated from pre-formed Zircaloy or Inconel strips (the bottom, and in some cases the top, spacer grid material is Inconel) interlocked in an egg crate fashion and welded together. Each cell of the spacer grid contains two leaf springs and four arches. The leaf springs press the rod against the arches to restrict relative motion between the grids and the fuel rods. The perimeter strips contain features designed to prevent hangup of grids during a refueling operation.

←(DRN 02-1538)

→(DRN 02-1538, R12; 04-502, R13)
The Zircaloy-4 spacer grids are fastened to the Zircaloy-4 guide tubes by welding, and each grid is welded to each guide tube at eight locations, four on the upper face of the grid and four on the lower face of the grid, where the spacer strips contact the guide tube surface. The lowest spacer grid (Inconel) is not welded to the guide tubes due to material differences. It is supported by an Inconel 625 skirt which is welded to the spacer grid and to the perimeter of the lower end fitting. For the assembly design with an Inconel top spacer grid, the grid is retained by ten Zircaloy-4 sleeves (five above and five below the grid) that are welded to the guide tubes at four locations per sleeve.
←(DRN 02-1538, R12; 04-502, R13)
→(LBDCR 15-025, R309)
The upper end fitting is an assembly consisting of two cast stainless steel plates, five machined posts and five helical Inconel X-750 springs, which attaches to the guide tubes to serve as an alignment and locating device for each fuel assembly and has features to permit lifting of the fuel assembly. The lower cast plate locates the top ends of the guide tubes and is designed to prevent excessive axial motion of the fuel rods.
←(LBDCR 15-025, R309)
The Inconel X-750 springs are of conventional coil design having a coil diameter of 1.844 in., a wire diameter of 0.299 in., and approximately 14 active coils. Inconel X-750 was selected for this application because of its previous use for coil springs and good resistance to relaxation during operation.

→(DRN 02-1538, R12)
The upper cast plate of the assembly, called the hold-down plate, together with the helical compression springs, comprise the hold-down device. The hold-down plate is movable, acts on the underside of the fuel alignment plate, and is loaded by the compression springs. Since the springs are located at the upper end of the assembly, the spring load combines with the fuel assembly weight to counteract upward hydraulic forces. The determination of upward hydraulic forces includes factors accounting for flow maldistribution, fuel assembly component tolerances, crud buildup, drag coefficient, and bypass flow. The springs are sized and the spring preload selected such that a net downward force will be maintained for all normal and anticipated transient flow and temperature conditions. The design criteria limit the maximum stress under the most adverse tolerance conditions to below yield strength of the spring material. The maximum stress occurs during cold conditions and decreases as the reactor heats up. The reduction in stress is due to a decrease in spring deflection resulting from differential thermal expansion between the Zircaloy fuel bundles and the stainless steel internals.
←(DRN 02-1538, R12)

During normal operation, a spring will never be compressed to its solid height. However, if the fuel assembly were loaded in an abnormal manner such that a spring were compressed to its solid height, the spring would continue to serve its function when the loading condition returned to normal.

The lower end fitting is a single piece stainless steel casting consisting of a plate with flow holes and four support legs which also serve as alignment posts. Precision drilled holes in the support legs mate with four core support plate alignment pins, thereby properly locating the lower end of the fuel assembly.

→(DRN 02-1538, R12)
The four outer guide tubes have a widened region at the upper end which contains an internal thread. Connection with the upper end fitting is made by passing the male threaded end of the guide posts through holes in the lower cast flow plate and into the guide tubes. When assembled, the flow plate is secured between flanges on the guide tubes and on the guide posts. The connection with the upper end fitting is locked with a mechanical crimp. Each outer guide tube has, at its lower end, a welded Zircaloy-4 fitting. This fitting has a female threaded portion which accepts a stainless steel bolt, which passes through a hole in the lower end fitting, to secure it. This joint is secured with a stainless steel locking ring tack welded to the lower end fitting in four places.
←(DRN 02-1538, R12)
The central guide tube inserts into a socket in the upper end fittings and is thus retained laterally by the relatively small clearance. The upper end fitting socket is created by the center guide tube post which is threaded into the lower cast flow plate and tack welded in two places.
→(EC-9533, R302)
The NGF design incorporates many of the same features and geometry as the standard fuel assembly, but incorporates a full complement of innovative components to improve fuel reliability, fuel cycle economics, fuel duty, manufacturability, burnup capability, and thermal performance. The major differences between the two designs are the following:

- The NGF assembly uses bulged joints to build the grid cage versus welded joints and uses a pull rod loading process versus the current push loading process. These process changes were selected for NGF to improve the fabricability of the design while preserving the rigidity of the fuel assembly structure.
- The guide thimbles are made of SRA Zircaloy-4 in the prior designs and SRA ZIRLO™ in the NGF design. This change was made because of ZIRLO™'s improved corrosion resistance and dimensional stability under irradiation.
- The NGF guide tube flange, which includes an anti-rotation feature to prevent the transmission of torque to the grids during post installation/removal, is connected to the guide tube by bulging instead of by welding as in the standard design. The bulged flange to guide tube connection retains adequate strength and is necessary to compensate for the axial shrinkage of the guide tubes due to bulging.
- The NGF top grid is made of Inconel-718 and has vertical springs and horizontal dimples. Stainless steel sleeves are brazed into the grid at guide tube locations and are bulged with the guide tubes during cage fabrication to secure the grid to the guide tubes. The design is comparable to others that have an extensive history of successful operation in Westinghouse NSSS nuclear power plants.

→(LBDCR 15-035, R309)
- The standard design Mid grids (HID-1L, Figure 4.2-5) are made using wavy strap Zircaloy-4, while the NGF Mid grids use straight strap Optimized ZIRLO™. The material change was made because of Optimized ZIRLO™'s improved corrosion resistance and dimensional stability under irradiation. The straight straps allow the incorporation of the "I-spring" design and mixing vanes for improved fretting and thermal performance, respectively. Sleeves fabricated from Optimized ZIRLO™ are laser-welded into the guide tube openings and secured to the guide tubes by bulges both above and below the grid.

←(LBDCR 15-035, R309)
- Two IFM grids are included to improve thermal performance in two critical grid spans near the top for active core. These grids are short, non-structural grids that are made from straight strap Optimized ZIRLO™ with side-supported mixing vanes and opposing dimples with small grid-to-rod gaps in lieu of an active (preloaded spring-dimple) support system. The IFM grids have sleeves that are similar to the Mid grid sleeves, except the protrusion of the sleeve above the IFM grids is less than above the Mid grids because the IFM sleeves are only bulged to the guide tubes below the grid.

←(EC-9533, R302)

→(EC-9533, R302; EC-30663, R307)

- The lower portion of the NGF assembly includes several changes to accommodate rod push loading. In lieu of welding, the NGF Guardian™ grid is retained by inserts that are laser-welded to the four outer guide tube openings and then clamped between the bottom of the guide tube and the lower end fitting. To facilitate the installation of the lower end fitting after the rods have been pulled into the grid cage, a small gap remains between the bottoms of the NGF fuel rods and the bottom nozzle. This gap, in combination with associated changes to the lower end cap design, result in the bottom of the active fuel column being 0.165 inches higher than the prior design. The head of the NGF bolt has a skirted region that is crimped into recesses in the lower end fitting to secure the bolt, rather than using a separate locking disc that is welded to the lower end fitting to secure the bolt. The NGF bolt also includes a hole through the center of the bolt to allow water to drain out of the guide tubes after washing the fuel assemblies during fabrication, or prior to the installation of the fuel assemblies in dry casks for spent fuel storage.

←(EC-30663, R307)

- The NGF fuel rod design includes several changes relative to the standard fuel rod design, the most significant of which are the reduced diameter/thickness of the cladding, a modified pellet geometry, the use of Optimized ZIRLO™ cladding, and an increase in the overall rod length. These changes, as well as the other design changes associated with the NGF fuel rods, are detailed in Section 4.2.2.2.

←(EC-9533, R302)

The five guide tubes have the effect of ensuring that bowing or excessive swelling of the adjacent fuel rods cannot result in obstruction of the control element pathway. This is so because:

a) There is sufficient clearance between the fuel rods and the guide tube surface to allow an adjacent fuel rod to reach rupture strain without contacting the guide tube surface.

b) The guide tube, having considerably greater diameter and wall thickness (and also being at a lower temperature) than the fuel rod, is considerably stiffer than the fuel rod and would, therefore, remain straight, rather than be deflected by contact with the surface of an adjacent fuel rod.

Therefore, the bowing or swelling of fuel rods would not result in obstruction of the control element channels such as could hinder CEA movement.

The fuel assembly design enables reconstitution, i.e., removal and replacement of fuel and poison rods, of an irradiated fuel assembly. The fuel and poison rod lower end caps are conically shaped to ensure proper insertion within the fuel assembly grid cage structure; the upper end caps are designed to enable grappling of the fuel and poison rod for purposes of removal and handling. Threaded joints which mechanically attach the upper end fitting to the control element guide tubes will be properly torqued and locked during service, but may be removed to provide access to the fuel and poison rods.

Loading and movement of the fuel assemblies is conducted in accordance with strictly monitored administrative procedures and, at the completion of fuel loading, an independent check as to the location and orientation of each fuel assembly in the core is required.

→(DRN 00-644; 02-1538, R12)

Markings provided on the fuel assembly upper end fitting enable verification of fuel enrichment and orientation of the fuel assembly. Identical markings are provided on the lower end fitting to ensure preservation of fuel assembly identity in the event of upper end fitting removal. Additional markings are provided on each fuel rod during the manufacturing process to distinguish between fuel enrichments and burnable poison rods, if present.

←(DRN 00-644; 02-1538, R12)

→(DRN 00-644; 02-1538, R12)
During the manufacturing process, each fuel rod is marked in order to facilitate a means of maintaining a record of pellet enrichment, pellet lot and fuel stack weight. In addition, a quality control program specification requires that measures be established for the identification and control of materials, components, and partially fabricated subassemblies. These means provide assurance that only acceptable items are used and also provide a method of relating an item or assembly from initial receipt through fabrication, installation , repair, or modification to an applicable drawing, specification, or other pertinent technical document.
←(DRN 00-644; 02-1538, R12)

4.2.2.2 Fuel Rod

→(DRN 02-1538, R12; 06-1059, R15)
The fuel rods consist of slightly-enriched UO_2 cylindrical ceramic pellets, a round wire Type 302 stainless steel compression spring, and an alumina spacer disc located at each end of the fuel column, all encapsulated within a Zircaloy-4 tube seal welded with Zircaloy-4 end caps. The upper alumina disc was removed in the Batch S rod assemblies, and both spacers were removed from the Batch U and subsequent reload fuel. Beginning with Batch U, a Tungsten Inert Gas (TIG) welding is utilized, using a friction fit of the cladding on a reduced diameter pedestal section of the end cap. Beginning with Batch Y, the ZIRLO^{TM} cladding tubes are used and are TIG welded with the Zircaloy-4 end caps. The fuel rods are internally pressurized with helium during assembly. Figure 4.2-10 depicts the fuel rod design.
←(DRN 02-1538, R12; 06-1059, R15)
Each fuel rod assembly includes a unique serial number. The serial number ensures traceability of the fabrication history of each fuel rod component. Finished fuel rods, prior to being loaded into bundles, are processed through a rod scanner to check pellet enrichment.
→(EC-9533, R302)
The fuel cladding is cold-worked and stress relief annealed Zircaloy-4 tubing 0.025 in. thick. The actual tube forming process consists of a series of cold working and annealing operations, the details of which are selected to provide the combination of properties discussed in Subsection 4.2.1.2.2.
←(EC-9533, R302)
The UO_2 pellets are dished at both ends in order to better accommodate thermal expansion and fuel swelling. The initial density of the UO_2 pellets is 10.44 g/cm^3, which corresponds to 95.25 percent of the 10.96 g/cm^3 theoretical density (TD) of UO_2. However, because the pellet dishes and chamfers constitute about three percent of the volume of the pellet stack, the average density of the pellet stack is reduced to 10.11 g/cm^3. This number is referred to as the "stack density."

→(DRN 06-1059, R15)
Note that the initial pellet density and stack density for Erbia pellets used in Erbia fuel rods (see Section 4.2.2.3) are slightly lower (respectively 10.41 and 10.09 g/cm^3) due to Erbia content. These densities for the ZrB_2 coated UO_2 (IFBA) pellets that were first introduced in Batch Y for Cycle 15 are consistent with those for the solid UO_2 pellets. However, the pellet stack density for the annular pellets used in the cutback zones of the pellet stack is lowered to 7.80 g/cm^3 (due to hollow center of 0.1625” diameter).
←(DRN 06-1059, R15)
→(DRN 02-1538, R12)
The compression spring located at the top of the fuel pellet column maintains the column in its proper position during handling and shipping. The fuel rod plenum, which is located above the pellet column, provides space for axial thermal differential expansion of the fuel column and accommodates the initial helium loading and evolved fission gases. (See Subsection 4.2.1.2.5.1 and 4.2.1.2.5.2). The specific manner in which these factors are taken into account, including the calculation of temperatures for the gas contained within the various types of rod internal void volume, is discussed in Reference 14.
→(EC-9533, R302)
Starting with Batch U, fuel rod fabrication was moved from Hematite, MO, to the Columbia, SC, facility. Figure 4.2-10A compares the Hematite and Columbia production urania rod assembly features. Figure 4.2-11A compares the corresponding erbia rod assemblies.
←(DRN 02-1538, R12; EC-9533, R302)

→(EC-9533, R302)
The basic configuration of the NGF fuel rod (Figure 4.2-10B) and IFBA rod (Figure 4.2-11B) are comparable to the prior rod designs, but there are significant differences in the detailed design of the rods.

- The NGF rods have a smaller outside diameter than prior designs (0.374" versus 0.382") to compensate for some of the pressure drop increase associated with the NGF spacer grids. The 0.374" diameter rod is the same as the standard Westinghouse 17x17 design, which precipitated the use of the 17x17 cladding dimensions and pellet geometry for the NGF design. Therefore, the cladding outside/inside diameters are 0.374" and 0.329", while the fuel and IFBA pellets have a diameter of 0.3225", a length of 0.387", and a spherical dish at each end instead of a truncated dish. The blanket pellet associated with the IFBA rod has a diameter of 0.3225", a length of 0.500", and a central hole of 0.155". The corresponding stack densities for these pellet configurations are 10.31 g/cc for the fuel and IFBA pellets, and 8.00 g/cc for the blanket pellets.

→(LBDCR 15-035, R309)
- Optimized ZIRLO™ fuel cladding has been used to replace the ZIRLO™ fuel cladding. The topical report, Reference 83, summarizes the material properties as they pertain to fuel rod cladding, design and licensing activities. The difference between Optimized ZIRLO™ fuel cladding and ZIRLO™ cladding is that Optimized ZIRLO™ has a slight reduction in Tin content for improved corrosion resistance (0.6% minimum for Optimized ZIRLO™ versus 0.8% minimum for ZIRLO™). Reference 85 updates the cladding corrosion model.

←(LBDCR 15-035, R309)
- The overall length of the NGF fuel rod is increased by 0.7" to minimize the loss of void volume associated with the diameter reduction of the rod. To further offset the effect of the diameter reduction, the initial fill gas pressure of the fuel rods has been reduced to approximately 275 psig.

→(EC-13881, R304)
- The nominal active length remains 150" for both the fuel and IFBA rods. The fuel rod stack continues to exclude any cutback/blanket pellets, while the IFBA rod stack has a cutback/ blanket zone at each end of the center pellet column (See Fig. 4.3A-19b).

←(EC-13881, R304)

- The bottom end cap has been modified to accommodate a recess in the bottom end that is necessary for pull-loading the rods into the fuel assemblies. The length of the upper end cap has been reduced and the "acorn" removed to allow as large an increase as possible to the plenum to facilitate the accommodation of fission gas release.

4.2.2.3 Burnable Poison Rod

→(DRN 02-1477, R12)
Fixed burnable neutron absorber (poison) rods, Figure 4.2-11, will be included in selected fuel assemblies to reduce the beginning-of-life moderator coefficient. They will replace fuel rods at selected locations. The poison rods will be mechanically similar to fuel rods. The poison material will be alumina with uniformly-dispersed boron carbide particles. The balance of the column will consist of two Zircaloy-4 spacers with the total column length the same as the column length in fuel rods. The burnable poison rod plenum spring is designed to produce a smaller preload on the pellet column than that in a fuel rod because of the lighter material in the poison pellets.

← (DRN 02-1477, R12; EC-9533, R302)
Each burnable poison rod assembly includes a unique serial number. The serial number is used to record fabrication information for each component in the rod assembly.

→(DRN 02-1477, R12; 06-1059, R15; EC-9533, R302)
← (DRN 02-1477, R12; 06-1059, R15; EC-9533, R302)

4.2.2.4 Control Element Assembly Description and Design Drawings

→(DRN 01-1103, R12; 02-1477, R12)

The Waterford 3 reactor contains a total of 87 CEAs. These are distributed among the fuel assemblies as shown in Figure 4.2-12. The CEA is shown in Figure 4.2-5. CEAs have four control elements arranged in a 4.050-in. square array plus one element at the center of the array. Each CEA interfaces with the guide tubes of one fuel assembly.

←(DRN 01-1103, R12; 02-1477, R12)

→(DRN 02-1477, R12)

←(DRN 02-1477, R12)

→(DRN 02-1477, R12)

The control elements of a CEA consist of an Inconel 625 tube loaded with a stack of cylindrical absorber pellets. The absorber material consists of 73 percent TD boron carbide (B_4C) pellets, with the exception of the lower portion of the elements, which contain silver-indium-cadmium (Ag-In-Cd) alloy cylinders.

←(DRN 02-1477, R12)

Two design objectives are realized by the use of Ag-In-Cd in the element tip zones:

a) CEA Cladding Dimensional Stability

Because of its high ductility and low strength, the Ag-In-Cd will not deform the CEA cladding. Buffering of the CEA following scram, which occurs when the corner element tips enter a reduced diameter portion of the fuel assembly guide tubes, is not degraded with long term exposure of the CEA to reactor operating conditions.

b) Adequate CEA Worth

Although some reduction in CEA worth arises because of the substitution of B_4C with Ag-In-Cd, the effect is small and is accounted for.

During normal powered operation, most of the CEAs are expected to be in the fully withdrawn position.

Above the poison column is a plenum which provides expansion volume for helium released from the B_4C. The plenum volume contains a Type 302 stainless steel hold-down spring, which restrains the absorber material against longitudinal shifting with respect to the clad while allowing for differential expansion between the absorber and the clad. The spring develops a load sufficient to maintain the position of the absorber material during shipping and handling.

→(DRN 02-1477, R12)

Each control element is sealed by welds which join the tube to an Inconel 625 nose cap at the bottom, and an Inconel 625 end fitting at the top. The end fittings, in turn, are threaded and pinned to the spider structure which provides rigid lateral and axial support for the control elements. The spider hub bore is specially machined to provide a point of attachment for the CEA extension shaft.

←(DRN 02-1477, R12)

→(DRN 01-1103, R12)

←(DRN 01-1103, R12)

→(DRN 00-644; 01-1103, R12; 02-1477, R12)

Each CEA is positioned by a magnetic jack control element drive mechanism (CEDM) mounted on the reactor vessel closure head. The extension shaft joins with the CEA spider and connects the CEA to the CEDM. CEAs may be connected to any extension shaft depending on control requirements. Mechanical reactivity control is achieved by positioning groups of CEAs by the CEDMs.

←(DRN 00-644; 02-1477, R12)

In the outlet plenum region, all CEAs are enclosed in CEA shrouds which provide guidance and protect the CEA and extension shaft from coolant cross flow. Within the core, each element travels in a Zircaloy guide tube. The guide tubes are part of the fuel assembly structure and ensure proper orientation of the control elements with respect to the fuel rods.

←(DRN 01-1103, R12)

When the extension shaft is released by the CEDM, the combined weight of the shaft and CEA causes the CEA to insert into the fuel assembly.

→(DRN 01-1103, R12; 02-1477, R12)

The lower ends of the four outer fuel assembly guide tubes are tapered gradually to form a region of reduced diameter which, in conjunction with the outer control element on the CEA, constitutes an effective hydraulic buffer for reducing the deceleration loads at the end of a trip stroke. This purely hydraulic damping action is augmented by a spring and plunger arrangement on the CEA spider. When fully inserted, CEAs rest on the central post of the fuel assembly upper end fitting.

←(DRN 01-1103, R12; 02-1477, R12)

The capability of the CEAs to scram within the allowable time is demonstrated as part of the flow testing discussed in Subsection 4.2.4.4.

4.2.3 DESIGN EVALUATION

4.2.3.1 Fuel Assembly

4.2.3.1.1. Vibration Analyses

Three sources of periodic excitation are recognized in evaluating the fuel assembly susceptibility to vibration damage. These sources are as follows:

a) Reactor Coolant Pump Blade Passing Frequency

Precritical vibration monitoring on previous C-E reactors indicates the peak pressure pulses are expected at the pump blade passing frequency, and a lesser but still pronounced peak at twice this frequency.

b) Core Support Plate Motion

Experience with earlier C-E reactors indicates that random lateral motion of the core support plate is expected to occur with an amplitude of 0.001 to 0.002-in. and a frequency range of between 2 and 10 Hz.

c) Flow-induced vibration resulting from coolant flow through the fuel assembly.

The capability of the Waterford 3 16 x 16 fuel assembly to sustain the effects of flow-induced vibration without adverse effects has been demonstrated in a dynamic flow test performed in CE's TF-2 flow test facility. The test utilized prototypical 16 X 16 reactor components consisting of a 16 X 16 type fuel assembly, a CEA shroud, control element drive mechanism, and a simulation of surrounding core internal support components and was performed under extreme flow and temperature conditions. The success of this test, similar previous tests of 16 X 16 fuel assemblies and the operation of CE's ANO-2 plant, demonstrate that flow-induced vibration will have no adverse effects on the Waterford 3 fuel assemblies.

→(EC-9533, R302)

The NGF fuel assembly design was designed to have a lateral stiffness comparable to the prior designs that have operated successfully in the Waterford plant. In addition, the NGF configuration was tested to confirm the hydraulic stability of the fuel assembly design and to demonstrate the acceptability of the fretting performance of the fuel assembly design. The testing included full scale single and dual bundle tests with both the NGF design and the standard design. The single bundle tests demonstrated the hydraulic stability of both designs over the expected range of flow rates. The dual bundle test was an endurance test that provided additional confirmation of the hydraulic stability of the designs and showed a significant improvement in the fretting performance of the NGF design compared to the standard design. These results indicate that the NGF design is even less susceptible to any vibration effects than the prior designs.

←(EC-9533, R302)

These sources of periodic motion are not expected to have an adverse effect on the performance of the Waterford 3 fuel assembly.

4.2.3.1.2 CEA Guide Tube

The CEA guide tubes were evaluated for structural adequacy using the criteria given in Subsection 4.2.1.1 in the following areas:

a) Steady axial load due to the combined effects of axial hydraulic forces and upper end fitting holddown forces.

   For normal operating conditions, the resultant guide tube stress levels satisfy the criteria given in Subsection 4.2.1.1.1.

b) Short-term axial load due to the impact of the spring loaded CEA spider against the top of the fuel assembly at the end of a CEA trip.

   For trips occurring during normal power operation, solid impact is not predicted to occur due to the kinetic energy of the CEA being dissipated in the hydraulic buffer and by the CEA spring.

c) Short-term differential pressure load occurring in the hydraulic buffer regions of the outer guide tubes at the end of each trip stroke.

   The buffer region slows the CEA during the last few inches of the trip stroke. The resultant differential pressure across the guide tube in this region is predicted to be 300 psi, and this gives rise to circumferential stresses of 3300 psi, which is less than one quarter of the yield stress, for a very short term. The trip is assumed to be repeated daily. However the resultant stress is too small to have a significant effect on fatigue usage.

For conditions other than normal operation, the additional mechanical loads imposed on the fuel assembly by an OBE (equivalent to one-half SSE), SSE, and large break LOCA and their resultant effect on the control element guide tubes are discussed in the following paragraphs:

4.2.3.1.2.1 Operating Basis Earthquake

During the postulated OBE, the fuel assembly is subjected to lateral and axial accelerations which, in turn, cause the fuel assembly to deflect from its normal shape. The method of calculating these deflections is described in Subsection 3.7.3.14. The magnitude of the lateral deflections and resultant stresses are evaluated for acceptability. The method for calculating stresses from deflected shapes is described in Reference 50. The results of the stress analysis demonstrate that the equipment stresses are less than the allowable values discussed in Subsection 4.2.1.1.

4.2.3.1.2.2 Safe Shutdown Earthquake

The axial and lateral loads and deformation sustained by the fuel assembly during a postulated SSE have the same origin as those discussed above for the OBE, but they arise from initial ground accelerations twice those used for the OBE. The analytical methods used for the SSE are identical to those used for the OBE. The predicted component stresses were less than the allowable values discussed in Reference 50.

4.2.3.1.2.3 Loss-of-Coolant Accident

→(DRN 03-2058, R14)
In the event of a large break LOCA, there will occur rapid changes in pressure and flow within the reactor vessel. Associated with the transient are relatively large axial and lateral loads on the fuel assemblies.
←(DRN 03-2058, R14)

→(DRN 03-2058, R14)
The response of a fuel assembly to the mechanical loads produced by a LOCA is considered acceptable if the fuel rods are maintained in a coolable array, i.e., acceptably low grid crushing. The methods used for analysis of combined seismic and LOCA loads and stresses is described in Reference 50. See Sections 3.6.2.1.1.1(d) and 3.6.3 for discussions on pipe break criteria and leak-before-break.
→(DRN 00-644)
←(DRN 03-2058, R14)
To qualify the complete fuel assembly, full-scale hot loop testing has been conducted. The tests were designed to evaluate fretting and wear of components, refueling procedures, fuel assembly uplift forces, holddown performance and compatibility of the fuel assembly with interfacing reactor internals, CEAs and CEDMs under conditions of reactor water chemistry, flow velocity, temperature, and pressure. Additional information on the test is given in Subsection 4.2.3.2.4.2. The test was run for approximately 2000 hours and was completed in 1976.
←(DRN 00-644)
Mechanical testing of the fuel assembly and its components has been performed to support analytical means of defining the assembly's structural characteristics. The test program consisted of static and dynamic tests of spacer grids and static and vibratory tests of a full size fuel assembly.

4.2.3.1.2.4 Combined SSE and LOCA

It is not considered appropriate to combine the stresses resulting from the SSE and LOCA events. Nevertheless for purposes of demonstrating margin in the design, the maximum stress intensities for each individual event were combined by a square root of the sum of the squares (SRSS) method. This was performed as a function of fuel assembly elevation and position, e.g., the maximum stress intensities for the center guide tube at the upper grid elevation (as determined in the analysis discussed in Subsections 4.2.3.1.2.2 and 4.2.3.1.2.3) were combined by the SRSS method. The results demonstrated that the allowable stresses described in Reference 50 were not exceeded for any position along the fuel assembly, even under the added conservatism provided by this load combination.

4.2.3.1.3 Spacer Grid Evaluation

As discussed in Subsection 4.2.2.1 the function of the spacer grids is to provide lateral support to fuel and burnable poison rods in such a manner that the axial forces are not sufficient to buckle or bow the rods and that the wear resulting at the grid-to-clad contact points will be limited to acceptably small amounts. It is also a criterion that the grid be capable of withstanding the lateral loads imposed during the postulated seismic and LOCA events.

→(DRN 02-1538, R12)
With respect to the design criterion that the axial restraint offered by the grids during initial assembly be such that the axial forces on a fuel rod are not sufficient to cause the rod to bow or buckle, it is currently understood that the observed instances of fuel rod bowing have occurred because the axial restraint of the spacer grids on the fuel rods was such that relative motion between the fuel rods and the grids (e.g., differential thermal expansion) could not occur except at axial forces high enough to cause slight bowing of the fuel rods. Fuel assemblies, however, are designed such that the combination of fuel rod rigidity, grid spacing, and grid preload will not cause significant fuel rod deformation under axial loads. The long-term effects of clad creep (reduction in clad OD), the reduction of grid stiffness with temperature, and the partial relaxation of the grid material during operation ensure that this criterion is also satisfied during all operating conditions. Moreover, visual inspection of irradiated fuel assemblies from the Maine Yankee (14 x 14), Palisades (15 x 15) and Fort Calhoun (14 x 14) reactors has not shown any significant bowing of the fuel rods. In view of these factors and the similarity of these designs to the Waterford 3 design, it is concluded that the axial forces applied by the grids on the cladding will not result in a significant degree of fuel rod bow. Additional discussion of the causes and effects of fuel rod bowing are contained in Subsection 4.2.3.2.6 and in References 53 and 75.
←(DRN 02-1538, R12)

→(EC-9533, R302)
The capability of the grids to support the clad without excessive clad wear has been demonstrated by out-of-pile flow testing, and by the results of post-irradiation examination of grid-to-clad contact points in Maine Yankee fuel assemblies which showed only negligible clad wear(51). An extensive flow test program was conducted to support the implementation of the NGF design. A full scale dual bundle test with a NGF fuel assembly and a standard fuel assembly was run to demonstrate the acceptability of the fretting performance of the NGF assembly design. The dual bundle test was an endurance test that provided confirmation of the hydraulic stability of the designs and showed a significant improvement in the fretting performance of the NGF design compared to the standard design.
←(EC-9533, R302)
→(DRN 00-644)
The capability of the grid to withstand the lateral loads produced during the postulated seismic and LOCA events is demonstrated by impact testing of the reference grid design and comparing the test results with the analytical predictions of the seismic and LOCA loads. The test methods are discussed in Reference 50.
←(DRN 00-644)
→(DRN 03-2058, R14)
For the original fuel design, the results of the load comparison were that under seismic loading no spacer grids in the core were subjected to loadings in excess of their capability based on test results. However, under LOCA conditions some fuel assemblies in the periphery of the core had spacer grids with predicted loads which exceeded the capability defined by testing. An ECCS analysis was performed for the core locations occupied by these fuel assemblies, and the results confirmed that the ECCS acceptance criteria (10CFR50.46) were still satisfied. The methods used in the ECCS evaluation were the same as used in previous analyses (Reference 77). In order to demonstrate margin in the design, spacer grid loadings from the SSE and LOCA events were combined by a square root of the sum of squares (SRSS) method, and no additional fuel assemblies were found to have grids which exceeded the capability defined by testing.

With the introduction of the HID-1L gird design, the grid strengths increased above those of the original fuel design such that the grid strengths exceeded the maximum grid impact loads. There was therefore no further need to perform the ECCS analysis to show that the HID-1L grid design was acceptable.

For the power uprate condition, updated LOCA loadings were determined which included a combination of power uprate and Leak-Before-Break effects. Seismic loadings remained unchanged. Because the loadings used in the analyses performed for the original fuel design are conservative and bounding with respect to the uprate loadings, there was no need to reevaluate the fuel assemblies.
←(DRN 03-2058, R14)
→(EC-9533, R302)
The NGF design utilizes straight-strip mid grids that have a higher spacer grid stiffness than the HID-1L spacer grids of the prior fuel designs. Due to this increased grid stiffness, the seismic and LOCA analyses were reevaluated for the mixed core and all NGF core cases. The results showed that the documented strengths of the NGF and HID-1L spacer grids exceeded predicted impact loads, but that the loading history simulated in the determination of the HID-1L grid strength did not bound the predicted loading history in some peripheral core locations. Instead of retesting the HID-1L grids with the predicted mixed core loading history, an ECCS evaluation was performed to demonstrate compliance with the ECCS acceptance criteria.

The Zircaloy-4 spacer grid material is of the same composition as the fuel rods and guide tubes with which it is in contact, thereby obviating any problem of chemical incompatibility with those components. For the same reason, adequate resistance to corrosion from the coolant is assured (see Subsection 4.2.3.2.3, for additional information relative to the corrosion resistance of Zircaloy-4 in the primary coolant environment). Similarly, the NGF design is not susceptible to chemical incompatibility since it utilizes Optimized ZIRLO™ spacer grids and Optimized ZIRLO™ cladding. In addition, the use of Optimized ZIRLO™ for the spacer grids offers improved corrosion resistance relative to the Zircaloy-4 spacer grids.
←(EC-9533, R302)

→(DRN 02-1538, R12; 06-1059, R15, LBDCR 15-025, R309)
The Inconel-625 material used for the lowest, and in some cases the uppermost, spacer grid is in contact with the coolant, the stainless steel lower end fitting (to which it is welded), the Zircaloy-4 or ZIRLO™ fuel and poison rods, and the Zircaloy-4 guide tubes. The mutual chemical compatibility of these materials in a reactor environment has been demonstrated by the use of these materials in fuel assemblies that have been operated in other C-E reactors and for which post irradiation examination has yielded no evidence of chemical reaction between these components. In addition, experiments have also been performed at C-E on Inconel type alloys and Zircaloy-4 which showed the eutectic reactions did not occur below 2200°F, a temperature far in excess of that anticipated at the lower grid location in the event of a LOCA.
←(DRN 02-1538, R12; 06-1059, R15, LBDCR 15-025, R309)
→(EC-9533, R302)
The Inconel-718 material used for the top spacer grid in the NGF design has similar material characteristics to the Inconel-625 material and has operated successfully in Westinghouse plants for many years with ZIRLO™ clad fuel rods. The slight reduction in tin content of the Optimized ZIRLO™ cladding compared to the ZIRLO™ cladding does not impact its compatibility with Inconel-718, as evidenced by the successful operation of the NGF lead fuel assemblies in Waterford and in other Westinghouse reactors.
←(EC-9533, R302)
The only dissimilarity, between the fuel for which post-irradiation examination data are presently available and the Waterford 3 design (other than dimensional variations), is that the Inconel-625 is used as a spacer grid for Waterford 3 and was used originally as a retention grid. However, the effect that such a change might have on fretting behavior has been evaluated in out-of-pile flow test programs (see Subsection 4.2.3.2.4.2).

→(EC-9533, R302)
4.2.3.1.4 Dimensional Stability of Zirconium-Based Alloys

→(DRN 06-1059, R15)
Zircaloy components are designed to allow for dimensional changes resulting from irradiation-induced growth. Extension analyses of in-pile growth data have been performed to formulate a comprehensive model of in-pile growth. The in-pile growth equations are used to determine the minimum axial differential growth allowance which must be included in the axial gap between the fuel rods and the upper end fitting. For determining the necessary fuel rod growth allowance, the growth correlations for fuel rod and guide tube growth are combined statistically such that the minimum initial gap is adequate to accommodate the upper 95 percent confidence level of differential growth between fuel rods and guide tubes in the peak burnup assembly for Zircaloy, ZIRLO™, and Optimized ZIRLO™ cladded rods. For the purpose of predicting axial and lateral growth of the fuel assembly structure (thereby establishing the minimum initial clearance with interfacing components), the equations are used in a conservative manner to ensure adequate margins to interference are maintained.
←(DRN 06-1059, R15; EC-9533, R302)
→(DRN 02-1538, R12)
Inspection of fuel assemblies after two cycles of operation at the Arkansas Nuclear One, Unit 2 reactor has shown higher rates of gap closure than predicted by the method described in Reference (3). Closure rates predicted by Reference (3) may remain valid for the Waterford 3 fuel assemblies because of differences in the Waterford and Arkansas designs. Nonetheless, additional shoulder gap has been provided in those fuel assemblies scheduled for three cycles of operation.
←(DRN 02-1538, R12)
The additional gap was selected to provide the maximum shoulder gap without violating other design criteria. Based on the shoulder gap reduction observed at ANO-2 at EOC2, the additional shoulder gap is expected to provide three cycle operation capability.
→(EC-9533, R302)
The NGF design incorporates material changes that improve the dimensional stability of the CEA guide tubes and the fuel rod cladding. These improvements allow a reduction in the NGF shoulder gap while still providing adequate space to accommodate rod burnups above 60,000 MWd/MTU.
←(EC-9533, R302)

4.2.3.1.5 Fuel Handling and Shipping Design Loads

Three specific design bases have been established for shipping and handling loads. These are as follows:

a) The fuel assembly, when supported in the new fuel shipping container, shall be capable of sustaining the effects of five g axial, lateral or vertical acceleration without sustaining stress levels in excess of those allowed for normal operation. The five g criterion was originally established experimentally, and its adequacy is continually confirmed by the presence of impact recorders as described in the following paragraph.

   Impact recorders are included with each shipment which indicate if loadings in excess of five g are sustained. A record of shipping loads in excess of five g indicates an unusual shipping occurrence in which case the fuel assembly is inspected for damage prior to releasing it for use.

   The axial shipping load path is through either end fitting to the guide tubes. A five g axial load produces a compressive stress level in the guide tubes less than the two-thirds yield stress limit that is allowed for normal condition events. The fuel assembly is prevented from buckling by being clamped at grid locations. For lateral or vertical shipping loads, the grid spring tabs have an initial preload which exceeds five times the fuel rod weight. Therefore, the spring tabs see no additional deflection as a result of five g lateral or vertical acceleration of the shipping container. In addition, the side load on the grid faces produced by a five g lateral or vertical acceleration is less than the measured impact strength of the grids.

b) The fuel assembly shall be capable of sustaining a 5000 pound axial load applied at the upper end fitting by the refueling grapple (and resisted by an equal load at the lower end fitting) without sustaining stress levels in excess of those allowed for normal operation. The 5000 pound load was chosen in order to provide adequate lift capability should an assembly become lodged. This load criterion is greater than any lift load that has been encountered in-service.

c) The fuel assembly shall be capable of withstanding a 0.125 in. deflection in any direction whenever the fuel assembly is raised or lowered from a horizontal position without sustaining a permanent deformation beyond the fuel assembly inspection envelope.

   Fuel handling procedures require the use of a strongback to limit the fuel assembly deflection to a maximum of 0.125 in. in any direction whenever the fuel assembly is raised or lowered to a horizontal position. This limits the stress and strain imposed upon the fuel assembly to values well below the limits set for normal operating conditions. The adequacy of the 0.125 in. criterion is based on the inclusion of this limitation in specifications and procedures for fuel handling equipment, which is thereby constrained to provide support that lateral deflection is limited to 0.125 in.

4.2.3.2 Fuel Rod Design Evaluation

The evaluations discussed in this section are based on assumed fuel rod operation within certain linear heat rate limits related to avoiding excessive fuel clad temperatures. Information concerning the bases for these limits is contained in Section 4.4.

4.2.3.2.1 Results of Vibration Analyses

Three sources of periodic excitation are recognized in evaluating the fuel rod susceptibility to vibration damage. These sources are as described in Subsection 4.2.3.1.1.

These sources of periodic motion are not expected to have an adverse effect on the performance of the fuel rod. Subsection 4.2.3.2.4 includes additional informaton on fuel rod response to the sources.

4.2.3.2.2 Fuel Rod Internal Pressure and Stress Analysis

→(DRN 02-1538, R12)

A fuel rod cladding stress analysis is conducted to determine the circumferential stress and strain resulting from normal, upset, and emergency conditions. The analysis includes the calculation of cladding temperatures and rod internal pressures during each of the occurrences listed in Subsection 4.2.1.1. The design criteria to be used to evaluate the analytical results are specified in Subsection 4.2.1.2.1. Fuel rod stresses resulting from seismic events are calculated, using the methodology described in Reference 50.

←(DRN 02-1538, R12)

4.2.3.2.3 Potential for Chemical Reaction

a) Corrosion

Corrosion tests of Zircaloy-4 fuel rod tubing which were conducted in excess of 4000 hours exposure include 600 and 650°F autoclave tests and 600°F loop tests with borated lithium hydroxide additives to the water chemistry. The test results agree with long term corrosion tests in lithium hydroxide reported by Bettis.(52) No deleterious effects have occurred.

→(DRN 02-1538, R12)

Experience at both Shippingport and Saxton Core I have shown under PWR conditions (hydrogen overpressure and chemical additives) that in reactor behavior with low heat flux was similar to autoclave behavior. Experience at the Saxton reactor in Cores II and III, however, have shown that with severe nucleate boiling, some accelerated corrosion was encountered. Similar accelerated corrosion with high crud deposits was also reported at KWO, but was terminated by using hydrogen overpressure and chemical additives.

→(DRN 00-644; 06-1141, R15; EC-9533, R302, LBDCR 15-035, R309)

Batch Y fuel rods were fabricated with ZIRLO™ cladding to improve the corrosion resistance of the fuel. Section 4.5 of Reference 80 presents corrosion data at high burnup for both Zircaloy-4 cladding and ZIRLO™ cladding and concludes that the ZIRLO™ cladding offers a significant improvement in the corrosion resistance of the cladding. NGF fuel rods are fabricated with Optimized ZIRLO™ cladding that has a slightly reduced tin content compared to ZIRLO™ specifically to improve its corrosion resistance. Autoclave steam testing demonstrated almost a 20% corrosion resistance improvement of Optimized ZIRLO™ compared to ZIRLO™. Reference 85 presents additional cladding corrosion data and provides updated cladding corrosion models for both ZIRLO™ and Optimized ZIRLO™ cladding.

←(EC-9533, R302, LBDCR 15-035, R309)

Coolant chemistry parameters have been specified that minimize corrosion product release rates and their mobility in the primary system. Specifically, the precore hot functional environment is controlled (ph and oxygen) to provide a thin, tenacious, adherent, protective oxide film. This approach minimizes corrosion product release and associated inventory on initial startup and subsequent operation. During operation, the specified lithium concentration range (0.2-3.5 ppm) effects a chemical potential gradient or driving force between hot and cooler surfaces (refuel cladding and steam generator tubing, respectively) such that soluble iron and nickel species will preferentially deposit on the steam generator surfaces. The associated ph also minimizes general corrosion product release rates from primary system surfaces. Moreover, the specified hydrogen concentration range (10-50 cm^3kg STP) ensures; reducing conditions in the core thereby avoiding low solubility Fe^{3+}. Additionally, dissolved hydrogen promotes rapid recombination of oxidizing species. Oxidizing species and a fast neutron flux are synergistic prerequisites to accelerated Ziraloy-4 corrosion.

←(DRN 00-644; 02-1538, R12; 06-1141, R15)

During operations lithium, dissolved oxygen, and dissolved hydrogen will be monitored at a frequency consistent with maintaining these parameters within their specifications.

→(EC-9533, R302)

Post-operational examinations of fuel cladding that has operated within these specifications, has shown no significant chemical or corrosive attack of the Zircaloy cladding. ZIRLO™ cladding and Optimized ZIRLO™ cladding are less sensitive to chemical or corrosive attack due to their better corrosion resistance.

←(EC-9533, R302)

b) External Hydriding

→(EC-9533, R302)

During operation of the reactor with exposure to high temperature, high pressure water, Zirconium-based cladding will react to form a protective oxide film in accordance with the following equation.

←(EC-9533, R302)

→(DRN 00-644)

$$Zr + 2H_2O = ZrO_2 + 2H_2$$

←(DRN 00-644)

Approximately 20 percent of the hydrogen is adsorbed by the Zircaloy. Based on data described in WAPD-MRP-107, the cladding would be expected to contain up to 250 ppm of hydrogen following three years of exposure.

A series of 600°F burst tests was performed on Zircaloy-4 tubes containing to 200 to 250 and 400 ppm of hydrogen precipitated as hydride platelets in various orientations from radial to circumferential. Additional burst tests have shown similar effects at 725°F. Little difference in burst test ductility was evident. Therefore, hydrogen normally adsorbed in Zr-4 tubing will not prove deleterious to the cladding integrity.

→(EC-9533, R302, LBDCR 15-035, R309)

The impact of hydrides and hydride reorientation in ZIRLO™ cladding is discussed in Section 4.4.2.5 of Reference 80, where it is concluded that the performance of the ZIRLO™ cladding will be similar to that of the Zircaloy-4 cladding since the hydride reorientation is primarily a function of the tensile stresses and temperatures in the cladding. Due to the similarity of the material composition of Optimized ZIRLO™ and ZIRLO™, the same conclusion applies for Optimized ZIRLO™ cladding. Reference 85 provides updated data and models for ZIRLO™ and Optimized ZIRLO™ cladding.

←(EC-9533, R302, LBDCR 15-035, R309)

c) Internal Hydriding

A number of reported fuel rod failures have resulted from excessive moisture available in the fuel. Under operation, this moisture would flash to steam and oxidize the Zircaloy.

The hydrogen, which was not absorbed during normal oxidation, would then be absorbed into the Zircaloy through a scratch in the oxide film. This localized hydrogen absorption by the cladding would shortly result in a localized fuel rod failure. Work performed at the Institt for Atomenergi, Halden, Norway, of which C-E is a member, demonstrated that a threshold value of water moisture is required for hydride sunbursts to occur. Through a series of in-pile experiments, the level of this threshold value was established. The allowable hydrogen limit in the fuel complies with this requirement, ensuring that hydride sunbursts will not occur.

d) Crud

The slow general corrosion of out-of-core plant surfaces will release corrosion products to reactor coolant, some of which will deposit on core surfaces as "crud". The major constituents of crud are iron and nickel, with lesser amounts of chromium and traces of manganese and cobalt, all present as oxides. Crud is essentially a nickel ferrite ($Ni_xFE_{3-x}O_4$) with "x" in the range 0.45-0.75. Chromium appears to enter the inverse spinel substantially to give a composition $CR_yNi_xFe_{3-x-y}O_4$ (Reference 69). The porosity of core crud deposits is typically given as 80 to 85 percent (density ~ 1.2 g/cm^3.)

Although there are significant efforts underway within the industry to develop mathematical models for crud transport in reactor coolant systems (e.g., see Reference 70), at present there are not analytical techniques available for estimating crud buildup on fuel surfaces.

Although heavy crud deposits have been observed in older plants (see Reference 71), measurements made on modern pressurized water reactors indicate that crud buildup is low, ranging from < 0.02 mils up to a few tenths of a mil (see Reference 72). As discussed in Subsection 4.2.3.2.3 a) above, coolant chemistry parameters have been specified to minimize crud deposition. Visual inspection of fuel removed from CE's Calvert Cliffs I plant, which operated under these specifications, revealed relatively light crud deposits, such that clad surface features from fabrication could be discerned (see Reference 73). Similar behavior is anticipated for the Waterford 3 core.

Enhanced corrosion of Zircaloy cladding should not occur under light deposits of porous crud. Water is free to flow through porosity in the crud, providing heat transfer through convection. Even heavy crud found in Yankee Rowe (Reference 71) was non-insulating because of its porosity.

e) Fuel-Cladding Chemical Reaction

An in-depth Post Irradiation Examination has been conducted wherein fuel-cladding chemical reactions were among those items studied. This study concluded that early unpressurized elements containing unstable fuel were more susceptible to stress corrosion attack than are those of the current design that utilizes stable fuel and pressurized cladding. Since stress corrosion attack is the result of a combination of stress imposed by the fuel on the cladding and the corrosive chemical species available to the cladding, irradiation programs are being pursued to define the conditions under which pellet-clad interaction will damage the cladding. These programs are currently underway both at Halden and in the Pathfinder test program being conducted jointly with KWU in the Obrigheim and Petten reactors.

4.2.3.2.4 Fretting Corrosion

The phenomenon of fretting corrosion, particularly in Zircaloy clad fuel rods supported by Zircaloy spacer grids, has been extensively investigated. Since irradiation-induced stress relaxation causes a reduction in grid spring load, spacer grids must be designed for end-of-life conditions as well as beginning-of-life conditions to prevent fretting caused by flow - induced tube vibrations. To ensure this, out-of-pile fretting tests have been performed concentrating on the more severe end-of-life conditions. Two testing approaches have been used; i.e., autoclave vibration tests and dynamic flow tests.

4.2.3.2.4.1 Autoclave Vibration Tests

The autoclave tests were performed by vibrating a fuel rod sample supported by two rigidly held spacer grid sections. Test conditions matched reactor coolant chemistry, temperature, and pressure. Variable parameters provided data to evaluate the effects of:

a) Frequency of tube vibration

b) Spacer grid spring load (preset)

c) Axial tube movement (simulating reactor load following characteristics)

Data from such tests have indicated that wear starts with a brief break-in period and then proceeds at a negligible rate. Changes in frequency, spring present (including zero preset) and amplitude within representative limits do not significantly alter fretting characteristics. At no time under any conditions was fretting significant.

4.2.3.2.4.2 Dynamic Flow Tests

Dynamic flow tests have been performed on four x four rod arrays (16 fuel rods) and on full size fuel assemblies. The four x four rod array testing was conducted under the following conditions:

a) Flow velocities ranged from 14 ft/sec to 25 ft/sec

b) Coolant temperature was 590°F

c) Coolant pressure was 2150 psia

In addition, the four x four rod arrays were subjected to cross-flow and a mechanically induced forced vibration of the lower end of the rod array at a frequency of 15 Hz and an amplitude of five mils (representing vibratory forces imparted by the reactor internals). The four x four rod array testing also included rod arrays with preset spacer grid springs ranging from approximately 10 mils interference to gaps of up to five mils, simulating both tightly held and loose rods. The four x four rod arrays were tested for intervals from 1000 hours up to 3182 hours for a total accumulated test time of 18,000 hours.

The fuel rods in the four x four assemblies were either of a 0.413 in. diameter on a 0.550 in. pitch or of a 0.440 in. diameter on a 0.580 in. pitch, which are representative of a 15 x 15 and 14 x 14 fuel array, respectively. All fuel rods were visually inspected at each spacer grid interface. The depth of wear marks was accurately determined using an optical micrometer. The maximum depth of wear noted for the conditions above was less than 1/2 mil. In a special test where a fuel rod was completely unsupported at its lower end for a distance of 15 in., a depth of wear of three mils was noted after 2000 hours of flow at 25 ft/sec. This test was not representative of any design condition, but was performed to demonstrate the need for supporting the lower end of the fuel rod. Based on test results of four x four assemblies which follow the same trend as found in the autoclave vibration test, the maximum expected clad wear at end-of-life will be will be less than three mils.

Separate full scale flow tests at or exceeding reactor flow conditions were run with an array of four full-size prototypical 15 x 15 fuel assemblies, four full size 14 x 14 fuel assemblies of which two were prototypical and two contained stainless steel fuel rods, several tests of individual full size 14 x 14 fuel assemblies and a prototype 16 x 16 fuel assembly. The test conditions were as follows:

a) Flow velocities ranged from 16 ft/sec for 15 x 15 fuel assemblies up to 23.7 ft/sec for some of the 14 x 14 fuel assemblies, and 22 ft/sec for the 16 x 16 fuel assembly. In all cases, the flow test velocities exceeded the maximum calculated velocity at operating conditions for fuel assemblies in each particular reactor.

b) A large number of fuel rods (in some cases all rods within a fuel assembly) were tested with zero preset Zircaloy spacer grid spring loads to conservatively represent end-of-life spacer grid conditions. A number of fuel rods were also loosely supported at various spacer grid locations, and, in some cases, over the entire length of the rod.

c) Test time accumulated exceeded 13,500 hours, with the longest single test 4000 hours in length.

The results of these tests are similar to those of the four x four fuel assemblies with a few exceptions. On the 14 x 14 fuel assemblies subjected to 4000 hours of continuous testing at 23.7 ft/sec and 1000 hours at 19.1 ft/sec, the maximum depth of wear on one assembly was 1.7 mils, while on the other assembly, one wear mark was found to be 2.2 mils deep and a few others ranged from 1.6 to 1.8 mils. The only incidence of significant wear on a full size fuel assembly occurred in special test of an off-design condition where the lower end of the fuel assembly was essentially unrestrained laterally. In this test, the depth of wear of one fuel rod was 10.9 mils after only 1188 hours of testing at 23.7 ft/sec. Again, this test, as in the case of the cantilevered fuel rod test in a four x four fuel assembly, showed the need for laterally restraining the lower end of the fuel assembly.

→(EC-9533, R302)
Results for the 16 x 16 fuel assembly test, where the Zircaloy spacer grid springs were preset to zero interference and the Inconel grid springs were preset to a small interference with the fuel rods, showed no evidence of fretting on any fuel rod after 1000 hours of testing.

An extensive flow test program was conducted to support the implementation of the NGF design. The NGF configuration was tested to confirm the hydraulic stability of the fuel assembly design and to demonstrate the acceptability of the fretting performance of the fuel assembly design. These tests included full scale single bundle tests of the NGF and standard designs, a full scale dual bundle test with a NGF fuel assembly and a standard fuel assembly, and a full cross-section/short length bundle test of the NGF design. The single bundle tests were run to evaluate the hydraulic stability of the fuel assemblies. The tests demonstrated the hydraulic stability of both designs over the expected range of flow rates. The dual bundle test was an endurance test to evaluate fretting performance of the two designs. This test provided additional confirmation of the hydraulic stability of the designs and showed a significant improvement in the fretting performance of the NGF design compared to the standard design. The short length bundle test was run to confirm the absence of flow-induced strip vibration within the spacer grids, which it did. The successful results of the flow test program demonstrate that the hydraulic performance of the NGF design is acceptable and superior to that of the prior designs.
←(EC-9533, R302)

4.2.3.2.5 Cycling and Fatigue

A fatigue analysis is performed to determine the cumulative fatigue damage of fuel rods exposed to lifetime power cycling conditions. The fatigue cycle is determined by considering combinations of normally anticipated events that would produce conservative estimates of strain in the clad. Some of the major conservative assumptions are as follows:

a) Hot spot fuel radii are used in the calculations

b) The most adverse tolerance conditions on the fuel and cladding dimensions are chosen to produce maximum interactions and hence maximum clad strains.

The chosen fatigue cycle represents daily operation at both full and reduced power. Clad strains are calculated from the primary creep rate of the clad and used to calculate the effective strain ranges. The cumulative fatigue damage fraction is determined by summing the ratios of the number of cycles at a given effective strain range to the permitted number at that range as taken from the fatigue curve presented in Figure 4.2-2.

4.2.3.2.6 Fuel Rod Bowing

Analysis of bowing data has shown that the bowing expected in the 16 x 16 design will have no effect on the margin to DNB beyond the allowance provided by the pitch, bowing and clad diameter enthalpy rise factor given in Table 4.4-1 and discussed in Section 4.4. A more complete discussion of the cause and effects of rod bowing is presented in References 53 and 75.

4.2.3.2.7 Irradiation Stability of Fuel Rod Cladding

The combined effects of fast flux and cladding temperature are considered in three ways as discussed below:

a) Cladding Creep Rate

→(EC-9533, R302)

The in-pile creep performance of Zircaloy-4, ZIRLO™, and Optimized ZIRLO™ are dependent upon both the local material temperature and the local fast neutron flux. The functional form of the dependencies for Zircaloy-4 cladding is presented in Reference 14 for gap conductance calculations, and in Reference 22 for cladding collapse time predictions. The corresponding functional form of the dependencies is presented in Reference 80 for ZIRLO™ cladding, while Reference 83 documents that the similarities between the ZIRLO™ cladding and the Optimized ZIRLO™ cladding result in the same correlation for the two materials.

←(EC-9533, R302)

b) Cladding Mechanical Properties

The yield strength, ultimate strength, and ductility of Zircaloy-4 are dependent upon temperature and accumulated fast neutron fluence. The temperature and fluence dependence is discussed in Subsection 4.2.1.2.2.1. Unirradiated or irradiated properties were used depending upon which is more restrictive for the phenomenon being evaluated.

c) Irradiation Induced Dimensional Changes

→(EC-9533, R302)

Zirconium-based alloys have been shown to sustain dimensional changes (in the unstressed condition) as a function of the accumulated fast fluence. These changes are considered in the appropriate clearances between the various core components. The irradiation induced growth correlation method is discussed in Reference 3 (see Subsection 4.2.3.1.4), with the rod growth correlations specified in Reference 82 for Zircloy-4 cladding, Reference 80 for ZIRLO™ cladding, and Reference 84 for Optimized ZIRLO™ cladding.

Zircaloy-4 fuel cladding has been utilized in pressurized water reactors at temperatures and burnups anticipated in current designs with no failures attributable to radiation damage. Mechanical property tests on Zircaloy-4 cladding exposed to neutron irradiation of 4.7×10^{21} nvt (estimated) have revealed that the cladding retains a significant amount of ductility (in excess of four percent elongation). Typical results are shown in Table 4.2-2. It is believed that the fluence of 4.7×10^{21} nvt is at saturation so that continued exposure to irradiation will not change these properties.(54) Similar performance has been experienced with ZIRLO™ cladding and Optimized ZIRLO™ cladding, as detailed in Reference 80 and 83, respectively.

←(EC-9533, R302)

4.2.3.2.8 Cladding Collapse Analysis

→(DRN 02-1538, R12)

A cladding collapse analysis is performed to ensure that no fuel rod in the core will collapse during its design lifetime. The clad collapse calculation method(22) itself does not include arbitrary safety factors. However, the calculation inputs are deliberately selected to produce a conservative result. For example, the as-built clad dimensional data are chosen to be worst case combinations which result in 95 percent confidence in minimum predicted collapse time; the internal pressure history is based on minimum fill pressure with no assistance from released fission gas; and the flux and temperature histories are based on conservative assumptions. The combined effect of using conservative inputs in the clad buckling analysis method is to produce computed collapse time in excess of three cycles of operation.

←(DRN 02-1538, R12)

4.2.3.2.9 Fuel Dimensional Stability

Fuel swelling due to irradiation (accumulation of solid and gaseous fission products) and thermal expansion results in an increase in the fuel pellet diameter. The design makes provision for accommodating both forms of pellet growth. The fuel-clad diametral gap is more than sufficient to accommodate the thermal expansion of the fuel. To accommodate irradiation-induced swelling, it is conservatively assumed that the fuel-clad gap is reduced by the thermal expansion and that only the volume due to fuel porosity and the dishes on each end of the pellets are available. Thermal and irradiation induced creep of the restrained fuel results in redistribution of fuel so that the swelling due to irradiation is accommodated by the free volume (eight percent of the fuel volume).

→(DRN 00-644)
For such restrained pellets, and at a total fission-product-induced swelling rate of 0.7 percent Δ V/V per 10^{20} fissions/cm^3, 0.54 percent would be accommodated by the fuel porosity and dished pellet ends through fuel creep, and 0.16 percent would increase the fuel diameter. Assuming peak burnup, this would correspond to using up a void volume equal to approximately 7.4 percent of the fuel volume and increasing the fuel rod diameter by a maximum of < 0.0025 in. (< 0.7 percent clad strain). When these numbers were compared to the minimum available volume and the maximum allowable strain, it was concluded that sufficient accommodation volume has been provided even under the most adverse burnup and tolerance conditions.

Demonstration of the margin which exists is seen in the large seed blanket reactor (LSBR) irradiation. Two rods which operated in the B-4 loop of the MTR offer an interesting simulation for current PWR design.(6) (7) (55)

Both rods were comprised of 95 percent theoretical density pellets with dished ends and clad in Zircaloy. The first of these, No. 79-21, was operated successfully to a burnup of 12.41 x 10^{20} fissions/cm^3 (>48.00 MWd/MTU). The second fuel pin, No. 79-25, operated successfully to 15.26 x 10^{20} fissions/cm^3 (>60,000 MWd/MTU). The linear heat rating ranged from 7.1 to 16.0 KW/ft. The wall thickness for the latter pin was 0.028 in. as compared with 0.016 in. for the former. All other parameters were essentially identical. The two rods were assembled by shrinking the cladding onto the fuel. The maximum diametral increase measured at the ridge heights for rod 79-21 was 0.005 in., while it was less than 0.002 in. for rod 79-25. From post-irradiation examination, it was concluded that approximately 84 percent of the total fuel swelling was accommodated by the porosity and dishes, while 16 percent caused diametral expansion of the clad and ridging at pellet interfaces. These results indicate that a comparable irradiation of the fuel elements for Waterford 3 (cold diametral gap 0.007 in., wall thickness of 0.025 in., density 94.75 percent TD) would allow adequate margin for swelling accommodation.

The successful combined VBWR-Dresden irradiation of Zircaloy-clad uranium dioxide pellets provides additional confidence with respect to the design conditions for the fuel rods for this core.(56)(57) Ninety-eight rods which had been irradiated in VBWR to an average burnup of about 10,700 MWd/MTU were assembled in fuel bundles and irradiated in Dresden to a peak burnup greater than 48,000 MWd/MTU. The reported maximum heat rating for these rods is 17.3 KW/ft which occurred in VBWR. Post-irradiation examination(58) revealed that diametral increases in the fuel rods ranged from 0.001 to 0.003 in. maximum. The maximum diametrical change corresponds to 1.42 percent Δ V/V, (or 0.12 percent Δ V/V per 10^{20} fission/cm^3) for these 0.424 in. diameter rods. The relevant fuel parameters are listed below for the above test and the Waterford 3 design.
←(DRN 00-644)

	Fuel Density %TD	Cold Diametral Gap (in.)	Peak Burnup (MWd/MTU)
VBWR-Dresden	95	0.004 to 0.008	>48,000
LSBR-MTR	95	0.001	50,000; 61,000
Waterford 3	94.75	0.007	55,000

A comparison of the design parameters above, relative to the test results, provides a demonstration of the clad strains resulting from swelling of fuel.

4.2.3.2.10 Potential for Waterlogging Rupture and Chemical Interaction

The potential for waterlogging rupture is considered remote. Basically, the necessary factor or combination of factors, include the presence of a small opening in the cladding, time to permit filling of the fuel rod with water, and finally a rapid power transient. The size of the opening necessary to cause a problem falls within a fairly narrow band. Above a certain defect size, the rod can fill rapidly, but during a

power increase it also expels water or steam readily without a large pressure buildup. Defects which could result in an opening in cladding are scrupulously checked for during the fuel rod manufacturing process by both ultrasonic and helium leak testing. Clad defects which could develop during reactor operation due to hydriding are also controlled by limiting those factors (e.g., hydrogen content of fuel pellets) which contribute to hydriding.

The most likely time for a waterlogging rupture incident would be after an abnormally long shutdown period. After this time, however, the startup rate is controlled so that even if a fuel rod were filled with coolant, it would "bake out", thus minimizing the possibility of additional cladding rupture. The combination of control and inspection during the manufacturing process and the limits on the rate of power change restrict the potential for waterlogging rupture to a very small number of fuel rods.

The UO_2 fuel pellets are highly resistant to attack by reactor coolant in the event cladding defects should occur. Extensive experimental work and operating experience have shown that the design parameters chosen conservatively account for changes in thermal performance during operation and that coolant activity buildup resulting from cladding rupture is limited by the ability of uranium dioxide to retain solid and gaseous fission products.

4.2.3.2.11 Fuel-Cladding Interaction

An analytical model to evaluate cladding response to pellet-clad interaction has been developed(21). This analysis which is based on an advanced version of the FATES computer code, considers generalized plane-strain of a unit section of fuel and clad. All of the physical phenomena calculational methods and input variables of the present FATES program(14) are included in the new version; and in addition, models are included for elastic and plastic stresses and strains in the clad and fuel, and fuel creep. A compatible interface modeled between the fuel and clad ensures that interaction is accurately accounted for.

The treatment of power history, axial power shapes and other operating parameters is handled similar to the current FATES version with the exception that power ramp rates and cycling can be considered. The response of the fuel and clad is calculated through an iteractive process, and the interaction between the fuel and clad is established.

The resulting analytical predictions of temperatures, stresses, strains and geometric configuration are thus made available for use in conjunction with operating experience and irradiation test results in demonstrating the acceptability of the various operating conditions to which the fuel may be subjected. A detailed discussion of the methods and capabilities of the pellet-clad interaction model is contained Reference 21.

4.2.3.2.12 Fuel Burnup Experience

→(EC-9533, R302)

Design bases for the Zircaloy-4, ZIRLO™, and Optimized ZIRLO™ cladding have been established which are conservative with respect to the reported data. Evidence currently available indicates that these claddings and UO_2 fuel performance is satisfactory to exposures in excess of 60,000 MWd/MTU.

←(EC-9533, R302)

a) High Linear Heat Rating Irradiation Experience

→(DRN 00-644)

The determination of the effect of linear heat rating and fuel cladding gap on the performance of Zircaloy-clad UO_2 fuel rods was the object of two experimental capsule irradiation programs conducted in the Westinghouse Test Reactor (WTR).(59) In the first program, 18 rods containing 94 percent theoretical density UO_2, pellets were irradiated at 11, 16, 18, and 25 kW/ft with cold diametral gaps of 0.006 in., 0.012 in., and 0.025 in. The wall thickness to diameter ratio (t/OD) of the Zircaloy cladding was 0.064 which is comparable to the 0.066 value in this design. Although

←(DRN 00-644)

these irradiations were of short duration (about 40 hours) significant results applicable to this design were obtained. No significant dimensional changes were found in any of the fuel rods. Only one rod, which operated at a linear heat rate of 24 kW/ft with an initial diametral gap of 0.025 in., experienced center melting. Rods which operated at 24 kW/ft with cold gaps of 0.006 in. and 0.012 in. did not exhibit center melting. On these bases, the initial gap of 0.007 in. and the maximum linear heat ratings for this design provide adequate margin against center melting, even when 112 percent overpower conditions are considered. These results also indicate that an initial diametral gap of 0.007 in. is adequate to accommodate radial thermal expansion without inducing cladding dimensional changes even at a linear heat rate of 24 kW/ft. This margin with respect to thermal expansion will be diminished with increasing burnup at a rate of 0.16 percent Δ V/V per 10^{20} fissions/cm^3. However, the linear heat rating will decrease with burnup and thus limit the sum of the strains to values below the allowable.

Further substantiation of the capability of operation at maximum linear heat ratings in excess of those in this design is obtained from later irradiation tests in WTR.(59) Fuel rods 38 in. long and 6 in. long were irradiated at linear heat ratings of 19 kW/ft and 22.2 kW/ft to burnups of 3450 and 6250 MWd/MTU. The cold diametral gaps in these Zircaloy clad rods containing 94 percent dense UO_2 were 0.002 in., 0.006 in., and 0.012 in. The cladding t/OD was 0.064. No measurable diameter changes were noted for the 0.006 in. or 0.012 in. fuel clad gap rods. Only small changes were observed for the rods with a 0.002 in. diametral gap.

b) Shippingport Irradiation Experience

Zircaloy clad fuel rods have operated successfully (three defects have been observed which were a result of fabrication defects) in the Shippingport blanket with burnups of about 37,000 MWd/MTU and maximum linear heat ratings of about 13 kW/ft. (59)(60)(61) Although higher linear heat ratings will be experienced, swelling (primarily burnup dependent) and thermal expansion (linear heat rating dependent) provide the primary forces for fuel cladding strain at the damage limit. Thus, the Shippingport irradiations have demonstrated that Zircaloy clad rods with a cladding t/OD less than that for this plant (0.066) can successfully contain the swelling associated with 37,000 MWd/MTU burnup while at the same time containing the radial thermal expansion associated with peak linear heat ratings. Irradiation test programs in support of Shippingport in-reactor loops demonstrated successful operation at burnups of 40,000 MWd/MTU and linear heat ratings of about 11 kW/ft with cladding t/OD ratios as low as 0.053.(62)

c) Saxton Irradiation Experience

→(DRN 02-1538)

Zircaloy-4 clad fuel rods containing UO_2-PuO_2 pellets of 94 percent theoretical density have been successfully irradiated in Saxton to peak burnups of 31,800 MWd/MTU at 15 kW/ft linear heat rate under USAEC Contract AT (30-1)-3385(63). The t/OD of the cladding was 0.059 which is less than that of this design. The amount of PuO_2, 6.6 percent is considered as insignificant with respect to providing any difference in performance when compared with that for UO_2. Subsequent tests on two of the above rods (18,000 MWd/MTU at 10.5 kW/ft) successfully demonstrated the capability of these rods to undergo power transients from 16.8 kW/ft to 18.7 kW/ft.

←(DRN 02-1538)

d) Vallecitos Boiling Water Reactor (VBWR) - Dresden Experience

→(DRN 02-1538)

The combined VBWR - Dresden irradiation of Zircaloy clad oxide pellets provides additional confidence with respect to the design conditions for the fuel rods for this core.[55][57][64] Ninety-eight rods which had been irradiated in VBWR to an average burnup of about 10,700 MWd/MTU were assembled in fuel bundles and irradiated in Dresden to a peak burnup greater than 48,000 MWd/MTU. The reported maximum heat ratings for these rods is 17.3 kW/ft which occurred in VBWR. The t/OD cladding ratio of 0.052, and the external pressure of about 1000 psia are conditions which are all in the direction of less conservatism with respect to fuel rod integrity when compared with the design values of 0.066 cladding t/OD ratio and an external pressure of 2250 psia. Ten of these VBWR - Dresden rods representing maximum combinations of burnup, linear heat rating, and pellet density have been examined in detail and found to be in satisfactory condition. The remaining 88 rods were returned to Dresden and successfully irradiated to the termination of the program.

←(DRN 02-1538)

e) Large Seed Blanket Reactor (LSBR) Rods Experience

Two rods operated in the B-4 loop at the Materials Testing Reactor (MTR) provide a very interesting simulation for current PWR designs [6][7][52]. Both rods were comprised of 95 percent theoretical density pellets with dished ends, clad in Zircaloy. The first of these No. 79-21, was operated successfully to a burnup of 12.41 x 10^{20} fiss/cm^3 (48,000 MWd/MTU) through several power cycles which included linear heat rates from 5.6 to 13.6 kW/ft. The second fuel pin, No. 79-25, operated successfully to 15.26 x 10^{20} fiss/cm^3 (60,000 MWd/MTU). The basic difference in this rod was the 0.028 in. wall thickness as compared to 0.016 in. (t/OD = 0.058) in the first rod. All other parameters were essentially identical.

The linear heat rating ranged from 7.1 to 16.0 kW/ft. After the seventh interim examination, the rod operated at a peak linear power of 12.9 kW/ft at a time when the peak burnup was 49,500 MWd/MTU. These high burnups were achieved with fuel elements which were assembled by shrinking the cladding onto the fuel and indicate that a comparable irradiation of the fuel elements for this reactor (cold diametral gap of 0.007 in.) would allow a considerable increase in swelling life at a given clad strain.

f) Central Melting in Big Rock Point Experience

→(DRN 00-644)

As part of a joint U.S. - Euratom Research and Development Program, Zircaloy clad UO_2 pellet rods (95 percent theoretical density) were irradiated under conditions designed to induce central melting in the Consumers Power Co. Big Rock Point Reactor[65]. The test includes 0.7 in. diameter fuel rods (cladding t/OD = 0.057; fuel clad gap of about 0.012 in.) at maximum linear heat ratings of about 27 kW/ft and 22 kW/ft with peak burnups up to 30,000 MWd/MTU. Result of these irradiations provide a basis for incorporating linear heat ratings well in excess of those calculated for this reactor, and show that the presence of localized regions of fuel melting is not catastrophic to the fuel rod.

←(DRN 00-644)

g) KWU Irradiations-Kraftwerk Union Reactor, Obrigheim, Germany

C-E has entered into a technical agreement with Kraftwerk Union (KWU) for the complete exchange of information and technology relating to pressurized water reactor systems including fuel.

This agreement makes available to C-E the experience of eight years successful operation of the KWO reactor at Obrigheim, Germany.

→(DRN 00-644; 02-1538, R12)

In the area of nuclear fuel performance, the experience at Obrigheim has shown successful operation through seven operating cycles. Fuel batches of 95 percent TD, both pressurized and nonpressurized, have been irradiated. Substantial testing has been performed in the reactor on the load following ability of both pressurized and nonpressurized fuel rods. Selected rods were subjected to power changes from 50 to 100 percent at rates of 20 percent/min for more than 900 cycles. Peak power densities in the rods were 15 kW/ft with maximum burnups in excess of 30,000 MWd/MTU. No failures have been observed to date. This experiment demonstrates the load-following capability of a design similar to C-E's in an operating PWRs.

←(DRN 00-644; 02-1538, R12)

h) Long Term Irradiation Testing

As indicated, C-E has several self-sponsored fuel irradiation programs in progress and several cooperative fuel development programs with Kraftwerk Union as part of a technical agreement. In addition, C-E has access to all data and results of Kraftwerk Union's own fuel development programs.

→(EC-9533, R302)

i) High Burnup Combustion Engineering Operational Experience

Reference 82 presents fuel performance data obtained during poolside examinations and hot cell examinations of high burnup fuel utilizing Zircaloy-4 cladding in Combustion Engineering cores. The data demonstrates the acceptability of the fuel’s performance to rod average exposures in excess of 60,000 MWD/MTU.

j) Westinghouse Experience

ZIRLO™ cladding material is in widespread use domestically in at least 38 nuclear power plants (Reference 80, Section 3.3). ZIRLO™ has been shown to have improved corrosion resistance compared to Zircaloy-4. Also, no oxide spalling has been observed in current ZIRLO™ fuel rods for normal operation.

→(LBDCR 15-035, R309)

Optimized ZIRLO™ cladding has a slightly lower allowed tin level than ZIRLO™ (lower by 0.2%) with the remainder of the material composition requirements being the same. The reduced tin level is to further enhance the corrosion resistance of the cladding. Reference 83 documents that ZIRLO™ material properties currently utilized in various models and methodologies are applicable to analyses for Optimized ZIRLO™ and shows the differences are negligible with no impact on any design or safety analyses. Reference 85 presents additional cladding corrosion data and provides updated cladding corrosion models for both ZIRLO™ and Optimized ZIRLO™ cladding. Therefore, in addition to the operational experience of Optimized ZIRLO™, the ZIRLO™ operational experience discussed above is applicable to Optimized ZIRLO™.

←(EC-9533, R302, LBDCR 15-035, R309)

4.2.3.2.12.1 Combustion Engineering Fuel Development Programs

→(DRN 02-1538, R12)

Since mid-1972, C-E has performed an extensive irradiation test program on fuel densification. When fuel densification became apparent, C-E immediately initiated an irradiation test program to determine the causes of densification and to define the specifications and processes required to limit densification of fuel. The first irradiation test program in the sequence confirmed that the phenomena is real and defined

←(DRN 02-1538, R12)

→(DRN 02-1538, R12)
the parameters important in the effect. An immediate response was a change in the C-E fuel pellet specification and a modification of the fuel fabrication process to provide densification resistant UO_2 fuel. The irradiation tests are continuing to establish conclusively that the current specification and process used is effective in minimizing densification.
←(DRN 02-1538, R12)
C-E is also a participating member of the Halden Reactor Project in Halden, Norway. The Halden project has underway a spectrum of fuel development programs from which C-E can further verify present fuel design models and continually evaluate advanced fuel design concepts.

4.2.3.2.12.2 Combustion Engineering/Kraftwerk Union Fuel Development Programs

The primary objectives of the cooperative fuel development programs are:

a) To assess the causes of fuel densification and provide process changes which will preclude densification. Then subsequently to verify through irradiation testing that the process changes have been effective.
b) To obtain long term data to further verify fuel performance models.

c) To evaluate advanced fuel design concepts in-reactor.

C-E and KWU currently have three densification test programs in progress in both United States and European test reactors. In addition, C-E and KWU are participating extensively in the densification test program under primary sponsorship of the Edison Electric Institute.

4.2.3.2.12.3 Kraftwerk Union Fuel Development Programs
→(DRN 00-644)
The design of the C-E fuel rods is very similar to the KWU fuel utilized in the Obrigheim reactor. The Obrigheim core has operated with peak power densities up to 15 kW/ft with maximum burnups in excess of 46,000 MWd/MTU without observed life limiting failures. Several fuel rods, both pressurized and unpressurized, from the Obrigheim reactor have undergone detailed hot cell examination under the direction of KWU. The results of all nondestructive fuel examinations performed during shutdowns and the complete results of the hot cell program are available to C-E under the technical agreement with KWU.
←(DRN 00-644)
In addition to the programs to routinely examine high burnup standard fuel, KWU also has comprehensive fuel development programs underway which utilize special test assemblies in the Obrigheim reactor. Under this program, fuel rod design parameters have been varied over significant ranges to experimentally establish the basis for further design optimization. One assembly has been irradiated annually since October 1973. Also included in this special assembly are segmented rods or "rodlets" which are connected to form a complete fuel rod. These rodlets are preirradiated in a test reactor. The test reactor irradiations provide data on fuel rod performance under transient conditions.

In summary, C-E has in process, or in the planning stages, fuel development programs that will provide additional assurance of fuel design adequacy.

4.2.3.2.13 Temperature Transient Effects Analysis

4.2.3.2.13.1 Waterlogged Fuel

The potential for a fuel rod to become waterlogged during normal operation is discussed in Subsection 4.2.3.2.10. In the event that a fuel rod does become waterlogged at low or zero power, it is possible that a subsequent power increase could cause a buildup of hydrostatic pressure. It is unlikely that the pressure would build up to a level that could cause cladding rupture because a fuel pin with the potential for rupture requires the combination of a very small defect together with a long period of operation at low or zero power.

Tests which have been conducted using intentionally waterlogged fuel pins (capsule drive core at SPERT)[66][67] showed that the resulting failures did eject some fuel material from the rod and greatly deformed the test specimens. However, these test rods were completely sealed, and the transient rates used were several orders of magnitude greater than those allowed in normal operation.

In those instances where waterlogged fuel rods have been observed in commercial reactors, it has not been clear that waterlogging was the cause, and not just the result, of associated cladding failures; and C-E has not observed any case in which material was expelled from waterlogged fuel rods.

It is therefore, concluded that the effect of normal power transients on waterlogged fuel rods is not likely to result in cladding rupture and even if rupture does occur it will not produce the sort of postulated burst failures which would expel fuel material or damage adjacent fuel rods or fuel assembly structural components.

4.2.3.2.13.2 Intact Fuel

The thermal effects of anticipated operational occurrences on fuel rod integrity are discussed in the following paragraphs.

a) Fuel rod thermal transient effects are basically manifested as the change in internal pressure, the changes in clad thermal gradient and thermal stresses, and the differential thermal expansion between pellets and clad. These effects are discussed in Subsections 4.2.3.2.2 and 4.2.3.2.11.

b) Another possible effect of transients would be to cause an axial expansion of the pellet column against a flattened (collapsed) section of the clad. However, the fuel rod design includes specific provisions to prevent clad flattening, and, therefore, such interactions will not occur.

4.2.3.2.14 Energy Release During Fuel Element Burnout

The Reactor Protection System provides fuel clad protection so that the probability of fuel element burnout during normal operation and anticipated operational occurrences is extremely low. Thus, the potential for fuel element burnout is restricted to faulted conditions. The LOCA is the limiting event since it results in the larger number of fuel rods experiencing burnout; thus the LOCA analysis, which is very conservative in predicting fuel element burnout, provides an upper limit for evaluating the consequences of burnout. The LOCA analysis explicitly accounts for the additional heat release due to the chemical reaction between the Zircaloy clad and the coolant following fuel element burnout in evaluating the consequences of this accident. LOCA analysis results are discussed in Subsection 15.6.3.

4.2.3.2.15 Energy Release on Rupture of Waterlogged Fuel Elements

A discussion of the potential for waterlogging fuel rods and for subsequent energy release is presented in Subsection 4.2.3.2.10.

4.2.3.2.16 Fuel Rod Behavior Effects from Coolant Flow Blockage

An experimental and analytical program was conducted to determine the effects of fuel assembly coolant flow maldistribution during normal reactor operation. In the experimental phase, velocity and static pressure measurements were made in cold, flowing water in an oversize model of a C-E 14 x 14 fuel assembly in order to determine the three-dimensional

flow distributions in the vicinity of several types of flow obstructions. The effects of the distributions on thermal behavior were evaluated, where necessary, with the use of a preliminary version of the TORC thermal and hydraulic code(68). Subjects investigated included:

a) The assembly inlet flow maldistribution caused by blockage of a core support plate flow hole. Evaluation of the flow recovery data indicated that even the complete blockage of a core support plate flow hole would not produce a W-3, Burnout Heat Flux Correlation, DNBR of less than 1.0 even though the reactor might be operating at a power sufficient to produce a DNBR of 1.3 without the blockage.

b) The flow maldistribution within the assembly caused by complete blockage of one to nine channels was also evaluated. Flow distributions were measured at positions upstream and downstream of a blockage one to nine channels. The influence of the blockage diminished very rapidly in the upstream direction. Analysis of the data for a single channel blockage indicated that such a blockage would not produce a W-3 DNBR of less than 1.0 downstream of the blockage even though the reactor might be operating at a power sufficient to produce a DNBR of 1.3 without the blockage.

→ (DRN 00-644)
The results presented above were obtained through flow testing an oversize model of a standard 14 x 14 fuel assembly. Because of the great similarity in design between the Waterford 3 16 x 16 assembly, and the earlier 14 x 14 array, these test results also constitute an adequate demonstration of the effects that flow blockage would have on the 16 x 16 assembly. This conclusion is also supported by the fact that the 16 x 16 assembly has been demonstrated to have a greater resistance to axial flow than the 14 x 14 assembly. The higher flow resistance of the 16 x 16 arrangement would lead to more rapid flow recovery downstream of any blockage than would occur with the 14 x 14 array. The effect of the higher flow resistance is to produce a more rapid flow recovery (i.e., more nearly uniform flow) and is analogous to the common use of flow resistance devices (screens or perforated plates) to smooth non-uniform velocity profiles in ducts or process equipment.
← (DRN 00-644)

4.2.3.2.17 Fuel Temperatures

Steady state fuel temperatures are determined by the FATES computer program. The calculational procedure considers the effect of linear heat rate, fuel relocation, fuel swelling, densification, thermal expansion, fission gas release, and clad deformations. The model for predicting fuel thermal performance is discussed in detail in Reference 14.
→ (DRN 00-644)
Two sets of burnup and axially dependent linear heat rate distributions are considered in the calculation. One is the hot rod, time averaged, distribution expected to persist during long term operation, and the other is the envelope of the maximum linear heat rate at each axial location. The long term distributions are integrated over selected time periods to determine burnup, which is in turn used for the various burnup dependent behavioral models in the FATES computer program. The envelope accounts for possible variations in the peak linear heat rate at any elevation which may occur for short periods of time and is used exclusively for fission gas release calculations.
← (DRN 00-644)

The power history used assumes continuous 100 percent power from beginning-of-cycle. Using this history, the highest fuel temperatures occur at beginning-of-life. It has been shown that fuel temperatures for a given power level and burnup are insensitive to the previous history (e.g., operating power transients, length and number of shutdowns, etc.) used to arrive at the given power level.

Fuel thermal performance parameters are calculated for the hot rod. These parameters for any other rod in the core can be obtained by using the axial location in the hot rod, whose local power and burnup corresponds to the local power and burnup in the rod being examined. this procedure will yield conservatively high stored energy in the fuel rod under consideration.

The maximum power density, including the local peaking as affected by anticipated operational occurrences, is discussed in Sections 4.3, 4.4, and Chapter 15.

4.2.3.3 Burnable Poison Rod

4.2.3.3.1 Burnable Poison Rod Internal Pressure and Cladding Stress

→(DRN 02-1538, R12; 06-1059, R15)

A poison rod cladding analysis will be performed to determine the stress and strain resulting from the various normal, upset, and emergency conditions discussed in Subsection 4.2.1.1. Specific accounting will be made for differential pressure, differential thermal expansion, cladding creep, and irradiation induced swelling of the burnable poison material. Owing to a lower linear heat generation rates in these rods, the cladding analyses can be accomplished using conventional strength of materials formula, except for determining clad collapse resistance which will be done using the CEPAN computer model(22).

←(DRN 06-1059, R15)

The design criteria used to evaluate the analytical results are specified in Subsection 4.2.1.3.1.

←(DRN 02-1538, R12)

4.2.3.3.2 Potential for Chemical Reaction

A discussion of possible chemical reaction between the poison material and the coolant was presented in Subsection 4.2.1.3.3.3, along with information on chemical compatibility between poison material and cladding. Since the cladding material is identical to that of the fuel rod (Subsection 4.2.1.3.2), the description of potential chemical reactions between cladding and coolant in Subsection 4.2.3.2.3 is applicable to both fuel and poison rods.

→(DRN 00-644)

The potential for waterlogging rupture in poison rods is much lower than that in fuel rods because of the smaller thermal and dimensional changes that occur in a poison rod during reactor power increases. Refer to Subsection 4.2.3.2.10 for a discussion of the potential for waterlogging rupture in fuel rods.

←(DRN 00-644)

4.2.3.4 Control Element Assembly

The CEAs are designed for 10 effective full power years based on estimates of neutron absorber burnup, allowable plastic strain of the Inconel 625 cladding and the resultant dimensional clearances of the elements within the fuel assembly guide tubes.

a) Internal Pressure

The value of internal pressure in the control element is dependent on the following parameters:

1) Initial fill gas pressure

2) Gas temperature

3) Helium generated and released

4) Available volume including B_4C porosity

→ (DRN 00-644)

Of the absorber materials utilized in the CEA design, only the B_4C contributes to the total quantity of gas which must be accommodated within the control element. The helium is produced by the nuclear reaction on ${}_0n^1 + {}_5B^{10} \rightarrow {}_3Li^7 + {}_2He^4$, and the fraction of the quantity generated which is actually released to the plenum is temperature dependent and is predicted by the empirical equation discussed in Subsection 4.2.1.4.4.A.3. Temperatures used for release fraction calculations are the maximum predicted to occur during normal operation.

← (DRN 00-644)

b) Thermal Stability of Absorber Materials

None of the materials selected for the control elements are susceptible to thermally induced phase changes at reactor operating conditions. Linear thermal expansion, thermal conductivity, and melting points are given in Subsection 4.2.1.4.

c) Irradiation Stability of Absorber Materials

Irradiated properties of the absorber materials are discussed in Subsection 4.2.1.4. Irradiation induced chemical transmutations are produced in both the B_4C and the Ag-In-Cd. Neutron bombardment of B10 atoms results in the production of lithium and helium. The percent of helium released is given by the expression in Subsection 4.2.1.4.

Ag-In-Cd alloy, which has an initial chemical composition of 79 w/o minimum Ag, 15 ± 0.35 w/o In, 5 ± 0.35 w/o Cd and 0.2 w/o maximum impurities, is expected to undergo small changes in composition. Formation of 3 w/o tin due to the transmutation of indium and an increase in cadmium content to about 10 w/o due to the transmutation of silver is expected. These affect the thermal conductivity and linear expansion characteristics of the alloy and are accounted for in the design of the control elements.

Irradiation enhanced swelling characteristics of the absorber materials are given in Subsection 4.2.1.4. Accommodations for swelling of the absorbers have been incorporated in the design of the control elements and include the following measures:

1) All B_4C pellets have chamfered edges to promote sliding of the pellets in the cladding due to differential thermal expansion and irradiation enhanced swelling.

2) Dimensionally stable Type 304 stainless steel spacers are located at the bottom of all absorber stacks adjacent to the nose cap to minimize strain at the weld joint.

3) A hole is provided in the center of the Ag-In-Cd cylinder to accommodate swelling in excess of the amount expected over the life of the control element.

d) Potential for and Consequences of CEA Functional Failure

The probability for a functional failure of the CEA is considered to be very small. This conclusion is based on the conservatism used in the design, the quality control procedures used during manufacturing and on testing of similar full size CEA/CEDM combinations under simulated reactor conditions for lengths of travel and numbers of trips greater than that expected to occur during the Waterford 3 design life. The consequences of CEA/CEDM functional failure are discussed in Chapter 15.

→ (DRN 00-644)

A postulated CEA failure mode is cladding failure. In the event that an element is assumed to partially fill with water under low or zero power conditions, the possibility exists that upon returning to power, the path of the water to the outside could be blocked. The expansion of the entrapped water could cause the element to swell. In tests, specimens of CEA cladding were filled with a spacer representing the poison material. All but nine percent of the remaining volume was filled with water. The sealed assembly was then subjected to a temperature of 650°F and an external pressure of 2,250 psia followed by a rapid removal of the external pressure. The resulting diametral increases of the cladding were on the order of 15 to 25 mils and were not sufficient to impair axial motion of the CEA, which has a 0.084 in. diametral clearance with the fuel assembly guide tubes. This test result, coupled with the low probability of a cladding failure leading to a waterlogged rod, demonstrates that the probability for a CEA functional failure from this cause is low.

← (DRN 00-644)

Another possible consequence of failed cladding is the release of small quantities of CEA filler materials, and helium and lithium (from the neutron-boron reactions). However, the amounts which would be released are too small to have significant effects on coolant chemistry or rod worth.

4.2.4 TESTING AND INSPECTION PLAN

Fuel bundle assembly and control element assembly quality assurance is attained by adherence to the ANS Quality Assurance Program Requirements for Nuclear Power Plants, ANSI N45.2-1971.

Vendor product certifications, process surveillance, inspections, tests, and material check analyses are performed to ensure conformity of all fuel assembly and control element assembly components to the design requirements from material procurement through receiving inspection at the plant site. The following are basic quality assurance measures which are performed.

4.2.4.1 Fuel Assembly

A comprehensive quality control plan is established to ensure that dimensional requirements of the drawings are met. In those cases where a large number of measurements are required and 100 percent inspection is impractical, these plans shall ensure with 95 percent confidence that 95 percent of these dimensions are within tolerance. Sensitivity and accuracy of all measuring devices are within $\pm$ 10 percent of the dimensioned tolerance. The basic quality assurance measures which are performed in addition to dimensional inspections and material verifications are described in the following sections.

4.2.4.1.1 Weld Quality Assurance Measures

The welded joints used in the fuel assembly design are listed below in a series of paragraphs which describe the type and function of each weld, and include a brief description of the testing (both destructive and non-destructive) performed to ensure the structural integrity of the joints. The welds are listed from top to bottom in the fuel assembly.

The CEA guide tube joints (between the tube and threaded upper and lower ends) are butt welds between the two Zircaloy subcomponents. The welds are required to be full penetration welds and must not cause violation of dimensional or corrosion resistance standards.

The upper end fitting center guide post to lower cast flow plate joint has a threaded connection which is prevented from unthreading by tack welding the center guide post to the bottom of the lower cast plate using the gas tungsten arc (GTA) process. Each weld is inspected for compliance with a visual standard.

→(DRN 02-1538, R12)
The spacer grid welds at the intersection of perpendicular Zircaloy-4 grid strips are made by the laser processes. Each intersection is welded at the top and at the bottom, and each weld is inspected by comparison with a visual standard.
←(DRN 02-1538, R12)

For the spacer grid to CEA guide tube weld (both components Zircaloy-4), each grid is welded to each guide tube with eight small welds, evenly divided between the upper and lower faces of the grid. Each weld is required to be free of cracks and burnthrough and each weld is inspected by comparison to a visual standard. Also, sufficient testing of sample welds is required to establish acceptable corrosion resistance of the weld region. Each guide tube is inspected after welding to ensure that welding has not affected clearance for CEA motion.

The bottom spacer grid welds at spacer strip intersections and between spacer and perimeter strips (all components Inconel 625) have the same configuration as for the Zircaloy and are all inspected for compliance with appropriate visual standards.

→(DRN 02-1538, R12; EC-9533, R302)
The bottom spacer grid (Inconel 625) to Inconel skirt weld was made using the GTA process. Each weld was inspected to ensure compliance with a visual standard. The debris-filtering bottom spacer grid has eliminated this weldment.
←(DRN 02-1538, R12; EC-9533, R302)

→(LBDCR 15-025, R309)
The Inconel skirt to lower end fitting (stainless steel) weld is made using the GTA process and each weld is inspected to ensure compliance with a visual standard.
←(LBDCR 15-025, R309)
The lower end fitting is fastened to the Zircaloy guide tubes using threaded connections. The connections are prevented from unthreading by stainless steel locking rings which are welded to the lower end fitting. Each ring is tack welded to the end fitting in four places using the GTA process, and each weld is inspected for compliance with a visual standard. The inspection requirements and acceptance standards for each of the welds are established on the basis of providing adequate assurance that the connections will perform their required functions.
→(EC-9533, R302)
The implementation of the NGF design eliminates four weld types while introducing three new weld types. As discussed in Section 4.2.2.1, the welds between the flange and the CEA guide tubes, between the Zircaloy-4 spacer grids and the guide tubes, between the bottom grid and the lower end fitting, and between the locking disc and the lower end fitting have all been eliminated. The three new weld types are discussed below:

- The Inconel top grid is a brazed design composed of Inconel-718 inner and outer straps and stainless steel sleeves. The braze joints are inspected for length and the absence of cracks.
- ZIRLO™ sleeves are laser welded to the Optimized ZIRLO™ inner straps of the mids grids and the IFMs. The welds are inspected for length and the absence of cracks.
- Stainless steel inserts are laser welded to the Inconel inner straps of the bottom grid. The welds are inspected by comparison to a visual standard and the absence of cracks.

←(EC-9533, R302)

4.2.4.1.2 Other Quality Assurance Measures

All guide tubes are internally gaged ensuring free passage within the tubes including the reduced diameter buffer region.

Each upper end fitting post to guide tube joint is inspected for compliance with a visual standard.

The spacer grid to fuel rod relationship is carefully examined at each grid location.
Stainless steel inserts are laser welded to the Inconel inner straps of the bottom grid. The welds are inspected by comparison to a visual standard and the absence of cracks.
→(EC-9533, R302)
For NGF assemblies, inspections of the bulges are performed for size, location, and absence of cracks.
←(EC-9533, R302)
→(DRN 06-895, R15)
Each completed fuel assembly is inspected for cleanliness, wrapped to preserve its cleanliness and loaded within shipping containers.
← DRN 06-895, R15)

Visual inspection of the conveyance vehicle, shipping container, and fuel assembly are performed at the reactor site. Approved procedures are provided for unloading the fuel assemblies. Following unloading, exterior portions of the fuel assembly components are inspected for shipping damage and cleanliness. If damage is detected, the assembly may be repaired onsite or returned to the manufacturing facility for repair. In the event the repair process were other than one normally used by the manufacturing facility, or that the repaired assembly did not meet the standard requirements for new fuel, the specific process or assembly would be reviewed by the appropriate design department before the process or assembly would be accepted.

4.2.4.2 Fuel Rod

4.2.4.2.1 Fuel Pellets
→(DRN 00-644; 02-1538, R12)
Beginning with Batch U, all urania fuel pellets will be fabricated at the Columbia, SC, manufacturing facility.
←(DRN 00-644; 02-1538, R12)

→(DRN 00-644; 02-1538, R12)
During the conversion of source material to ceramic grade uranium dioxide powder, the UO_2 powder is divided into lots blended to form uniform isotopic, chemical and physical characteristics. Samples are tested from each powder blend to verify compliance with the specification limits for the blend. Additional finished pellets are tested for the final enrichment certification of the pellets.

Pellets are divided into lots during fabrication with all pellets within the lot being processed under the same conditions, as defined per the pellet specification. Representative samples are obtained from each lot for product acceptance tests. Hydrogen content of the finished ground pellets is restricted. The pellets' diameters are inspected and certified to meet the design tolerance requirements at a 95/99 confidence level. All other pellet dimensions meet a 90/90 confidence level. Density requirements of the sintered pellets must meet a 95/95 confidence level. Sample pellets from each pellet lot are prepared for metallographic examination to ensure conformance to microstructural requirements. Surface finish of ground pellets is restricted and meets a 90/90 confidence level. Pellet surfaces are inspected for chips, cracks, and fissures in accordance with approved standards.
←(DRN 00-644; 02-1538, R12)

→(DRN 02-1538, R12)
←(DRN 02-1538, R12)

4.2.4.2.2 Cladding

→(DRN 02-1538, R12)
Lots are formed from tubing produced from the same ingot, annealed in the same final vacuum annealing charge and fabricated using the same procedures. Samples randomly selected from each lot of finished tubing are chemically analyzed to ensure conformance to specified chemical requirements, and to verify tensile properties and hydride orientation. Samples from each lot are also used for metallographic tests, and burst tests. Each finished tube is ultrasonically tested for internal soundness; visually inspected for cleanliness and the absence of acid stains, surface defects, and deformation; and inspected for inside dimension and wall thickness. The following summarizes the test requirements:
←(DRN 02-1538, R12)

a) Test (refer to Subsection 4.2.1.2.2)

1) Chemical Analysis

→(DRN 02-1538, R12)
Ingot analysis is required for top, middle, and bottom of each ingot. Finished intermediate TREX or finished tube product is tested for hydrogen, nitrogen, and oxygen per ASTM E353.
←(DRN 02-1538, R12)

2) Tensile Test at Room Temperature (ASTM E8-69)

3) Corrosion Resistance Test (ASTM G2-67)

4) Grain Size (ASTM E112-63)

→(DRN 02-1538, R12)
5) Deleted
←(DRN 02-1538, R12)

6) Surface Roughness

7) Visual Examination

8) Ultrasonic Test

9) Wall Thickness

10) Straightness

11) Inside Diameter

4.2.4.2.3 Fuel Rod Assembly

→(DRN 02-1538, R12)

Immediately prior to loading pellets must be capable of passing approved visual standards. Each fuel pellet stack is weighed to within 0.1 percent accuracy. The loading process is such that cleanliness and dryness of all internal fuel rod components are maintained until after the final end cap weld is completed. Loading and handling of pellets is carefully controlled to minimize chipping of pellets.

←(DRN 02-1538, R12)

The following procedures are used during fabrication to assure that there are no axial gaps in fuel rods.

4.2.4.2.3.1 Stack Length Gage

→(DRN 02-1538, R12)

The pellet stacks for Batches A through T were preassembled in "V" troughs that had been gauge marked to the proper length. They were then pushed into cladding tubes and the distance from the end of the tube to the end of the pellet stack checked with a gauge. The rods for Batches U and later are fabricated at the Columbia facility, which builds its pellet stacks directly in the cladding tubes. Their stacks are built up, 25 at a time, from a series of shorter preassembled segments that are fed into a like number of tubes by a vibratory feeder. Before feeding the last row of segments into the tubes, the distance from the end of the tube to the end of the pellet stack is checked with a gauge. If necessary, an appropriate number of pellets are added to or removed from each segment in the row. As before, the distance from the end of the tube to the end of the pellet stack is then checked with a gauge.

4.2.4.2.3.2 Rod Scanner

Before being loaded into bundle assemblies, the finished fuel rods are gamma scanned to ensure that no gaps exist within them.

Loaded fuel rods are pressurized with helium to a prescribed pressure as determined for the fuel batch. Impurity content of the fill gas shall not exceed 0.5 percent.

In Batches A through T, the fuel rod upper end cap to cladding tube weld is a Magnetic Force (i.e., resistance) Weld whose outer surface is subsequently machined (i.e., deflashed). Beginning with Batch U, the joint was converted to Tungsten Inert Gas (TIG) welding. The latter also utilizes a separate (TIG) seal weld to close the opening through which the rod is pressurized. Quality assurance on the end cap weld is as follows:

→(DRN 04-502, R13)

a) Non-destructive examination in accordance with approved procedures of all end cap welds (Batches U and later only) to certify bond length and to detect porosity or undercut.

←(DRN 04-502, R13)

b) Visual examination of all end cap welds to establish freedom from cracks, seams, inclusions and foreign particles (Note: In Batches A through T, this examination was performed after final machining of the weld).

c) Destructive examination of a sufficient number of weld samples to establish that the allowable percent of unbonded wall thickness and the maximum allowable continuous unbonded region are satisfied.

←(DRN 02-1538, R12)

→(DRN 02-1538)

d) Helium Leak checking of all end cap welds to establish that no leak rate greater than $10^{-8cc}/_{sec}$ is present.

e) Corrosion testing of a sufficient number of samples to establish that weld zones do not exhibit excessive corrosion compared to a visual standard.

←(DRN 02-1538)

All finished fuel rods are visually inspected to ensure a proper surface finish (scratches that measure greater than 0.001 in. depth, cracks, slivers and other similar defects are not acceptable).

Each fuel rod is marked to provide a means of identification.

4.2.4.3 Burnable Poison Rod

4.2.4.3.1 Burnable Poison Pellets

B_4C powder is sampled to verify particle size and w/o boron requirements prior to its use in pellet production. Finished pellets are 100 percent inspected for diameter and must satisfy a 90/90 confidence level on other dimensions. Samples are taken from each of the pellet lots and examined for uniform dispersion of the B_4C in $A1_2O_3$. Conformance with density range requirements is demonstrated at a 95/95 confidence level and with B_4C loading requirements at a 90/90 level. Samples are drawn from each lot to verify acceptable impurity levels. Finally, all pellets are inspected for conformance with surface chip and crack standards.

4.2.4.3.2 Cladding

The testing and inspection plan for burnable poison rod cladding is identical to that for fuel rod cladding (Subsection 4.2.4.2.2).

4.2.4.3.3 Burnable Poison Rod Assembly

The moisture content of poison pellets prior to loading is limited. The loading process is such that cleanliness and dryness of all internal poison rod components are maintained until the final end cap weld is completed.

The following procedure is used during fabrication to assure that there are no axial gaps in poison rods:

The operator stacks pellets onto V troughs that are gage marked to the proper column height. When pellet stacking is completed, all column heights are checked by Quality Control. The pellets are subsequently loaded into tubes. After loading, the distance from the end of the tube to the end of the pellet column is checked with a gage.

Loaded poison rods are evacuated and backfilled with helium to a prescribed level. Impurity content of the fill gas must not exceed 0.5 percent.

→(DRN 02-1538)

End cap weld integrity and corrosion resistance is ensured by a Quality Control plan identical to that used in fuel rod fabrication (Subsection 4.2.4.2.3).

←(DRN 02-1538)

All finished rods are visually inspected to ensure a proper surface finish (scratches greater than 0.001 in. in depth, cracks, slivers, and other similar defects are not acceptable).

4.2.4.4 Control Element Assemblies

The CEAs are subjected to numerous inspections and tests during manufacturing and after installation in the reactor. A general product specification controls the fabrication, inspection, assembly, cleaning, packaging, and shipping of CEAS. All materials are procured to AMS, ASTM or C-E specifications. In addition, various CEA hardware tests have been conducted or are in progress.

During manufacturing, the following inspections and tests are performed:
→ (DRN 01-1103, R12; 02-1477, R12)

a) The loading of each control element is carefully controlled to obtain the proper amounts and types of filler materials.

← (DRN 01-1103, R12; 02-1477, R12)

b) All end cap welds are liquid penetrant examined and helium leak tested. A sampling plan is used to section and examine end cap welds.

→ (DRN 02-1477, R12)

c) Deleted.

d) Each CEA has unique serialization on the spider. See Figures 4.2-5.

← (DRN 02-1477, R12)
→(DRN 00-644)

e) Fully assembled CEAs are checked for proper alignment of the neutron absorber elements using a special fixture. The alignment check ensures that the frictional force that could result from adverse tolerances is below the force which could significantly increase trip time.

← (DRN 00-644)

In addition to the basic measurements discussed above, the manufacturing process includes numerous other quality control steps for ensuring that the individual CEA components satisfy design requirements for material quality, detail dimensions, and process control.

After installation in the reactor, but prior to criticality, each CEA is traversed through its full stroke and tripped. A similar procedure will also be conducted at refueling intervals.

→(LBDCR 16-063, R310)

The integrity of each CEA was tested at the beginning of the initial fuel cycle by performing a CEA symmetry test as part of the low power physics testing. The CEA symmetry test determined whether the reactivities of symmetric CEAs are equal within the measurement limitation. The successful completion of these tests demonstrated that no core loading or fabrication errors or loss in rod integrity exist that are sufficient to result in measurable CEA asymmetries. Following the initial fuel cycle, CEA integrity is confirmed at the beginning of each cycle through the combination of the following tests: CEA Coupling Check, CEA Drop Time, Incore Flux Symmetry and Power Distribution Tests (per WCAP-16011-P-A,"Startup Test Activity Reduction Program").

←(LBDCR 16-063, R310)

Hardware tests to date have been performed using CEA components developed primarily for CEs 800 MWe class reactors which use 14 x 14 fuel assemblies.

→(DRN 01-1103, R12; 02-1477, R12)
CEAs used in the Waterford 3 reactor are essentially similar in design and construction to the 800 MWe class CEA. The CEA spider arms are shorter and the neutron absorber elements are smaller in diameter for compatibility with the 16 x 16 fuel assembly guide tube dimensions employed in Waterford 3.
←(DRN 01-1103, R12)
→(LBDCR 15-039, R309)
Safety analyses assume the average CEA position is at least 90% inserted at 3.2 seconds after trip breakers open. CEAs meet the 3.2 second average even under worst case conditions to reach 90 percent insertion in 3.2 seconds to agree with assumptions in Section 15.0.2.
←(DRN 02-1477, R12)
The reactivity worth of a CEA depends on the power (i.e., neutron flux) surrounding the CEA. During a reactor trip faster CEAs move into higher flux regions sooner and, thus, add more negative reactivity than slower CEAs. Note, CEAs do not necessarily fall with the same insertion times or at the same rate during a reactor trip. Therefore, the amount of negative reactivity inserted correlates to the average CEA insertion rate rather than the slowest CEA insertion rate. This relation between CEA insertion and reactivity insertion is cycle independent if the mechanical design, CEDM design, plus core physics and core thermohydraulics (pertinent to the CEAs) remain unchanged.
→(DRN 02-1477, R12)
CE performed three-dimensional space-time calculations with the NRC approved HERMITE computer program. The calculations adequately cover possible operating conditions and limits on the as-measured CEA distributions (Safety Evaluation Report for Amendment 58, dated October 31, 1989). The calculations show that for any reasonable distribution around an average CEA position during a trip, CEAs add negative reactivity at a rate directly related to the average CEA position. Thus, Technical Specification limits should exist for the average CEA position. Thus, Technical Specification limits should exist for the average CEA drop time and Safety Analysis should assume that all CEAs fall in a "window shade" pattern with the average CEA drop time. However, if the time between the fastest and slowest CEA becomes too large, or the CEA distribution deviates from the one modeled by CE, then the "window shade" may not necessarily represent the time dependent negative reactivity insertion. Therefore, besides the 3.2 second average insertion time limit, the Technical Specifications limit the maximum drop time for the slowest CEA to 3.5 seconds.
←(DRN 02-1477, R12, LBDCR 15-039. R309)

SECTION 4.2: REFERENCES

1. Timoshenko, S., Strength of Materials, Part II Chapter IX, D. Van Nostrand Co., Inc., New York, 1956.

2. "High Temperature Properties of Zircaloy and UO_2 for use in LOCA Evaluation Models," Combustion Engineering, Inc., CENPD-136 (Proprietary).

3. "Zircaloy Growth-In-Reactor Dimensional Changes in Zircaloy-4 Fuel Assemblies." Combustion Engineering, Inc., CENPD-198P (Proprietary), December 1975.

4. O'Donnell, W.J., "Fracture of Cylindrical Fuel Rod Cladding due to Plastic Instability," WAPD-TM-651, April 1967.

5. Weber, J.M., "Plastic Stability of Zr-2 Fuel Cladding, Effects of Radiation on Structural Metals," ASTM STP 426, AM. Soc. Testing Mats., pp 653-669, 1967.

6. Engle, J.T. and Meieran, H.B., "Performance of Fuel Rods Having 97 Percent Theoretical Density UO_2 Pellets Sheathed in Zircaloy-4 and Irradiated at Low Thermal Ratings," WAPD-TM-631, July 1968.

7. Duncombe, E., Meyer, J.E., and Coffman, W.A., "Comparisons with Experiment of Calculated Dimensional Changes and Failure Analysis of Irradiated Bulk Oxide Fuel Test Rods Using the CYGRO-1 Computer Program," WAPD-TM-583, December 1966.

8. McCauley, J.E., et al., "Evaluation of the Irradiation Performance of Zircaloy-4 Clad Test Rod Containing Annular UO_2 Fuel Pellets (Rod 79-19)," WAPD-TM-595, December 1966.

9. Notley, M.J.F., Bain, A.S., and Robertson, J.A.L., "The Longitudinal and Diametral Expansion of UO_2 Fuel Elements," AECL-2143, November 1964.

10. Notley, M.J.F., "The Thermal Conductivity of Columnar Grains in Irradiated UO_2 Fuel Elements," AECL-1822 July 1962.

11. Manson, S.S., "Fatigue: A Complex Subject - Some Simple Approximations," Experimental Mechanics, Vol. 22, No. 2, pp 193-226, July 1965.

12. O'Donnell, W.J. and Langer, B.F., "Fatigue Design Basis for Zircaloy Components,' Nuc. Sci. Eng., Vol. 20, pp 1-12, 1964.

13. CESSAR Proprietary Appendix, Docket 50-470.

14. "C-E Fuel Evaluation Model Topical Report," Combustion Engineering, Inc., CENPD-139 (Proprietary), CENPD-139 Rev. 01 (Non-Proprietary) CENPD-139 Supplement 1 (Proprietary), CENPD-139 Supplement 1, Rev. 01 (Non-Proprietary), July 1974.

SECTION 4.2: REFERENCES (Cont'd)

15. Conway, J.B., "The Thermal Expansion and Heat Capacity of UO_2 to 2200°C", GE-NMPD-TM-63-6-6.

16. Christensen, J.A., "Thermal Expansion of UO_2", HW-75148, 1962.

17. Jones, J.M., et. al., "Optical Properties of Uranium Oxides," Nature, 205, 663-65, 1965.

18. Cabannes, F. and Stora, J.P., "Reflection and Emission Factors of UO_2 at High Temperatures", C.R. Acad. Sci., Paris, Ser. B. 264 (1) 45-48, 1967.

19. Held, P.C. and Wilder, D.R., "High Temperature Hemispherical Spectral Emittance of Uranium Dioxide at 0.65 and 0.70 m," J.Am. Cer. Soc., Vol. 52, No. 4, 1969.

20. Brassfield, M.C., "Recommended Property and Reaction Kinetics Data for Use in Evaluating a Light Water Cooled Reactor Loss-of-Coolant Incident Involving Zircaloy-4 or 324-53 Clad UO_2," GEMP-482, 1968.

21. "C-E Thermo-Structural Fuel Evaluation Method," Combustion Engineering, Inc., CENPD-179, April 1976.

22. "CEPAN, Method of Analyzing Creep Collapse of Oval Cladding," Combustion Engineering, Inc. CENPD-179, April 1976.

23. "STRIKIN-II, A Cylindrical Geometry Fuel Rod Heat Transfer Program," Combustion Engineering, Inc., CENPD-135P (Proprietary), CENPD-135 (Non-Proprietary), August 1974.

24. Deverall, J.E., LA-2669 USAEC, Vol. 62, 1954.

25. Rudkin, R.L., Parker, J.W., and Jenkins, R.J., ASD-TDR-62-24, Vol. 1, p. 20, 1963.

26. Thorne, R.P. and Howard, V.C. "Changes in Polycrystalline Alumina by Fast Neutron Irradiation," p. 415, Proceedings, of the British Ceramic Society, No. 7, February 1967.

27. Simnad, M.T. and Meyer, R.S., "BeO Review of Properties for Nuclear Reactor Applications," Proceedings of the Conference on Nuclear Applications of Nonfissionable Ceramics, p 209-210, May 9-11, 1966.

28. Rason, N.S. and Smith, A.W., "NAA-SR-862", Vol. 37 (AD85006), 1954.

29. Saba, W.G. and Sterret, K.F., "J. Am. Chem. Soc." Vol. 79, pp 3637-38.

30. "Fuels and Materials Development Quarterly Progress Report," pp 38-58, ONRL-TM-3703, December 31, 1971.

SECTION 4.2: REFERENCES (Cont'd)

31. Kingery, W.D., "Introduction to Ceramics," John Wiley & Sons, pp 486-504.

32. Toulookan, Y.S., "Thermophysical Properties of High Temperature Solid Materials," Vol. 4 and 5, MacMillan.

33. Moore, G.E. and Kelley, K.K. , "J. Am. Chem. Soc.", Vol. 69, pp 309-16, 1947.

34. Keilholtz, G.W. Moore, R.E., and Robitson, M.E., "Effects of Fast Neutrons on Polycrystalline Alumina and Other Electric Insulators at Temperatures From 60C-1230C" ORNL 4678, May 1971.

35. Burian, R.J., Fromm, E.O., and Gates, J.E, "Effect of High Boron Burnups on B_4C and ZrB Dispersions in $A1_2O_3$ and Zircaloy-2," BM1-1627, April 24, 1963.

36. Cunningham, G.W., "Compatibility of Metals and Ceramics, "Proceedings of Nuclear Applications of Nonfissionable Ceramics, pp 279-289, May 1966.

37. Graber, M.J., "A Metallurgical Evaluation of Simulated BWR Emergency Core Cooling Tests,' Idaho Nuclear Corporation, IN-1453, March 1971.

38. Pitner, A.L., "The WDC -1-1 Instrumental Irradiation of Boron Carbide in a Spectrum-Hardened ETR Flux" HEDL-TME-73-38, April 1973.

39. Gray, R.G. and Lynam, L.R., "Irradiation Behavior of Bulk B_4C and B_4C-SiC Burnable Poison Plates," WAPD-261, October 1963.

40. "HEDL Quarterly Technical Report for October, November, and December 1974," Vol. 1, HEDL-TME-74-4, pp A-51 to A-53, January 1975.

41. Mahagan, D.E., "Boron Carbide Thermal Conductivity," HEDL-TME-73-78, September 1973.

42. Homan, F.J., "Performance Modeling of Neutron Absorbers," Nuclear Technology, Vol. 16, pp 216-225, October 1972.

43. Pitner, A.L. and Russcher, G.E., Irradiation of Boron Carbide Pellets and Powders in Hanford Thermal Reactors," WHAN-FR-24, December 1970.

44. Pitner, A.L. and Russcher, G.E., "A Function of Predict LMFBR Helium Release Bound on Boron Carbide Irradiation Data from Thermal Reactors," HEDL-TME-71-127, September 30, 1971.

45. HEDL-73-6, "Materials Technology Program Report for October, November, and December 1973," pp A-69 to A-72.

SECTION 4.2: REFERENCES (Cont'd)

46. Cohen, I., "Development and Properties of Silver-Base Alloys as Control Rod Materials for Pressurized Water Reactors," WAPD-214, December 1959.

47. Tipton, C.R., "Reactor Handbook," Vol. 1, Materials, Interscience, p 827, 1960.

48. "National Alloy Development Program Information Meeting," pp 39-63, TC-291, May 22, 1975.

49. "Quarterly Progress Report - Irradiation Effects on Structural Materials," HEDL-TME-161, pp GE-5 - GE-10.

50. "Structural Analysis of Fuel Assemblies for Combined Seismic and Loss of Coolant Accident Loadings," Combustion Engineering, Inc., CENPD-178, August 1976.

51. "Joint C-E/EPRI Fuel Performance Evaluation Program, Task C, Evaluation of Fuel Rod Performance on Maine-Yankee Core I," Combustion Engineering, Inc., CENPD-221, December 1975.

52. "Pressurized Water Reactor Project Period January 24, 1964 to April 23, 1964," WAPD-MRP-108.

53. "Fuel and Poison Rod Bowing," Combustion Engineering, Inc., CENPD-225-P (Proprietary), October 1976.

54. Caye, T.E., "Saxton Plutonium Project, Quarterly Progress Report for the Period Ending March 31, 1972," WCAP-3385-31, November 1972.

55. Berman, R.M., Meieran, H.B., and Patterson, P., "Irradiation Behavior of Zircaloy-Clad Fuel Rods Containing Dished End UO_2 Pellets," (LWBR-LSBR Development Program), WAPD-TM-629, July 1967.

56. Baroch, S.J., et al., "Comparative Performance of Zircaloy and Stainless Steel Clad Fuel Rods Operated to 10,000 MWd/MTU in the VBWR," GEAP-4849, April 1966.

57. Megerth, F.H., Zircaloy-Clad UO_2 Fuel Rod Evaluation Program," Quarterly Progress Report No. 8, August 1969-October 1969. GEAP-10121, November 1969.

58. Megerth, F.H., "Zircaloy-Clad UO_2 Fuel Rod Evaluation Program," Quarterly Progress Report No. 1, November 1967-January 1968, GEAP-5598, March 1968.

59. Indian Point Nuclear Generating Unit No. 2, Preliminary Safety Analysis Report - Appendix A, Docket No. 50-247.

60. Stiefel, J.T., Feinroth, H., and Oldham, G.M., "Shippingport Atomic Power Station Operating Experience, Developments and Future Plans," WAPD-TM-390, April, 1963.

SECTION 4.2: REFERENCES (Cont'd)

61. Question V.B. 2, Prairie Island Nuclear Generating Plant, Preliminary Safety Analysis Report, Docket No. 50-306.

62. Anderson, T.D., "Effects of High Burnup on Bulk UO_2, Fuel Elements," Nuclear Safety Vol. 6, No. 2, Winter 1964-65 pp 164-169.

63. Miller, R.S., et.al., "Operating Experience with the Saxton Reactor Partial Plutonium Core - II," paper presented at AEC Plutonium Meeting in Phoenix, August, 1967.

64. Megerth, F.H., "Zircaloy-Clad UO_2 Fuel Rod Evaluation Program," Quarterly Progress Report No. 2, February 1968 April 1968, CEAP-5624, May, 1968.

65. Blakely, J.P., "Action on Reactor and Other Projects Undergoing Regulatory Review of Consideration," Nuclear Safety, Vol. 9, No. 4, p 326, July-August, 1968.

66. Stephan, L.A., "The Response of Waterlogged UO_2 Fuel Rods to Power Bursts," IDO-ITR-105, April, 1969.

67. Stephan, L.A., "The Effects of Cladding Material and Heat Treatment on the Response of Waterlogged UO_2 Fuel Rods to Power Burst," IM-ITR-111, January, 1970.

68. "TORC Code: A Computer Code for Determining the Thermal Margin of a Reactor Core," Combustion Engineering, Inc., CENPD-161-P, (Proprietary) July 1, 1975.

69. Sandler, Y.L., "Structure of PWR Primary Corrosion Products," presented during NACE Corrosion/78, March, 1978, Houston, Texas. Published in NACE-CORROSION, Vol. 35, No. 5, May, 1979.

70. Lister, D.H., "The Accumulation of Radioactive Corrosion Products in Nuclear Steam Generators," presented during NACE Corrosion/76, March, 1976, Houston, Texas.

71. Yankee Core Evaluation Program,-Final Report, WCAP-3017-6094, 1971.

72. Solomon, Y., Roesmer, T., "Measurement of Fuel Element Crud Deposits in Pressurized Water Reactors," Nuclear Technology, Vol 29, May, 1976, pp 166-173.

73. Bessette, D.E., et al., CE/EPRI Fuel Performance Evaluation Program, RP-586-1, Task A, Examination of Calvert Cliffs I Test Fuel Assemblies at End of Cycles 1 and 2, September, 1978.

74. Hillner, E., "Corrosion of Zirconium Base Alloys - An Overview," Zirconium in the Nuclear Industry, ASTM STP 633, pp.211-235, 1977.

75. "Fuel and Poison Rod Bowing," Combustion Engineering, Inc., CENPD--225-P, Supplement 3-P (Proprietary), August 1979.

SECTION 4.2: REFERENCES (Cont'd)

76. J.A. Christensen, et. al., "Melting Point of Irradiated Uranium Dioxide," ANS Transactions, Volume 7:2, November 1964, p 390.

77. Final Safety Analysis Report, San Onofre Nuclear Generating Station Units 2 and 3, NRC Docket Nos. 50-361 and 50-362, Response to NRC Question 231.26.

78. CEN-382-P-A, “Methodology for Core Designs Containing Erbium Burnable Absorbers,” ABB Combustion Engineering Nuclear Fuel, August 1993.

→(DRN 03-1821, R13)
79. “Fuel Rod Maximum Allowable Gas Pressure,” CEN-372-P-A, May 1990.
←(DRN 03-1821, R13)

→(DRN 06-1059, R15)
80. CENPD-404-P-A, “Implementation of ZIRLO™ Material Cladding in CE Nuclear Power Fuel Assembly Designs,” November 2001.

81. WCAP-16072-P-A, “Implementation of Zirconium Diboride Burnable Absorber Coatings in CE Nuclear Power Fuel Assembly Designs,” August 2004.
←(DRN 06-1059, R15)
→(EC-9533, R302)
82. CEN-386-P-A, “Verification of the Acceptability of a 1-Pin Burnup limit of 60 MWD/kg for Combustion Engineering 16x16 PWR Fuel”, August 1992.

83. WCAP-12610-P-A and CENPD-404-P-A Addendum 1-A, “Optimized ZIRLO™”, July 2006.

84. WCAP-16500-P-A, “CE 16x16 Next Generation Fuel Core Reference Report”, August 2007.
←(EC-9533, R302)
→(LBDCR 15-035, R309)
85. WCAP-12610-P-A and CENPD-404-P-A Addendum 2-A, “Westinghouse Clad Corrosion Model for ZIRLO™ and Optimized ZIRLO™,” October 2013.
←(LBDCR 15-035, R309)

TABLE 4.2-1 (Sheet 1 of 4) Revision 302 (12/08)

MECHANICAL DESIGN PARAMETERS

Core Arrangement

→(EC-9533, R302)

		NGF
Number of fuel assemblies in core, total	217	
→(DRN 01-1103, R12) Number of CEAs ←(DRN 01-1103, R12)	87	
Number of fuel rod locations	51,212	
Spacing between fuel assemblies, fuel rod surface to surface, in.	0.208	0.216
Spacing, outer fuel rod surface to core shroud, in.	0.214	0.218
Hydraulic diameter, nominal channel, ft.	0.0394	0.0415
Total flow area (excluding guide tubes), ft^2	54.8	56.5
Total core area, ft^2	101.1	
Core equivalent diameter, in.	136	
Core circumscribed diameter, in.	143	
Total fuel loading, Kg U	90×10^3	93×10^3
Total fuel weight, lbm. UO_2	224×10^3	234×10^3
Total weight of Zircaloy, lbm.	64,092	61,385
Fuel volume (including dishes), ft^3	356	359
Fuel Rod Array, square	16 x 16	
Fuel Rod Pitch, in.	0.506	

←(EC-9533, R302)

TABLE 4.2-1 (Sheet 2 of 4) Revision 302 (12/08)

Fuel Assemblies (Cont'd)

→(EC-9533, R302)

		NGF
Spacer Grid		
Type – HID-1L	Cantilever Spring	
Material	Zircaloy-4	
→(DRN 02-1538, R12)		
Number per assembly	11	
←(DRN 02-1538, R12)		
Weight each, lb	1.7	
→(DRN 02-1538, R12; 06-1059, R15)		
←(DRN 02-1538, R12; 06-1059, R15)		
Type	Cantilever Spring	Vertical Spring
Material	Inconel 625	Inconel-718
Number per assembly	1*	1
Weight each, lb	2.3	1.5
Type – Vaned Mid Grid		I-Spring
Material		Optimized ZIRLO™
Number per Assembly		6
Weight, each, lb		2.8
Type – Unvaned Mid Grid		I-Spring
Material		Optimized ZIRLO™
Number per Assembly		3
Weight, each, lb		2.7
Type – IFM Grid		Co-planar Dimples
Material		Optimized ZIRLO™
Number per Assembly		2
Weight, each, lb		1.1
Type – Inconel Bottom Grid	Cantilever Spring	Cantilever Spring
Material	Inconel-625	Inconel-625
Number per Assembly	1	1
Weight, each, lb	2.6	2.3
Weight of fuel assembly, lbm.	1,435	1,416
Outside Dimensions		
Fuel rod to fuel rod, in.	7.972 x 7.972	7.96x7.964
Fuel Rod		
Fuel rod material (sintered pellet)	UO_2	
→(DRN 06-1059, R15)		
Pellet diameter, in., OD (annular ID)	0.325 (0.1625)	0.3225 (0.1550)
Pellet length, in., solid (annular)	0.390 (0.500)	0.387 (0.500)
Pellet density, g/cm^3	10.44	
←(DRN 06-1059, R15)		
Pellet theoretical density, g/cm^3	10.96	
→(DRN 06-1059, R15)		
Pellet density (% theoretical)	95.25	
Stack density, g/cm^3, solid (annular)	10.11 (7.80)	(10.31 (8.00)
Clad material	Zircaloy-4, ZIRLO™	Optimized ZIRLO™
←(DRN 06-1059, R15)		
Clad ID, in.	0.332	0.329
Clad OD, (nominal), in.	0.382	0.374
→(DRN 06-1059, R15)		

* some fuel assemblies in Batch U; all fuel assemblies beginning w/Batch W

←(DRN 06-1059, R15)

Fuel Assemblies (Cont'd)

→(EC-9533, R302)

		NGF
Clad thickness, (nominal), in.	0.025	0.0225
Diametral gap, (cold, nominal), in.	0.007	0.0065
Active length, in.	150	
→(DRN 02-1477, R12; 04-502, R13) Plenum length, in.	8.888 (Batch T) 9.138 (Batches U&W)	10.013
→(DRN 06-992, R15) Uranium weight (nominal) grams	1830	1825

←(DRN 04-502, R13; 06-992, R15; EC-9533, R302)

Control Element (CEA)

←(DRN 02-1477, R12)

→(DRN 01-1103, R12)

Number	87
Absorber elements, No. per assy.	5
Type	Cylindrical rods
Clad material	Inconel 625
Clad thickness, in.	0.035
Clad OD, in.	0.816
Diametral gap, in.	0.009
Outside elements	
Poison material	B_4C/Ag-In-CD
Poison length, in.	135.5/12.5
B_4C Pellet	
Diameter, in.	0.737
Density, % of theoretical density of 2.52 g/cm^3	73
Weight % boron, minimum	77.5

←(DRN 01-1103, R12)

TABLE 4.2-1 (Sheet 4 of 4)

Burnable Poison Rod

Absorber material	$A1_20_3$-B_4C
Pellet diameter	.307
Pellet length, min.	1.000
Pellet density, (% theoretical), min.	93
Theoretical density, $A1_20_3$, g/cm^3	3.94
Theoretical density, B_4C, g/cm^3	2.52
Clad material	Zircaloy-4
Clad ID, in.	0.332
Clad OD, in.	0.382
Clad thickness, (nominal), in.	0.025
Diametral gap, (cold, nominal), in.	.025
Active length, in.	136.0
Plenum length, in.	11.090

TABLE 4.2-2

TENSILE TEST RESULTS ON IRRADIATED

SAXTON CORE III CLADDING (54)

Fluence (1 MeV) 4.7 x 10^{21} n/cm^2 (estimated)

Rod ID	Location From Bottom (in.)	Testing Temp (F)	0.2% Yield Stress (psi x 103)	Ultimate Tensile Strength (psi x 103)	Uniform Strain In 2 in. Gage Length (%)	Total Strain In 2 in. Gage Length
BO	11-17	650	61.4	65.6	2.2	6.8
BO	26-32	650	58.1	68.9	2.4	11.3
RD	3-9	650	62.2	70.0	2.0	4.2
RD	12-18	650	60.5	65.4	1.7	5.8
MQ	12-18	675	70.4	77.4	1.9	6.1
MQ	28-34	675	66.0	75.1	1.6	6.2
FS	28-34	675	57.2	71.4	3.9	12.9
GL	12-18	675	60.5	71.5	2.4	9.3

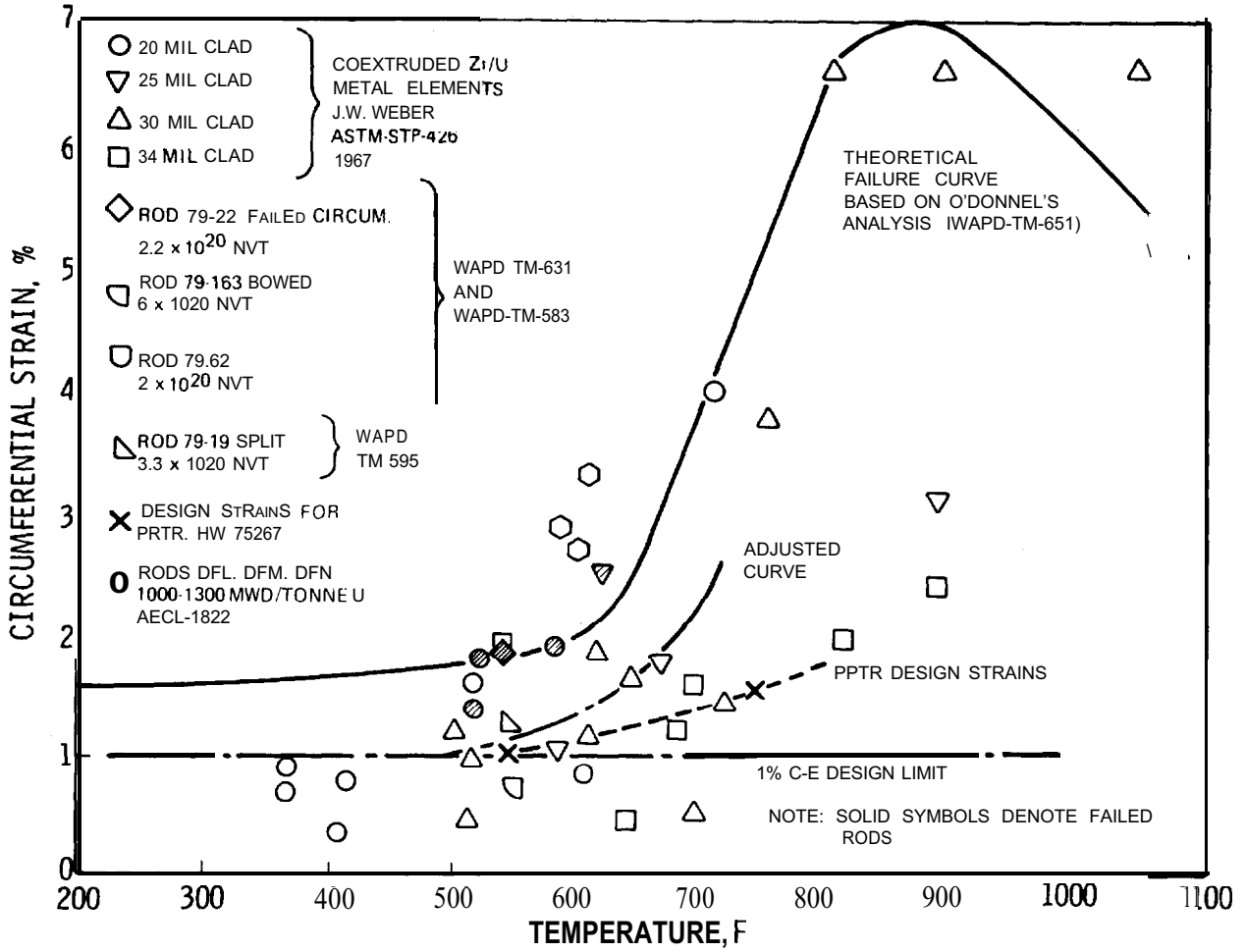

LOUISIANA POWER & LIGHT CO. Waterford Steam Electric Station	**CIRCUMFERENTIAL STRAIN VS. TEMPERATURE**	**Figure 4.2-I**

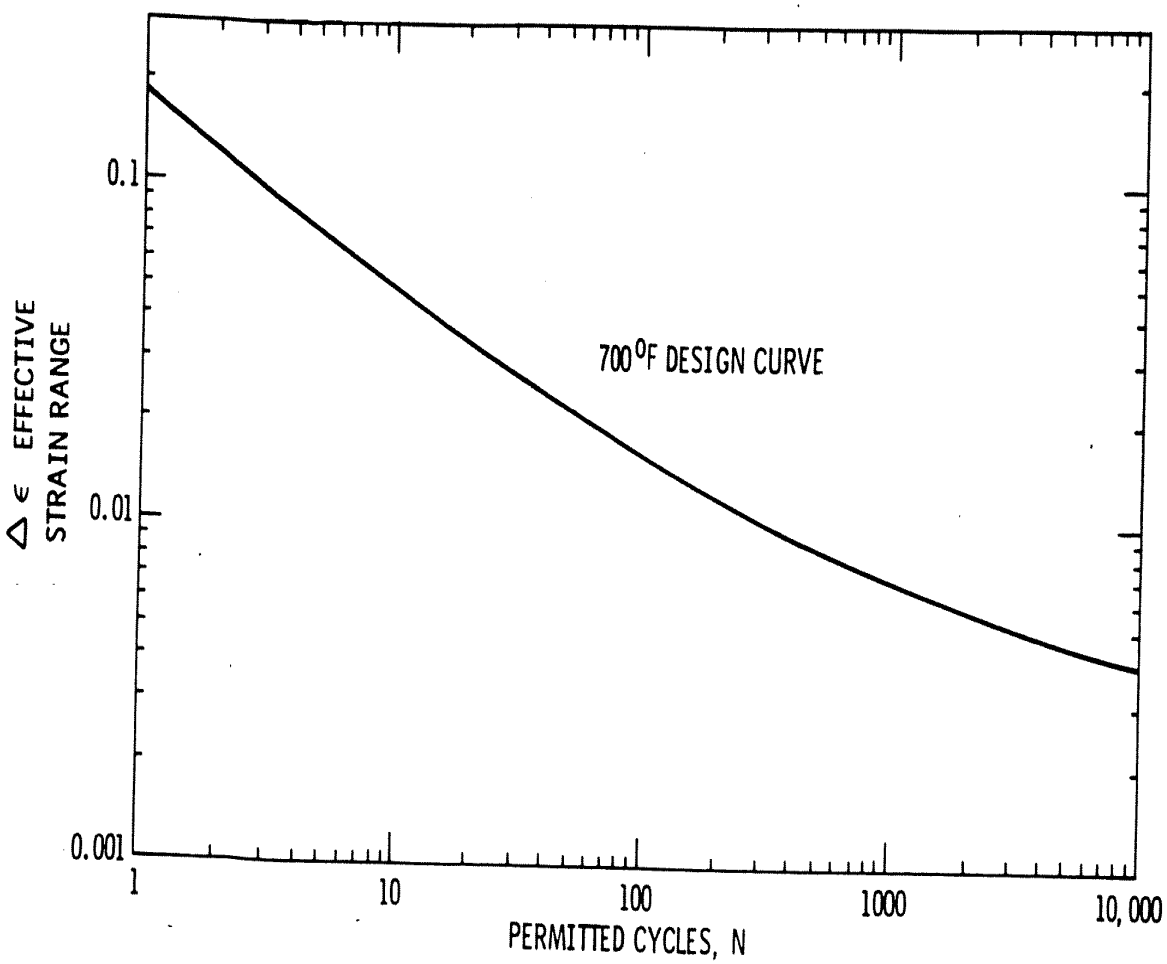

Revision 11 (05/01)

Waterford Steam Electric Station #3	DESIGN CURVE FOR CYCLIC STRAIN USAGE OF ZIRCALOY – 4 AT 700° F	Figure 4.2-2

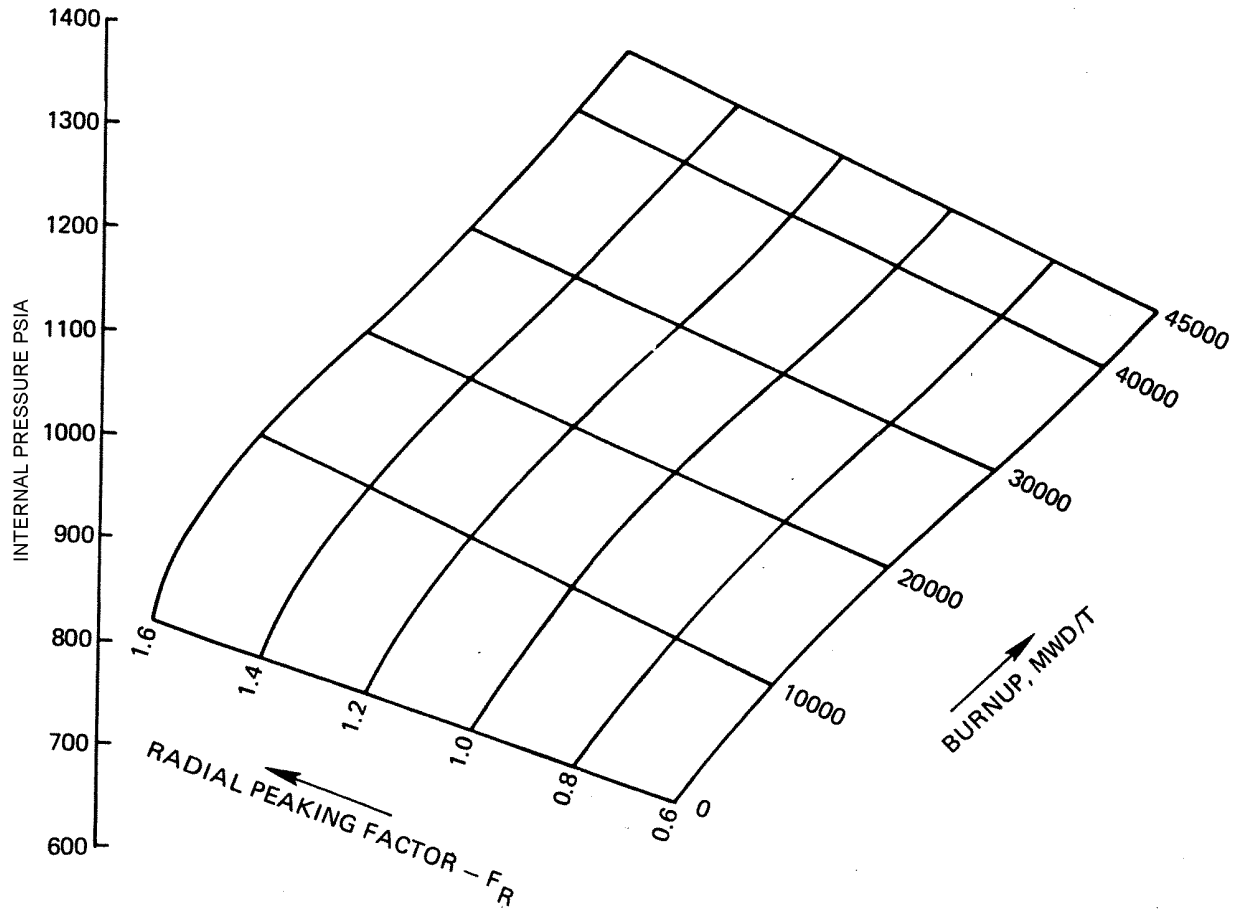

Revision 11 (05/01)

Waterford Steam Electric Station #3	FUEL ROD INTERNAL PRESSURE VARIATION WITH BURNUP & POWER LEVEL MINIMUM PRESSURE ROD	Figure 4.2-3

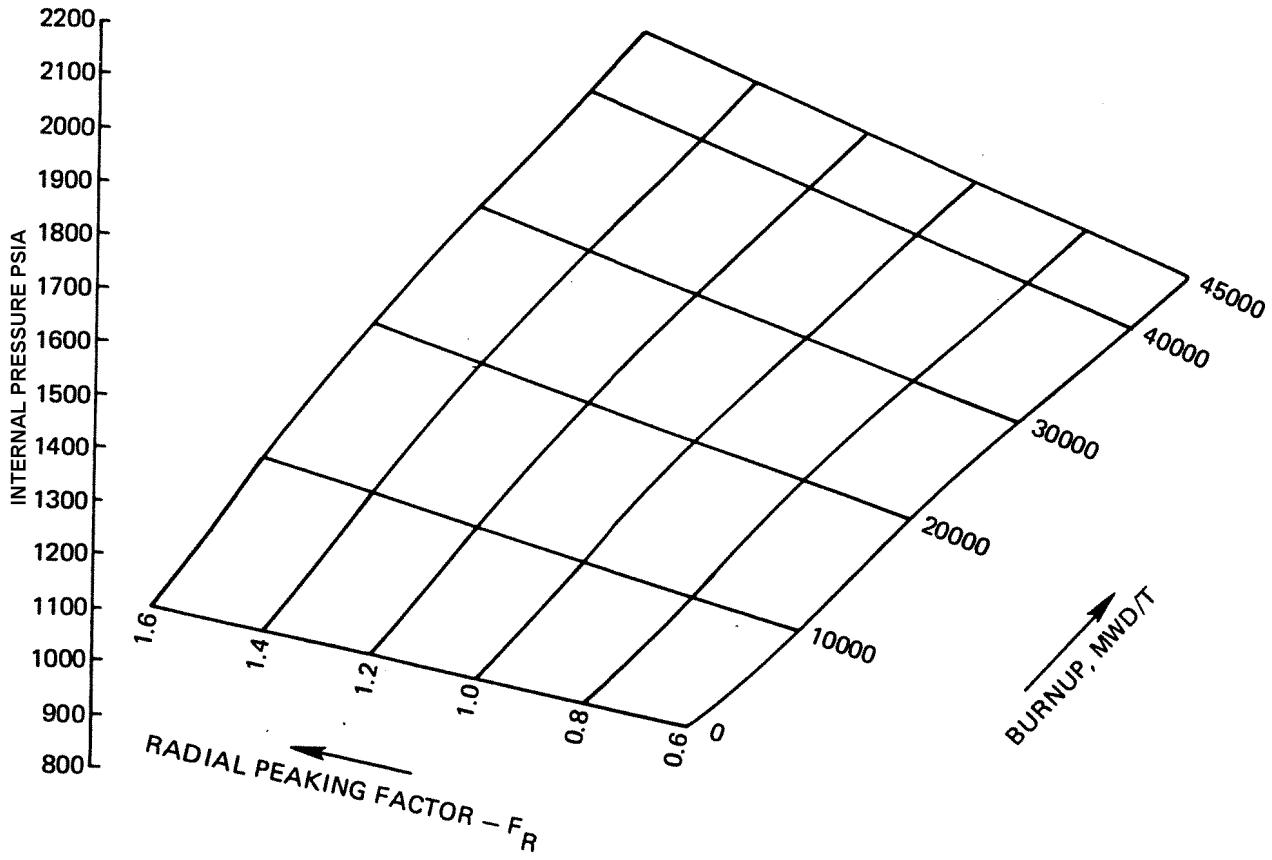

Revision 11 (05/01)

Waterford Steam Electric Station #3	FUEL ROD INTERNAL PRESSURE VARIATION WITH BURNUP & POWER LEVEL MAXIMUM PRESSURE ROD	Figure 4.2-4

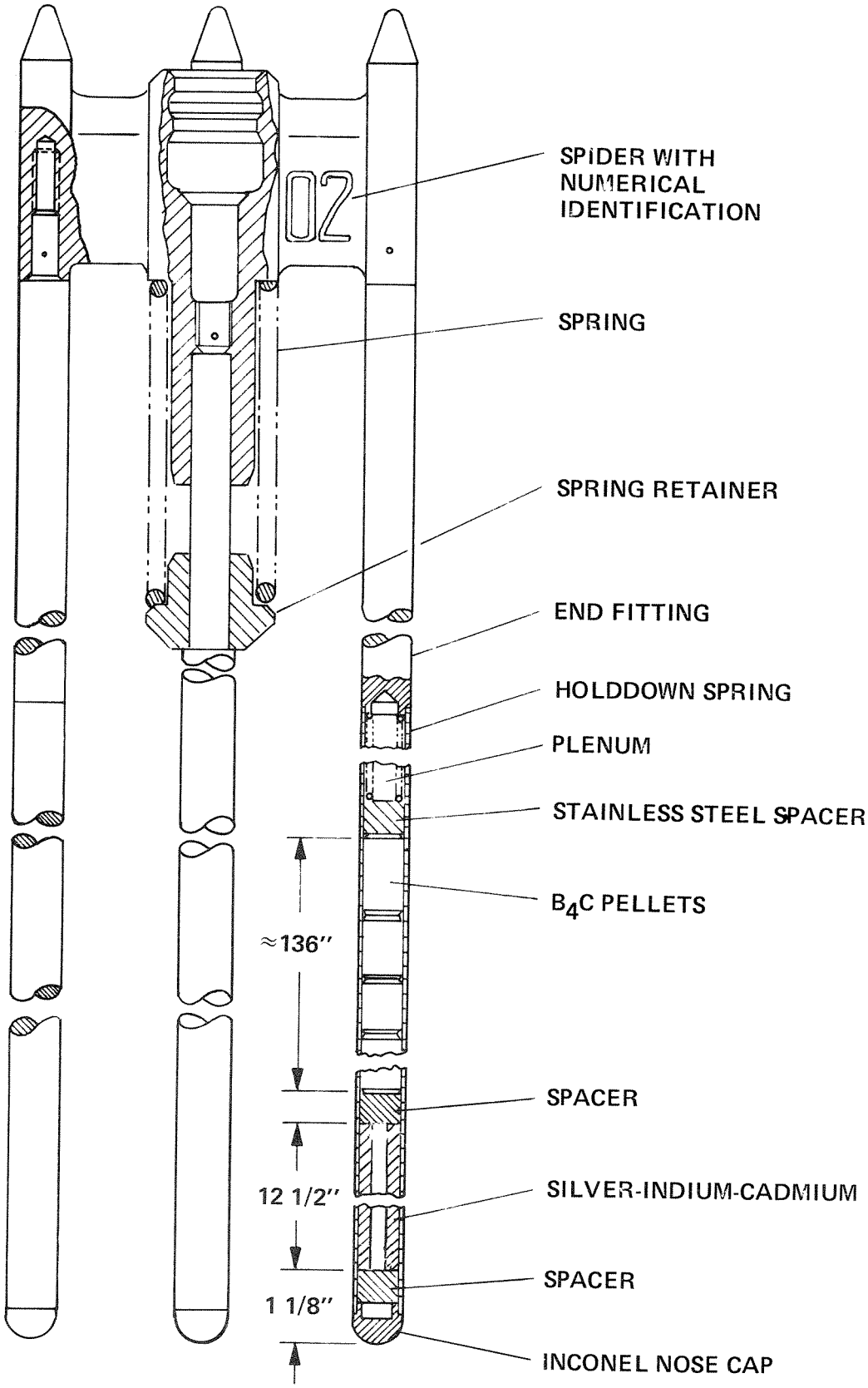

Revision 12 (10/02)

LOUISIANA POWER & LIGHT CO. Waterford Steam Electric Station	CONTROL ELEMENT ASSEMBLY	Figure 4.2-5

→(DRN 01-1103)

Figure 4.2-6 has been intentionally deleted.

←(DRN 01-1103)

→(DRN 01-1103)

Figure 4.2-7 has been intentionally deleted.

←(DRN 01-1103)

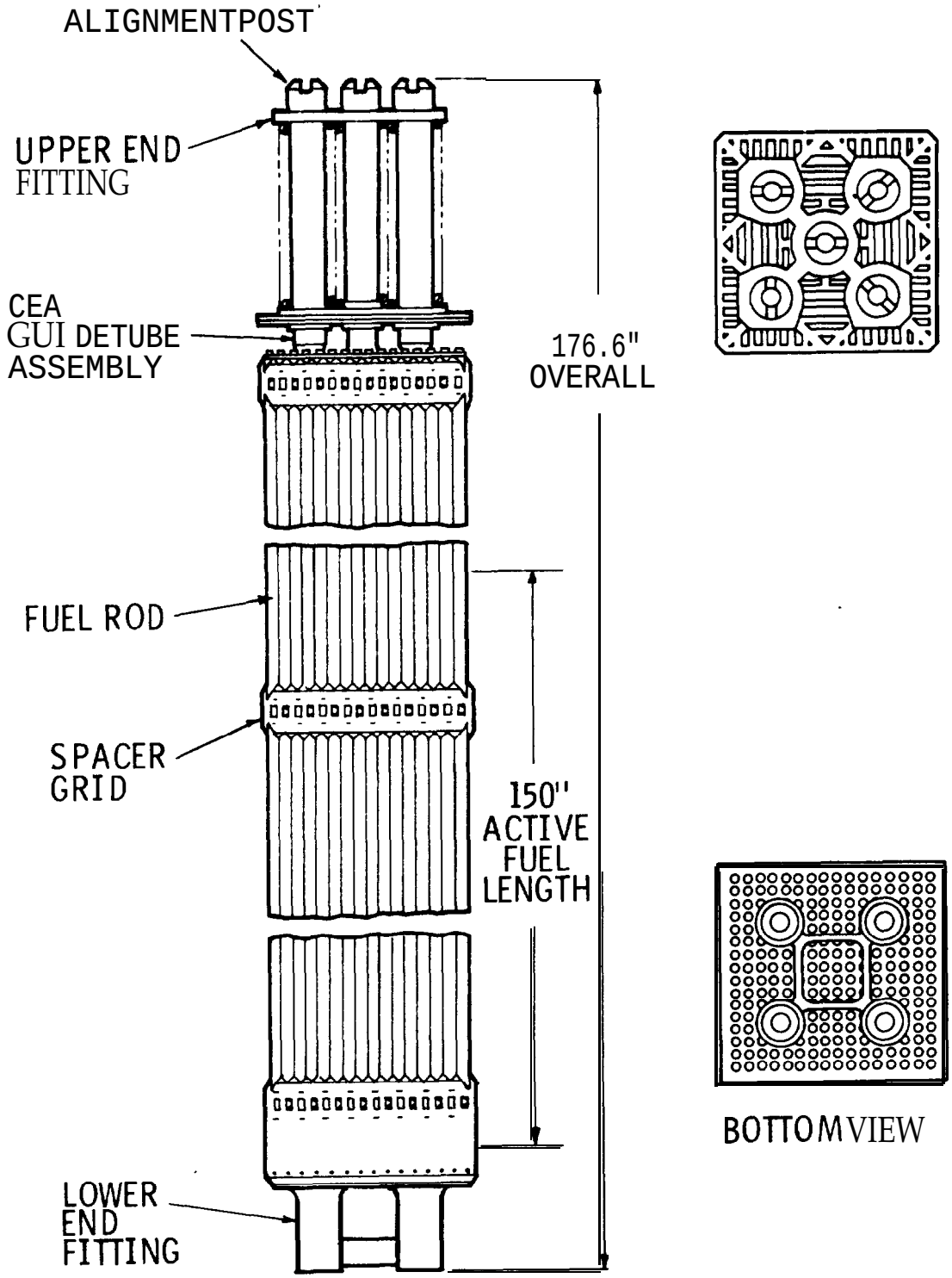

LOUISIANA POWER & LIGHT CO.
Waterford Steam Electric Station

FUEL ASSEMBLY

Figure 4.2-8

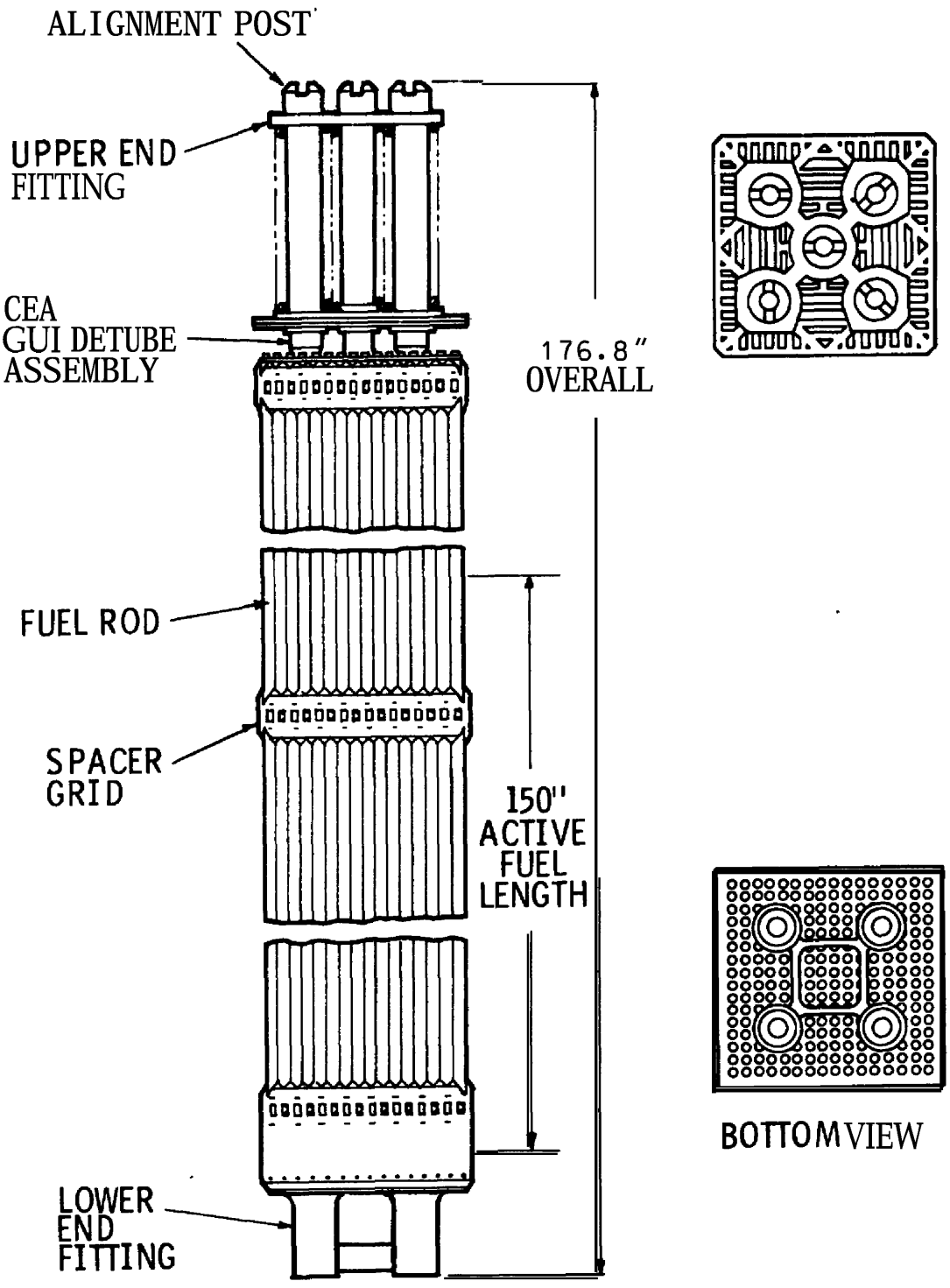

REVISION 302 (12/08)

LOUISIANA POWER & LIGHT CO. Waterford Steam Electric Station	FUEL ASSEMBLY (NGF)	Figure 4.2-8a

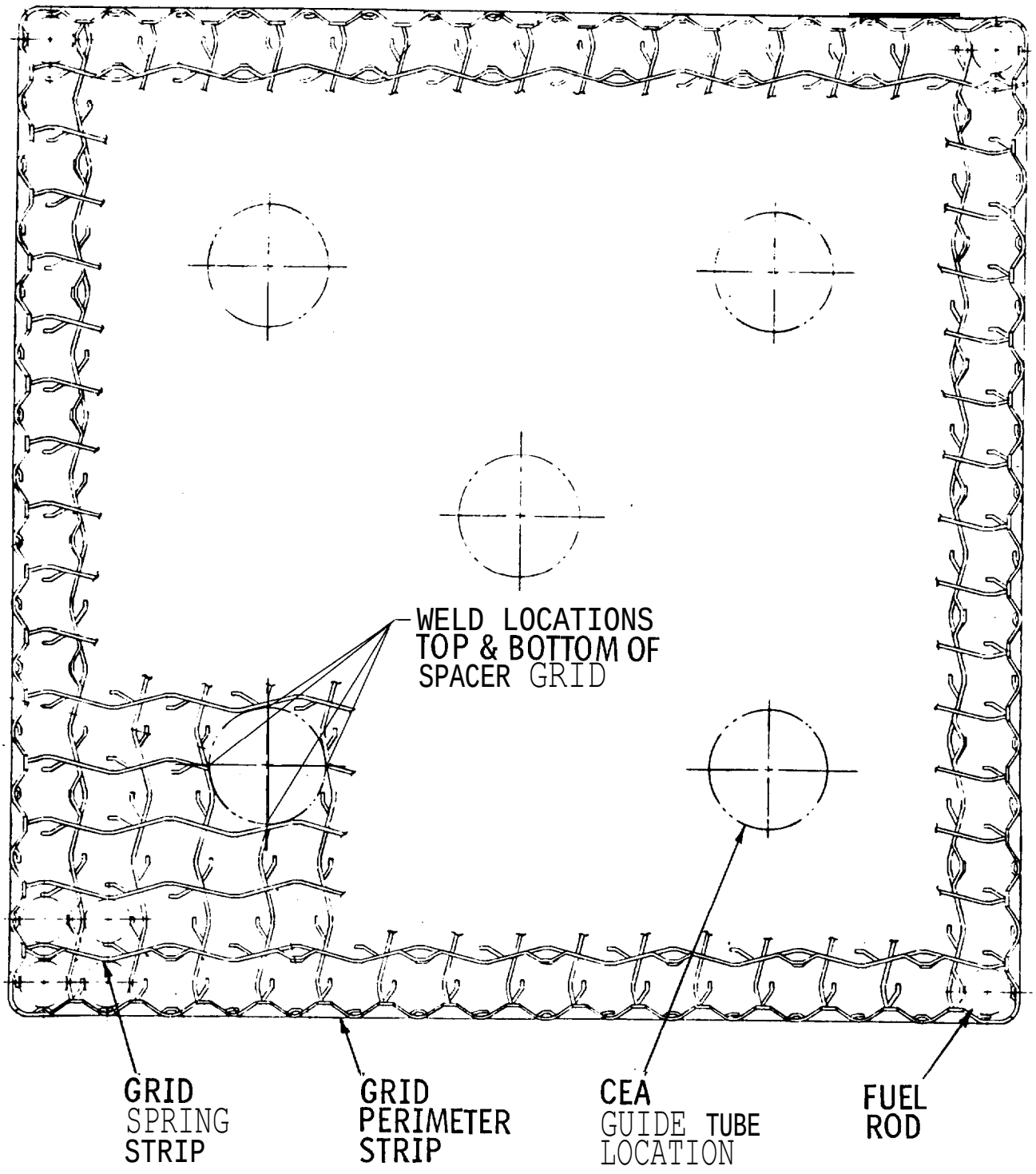

LOUISIANA POWER & LIGHT CO. Waterford Steam Electric Station	FUEL SPACER GRID	Figure 4.2-9

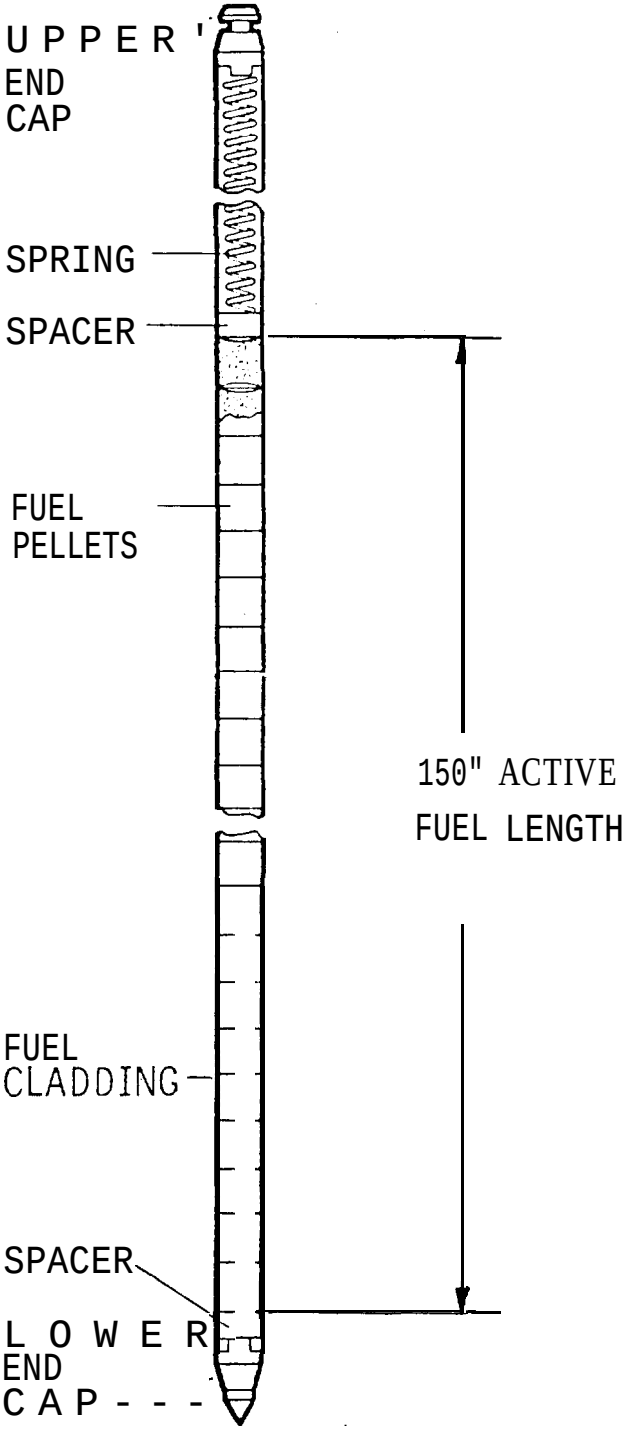

LOUISIANA POWER & LIGHT CO. Waterford Steam Electric Station	FUEL ROD	Figure 4.2-I 0

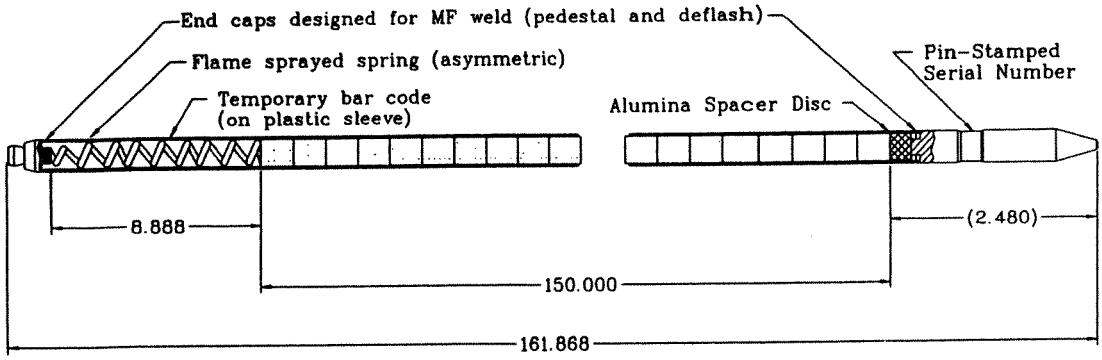

Batch T Rod Assembly with MF Welds (Hematite Production)

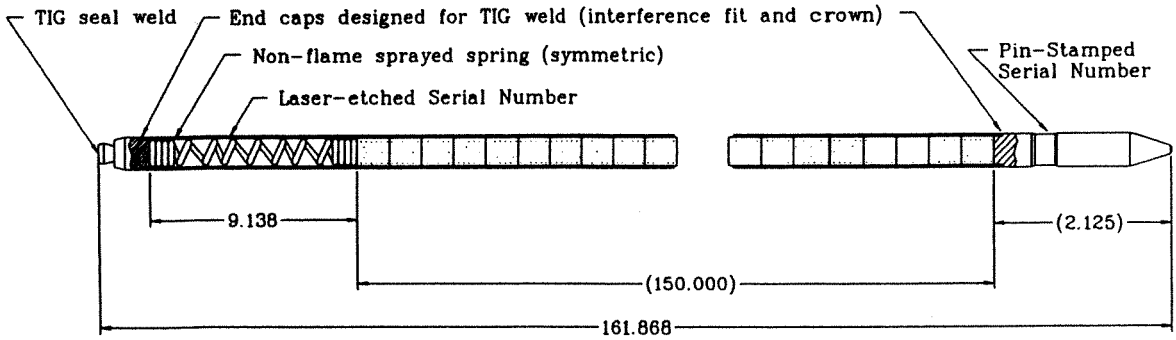

Batch U Rod Assembly with TIG Welds (Columbia Production)

Revision 12 (10/02)

Waterford Steam Electric Station #3	Comparison of Urania Rod Assembly Features	Figure 4.2-10A

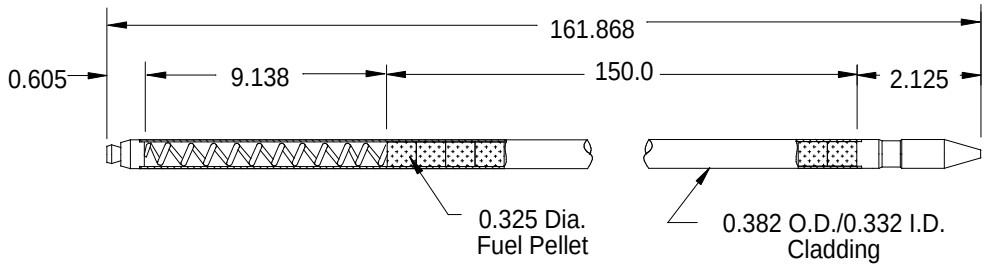

WSES Urania Rod Design
(Batches U, X, and Y)

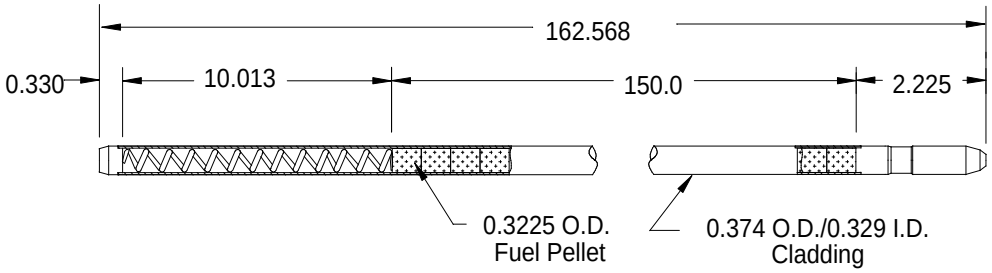

WSES NGF Urania Rod Design
(begins w/Batch Z)

Waterford Steam Electric Station #3	Comparison of Urania Rod Assembly Features	Figure 4.2-10B

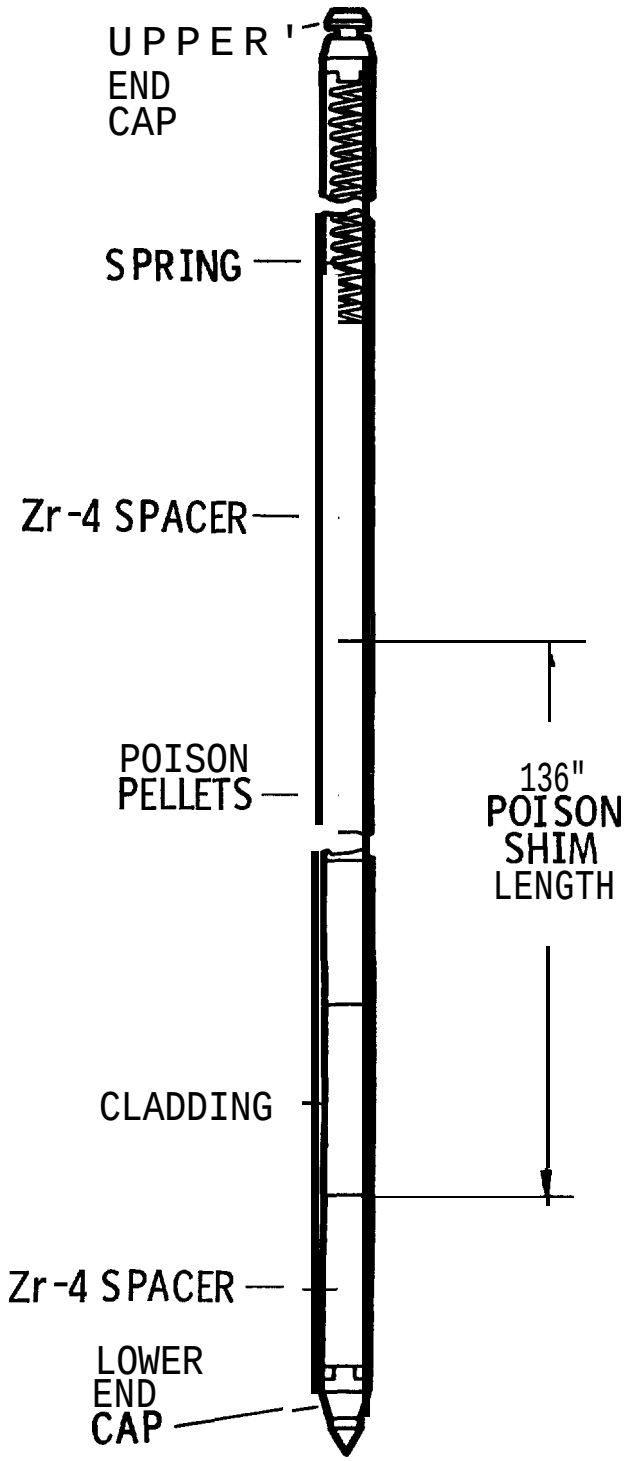

LOUISIANA POWER & LIGHT CO. Waterford Steam Electric Station	BURNABLE POISON ROD	Figure **4.2-11**

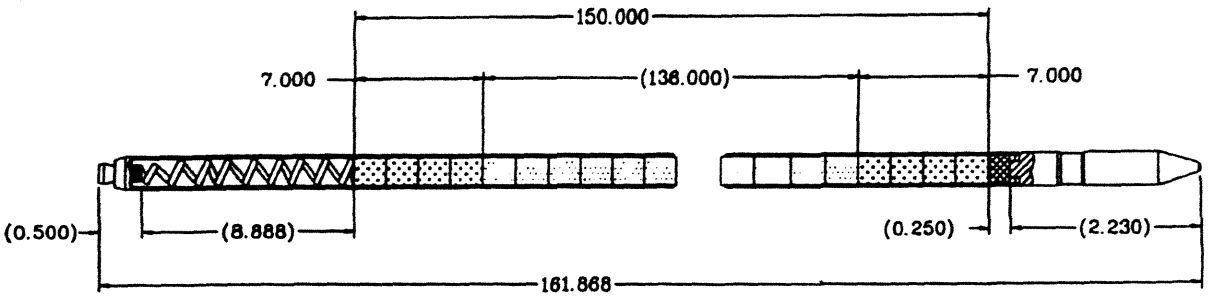

WSES-3 Batch T Erbia Rod Design (Hematite)

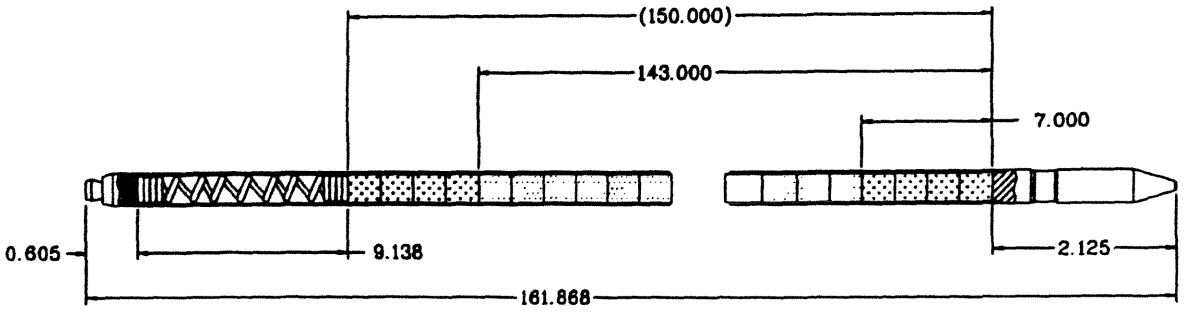

WSES-3 Columbia Rod Design
Erbia (Batches U-X), IFBA (begins w/Batch Y)

Revision 15 (03/07)

Waterford Steam Electric Station #3	Comparison of Burnable Absorber Rods	Figure 4.2-11A

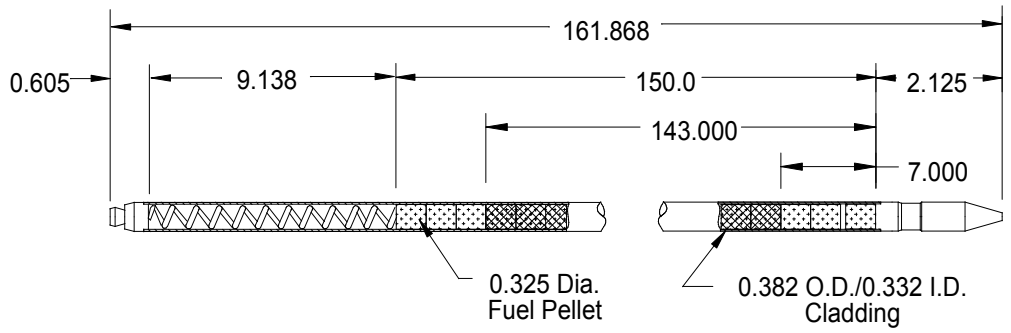

WSES IFBA Rod Design
(Batch Y)

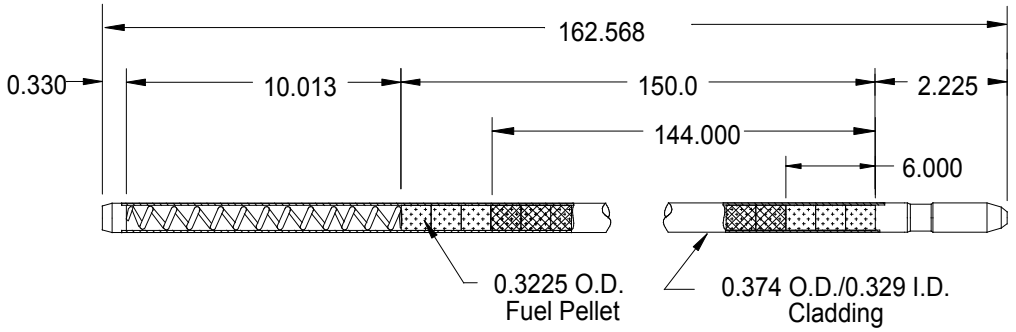

WSES NGF IFBA Rod Design
(begins w/Batch Z)

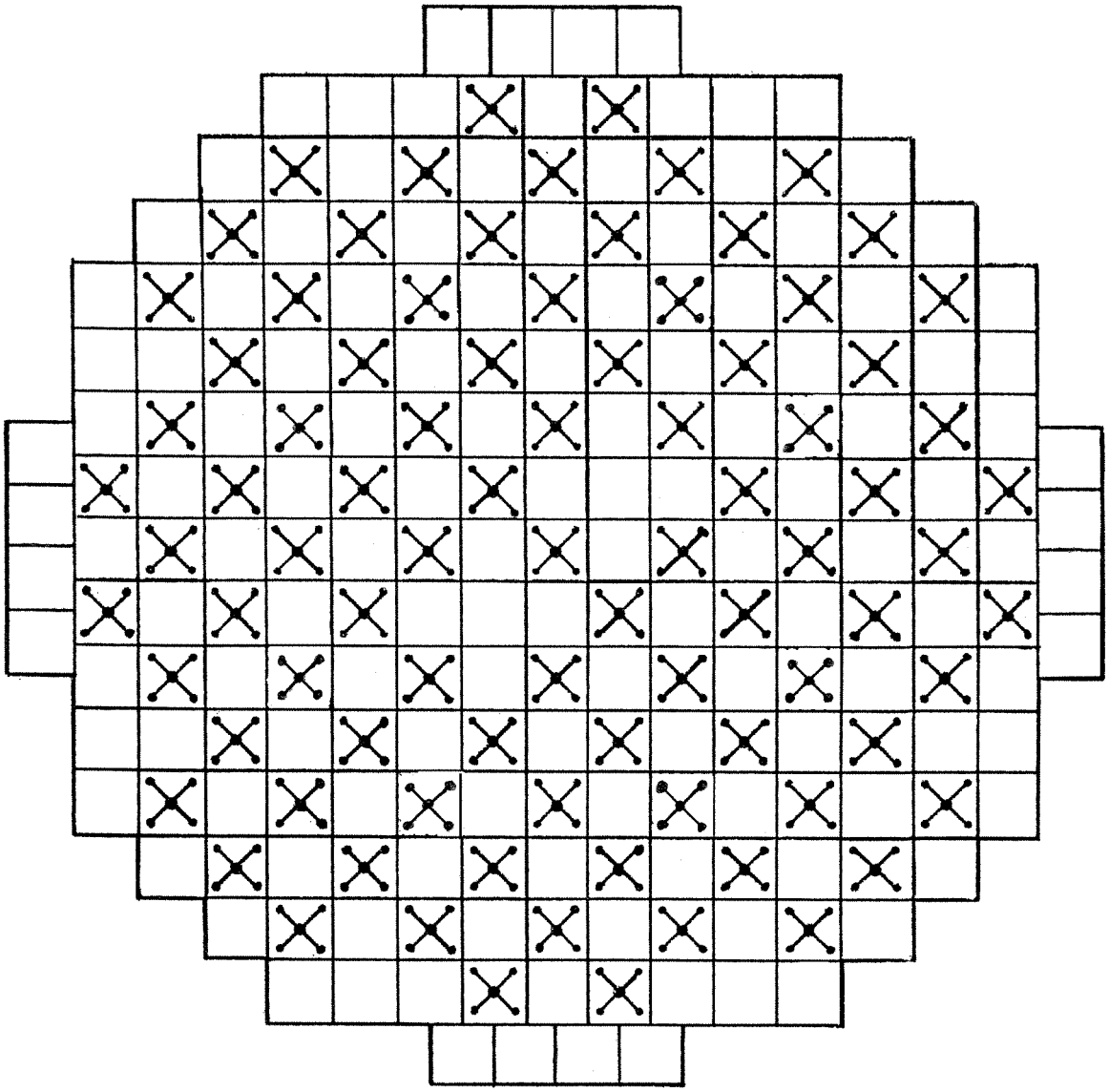

CEA's 87

Revision 12 (10/02)

LOUISIANA POWER & LIGHT CO. Waterford Steam Electric Station	CONTROL ELEMENT ASSEMBLY LOCATIONS	Figure 4.2-12

4.3 NUCLEAR DESIGN

4.3.1 DESIGN BASES

→(DRN 02-1538)
The bases for the nuclear design of the fuel and reactivity control systems are discussed in the following subsections. The Cycle 1 information presented in these sections is representative of the current cycle as modified by Appendix 4.3A.
←(DRN 02-1538)

4.3.1.1 Excess Reactivity and Fuel Burnup

The excess reactivity provided for a cycle is based on the depletion characteristics of the fuel and burnable poison and on the desired burnup for the cycle. The desired burnup is based on the projected operating cycle for Waterford 3. The average burnup is chosen to ensure that the peak burnup is within the limits discussed in Subsection 4.2.3.2.12. This design basis, along with the design basis in Subsection 4.3.1.8, satisfies General Design Criterion 10.

4.3.1.2 Core Design Lifetime and Fuel Replacement Program

The core design lifetime and fuel replacement program for Cycle 3 and beyond is based on approximately eighteen month refueling with roughly 40% of the fuel assemblies replaced at each refueling outage.

4.3.1.3 Negative Reactivity-Feedback

In the power operating range, the net effect of the prompt inherent nuclear feedback characteristics (fuel temperature coefficient, moderator temperature coefficient, and moderator pressure coefficient) tends to compensate for a rapid increase in reactivity. The negative reactivity feedback provided by the design satisfies General Design Criterion 11.

4.3.1.4 Reactivity Coefficients

→(DRN 02-1538)
The values of each coefficient of reactivity are consistent with the design bases for net reactivity feedback (Subsection 4.3.1.3), and analyses that predict acceptable consequences of postulated accidents and anticipated operational occurrences, where such analyses include the response of the Reactor Protection System ((RPS).
←(DRN 02-1538)

4.3.1.5 Burnable Poison Requirements

The burnable poison reactivity worth provided in the design is sufficient to ensure that the moderator coefficients of reactivity are consistent with the design bases in Subsection 4.3.1.4.

4.3.1.6 Stability Criteria

The reactor and the instrumentation and control systems are designed to detect and suppress xenon-induced power distribution oscillations that could, if not suppressed, result in conditions that exceed the specified acceptable fuel design limits. The design of the reactor and associated systems precludes the possibility of power level oscillations. This basis satisfies General Design Criterion 12.

4.3.1.7 Maximum Controlled Reactivity Insertion Rate

The core, control element assemblies (CEAs), Reactor Regulating System, and boron charging portion of the Chemical and Volume Control System are designed so that the potential amount and rate of reactivity insertion due to normal operation and postulated reactivity accidents do not result in:

a) Violation of the specified acceptable fuel design limits

b) Damage to the reactor coolant pressure boundary

c) Disruption of the core or other reactor internals sufficient to impair the effectiveness of emergency core cooling.

This design basis, along with Subsection 4.3.1.11 satisfies General Design Criteria 25 and 28.

4.3.1.8 Power Distribution Control

→(DRN 02-1538)
The core power distribution is controlled such that, in conjunction with other core operating parameters, the power distribution does not result in violation of the limiting conditions for operation. Limiting conditions for operation and limiting safety system settings are based on the accident analyses described in Chapter 15, such that: specified acceptable fuel design limits are not exceeded as a result of anticipated operational occurrences, and the limits of acceptable consequences are not exceeded for other postulated accidents. This basis, along with Subsection 4.3.1.2, satisfies General Design Criterion 10.
←(DRN 02-1538)

4.3.1.9 Shutdown Margins and Stuck Rod Criteria

The amount of reactivity available from insertion of withdrawn CEAs under all power operating conditions, even when the highest worth CEA fails to insert, will provide for at least one percent shutdown margin after cooldown to hot zero power, and any additional shutdown reactivity requirements assumed in the safety analyses. This basis, along with Subsection 4.3.1.10, satisfies General Design Criteria 26 and 27.

4.3.1.10 Chemical Shim Control

The Chemical and Volume Control System (CVCS) (Subsection 9.3.4) is used to adjust the dissolved boron concentration in the moderator. After a reactor shutdown, this system is able to compensate for the reactivity changes associated with xenon decay and reactor coolant temperature decreases to ambient temperature, and it provides adequate shutdown margin during refueling. This system also has the capability of controlling, independently of the CEAs, long-term reactivity changes due to fuel burnup and reactivity changes during xenon transients resulting from changes in reactor load. In particular, any xenon burnout transient may be accommodated at any time in the fuel cycle. This design basis, along with Subsection 4.3.1.9 satisfies General Design Criteria 26 and 27.

4.3.1.11 Maximum CEA Speeds

Maximum CEA speeds are consistent with the maximum controlled reactivity insertion rate design basis discussed in Subsection 4.3.1.7. Maximum CEA speeds are also discussed in Section 4.2.

→(LBDCR 13-014, R309)

4.3.2 DESCRIPTION

←(LBDCR 13-014, R309)

4.3.2.1 Nuclear Design Description

→(DRN 00-644; 02-1477, R12)

This section summarizes the nuclear characteristics of the core and discusses the important design parameters that affect the performance of the core in steady-state and normal transient operation. Summaries of nuclear design parameters for Cycle 1 are presented in Table 4.3-1, and Figure 4.3-1. Design limit values for these and other parameters are discussed in the appropriate sections.

←(DRN 02-1477, R12)

The first cycle design features a 3 batch loading scheme in which the type B and C fuel assemblies contain rods of two different enrichments. In this approach, the three pins in each of the corners of every B assembly and every C assembly were replaced by pins containing a lower fuel enrichment. This unique system of enrichment zoning offers improved long-term control over the local assembly power distribution.

←(DRN 00-644)

Fuel enrichment and burnable poison distributions are shown in Figure 4.3-1. The other three quadrants of the core are symmetric to the displaced quadrant. Physical features of the lattice, fuel assemblies, and CEAs are described in Section 4.2.

→(DRN 00-644)

Assembly enrichments, core burnup, critical soluble boron concentrations and worths, plutonium buildup, and delayed neutron fractions and neutron lifetime are shown in Table 4.3-1. The soluble boron insertion rate shown in this table, as discussed in Subsection 9.3.4, are sufficient to compensate for the maximum reactivity addition due to xenon burnout and normal plant cooldown. This maximum reactivity addition rate for which the CVCS will be required to compensate is given in Table 4.3-1. The maximum value occurs for an end-of-cycle cooldown, where the moderator temperature coefficient is most negative.

←(DRN 00-644)

4.3.2.2 Power Distribution

4.3.2.2.1 General

→(DRN 04-1096, R14)

At all times during operation, it is intended that the power distribution and coolant conditions be controlled so that the peak fuel centerline temperature and the minimum departure from nucleate boiling ratio (DNBR) are maintained within operating limits supported by the safety analyses (Chapter 15) with due regard for the correlation between measured quantities, the power distribution, and uncertainties in the determination of power distribution.

←(DRN 04-1096, R14)

→(DRN 01-1103; 02-1477)
Methods of controlling the power distribution include the use of CEAs to alter the axial power distribution, decreasing CEA insertion by boration, thereby improving the radial power distribution, and correcting off-optimum conditions which cause margin degradations (e.g., CEA misoperation).
←(DRN 01-1103; 02-1477)
As an operator aide, the Core Operating Limit Supervisory System (COLSS) will indicate to the operator how far the core is from the operating limits and give an audible alarm should an operating limit be exceeded. Such a condition signifies a reduction in the capability of the plant to withstand an anticipated transient, but does not necessarily imply a violation of fuel design limits. If the margin to fuel design limits continues to decrease, the RPS assures that the specified acceptable fuel design conditions are not exceeded by initiating a trip.

The COLSS, described in Section 7.7 and Reference 1, continually generates an assessment of the margin to linear heat rate and DNBR operating limits. The data required for these assessments include measured in-core neutron flux data, CEA positions, and coolant inlet temperature, pressure, and flow. In the event of an alarm indicating that an operating limit has been exceeded, power must be reduced unless the alarm can be cleared by improving either the power distribution or another process parameter. The adequacy of the COLSS calculations is verified periodically.

In addition to the monitoring performed by COLSS, the RPS continually infers the core power distribution and thermal margin by processing reactor coolant data, signals from ex-core neutron flux detectors, each containing three axially stacked elements, and input from redundant reed switch assemblies to indicate CEA position. In the event the power distributions or other parameters are perturbed as the result of an anticipated operational occurrence that would violate fuel design limits, the high local power density or low DNBR trips in the RPS will initiate a reactor trip. The relationship between the design power distributions and the monitoring instrumentation is discussed in detail in Reference 1. The dependence of the excore detector readings on the power distributions is also detailed in Subsection 4.3.3.1.1.

4.3.2.2.2 Nuclear Design Limits on the Power Distribution

The design limits on the power distribution stated here were employed during the design process both as design input and as initial conditions for accident analyses described in Chapters 6 and 15. However, for the monitoring system, it is the final operating limit determination that is used to assure that the consequences of an anticipated operational occurrence or postulated accident will not be any more severe than the consequences shown in Chapter 15. The initial conditions used in this operating limit determination are actually stated in terms of PLHGR and required power margin for minimum DNBR.

The design limits on power distribution are as follows:

a) The limiting three-dimensional heat flux peaking factor, F_q^n was established for full power conditions at 2.28 and 2.35, for, first and equilibrium cycles, respectively. The lower value for the first cycle reflects the presence of burnable poison shims in the fuel lattice and a corresponding reduction in the number of fuel rods. F_q^n is defined in Subsection 4.4.2.2.2.1, listing C and is termed the nuclear heat flux factor or the total nuclear peaking factor.

An F_q^n of 2.28 in combination with uncertainties and allowances on heat flux which give the initial peak linear heat rate assumed in the safety analyses constituted one limiting combination of parameters for full power operation in the first cycle. Other combinations of parameters which will result in acceptable consequences of the safety analysis do exist; e.g., a higher F^n is acceptable at a reduced power level. Implementation in the technical specification is via an operating limit on the monitored peak linear heat generation rate.

→(EC-13881, R304)

b) The margin to the minimum DNBR (using the ABB-NV and WSSV-T DNBR correlations as discussed in Subsection 4.4.2.2 and 4.4.4.1), which is available to accommodate anticipated operational occurrences, will be as acceptable as the margin calculated with the following combination of:

←(EC-13881, R304)

1) The coolant conditions

2) The axial power distribution

3) The axially integrated radial peaking factor, F_r^n, is the rod radial nuclear factor or the rod radial peaking factor and is defined in Subsection 4.4.2.2.2.1, listing A.

An F_r^n of 1.55, the set of axial shapes displaced in Figure 4.4-3, and the coolant conditions assumed in the safety analyses constitute one limiting combination of parameters for full power operation. Other combinations giving acceptable accident analysis consequences are equally acceptable. Implementation of these limits in the technical specification is via an operating limit on allowed minimum monitored DNBR underflow vs. measured incore axial shape index. This operating limit is based on consideration of many different allowed operating conditions (axial and radial power distributions as well as coolant conditions) at any axial shape index.

It will be shown in the following subsections that operation within these design limits is achievable.

4.3.2.2.3 Expected Power Distributions

→(DRN 01-1103; 02-1477)

Figures 4.3-2 through 4.3-13 and 4.3-14 through 4.3-18 show typical first cycle planar radial and unrodded core average axial power distributions, respectively. They illustrate conditions expected at full power for various times in the fuel cycle as specified on the figures. It is expected that the normal operation of the reactor will be with limited CEA insertion so that these power distributions represent the expected power distribution during most of the cycle. The three-dimensional peaking factor, F_q expected during steady-state operation is then just the product of the unrodded planar radial peaking factor (F_r) and the axial peaking factor. The maximum expected value of F^n is 1.85 during the first cycle and, as can be seen from the above figures, occurs near the beginning-of-cycle for steady-state, base loaded operation with no CEA insertion. The uncertainty associated with these calculated power distributions is discussed in Subsection 4.3.3.1.2.2.6.

The capability of the core to follow load transients without exceeding power distribution limitations depends on the margin to operating limits compared to the margin required for base loaded, unrodded operation. In order to illustrate the maneuvering capability available in Waterford 3, the results of calculations of the power distributions and power peaking factors during distributions are calculated by QUIX (see Subsection 4.3.3.1.1), a one-dimensional spatial flux calculational model that considers the effects of the time and spatial variations of xenon and iodine concentration, CEA position, thermal and moderator density feedback mechanisms, as well as the effect of the burnup distribution near end-of-cycle. Since QUIX does not have fuel depletion capability, axial-dependent depletion effects are included in end-of-cycle calculation by using and end-of-cycle axial nuclide distribution computed from one-dimensional (axial) PDQ depletion calculations. Estimates of F_q and F^n are obtained by synthesis of the three-dimensional power QUIX calculations. The QUIX model accepts values of radial peaking factors for each type of CEA bank insertion (unrodded, bank six inserted, bank five inserted, etc.). These radial peaking factors are input for the appropriate core average burnup condition and are applied over that axial region of the core having the specified CEA bank configuration (e.g., unrodded, bank six inserted, etc.). These radial peaking factors are weighted by the axial power distribution to obtain an axially integrated radial peaking factor. The value of this integrated radial peaking factor of each planar region is not, in general, expected to occur at the same fuel pin location. The magnitude of the input radial peaking factors is determined primarily by the number and location of the inserted CEAs; it is evaluated at the full power conditions and taken to be independent of power level.

←(DRN 01-1103; 02-1477)

→(DRN 01-1103; 02-1477)
Figures 4.3-25 through 4.3-32 show the calculated axial power distributions and associated nuclear peaking factors during a typical day of a maneuvering transient to either 50 or 35 percent of the full power conditions. Also shown on these figures are the CEA locations during the transient.
←(DRN 01-1103; 02-1477)
The detailed axial power distribution within any assembly is a function of the location of that assembly within the core as well as the time in life, CEA insertion, etc. For DNB analysis, a conservatively flat local radial distribution is used to evaluate intra-assembly mixing and crossflow. The conservative distribution is shown on Figure 4.3-33; the power in the hottest rod in that assembly is assumed to be at the design limit peaking factor. Care is taken in the fuel management to ensure in effect that no flatter distribution occurs in assemblies that are limiting or near limiting with respect to DNB. In Subsection 4.3.3.1.2, the accuracy of calculations of the power distribution within a fuel assembly is discussed.

4.3.2.2.4 Allowances and Uncertainties on Power Distributions

In comparing the expected power distributions and implied peak linear heat generation rate (PLHGR) produced by analysis with the design limits stated in Subsection 4.3.2.2.2 consideration must be given to the uncertainty and allowances associated with on-line monitoring by COLSS.

Reference 1, a CE Topical Report on COLSS, contains the conclusion based on detailed numerical evaluations for cores similar to Waterford 3 that a penalty factor of 7.5 percent should be applied to COLSS determinations of F^n. The uncertainty analysis provided for Waterford 3 is described in Subsection 7.7.1.5. In addition, a power level uncertainty factor of 1.02, an engineering factor of 1.03, and an augmentation factor to account for power spiking associated with fuel densification are customarily included. The latter factor varies axially, but can be expected to have a value on the order of 1.03 at the elevation of the axial peak. A multiplicative combination of these factors leas to an overall penalty of 16.3 percent on monitored PLHGR. Similarly, it has been demonstrated in Reference 1 than an uncertainty of 4.6 percent is associated with the thermal margin calculation performed by COLSS.

4.3.2.2.5 Comparisons Between Limiting and Expected Power Distributions
→(DRN 02-1477)
As was discussed in Subsection 4.3.2.2.3, Expected Power Distributions, the maximum expected unrodded F^n that occurs during the first cycle at full power is 1.85. Augmenting this value by the uncertainties and allowances discussed above provides an upper limit on F_q^n of 2.16 which is well below the design target of 2.28.
←(DRN 02-1477)

→(DRN 02-1477)
←(DRN 02-1477)

Similarly, even allowing for the 4.6 percent uncertainty on the monitoring of thermal margin the maximum expected unrodded F^n that occurs at full power is well below the design limit of 1.55 stated in Subsection 4.3.2.2. Again, as demonstrated by the calculations of the power distributions expected to occur during maneuvering transients, no appreciable loss in thermal margin is expected to occur during these transients.

4.3.2.3 Reactivity Coefficients

Reactivity coefficients relate changes in core reactivity to variations in fuel or moderator conditions. The data presented in this section and associated tables and figures illustrate the range of reactivity coefficient values calculated for a variety of operating accident conditions. Subsection 4.3.3 presents comparisons of calculated and measured moderator temperature coefficients and power coefficients for operating reactors. The good agreement shown in that subsection provides confidence that the data presented in this section adequately characterize the Waterford 3 reactor. Table 4.3-3 presents a comparison of the reactivity coefficients calculated for the Waterford 3 reactor with those used in the safety analyses described in Chapter 15. For each accident analysis, suitably conservative reactivity coefficient values are used. Since uncertainties in the coefficient values, as discussed in Subsection 4.3.3.1.2, and other conservatisms are taken into account in the safety analyses, values used in the safety analyses may fall outside the ranges in a conservative direction of the data presented in this section. A more extensive list of reactivity coefficients is given in Table 4.3-4.

The calculational methods used to compute reactivity coefficients are discussed in Subsection 4.3.3.1.1. All data discussed in subsequent subsections are calculated with two-dimensional, quarter-core nuclear models. Spatial distributions of materials and flux weighting are explicitly performed for the particular conditions at which the reactivity coefficients are calculated. The adequacy of this method is discussed in Subsection 4.3.3.1.2.

4.3.2.3.1 Fuel Temperature Coefficient

The fuel temperature coefficient (FTC) is the change in reactivity per unit change in fuel temperature. A change in fuel temperature affects not only the thermal expansion of the fuel pellet but, in addition, the reaction rates in both the thermal and epithermal neutron energy regimes. Epithermally, the principal contributor to the change in reaction rate with fuel temperature is the Doppler effect arising from the increase in absorption widths of the resonances with an increase in fuel temperature. The ensuing increase in absorption rate with fuel temperature causes a negative FTC. In the thermal energy regime, a change in reaction rate with fuel temperature arises from the effect of temperature dependent scattering properties of the fuel matrix on the thermal neutron spectrum. In typical

PWR fuels containing strong resonance absorbers such as U-238 and Pu-240, the magnitude of the component of the FTC arising from the Doppler effect is more than a factor of 10 larger than the magnitude of the thermal energy component.

Figure 4.3-34 shows the dependence of the calculated FTC on the fuel temperature, both at the beginning and the end of the first cycle.

4.3.2.3.2 Moderator Temperature Coefficient

The moderator temperature coefficient (MTC) relates changes in reactivity to uniform changes in moderator temperature, including the effects of moderator density changes with changes in moderator temperature. Typically, an increase in the moderator temperature causes a decrease in the core moderator density and, therefore, less thermalization, which reduces the core reactivity. However, when soluble boron is present in the moderator, a reduction in moderator density causes a reduction in the content of soluble boron in the core, thus producing a positive contribution to the MTC. In order to limit the dissolved boron concentration, burnable poison rods (shims) are provided in the form of cylindrical pellets of alumina with uniformly dispersed boron carbide particles. The number of shims is given in Table 4.3-1 and their distribution in one quadrant of the core is shown in Figure 4.3-1. The distribution is identical for the other three quadrants. The reactivity control provided by the shims is given in Table 4.3-1. This control makes possible a reduction in the dissolved boron concentration to the values given in Table 4.3-1.

→(DRN 00-644; 06-895, R15)
The calculated MTC for various core conditions at beginning and end of first cycle are given in Table 4.3-4. The MTC are more negative at end-of-cycle (EOC) because the soluble boron n the coolant is reduced. The build-up of equilibrium xenon produces a net negative change of $-0.45 \times 10^{-4} \Delta\rho/°F$ in the MTC; this change is due mainly to the concomitant reduction in critical soluble boron. The changing fuel isotopic concentrations and the changing neutron spectrum during the fuel cycle depletion also contribute a small negative component to the MTCl.
←(DRN 00-644; 06-895, R15)

The dependence of the MTC on moderator temperature at beginning-of-cycle (BOC) and EOC (at constant soluble boron) is shown in Figures 4.3-35 and 4.3-36, respectively. These figures also show the expected MTC at reduced power levels (corresponding to reduced moderator temperatures) based on power reductions accomplished with soluble boron only and with CEAs only. These two modes of power reduction result in the most positive and most negative MTC expected to occur at reduced power levels. These figures show the expected MTC for the full range of expected operating conditions and accident conditions addressed in Chapter 15.

4.3.2.3.3 Moderator Density Coefficient

The moderator density coefficient is the change in reactivity per unit change in the average core moderator density at constant moderator temperature. A positive moderator density coefficient translates into a negative contribution to the total moderator temperature coefficient, which is defined in Subsection 4.3.2.3.2. The density coefficient is always positive in the operating range, although the magnitude decreases as the soluble boron level in the core is increased. The calculated density coefficient is shown in Table 4.3.-4, and curves of density coefficient as a function of density for several soluble boron concentrations are presented in Figure 4.3-37. These curves are based upon two-dimensional PDQ calculations and have been generated over a wide range of core conditions including the range of both normal operating conditions and accident conditions. The density coefficients explicitly used in the accident analyses are based upon core conditions with the most limiting temperature coefficients allowed by the technical specification. Table 4.3-3 shows comparison of the expected values of the moderator temperature coefficients with those actually used in the accident analyses.

4.3.2.3.4 Moderator Nuclear Temperature Coefficient

The moderator nuclear temperature coefficient is the change in reactivity per unit change in core average moderator nuclear temperature, at constant moderator density. The source of this reactivity dependence is the spectral effects associated with the change in thermal scattering properties of water molecules as the internal energy, which is represented by the bulk water temperature, is changed. The magnitude of the moderator nuclear temperature coefficient is equal to the difference between the MTC, defined in Subsection 4.3.2.3.2, and the moderator density coefficient, defined in Subsection 4.3.2.3.3.

4.3.2.3.5 Moderator Pressure Coefficient

The moderator pressure coefficient is the change in reactivity per unit change in reactor coolant system pressure. Since an increase in pressure increases the water density, the pressure coefficient is merely the density coefficient expressed in a different form. The calculated pressure coefficient at full power is shown in Table 4.3-4.

4.3.2.3.6 Moderator Void Coefficient

The anticipated occurrence of small amounts of local subcooled boiling in the reactor during full power operation results in a predicted core average steam (void) volume fraction of substantially less than one percent. Changes in the moderator void fraction produce reactivity changes that are quantified by the void coefficient of reactivity. An increase in voids decreases core reactivity, but the presence of soluble boron tends to add a positive contribution to the coefficient.

The calculated values of moderator void coefficient are shown in Table 4.3-4. Curves showing void coefficient vs. void content can be inferred directly from the density coefficient curves provided in Figure 4.3-37.

4.3.2.3.7 Power Coefficient

The power coefficient is the change in reactivity per unit change in core power level. All previously described coefficients contribute to the power coefficient, but only the MTC and the FTC contributions are significant. The contributions of the pressure and void coefficients are negligible, because the magnitudes of these coefficients and the changes in pressure and void fraction per unit change in power level are small. The contribution of moderator density change is included in the MTC contribution.

In order to determine the change in reactivity with power, it is necessary to know the changes in the average moderator and effective fuel temperatures with power. The average moderator (coolant) temperature is controlled to be a linear function of power.

The core average linear heat rate is also linear with power. The average effective fuel temperature dependence on the core average linear heat rate is calculated from the following seem-empirical relation:

$$T_f = T_m + 128.36\,\alpha \underline{P}^2 \qquad (1)$$

T_m is the average moderator temperature (°F), α is a weighting factor accounting for the number of spatial dimensions used in the calculations, $\underline{P}$ is the average thermal power generated per unit fuel rod length (kW/ft), and T_f is the average effective fuel temperature (°F). The basis for this relation is discussed in Subsection 4.3.3.1.2.2.4.

The total power coefficient at a given core power can be determined by evaluating, for the conditions associated with the given power level, the following expression:

$$\frac{dp}{dP} = \frac{\partial p}{\partial T_f} \cdot \frac{\partial T_f}{\partial P_m} + \frac{\partial p}{\partial T_m} \cdot \frac{\partial T_m}{\partial P} \qquad (2)$$

The first term of equation (2) provides the fuel temperature contribution to the power coefficient, which is shown as a function of power in Figure 4.3-38.

The first factor of the first term is the fuel temperature coefficient of reactivity discussed in Subsection 4.3.2.3.1 and shown in Figure 4.3-34. The second factor of the first term is obtained by calculating the derivative of equation (1).

$$\frac{\partial T_f}{\partial P} = 128.36\alpha - 3.5664\alpha P \qquad (3)$$

The second term in equation (2) provides the moderator contribution to the power coefficient. The first factor, the MTC, is discussed in Subsection 4.3.2.3.2 and shown in Figures 4.3-35 and 4.3-36. The second factor is a constant since the moderator temperature is controlled to be a linear function of power.

→(DRN 00-644)
Since the factors $\partial p / \partial T_f$ and $\partial p / \partial T_m$ are functions of one or more independent variables; e.g., burnup, temperature, soluble boron content, xenon worth, and CEA insertion, the total power coefficient, $d\rho / dP$ also depends on these variables.
←(DRN 00-644)
The power coefficient tends to become more negative with burnup because the FTC and MTC become more negative (see Figures 4.3-34 through 4.3-36). The insertion of CEAs, while maintaining constant power, results in a more negative power coefficient, because the soluble boron level is reduced and because of the spectral effects of the CEAs.

The full power values of the overall power coefficient for the unrodded core at BOC and EOC are shown in Table 4.3-4.

4.3.2.4 Control Requirements

There are three basic types of control requirements that influence the design of this reactor;

a) Reactivity control so that the reactor can be operated in the unrodded, critical, full power mode for the design cycle length.

b) Power level and power distribution control so that the reactor power may be safely varied from full-rated power to cold shutdown, and so that the power distribution at any given power level is controlled within acceptable limits.

c) Shutdown reactivity control sufficient to mitigate the effects of postulated accidents.

→(LBDCR 13-014, R309)
Reactivity control is provided by several different means. The amount and enrichment of the fuel and burnable poison shims are design variables that determine the beginning-of-cycle and end-of-cycle reactivity for an unrodded, unborated condition. Soluble boron and CEA poisons are flexible means of controlling long-term and short-term reactivity changes, respectively.
←(LBDCR 13-014, R309)
The following paragraphs discuss the reactivity balances associated with each type of control requirement.

4.3.2.4.1 Reactivity Control at BOC and EOC

The reactivities of the unrodded core at BOC and EOC with no soluble boron are shown in Table 4.3.2. This table includes the reactivity worth of equilibrium xenon and samarium, and shows the reactivity available to compensate for burnup and fission product poisoning. Soluble boron concentrations required for criticality at various core conditions are shown in Table 4.3-1. Soluble boron is used to compensate for slow reactivity changes such as those due to burnup, changes in xenon content, etc. The reactivity controlled by burnable poison shims is also given in Table 4.3-1. At EOC, the reactivity worth of the residual poison is less than one percent, and the soluble boron concentration is near zero. The reactor is to be operated in essentially an unrodded condition at power. The CEA insertion at power is limited by the power dependent insertion limit (PDIL) for short term reactivity changes.

4.3.2.4.2 Power Level and Power Distribution Control

→(DRN 00-644; 01-1103, R12)

The regulating CEA groups may be used to compensate for changes in reactivity associated with routine power level changes. In addition, CEAs may be used to compensate for minor variations in moderator temperature and boron concentrations during operation at power. The reactivity worth of regulating CEA control groups is shown in Table 4;.3-5. Soluble boron is used to maintain shutdown reactivity at cold zero power conditions.

←(DRN 00-644; 01-1103, R12)

4.3.2.4.3 Shutdown Reactivity Control

The reactivity worth requirements of the full complement of CEAs is primarily determined by the power defect, and the shutdown margin and the stuck rod criteria discussed in Subsection 4.3.1.9. Table 4.3-6 shows the reactivity component allowances that define the total reactivity allowance. These data are based on the EOC conditions when the fuel and moderator temperature coefficients are the most negative and thus when the shutdown reactivity requirement is a maximum. Each allowance component is further discussed below. No CEA allowance is provided for xenon reactivity effects; e.g., undershoot, since these effects are controlled with soluble boron rather than with CEAs.

→(LBDCR 13-014, R309)

The worth of all CEAs except the most reactive, which is assumed stuck in the fully withdrawn position, provides more shutdown capability than required by the total reactivity allowance shown in Table 4.3-6. This excess shutdown margin is shown in Table 4.3-7 for BOC and EOC. The margin is more than sufficient to compensate for calculational uncertainties in the nominal design allowances and in the CEA reactivity worth. Thus, the shutdown reactivity control provided in this design is sufficient at all times in the cycle.

←(LBDCR 13-014, R309)

4.3.2.4.3.1 Fuel Temperature Variation

The increase in reactivity that occurs when the fuel temperature decreases from the full power value to the zero power value is due primarily to the Doppler effect in U-238. The CEA reactivity allowance for fuel temperature variation shown in Table 4.3-6 is a conservative allowance for the EOC conditions. Measurements of first cycle power coefficients at Fort Calhoun, Calvert Cliffs, and Millstone-2 lead to a power defected of 1.2 percent $\Delta\rho$ (Subsection 4.3.3.1.2.2.4). The slight increase in power defect with exposure due to the presence of plutonium isotopes is offset by the reduction in the fuel temperature resulting from fuel swelling and clad creep-down. Therefore, the power defect does not change significantly with increasing cycle number and the value of 1.4 percent $\Delta\rho$ in Table 4.3-6 is an adequately conservative variation allowance.

4.3.2.4.3.2 Moderator Temperature Variation

The moderator temperature variation allowance is large enough to compensate for any reactivity increase that may occur when the moderator temperature decreases from the full power value to the zero power (hot standby) value. This reactivity increase, which is primarily due to the negative MTC, is largest at the EOC when the soluble boron concentration is near zero and the moderator coefficient is strongly negative. At BOC when the MTC is less negative, the reactivity change is smaller.

The CEA reactivity allowance for moderator temperature variation given in Table 4.3-6 is actually the sum of three allowances. The first, and most important, is the allowance for the MTC effect. The second is an allowance for the reduction in CEA worth resulting from the shorter neutron diffusion length at the zero power moderator density relative to the full power moderator density. This allowance is necessary because the CEA worths shown in Table 4.3-5 were calculated at full power. The third allowance is intended to cover the reactivity effects associated with the greatest expected axial flux redistribution resulting from the difference in moderator temperature profile between full and zero power, and the asymmetric axial burnup distribution at EOC.

4.3.2.4.3.3 Moderator Voids

Reducing the power level from full power to zero power causes an increase in reactivity resulting from the collapsing of steam bubbles caused by local boiling at full power. The amount of void in the core is small and is estimated to be substantially less than one percent at full power. As with the moderator temperature effect, the maximum increase in reactivity from full to zero power occurs at EOC when the least amount of dissolved boron is present. The reactivity effect is small, and the allowance for this effect is shown Table 4.3-6.

4.3.2.4.3.4 Control Element Assembly Bite

→(DRN 01-1103; 02-1477)

The CEA bite is the amount of reactivity worth in CEAs that can be inserted in the core at full power to initiate ramp changes in reactivity associated with load changes, and to compensate for minor variations in moderator temperature, boron concentration, xenon concentration, and power level. The reactivity allowance for this effect is shown in Table 4.3-6.

←(DRN 01-1103; 02-1477)

→(DRN 01-1103)

←(DRN 01-1103)

4.3.2.4.3.6 Shutdown Margin and Accident Analysis Allowance

The allowance shown in Table 4.3-6 for shutdown margin is consistent with that assumed under various postulated accident conditions addressed in Chapter 15, which result in predicted acceptable consequences.

4.3.2.4.3.7 Available Reactivity Worth

Table 4.3-7 shows the reactivity worths of the full complement of CEAs, and the highest reactivity worth of a single CEA in the fully withdrawn position, at BOC and EOC. This table also compares the available net shutdown worth (including the effects of the stuck CEA) to the reactivity worth requirements from Table 4.3-6.

As discussed in Subsection 4.3.3, the uncertainty in total CEA reactivity worth is five percent and the uncertainty in the stuck CEA worth is less than 10 percent. Even allowing for the maximum calculated errors for total CEA worth in both of the adverse directions, sufficient shutdown margin is available.

4.3.2.5 Control Element Assembly Patterns and Reactivity Worths

→ (DRN 00-644)

The locations of all CEAs in one of four symmetrically rodded core quadrants are shown in Figure 4.3-39. The CEAs designated as regulating control rods are divided into six groups; the shutdown CEAs are divided into two groups. These groups are identified, for first cycle operation, in Figure 4.3-39. All CEAs in a group are withdrawn or inserted quasisimultaneously. Shutdown groups are inserted after the regulating groups are inserted and are withdrawn before the regulating groups are withdrawn. The reactivity worths of sequentially inserted CEA groups at beginning of life and end of first cycle are shown in Table 4.3-5, and the rod radial peaking factors (F_r^n) for these configurations are shown in Table 4.3-8.

It is expected that the core will be essentially unrodded during full power steady-state operation, except for limited insertion of the first regulating group in order to compensate for minor variations in moderator temperature and boron concentration as described in Subsection 4.3.2.5.4. For operation with substantial CEA insertion, the relationship between power level and the maximum permitted CEA insertion is typified in Figure 4.3-40. This figure also illustrates the regulating group insertion order (6-5-43-2) and the 40 percent fixed overlap between successive regulating groups. Compliance with the power dependent insertion limits throughout the cycle ensures that adequate shutdown margin is maintained and that the core conditions are no more severe than the initial conditions assumed in the accident analyses described in Chapter 15.

Reactivity insertion rates for the safety analysis of the Waterford 3 core are presented in Chapter 15. The full power CEA ejection accident (Subsection 15.4.3.2) considers the ejection of one CEA from a fully inserted lead bank. The ejected CEA worth is calculated

← (DRN 00-644)

→(DRN 01-1103; 02-1477)
by the difference between the preejection and the post ejection reactivity of the core computed static methods. The maximum ejected CEA worth used in the safety analysis is conservative since (1) the lead regulating bank is not expected to be fully inserted at full power, and (2) a 10 percent conservatism is applied to the ejected CEA worth. A similar analysis is performed for the CEA ejection analysis from zero power, except that the initial condition for this incident assumes that all regulating banks are fully inserted.
←(DRN 01-1103; 02-1477)
The CEA withdrawal incident from low power (Subsection 15.4.1.2) is analyzed with the maximum calculated differential reactivity insertion rate resulting from a sequential CEA bank withdrawal with 40 percent overlap, including a 10 percent reactivity uncertainty. As discussed in Subsection 15.4.1.3., the CEA withdrawal incident from full power is analyzed from the insertion of the lead bank which maximizes the reactivity insertion and the power shape change during the CEA withdrawal. Reactivity insertion rates are calculated by a static axial model of the Waterford 3 core. The calculated reactivity insertion rate resulting from the sequential CEA withdrawal is presented in Figures 4.3-41 and 4.3-42.
→(DRN 02-1477)
The CEA drop incident (Subsection 15.4.1.4) is analyzing by selecting the dropped CEA that maximizes the increase in the radial peaking factor. A conservatively small negative reactivity insertion is used in the accident analysis.
←(DRN 02-1477)
The typical reactivity insertion during a reactor SCRAM is presented in Section 15.0. This reactivity insertion is computed by static axial models at various scram CEA positions, and it is used for all accidents which are terminated by a scram, unless otherwise indicated. The reactivity insertion is conservative since (1) a flat end-of-cycle power shape is assumed for the calculations, (2) only the minimum shutdown worth of 8.85 percent $\Delta\rho$ is assumed to available, and (3) the influence of delayed neutrons on the transient power shape is neglected. The scram reactivity for other incidents such as the loss of flow are performed by a parametric analysis considering various initial power shapes and the scram reactivity associated with those power shapes.

4.3.2.6 Criticality of Reactor During Refueling

The soluble boron concentrations during refueling are shown in Table 4.3-1. These concentrations ensure that the k_{eff} of the core during refueling does not exceed 0.95.

4.3.2.7 Stability

4.3.2.7.1 General

Pressurized water reactors (PWRs) with negative overall power coefficients are inherently stable with respect to power oscillations. Therefore, this discussion will be limited to xenon induced power distribution oscillations. Xenon induced oscillations occur as a result of rapid perturbations to the power distribution which cause the xenon and iodine distributions to be out of phase with the perturbed power distribution. This results in a shift in the iodine and xenon distribution that causes the power distribution to change in an opposite direction from the initial perturbation and thus an oscillating condition is established. The magnitude of the power distribution oscillation can either increase or decrease with time. Thus, the core can be considered to be either unstable or stable with respect to these oscillations. Discussed below are the methods of analyzing the stability of the core with respect to xenon oscillations. The tendency of certain types of oscillations to increase or to de crease is calculated, and the method of controlling unstable oscillations is presented.

4.3.2.7.2 Method of Analysis

Xenon oscillations may be analyzed by two methods. The first method consists of an explicit analysis of the spatial flux solution accounting for the space-time solution of the xenon concentrations. Such a method is useful for testing various control strategies and evaluating transitional effects (such as power maneuvers). The second method consists of modal perturbation theory analysis, which is useful for the evaluation of the sensitivity of the stability to changes in the reactor design characteristics, and for the determination of the degree of stability for a particular oscillatory mode.

The stability for a reactor can be characterized by a stability index or a damping factor which is defined as the natural exponent which describes the growing or decaying amplitude of the oscillation. A xenon oscillation may be described by the following equation:

→(DRN 06-914, R15)

$$\phi(\bar{r},t) = \phi_o(\bar{r}) + \Delta\phi_o(\bar{r})\, e^{bt}\, sin(wt + \delta)$$

←(DRN 06-914, R15)

where

$\phi(\bar{r},t)$ is the space-time solution of the neutron flux

$\phi_o(\bar{r})$ is the initial fundamental flux

$\Delta\phi_o(\bar{r})$ is the perturbed flux mode

b is the stability index

ω is the frequency of the oscillation

δ is a phase shift

Modal analysis consist of an explicit solution of the stability index b using known fundamental and perturbed flux distributions. A positive stability index b indicates an unstable core, and a negative value indicates stability for the oscillatory mode being investigated. The stability index is generally expressed in units of inverse hours, so that a value of -0.01/hr would mean that the amplitude of each subsequent oscillation cycle decreases by about 25 percent (for a period of about 30 hours for each cycle).

Xenon oscillation modes in PWRs can be classified into three general types: radial, azimuthal, an axial. To analyze the stability for each oscillation mode, only the first overtone needs to be considered since higher harmonic modes decay more rapidly than the first overtone Furthermore, since the first overtone of a radial oscillation decays more rapidly than the first overtone of an azimuthal oscillation, only the latter of these two modes will be considered in detail.

4.3.2.7.3 Expected Stability Indices

4.3.2.7.3.1 Radial Stability

A radial xenon oscillation consists of a power shift inward and outward from the center of the core to the periphery. This oscillatory mode is generally more stable than an azimuthal mode. This effect is illustrated in Figure 4.3-43, which shows that for a bare cylinder the radial mode is more stable than the azimuthal mode. Discussion of the stability for radial oscillator mode is therefore deferred to the azimuthal mode.

4.3.2.7.3.2 Azimuthal Stability

An azimuthal oscillation consists of an X-Y power shift from one side of the reactor to the other. Modal analysis for this type of oscillation is performed for a range of expected reactor operating conditions.

The expected variation of the stability index during the first cycle is shown in Figure 4.3-44. These results are obtained from analyses which consider the spatial flux shape changes during the cycle, the changes in the moderator and Doppler coefficient during the cycle, and the change in xenon and iodine fission yield due to plutonium buildup during the cycle. As is shown on the figure, the expected stability index is no greater than -0.035/hr at any time during the cycle for the expected mode of reactor operation. Comparison of predicted stability index with those actually measured on operating cores, as discussed in Subsection 4.3.3.2.3, provide a high confidence level in the prediction of azimuthal stability. Measurements of xenon spatial stability in large cores have been made[2] which provide confidence in the methods that are used to predict the azimuthal stability of this core.

4.3.2.7.3.3. Axial Stability

→(DRN 02-1477)

Axial xenon oscillations consist of a power shift toward the top and bottom of the reactor core. This type of oscillation may be unstable during the first cycle. Table 4.3-9 shows the calculated variation of the axial stability index during the first cycle. It is anticipated that control action with CEAs may be required to limit the magnitude of the oscillation. As discussed in Subsection 4.3.2.2, the axial power

←(DRN 02-1477)

→(DRN 01-1103; 02-1477)
distribution is monitored by COLSS and the RPS. Based on the COLSS measurement of the axial power distribution, the operator may move CEAs so as to control any axial oscillations.

4.3.2.7.4 Control of Axial Instabilities

The control of axial oscillations during a power maneuver is illustrated in Figures 4.3-25 through 4.3-32. CEAs are used throughout these maneuvers to limit the change in the power distribution. The difference between an uncontrolled and a controlled xenon oscillation is illustrated in Figure 4.3-45. It was assumed in the calculation of the controlled oscillation that the CEAs were moved in such a way as to preserve the initial shape in the core prior to the initiating perturbation. The calculations are performed at the end of the first cycle which corresponds to the expected least stable condition for axial xenon oscillations.
←(DRN 01-1103; 02-1477)

4.3.2.7.5 Summary of Special Features Required by Xenon Instability

The RPS described in Subsection 7.2.2 is designed to prevent exceeding acceptable fuel design limits and to limit the consequences of postulated accidents. In addition, a means is provided to assure that under all allowed operating modes, the state of the reactor is confined to conditions not more severe than the initial conditions assumed in the design and analysis of the RPS.

Since the reactor is predicted to be stable with respect to azimuthal xenon oscillations, no special protective system features are needed to accommodate azimuthal mode oscillations. Nevertheless, a maximum quadrant tilt is prescribed in the technical specifications along with prescribed operating restrictions in the event that the tilt is exceeded. The azimuthal power tilt is determined by COLSS and included in the COLSS determination of core margin. The azimuthal power tilt limit is accounted for in the RPS.

4.3.2.7.5.1 Features Provided for Azimuthal Xenon Effects

a) Administrative limits on azimuthal power tilt

b) Monitoring and indicating the azimuthal power tilt in COLSS as well as accounting for this tilt in the COLSS determination of core margin

c) Accounting for azimuthal power tilt limit in the RPS.

4.3.2.7.5.2 Features Provided for Axial Xenon Effects and Power Distribution Effect and Control

→(DRN 01-1103)

a) CEAs for control of the axial power distribution, if required

←(DRN 01-1103)

b) Monitoring and accounting for changes in the axial power distribution in COLSS

c) Monitoring and accounting for the axial power distribution in the RPS.

4.3.2.8 Vessel Irradiation

The design of the reactor internals and of the water annulus between the active core and vessel wall is such that for reactor operation at the full power rating and an 80 percent capacity factor, the vessel fluence greater than 1 MeV at the vessel wall will not exceed 3.68×10^{19} n/cm^2 over the 40 year design life of the vessel. The calculated exposure includes a 10 percent uncertainty factor.

→(LBDCR 16-060, R310)
The initially-calculated maximum fast neutron fluxes greater than one MeV incident on the vessel ID and shroud ID are as shown in Table 4.3-10. The fluxes are based on a time averaged equilibrium cycle radial power distribution and an axial power distribution with a peak to average of 1.20. The calculation assumed a thermal power of 3560 MWt. The models used in these calculations, ANISN and SHADRAC, are discussed in Subsection 4.3.3.3.
←(LBDCR 16-060, R310)

→(LBDCR 17-020, R310)
Updated reactor vessel fluence analysis was performed in conjunction with the testing of surveillance capsule W-263 at the end of cycle 11. This analysis used the DORT code to predict a peak vessel wall fluence of 2.48×10^{19} n/cm^2 (E > 1 MeV) at the end of the 40-year vessel design life. Thermal power assumptions were 3390 MWt for the first 11 cycles, 3441 MWt for the 12th and 13th cycles, and 3716 MWt from cycle 14 through the end of the design life. Fuel enrichment, core power distributions, and fuel burnup were based on cycle-specific fuel designs and used to develop spatial- and energy-dependent core source distributions, which were averaged over each fuel cycle. The DORT model used in this calculation is discussed in Subsection 4.3.3.3.
←(LBDCR 17-020, R310)

4.3.3 ANALYTICAL METHODS

4.3.3.1 Reactivity and Power Distribution

4.3.3.1.1 Method of Analysis

→ DRN 06-871, R15)
The nuclear design analysis for low enrichment PWR cores is based on a combination of multigroup neutron spectrum calculations, which provide cross-sections appropriately averaged over a few broad energy groups, and few-group one, two, and three dimensional diffusion theory calculations of integral and differential reactivity effects and power distributions. Multigroup calculations include spatial effects in those portions of the neutron energy spectrum where volume homogenization is inappropriate; e.g., the thermal neutron energy range. Most of the calculations are performed with the aid of computer programs embodying analytical procedures and fundamental nuclear data consistent with the current state of the art.
←(DRN 06-871, R15)

Comparisons between calculated and measured data that validate the design procedures are presented in Subsection 4.3.3.1.2. As improvements in analytical procedures are developed, and improved nuclear data become available, they will be added to the design procedure, but only after validation by comparison with related experimental data.

Few-group cross-sections for subregions of the core that are represented in spatial diffusion theory codes; e.g., fuel pin cells, moderator channels, structural member cells, etc., are calculated by the CEPAK lattice program. This program is the synthesis of a number of computer codes, many of which were developed elsewhere; e.g., FORM,[3] THERMOS[4] and CINDER[5]. These programs are interlinked in a consistent way with inputs from differential cross-section data from an extensive library.

The entire neutron spectrum is represented by 83 neutron groups between 0 and 10 MeV. Neutron leakage in a single Fourier mode is represented by either P-1 or B-1 approximations to transport theory throughout this entire range. Resonance shielding is determined analytically; the Hellstrand correlation is employed for U-238, with appropriate adjustments guided by Monte Carlo calculations of resonance capture in U-238 so as to provide agreement

with selected measurements of the conversion ratio. Plutonium resonance integrals are determined from an intermediate resonance formulation using equivalence relationships for the lattice representation.[7]

Appropriate Dancoff correction factors are determined for uniform lattices by three-region model of the unit cell to provide a better description of the effect of scattering in the clad on resonance capture. For heterogeneous lattices, this calculation is extended to include heterogeneities by nearest neighbor approximations. Included also in the resonance shielding calculation is an appropriate account of resonance overlap effects between different uranium and plutonium isotopes. In the thermal energy range, the effects of cell environment on the spatially dependent neutron spectrum within the lattice cell can be included in those cases where such effects are important. An isotropic scattering and temperature-dependent effects associated with the hydrogenous moderator are approximated by the use of transport-corrected, temperature-dependent scattering kernels generated by the GAKER program.[8] A major subroutine of CEPAK provides depletion calculations in the reactor cell to describe the evolution of the reactor spectrum and the appropriate cross-section averages, the production of fission products, including xenon, and samarium , and the production of conversion products as plutonium isotopes. Various criticality search options are available to approximate the effects of reactivity control on the neutron spectrum and thus on the few-group cross-section averages over energy.
→ (DRN 00-644)
Boundary conditions and equivalent diffusion theory constants for individual elements of a CEA are calculated by the CERES program. For a one region CEA in cylindrical geometry boundary conditions are calculated in each multi-group by the method of successive generations, with capture probabilities based on the tabulations of Stuart and Woodruff[9]. Two region CEAs are transformed to fictitious homogeneous CEAs by matching extrapolation lengths on the outer surface as defined by Kear and Ruderman.[10] The homogeneous CEAs are then treated as above. Fictitious few-group diffusion parameters for use in multidimensional diffusion theory calculations are obtained using methods defined by Wachspress[11] and Henry.[12]

Effective diffusion theory constants for burnable poison rod shim cells are calculated by a sequence of programs consisting of HAMMER[13] DTFIV,[14] and MO-807[15]. HAMMER is employed as a few-group region wise cross-section generator for the shim cell; DTF-IV is employed in a one dimensional representation of the shim cell and environment to define relative reaction rates between shim and fuel cells; and MO-807 is employed to calculate the effective diffusion theory constants.
← (DRN 00-644)
Static and depletion dependent reactivities and nuclide concentration, flux, and power distributions in one, two, and three-dimensional representations of the core are determined by a diffusion-depletion program, PDQ-X. This program is an extension of the PDQ-7[16] and HARMONY[17] programs to include the following optional capabilities:

a) Moderator and fuel temperature feedback in the three-dimensional geometry option, fuel temperature feedback in two-dimensional geometry.

b) Poison content criticality searches as well as spatial feedback on the power distribution by fuel and moderator temperature in the one dimensional geometry option.

These calculations employ macroscopic or microscopic cross-section data for time independent or depletion effects respectively generated by the methods described in the preceding paragraph.
→ (DRN 00-644)
The spatial flux in the reactor core is customarily assumed to be separable into radial and axial components. Thus the detailed spatial variations of the flux and power are obtained from the calculation of the broad group fluxes in a two-dimensional calculation of a typical plane in the reactor. The calculation is corrected for axial leakage effects by the use of a group dependent buckling, which is obtained from a one dimensional core average axial calculation.
← (DRN 00-644)
For detailed calculations of pinwise power distributions, a mesh rectangle is assigned to each pin cell. The inter-assembly water channel, the core shroud, and the core barrel are each represented explicitly in standard fine-mesh design calculations. In addition, water holes, shim boron cells, and control rods are each represented. For first cycle calculations a quarter-core representation with reflective boundary conditions at the core centerlines is usually adequate. For cores with an asymmetric fuel loading or for the calculation of ejected rod worths, full-core representations are used.

The quarter-core fine mesh representation described above requires about 25,000 mesh points to describe the geometry of a 217 assembly reactor core. For some applications this detail is not required. For these purposes coarse-mesh calculations are constructed having only a few mesh regions per assembly (typically 16). Coarse-mesh calculations are capable of accurately predicting gross power distributions, core reactivity, and depletion characteristics but cannot accurately calculate pin power peaks. Cross-sections for coarse-mesh calculations are obtained by spatially collapsing, by batch type, the fine mesh cross-sections in such a way as to preserve the individual reaction rates.. To improve the gross power distribution in coarse mesh calculations, it has been found necessary to use a non-regular mesh structure within individual assemblies in order to reproduce the large thermal flux gradients at the assembly interfaces.

In a large PWR core, the calculated power distributions are fairly sensitive to the treatment of the reflector cross-section. Terney[18] has compared transport and diffusion calculations of the albedo and shown that the latter substantially underpredicts the reflector albedos in the fast (top) group and that the power distribution is shifted toward the core center when compared to multigroup transport theory results. When the fast diffusion coefficients in the reflector are altered to make the transport and diffusion theory albedos agree, the power distributions are also brought into agreement.

In addition, Terney[18] has obtained an additional correction factor for mesh size effects that is applicable to coarse mesh problems. The use of this formula gives the correct albedos at the reflector-core interface, as well as improved distributions for coarse mesh problems.

The HARMONY[17] scheme of cross-section organization is used to input cross-sections for the PDQ spatial calculations. The fuel cross-sections are calculated for each batch type at the batch average conditions. For the more important cross-section, the microscopic cross-sections is tabulated as a function of the fuel exposure (in MWd/MTU). For other

crossections, a value is input that has been averaged over the exposure history of the core. Separate cross-section sets are generated for the water holes, poison rods, water channels, reflectors, and control rods.

The depletion of the core is accomplished by utilizing a set of linearized depletion chains specifying the coupling (neutron capture or fission) between the isotopes in the chain. Except for I-135, Xe-135 and Sm-149, the fission products are added together into a single lumped fission product. The exposure intervals of the depletion calculations are usually chosen to be 1000 MWd/MTU during which is assumed that the flux and microscopic cross-sections are unchanged. At the end of each exposure interval, the fluxes and cross-sections are recalculated. Shorter exposure intervals are used for recalculation of cross-sections, which vary rapidly with depletion, such as shim boron. As in the spectrum calculation, the soluble boron concentration and axial leakages are modified at each exposure interval.

The local fuel temperature has a large effect upon the spatial power distribution and therefore has to be factored into the spatial calculations. This effect is included by the following form of power feedback calculation. The simplest method of modeling this feedback is by introducing in the batch-wise spectrum calculation the appropriate power level and effective fuel temperature. The broad-group cross-sections then reflect the average batch conditions.

A more detailed treatment of the Doppler feedback is obtained by introducing a set of power dependent microscopic cross-sections to account for the change in a cross-section due to the change in local power level. In this way a detailed Doppler feedback calculation can be performed for each fuel pin cell.
→(DRN 00-644)
The treatment of thermal hydraulic effect in the axial direction is more complex because the effect of moderator temperature on the local moderator density and neutron spectrum must be included for all isotopes. Thus, the fuel cross-sections must include both a fuel temperature and moderator density dependence, and both moderator and fuel temperature are allowed to vary in the axial direction.
←(DRN 00-644)
→(DRN 02-1477)
Axial depletion calculations are performed by the PDQ-X code, whose results are used to supply the necessary input to the QUIX code, which generates the data required by the monitoring and control systems. In addition to the eigenvalue problem, QUIX will perform four types of search calculations to attain a specified eigenvalue; viz., a poison search, buckling search, CEA region boundary search, and moderator density dependent poison search. The effects of moderator and fuel temperature feedback on the power distribution can be treated.
←(DRN 02-1477)
The QUIX code has the capability of simulating excore detector responses expected during operation. The calculated normalized core average power distribution is first corrected by the application of CEA shadowing factors to simulate the peripheral fuel assembly power distribution. Shape annealing factors (defined below) are then applied to the peripheral axial power distribution to simulate the integrated response of the subchannels of the three-element excore detectors.

CEA shadowing is the change in excore detector response resulting from changing the core configuration from an unrodded condition to a condition with CEAs inserted, while maintaining constant power operation. Although CEA shadowing is a function of azimuthal location, its effect is minimized by placing the excore detectors at azimuthal locations where minimum CEA shadowing occurs. CEA shadowing factors can be determined using detailed two-dimensional power distribution (XY-PDQ's) representing the cumulative presence of the various CEA banks and the shielding code SHADRAC.(19) SHADRAC calculates fast neutron and gamma ray spectra, heating and dose rates in a three-dimensional system utilizing a moments method solution of the transport equation. The core, vessel internals, vessel, and excore detector location are rated explicitly in the calculation.

Normalized CEA shadowing factors are relatively constant with burnup and power level changes made without moving CEAs. CEA shadowing factors at beginning and end of first cycle life are as shown in Table 4.3-11.

Figure 4.3-46 shows the typical behavior of the CEA shadowing factor during a CEA insertion and withdrawal sequence. QUIX simulated factors and experimentally measured CEA shadowing factors during this transient situation are shown to have quite good agreement over a significant range of CEA insertions.

Shadowing factors account for the radial effects and annealing accounts for the axial effects on the excore detector responses. Due to neutron scattering in the various regions separating the core and the excore detectors, each detector sub-channel responds to neutrons from the entire length of the core and not just from the section immediately opposite the sub-channel. This effect is independent of the axial power shape and the azimuthal CEA shadowing factors. Typical shape annealing functions, given as fractional response per percent of core height for a three sub-channel system, are shown in Figure 4.3-47.

Shape Annealing Functions (SAFs) are determined from a series of fixed source calculations in which the source is given by an isotropic fission spectrum distributed uniformly, radially and axially throughout successive horizontal slices of the core. The result of each fixed-source calculation is the response in each of the excore detectors. These results are then normalized so that the sum over all the detectors and fixed-source calculations representing the entire height of the core would equal 1.0. The effect of variations in the core height used for each fixed source calculation is removed and the units of the SAF converted to percent of axial height of the core by dividing the results for each case by the respective percent of core height used for the source of that calculation. The SAF is then plotted for each ex-core detector as the fraction of the total response percent of core height versus the percent of core height.

Cases Involving Geometric Models with Azimuthal Symmetry

For cases which may be described adequately by azimuthally symmetric models of the geometry (see Figure 4.3-48), the response at the detector given a fixed source in some increment of the core, may be determined by first solving the Boltzmann transport equation in Rz - cylindrical geometry (Reference 20).

Using the method of discrete ordinates the DOT II W or DOT III codes (References 21 and 43) can be used to solve an approximation to the Boltzman transport equation. DOT III is a more recent version of DOT II W. The major features of the method used in both codes are as follows:

a) Energy dependence is considered using the multigroup treatment.

b) The derivative terms and spatial dependence are approximated using a finite difference technique.

c) Dependence upon the direction variables is treated using the discrete ordinates method.

d) The scattering integral in Equation (A) is evaluated using a discrete ordinates quadrature in combination with a Legendre expansion of the scattering kernel to approximate anistropic scattering.

The use of DOT III provides the additional option of "bootstrapping" the calculation to overcome computer core storage limitations. In this technique the problem geometry is divided into sequential, overlapping regions and each is calculated separately, but in sequence with the appropriate angular fluxes used as a source in a subsequent calculation for an adjacent region.

Cases Involving Geometric Models with Partial Azimuthal Symmetry

In some problems it is not possible to adequately model the geometry unless a three-dimensional representation is used. In these cases the response of each detector is obtained by first solving the 3-D form of the transport equation.

The current state-of-the-art in solving the transport equation involves the use of the Monte Carlo method and for this work in particular the MORSE code. (Reference 44) The major features of the MORSE code are as follows:

a) Multigroup treatment of energy dependence,

b) Combinatorial geometry representation of the problem geometry,

c) Generalized Gaussian Quadrature for the treatment of the angular distribution of group-to-group transfers.

The usual problem in utilizing MORSE is that the amount of computer CPU time required to calculate the desired results to the necessary statistical precision is too large for practical consideration. This typically occurs in problems with overall dimensions of many mean-free-paths and moderate geometric complexity.

→ (DRN 00-644)
The existence of even a partial azimuthal symmetry in the problem geometry, such as is shown in Figure 4.3-48, reduces the difficulty of the calculation greatly. The geometry may be divided into two overlapping parts, one with complete azimuthal symmetry. The radiation field in this portion of the geometry may then be calculated using the DOT II W/DOT III codes and the other portion calculated using the MORSE code and a source generated along an interface between the two portions of the geometry.
← (DRN 00-644)
This source is generated for MORSE by the DOMINO code (Reference 45), a utility code which converts the boundary angular flux from a DOT II-W/DOT III "RZ" geometry, calculation into the appropriate format for use as a source in MORSE.

The Rz-DOTs and MORSE use P^3, scattering cross-sections based on the CASK (DLC-23E) cross-section set (Reference 46).

The shape annealing factors are purely geometric correction factors applied to the peripheral axial power distribution. As such, the effects of time in fuel cycle, transient xenon redistribution and CEA insertion, although affecting the peripheral bundle power shape, do not effect the geometric shape annealing correction factors. Figure 4.3-49 compares the peripheral axial shape index with the external shape index during a CEA and PLCEA motion test for the Palisades reactor. Shown are the result of QUIX simulations of the test as well as experimental data taken during the test.

From this curve, we can conclude that even though the axial power distribution in the core and on the core periphery were changing during this transient, the relationship between the excore response and the peripheral response was not changing. These results justify not only the separability of CEA shadowing and shape annealing as summed in QUIX but also demonstrate that shape annealing is purely a geometric effect, independent of the peripheral axial power distribution.

The excore detector temperature decalibration effect is the relative change in detector response as a function of reactor water inlet temperature. The temperature decalibration effect is calculated utilizing SHADRAC with explicit representation of core, vessel internals, vessel, and detector location for various reactor inlet temperatures. Typical detector temperature decalibration effect as a function of inlet temperature normalized to an inlet temperature of 525°F is as shown in Figure 4.3-50.

Final normalization of the CEA shadowing, shape annealing, and temperature decalibration constants will be accomplished during start-up testing.

4.3.3.1.2 Comparisons with Experiments

The nuclear analytical design methods in use for Waterford 3 have been checked against a variety of critical experiments and operating power reactors. In the first type of analysis, reactivity and reaction rates calculations are performed, which leads to information concerning the validity of the basic fuel cell calculation. The second type of analysis consists of a core follow program in which power distributions, reactivity coefficients, reactivity depletion rate, and CEA worths are analyzed to provide a global verification of the nuclear design package.

4.3.3.1.2.1 Critical Experiments

Table 4.3-12 summarizes the properties of the fuel rods employed in the lattices analyzed. The enrichments, pin dimensions, and water-to-fuel ratios are similar to those used in pressurized power reactors. Tables 4.3-13 and 4.3-14 summarize pertinent characteristics of the lattices and the eigenvalues calculated for the uranium and mixed oxide lattices, respectively.

The average eigenvalue for the uranium oxide lattices is 1.0020 ± 0.0020 and for the mixed oxide lattices it is 1.0043 ± 0.0034.

Reaction rates were measured in some of the lattices noted in the previous section and are shown, along with definitions of the measured quantities, in Table 4.3-15.

→(DRN 00-644; 06-895, R15)
Although some scatter can be seen in the differences between measured and calculated values, the average error in the prediction of reaction rates is of the order of one percent only, except for the epicadmium-to-subcadmium fission rate for U-235, which is consistently overestimated by seven to eight percent. This overprediction of the fast fission rate in U-235 is due to simplifying assumptions in the resonance shielding, which were shown not to affect the reactivity level or the isotopic depletion rates.
←(DRN 00-644; 06-895, R15)

4.3.3.1.2.2 Power Reactors

The accuracy of the calculational system in its entirety can only be assessed through the analysis of experimental data collected on operating power reactors. The data under investigation consists of critical conditions, reactivity coefficients, and rod worths measured during the startup period, and of critical conditions, power distributions, and reactivity coefficients measured throughout the various cycles.

4.3.3.1.2.2.1 Startup Data

Because of the clean core configuration prevailing during the initial zero power operation, the startup data is extremely valuable in assessing the validity of the physics design package.

The soluble boron concentration that has to be added to the moderator to bring the unrodded reactor critical is a measure of the excess reactivity present in the core to accommodate the negative reactivity insertion due to the power escalation and the fuel depletion. The boron concentrations measured in cold and hot conditions for various reactors are compared with the calculated predictions in Table 4.3-16, showing an average error of -8 ± 13 ppm.
→(DRN 00-644)
The moderator temperature coefficient is the change in reactivity resulting from a unit change in moderator temperature. As the temperature increases and the moderator density decreases, two phenomena take place, affecting the reactivity in two opposite directions. The reduced water density affects adversely the slowing down of neutrons to thermal energies, reducing the fissions rates and thus the reactivity. Another effect of the reduced water density is a displacement of the soluble boron, which results in a reduction of the thermal absorption rate and an increase in reactivity. In a fresh core, when the
←(DRN 00-644)

soluble boron concentration is at its maximum, the second effect may overcome the first one and the moderator temperature coefficient may be positive at low power levels. As the core depletes and the boron concentration is reduced to maintain criticality, the first effect becomes predominant, and the moderator temperature coefficient becomes increasingly negative. The result of analyses of beginning of cycle temperature coefficients is given in Table 4.3-16, showing an excellent agreement between measured and calculated values. The average-error in the eight coefficients given in the table is only $-0.04 \pm 0.08 \times 10^{-4}$ $\Delta\rho/°F$.

4.3.3.1.2.2.2 CEA Reactivity Worth

Comparisons were made between the predicted and measured CEA worths for individual banks inserted sequentially, for the Maine Yankee, Fort Calhoun, Calvert Cliffs, and Millstone II reactors. Table 4.3-17 summarizes this comparison between calculation and experiment. In the evaluation of the experimental data, revised values of delayed neutron fractions published in Reference 31 were used. The comparisons demonstrate that CEA reactivity worths can be calculated to within seven percent of the experimental value. A comparison between calculation and measurement of ejected, stuck and dropped CEA worths is given in Table 4.3-18 for Palisades, Fort Calhoun, and Maine Yankee. The differences between calculation and measurement are approximately the same as in the individual CEA bank calculations. For these comparisons the stuck, ejected, and dropped CEA worths are calculated to within eight percent of the experimental value.

4.3.3.1.2.2.3 Depletion Calculation

Over 50 spent fuel samples from Yankee Rowe Core I were subjected to isotopic and radio-chemical analyses which were performed in the Tracerlab Laboratory at Richmond, California and by the Vallecitos Atomic Laboratory of the General Electric Company(32). Depletion calculations were performed on the Yankee core for comparison with the above measurements. Figure 4.3-51 compares measured and calculated values of the Pu/U mass ratio versus exposure, and Figure 4.3-52 shows a comparison for the relative isotopic composition of plutonium as a function of fractional U-235 depletion.
→ (DRN 00-644)
Comparisons of the depletion behavior of the measured and calculated critical boron concentrations for the Palisades Maine Yankee, and Fort Calhoun reactors are shown in Figures 4.3-53, 4.3-54, and 4.3-55, respectively. These comparisons indicate good agreement for the Palisades reactor and a relatively consistent bias between calculation and measurement for the Maine Yankee and Fort Calhoun reactors of approximately 50 to 70 ppm for the range of conditions shown in the figures. Best estimate reactivity predictions for these latter two classes of reactors are currently obtained by increasing the calculated critical boron concentration by approximately 50 ppm. The a priori knowledge of the expected bias between measured and calculated soluble boron concentration is factored into the design calculations; and results in better estimates of these characteristics which are sensitive to the boron level such as moderator temperature coefficients, power distributions, and cycle length. The resulting difference between the best estimate predicted soluble boron concentration and the measured critical soluble boron concentrations after adjustment to standard conditions is within approximately 0.4 percent reactivity, of which a significant fraction is associated with the spread in the experimental data.
← (DRN 00-644)

4.3.3.1.2.2.4 Fuel Temperature and Power Coefficients

The power coefficient is expressed in terms of reactivity change per unit change in power. This coefficient consists mostly of two components: one results from the reactivity change associated with the core average coolant temperature, and the other, which will be discussed here, is due to the change in fuel temperature. At each power level, an equilibrium exists between the power produced in the fuel, the fuel temperature, the heat transfer between the fuel and the coolant, and the energy removed by the coolant. The fuel temperature can be calculated directly by a heat transfer calculation, or indirectly by the analysis of the reactivity effects associated with a fuel temperature change. Both approaches have been used and lead to very consistent results.

The reactivity effects attributable to the fuel temperature are due to the Doppler broadening of the cross section resonances, mostly those of uranium 238, as well as to the change in scattering properties of the oxygen present in the fuel. The power coefficient can be expressed as

$$\frac{\partial \rho}{\partial P} = \frac{\partial \rho}{\partial T} \cdot \frac{\partial T}{\partial P}$$

The determination of the first term, $\partial\rho/\partial T$, is performed by the lattice code CEPAK, in which the Hellstrand correlation is used to calculate the Doppler broadening of U-238[6] and an equivalence principle is used for the plutonium isotopes[7]. The second term, $\partial T/\partial P$, is calculated by the FATES code[33], Waterford 3 fuel pin as well as for a Millstone II fuel pin, which has different dimensions but the same fuel densification properties. FATES shows that the fuel temperature is insensitive to the pellet diameter, and therefore that the measured power coefficients $\partial\rho/\partial P$ for Millstone II can be used to establish the validity of the fuel temperature correlation.

The following correlation is semi-empirically derived from the FATES results and the analysis of the Millstone II power coefficients.

$$T_f(F) = T_m + 128.36\alpha\underline{P} - 1.7832\alpha\underline{P}^2$$

in which α is a weighting factor accounting for the number of dimensions in spatial calculations.

$\alpha = 1.0$ in three dimensional,
$\alpha = 1.1415$ in two dimensional,
$\alpha = 1.0198$ in one dimensional axial calculations,

$\underline{P}$ is the linear heat generation rate in the fuel rod in kW/ft; T_m is the coolant temperature; and T_f the pellet average fuel temperature used in the resonance broadening calculation.

The results of the Millstone II power coefficient analysis are displayed in Figure 4.3-56.

4.3.3.1.2.2.5 Moderator Temperature Coefficients

Moderator temperature coefficients were measured at or near full power for a number of reactors of the 133 or 217 assembly design, at various core exposure throughout the cycles. The analysis of this data is a complement to the analysis of beginning-of-life, zero power coefficients presented earlier. The accuracy of the full power temperature coefficient predictions has a direct bearing on the prediction of most fast transients. Table 4.3-19 gives the results of the analysis, and shows that with standard two dimensional calculations, the average error is $(0.008 \pm 0.10) \times 10^{-4}$ $\Delta\rho/°F$. Three dimensional calculations, performed with full feedback, lead to essentially the same results, demonstrating the validity of two dimensional calculations.

4.3.3.1.2.2.6 Core Power Distributions

→ (DRN 00-644)

The accuracy of the power distribution predictions cannot be disassociated from the accuracy of the instrumentation which is used to measure these power distributions. The instrumentation in C-E reactors consists of fixed self-powered rhodium detectors, whose signals are fed into the computer code system INCA(34) which unfolds a full core power distribution with the help of precalculated coupling coefficients. The uncertainties associated with each step of this process, and the differences observed between calculated and measured three dimensional power distributions, are documented in detail in References 35 and 36. The overall errors or uncertainties presented in these topical reports are summarized in Table 4.3-20, showing a 6.9 percent uncertainty in the three-dimensional peak F_q^n.

← (DRN 00-644)

4.3.3.2 Spatial Stability

4.3.3.2.1 Methods of Analysis

An analysis of xenon-induced spatial oscillations may be done by two methods: time-dependent spatial calculations and linear modal analysis. The first method is based on computer simulation of the space, energy, and the time dependence of neutron flux and power density distributions. The second method calculates the damping factor based on steadystate calculations of flux, importance (adjoint flux), xenon and iodine concentrations, and other relevant variables.

The time-dependent calculations are indispensable for studies of the effects of CEA, core margin, out-of-core and in-core detector responses, etc., and are performed in one, two, and three dimensions with few-group diffusion theory, using tested computer codes and realistic modeling of the reactor core.

→(DRN 00-644)

The linear modal analysis methods are used to calculate the effect on the damping factor of changes in fuel zoning, enrichment, CEA patterns, operating temperature, and power levels. These methods, using information at a single point in time, are particularly suited to survey type calculations. Methods are based on the work of Randall and St. John(37) as extended by Stacey(38). These methods are verified by comparison with time-dependent calculations.

← (DRN 00-644)

4.3.3.2.2 Radial Xenon Oscillations

→ (DRN 00-644)

To confirm that the radial oscillation mode is extremely stable, a spacetime calculation was run for a reflected, zoned core 11 ft. in diameter without including the damping effects of the negative power coefficient. The initial perturbation was a poison worth of 0.4 percent in reactivity placed in the central 20 percent of the core for one hour. Following removal of the perturbation, the resulting oscillation was followed in four hour time steps for a period of 80 hours. The resulting oscillation diminished very rapidly with a damping factor of about -0.06 per hour. When this damping factor is corrected for a finite-time step size by the formula in Reference 39, a more negative damping factor is obtained indicating an even more strongly convergent oscillation. On this basis, it is concluded that a radial oscillation instability will not occur.

← (DRN 00-644)

4.3.3.2.3 Azimuthal Xenon Oscillations

→ (DRN 00-644)

Two-dimensional modal analysis techniques were used to calculate the damping factor for azimuthal oscillations, and included both the fuel temperature and moderator temperature components of the total power coefficient. These calculational techniques were used to predict the results of azimuthal oscillation tests at Maine Yankee at 75 percent power. The predicted damping factor of -0.045 per hour for azimuthal oscillations was found to agree well with the measured value of -0.047 ± 0.005 per hour.

← (DRN 00-644)

Measurements of the azimuthal damping factor on other (earlier) reactors near full power further substantiate the techniques used to predict the damping factor for Waterford 3.

4.3.3.2.4 Axial Xenon Oscillations

→ (DRN 00-644)

To check and confirm the predictions of the linear modal analysis approach, numerical space-time calculations were performed for both beginning and end-of-cycle. The fuel and poison burnup distributions were obtained by depletion with soluble boron control, so that the power distribution was strongly flattened. Spatial Doppler feedback was included in these calculations. In Figure 4.3-57, the time variation of the power distribution along the core axis is shown near end-of-cycle with reduced Doppler feedback. The initial perturbation used to excite the oscillations was a 50 percent insertion into the top of the core of a 1.5 percent reactivity CEA bank for one hour. The damping factor for this case was calculated to be about +0.02 per hour; however, when corrected for finite-time step intervals by the methods of Reference 39, the damping factor is increased to approximately +0.04 per hour. When this damping factor is plotted on Figure 4.3-58 at the appropriate eigenvalue separation for this mode at end of cycle, it is apparent that good agreement is obtained with the modified Randall-St. John prediction. This good agreement is a result of the generally antisymmetric distribution of the moderator coefficient about the core midplane, and its flux and adjoint weighted integrals of approximately zero.

← (DRN 00-644)

Axial xenon oscillation experiments performed at Fort Calhoun at a core exposure of 7000 MWd/MTU and at Stade at beginning of cycle and at 12000 MWd/MTU[40] were analyzed with a space-time one-dimensional axial model. The results are given in Table 4.3-21 and show no systematic error between the experimental and analytical results.

4.3.3.3 Reactor Vessel Fluence Calculation Model

→(LBDCR 16-060, R310)
The initially calculated vessel fluence was obtained by combining the results of ANISN[41] and SHADRAC[19] in the following manner:
←(LBDCR 16-060, R310)

$$\phi(E) = \phi(ANISN) \cdot \frac{\phi A(SHADRAC)}{\phi B(SHADRAC)} \qquad (6)$$

where:

ϕ(E) is the neutron energy flux at the inner surface of the vessel,

ϕ(ANISN) is the neutron energy flux obtained from ANISN,

ϕA (SHADRAC) is the neutron energy flux as calculated by SHADRAC in which the exact source geometry and a three-dimensional time averaged power distribution are used.

ϕB (SHADRAC) is the neutron energy flux as calculated by SHADRAC using a cylindrical source geometry and the power distribution obtained from ANISN.
→ (DRN 00-644)
The neutron flux as calculated by the above method has uncertainty limits of +10 percent, -40 percent. The total uncertainty is composed of 0 percent, -30 percent in the calculational method and ± 10 percent uncertainty in the combined radial and axial power distribution. The calculational uncertainty factors are obtained by comparing the ANISN-SHADRAC results with measurements from various operational reactors[42].
← (DRN 00-644)

→(LBDCR 17-020, R310)
Calculation of vessel fluence in conjunction with analysis of surveillance capsule W -263 was performed using the DORT[47] code and BUGLE-96 cross-section library[48]. DORT is a two-dimensional discrete ordinates transport code. Synthesis of a solution in 3 dimensions is accomplished by combining cycle-specific forward transport calculations using the following method:

$$\phi(r,\theta,z) = \phi(r,\theta) \times \frac{\phi(r,z)}{\phi(r)}$$

Where $\phi(r,\theta,z)$ is the synthesized three dimensional flux distribution,

$\phi(r,\theta)$ is the transport solution in (r,θ) geometry,

$\phi(r,z)$ is the two-dimensional solution for a cylindrical reactor model using the actual axial core power distribution, and

$\phi(r)$ is the one-dimensional solution for a cylindrical reactor model using the same source per unit height as that used in the (r,θ) calculation.

The DORT method meets the requirements of Reg. Guide 1.190[49,50] and was approved by the NRC for industry use. The calculation method uncertainties were calculated based on the requirements of the Reg. Guide and were determined to be 12% for the surveillance capsule fluence and 13% for the WF3 reactor vessel fluence[51]. No systematic bias was applied to the analysis results. WF3-specific dosimetry measurements from surveillance capsules W-97 and W-263 validate the uncertainties.
←(LBDCR 17-020, R310)

4.3.3.4 Local Axial Power Peaking Augmentation

A reduction in UO_2 volume associated with fuel densification results in a shortening of the active fuel pellet stack height. If it is assumed that the reduction in the active stack length is not reflected by an equivalent increase in the length of the gas plenum but, instead, results in the formation of axial gaps within the fuel column, local power peaking is experienced in the vicinity of the fuel gaps. This arises because the decreasing neutron absorption, due to fuel removal, more than compensates for the fission loss.

Since the magnitude of the local power peaking in a given rod is a function of both the size and number of gaps in surrounding fuel rods, and the distribution of gaps within a given volume of the core cannot be defined explicitly, a statistical approach to the determination of the local peaking factor, resulting from the presence of gaps, is employed. This additional peaking due to gaps is called the augmentation factor. The augmentation factor, at any given plane, is defined as the ratio of the maximum power in that plane with the statistically expected distribution of gaps to the maximum power without gaps. The peaking augmentation factors are based on a 95 percent confidence level. That is to say, for each axial region, the augmented power is chosen so that there is a 95 percent probability that no more than one rod exceeds the augmented power.

A detailed discussion of the theoretical model, a description of the gap distribution characteristics employed in the model, the data from which these characteristics were established, and a discussion of the application of the model to the calculation of axial peaking augmentation factors are presented in Reference 33. Reference 33 describes the model in detail and gives as an example a calculation using input characteristics for a typical reactor.

Input information, which is specific to the reactor under consideration and is required for the calculation of augmentation factors, includes the fuel densification characteristics, the radial pin power distribution, and the single gap peaking factors. The fuel densification characteristics used in the calculation of augmentation factors for Waterford 3 are presented in Table 4.3-22. The radial pin power census used in calculation of the augmentation factors is given in Table 4.3-23. The integration of this radial pin power census into the R(x) function described in Reference 33 is illustrated here as Figure 4l.3-56. Figure 4.3-59 shows the specific assignment of fuel rod locations to radial groups and gives the power peaking associated with a single gap at each of these locations used in the calculation of the limiting augmentation factors for Waterford 3.

The axial dependent peaking augmentation factors for noncollapsed gaps are presented in Figure 4.3-60 for Waterford 3. Augmentation factors were calculated using limiting radial pin power distributions and single gap peaking factors, and therefore can be used throughout the first cycle.

4.3.4 CHANGES

A significant amount of core operating data has been incorporated into the nuclear design methods used for the design of this reactor. Operating reactor power distributions, critical boron concentrations, reactivity coefficients, and control rod worths were measured on the Maine Yankee, Fort Calhoun, Calvert Cliffs, and Millstone II reactors. The design methodology used for Waterford 3 is essentially identical to the methodology used in the analysis of the experimental data reported in Subsection 4.3.3.1.2. The good agreement between measured values and those predicted by the analytic methods used at C-E, as described in Subsection 4.3.3, lends confidence to the methods used in the design of this reactor.

As more experimental data becomes available, the methods verification program is extended, and the results of these analyses are implemented in the design of future cores.

SECTION 4.3: REFERENCES

1. "COLSS, Assessment of the Accuracy of PWR Operating Limits as Determined by the Core Operating Limit Supervisory System," CENPD-169 C-E Proprietary Topical Report, July 1975.

2. Krebs, W.D., and Brinkman, H., Proceedings of Reaktortagung 1976, Dusseldorf, Germany, March 1976.

3. McGoff, D.J., FORM-A Fourier Transform Fast Spectrum Code for the IBM-7090, NAA-SR-Memo, September 1960.

SECTION 4.3: REFERENCES (Cont'd)

4. Honeck, H., "THERMOSA Thermalization Transport Theory Code for Reactor Lattice Calculations," BNL-5816, July 1961.

5. England, T.R., "CINDER-A One Point Depletion and Fission Product Program," WAPD-TM-334, Revised June 1964.

6. Hellstrand, E., Measurement of Resonance Integral, Proceedings of National Topical Meeting of the Ans. San Diego, The M.I.T. Press, February 7-9, 1966.

7. Goldstein, R., "Temperature-Dependent Intermediate Neutron Resonance Integrals," Nuclear Science and Engineering 48, 248, 1972.

8. Honeck, H., Description of the Code GAKER, BNL Memorandum, January 6, 1964.

9. Stuart, G.W. and Woodruff, R.W., "Method of Successive Generations," Nuclear Science and Engineering, Vol. 3, p 339, 1958.

10. Kear, G.N. and Ruderman, M.J., "An Analysis of Methods in Control Rod Theory and Comparison with Experiment," GEAP-3937, May 1962.

11. Wachspress, E.L., "Thin Regions in Diffusion Theory Calculations," Nuclear Science and Engineering, Vol. 3, p 186, 1958.

12. Henry, A.F., "A Theoretical Method for Determining the Worth of Control Rods," WAPD-218, August 1959.

13. Suich, J.E. and Honeck, H.C., "The HAMMER System," DP-1064, January 1967.

14. Lathrop, L.D., "DTF-IV, A Fortran IV Program for Solving the Multigroup Transport Equation with Anisotropic Scattering," LA-3373, July 15, 1965.

15. Rutherford, C.N., "MO-807 - A Diffusion Theory Fitting Program Using Fortran-IV," WAPD-TM-671, September 1967.

16. Cadwell, W.R., "PDQ-7 Reference Manual," WAPD-TM-678, January 1968.

17. Breen, R.J., et al.,"HARMONY-System for Nuclear Reactor Depletion Computation," WAPD-TM-478, January 1965.

18. Terney, W.C., "Albedo Adjusted Reflector Fast Diffusion Coefficient," Transactions American Nuclear Society, 18, 312, 1974.

19. SHADRAC, "Shield Heating and Dose Rate Attenuation Calculation," G30-1365, March 25, 1966.

20. F.R. Mynatt, Development of Two-Dimensional Discrete Ordinates, Transport Theory for Radiation Shielding CTC-INF-952, August 11, 1969.

SECTION 4.3: REFERENCES (Cont'd)

21. DOT-IIW, Users Manual Two-Dimensional Discrete Ordinates, Transport Code, WANL-TME-1982, December 1969.

22. Engeloer, T.C., et al., "Spectral Shift Control Reactor, Basic Physics Program," B & W - 1273, November 1963.

23. Clark, R.H., et al., "Physics Verification Program," Final Report B & W - 3647-3, March 1967.

24. Davidson, P.W., et al., "Yankee Critical Experiments," YAEC-94, April 1969.

25. Eich, W.J. and Rocacik, W.P., "Reactivity and Neutron Flux Studies in Multi-Region Loaded Cores," WCAP-1443, 1961.

26. Fayers, F.J., et al., "An Evaluation of Some Uncertainties in the Comparison Between Theory and Experiments for Regular Light Water Lattices," British Nuclear Engineering Society Journal, April 6, 1967.

27. Brown, J.R., et al., "Kinetic and Buckling Measurements on Lattices of Slightly Enriched Uranium and UO_2 Rods in Light Water," -WAPD-176, 1958.

28. Schmid, L.C., et al., "Critical Masses and Buckling of Pu 02-UO21120 System," ANS Transactions, 1, 216, 1964.

29. Dawson, F.D., "Plutonium Utilization Program Annual Report," BNWL-624, December 1964.

30. Leamer, R.D., "PuO_2 -H_2O Fueled Critical Experiments," WCAP-3726-1, July 1967.

31. Tomlinson, L., "Delayed Neutrons for Fission," UKAEA Report AERE-R-6993, Harwell, Berkshire, 1972.

32. Chajson, L., et al., "Yankee Core Evaluation Program - Quarterly Report for the Period Ending September 30, 1963," WCAP-6056, October 1963.

33. CENPD-139 "C-E Fuel Evaluation Model Topical Report" (Chapter 3, Augmentation Factors), C-E Proprietary Topical Report, July 1, 1974.

34. "A Method of Analyzing In-Core Detector Data in Power Reactors," CENPD-145, C-E Topical Report, April 1975.

35. "Evaluation of Uncertainty in the Nuclear Form Factor Measured by Self-Powered Fixed In-Core Detector System," CENPD-153, C-E Topical Report, August 1975.

36. C-E Setpoint Methodology: Local Power Density and DNB LSSS and LCO Setpoint Methodology for Analog Protection Systems, CENPD-199, C-E Topical Report, April 1976.

SECTION 4.3: REFERENCES (Cont'd)

37. Randall, D. and St. John, D.S., "Xenon Spatial Oscillations," Nucleonics, 16, 3, pp 82-86, 1958.

38. Stacey, Jr., W.M., "Linear Analysis of Xenon Spatial Oscillations," Nuclear Science Engineering, 30, pp 453-455, 1967.

39. Poncelet, C.G., "The Effect of a Finite Time Step Length on Calculated Spatial Xenon Stability Characteristics in Large PWR's," Trans. ANS. 10, 2, p 571.

40. Gruen, A., "Messung Physikalischer Kenngroessen and Leistungsreakoren," Atom Kernenergie, 25, 2, 1975.

41. Engle, Wald M., Jr., "A User's Manual for ANISN, A One-Dimensional Discrete Ordinates Transport Code with Anisotropic Scattering," K-1693, March 30, 1967.

42. Stephen, D.W., "Fast Neutron Attenuation by the ANISN-SHADRAC Analytical Method," CENPD-105, June 1973.

43. DOT-III Two-Dimensional Discrete Ordinates Transport Code, ORNL-TM-4280, September 1973.

44. MORSE Code with Combinatorial Geometry, E.A. Straker et al., DNA 2860T, May 1972.

45. DOMINO, A General Purpose Code for Coupling Discrete Ordinates and Monte Carlo Radiation Transport Calculations, M.B. Emmett, ORNL4853, July 1973.

46. CASK, 40 Group Coupled Neutron and Gamma Cross Section Date, RSIC Publication DLC-23E, March 1975.

→(DRN 06-1059, R15; EC-9533, R302)

←(DRN 06-1059, R15; EC-9533, R302)

→LBDCR 17-020, R310)

47. RSIC Computer Code Collection CCC-650, "DOORS 3.1 One, Two-, and Three-Dimensional Discrete Ordinates Neutron/Photon Transport Code System," August 1996.

48. RSIC DLC-185, "BUGLE-96 Couple 47 Neutron, 20 Gamma-Ray Group Cross-Section Library Derived from ENDF/B-VI for LWR Shielding and Pressure Vessel Dosimetry Applications," March 1996.

49. NRC Regulatory Guide 1.190, "Calculational and Dosimetry Methods for Determining Pressure Vessel Neutron Fluence," March 2001.

50. Letter from Herbert N. Berkow to Mr. Gordon Bischoff, “Final Safety Evaluation for Topical Report WCAP-14040, Revision 3, ‘Methodology Used to Develop Cold Overpressure Mitigating System Setpoints and RCS Heatup and Cooldown Limit Curves (TAC No. MB5754).’” February 27, 2004. ADAMS Accession No. ML050120209.

51. WCAP-16002-NP, "Analysis of Capsule 263 from the Entergy Operations Waterford Unit 3 Reactor Vessel Radiation Surveillance Program," March 2003.

←(LBDCR 17-020, R310)

TABLE 4.3-1 (Sheet 1 of 2) Revision 307 (07/13)

NUCLEAR DESIGN CHARACTERISTICS

Item	Value
General Characteristics	
Fuel management	3-batch, mixed central zone
First cycle average burnup, MWd/MTU	12,731
First cycle lifetime, full power hours	8,075
U-235 enrichments, w/o	
18,188 rods	1.87
17,408 rods	2.41
13,984	2.91
Core average	2.35
Core average H_2O/UO_2 volume ratio, first cycle, hot	2.08
→(DRN 02-1477, R12; 06-895, R15; EC-2800, R307) Number of control element assemblies ←(DRN 02-1477, R12; 06-895, R15; EC-2800, R307)	87
→(DRN 01-1103, R12; 02-1477, R12) ←(DRN 01-1103, R12; 02-1477, R12)	
Burnable Poison Rods	
Number	1,632
→(DRN 06-895, R15) Material ←(DRN 06-895, R15)	B_4C-Al_2O_3
Worth W%p, at BOC	
Hot, 583°F	7.5
Cold, 68°F	6.0
Dissolved Boron	
Dissolved boron content for criticality, ppm, (CEAs withdrawn, BOC)	
Hot, zero power, clean 545°F	832
Cold, 68°F	899
Hot, full power, clean, 583°F	719
Hot, full power, equilibrium Xe	452

→(DRN 06-895, R15; EC-2800, R307)

←(DRN 06-895, R15; EC-2800, R307)

TABLE 4.3-1 (Sheet 2 of 2) Revision 6 (12/92)

NUCLEAR DESIGN CHARACTERISTICS

Item	Value
Dissolved boron content (ppm) for:	
Refueling, first cycle/later cycles	1,720/2,150
10% subcritical, cold, first cycle (all CEAs out)	1,530
10% subcritical, hot, first cycle (all CEAs out)	1,590
Design maximum soluble boron addition rate required to compensate for reactivity addition due to system cooldown and xenon decay, ppm/hr	370
Maximum reactivity addition rate due to system cooldown and xenon decay, $\%\Delta\rho$	2.9
Boron worth, ppm/$\%\Delta\rho$	
Hot, 583°F	79
Cold, 68°F	62
Neutron Parameters	
Neutron lifetime (minimum), microseconds	30
Delayed neutron fraction	
Beginning-of-cycle	0.0072
End-of-cycle	0.0053

Table 4.3-2

Intentionally Deleted

TABLE 4.3-3 Revision 6 (12/92)

COMPARISON OF CORE REACTIVITY COEFFICIENTS WITH THOSE USED N VARIOUS SAFETY ANALYSES

	Moderator Temperature Coefficient ($\Delta\rho/°F \times 10^4$)	Doppler[a] (Coefficient)	Density Coefficient ($\Delta\rho/gm/cm^3$)
Coefficients from Table 4.3-4			
Full power			
BOC	-0.8	Figure 4.3-34	0.48
EOC 1	-2.3	Figure 4.3-34	N/A[b]
Zero power, CEAs at PDIL			
BOC	-1.1	Figure 4.3-34	N/A
EOC 1	-2.0	Figure 4.3-34	N/A
Coefficients used in Cycle 1 Accident Analyses			
CEA withdrawal			
Full/zero power	+0.5/+0.5	0.85	N/A
CEA misoperation (full length)			
Dropped CEA	-3.3	1.15	N/A
CEA misoperation (part length)			
Dropped CEA	+0.5/-3.3	0.85/1.15	N/A
Loss of flow	+0.5	0.85	N/A
CEA ejection		$0.85 \times W_R$	N/A
BOC, full/zero power	+0.5/+0.2	1.0/1.57[c]	N/A
EOC 1, full/zero power	-1.3/-1.0	1.0/2.15	N/A
Loss-of-coolant accident	N/A	1.0	(d)

(a) Nominal values of the Doppler coefficient ($\Delta\rho/°F$) as a function of the fuel temperature are shown on Figure 4.3-34. The numbers entered in the Doppler column of this table are the multipliers applied to the nominal value for analysis of designated accidents.

(b) Not applicable.

(c) These are the values of W_R, where W_R is a reactivity dependent factor, the origin of which is explained in Subsection 15.4.3.2.

(d) A curve of reactivity vs. moderator density is used for the LOCA evaluation. The value of density coefficient used corresponds to a $+ 0.5 \times 10^{-4}$ MTC for the large break analysis, and to a $+ 0.15 \times 10^{-4}$ MTC for the small break analysis.

TABLE 4.3-4

REACTIVITY COEFFICIENTS

Moderator Temperature Coefficient, $\Delta\rho$/°F	
Beginning-of-cycle (719 ppm, soluble boron)	
Cold, 68°F	-0.1×10^{-4}
Hot, zero power, 545°F, no CEAs	-0.5×10^{-4}
Hot full power, 583°F no CEAs	-0.8×10^{-4}
Hot full power, equilibrium Xe, no CEAs	-1.2×10^{-4}
Hot zero power, regulating CEAs inserted	-1.1×10^{-4}
End-of-Cycle (0 ppm, soluble boron)	
Cold, 68°F	0.0
Hot zero power, 545°F, no CEAs	-1.5×10^{-4}
Hot full power, equilibrium Xe, no CEAs	-2.3×10^{-4}
Hot zero power, rodded, regulating CEAs inserted	-2.0×10^{-4}
Moderator Density Coefficient, $\Delta\rho$/gm/cm^3	
Hot, operating, 583°F	
Beginning-of-cycle, 719 ppm soluble boron	+0.048
Fuel temperature contribution to power coefficient, /(kW/ft)	
Hot zero power	-4.0×10^{-3}
Full power	-1.5×10^{-3}
Moderator void coefficient $\Delta\rho$/% void	
Hot operating, 583°F	
Beginning-of-cycle, 719 ppm soluble boron	-0.36×10^{-3}
Moderator pressure coefficient, $\Delta\rho$/psi	
Hot, operating, 583°F	
Beginning-of-cycle, 719 ppm soluble boron	$+0.7\times10^{-6}$
Overall power coefficient, $\Delta\rho$/(kW/ft)	
Hot, operating, 583°F	
Beginning-of-cycle, 719 ppm soluble boron	-1.9×10^{-3}
End-of-cycle, 0 ppm soluble boron	-2.9×10^{-3}

TABLE 4.3-5

WORTHS OF CEA GROUPS (%Δρ)

	BOC	EOC
Shutdown CEAs	6.5	6.6
Regulating CEAs		
Group 1	1.3	1.1
Group 2	0.7	0.6
Group 3	1.0	1.1
Group 4	1.0	1.0
Group 5	0.4	0.5
Group 6 (lead bank)	0.4	0.4
	11.3	11.3

TABLE 4.3-6

CEA REACTIVITY ALLOWANCES (%$\Delta\rho$)

(Hot Full Power to Hot Zero Power)

Fuel temperature variation	1.4
Moderator temperature	2.0
Moderator voids	0.1
CEA bite	0.2
Part-length CEA effects	0.0
Shutdown margin and accident analysis allowance	5.15
Total reactivity allowance	8.85

TABLE 4.3-7 Revision 6 (12/92)

CALCULATED CEA WORTHS AND ALLOWANCES (%$\Delta\rho$)

Condition	BOC	EOC
All full-length CEAs inserted, hot, 583°F	11.35	11.30
Total reactivity allowance, full power (from Table 4.3-6)	8.85	8.85
Stuck rod worth	1.5	1.3
Excess over nominal design allowance	1.00	1.15
Excess over nominal, assuming most adverse stack-up of CEA worth uncertainties	0.10	0.25

TABLE 4.3-8

COMPARISON OF RODDED AND UNRODDED PEAKING FACTORS FOR VARIOUS RODDED CONFIGURATIONS AT BOC AND EOC

Configurations	Maximum Rod Radial Peaking Factor F_r^n	
	BOC	EOC
Unrodded	1.30	1.31
Bank 6	1.33	1.38
PLCEA	1.33	1.39
Bank 6 and PLCEA	1.43	1.46
Bank 5+6(a)	1.48	1.54
Bank 4+5+6(a)	1.54	1.50
Bank 3+4+5+6(a)	2.09	1.73
Bank 2+3+4+5+6(a)	1.70	1.71
Bank 1+2+3+4+5+6(a)	1.63	1.71

(a) No PLCEAs.

TABLE 4.3-9

CALCULATED VARIATION OF THE AXIAL STABILITY INDEX

DURING THE FIRST CYCLE[a] (hr^{-1})

Power Level (% of Full Power)	BOC	MOC [b]	EOC
100	+0.043	+0.036	+0.090
75	+0.016	+0.012	+0.063
50	-0.018	-0.020	+0.025

(a) Equilibrium xenon conditions.

(b) Middle of cycle.

TABLE 4.3-10 Revision 6 (12/92)

MAXIMUM FAST FLUX GREATER THAN 1 MeV (n/cm^2-sec)

Neutron Group	Lower Bound On Energy (MeV)	Flux, Shroud, ID and Core Periphery	Flux, Vessel, ID
1	7.41	2.69 (+11)[a]	1.29 (+9)
2	4.97	1.39 (+12)	4.09 (+9)
3	3.33	3.09 (+12)	4.51 (+9)
4	2.23	6.49 (+12)	8.78 (+9)
5	1.50	6.74 (+12)	9.09 (+9)
6	1.22	3.86 (+12)	4.86 (+9)
7	1.00	3.28 (+12)	4.17 (+9)
Total		2.51 (+13)	3.68 (+10)

(a) () Denotes power of ten

TABLE 4.3-11

CONTROL ELEMENT ASSEMBLY SHADOWING FACTORS

	BOC	EOC
Unrodded	1.000	1.000
Reg. Bank 3	1.133	1.116
PLR 9	1.054	1.054
Reg. Bank 3 + PLR 9	1.197	1.175

TABLE 4.3-12

FUEL ROD DESCRIPTION

Laboratory	Clad OD (in.)	Clad Thickness (in.)	Clad Material	Fuel Pellet OD (in.)	Fuel Density (g/cm^3)	Fuel Enrichment Wt % U-235	Wt % PuO_2
B&W	0.4755	0.016	SS 304	0.440	9.46	4.020	0
B&W	0.4748	0.032	AL 6061	0.4054	10.24	2.459	0
Yankee	0.3383	0.0161	SS 304	0.3000	10.18	2.700	0
Winfrith	0.4301	0.01051	SS 304	0.3984	10.44	3.003	0
Bettis	0.453	0.028	A1	0.3830	10.53	1.311	0
Hanford	0.426	0.027	Zr-2	0.372	9.646(a)	0.22	1.50
Battele N.W. Westinghouse	0.568	0.030	Zr-2	0.508	9.869(a)	0.72	2.20

(a) Effective fuel density

TABLE 4.3-13

RESULTS OF ANALYSIS OF CRITICAL UO_2 SYSTEMS

Lattice		W/O U-235	Pitch (in.)	H_2O/UO_2	Boron (ppm)	K_{eff}	Ref
B&W-1273	1	4.020	0.595	1.137	0	1.0012	22
	2	4.020	0.595	1.137	3390	1.0053	22
	3	4.020	0.571	0.956	0	0.9984	22
	4	2.459	0.595	1.371	0	1.0042	22
	5	2.459	0.595	1.371	1075	1.0055	22
B&W-3647	6	2.459	0.644	1.846	0	1.0027	23
	7	2.459	0.644	1.846	846	1.0044	23
	8	2.459	0.644	1.846	1536	1.0033	23
Yankee	9	2.700	0.405	1.048	0	1.0009	24
	10	2.700	0.435	1.405	0	1.0011	24
	11	2.700	0.470	1.853	0	1.0014	24
	12	2.700	0.493	2.166	0	1.0034	25
Winfrith	13(20°C)	3.003	0.520	1.001	0	1.0021	26
	14(80°C)	3.003	0.520	1.001	0	0.9994	26
	15	3.003	0.735	3.164	0		
	16	3.003	0.492	0.779	0		26
Bettis	17	1.311	0.6133[(a)]	1.429	0	1.0005	27
	18	1.311	0.6504[(a)]	1.781	0	1.0004	27
	19	1.311	0.7110[(a)]	2.401	0	1.0011	27
Average						1.0020±	0.0020

(a) Triangular pitch

TABLE 4.3-14

RESULTS OF ANALYSIS OF PuO2-UO2 FUELED LATTICES

Lattice	W/O U-235	W/O PuO_2	Pitch (in.)	H_2O/Fuel	Boron (ppm)	K_{eff}	Ref
Hanford	0.22	1.50	0.55[b]	1.099	0	0.9998	28
			0.60[b]	1.557	0	1.0026	28
			0.71[b]	2.705	0	1.0081	28
			0.80[b]	3.783	0	1.0071	28
BNWL	0.72	2.2[a]	0.85[b]	1.837	0	1.0068	29
			0.93[b]	2.445	0	1.0093	29
WCAP	0.72	2.2[a]	0.69	1.099	0	1.0019	30
			0.75	1.525	0	1.0067	30
			0.67	1.099	201	1.0013	30
			0.69	1.099	526	1.0011	30
				Average		1.0043 ± 0.0034	

(a) 7.654 W/O Pu-240 in Pu
(b) Triangular pitch

TABLE 4.3-15

REACTION RATES [a]

Lattice Number	Measured	Calculated	Measured	Calculated	Measured	Calculated
Babcock and Wilcox		ρ28		δ^{25}		
1	4.12±0.31	4.38	0.254±0.006	0.292		
3	5.08±0.10	5.19	0.307±0.002	0.351		
4	2.28±0.03	2.40	0.151±0.001	0.163		
		ρ28		δ^{28}	MCR	
6	1.85±0.02	1.81	0.063±0.006	0.056	0.484±0.011	0.480
Winfrith		RCR		δ^{28}	Pu239/U235	Fission
13	4.158±0.03	4.203	0.0845±0.0009	0.0884	1.589±0.009	1.568
14	4.293±0.047	4.311	0.0881±0.0027	0.0903	1.637±0.009	1.608
16	4.789±0.053	4.874	0.1050±0.0018	0.1056	1.611±0.009	1.633
Bettis		ρ28		δ^{28}	δ^{25}	
17	1.43±0.01	1.40	0.078±0.004	0.078	0.089±0.002	0.091
18	1.15±0.01	1.16	0.070±0.004	0.067	0.072±0.001	0.074
19	0.934±0.01	0.907	0.057±0.003	0.055	0.055±0.001	0.057

(a) Definitions:

ρ28 = epicadmium captures in U-238/subcadmium captures in U-238

δ^{25} = epicadmium fissions in U-235/subcadmium fissions in U-235

δ^{28} = Total fissions in U-238/total fissions in U-235

MCR = captures in U-238/fissions in U-235

RCR = MCR in lattice/MCR in thermal column

TABLE 4.3-16

BEGINNING OF CYCLE, ZERO POWER UNRODDED CHARACTERISTICS

Reactor	Temperature F	Critical Boron (ppm)		Temperature Coefficient x 10^{-4} $\Delta\rho$/F	
		Measured	Cal culated	Measured	Calculated
Maine-Yankee I	260	955	952	0.18	0.08
	525	988	989	0.13	0.23
Maine-Yankee II	525	809	799	-0.24	-0.29
Fort Calhoun	260	900	889	0.22	0.08
	525	933	911	0.26	0.21
Calvert Cliffs	260	1048	1062	0.20	0.14
	525	1106	1078	0.22	0.26
Millstone II	532	960	951	0.08	0.02
Average Error (calc.-meas.)		-8 $\pm$ 13		-0.04 $\pm$ 0.08	

TABLE 4.3-17 Revision 6 (12/92)

CONTROL ROD WORTH, BEGINNING OF CYCLE, ($\Delta\rho$) HOT - ZERO POWER

	Main-Yankee		Fort Calhoun		Calvert Cliffs		Millstone II	
Rod Banks	Measured	Calculated	Measured	Calculated	Measured	Calculated	Measured	Calculated
7	-	-	-	-	-	-	0.76	0.74
6	-	-	-	-	-	-	0.50	0.47
5	0.57	0.58	-	-	0.55	0.54	0.33	0.29
4	0.37	0.38	0.60	0.54	0.35	0.35	1.37	1.36
3	0.92	0.93	0.58	0.57	0.93	0.90	0.62	0.62
2	0.86	0.95	2.10	2.01	0.78	0.74	1.40	1.40
1	0.80	0.80	0.99	0.91	0.95	1.04	0.69	0.70
C	1.21	1.23	-	-	1.30	1.40	-	-
B	0.76	0.75	2.13	2.09	0.99	0.87	0.39	0.46
Total	5.49	5.62	6.40	6.12	5.85	5.84	6.06	6.04
Average relative error (%) (Calc-meas)/measured			2.3 $\pm$ 3.8		-5.2 $\pm$ 3.7		-0.2 $\pm$ 7.4	-0.3 $\pm$ 8.6

Average relative error, all cases (%): -0.6 $\pm$ 6.7

TABLE 4.3-18 Revision 6 (12/92)

COMPARISONS OF CALCULATED AND MEASURED CEA WORTHS ($\Delta\rho$)

Condition	CEA Worth	
	Calculated	Measured
Ejected CEA		
Maine Yankee		
9 CEA pattern	0.15	0.14
Fort Calhoun		
17 CEA pattern	0.29	0.28
Palisades		
9 Rod pattern	0.25	0.28
13 Rod pattern	0.71	0.67
Dropped CEA		
Maine Yankee		
Dual CEA	0.15	0.14
Fort Calhoun		
Dual (peripheral) CEA	0.14	0.15
Dual (central) CEA	0.18	0.19
Stuck CEA (with all other CEAs inserted)		
Maine Yankee		
Dual CEA	1.89	2.14
Fort Calhoun		
Dual CEA	1.57	1.46

TABLE 4.3-19

AT-POWER ISOTHERMAL TEMPERATURE COEFFICIENTS

Core	Exposure (MWD/T)	Boron (PPM)	Temperature Coefficient (x10 $\Delta\rho$/F) Measured	Calculated 2-D	Calculated 3-D
Fort Calhoun	3000	597	-0.13	-0.29	
	8200	300	-0.97	-0.91	
Maine Yankee 1	2000	750	0.03	-0.01	
	4400	760	0.13	0.06	
	4400	712	-0.06	-0.04	-0.04
	6500	640	-0.19	-0.19	-0.21
	9000	500	-0.47	-0.46	-0.48
	10360	420	-0.61	-0.67	-0.58
	6700	537	-0.50	-0.45	
Maine Yankee II	400	525	-0.93	-0.69	
	4700	521	-0.42	-0.48	
Average difference X (Calc-meas)				0.008	0.005
Standard deviation of difference				0.100	0.024

TABLE 4.3-20 Revision 6 (12/92)

POWER DISTRIBUTIONS
SUMMARY OF CALCULATIONAL AND MEASUREMENT UNCERTAINTIES

1. Calculational Uncertainty on F_q^n	6.9%
2. Measurement Uncertainty on F_q^n	5.8%
3. Calculational Uncertainty on F_r^n	4.6%
4. Measurement Uncertainty on F_r^n	4.6%

TABLE 4.3-21 Revision 6 (12/92)

AXIAL XENON OSCILLATIONS

Reactor	Exposure (MWd/MTU)	Period (hr)		Dampling (hr^{-1})	
		Measured	Calculated	Measured	Calculated
Fort Calhoun	7075	29	32	-0.027	-0.030
Stade	BOC	36	36	-0.096	-0.090
Stade	12200	27	30	-0.021	-0.019

TABLE 4.3-22 Revision 6 (12/92)

DENSIFICATION CHARACTERISITCS

Core Height	150 in.
Fractional Density Change	0.01
Clad Growth Allowance	0.007 in./in.

TABLE 4.3-23

RADIAL PIN POWER CENSUS

Pin Power Interval[a]	Number of Pins with power in Interval
0.00 - 1.00	15,700
1.00 - 1.05	6,324
1.05 - 1.10	10,516
1.10 - 1.20	11,344
1.20 - 1.29	5,696

(a) F_q^n within the interval given.

ASSEMBLY TYPE	NUMBER OF ASSEMBLIES	FUEL ENRICHMENT WT % U235	NO. OF FUEL RODS PER ASSEMBLY	NO. OF SHIM RODS/ ASSEMBLY	WT % B_4C	gm B^{10}/IN.
A	73	1.87	236	0		
B	80	187 2.41	12 208	16	3.60	0.02276
C	40	2.41 2.91	12 224	0	1.62	0.01034
C.	8	2.41 2.91	12 212	12	1.62	0.01034
C+	16	2.41 2.91	12 208	16	1.62	0.01034

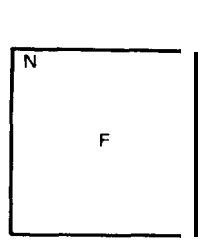

N = BOX NO.
F = ASSEMBLY TYPE

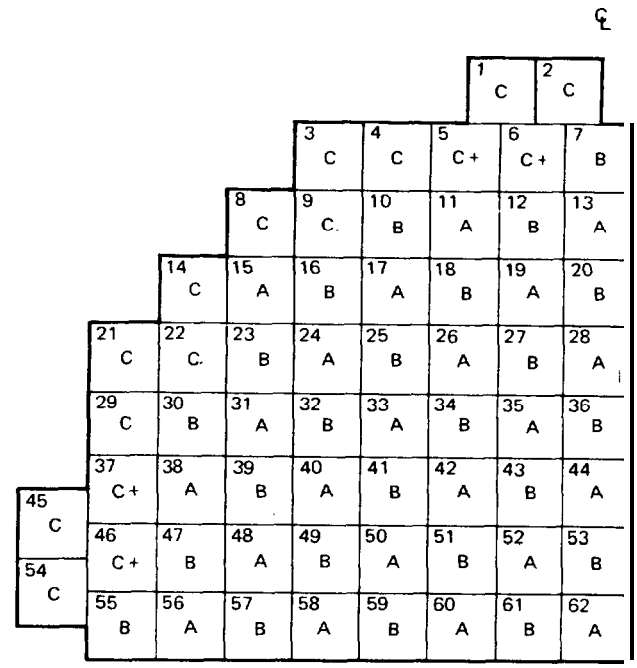

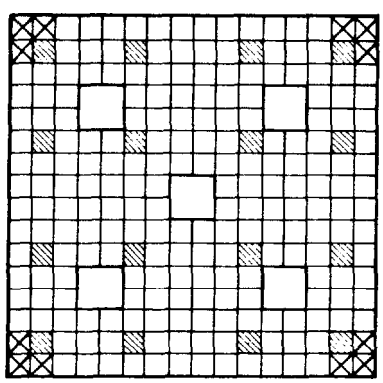

B OR C+

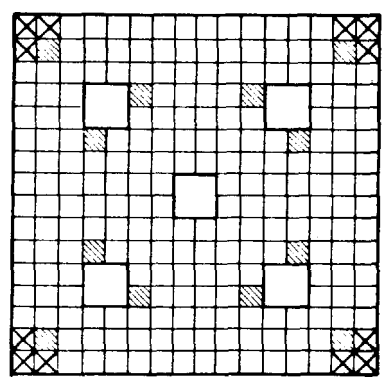

C.

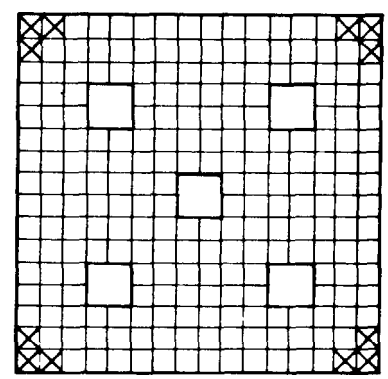

C

LOWER ENRICHED FUEL PIN
HIGHER ENRICHED FUEL PIN
SHIM PIN

LOUISIANA POWER & LIGHT CO. Waterford Steam Electric Station	FUELMANAGEMENTPATTERN	Figure 4.3-1

X.XX BOX AVERAGE (BOX POWER / CORE AVERAGE POWER)
X.XX MAX. ENTHALPY RISEFACTOR (Max. of the Average Power of 4 Neighboring Pins / Core Average Power)
X.XX MAX. ONE-PIN FACTOR (Max. Pin Power / Core Average Power)

							C 1 0.67 1.08 1.10	C 2 0.90 1.17 1.19
				C 3 0.60 0.97 0.99	C 4 0.83 1.10 1.13	C+ 5 0.96 1.19 1.23	C+ 6 1.12 1.19 1.23	B 7 1.00 1.08 1.11
			C 8 0.67 1.03 1.05	C 9 0.96 1.06 1.09	B 10 0.95 1.04 1.09	A 11 0.99 1.07 1.09	B 12 1.05 1.11 1.15	A 13 1.03 1.11 1.13
		C 14 0.67 1.03 1.05	A 15 0.81 0.90 0.92	B 16 0.95 1.03 1.08	A 17 0.98 1.06 1.08	B 18 1.08 1.13 1.18	A 19 1.06 1.14 6	B 20 1.12 1.16 0
	C 21 0.60 0.97 0.99	C 22 0.96 1.06 1.09	B 23 0.95 1.03 1.08	A 24 0.98 1.06 1.08	B 25 1.08 1.13 1.18	A 26 1.07 1.15 1.18	B 27 1.14 1.19	A 28 1.10 1.19
	C 25 0.83 1.10 1.13	B 30 0.95 1.04 1.09	A 31 0.98 1.06 1.08	B 32 1.08 1.13 1.18	A 33 1.08 1.16 1.18	B 34 1.16 1.20 1.25	A 35 1.13 1.21 1.24	B 36 1.18 1.22 1.26
C 45 0.67 1.08 1.10	C+ 37 0.96 1.19 1.23	A 38 0.99 1.07 1.09	B 39 1.08 1.13 1.18	A 40 1.07 1.15 1.18	B 41 1.16 1.20 1.25	A 42 1.14 1.22 1.25	B 43 1.20 1.24	A 44 1.16 1.25 1.27
C 54 0.90 1.17 1.19	C+ 46 1.12 1.20 1.23	B 47 1.05 1.11 1.15	A 48 1.06 1.14 1.16	B 49 1.14 1.19 1.23	A 50 1.13 1.21 1.24	B 51 1.20 1.24 1.29	A 52 1.17 1.26 1.28	B 53 1.23 1.26 1.30
	B 55 1.00 1.08 1.11	[illegible] 1.11 1.13	B 57 1.12 1.16 1.20	A 58 1.10 1.19 1.21	B 59 1.18 1.22 1.26	A 60 1.16 1.25 1.27	B 61 1.23 1.26 1.30	A 62 1.18 1.27 1.29

LOUISIANA POWER & LIGHT CO. Waterford Steam Electric Station	**PLANAR AVERAGE POWER DISTRIBUTION BOC, UNRODDED, FULL POWER, NO XENON**	Figure 4.3-2

x.xx x.xx x.xx

BOX AVERAGE (BOX POWERICOREAVERAGEPOWER)
MAX. ENTHALPY RISEFACTOR (Max. of the Average Power of 4 Neighboring Pins/ Core Average Power)
MAX. ONE-PINFACTOR (Max. Pin Power/Core Average Power)

							C 1 0.62 1.01 1.03	C 2 0.83 1.08 1.11
				C 3 0.58 0.93 0.96	c 4 0.80 1.06 1: 10	C+ 5 0.92 1.15 1.19	C+ 6 1.06 1.13 1.17	B 7 0.95 1.04 1.07
			C 8 0.65 1.01 1.04	C. 9 0.93 1.04 1.08	B 10 0.93 1.03 1.08	A 11 0.98 1.06 1.09	B 12 1.04 1.10 1.15	A 13 1.01 1.10 1.12
		C 14 0.65 1.01 1.04	A 15 0.81 0.90 0.93	B 16 0.95 1.04 1.09	A 17 0.99 1.08 1.10	B 18 1.08 1.14 1.20	A 19 1.07 1.16 1.18	B 20 1.12 1.17 1.22
	C 21 0.58 0.93 0.96	C. 22 0.93 1.04 1.08	B 23 0.95 1.04 1.09	A 24 1.00 1.08 1.10	B 25 1.10 1.16 1.21	A 26 1.10 1.19 1.21	B 27 1.17 1.22 1.27	A 28 1.13 1.22 1.25
	C 29 0.80 1.06 1.10	B 30 0.93 1.03 1.08	A 31 0.99 1.08 1.10	B 32 1.10 1.16 1.21	A 33 1.11 1.20 1.22	B 34 1.19 1.24 1.29	A 35 1.17 1.26 1.29	B 36 1.22 1.26 1.31
	C+ 37 0.92 1.15 1.19	A 38 0.98 1.06 1.09	B 39 1.08 1.14 1.20	A 40 1.10 1.19 1.21	B 41 1.19 1.24 1.29	A 42 1.18 1.27 1.30	B 43 1.25 1.26 1.34	A 44 1.21 1.30 1.33
C 45 0.62 1.01 1.03	C+ 46 1.06 1.13 1.17	B 47 1.04 1.10 1.15	A 48 1.07 1.17 1.18	B 49 1.17 1.22 1.27	A 50 1.17 1.26 1.29	B 51 1.25 1.28 1.34	A 52 1.22 1.31 1.34	B 53 1.27 1.31 1.35
C 54 0.83 1.08 1.11	B 55 0.95 1.04 1.07	A 56 1.02 1.10 1.12	B 57 1.12 1.17 1.22	A 58 1.13 1.22 1.25	B 59 1.22 1.26 1.31	A 60 1.21 1.30 1.33	B 61 1.27 1.31 1.35	A 62 1.23 1.32 1.35

LOUISIANA POWER & LIGHT CO. Waterford Steam Electric Station	PLANAR AVERAGE POWER DISTRIBUTION BOC, UNRODDED FULL POWER, EQUILIBRIUM XENON	Figure 4.3-3

x.xx x.xx x.xx

BOX AVERAGE (BOX POWERICOREAVERAGE POWER))
MAX. ENTHALPY RISEFACTOR (Max. of the Average Power of 4 Neighboring Pins/ Core Average Power)
MAX. ONE-PIN FACTOR (Max. Pin Power / Core Average Power)

					C 1 0.61 0.97 0.99	C 2 0.77 1.03 1.05
			C 3 0.59 0.96 0.99	C 4 0.80 1.08 1.11	C+ 5 1.00 1.20 1.25	C+ 6 1.17 1.28 1.31	B 7 1.13 1.20 1.22
		C 8 0.65 1.02 1.05	C 9 1.04 1.21 1.25	B 10 1.10 1.17 1.19	A 11 1.02 1.07 1.08	B 12 1.19 1.22 1.24	A 13 1.06 1.08 1.09
	C 14 0.65 1.02 1.05	A 15 0.86 1.00 1.02	B 16 1.13 1.19 1.20	A 17 1.04 1.06 1.08	B 18 1.18 1.20 1.23	A 19 1.05 1.07 1.08	B 20 1.18 1.21 1.23
C 21 0.59 0.96 0.99	C 22 1.04 1.21 1.25	B 23 1.13 1.19 1.20	A 24 1.04 1.06 1.07	B 25 1.18 1.20 1.23	A 26 1.03 1.06 1.07	B 27 1.15 1.18 1.20	A 28 1.02 1.05 1.06
C 29 0.80 1.08 1.11	B 30 1.10 1.17 1.19	A 31 1.04 1.06 1.08	B 32 1.18 1.20 1.23	A 33 1.03 1.06 1.07	B 34 1.14 1.17 1.19	A 35 0.99 1.03 1.04	B 36 1.11 1.14 1.16
C+ 37 1.00 1.20 1.25	A 38 1.02 1.07 1.08	B 39 1.18 1.20 1.23	A 40 1.03 1.06 1.07	B 41 1.14 1.17 1.19	A 42 0.99 1.02 1.03	B 43 1.09 1.12 1.14	A 44 0.96 0.99 1.00
C 45 0.61 0.97 0.99	C+ 46 1.17 1.28 1.31	B 47 1.19 1.22 1.24	A 48 1.05 1.07 1.08	B 49 1.15 1.18 1.20	A 50 0.99 1.03 1.04	B 51 1.09 1.12 1.14	A 52 0.95 0.98 0.99	B 53 1.07 1.09 1.11
C 54 0.77 1.03 1.05	B 55 1.13 1.20 1.22	A 56 1.06 1.08 1.09	B 57 1.18 1.21 1.23	A 58 1.02 1.05 1.06	B 59 1.11 1.14 1.16	A 60 0.96 0.99 1.00	B 61 1.07 1.09 1.11	A 62 0.94 0.96 0.97

LOUISIANA POWER & LIGHT CO. Waterford Steam Electric Station	PLANAR AVERAGE POWER DISTRIBUTION EOC, UNRODDED, FULL POWER, EQUILIBRIUM XENON	Figure 4.3-4

x.xx
x.xx
x.xx

BOX AVERAGE (BOX POWER/CORE AVERAGE POWER)
MAX. ENTHALPY RISE FACTOR (Max. of the Average Power of 4 Neighboring Pins / Core Average Power)
MAX. ONE-PIN FACTOR (Max. Pin Power / Core Average Power)

									C 1 0.74 1.19 1.22	C 2 1.00 1.29 1.31				
					C 3 0.68 1.09 1.12	C 4 0.93 1.22 1.25	C+ 5 1.05 1.28 1.32	C+ 6 1.21 1.29 1.33	B 7 1.08 1.13 1.17					
			C 8 0.76 1.17 1.20	C 9 1.08 1.19 1.22	B 10 1.05 1.11 1.16	A 11 1.05 1.14 1.16	B 12 1.08 1.13 1.16	A 13 1.03 1.11 1.14						
		C 14 0.76 1.17 1.20	A 15 0.92 1.02 1.04	B 16 1.06 1.12 1.17	A 17 1.06 1.13 1.16	B 18 1.08 1.12 1.16	A 19 0.97 1.05 1.08	B 20 0.93 1.04 1.09						
	C 21 0.68 1.09 1.12	C 22 1.08 1.19 1.22	B 23 1.05 1.12 1.17	A 24 1.06 1.14 1.16	B 25 1.11 1.14 1.18	A 26 1.03 1.11 1.14	B 27 0.93 1.04 1.09	A 28 0.59 0.70 0.73						
	C 29 0.93 1.22 1.25	B 30 1.05 1.11 1.16	A 31 1.05 1.16	B 32 1.11 1.14 1.18	A 33 1.07 1.15 1.17	B 34 1.09 1.14 1.18	A 35 0.98 1.06 1.08	B 36 0.94 1.05 1.10						
	C+ 37 1.05 1.29 1.32	A 38 1.05 1.14 1.16	B 39 1.08 1.12 1.16	A 40 1.03 1.11 1.14	B 41 1.09 1.14 1.18	A 42 1.06 1.14 1.17	B 43 1.10 1.15 1.19	A 44 1.05 1.14 1.16						
C 45 0.74 1.19 1.22	C+ 46 1.21 1.29 1.33	B 47 1.08 1.13 1.16	A 48 0.97 1.05 1.08	B 49 1.04 1.09	A 50 0.98 1.06 1.08	B 51 1.10 1.15 1.19	A 52 1.10 1.18 1.20	B 53 1.15 1.19 1.23						
C 54 1.00 1.29 1.31	B 55 1.08 1.13 1.17	A 56 1.03 1.11 1.14	B 57 0.93 1.04 1.09	A 58 0.59 0.70 0.73	B 59 0.94 1.05 1.10	A 60 1.05 1.14 1.16	B 61 1.15 1.19 1.23	A 62 1.12 1.20 1.23						

LOUISIANA POWER & LIGHT CO. Waterford Steam Electric Station	**PLANAR AVERAGE POWER DISTRIBUTION** **BOC, BANK 6 FULL'IN, FULL POWER, NO XENON**	Figure **4.3-5**

x.xx
x.xx
x.xx

BOX AVERAGE (BOX POWER / CORE AVERAGE POWER)
MAXENTHALPY RISE FACTOR (Max. of the Average Power of 4 Neighboring Pins / Core Average Power)
MAX. ONE-PIN FACTOR (Max Pin Power/ Core Average Power)

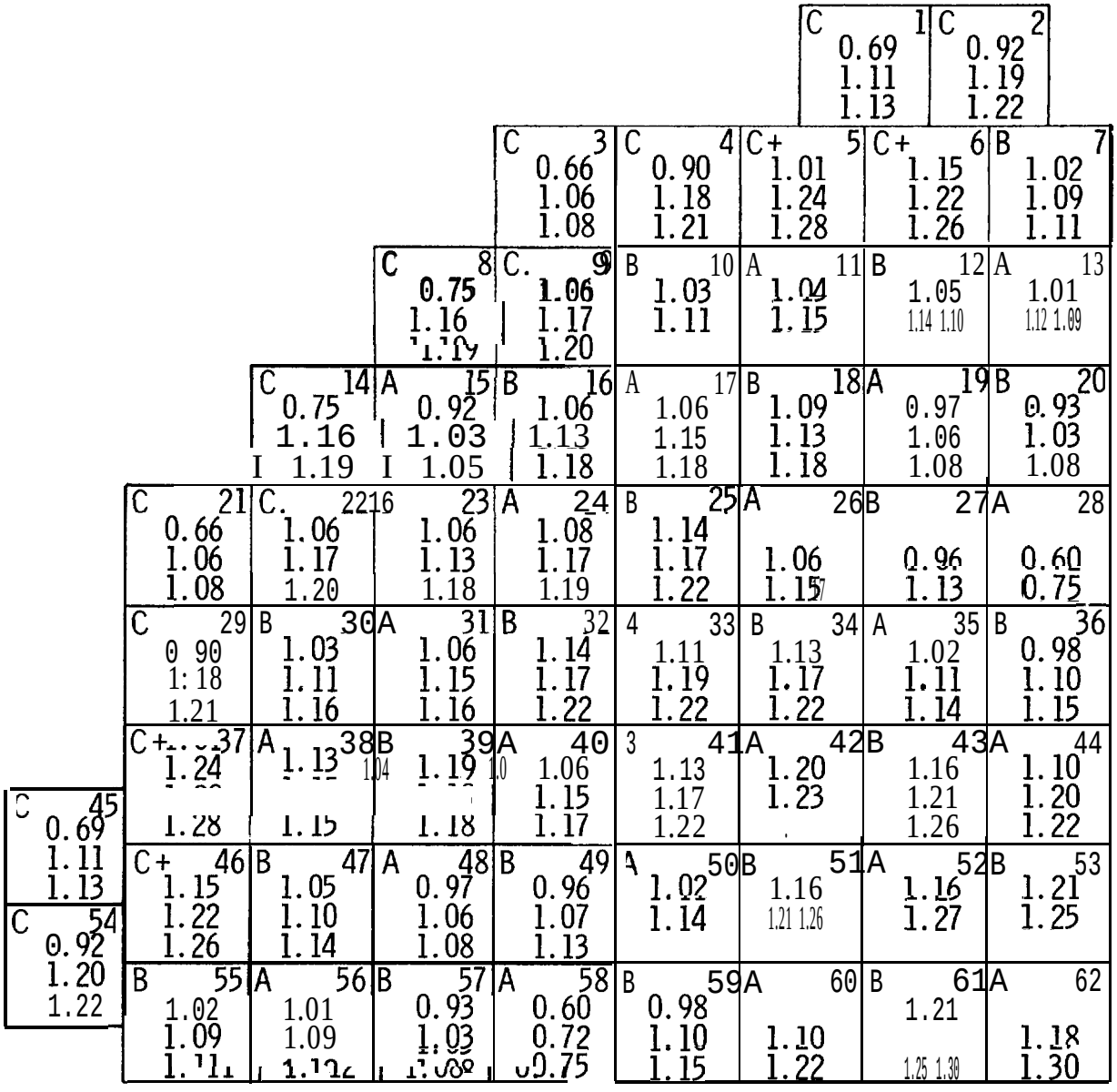

LOUISIANA POWER & LIGHT CO. Waterford Steam Electric Station	PLANAR AVERAGE POWER DISTRIBUTION – BOC, **BANK 6 FULL IN, FULL POWER EQUILIBRIUM XENON**	Figure 4.3-6

x.xx
x.xx
x.xx

BOX AVERAGE (BOX POWER / CORE AVERAGE POWER)
MAX. ENTHALPY RISE FACTOR (Max. of the Average Power of 4 Neighboring Pins/ Core Average Power)
MAX. ONE-PINFACTOR (Max. Pin Power / Core Average Power)

										C 1 0.67 1.05 1.07	C 2 0.84 1.11 1.13				
				C 3 0.66 1.07 1.10	C 4 0.88 1.18 1.21	C+ 5 1.08 1.29 1.33	C+ 6 1.25 1.35 1.37	B 7 1.20 1.26 1.28							
			C 8 0.74 1.15 1.18	C. 9 1.16 1.34 1.38	B 10 1.20 1.27 1.29	A 11 1.08 1.11 1.13	B 12 1.21 1.26 1.28	A 13 1.06 1.12 1.13							
		C 14 0.74 1.15 1:18	A 15 0.96 1.11 1.13	B 16 1.25 1.29 1.32	A 17 1.11 1.14 1.16	B 18 1.19 1.25 1.26	A 19 0.97 1.07 1.08	B 20 1.00 1.12 1.14							
	C 21 0.66 1.07 1.10	c. 22 1.16 1.34 1.38	B 23 1.25 1.29 1.32	A 24 1.12 1.14 1.16	B 25 1.22 1.28 1.29	A 26 1.00 1.08 1.10	B 27 0.95 1.07 1.10	A 28 0.56 0.74 0.78							
	C 29 0.88 1.18 1.21	B 30 1.20 1.27 1.29	A 31 1.11 1.14 1.16	B 32 1.22 1.28 1.29	A 33 1.03 1.10 1.11	B 34 1.08 1.14 1.16	A 35 0.86 0.92 0.94	B 36 0.88 0.95 0.96							
	C+ 37 1.08 1.29 1.33	A 38 1.08 1.11 1.13	B 39 1.19 1.25 1.26	A 40 1.00 1.08 1.10	B 41 1.08 1.14 1:16	A 42 0.92 0.98 0.99	B 43 0.99 1.03 1.04	A 4 0.86 0.89 0.90							
C 45 0.67 1.05 1.07	C+ 46 1.25 1.35 1.37	B 47 1.21 1.26 1.28	A 48 0.97 1.07 1.08	B 49 0.95 1.07 1:10	A 50 0.86 0.92 0.94	B 51 0.99 1.03 1.04	A 52 0.88 0.90 0:91	B 53 0.99 1.01 1.03							
C 54 0.84 1.12 1.13	B 55 1.20 1.26 1.28	A 56 1.06 1.12 1.13	B 57 1.00 1.12 1.14	A 58 0.56 0.74 0.78	B 59 0.88 0.95 .0.96	A 60 0.86 0.89 0.90	B 61 0.99 1.01 0	A 62 0.88 0.89 0.90							

LOUISIANA POWER & LIGHT CO. Waterford Steam Electric Station	PLANAR AVERAGE POWER DISTRIBUTION – EOC, BANK 6 FULL IN, FULL POWER EQUILIBRIUM XENON	Figure 4.3-7

x.xx
x.xx
x.xx

BOX AVERAGE (BOX POWER / CORE AVERAGE POWER)
MAX. ENTHALPY RISE FACTOR (Max. of the Average Power of 4 Neighboring Pins / Core Average Power)
MAX. ONE-PIN FACTOR (Max. Pin Power / Core Average Power)

										C 1 0.72 1.17 1.19	C 2 0.98 1.27 1.29			
					C 3 0.63 1.02 1.04	c 4 0.88 1.15 1.19	C+ 5 1.02 1.25 1.29	C+ 6 1.20 1.28 1.31	B 7 1.08 1.14 1.17					
			C 8 0.70 1.07 1.09	C. 9 0.09 1.09 1.12	B 10 0.98 1.06 1.09	A 11 1.02 1.11 1.13	B 12 1.09 1.14 1.18	A 13 1.07 1.16 1.18						
		C 14 0.70 1.07 1.09	A 15 0.84 0.93 0.95	B 16 0.96 1.02 1.06	A 17 0.97 1.04 1.06	B 18 1.03 1.09 1.14	A 19 1.05 1.13 1.15	B 20 1.12 1.15 1.18						
	C 21 0.63 1.02 1.04	C. 22 0.99 1.09 1.12	B 23 0.96 1.02 1.06	A 24 0.96 1.03 1.06	B 25 1.01 1.04 1.08	A 26 0.86 0.91 0.92	B 27 1.08 1.14 1.20	A 28 1.08 1.16 1.19						
	C 29 0.88 1.15 1.19	B 30 0.98 1.06 1.09	A 31 0.97 1.04 1.06	B 32 1.01 1.04 1.08	A 33 1.00 1.08 1.10	B 34 1.07 1.15 1.21	A 35 1.09 1.18 1.20	B 36 1.16 1.21 1.25						
C	C+ 37 1.02 1.25 1.29	A 38 1.02 1.11 1.13	3 39 1.03 1.09 1.14	A 40 0.86 0.91 0.92	B 41 1.07 1.15 1.21	A 42 1.10 1.19 1.22	B 43 1.20 1.25 1.30	A 44 1.16 1.25 1.28						
45 0.72 1.17 1.19	C+ 46 1.20 1.28 1.31	B 47 1.09 1.14 1.18	4 1.05 48 1.13 1.15	B 1.08 49 1.14 1.20	A 50 1.09 1.18 1.20	B 1.20 51 1.25 1.30	A 52 1.27 1.18 1.30	B 53 1.25 1.29 1.33						
C 54 0.98 1.27 1.29	B 55 1 1.14 1.17	A 56 1.07 1.18 1.16	3 57 1.12 1.15 1.18	A 58 1.08 1.16 1.19	B 59 1.16 1.21 1.25	A 60 1.16 1.25 1.28	B 61 1.25 1.29 1.33	A 62 1.21 1.30 1.32						

LOUISIANA POWER & LIGHT CO. Waterford Steam Electric Station	**PLANAR AVERAGE POWER DISTRIBUTION BOC, PART-LENGTH ROD AS IF FULL LENGTH, FULL POWER, NO XENON**	Figure 4.3-8

x.xx
x.xx
x.xx

BOX AVERAGE (BOX POWER / CORE AVERAGE POWER)
MAX. ENTHALPY RISE FACTOR (Max. of the Average Power of 4 Neighboring Pins / Core Average Power)
MAX. ONE-PIN FACTOR (Max. Pin Power / Core Average Power)

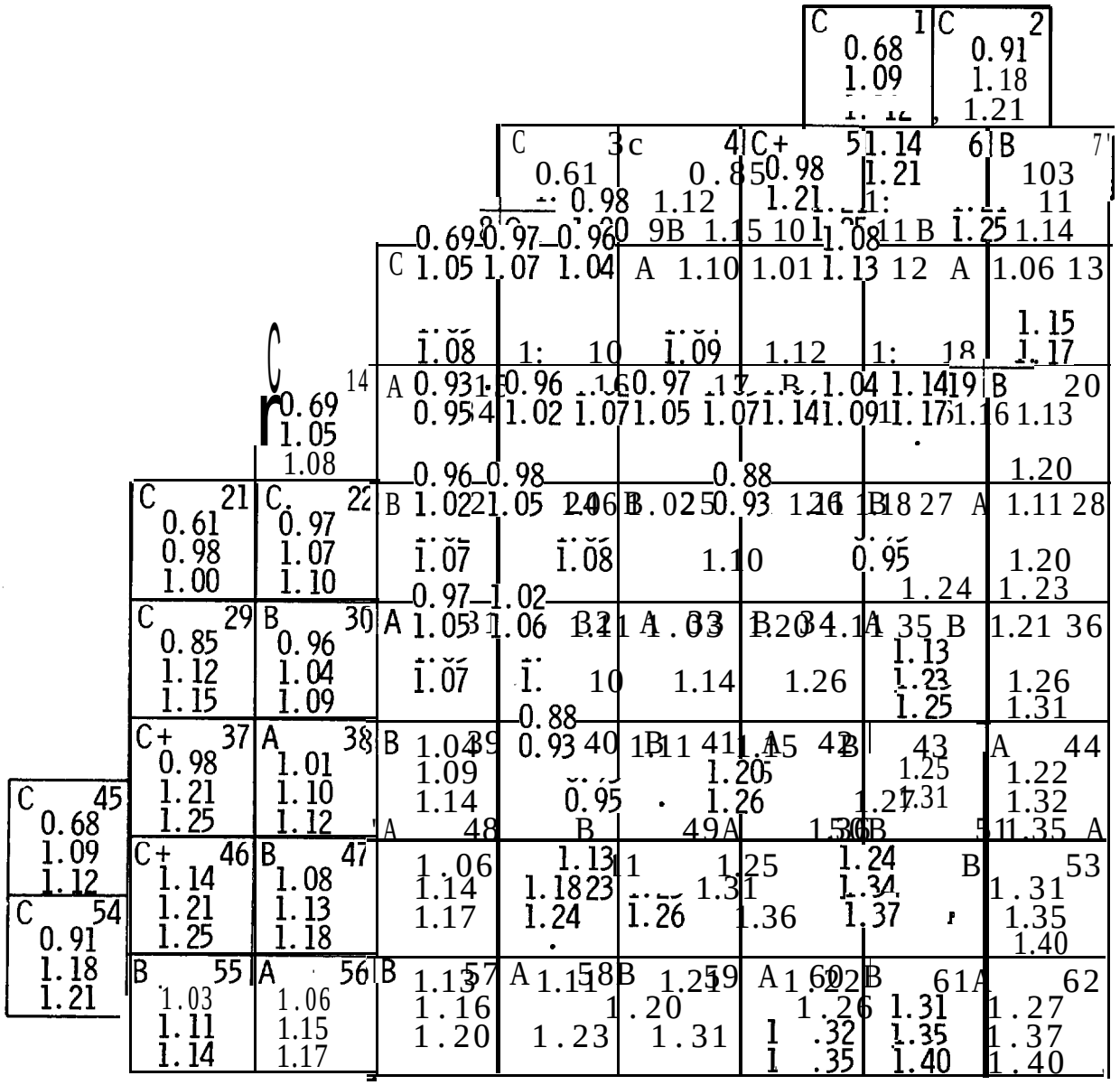

LOUISIANA POWER & LIGHT CO. Waterford Steam Electric Station	PLANAR AVERAGE POWER DISTRIBUTION **BOC, PART-LENGTH ROD AS IF** FULL LENGTH, FULL POWER, EQUILIBRIUM XENON	Figure 4.3-9

x.xx
x.xx
x.xx

BOX AVERAGE (BOX POWER / CORE AVERAGE POWER)
MAX. ENTHALPY RISE FACTOR (Max. of the Average Power of 4 Neighboring Pins / Core Average Power)
MAX. ONE-PIN FACTOR (Max. Pin Power / Core Average Power)

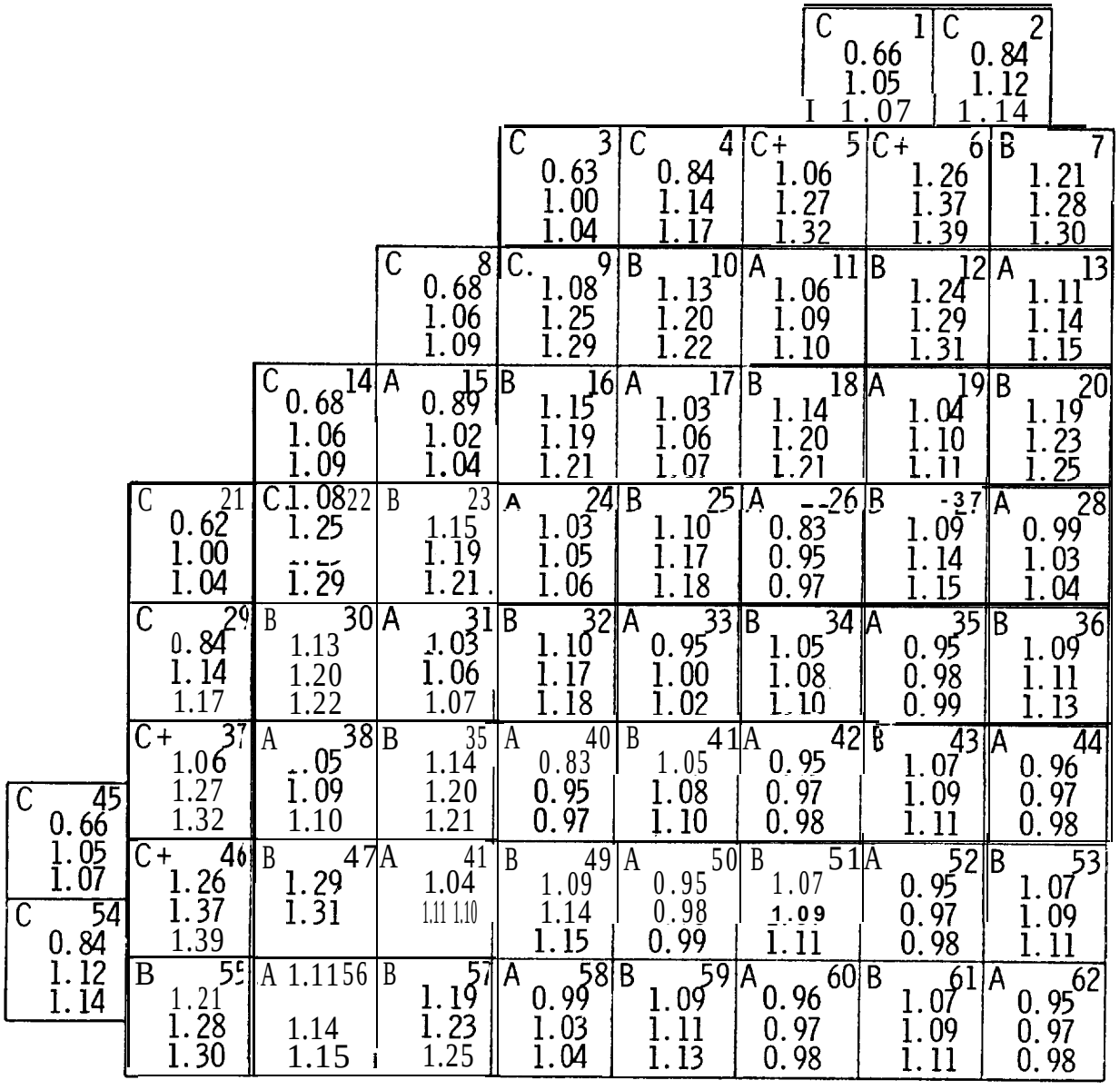

LOUISIANA POWER & LIGHT CO. Waterford Steam Electric Station	PLANAR AVERAGE POWER DISTRIBUTION EOC, PART-LENGTH ROD AS IF FULL LENGTH, FULL POWER, EQUILIBRIUM XENON	Figure 4.3-10

x.xx
x.xx
x.xx

BOX AVERAGE (BOX POWER / CORE AVERAGE POWER)
MAX. ENTHALPY RISE FACTOR (Max. of the Average Power of 4 Neighboring Pins / Core Average Power)
MAX. ONE-PIN FACTOR (Max. Pin Power / Core Average Power)

						C 1 0.80 1.30 1.32	C 2 1.09 1.40 1.43
			C 3 0.72 1.15 1.18	C 4 0.99 1.28 1.31	C+ 5 1.12 1.36 1.40	C+ 6 1.30 1.39 1.43	B 7 1.17 1.23 1.26
		C 8 0.80 1.22 1.25	C 9 1.13 1.23 1.27	B 10 1.08 1.15 1.18	A 11 1.09 1.18 1.21	B 12 1.12 1.18 1.21	A 13 1.08 1.17 1.20
	C 14 0.80 1.22 1.25	A 15 0.95 1.05 1.07	B 16 1.07 1.12 1.15	A 17 1.04 1.12 1.15	B 18 1.04 1.12 1.17	A 19 0.96 1.05 1.07	B 20 0.94 1.07 1.12
C 21 0.72 1.15 1.18	C 22 1.13 1.23 1.27	B 23 1.07 1.12 1.15	A 24 1.04 1.12 1.14	B 25 1.04 1.10 1.15	A 26 0.82 0.88 0.89	B 27 0.87 0.95 0.99	A 28 0.57 0.60 0.71
C 29 0.99 1.28 1.31	B 30 1.08 1.15 1.18	A 31 1.04 1.12 1.15	B 32 1.04 1.10 1.15	A 33 0.99 1.06 1.09	B 34 1.00 1.06 1.09	A 35 0.92 1.01 1.03	B 36 0.91 1.03 1.07
C+ 37 1.12 1.36 1.40	A 38 1.09 1.18 1.21	B 39 1.04 1.12 1.17	A 40 0.82 0.88 0.89	B 41 1.00 1.06 1.09	A 42 1.02 1.09 1.12	B 43 1.08 1.13 1.18	A 44 1.03 1.12 1.14
C 45 0.81 1.30 1.32	C+ 46 1.30 1.39 1.43	B 47 1.12 1.18 1.21	A 48 0.96 1.05 1.07	B 49 0.87 0.95 0.99	A 50 0.92 1.01 1.03	B 51 1.08 1.13 1.18	A 52 1.09 1.17 1.20	B 53 1.15 1.19 1.23
C 54 1.09 1.40 1.43	B 55 1.17 1.23 1.26	A 56 1.08 1.18 1.20	B 57 0.94 1.07 1.12	A 58 0.57 0.60 0.71	B 59 0.91 1.03 1.07	A 60 1.03 1.12 1.14	B 61 1.15 1.19 1.23	A 62 1.12 1.21 1.23

LOUISIANA POWER & LIGHT CO. Waterford Steam Electric Station	PLANAR AVERAGE POWER DISTRIBUTION BOC, PART-LENGTH ROD AS IF FULL LENGTH, BANK 6 FULL IN, FULL POWER NO XENON	Figure 4.3-11

X.XX
X.XX
X.XX

BOX AVERAGE (BOX POWER / CORE AVERAGE POWER)
MAX. ENTHALPY RISE FACTOR (Max. of the Average Power of 4 Neighboring Pins / Core Average Power)
MAX. ONE-PINFACTOR (Max. Pin Power / Core Average Power)

										C 0.76 1 1.21 1.23	C 2 1.31 1.01 1.34			
					C 0.70 3 1.12 1.14	c 0.95 4 1.24 1.28	C 5 1.31 1.35	C+ 6 1.24 1.32 1.36	B 7 1.11 1.16 1.20					
			C 8 0.79 1.21 1.24	C 9 1.11 1.25	B 10 1.07 1.17 1.13	A 11 1.08 1.19	B 12 1.10 1.18 1.15	A 13 1.06 1.11 1.15						
		C 14 0.79 1.21 1.24	A 15 0.96 1.06 1.09	B 16 1.08 1.12 1.17	A 17 1.05 1.14 1.16	B 18 1.05 1.12 1.17	A 19 0.96 1.05 1.08	B 20 0.94 1.06 1.11						
	C 21 0.70 1.12 1.14	C 22 1.11 1.21 1.25	B 23 1.08 1.12 1.17	4 24 1.06 1.14 1.17	B 25 1.06 1.12 1.16	A 26 0.84 0.89 0.90	B 27 0.89 0.96 1.01	A 28 0.58 0.69 0.72						
	C 29 0.95 1.24 1.28	B 1.01 1.13 1.17	A 31 1.05 1.14 1.16	3 32 1.06 1.12	A 33 1.02 1.10	B 34 1.04 1.10	A 35 0.97 1.06 1.08	B 36 0.95 1.08 1.13						
	C+ 37 1 08 1.31 1.35	A 38 1.08 1.17 1.19	3 39 1.05 1.12 1.17	A 40 0.84 0.89 0.90	B 41 1.04 1.11 1.15	A 42 1.07 1.16 1.18	B 43 1.13 1.20 1.26	A 44 1.09 1.19 1.22						
C 0.7% 1.21 1.23	C+ 46 1.24 1.32 1.36	B 47 1.10 1.15 1.18	A 48 0.96 1.06 1.08	3 49 0.89 0.97 1.01	A 50 0.97 1.06 1.08	B 51 1.13 1.20 1.26	A 52 1.16 1.25 1.28	B 53 1.22 1.27 1.31						
C 54 1.01 1.31 1.34	B 55 1.11 1.16 1.20	A 66 1.0 1.15 1.18	3 57 0.94 1.06 1.11	A 58 0.58 0.69 0.72	B 59 0.95 1.08 1.13	A 60 1.09 1.19 1.22	B 61 1.22 1.27 1.31	A 62 1.20 1.29 1.32						

LOUISIANA POWER & LIGHT CO. Waterford Steam Electric Station	PLANAR AVERAGE POWER DISTRIBUTION BOC, PART-LENGTH ROD AS IF FULL LENGTH., BANK 6 FULLY, FULL POWER EQUILIBRIUM XENON	Figure 4.3-12

X.XX
X.XX
r X.XX

BOX AVERAGE (BOX POWER / CORE AVERAGE POWER)
MAX. ENTHALPY RISEFACTOR (Max. of the Average Power of4 Neighboring Pins / Core Average Power)
MAX. ONE-PIN FACTOR (Max. Pin Power / Core Average Power)

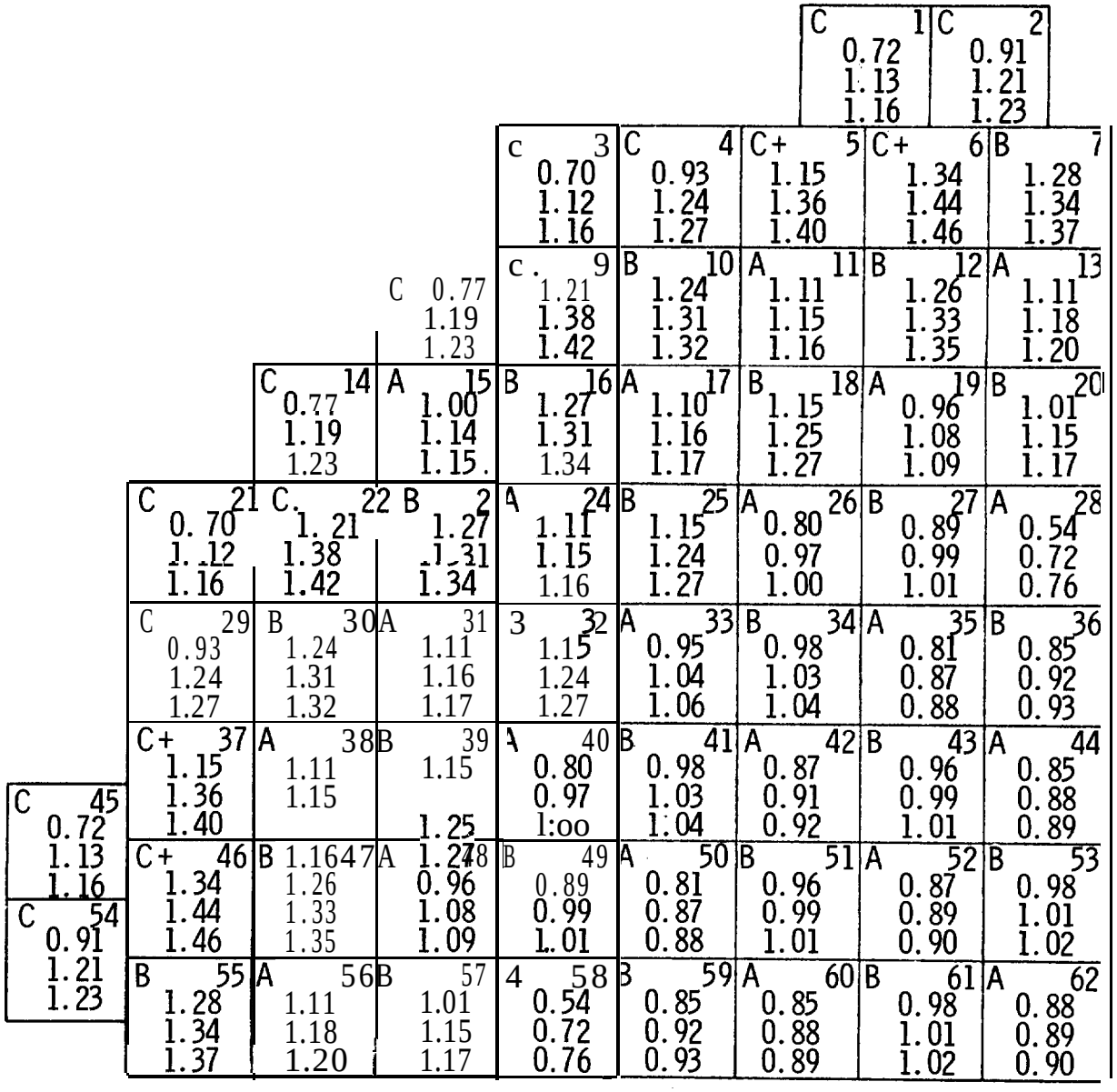

LOUISIANA POWER & LIGHT CO. Waterford Steam Electric Station	PLANAR AVERAGE POWER DISTRIBUTION EOC, PART-LENGTH ROD AS IF FULL LENGTH BANK 6 FULL IN, FULL POWER EQUILIBRIUM XENON	Figure 4.3-13

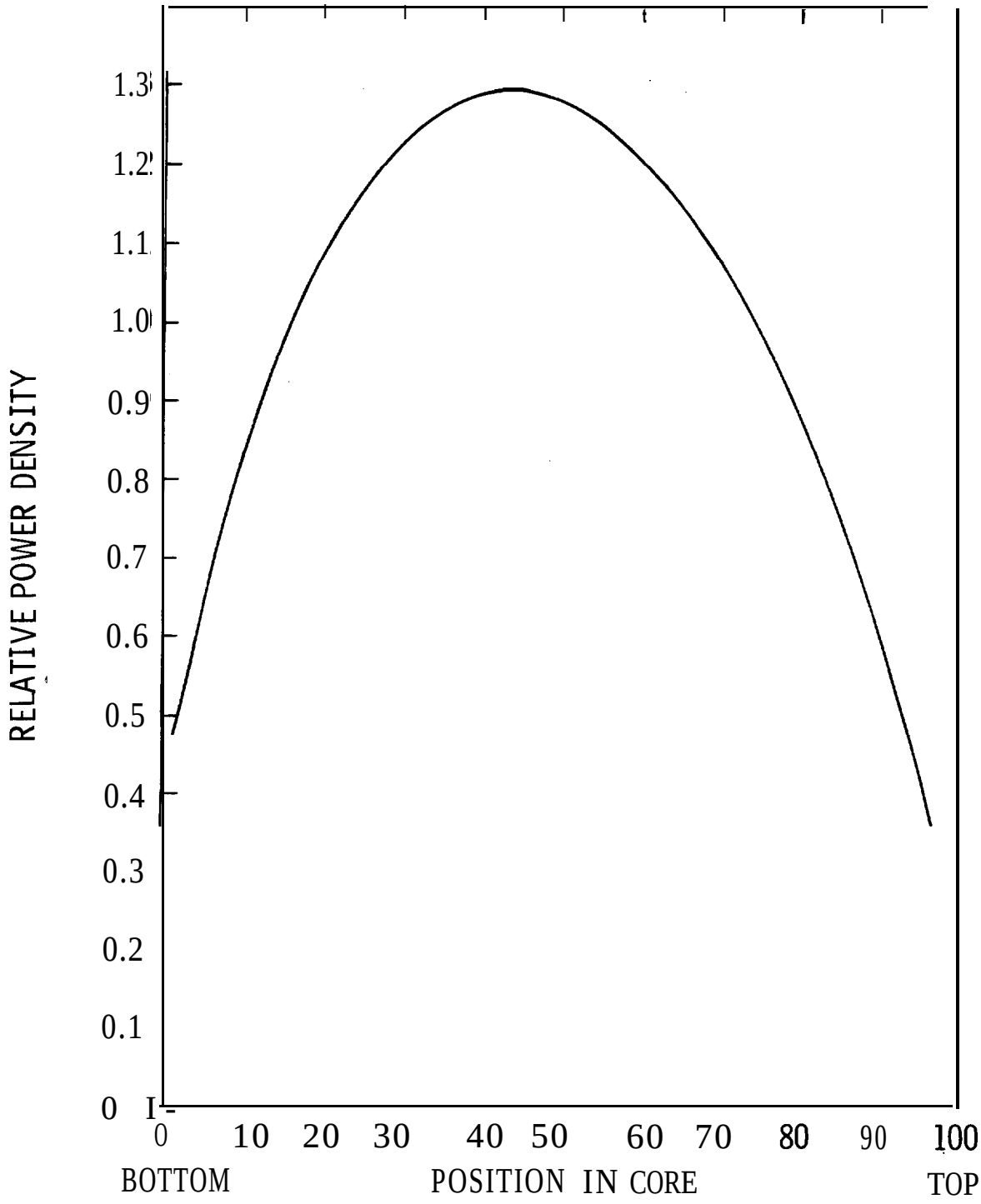

LOUISIANA POWER & LIGHT CO. Waterford Steam Electric Station	**AXIAL POWER DISTRIBUTION, BOC, UNRODDED**	**Figure** 4.3-I 4

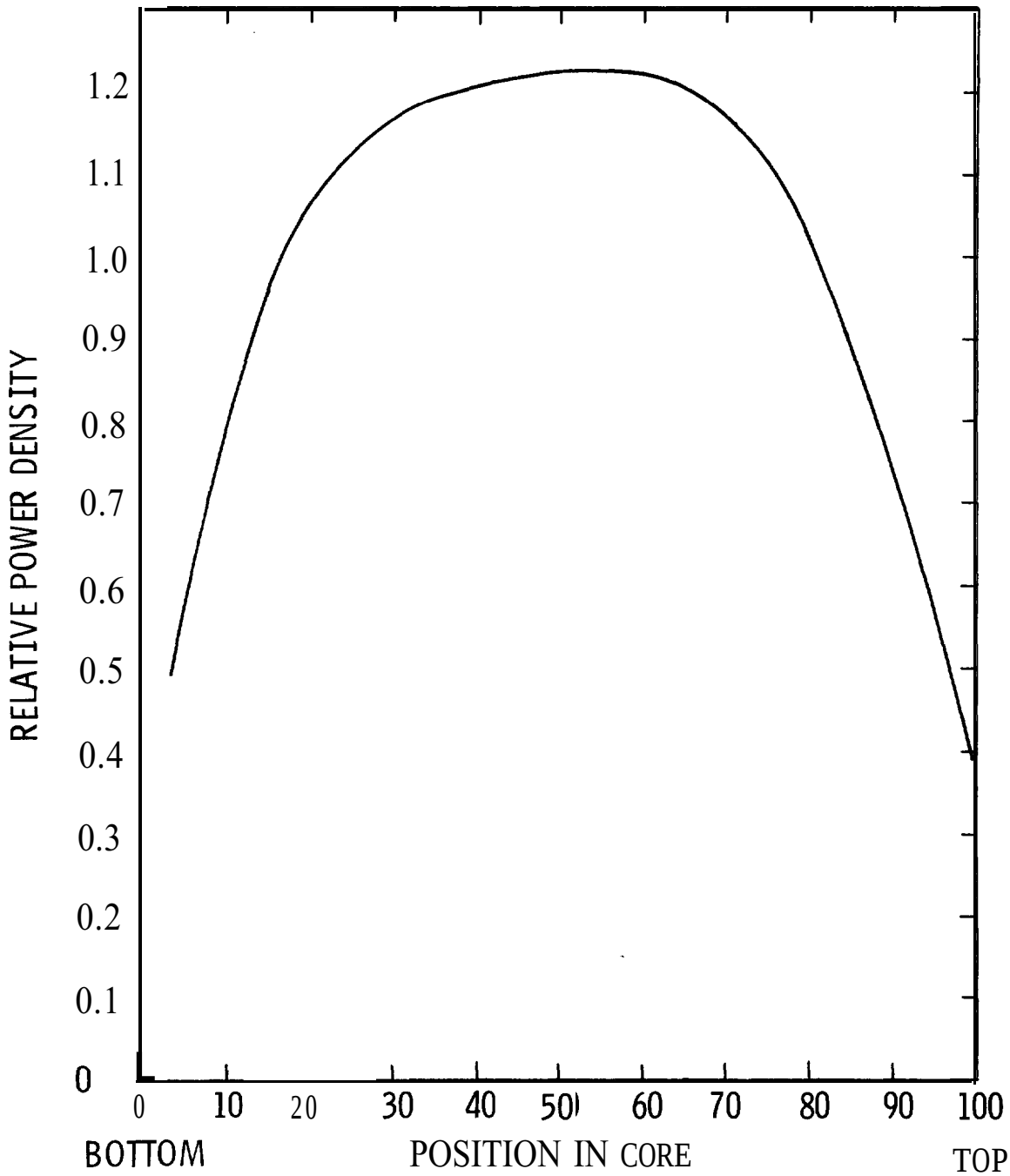

LOUISIANA
POWER & LIGHT CO.
Waterford Steam
Electric Station

AXIAL POWER DISTRIBUTION AT 3000 MWD/MTU, UNRODDED

Figure
4.3-15

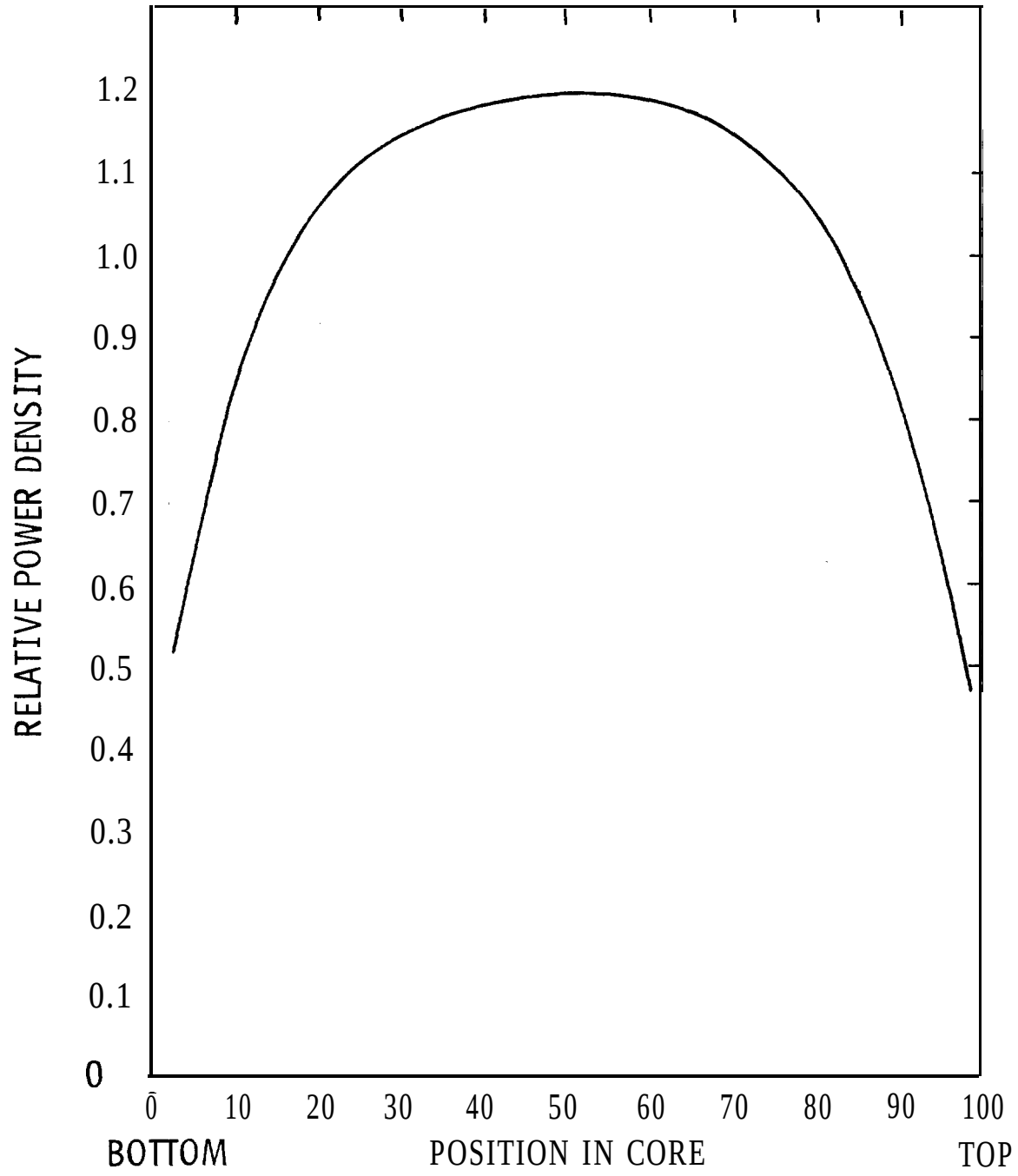

LOUISIANA
POWER & LIGHT CO.
Waterford Steam
Electric Station

AXIAL POWER DISTRIBUTION AT
6000 MWD/MTU, UNRODDED

Figure
4.3-16

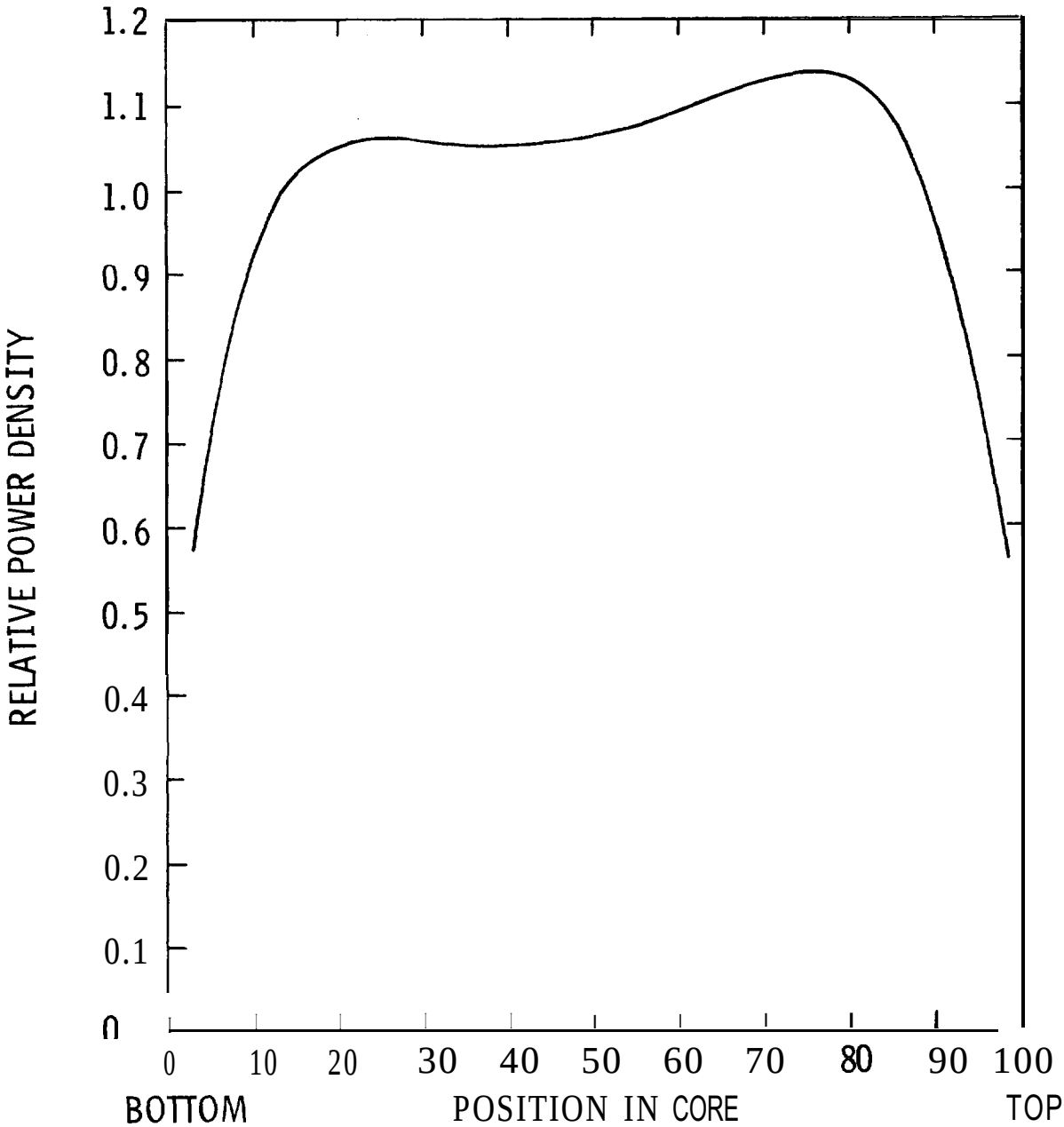

LOUISIANA POWER & LIGHT CO. Waterford Steam Electric Station	AXIAL POWER DISTRIBUTION AT 9000 MWD/MTU, UNRODDED	Figure 4.3-I 7

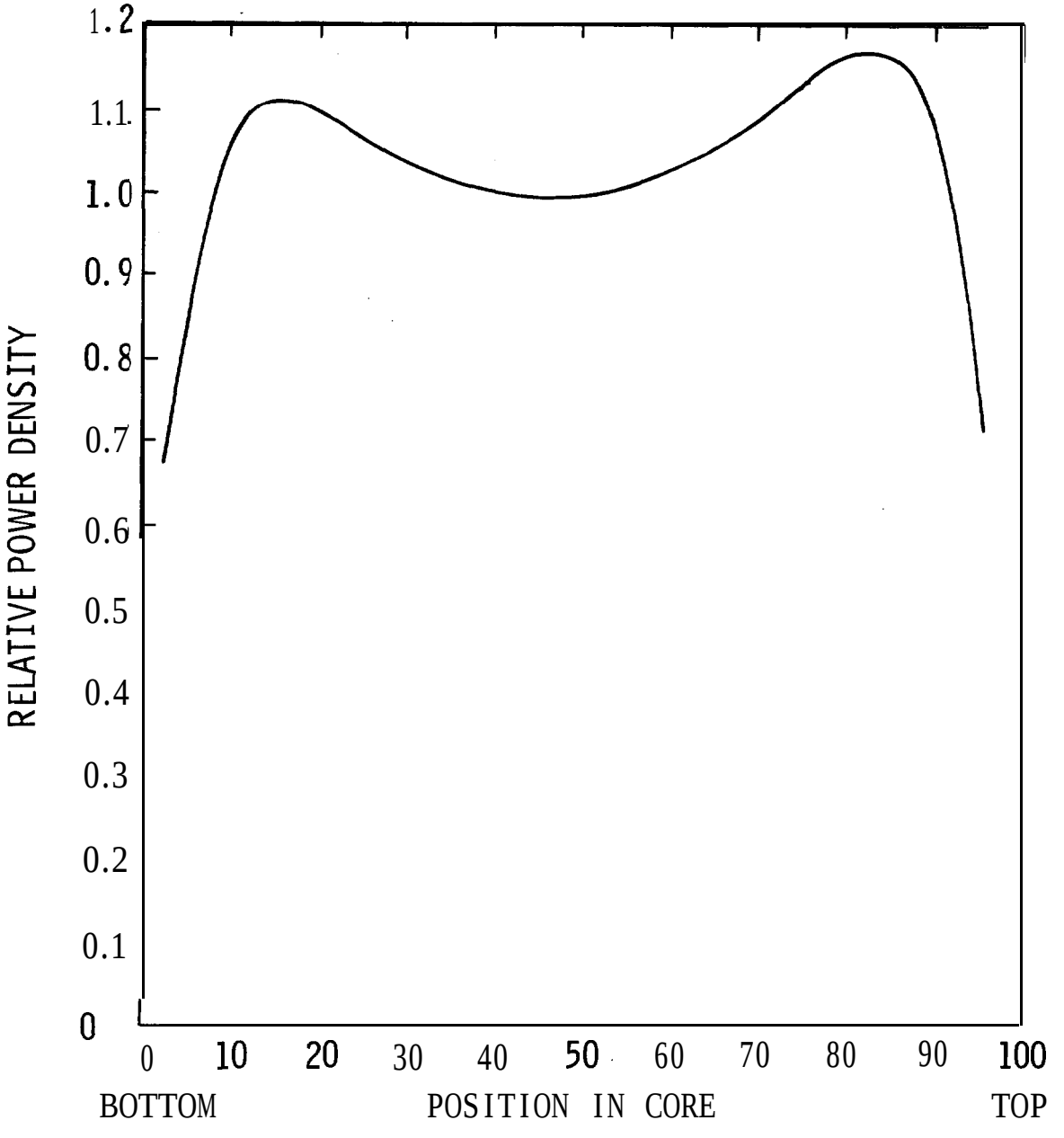

LOUISIANA POWER & LIGHT CO. Waterford Steam Electric Station	AXIAL POWER DISTRIBUTION AT THE END OF THE FIRST CYCLE, UNRODDED	Figure 4.3-1 8

FIGURE 4.3-19
HAS BEEN INTENTIONALLY
DELETED

REVISION 6 (12/92)

Waterford Steam Electric Station ● 3	PLANAR AVERAGE POWER DISTRIBUTION AT THE BEGINNING OF THE SECOND CYCLE, UNRODDED	Figure 4.3-I 9

FIGURE 4.3-20
HAS BEEN INTENTIONALLY
DELETED

REVISION 6 (12/92)

Woterford Steam Electric Station •3	PLANAR AVERAGE POWER DISTRIBUTION AT THE END OF THE SECOND CYCLE. UNRODDED	Figure 4.3-20

FIGURE 4.3-21
HAS BEEN INTENTIONALLY
DELETED

REVISION 6 (12/92)

Waterford Steam Electric Station ● 3	PLANAR AVERAGE POWER DISTRIBUTION AT THE BEGINNING OF THE THIRD CYCLE. UNRODDED	Figure 4.3-21

FIGURE 4.3-22
HAS BEEN INTENTIONALLY
DELETED

REVISION 6 (12/92)

Woterford Steam Electric Station ● 3	PLANAR AVERAGE POWER DISTRIBUTION AT THE END OF THE TH IRD CYCLE • UNRODDED	Figure 4.3-22

F I GURE 4 . 3-23
HAS BEEN INTENTIONALLY
DELETED

REVISION 6 (12/92)

Waterford Steam Electric Station ● 3	PLANAR AVERAGE POWER DISTRIBUTION AT THE BEGINNING OF THE FOURTH CYCLE. UNRODDED	Figure 4.3-23

F IGURE 4.3-24
HAS BEEN INTENTIONALLY
DELETED

REVISION 6 (12/92)

Waterford Steam Electric Station •3	PLANAR AVERAGE POWER DISTRIBUTION AT THE END OF THE FOURTH CYCLE. UNRODDED	Figure 4.3-24

LOUISIANA POWER & LIGHT CO.
Waterford Steam Electric Station

DAILY REACTOR POWER MANEUVERING NEAR BEGINNING OF CYCLE (100% TO 35% TO 100% POWER)

Figure 4.3-25

100% TO 35% TO 100% POWER – TWO HOUR RAMPS – 6 HOURS AT 35% POWER – WITH PART LENGTH RODS
POWER CONTROL ON RODS, XENON CONTROL ON BORON – EQUILIBRIUM DAILY MANEUVERING CYCLE

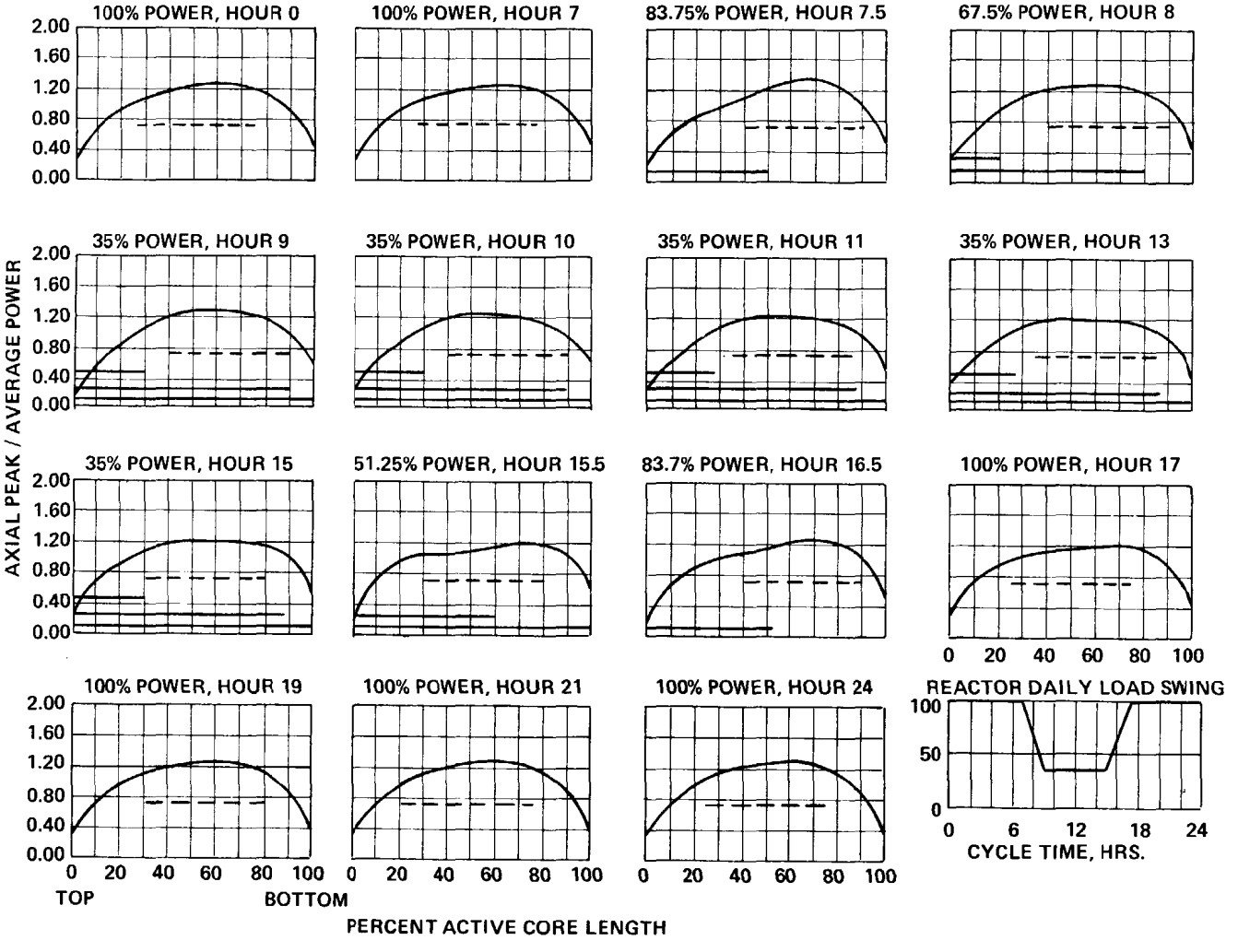

LEGEND:
——— Regulating Bank
– – – – Part Length Rod

LOUISIANA POWER & LIGHT CO.
Waterford Steam Electric Station

DAILY REACTOR POWER MANEUVERING NEAR END OF CYCLE (100% TO 35% TO 100% POWER)

Figure 4.3-26

100% TO 35% TO 100% POWER — TWO HOUR RAMPS — 6 HOURS AT 35% POWER — WITH PART LENGTH RODS
POWER CONTROL ON RODS, XENON CONTROL ON BORON — EQUILIBRIUM DAILY MANEUVERING CYCLE

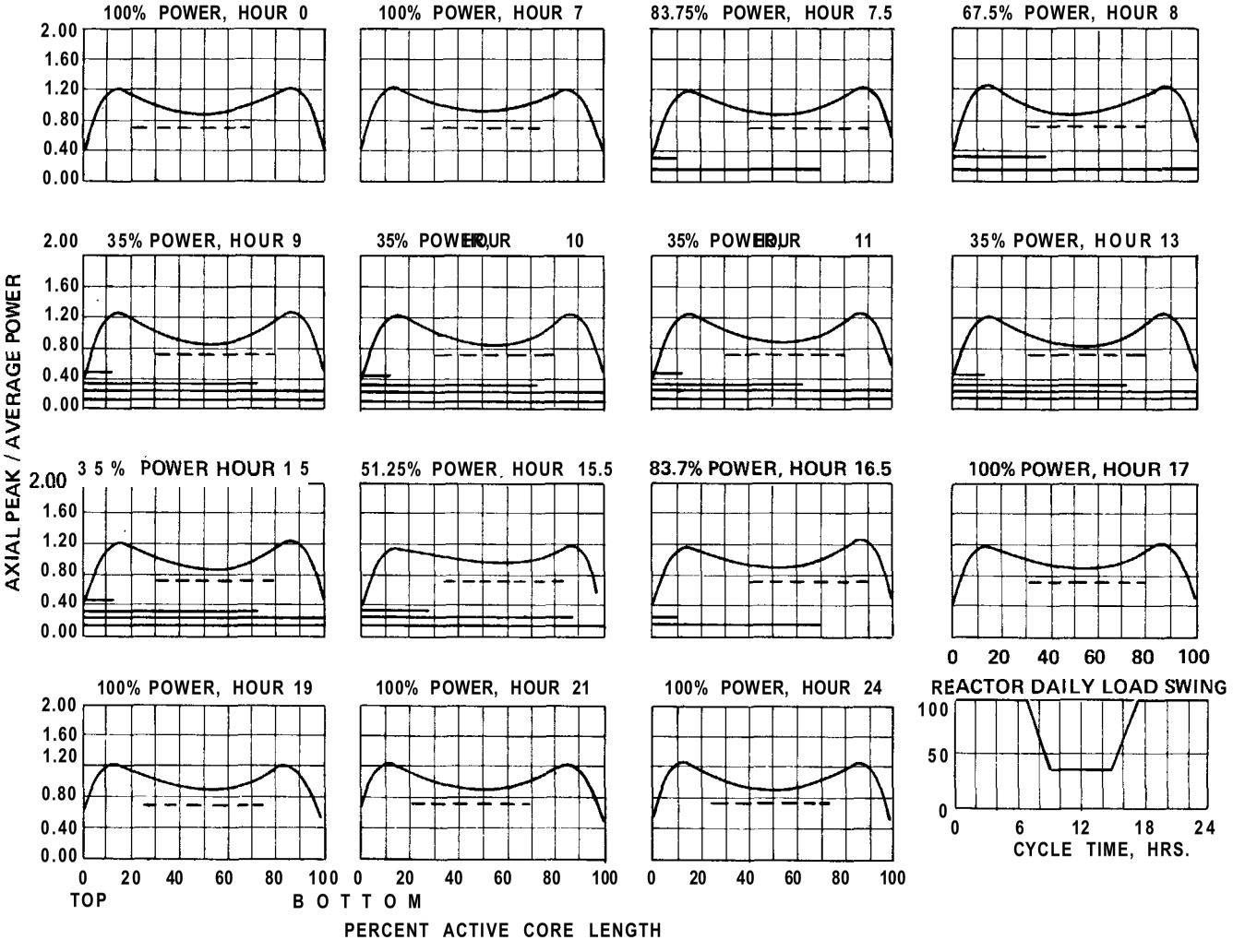

LEGEND:

——— Regulating Bank

- - - Part Length Rod

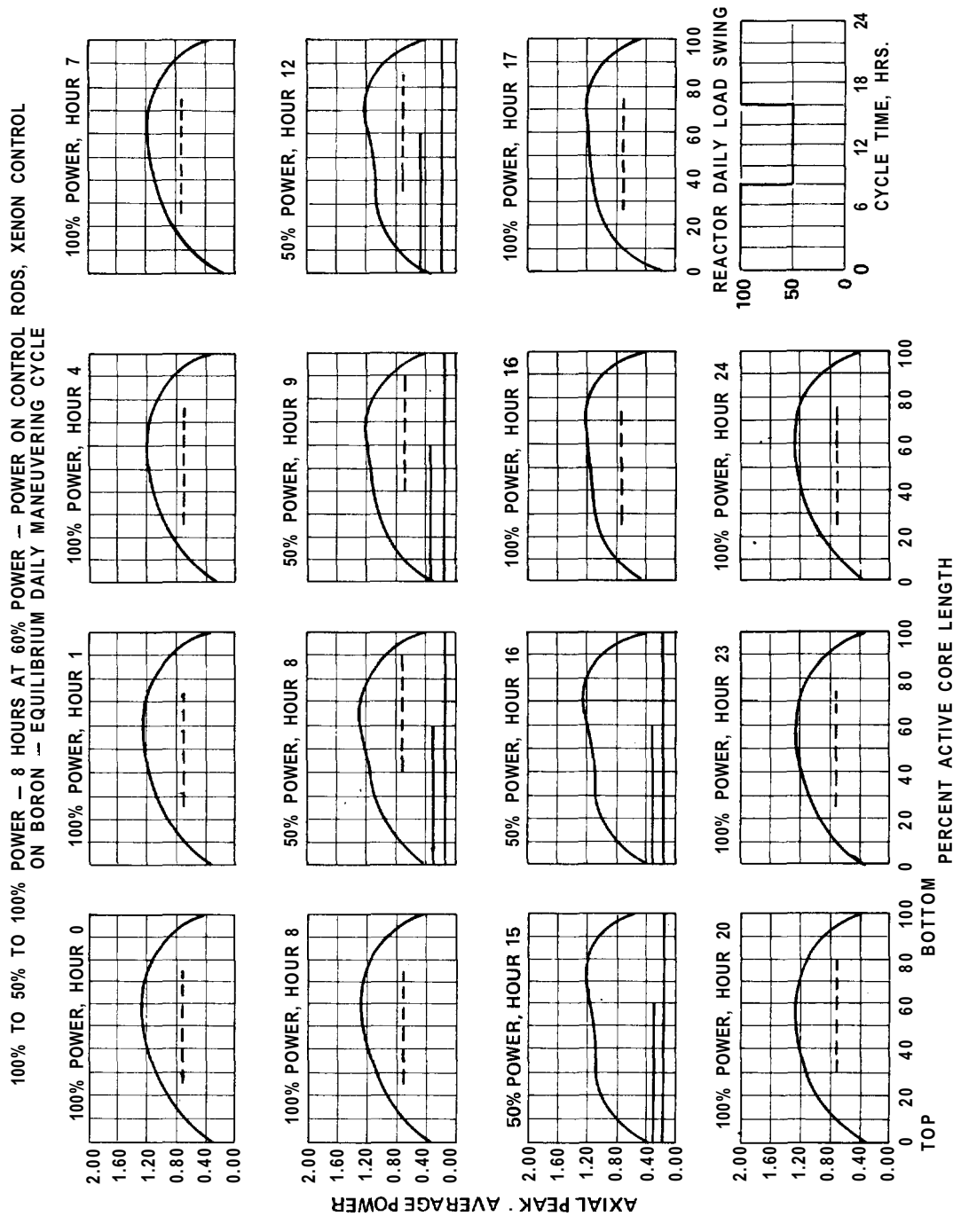

LOUISIANA
POWER & LIGHT CO
Waterford Steam
Electric Station

DAILY REACTOR POWER MANEUVERING NEAR THE BEGINNING OF CYCLE (100% TO 50% TO 100% POWER)

Figure
4.3-27

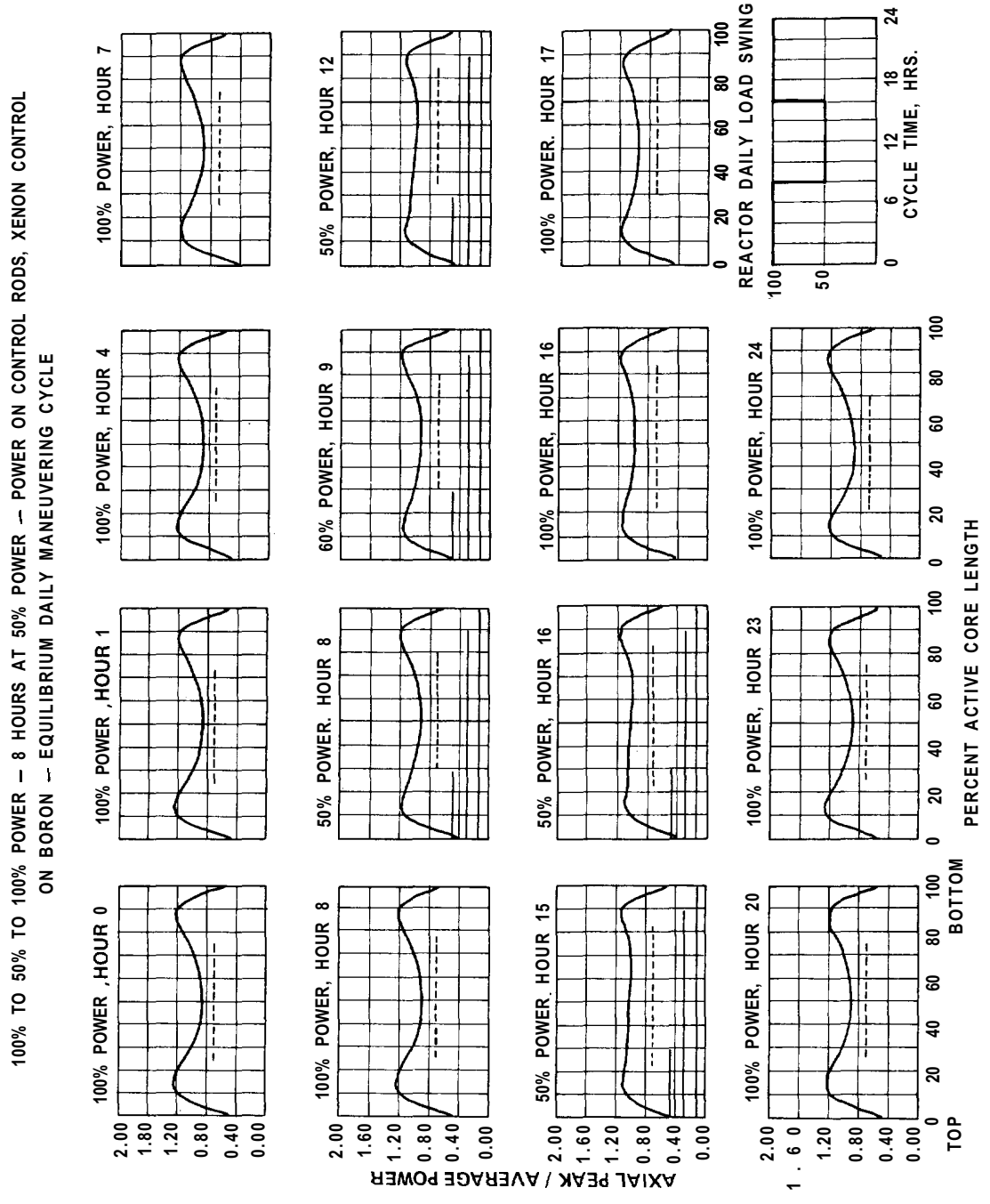

LOUISIANA POWER & LIGHT CO. Waterford Steam Electric Station	DAILY REACTOR POWER MANEUVERING NEAR THE END OF CYCLE (100% TO 50% TO 100% POWER)	Figure 4.3-28

LOUISIANA
POWER & LIGHT CO.
Waterford Steam
Electric Station

DAILY REACTOR POWER MANEUVERING NEAR THE BEGINNING OF CYCLE (2-HOUR RAMPS)

Figure
4.3-29

100% TO 50% TO 100% POWER -TWO HOUR RAMPS – 6 HOURS AT 50% POWER – POWER ON CONTROL RODS
XENON CONTROL ON BORON – EQUILIBRIUM DAILY MANEUVERING CYCLE

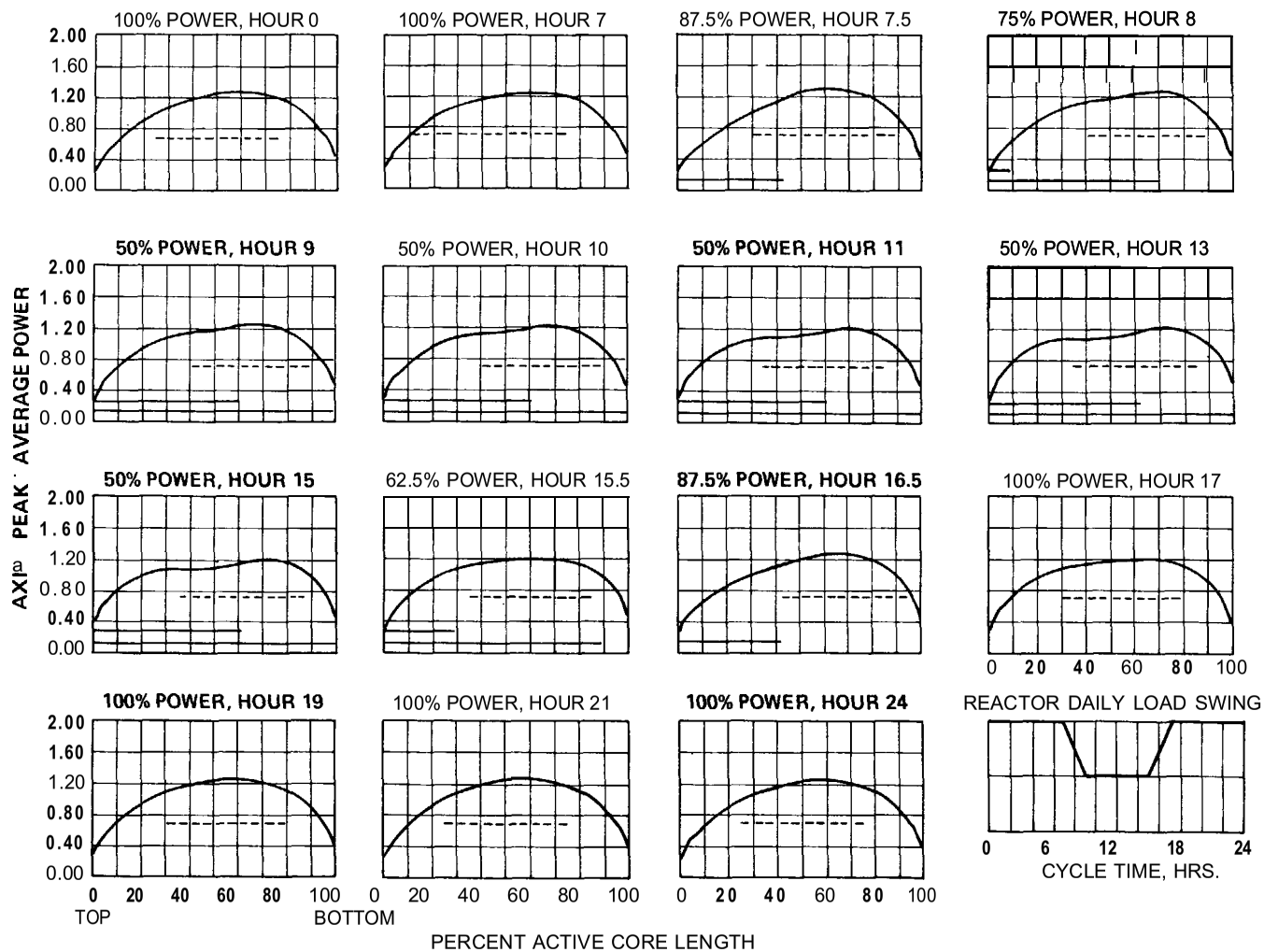

LEGEND:
——— Regulatiny Bank
– – – – Part Length Rod

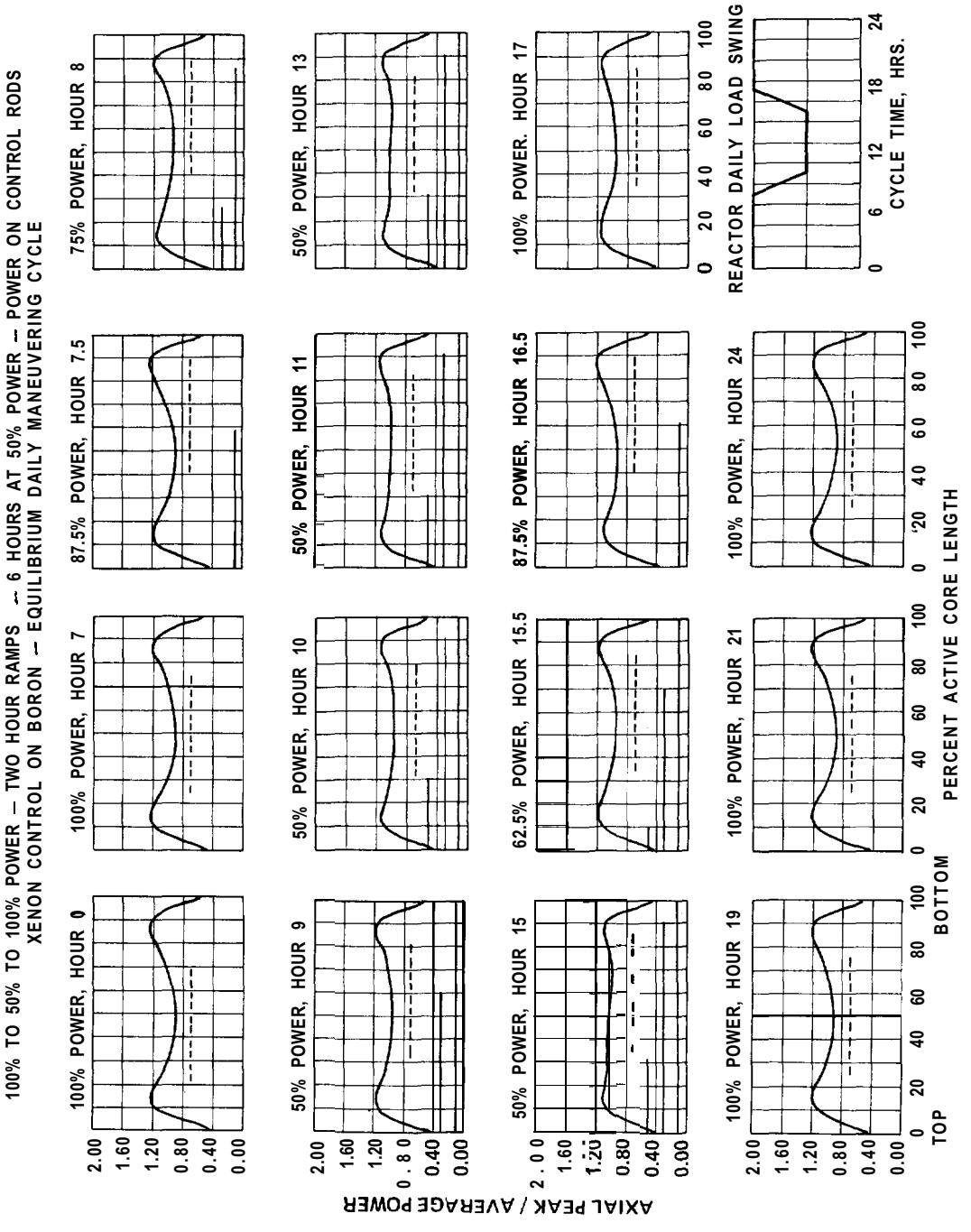

LOUISIANA POWER & LIGHT CO. Waterford Steam Electric Station	DAILY REACTOR POWER MANEUVERING NEAR THE END OF CYCLE (2-HOUR RAMPS)	Figure 4.3-30

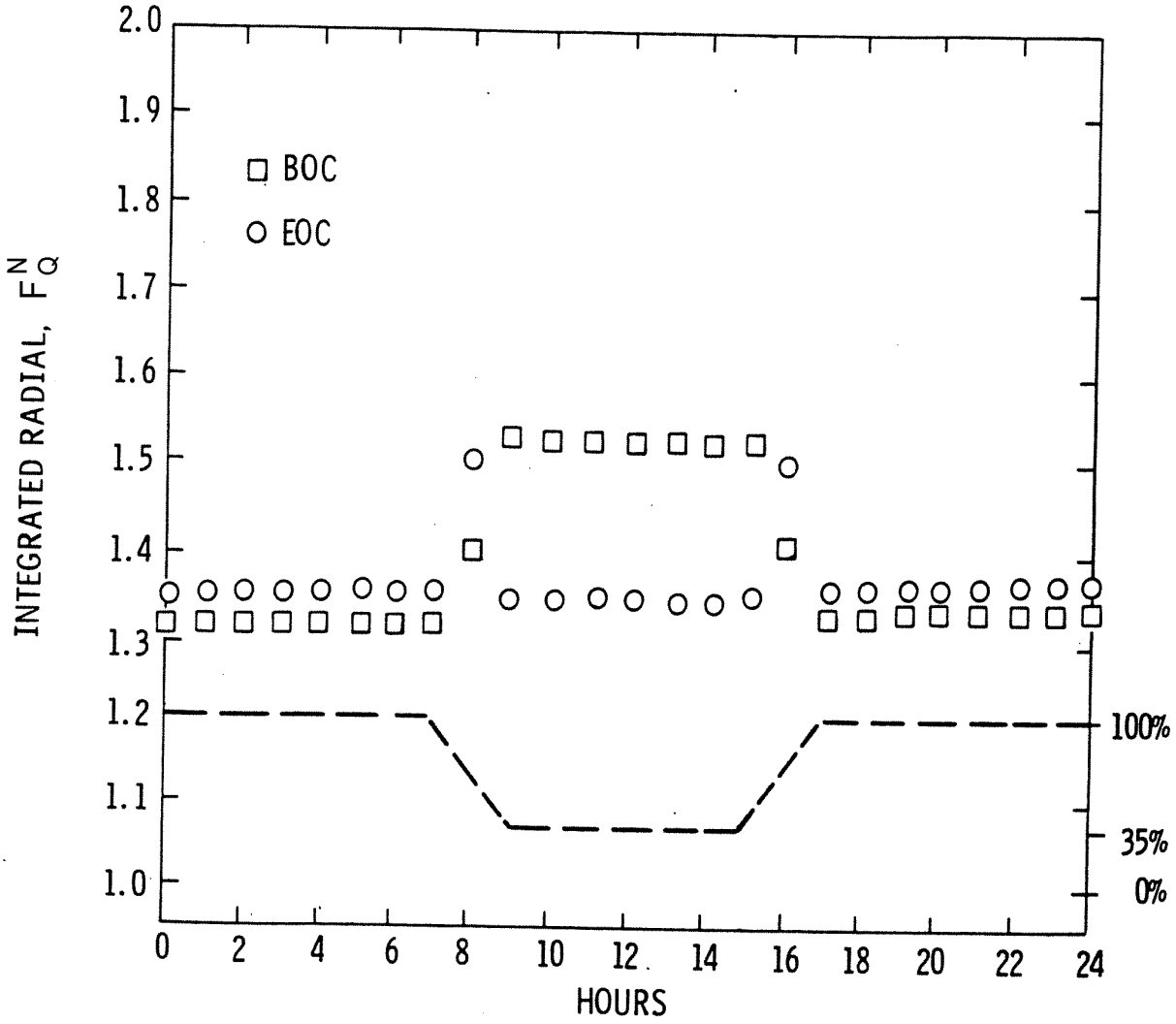

Revision 11 (05/01)

Waterford Steam Electric Station #3	F_Q^N VS. TIME FOR A LOAD FOLLOWING TRANSIENT (SHEET 1 OF 3)	Figure 4.3-31

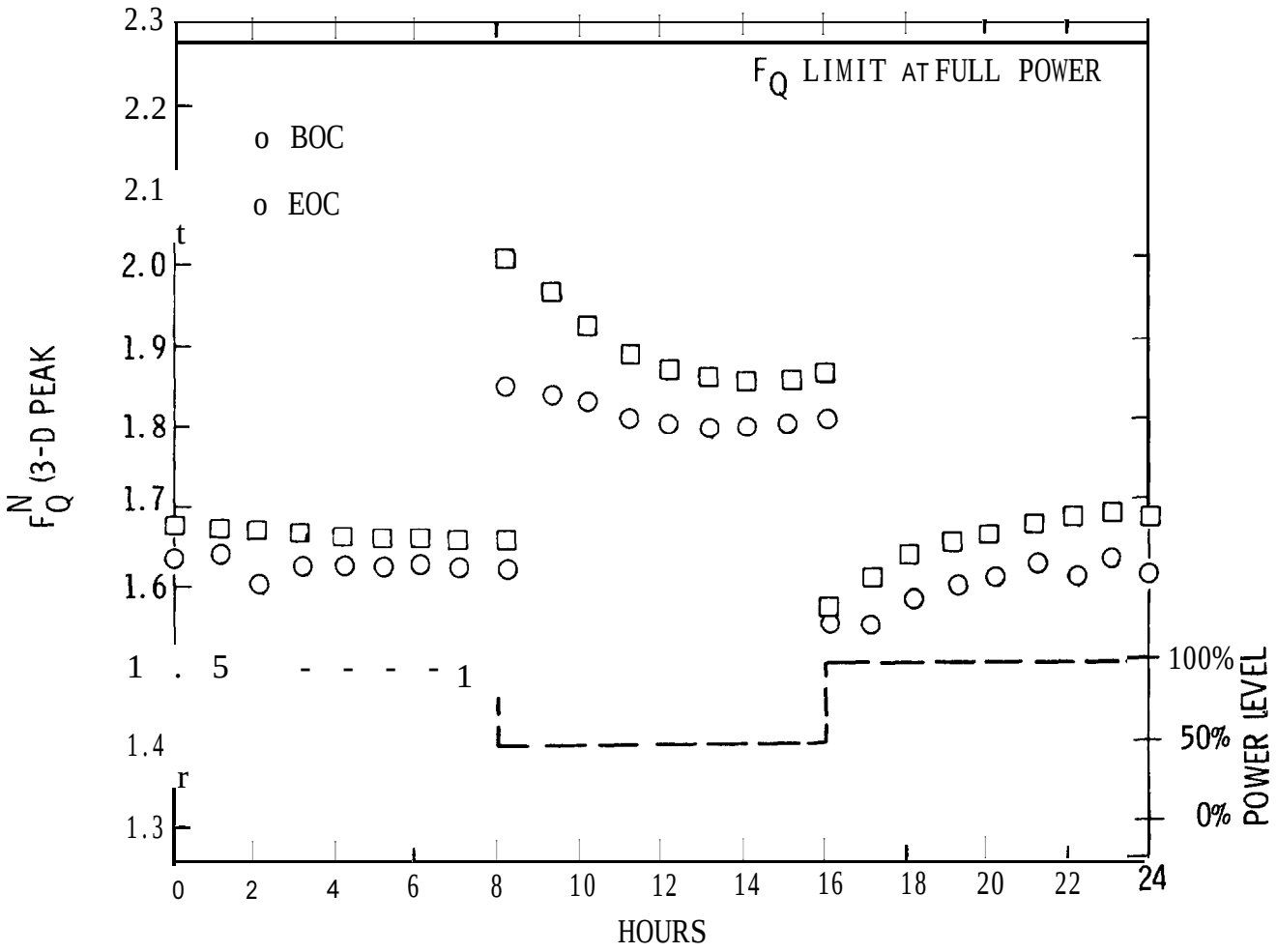

LOUISIANA POWER & LIGHT CO. Waterford Steam Electric Station	F_Q^N VS. TIME FOR A LOAD FOLLOWING TRANSIENT (SHEET 2 OF 3)	Figure 4.3-31

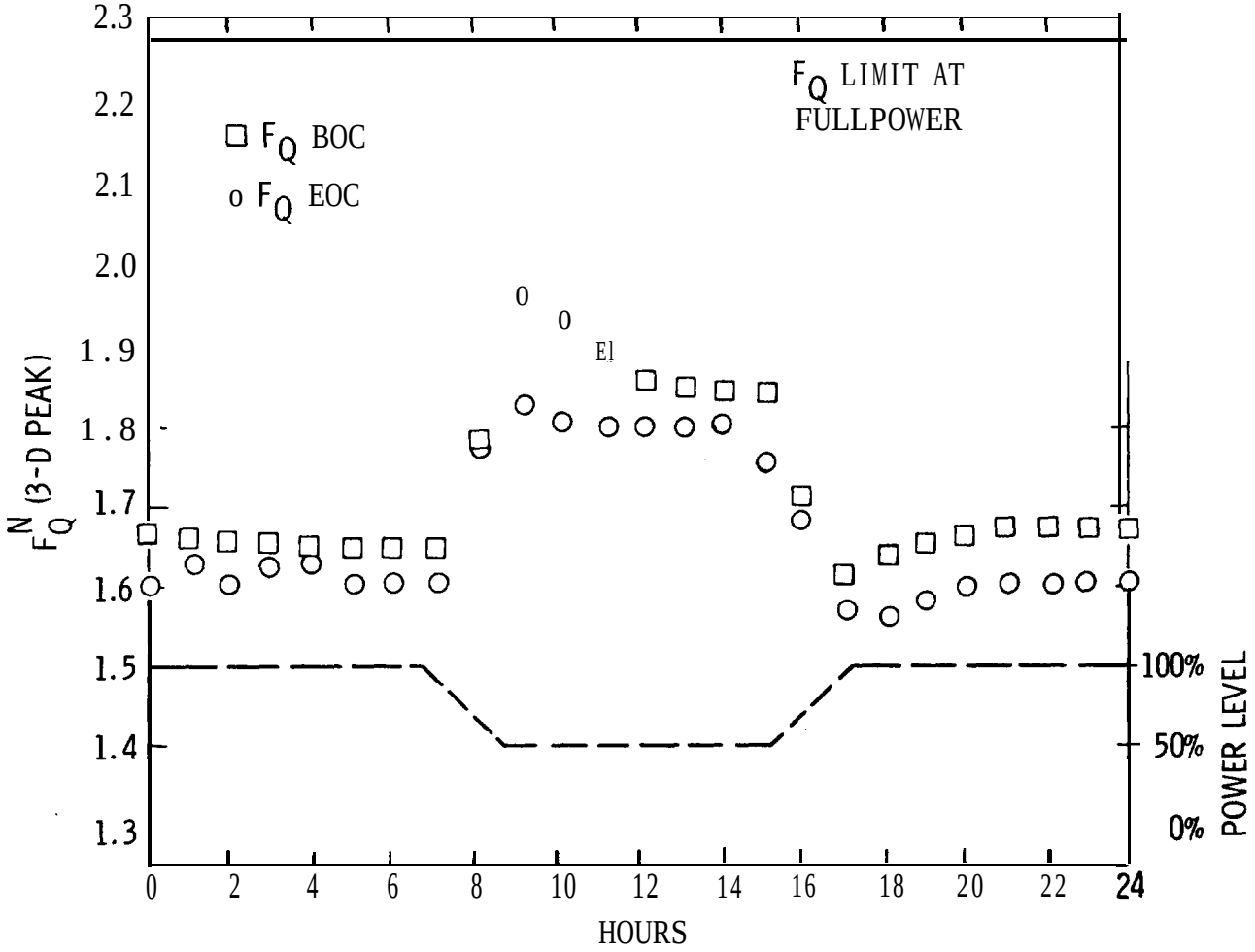

LOUISIANA POWER & LIGHT CO. Waterford Steam Electric Station	F_Q^N VS. TIME FOR A LOAD FOLLOWING TRANSIENT (SHEET 3 OF 3)	Figure 4.3-31

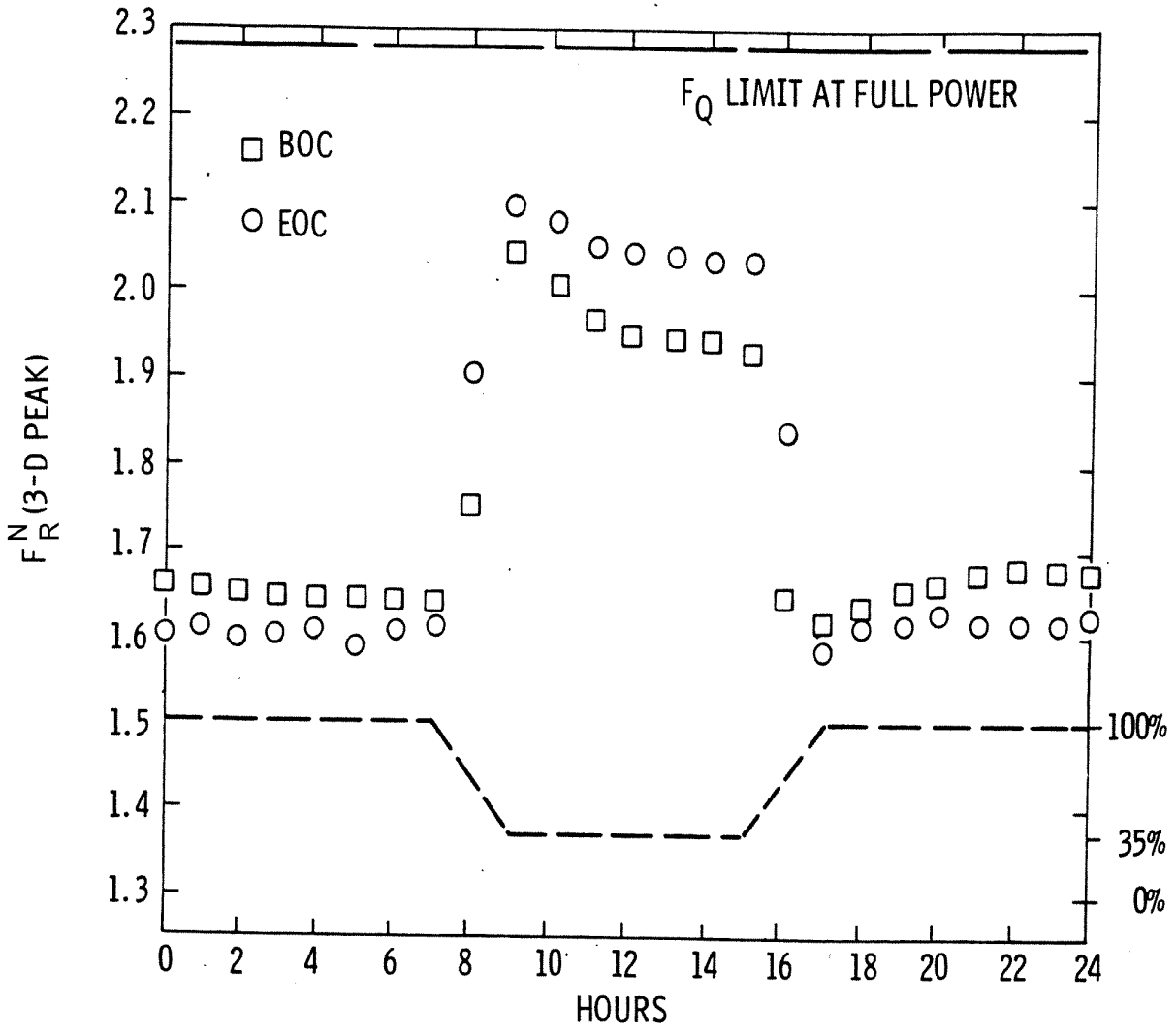

Revision 11 (05/01)

Waterford Steam Electric Station #3	F_R^N VS. TIME FOR A LOAD FOLLOWING TRANSIENT (SHEET 1 OF 3)	Figure 4.3-32

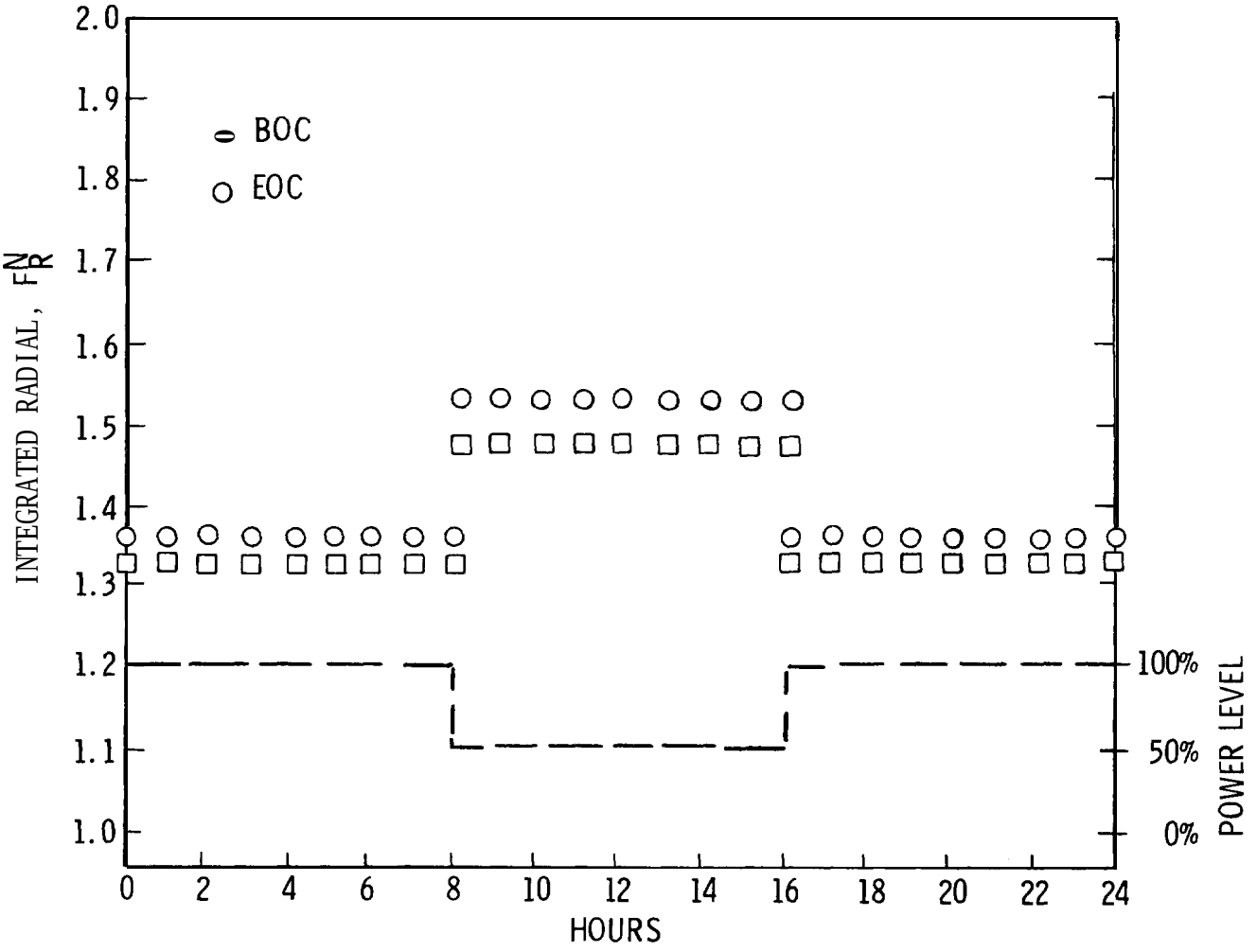

LOUISIANA POWER & LIGHT CO. Waterford Steam Electric Station	F_R^N VS. TIME FOR A LOAD FOLLOWING TRANSIENT (SHEET 2 OF 3)	Figure 4.3–32

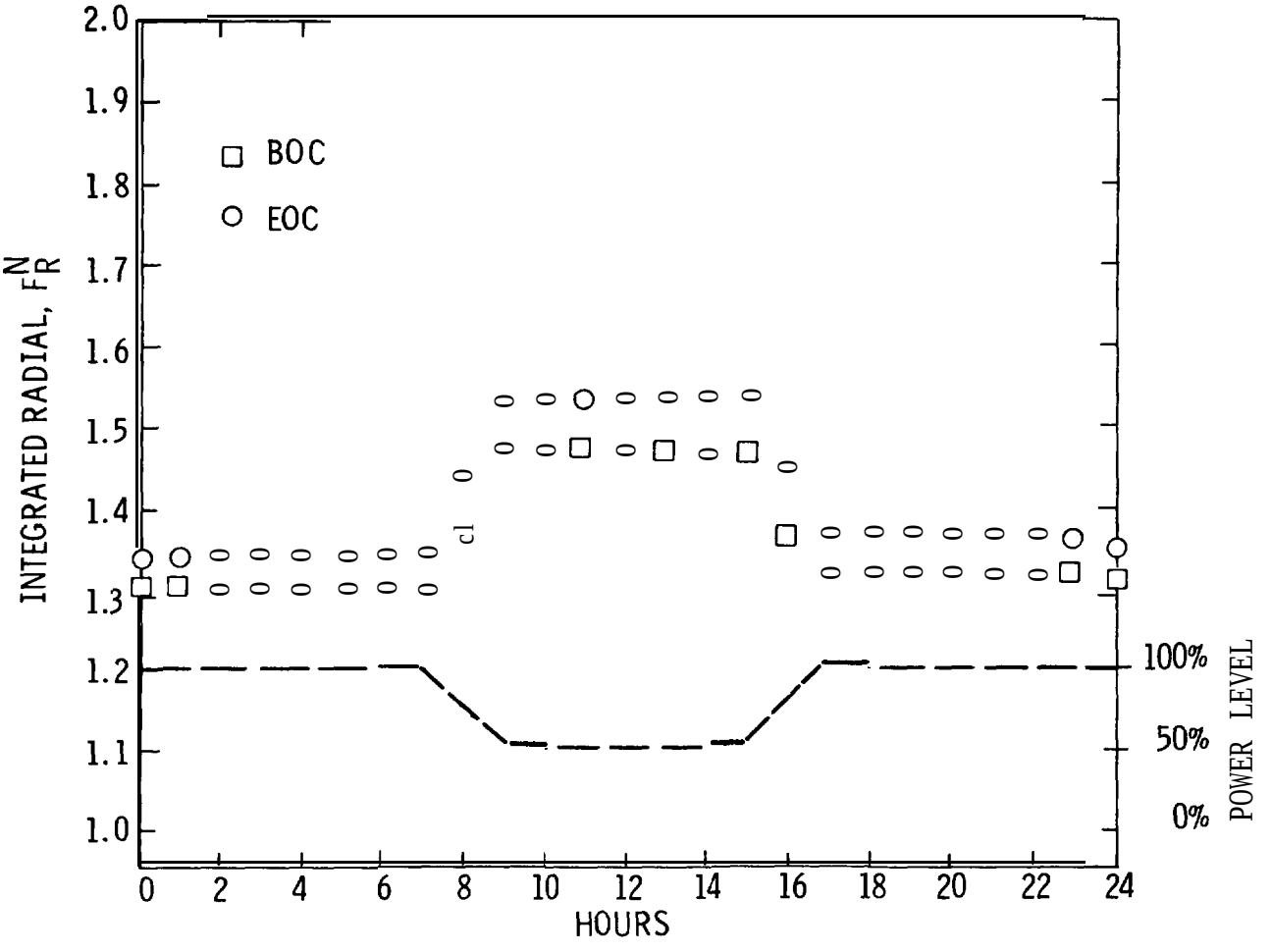

LOUISIANA POWER & LIGHT CO. Waterford Steam Electric Station	F_R^N VS. TIME FOR A LOAD FOLLOWING TRANSIENT (SHEET 3 OF 3)	Figure 4.3–32

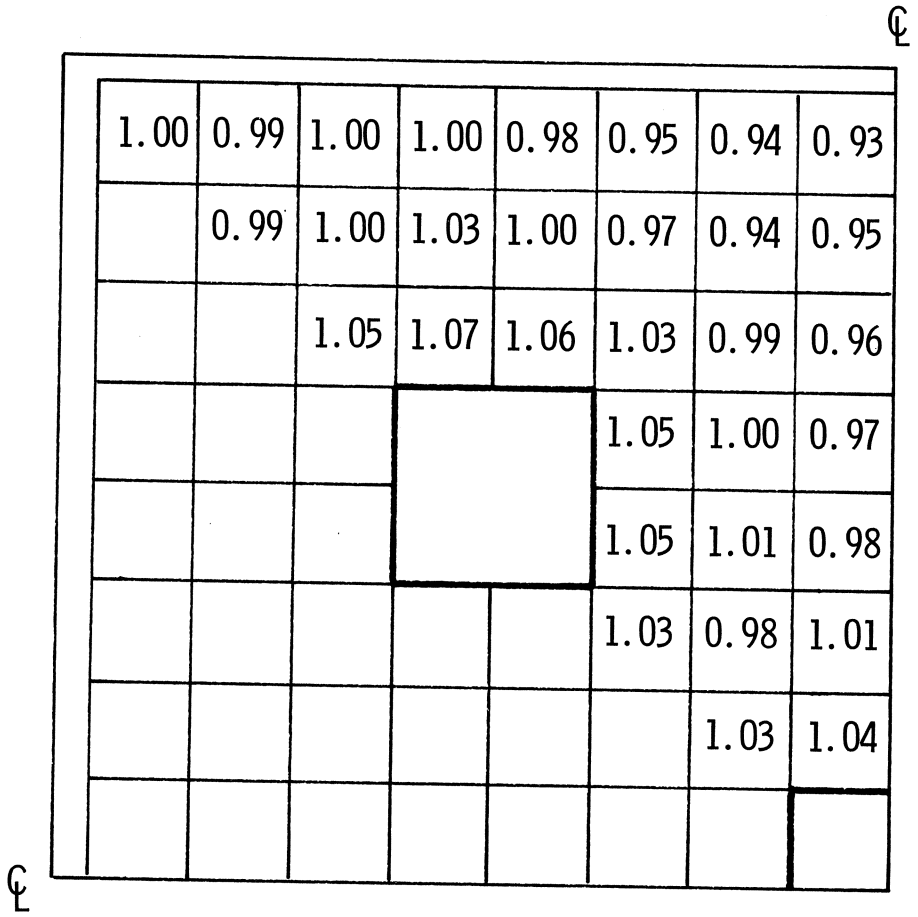

LOUISIANA POWER & LIGHT CO. Waterford Steam Electric Station	NORMALIZED POWER DISTRIBUTION WITHIN TYPICAL UNSHIMMED ASSEMBLY	Figure 4.3-33

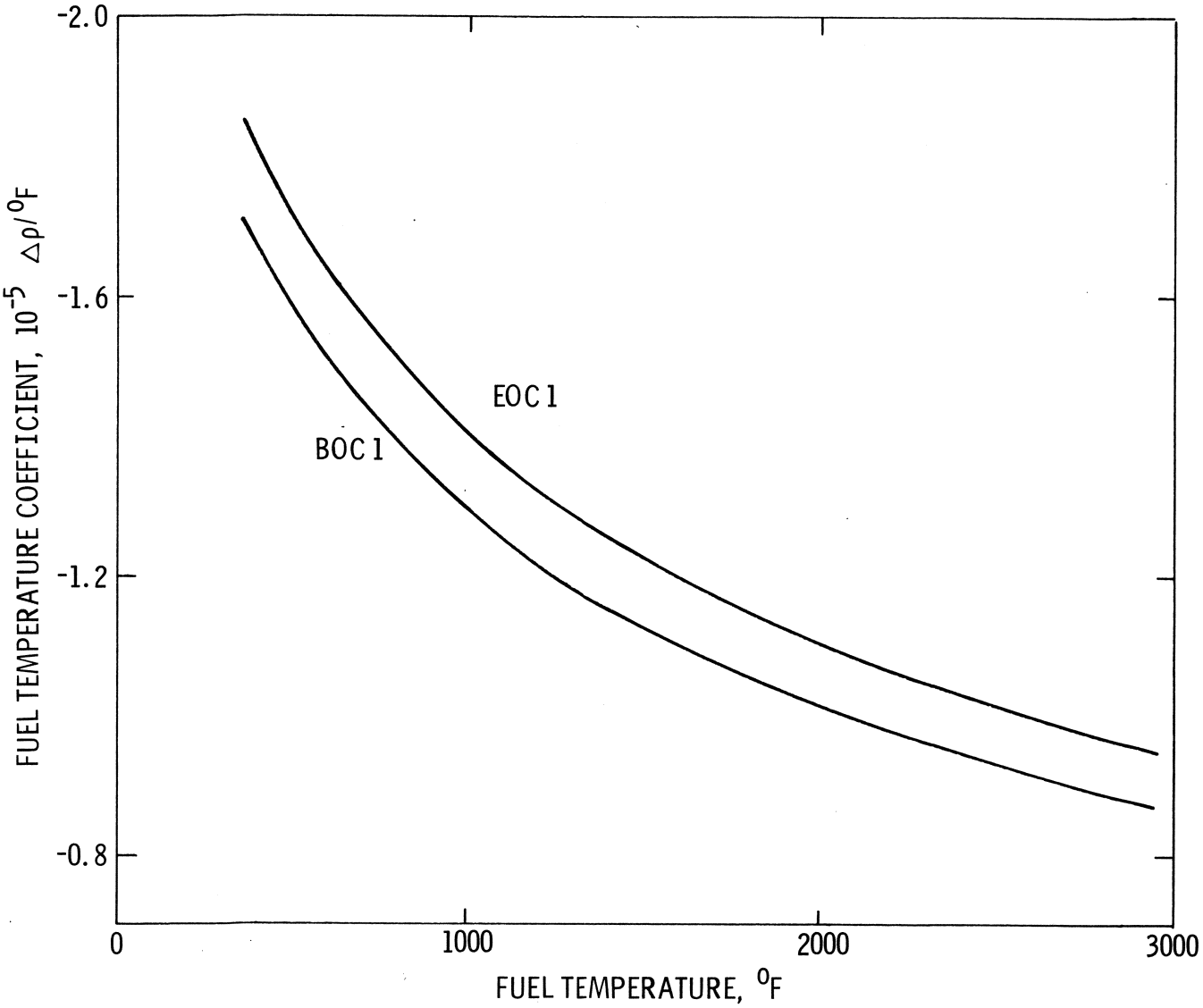

LOUISIANA POWER & LIGHT CO. Waterford Steam Electric Station	FUEL TEMPERATURE COEFFICIENT VS. EFFECTIVE FUEL TEMPERATURE	Figure 4.3-34

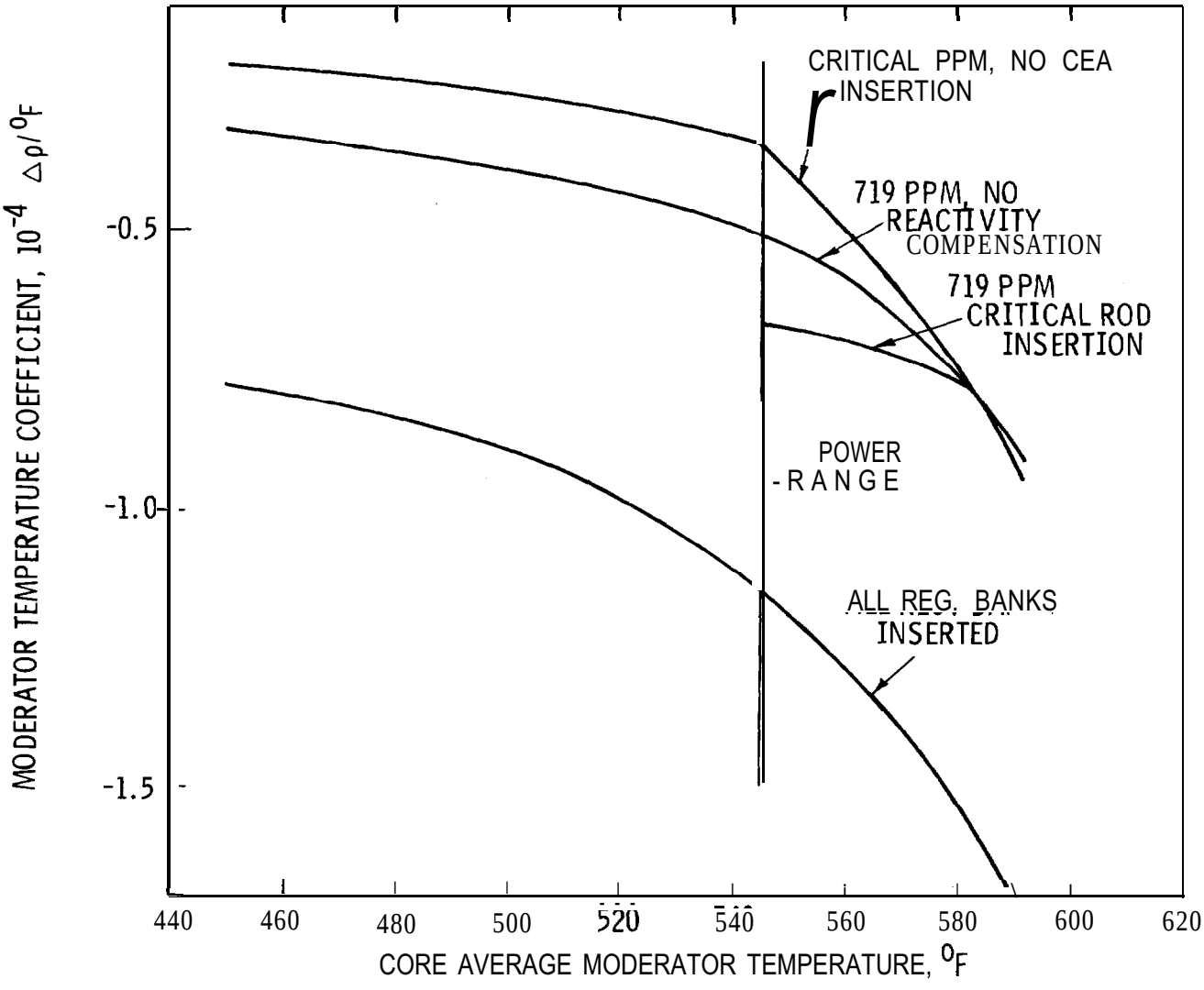

LOUISIANA POWER & LIGHT CO. Waterford Steam Electric Station	**MODERATOR TEMPERATURE COEFFICIENT VS. MODERATOR TEMPERATURE AT BOC1**	Figure 4.3-35

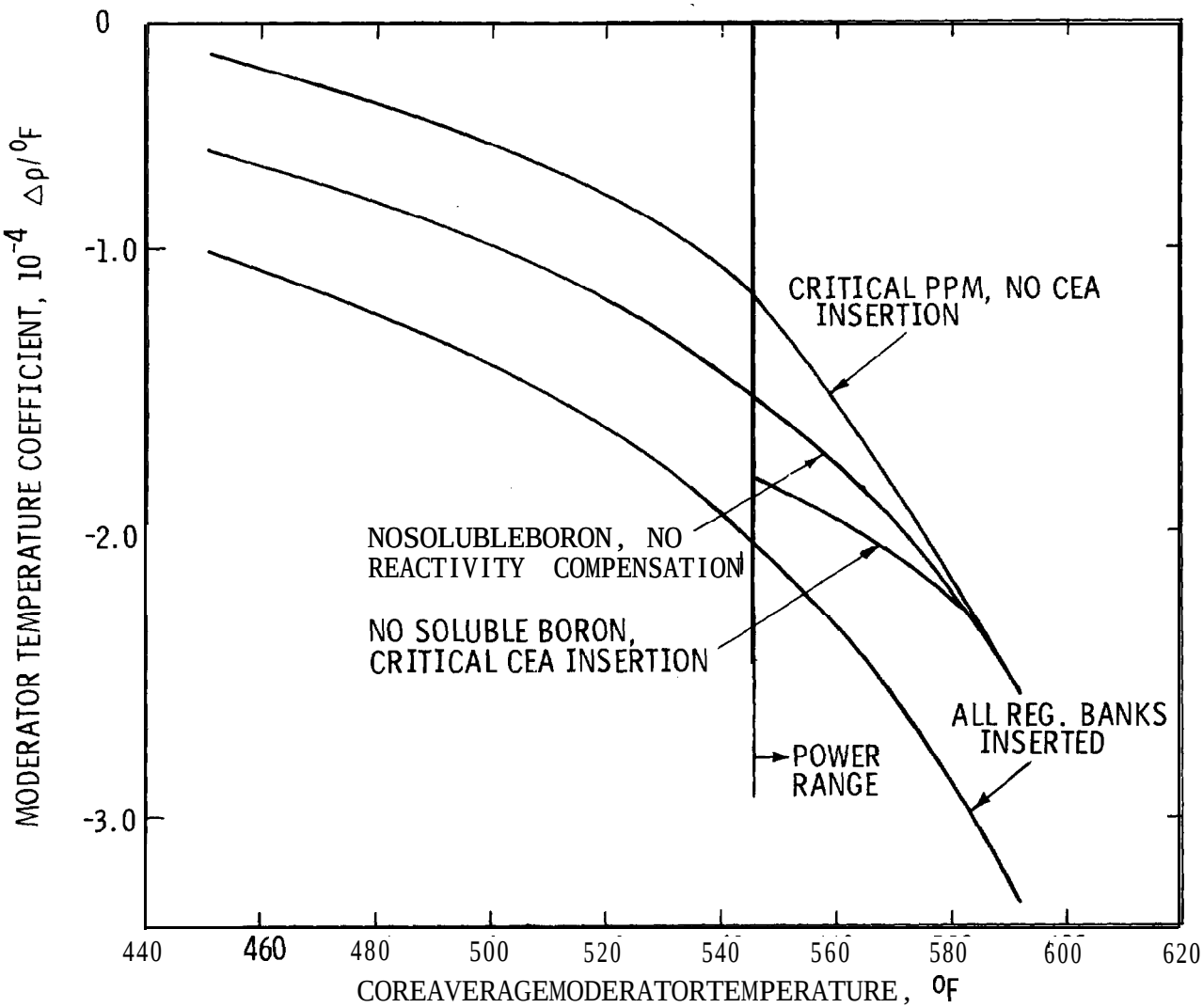

LOUISIANA POWER & LIGHT CO. Waterford Steam Electric Station	**MODERATOR TEMPERATURE COEFFICIENT VS. MODERATOR TEMPERATURE AT EOC1**	Figure 4.3-36

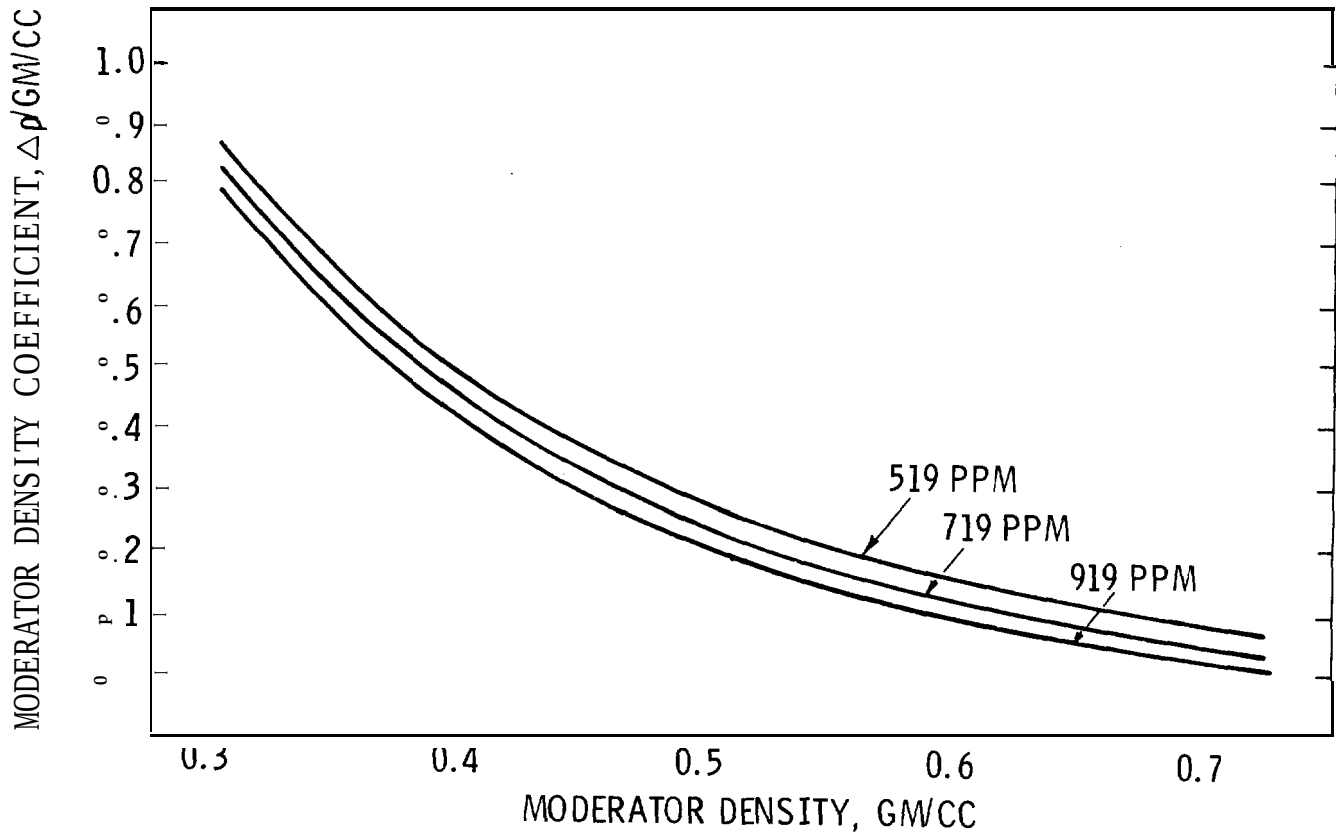

LOUISIANA POWER & LIGHT CO. Waterford Steam Electric Station	MODERATOR DENSITY COEFFICIENT VS. DENSITY	Figure 4.3-37

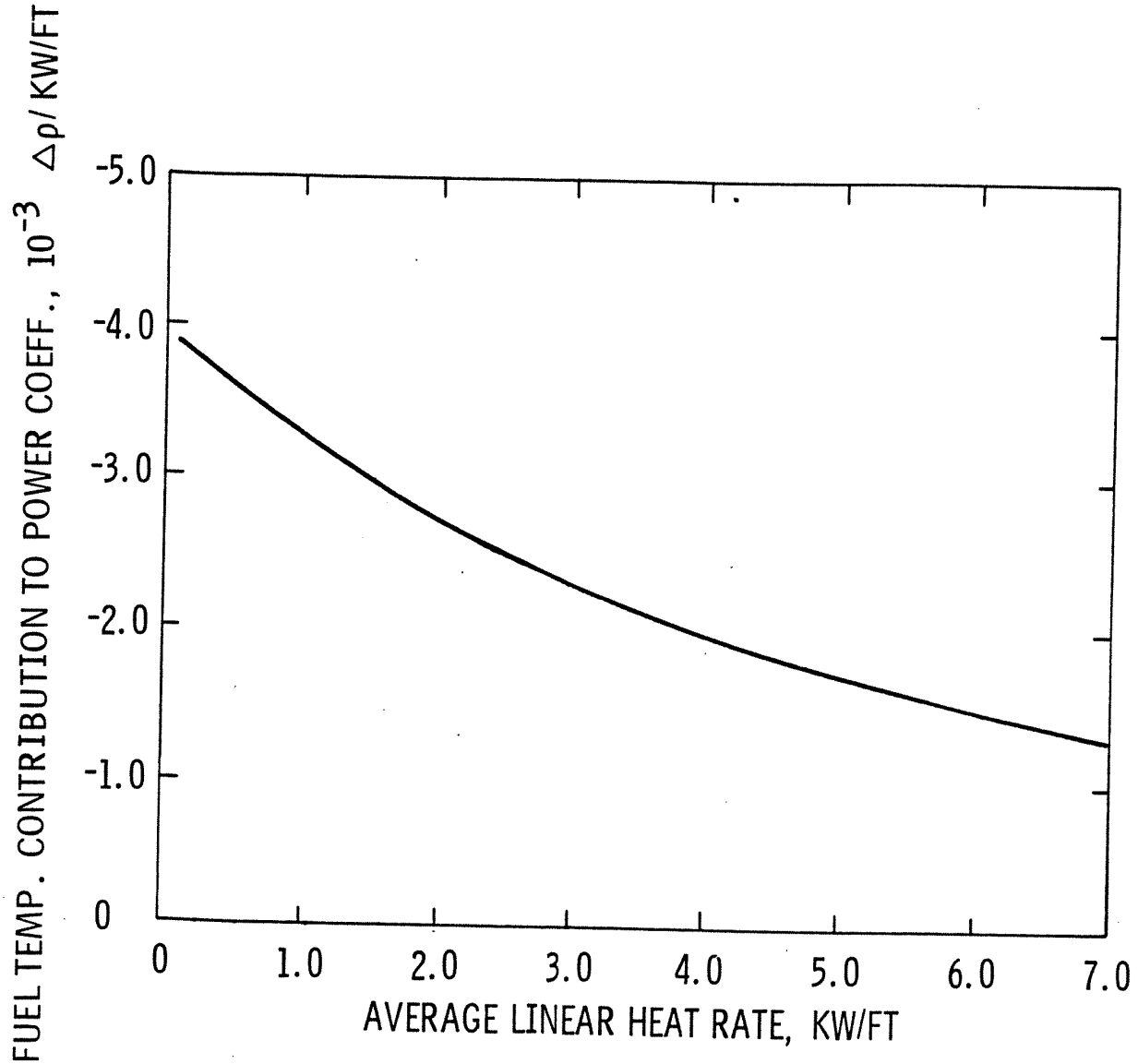

Revision 11 (05/01)

Waterford Steam Electric Station #3	FUEL TEMPERATURE CONTRIBUTION TO POWER COEFFICIENT AT EOC VS. LINEAR HEAT RATE	Figure 4.3-38

P - REGULATING BANK P
6 - LEAD REGULATING BANK
5 - SECOND REGULATING BANK
4 - THIRD REGULATING BANK
3 - FOURTH REGULATING BANK
2 - FIFTH REGULATING BANK
1 - LAST REGULATING BANK
S_B - SHUTDOWN BANK B
S_A - SHUTDOWN BANK A

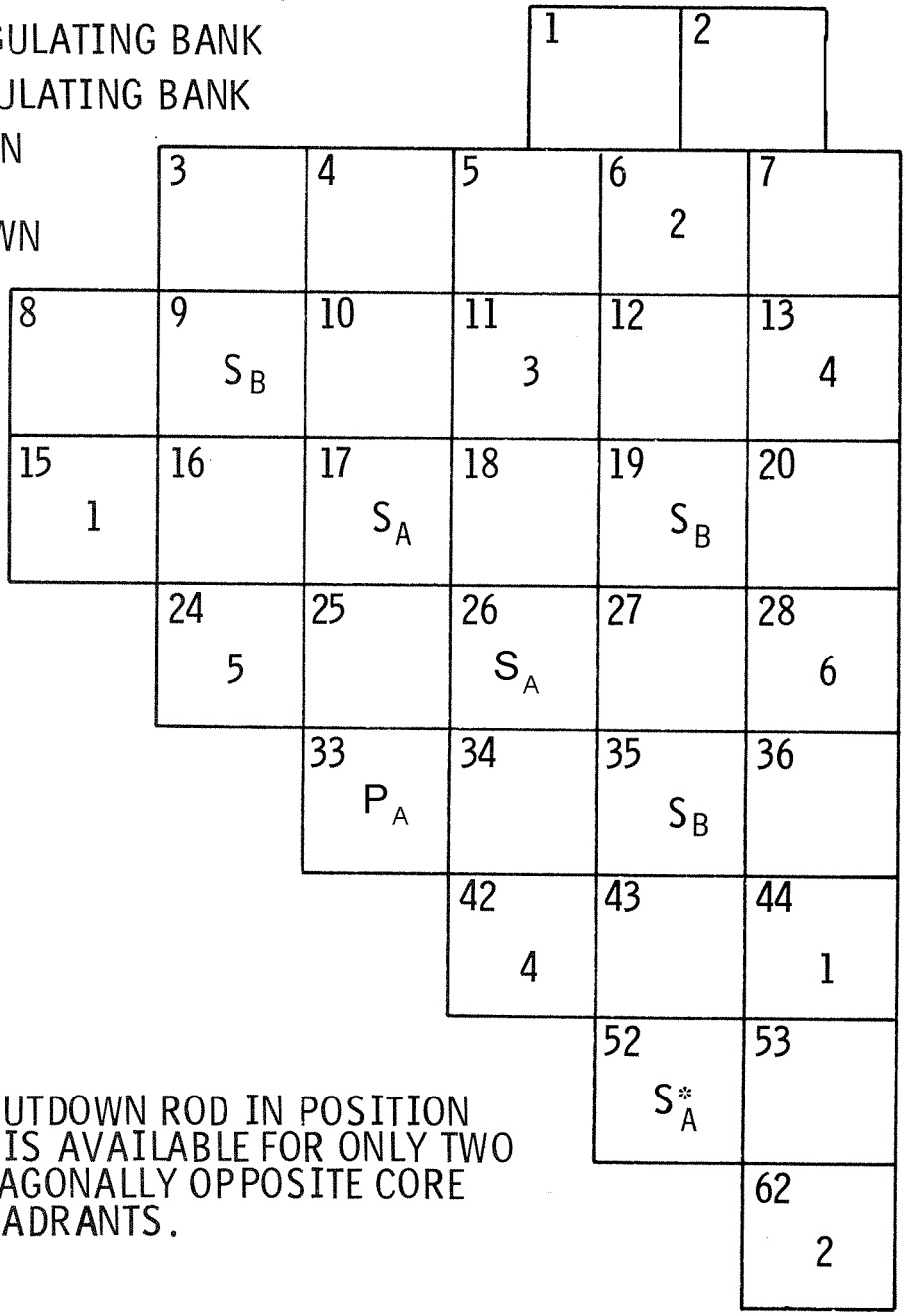

*SHUTDOWN ROD IN POSITION 52 IS AVAILABLE FOR ONLY TWO DIAGONALLY OPPOSITE CORE QUADRANTS.

Revision 12 (10/02)

LOUISIANA POWER & LIGHT CO. Waterford Steam Electric Station	CEA BANK IDENTIFICATION	Figure 4.3-39

LOUISIANA POWER & LIGHT CO.
Waterford Steam Electric Station

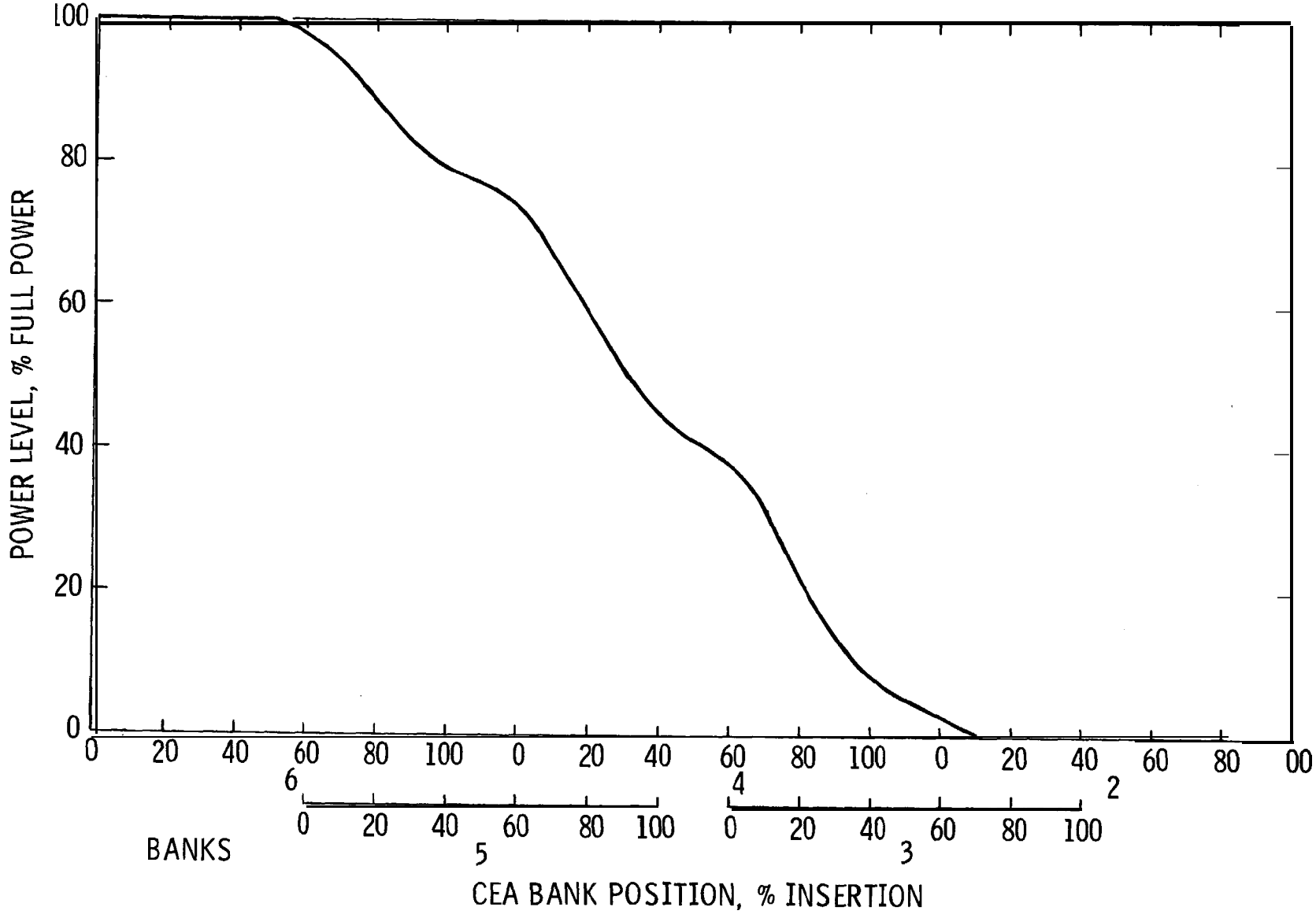

TYPICAL POWER DEPENDENT CEA INSERTION LIMIT

Figure 4.3-40

LOUISIANA POWER & LIGHT CO.
Waterford Steam Electric Station

INTEGRAL WORTH VS. WITHDRAWAL AT ZERO POWER, EOC CONDITIONS

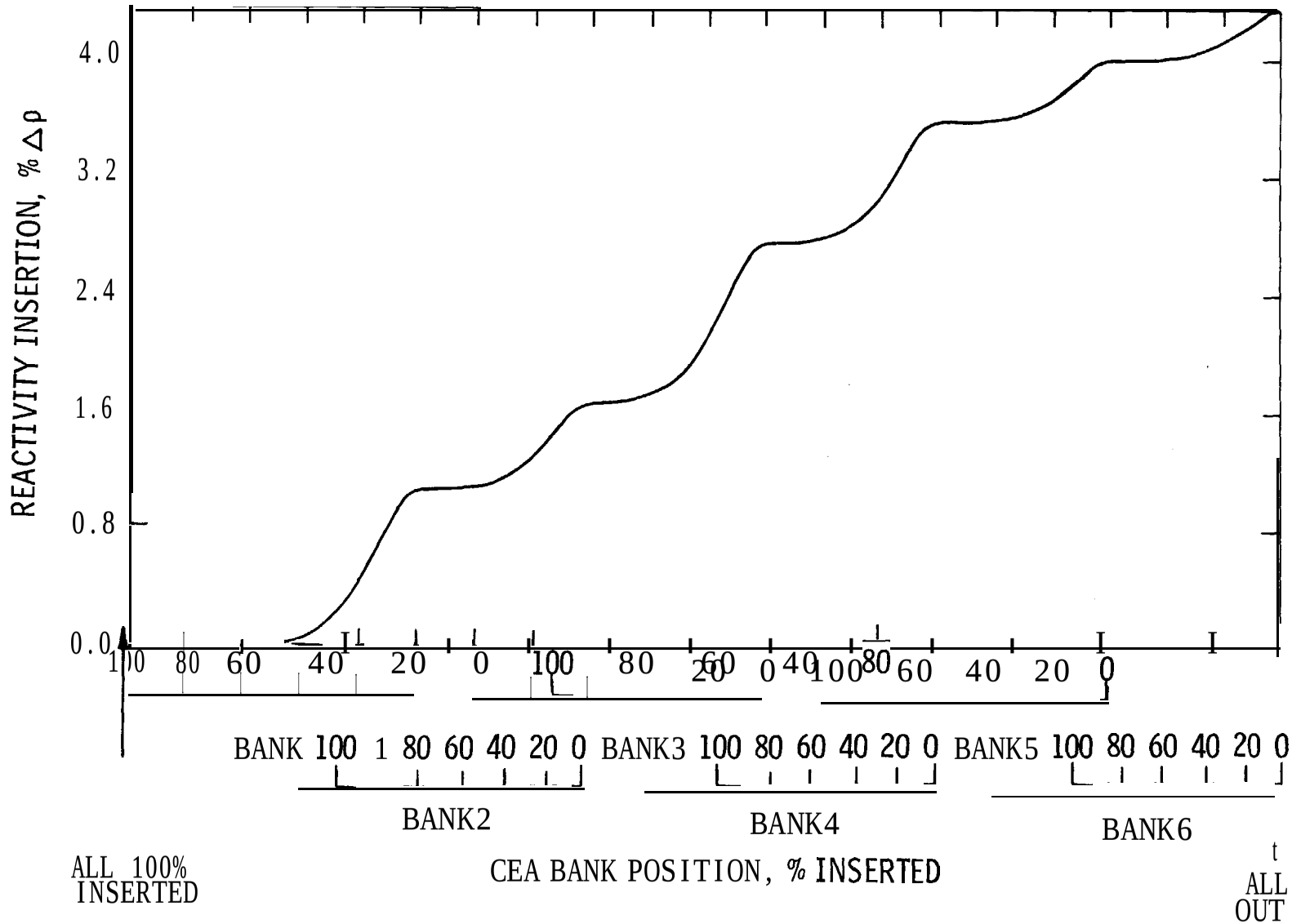

Figure 4.3-41

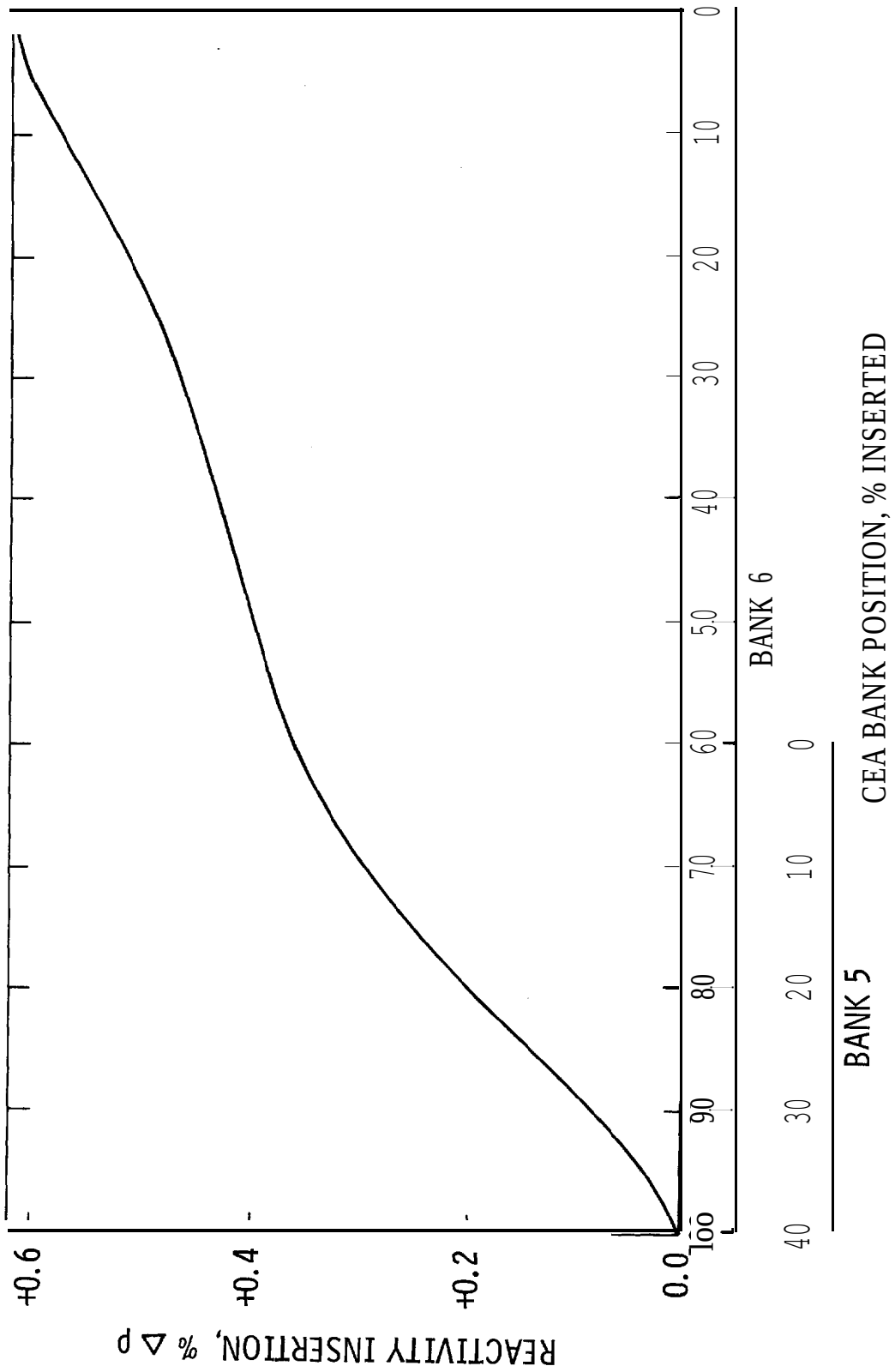

LOUISIANA POWER & LIGHT CO. Waterford Steam Electric Station	INTEGRAL WORTH VS. WITHDRAWAL AT FULL POWER EOC, EQUILIBRIUM XENON CONDITIONS	Figure 4.3-42

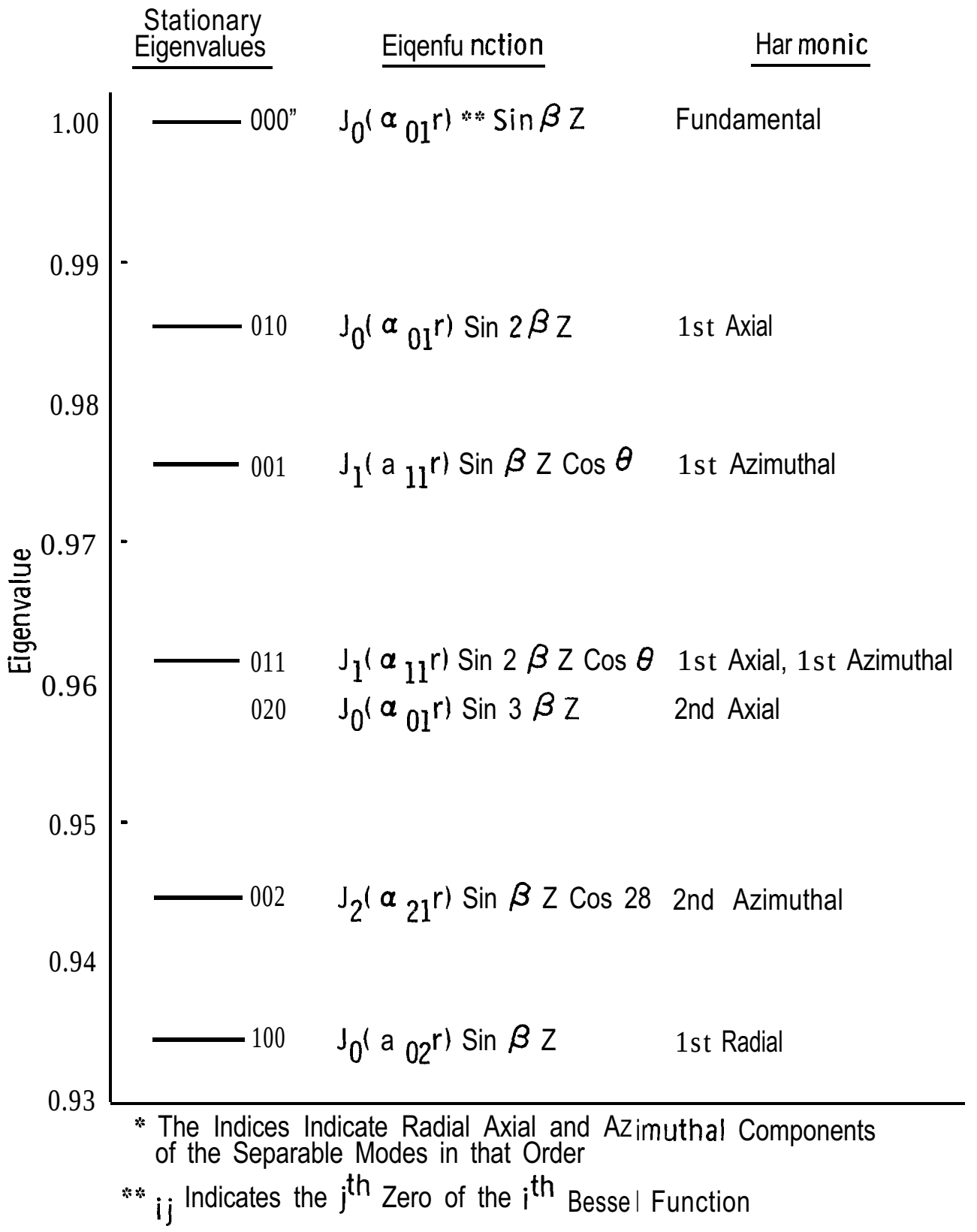

* The Indices Indicate Radial Axial and Azimuthal Components of the Separable Modes in that Order

** $_{ij}$ Indicates the j^{th} Zero of the i^{th} Bessel Function

LOUISIANA POWER & LIGHT CO. Waterford Steam Electric Station	REACTIVITY DIFFERENCE BETWEEN FUNDAMENTAL AND EXCITED STATES OF A BARE CYLINDRICAL REACTOR	Figure 4.3-43

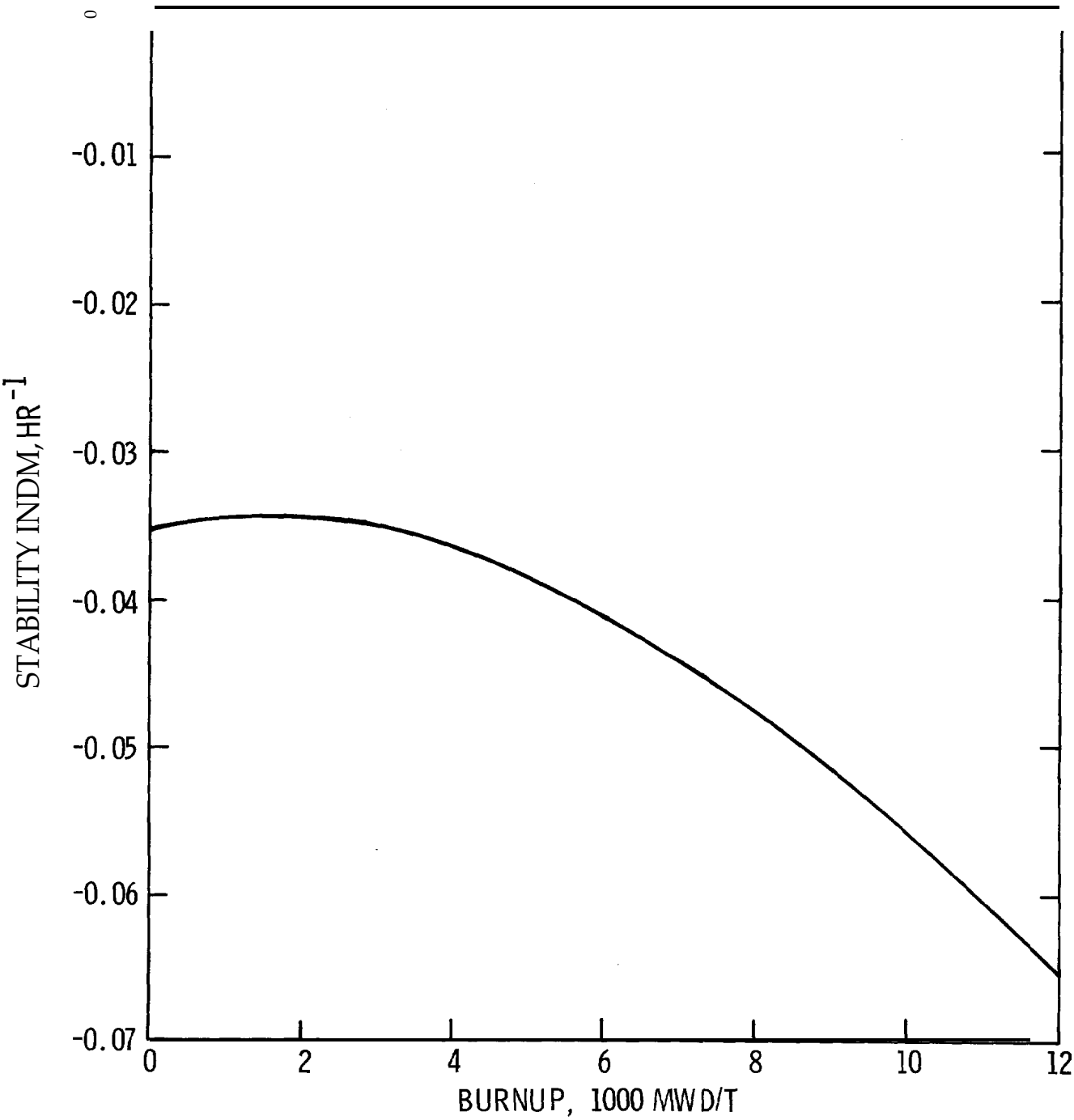

LOUISIANA POWER & LIGHT CO. Waterford Steam Electric Station	EXPECTED VARIATION OF THE AZIMUTHAL STABILITY INDEX	Figure 4.3-44

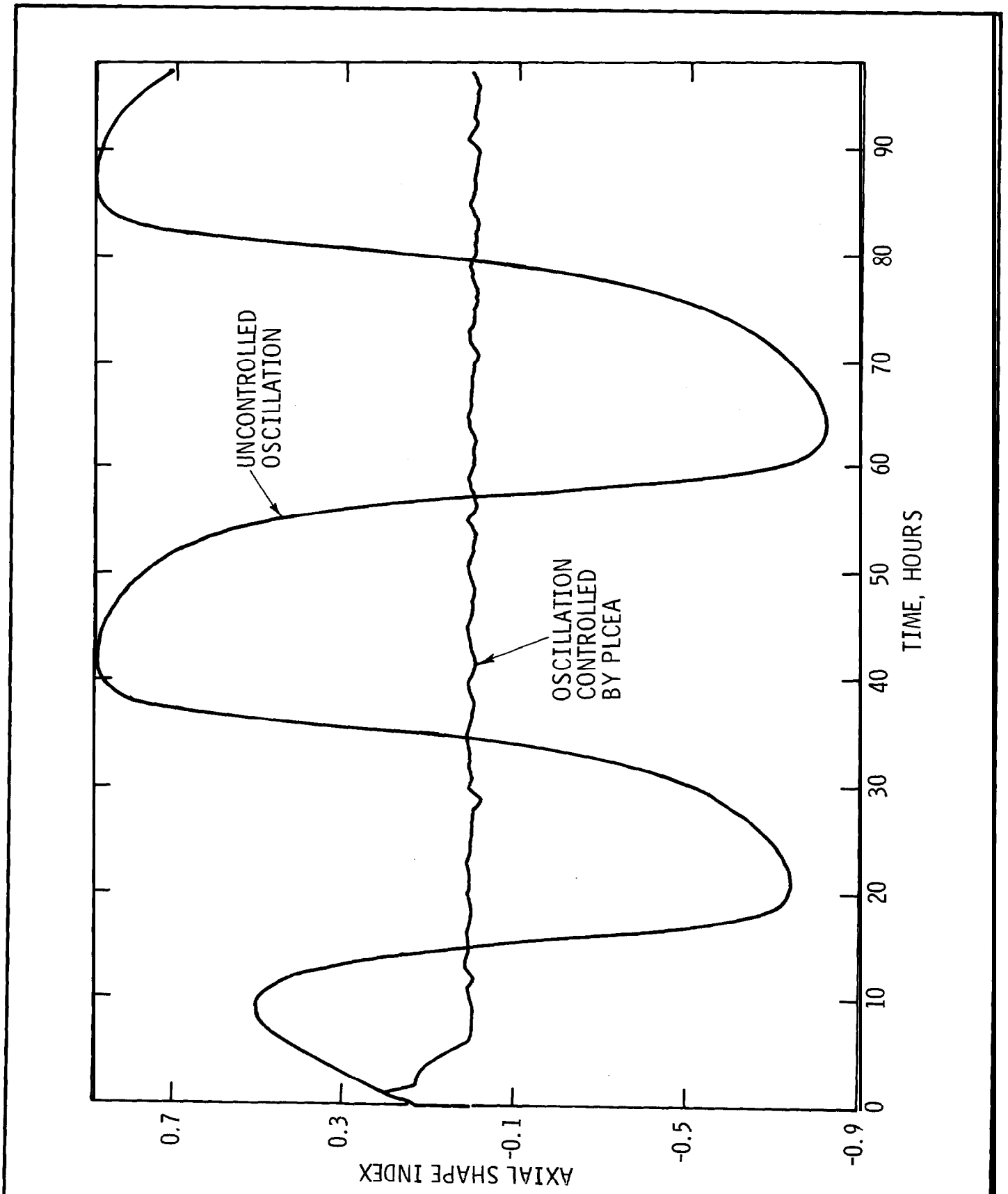

LOUISIANA
POWER & LIGHT CO.
Waterford Steam
Electric Station

STABILI TY INDEX

Figure
4.3-45

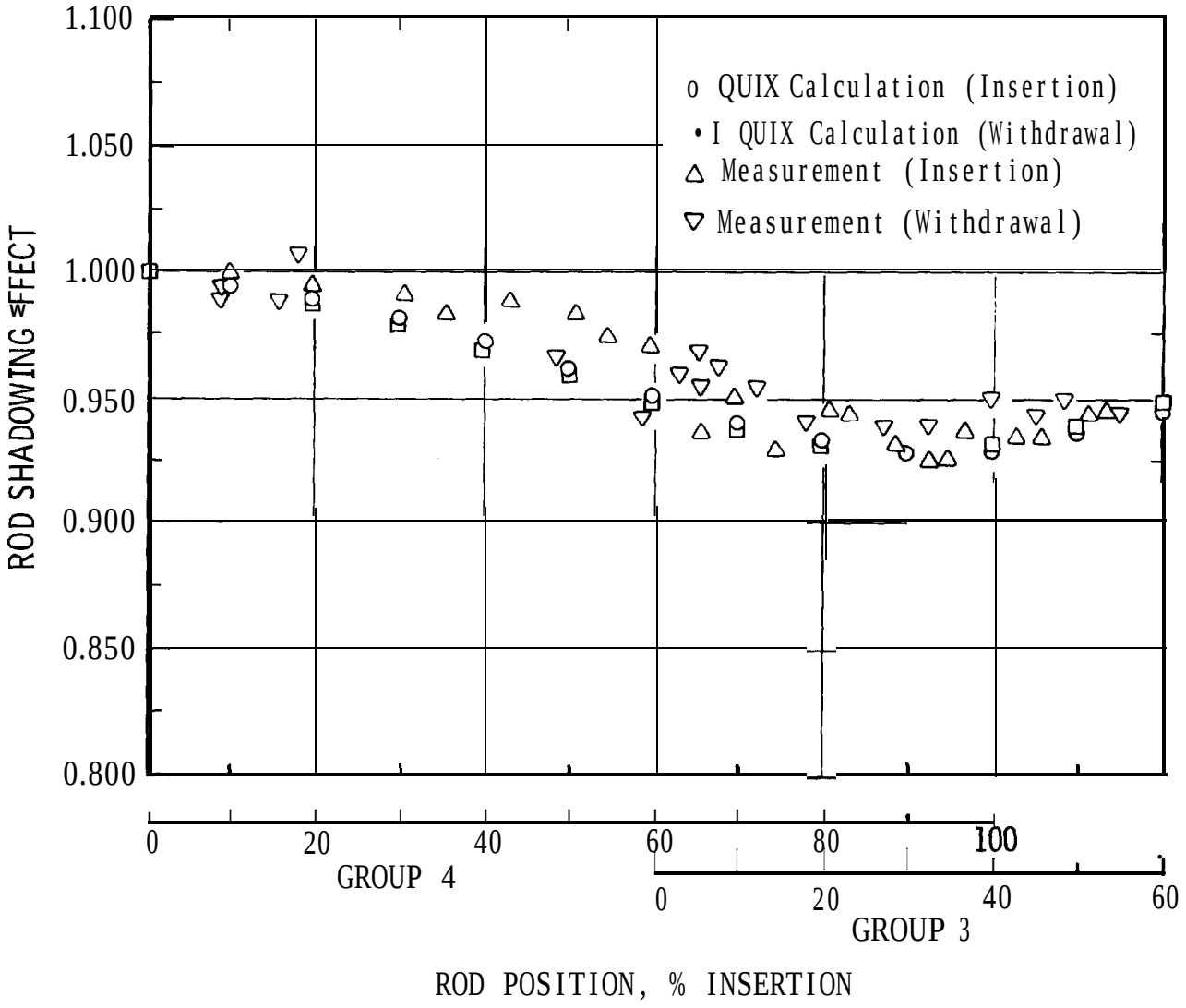

LOUISIANA POWER & LIGHT CO. Waterford Steam Electric Station	**ROD SHADOWING EFFECT VS. ROD POSITION FOR ROD INSERTION AND WITHDRAWAL TRANSIENTS AT PALISADES**	Figure 4.3-46

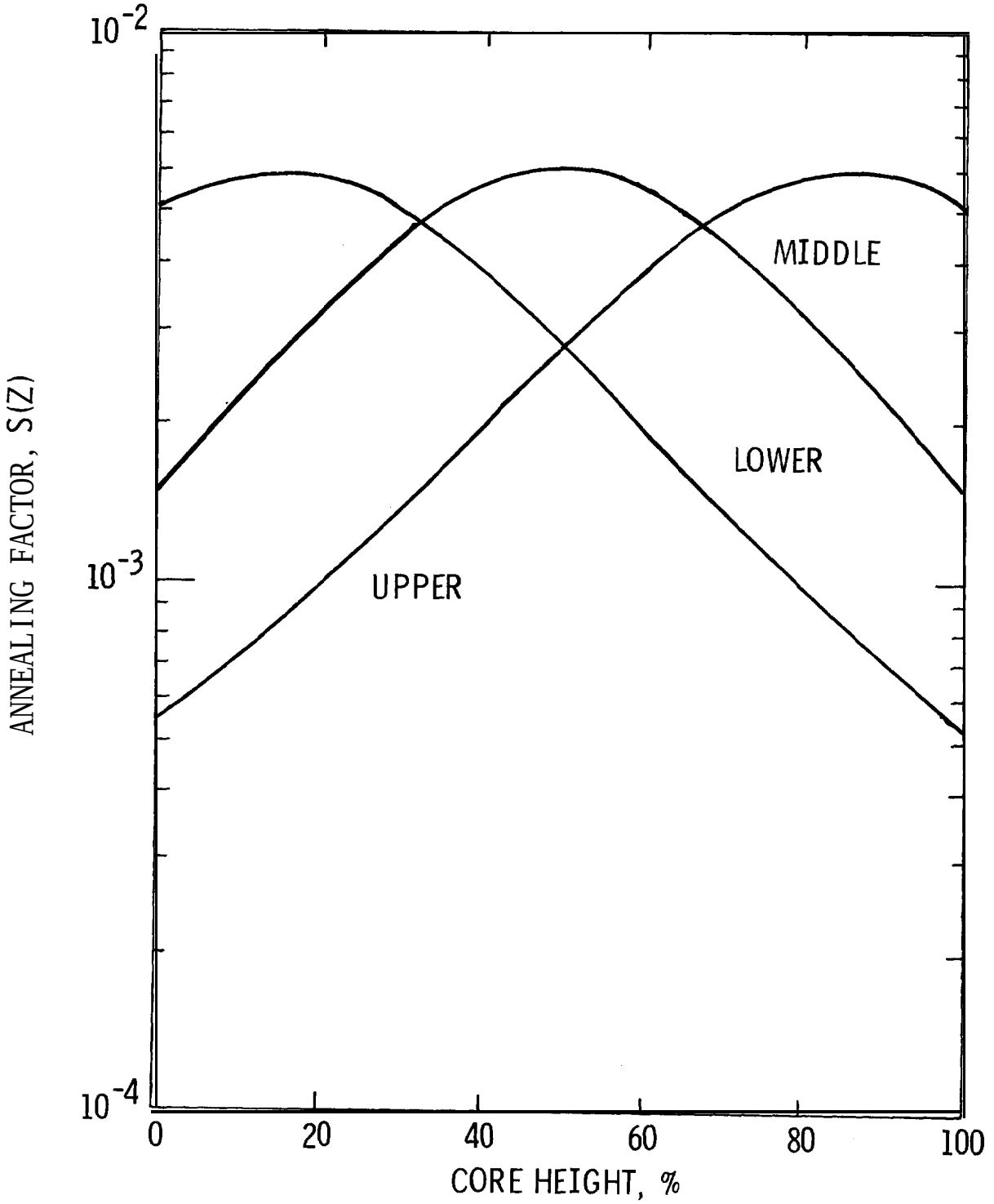

LOUISIANA POWER & LIGHT CO. Waterford Steam Electric Station	TYPICAL THREE-SUBCHANNEL ANNEALING	Figure 4.3-47

GEOMETRY WITH AZIMUTHAL SYMMETRY

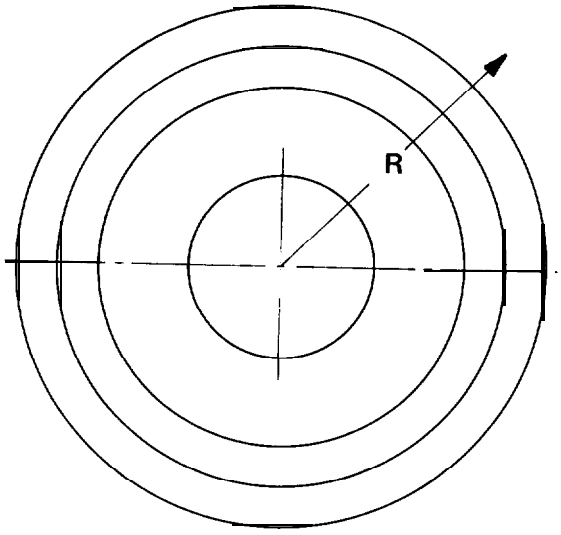

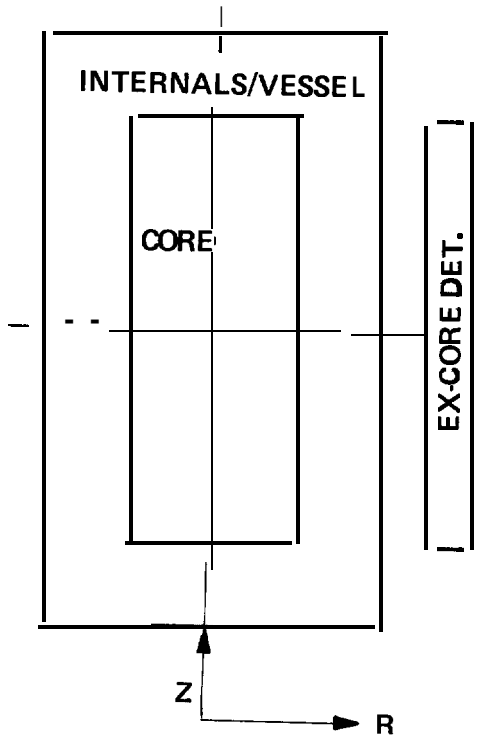

GEOMETRY WITH PARTIAL AZIMUTHAL SYMMETRY

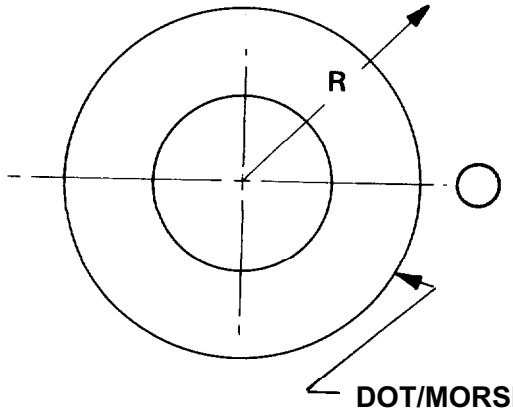

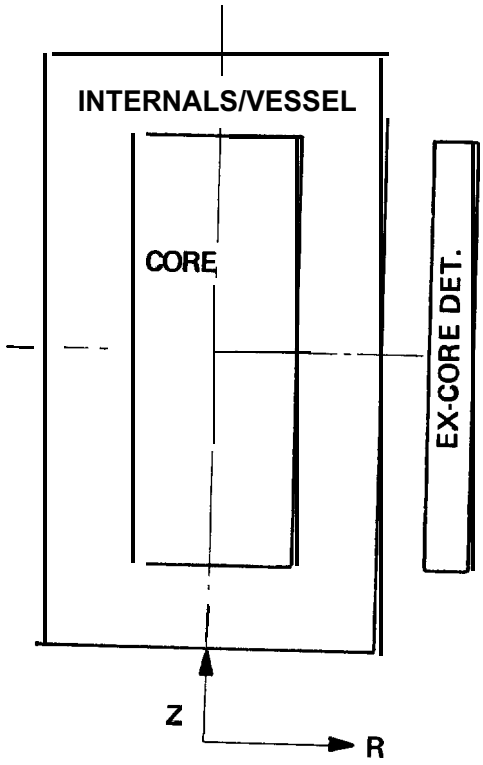

LOUISIANA POWER & LIGHT CO. Waterford Steam Electric Station	GEOMETRY LAYOUTS	Figure 4.3-48

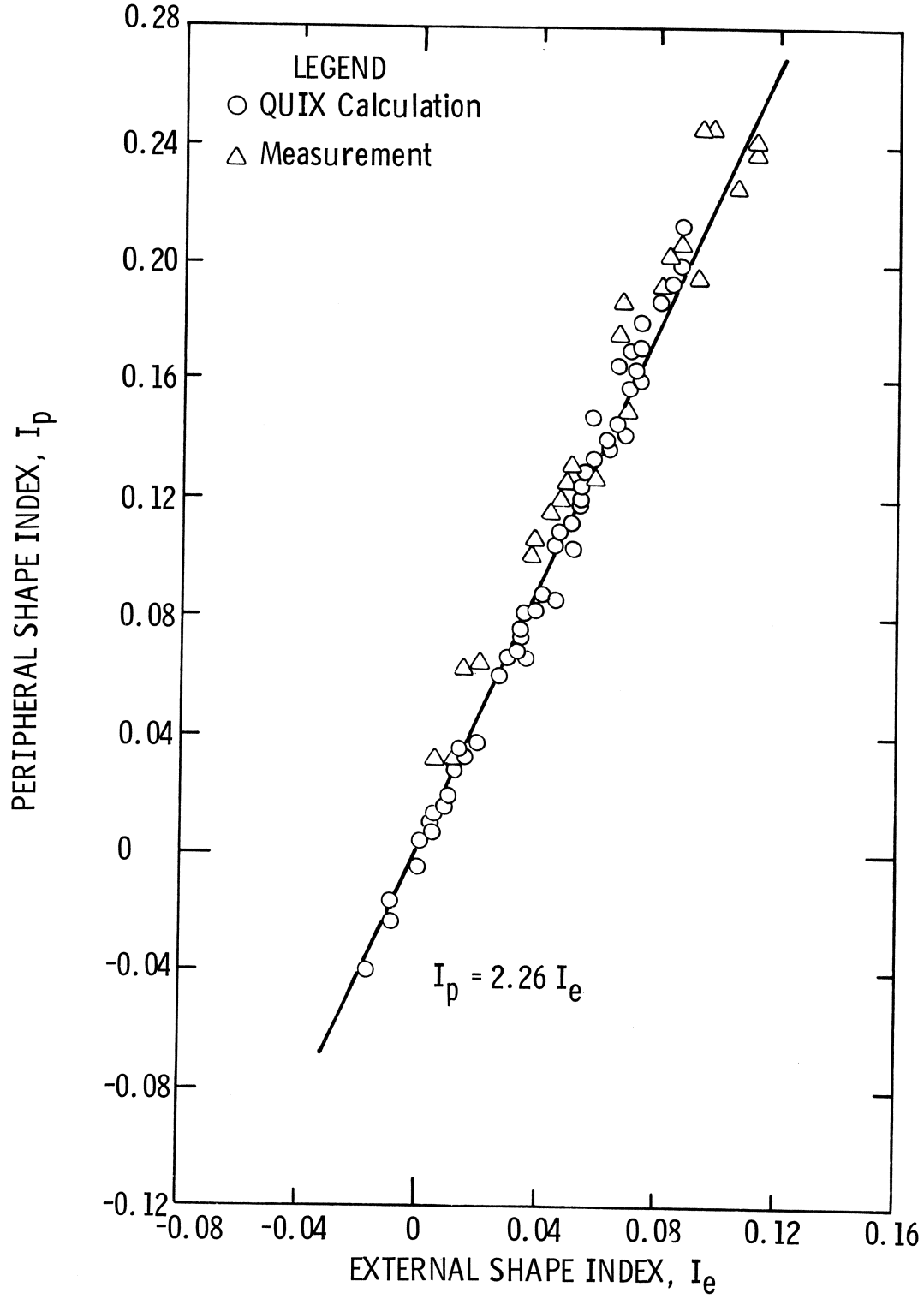

LOUISIANA POWER & LIGHT CO. Waterford Steam Electric Station	COMPARISON OF MEASURED AND CALCULATED SHAPE ANNEALING CORRECTION FOR PALISADES	Figure 4.3-49

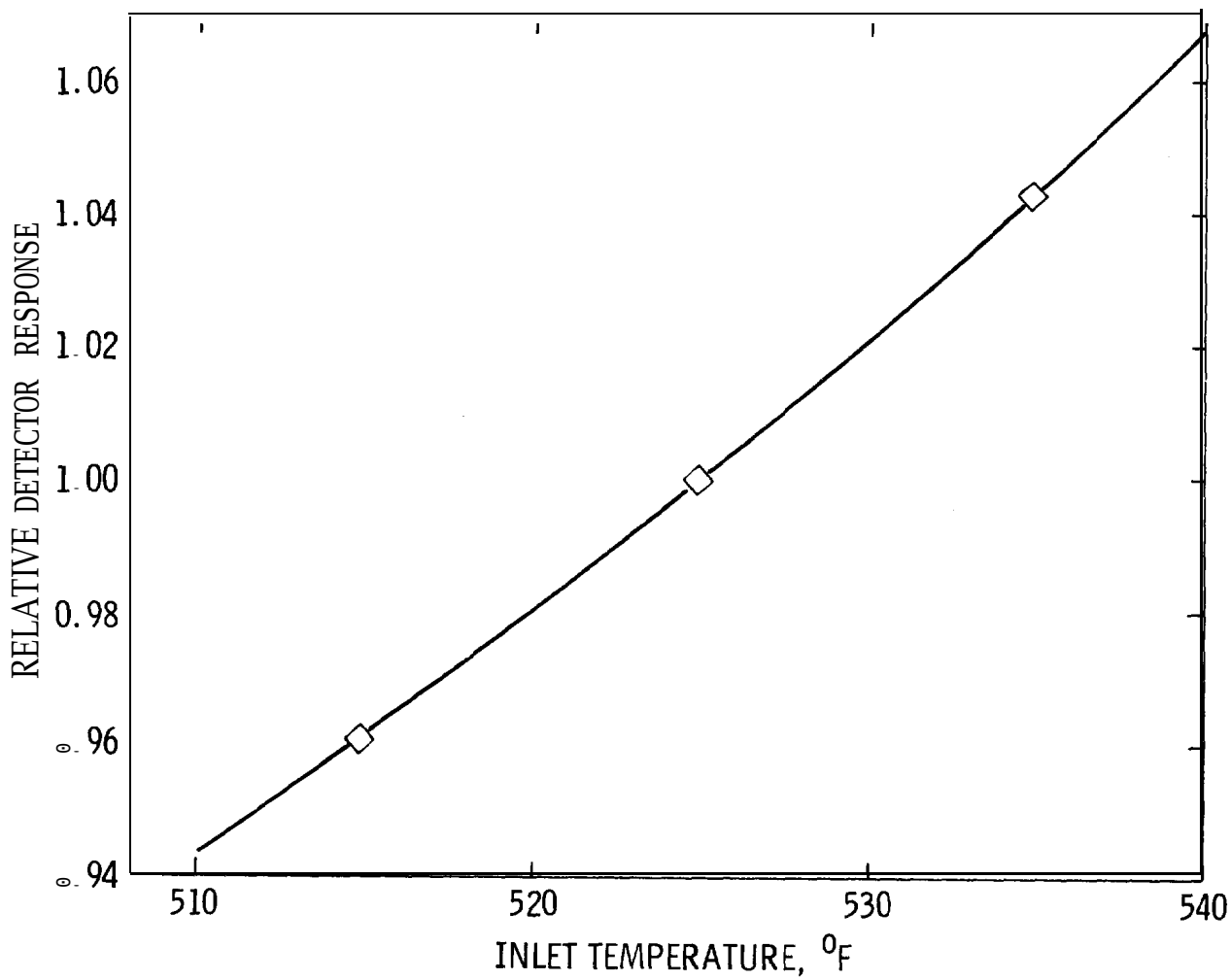

LOUISIANA POWER & LIGHT CO. Waterford Steam Electric Station	TYPICAL TEMPERATURE DEFECT VS. REACTOR INLET TEMPERATURE	Figure 4.3-50

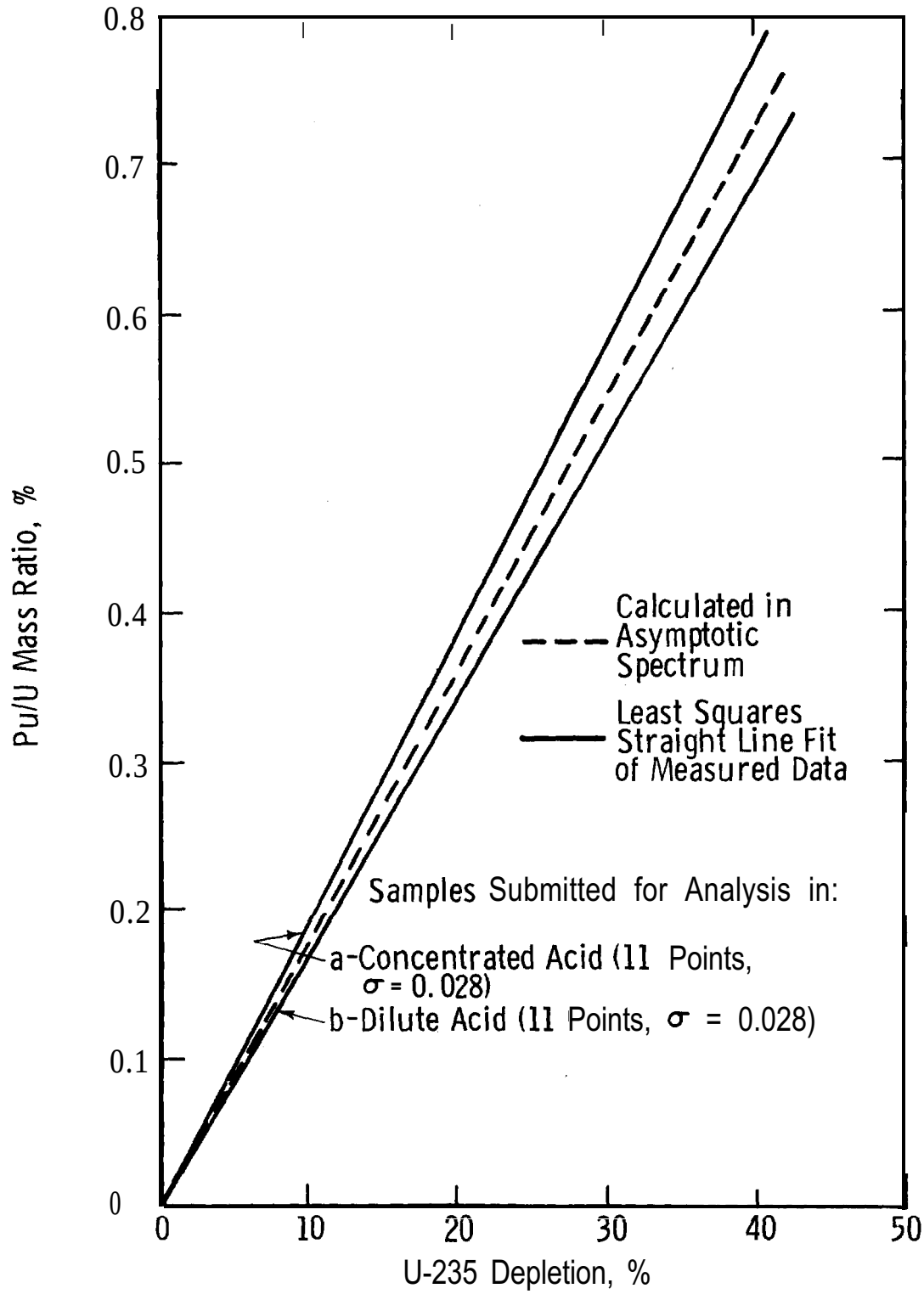

LOUISIANA POWER & LIGHT CO. Waterford Steam Electric Station	COMPARISON OF CALCULATED AND MEASURED PLUTONIUM TO URANIUM MASS RATIO IN THE ASYMPTOTIC NEUTRON SPECTRUM FOR YANKEE	Figure 4.3-51

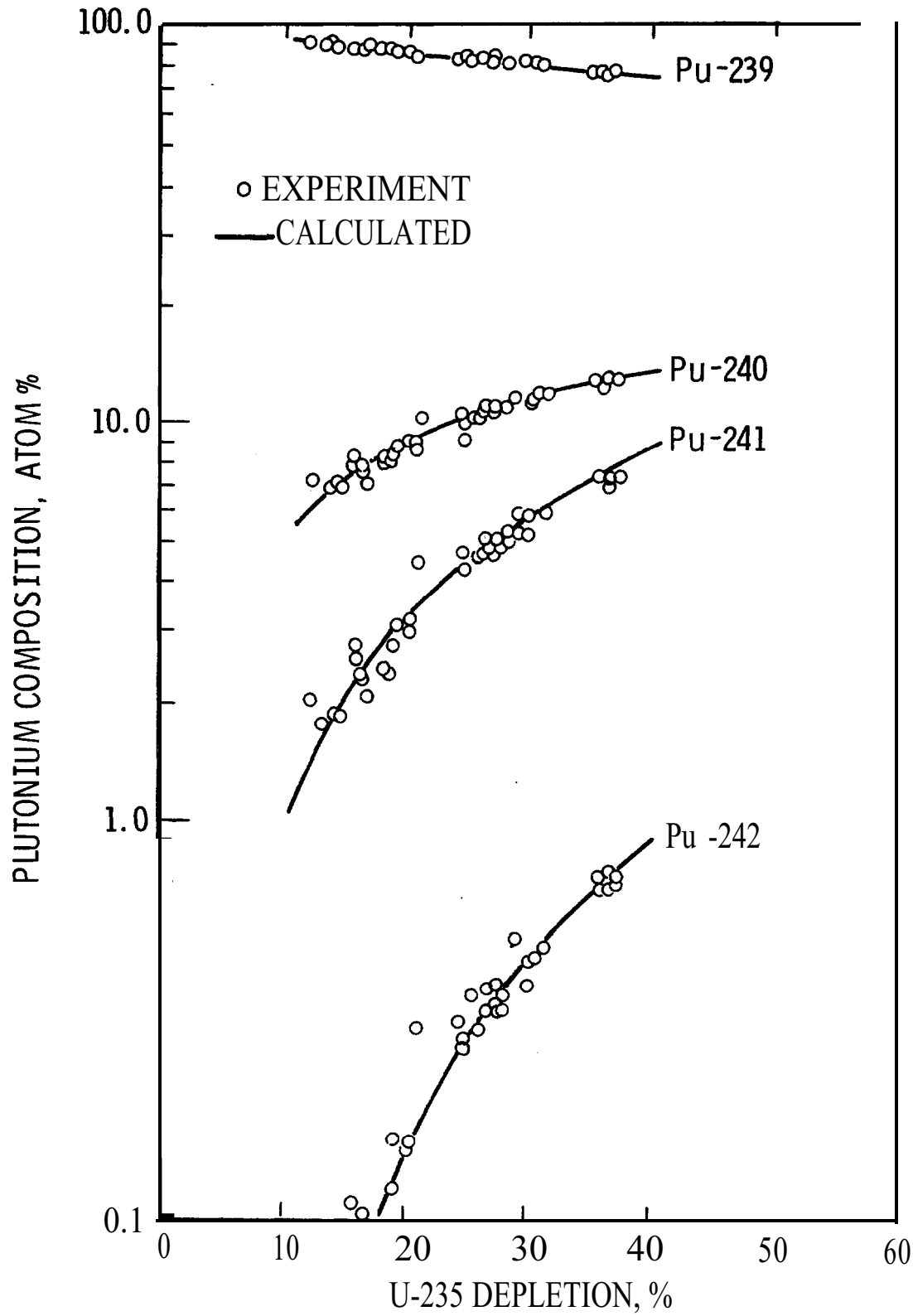

LOUISIANA POWER & LIGHT CO. Waterford Steam Electric Station	**PLUTONIUM ISOTOPIC COMPOSITION VS. FUEL DEPLETION IN THE ASYMPTOTIC SPECTRUM FOR YANKEE**	Figure 4.3-52

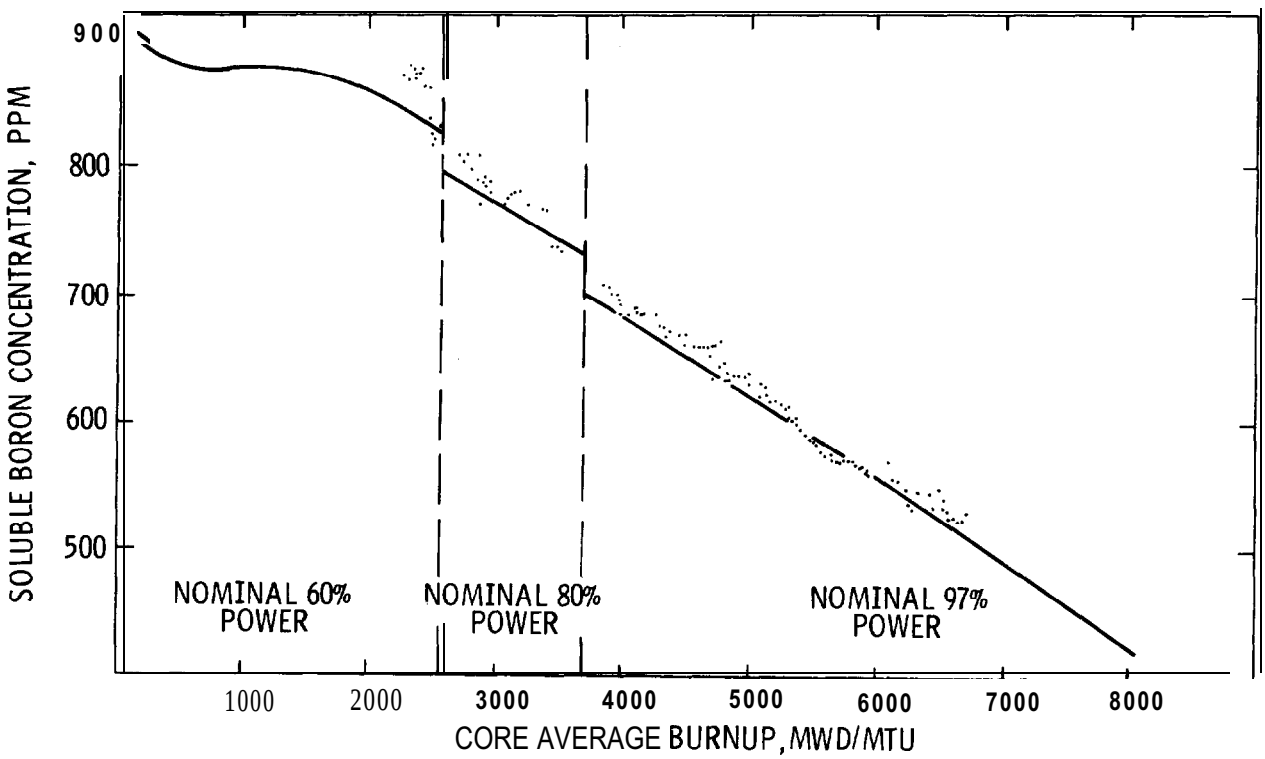

LOUISIANA POWER & LIGHT CO. Waterford Steam Electric Station	CRITICAL BORON-REACTIVITY DEPLETION OF PALISADES	Figure 4.3-53

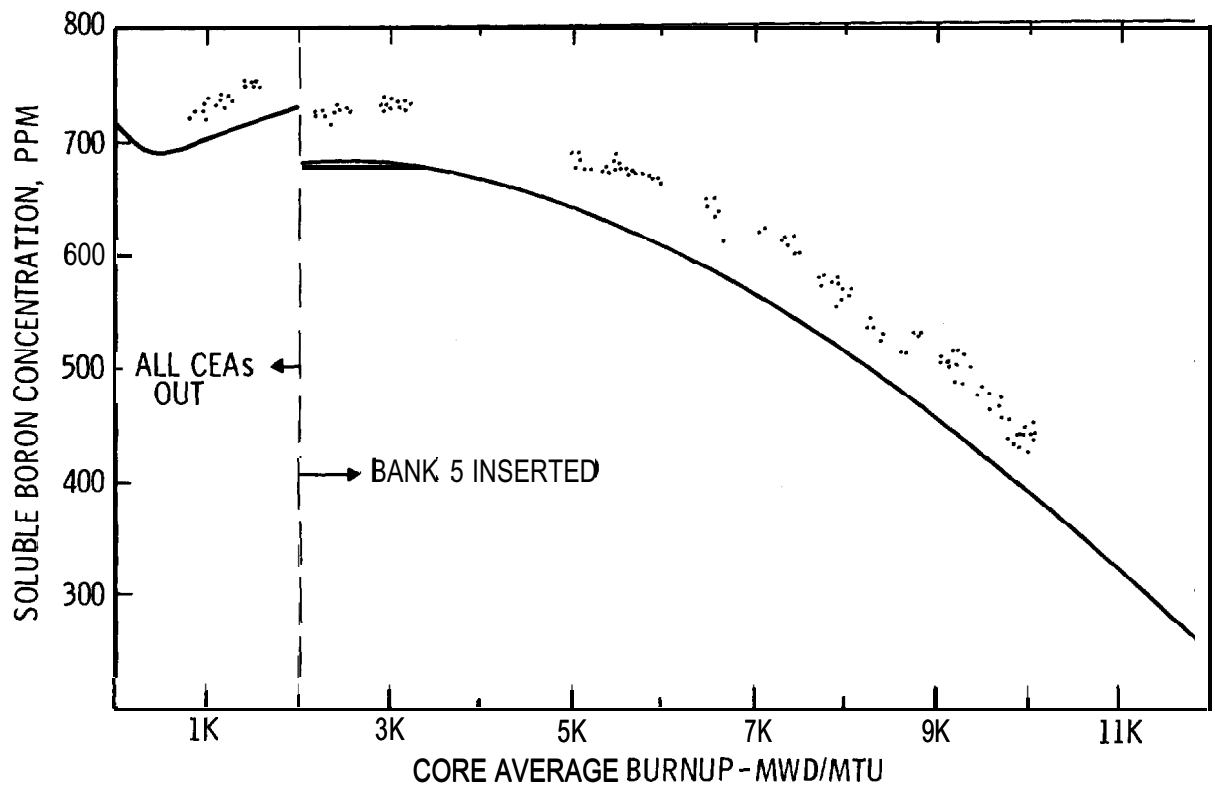

LOUISIANA POWER & LIGHT CO. Waterford Steam Electric Station	CRITICAL BORON FOR MAINE YANKEE	Figure 4.3-54

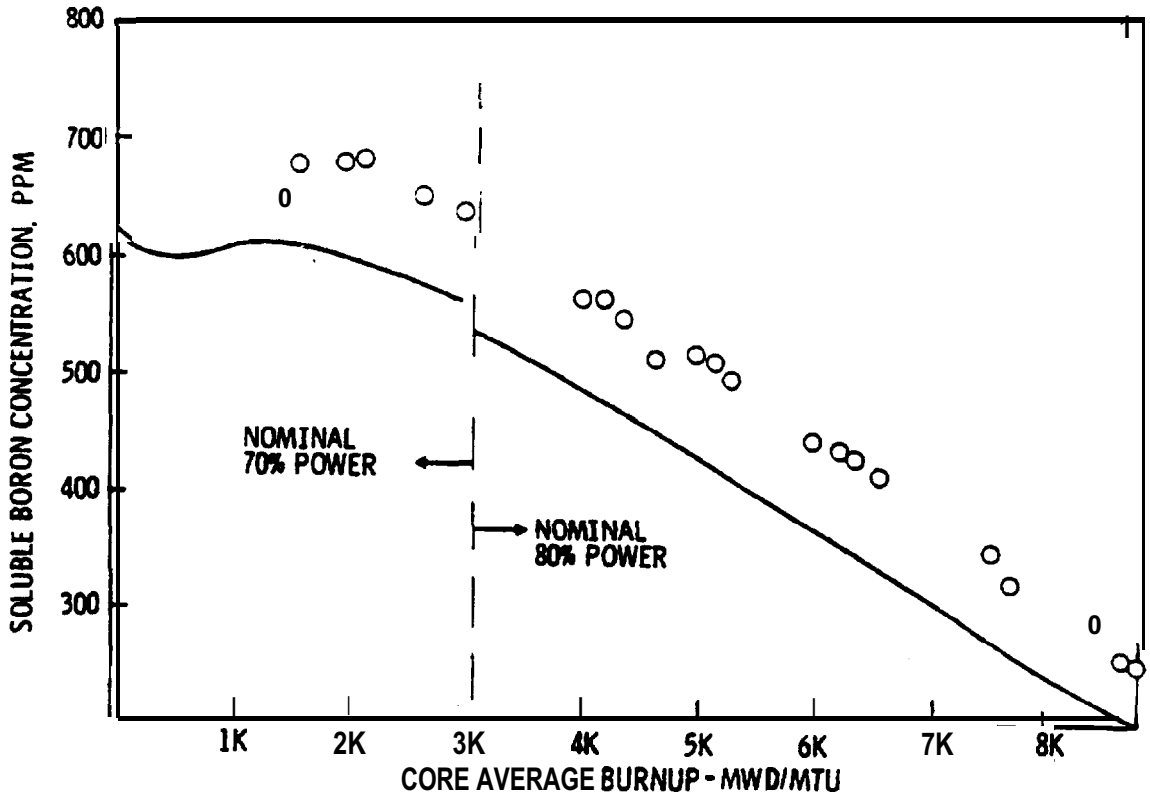

REVISION 6(12/92)

Waterford Steam Electric Station •3	CRITICAL BORON FOR FORT CALHOUN	Figure 4.3-5,5

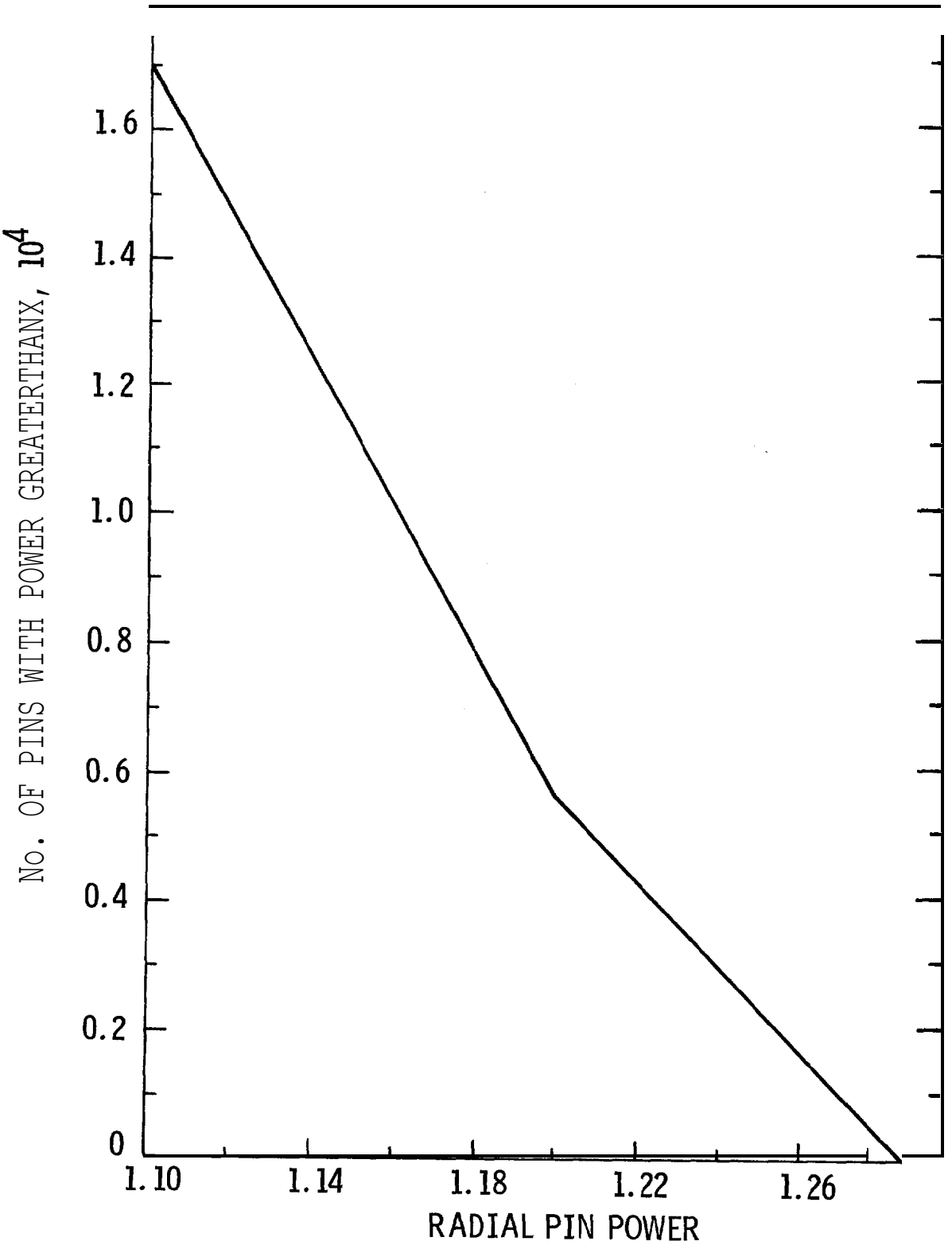

LOUISIANA POWER & LIGHT CO. Waterford Steam Electric Station	LIMITING INTEGRAL RADIAL PIN POWER DISTRIBUTION	Figure 4.3-56

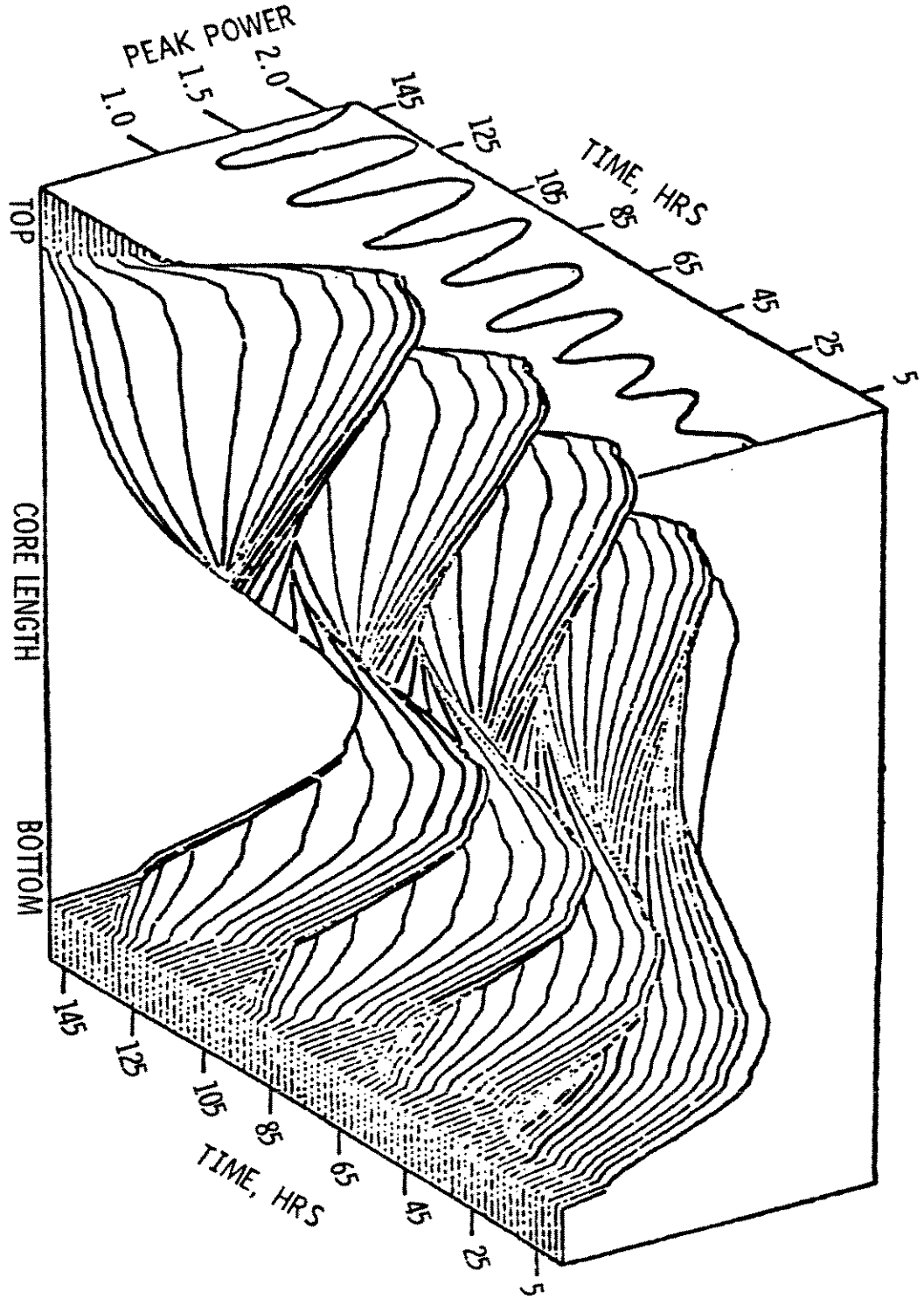

Revision 15 (03/07)

Waterford Steam Electric Station #3	A DIVERGENT AXIAL OSCILLATION IN AN EOC CORE WITH REDUCED POWER FEEDBACK ($\alpha = 0.96 \times 10^{-4}$ $\Delta\rho$(KW/FT)	Figure 4.3-57

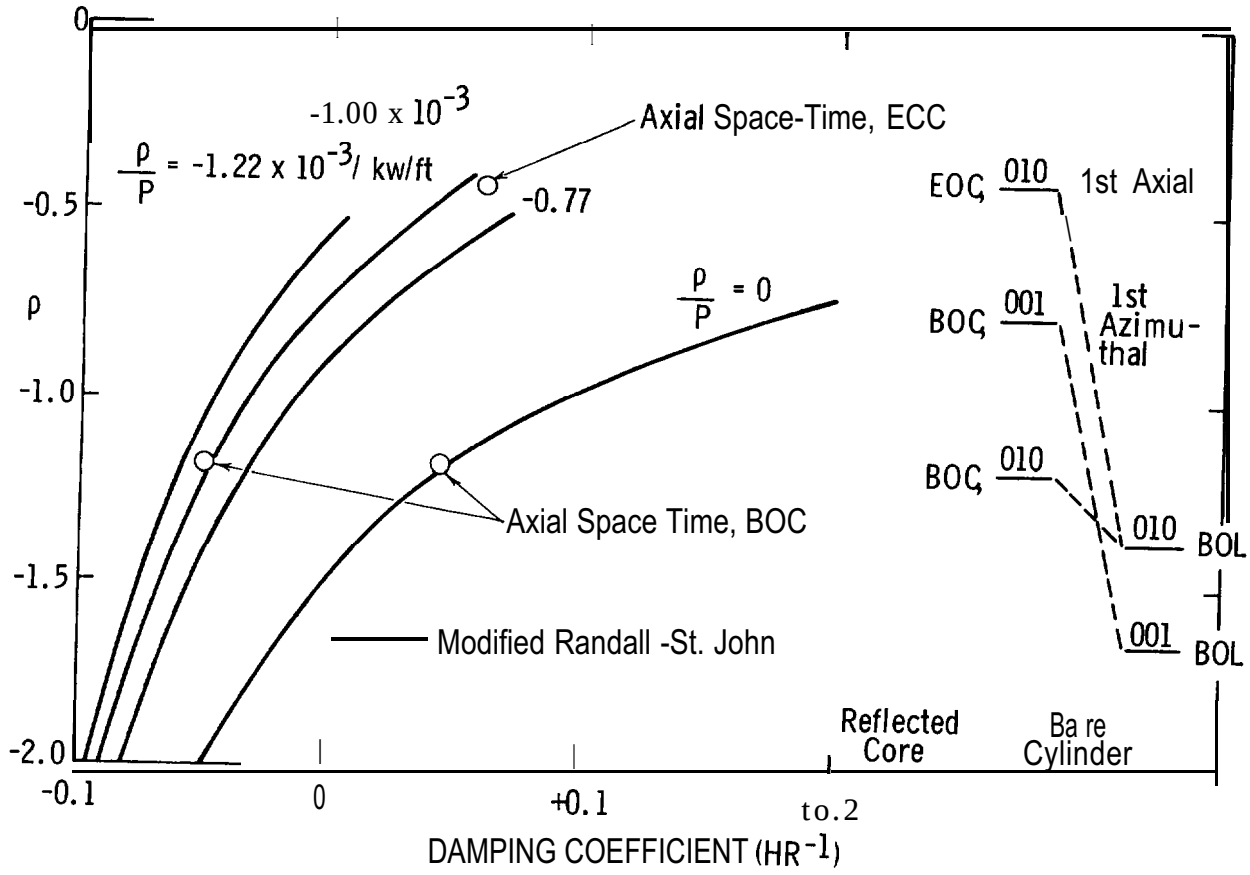

LOUISIANA POWER & LIGHT CO.
Waterford Steam Electric Station

DAMPING COEFFICIENT VS. REACTIVITY DIFFERENCE BETWEEN FUNDAMENTAL AND EXCITED STATE

Figure 4.3-58

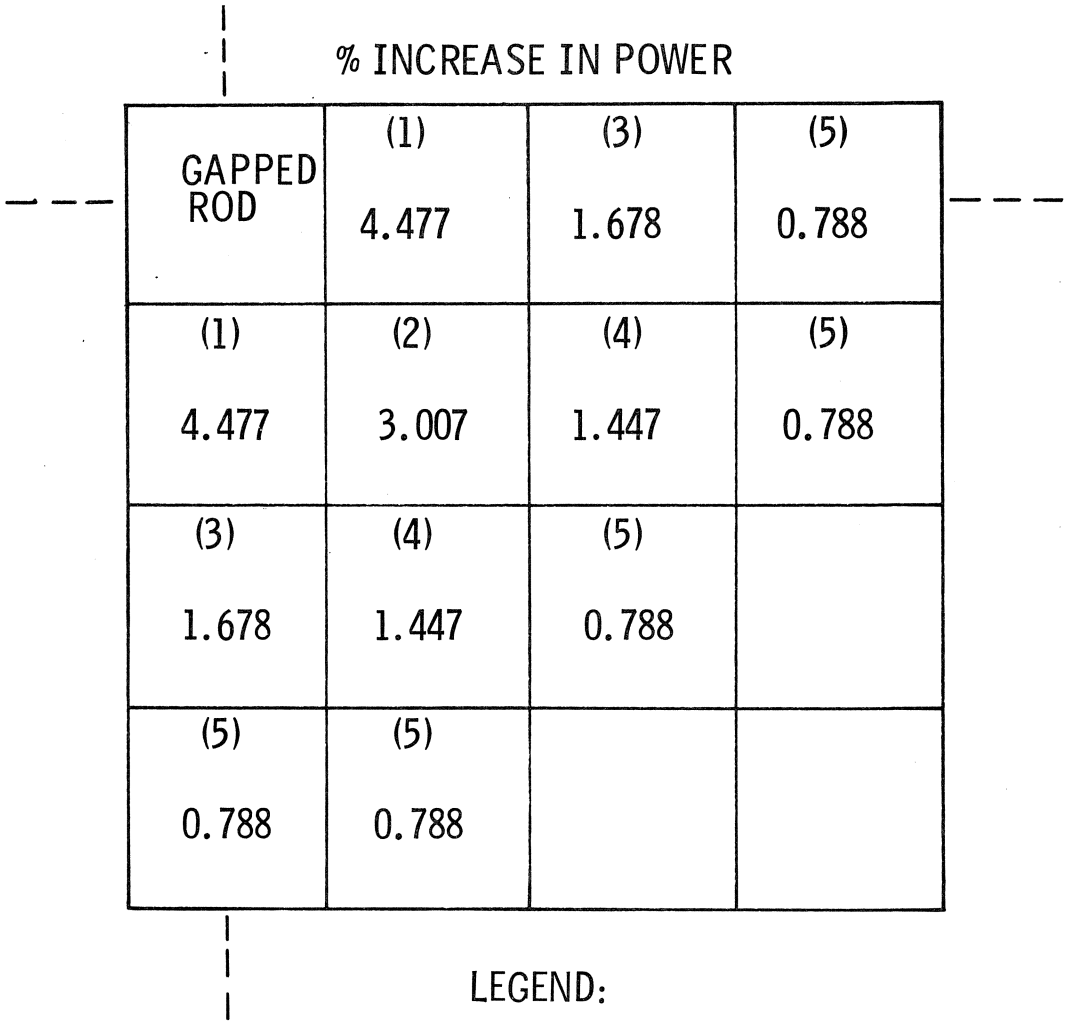

LOUISIANA POWER & LIGHT CO. Waterford Steam Electric Station	LIMITING SINGLE GAP POWER PEAKING AND ASSOCIATED ROD LOCATION RELATIVE TO THE GAP LOCATION	Figure 4.3-59

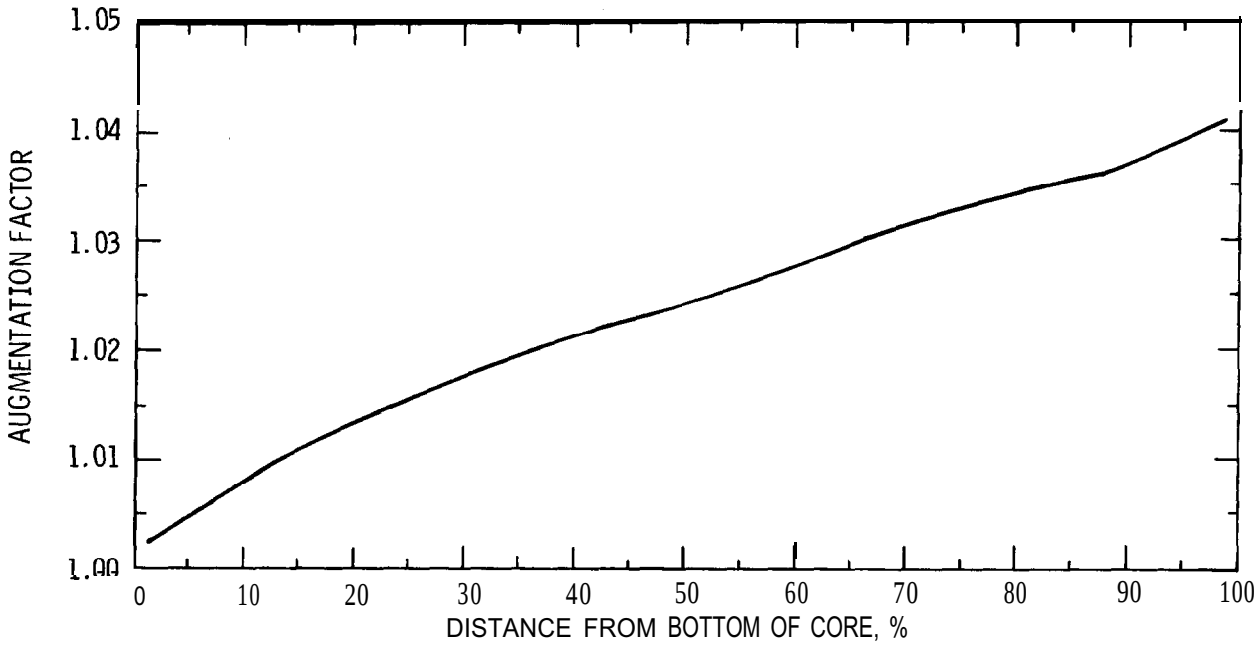

LOUISIANA
POWER & LIGHT CO.
Waterford Steam
Electric Station

AUGMENTATION FACTOR

Figure
4.3-60

APPENDIX 4.3A

→(DRN 00-1820, R10; 02-1477, R12; 04-502, R13; 05-508, R14; 06-1059, R15; EC-9533, R302, EC-13881, R304; EC-30663, R307, LBDCR 14-008, R308, LBDCR 15-035, R309; LBDCR 17-015, R310)

4.3A FUEL CYCLE 22

The following subsections discuss the fuel system design, nuclear design, thermal-hydraulic design and reactor protection and monitoring system changes for the subject fuel cycle at Waterford 3.
←(DRN 04-502, R13; 05-508, R14; 06-1059, R15; EC-9533, R302; EC-13881, R304; EC-30663, R307, LBDCR 14-008, R308; LBDCR 17-015, R310)
Operating conditions for this cycle were assumed to be consistent with those of previous cycles and are summarized as full power operation under base load conditions.
←(DRN 02-1477, R12)

Cycle 2 information was submitted to the NRC via References 1 and 2. The NRC's Safety Evaluation Report for Cycle 2 was provided in Reference 3.

4.3A.1 GENERAL DESCRIPTION

→(DRN 02-1477, R12; 04-502, R13; 05-508, R14; 06-1059, R15; EC-9533, R302; EC-13881, R304; EC-30663, R307, LBDCR 14-008, R308; LBDCR 17-015, R310)
The Waterford-3 Cycle 22 core will consist entirely of assemblies of the Next Generation Fuel (NGF) design; specifically, Fresh Region GG assemblies, once burned Region EE, and twice burned Region DD and AA assemblies. See Sections 4.2.2.1 and 4.2.2.2 for details of the NGF fuel assembly and fuel rod designs.
←(DRN 00-1820, R10; 02-1477, R12; 04-502, R13; 05-508, R14; 06-1059, R15; EC-9533, R302; EC-13881, R304; EC-30663, R307, LBDCR 14-008, R308; LBDCR 17-015, R310)

Control element assembly patterns and in-core instrument locations are shown in Figure 4.3A-4 and Figure 4.3A-5 respectively.

4.3A.2 FUEL SYSTEM DESIGN

4.3A.2.1 Mechanical Design

4.3A.2.1.1 Fuel Design

→(DRN 02-1477, R12; 04-502, R13; 05-508, R14; 06-1059, R15; EC-9533, R302; EC-13881, R304; EC-30663, R307, LBDCR 14-008, R308; LBDCR 17-015, R310)
The Cycle 22 core consists of those assembly types and numbers listed in Table 4.3A-1. All fuel assemblies in the Cycle 22 core are of the NGF design.
←(DRN 02-1477, R12; 04-502, R13; 05-508, R14; 06-1059, R15; EC-9533, R302; EC-13881, R304; EC-30663, R307, LBDCR 14-008, R308; LBDCR 17-015, R310)

→(DRN 02-1477, R12; 04-502, R13; 05-508, R14)
←(DRN 02-1477, R12; 04-502, R13; 05-508, R14)

→(DRN 04-502, R13)
←(DRN 04-502, R13)

→(DRN 00-1820, R10)
←(DRN 00-1820, R10)

4.3A.2.1.2 Clad Collapse

→(DRN 06-1059, R15; EC-9533, R302; EC-13881, R304)
The NGF fuel (UO_2) and IFBA rods in this cycle are initially pressurized with helium to the amount determined to be sufficient to prevent any gross clad deformation under the combined effect of external pressure and long term creep. The analyses of these rods credit the support of pellets and/or the holddown spring to prevent gross deformation (see also Sections 4.2.1.2.1 and 4.2.1.2.5).
←(DRN 06-1059, R15; EC-9533, R302; EC-13881, R304, LBDCR 15-035, R309)

4.3A.2.2 Mitigation of Guide Tube Wear

All fuel assemblies have stainless steel sleeves installed in the guide tubes to prevent guide tube wear.

4.3A.2.3 Thermal Design

→(DRN 02-1477, R12; 04-502, R13; 05-508, R14; 06-1059, R15; EC-9533, R302; EC-13881, R304; EC-30663, R307, LBDCR 14-008, R308, LBDCR 15-035, R309; LBDCR 17-015, R310)

The thermal performance of composite fuel rods that envelope the rods of fuel batches present in Cycle 22 have been evaluated using the NRC approved FATES3B version of the C-E fuel evaluation model (References 6, 7 and 32) and the Zirconium Diboride (ZrB_2) burnable absorber methodology described in Reference 35. The analysis was performed using a power history that enveloped the power and burnup levels representative of the peak pin at each burnup interval, from beginning of cycle to end of cycle burnups. The burnup range analyzed is in excess of that expected at the end of the Cycle.

←(EC-30663, R307, LBDCR 14-008, R308; LBDCR 17-015, R310)

Reference 35 describes Westinghouse's 15 year fabrication and operational experience with ZrB_2 IFBA and the implementation and effect of using the coating on the C-E fuel assembly design and safety analyses. The neutronics effect, the helium production effect on internal gas pressure, and the mechanical and thermal effects of the coating thickness are all taken into account in the design and safety evaluations for C-E designed PWRs as described in that Reference.

←(DRN 02-1477, R12; 04-502, R13; 05-508, R14; 06-1059, R15; EC-9533, R302)

→(EC-9533, R302)

The methodology for modeling the NGF design is described in the CE 16x16 Next Generation Fuel Topical Report, Reference 43.

←(EC-13881, R304)

4.3A.2.4 Chemical Design

→(EC-13881, R304; EC-30663, R307, LBDCR 14-008, R308; LBDCR 17-015, R310)

The metallurgical design specifications of the fuel cladding and other fuel assembly components for the NGF fuel used in Cycle 22 are essentially the same as those of the fuel regions included in Cycle 1. The NGF design of Region GG, Region EE, Region DD and Region AA include Optimized ZIRLO™ for the cladding and spacer grids (Reference 44) and ZIRLO™ for the CEA guide tubes (Reference 43). The introduction of these material changes does not impose any new water chemistry requirements relative to those employed for the standard fuel assembly.

←(EC-13881, R304; EC-30663, R307, LBDCR 14-008, R308; LBDCR 17-015, R310)

4.3A.2.5 Shoulder Gap Adequacy

→(DRN 02-1477, R12; 04-502, R13; 05-508, R14; 06-1059, R15; EC-13881, R304; EC-30663, R307, LBDCR 14-008, R308; LBDCR 17-015, R310)

Adequate shoulder gap is predicted for all NGF Regions of fuel in Cycle 22. This conclusion is based upon the fuel rod growth models of Reference 34 for Zircaloy, Reference 45 for ZIRLO™, and Reference 43 for Optimized ZIRLO™. The shoulder gap evaluation for Regions with the NGF design demonstrates that the initial shoulder gap reduction of approximately 0.5 inches relative to the non-NGF design is accommodated by the improved dimensional stability of the NGF cladding and CEA guide tube materials (Optimized ZIRLO™ and ZIRLO™, respectively).

←(DRN 02-1477, R12; 04-502, R13; 05-508, R14; 06-1059, R15; EC-9533, R302; EC-13881, R304; EC-30663, R307, LBDCR 14-008, R308; LBDCR 17-015, R310)

4.3A.3 NUCLEAR DESIGN

4.3A.3.1 Physics Characteristics

4.3A.3.1.1 Fuel Management

→(DRN 00-1820, R10; 02-1477, R12; 04-502, R13; 05-508, R14; 06-1059, R15; EC-9533, R302; EC-13881, R304; EC-30663, R307, LBDCR 14-008, R308; LBDCR 17-015, R310)

The Cycle 22 core consists of those assembly types and numbers listed in 4.3A-1. Twenty (20) Region CC and eighty (80) Region DD assemblies irradiated during Cycle 21 will be removed from the core and replaced with one hundred (100) fresh Region GG assemblies and one (1) twice-burned Region AA assembly that was not loaded in the Cycle 21 core. Ninety-six (96) Region EE and twenty (20) Region DD assemblies in the core during Cycle 21 will be retained for Cycle 22.

←(DRN (00-1820, R10; 02-1477, R12; 04-502, R13; EC-9533, R302; EC-13881, R304; EC-30663, R307, LBDCR 14-008, R308, LBDCR 15-035, R309; LBDCR 17-015, R310)

→(DRN 00-1820, R10; 02-1477, R12; 04-502, R13; 05-508, R14; 06-1059, R15; EC-9533, R302; EC-13881, R304; EC-30663, R307, LBDCR 14-008, R308, LBDCR 15-035, R309; LBDCR 17-015, R310)
The Cycle 22 core makes use of a low-leakage fuel management scheme in which four (4), sixteen (16), eight (8), twelve (12), and eight (8) previously burned Sub-Region DA, DG, EA, ED, and EE assemblies are each placed on the core periphery. One (1) previously burned Sub-Region AD assembly is placed in the center location. The one hundred (100) fresh Region GG (Sub-Regions GA, GB, GC, GD, and GU) assemblies are located throughout the interior of the core, where they are arranged with other previously burned Region EE fuel assemblies in a pattern that minimizes power peaking, and reduces both core leakage and the total neutron fluence to the reactor vessel.

The Cycle 22 center assembly is a twice-burned Region AA assembly that was held in the Spent Fuel Pool during the Cycle 19, Cycle 20, and Cycle 21 operations. It had previously been loaded in the core for the Cycle 17 and Cycle 18 operations. Fuel rod enrichment and Zirc Diboride configurations for the Region GG fuel are presented in
Figure 4.3A-1.

The Cycle 22 reload fuel enrichment and region size will provide a nominal best estimate cycle length of 569 EFPD (582 EFPD with coastdown) based on operation at 3716 MWth and a Cycle 21 nominal endpoint of 472 EFPD. Depending on the actual Cycle 21 endpoint, the Cycle 22 core could deliver as much as 582 EFPD (595 EFPD with coastdown) or as little as 561 EFPD (574 EFPD with coastdown) on a best estimate basis. The Cycle 21 termination burnup has been assumed to be between 447 and 487 EFPD.

Figures 4.3A-3a and 4.3A-3b display the beginning of Cycle 22 and the end of Cycle 22 (586 EFPD) assembly average burnup distributions. These burnup distributions are based on Cycle 21 endpoints of 447 and 487 EFPD, respectively.

Table 4.3A-2 provides a comparison of characteristic physics parameters for Cycle 22 to the same parameters for Cycle 21, the Reference Cycle. The values in this table are intended to represent nominal core parameters. Those values used in the safety analyses (see Chapter 15) contain appropriate uncertainties, or incorporate values to bound future operating cycles, and in all cases are conservative with respect to the values calculated for Cycle 22.

Table 4.3A-3 presents a summary of CEA reactivity worths and allowances for the end of Cycle 22 full power steam line break transient. The full power steam line break was chosen as a reasonable illustration of the CEA reactivity worth.
←(DRN (00-1820, R10; 02-1477, R12; 04-502, R13; EC-9533, R302; EC-13881, R304; EC-30663, R307, LBDCR 14-008, R308, LBDCR 15-035, R309; LBDCR 17-015, R310)

→(DRN 02-1477, R12; 04-502, R13)
The CEA core locations and group identifications are shown in Figure 4.3A-4. At the end of Cycle 11, the eight (8) Part-Length CEAs comprising Bank P were replaced with full-length, full strength CEAs and reassigned to Bank A. Four (4) full-length CEAs in Shutdown Bank A were reassigned to Bank P. Additionally, the four 4 Element CEAs in Shutdown Bank A, that span two fuel assemblies at the core periphery's major axes, were removed from the core. The Waterford 3 CEA Bank configurations are shown in Figure 4.3A-4. Commencing with Cycle 12, the Waterford 3 core has a total of 87 CEAs, all of the standard five element design. The assumed power dependent insertion limits (PDIL) for regulating groups and CEA Group P are shown in Figures 4.3A-6 and 4.3A-7 respectively. Table 4.3A-4 shows the reactivity worths of various CEA groups calculated at full power conditions for this cycle and the Reference Cycle.
←(DRN 02-1477, R12; 04-502, R13; 05-508, R14; 06-1059, R15)

4.3A.3.1.2 Power Distribution

Figures 4.3A-8 through 4.3A-10 illustrate the calculated All Rods Out (ARO) planar radial power distributions during this cycle. The one-pin planar radial power peaks presented in these figures represent the middle region of the core. Time points at the beginning, middle, and end of cycle were chosen to display the variation in maximum planar radial peak as a function of burnup.

The calculated radial power distributions described in this section do not include any uncertainties or allowances. The calculations performed to determine these radial power peaks explicitly account for augmented power peaking which is characteristic of fuel rods adjacent to the water holes.
→(DRN 02-1477, R12; 04-502, R13)
The following endpoints apply to Figures 4.3A-8 through 4.3A-10:
→(DRN 05-508, R14; 06-1059, R15; EC-9533, R302; EC-13881, R304; EC-30663, R307, LBDCR 14-008, R308, LBDCR 15-035, R309; LBDCR 17-015, R310)

BOC22 values based on EOC21 = 447 EFPD, BOC22 = 0 EFPD
MOC22 values based on EOC21 = 487 EFPD, MOC22 = 280 EFPD
EOC22 values based on EOC21 = 487 EFPD, EOC22 = 586 EFPD

←(DRN 02-1477, R12; 04-502, R13; 05-508, R14; 06-1059, R15; EC-9533, R302; EC-13881, R304, LBDCR 14-008, R308, LBDCR 15-035, R309; LBDCR 17-015, R310)

4.3A.3.1.3 Maximum Fuel Rod Burnup
→(DRN 00-1820, R10; 02-1477, R12; 04-502, R13; 05-508, R14; 06-1059, R15; EC-9533, R302; EC-13881, R304, LBDCR 14-008, R308, LBDCR 15-035, R309; LBDCR 17-015, R310)
The Cycle 22 length will be limited to assure the maximum projected fuel rod burnup is less than the 60,000 MWD/T limit presented in Reference 34. The physics data which are input to cycle safety and fuel performance analyses are developed from explicit fine mesh calculations of fuel rod power and exposure. Burnup dependent physics data (e.g., maximum fuel rod fluence and fuel rod power histories) conservatively envelope core and fuel rod behavior at maximum burnups as well as lower burnups.
←(DRN 00-1820, R10; 02-1477, R12; 04-502, R13; 05-508, R14; 06-1059, R15; EC-9533, R302; EC-13881, R304; EC-30663, R307, LBDCR 14-008, R308, LBDCR 15-035, R309; LBDCR 17-015, R310)

4.3A.3.2 Safety Related Data

4.3A.3.2.1 Augmentation Factors

As indicated in Reference 5, the increased power peaking associated with the small interpellet gaps found in modern fuel rods (non-densifying fuel in pre-pressurized tubes) is insignificant compared to the uncertainties in the safety analyses. The report concluded that augmentation factors can be eliminated from the reload analyses of any reactor loaded exclusively with this type of fuel. Therefore, augmentation factors have been eliminated for Waterford 3.

4.3A.3.3 Physics Analysis Methods

4.3A.3.3.1 Analytical Input To In-Core Measurements
→(EC-9533, R302)
In-core detector measurement constants to be used in evaluating the reload cycle power distributions were calculated in accordance with Reference 42.
←(EC-9533, R302)

4.3A.3.3.2 Uncertainties In Measured Power Distribution
→(EC-9533, R302)
The planar radial power distribution measurement uncertainty based upon Reference 42 is applied to the COLSS and CPC on-line calculations which use planar radial power peaks. The axial and three dimensional power distribution measurement uncertainties were determined using the values in Reference 42 in conjunction with other monitoring and protection system measurement uncertainties.
←(EC-9533, R302)

4.3A.3.3.3 Nuclear Design Methodology

→(DRN 06-1059, R15)

Beginning with Cycle 15, the Advanced Nodal Code (ANC) (References 37, 38, and 39) was implemented in the reload design analysis. ANC is an advanced nodal analysis theory code capable of two- or three-dimensional calculations. Also, beginning with Cycle 15, PARAGON (Reference 40) computer code was implemented in the reload design analysis. PARAGON is a two-dimensional transport theory based code that calculates lattice physics constants. These are the same methods and models that have been used in other Westinghouse reload cycle designs. These codes are replacements for the ROCS/DIT computer codes.

The primary purpose of PARAGON is to provide input data for use in three dimensional core simulator codes. This includes macroscopic cross sections, microscopic cross sections for feedback adjustments to the macroscopic cross sections, pin factors for pin power reconstruction calculations, and discontinuity factors for a nodal method solution. PARAGON can be used as a standalone or as a direct replacement for all the previously licensed Westinghouse Pressurized Water Reactor ("PWR") lattice codes, such as PHOENIX-P, as approved by the NRC in Reference 40.

→(EC-9533, R302)

PARAGON is a two-dimensional multi-group neutron (and gamma) transport code. The PARAGON flux solution calculation uses Collision Probability theory within the interface current method to solve the integral transport equation. Throughout the whole calculation, PARAGON uses the exact heterogeneous geometry of the assembly and the same energy groups as in the cross-section library to compute the multi-group fluxes for each micro-region location of the assembly.

In order to generate the multi-group data that will be used by a core simulator code, PARAGON goes through four steps of calculations: resonance self-shielding, flux solution, homogenization, and burnup calculation.

ANC (for Advanced Nodal Code) is the three-dimensional core simulator code in the Westinghouse nuclear design code system. The ANC nodal flux solution is based on a set of two-group diffusion theory nodal balance equations that are solved using a solution method based on the nodal expansion method (NEM). This method and the specific approximations made in the ANC implementation provide an accurate representation of the core nodal neutronics. ANC is used to calculate core reactivity, reactivity coefficients, critical boron, rod worths, and core, assembly, and rod power distributions for normal and off-normal conditions for use in design and safety analyses. The ANC computer code is also used in the COLSS/CPC uncertainty analysis, as a replacement for the ROCS code, which in turn was a replacement for the FLAIR computer code.

←(DRN 06-1059, R15; EC-9533, R302)

4.3A.4 THERMAL-HYDRAULIC DESIGN

4.3A.4.1 DNBR Analysis

→(DRN 02-523, R12; 03-2058, R14; EC-9533, R302; EC-13881, R304; EC-30663, R307)

Steady state DNBR analyses at the rated power level of 3716 MWT have been performed using the TORC computer code described in Reference 11, the WSSV-T and ABB-NV critical heat flux correlations applicable to NGF assemblies described in Reference 41 and 46, respectively, the TORC modeling methods described in References 11 and 13, and the CETOP code described in Reference 14.

←(DRN 02-523, R12; 03-2058, R14; EC-9533, R302; EC-30663, R307)

Table 4.3A-5 contains a list of pertinent thermal-hydraulic design parameters. The Modified Statistical Combination of Uncertainties (MSCU) methodology presented in Reference 15 was applied with Waterford 3 specific data using the calculational factors listed in Table 4.3A-5 and other uncertainty factors at the 95/95 confidence/probability level to define a design limit of 1.24 over a DNBR range of 1.0 to 1.24, applicable to both the ABB-NV and WSSV-T correlations.

←(EC-13881, R304)

The DNBR limit includes the following allowances:
→(EC-13881, R304)
1. NRC specified allowances for TORC code uncertainty.

2. Rod bow penalty as discussed in Section 4.3A.4.2 below.
→(EC-9533, R302)
←(EC-9533, R302; EC-13881, R304)

4.3A.4.2 Effects Of Fuel Rod Bowing on DNBR Margin
→(DRN 03-2058, R14; EC-9533, R302; EC-13881, R304)
Effects of fuel rod bowing on DNBR margin have been incorporated in the safety and setpoint analyses in the manner discussed in Reference 19. The penalty used for this analysis is valid for bundle burnups up to 33,000 MWD/T. This penalty is included in the 1.24 DNBR limit, applicable to both the ABB-NV and WSSV-T correlations.
←(EC-9533, R302; EC-13881, R304)

For assemblies with burnup greater than 33,000 MWD/T sufficient available margin exists to offset rod bow penalties due to the lower radial power peaks in these higher burnup batches. Hence the rod bow penalty based upon Reference 19 for 33,000 MWD/T is applicable for all assembly burnups expected.
←DRN 03-2058, R14)

4.3A.5 REACTOR PROTECTION AND MONITORING

4.3A.5.1 Introduction

The Core Protection Calculator (CPC) System is designed to provide the low DNBR and high Local Power Density (LPD) trips to (1) ensure that the specified acceptable fuel design limits on departure from nucleate boiling and centerline fuel melting are not exceeded during Anticipated Operational Occurrences (AOOs) and (2) assist the Engineered Safety Features System in limiting the consequences of certain postulated accidents. The CPCS is further described in subsection 7.2.1.1.2.5.

The CPC/CEAC in conjunction with the balance of the Reactor Protection System (RPS) must be capable of providing protection for certain specified design basis events, provided that at the initiation of these occurrences the Nuclear Steam Supply System, its sub-systems, components and parameters are maintained within operating limits and Limiting Conditions for Operation (LCOs).

4.3A.5.2 CPCS Software Modifications

The CPC/CEAC software for Waterford 3 was modified prior to Cycle 2. This modification implemented the CPC Improvement Program, including algorithms and plant specific data base changes, changes to the list of addressable constants and implementation of the Reload Data Block (RDB).

The Waterford 3 CPC/CEAC algorithms are the same as those implemented at SONGS-2 and -3 (Cycle 3) and at ANO-2 (Cycle 6) and described in References 21 and 22. The revised list of addressable constants are defined in Reference 23. The software modifications are described in References 23, 24, 25, and 29. All changes were implemented per the established software change procedures, References 26 and 27.

4.3A.5.3 Addressable Constants

Certain CPC constants are addressable so that they can be changed as required during operation. Addressable constants include (1) constants that are measured during startup (e.g., shape annealing matrix, boundary point power correlation coefficients, and adjustments for CEA shadowing and planar radial peaking factors), (2) uncertainty factors to account for processing and measurement uncertainties in DNBR and LPD calculations (BERRO through BERR4), (3) trip setpoints and (4) miscellaneous items (e.g., penalty factor multipliers, CEAC penalty factor time delay, pre-trip setpoints, CEAC inoperable flag, calibration constants, etc.).

Trip setpoints, uncertainty factors and other addressable constants have been determined consistent with the software and methodology established in the CPC Improvement Program (Reference 23, 24 and 25) and the cycle design, performance, and safety analyses.

4.3A.5.4 Digital Monitoring System (COLSS)

The Core Operating Limit Supervisory System (COLSS) is a monitoring system that initiates alarms if the LCO on DNBR, peak linear heat rate, core power, axial shape index, or core azimuthal tilt are exceeded. The COLSS is further described in subsection 7.7.1.5. The COLSS data base and uncertainties have been updated to reflect the current core design.

4.3A.6 REFERENCES TO APPENDIX 4.3A

1. W3P86-1686 dated August 29, 1986.

2. W3P86-3328 dated October 1, 1986.

3. J.H. Wilson (NRC), to J.G. Dewease (LP&L), "Reload Analysis Report for Cycle 2 at Waterford 3," January 16, 1987.

4. C.O. Thomas (NRC), to A.E. Scherer (C-E), "Acceptance for Referencing of Licensing Special Report LD-84-043, CEA Guide Tube Wear Sleeve Modification," September 7, 1984.

5. EPRI NP-3966-CCM, "CEPAN Method of Analyzing Creep Collapse of Oval Cladding Volume 5: Evaluation of Interpellet Gap Formation and Clad Collapse in Modern PWR Fuel Rods," April 1985.

6. CENPD-139-P-A, "C-E Fuel Evaluation Model Topical Report," July 1974.

7. CEN-161(B)-P-A, "Improvements to Fuel Evaluation Model," August 1989.

8. R.A. Clark (NRC) to A.E. Lundvall, Jr., (BG&E), "Safety Evaluation of CEN-161 (FATES3)," March 31, 1983.

9. ENEAD-02-NP, “Verification of CECOR Coefficient Methodology for Application to Pressurized Water Reactors of the Entergy System,” September 1994.

10. CENPD-266-P-A, "The ROCS and DIT Computer Codes for Nuclear Design," April 1983.

10B. CENPD-275-P-A, "C-E Methodology for Core Designs Containing Gadelinia-Urania Burnable Absorbers," May 1988.

11. CENPD-161-P-A, "TORC Code, A Computer Code for Determining the Thermal Margin of a Reactor Core," April 1986.

12. CENPD-162-P-A, "Critical Heat Flux Correlation for C-E Fuel Assemblies with Standard Spacer Grids, Part 1, Uniform Axial Power Distribution," September 1976.

13. CENPD-206-P-A, "TORC Code, Verification and Simplified Modeling Methods," June 1981.

14. CEN-160(S)-P, Rev. 1-P, "CETOP Code Structure and Modeling Methods for San Onofre Nuclear Generating Station Units 2 and 3," September 1981.

15. CEN-356(V)-P-A, Revision 01-P-A, "Modified Statistical Combination of Uncertainties, Part 1, Combination of System Parameter Uncertainties," May 1988.

→(EC-13881, R304)
16. Deleted

17. Deleted
←(EC-13881, R304)

18. NUREG-0787, Supplement 1, "Safety Evaluation Report Related to the Operation of Waterford Steam Electric Station, Unit No. 3," Docket No. 50-382, October 1981.

19. CENPD-225-P-A, "Fuel and Poison Rod Bowing," June 1983.

20. Robert A. Clark (NRC) to William Cavanaugh III, (AP&L), "Operation of ANO-2 During Cycle 2," July 21 1981 (Safety Evaluation Report and License Amendment No. 26 for ANO-2).

21. CEN-304-P, Rev. 01-P, "Functional Requirements for a Control Element Assembly Calculator," May 1986.

22. CEN-305-P, Rev. 01-P, "Functional Requirements for a Core Protection Calculator," May 1986.

23. CEN-308-P-A, "CPC/CEAC Software Modifications for the CPC Improvement Program," April 1986.

24. CEN-310-P-A, "CPC and Methodology Changes for the CPC Improvement Program," April 1986.

25. CEN-330-P-A, "Rev. 00-P, "CPC/CEAC Software Modifications for the CPC Improvement Program Reload Data Block," October 1987.

26. CEN-39(A)-P, Rev. 03, "CPC Protection Algorithm Software Change Procedure," January 1986.

27. CEN-39(A)-P, Supplement 1-P, Rev. 03-P, "CPC Protection Algorithm Software Change Procedure Supplement 1," April 1986.

28. CEN-323-P-A, "Reload Data Block Constant Installation Guidelines," September 1986.

29. CEN-281(S)-P, "CPC/CEAC Software Modifications for San Onofre Nuclear Steam Generating Station Units No. 2 and 3," July 1984.

30. LP&L (KW Cook) letter to NRC, "Cycle 3 Shoulder Gap Evaluation," July 24, 1987.

31. Deleted.

32. CEN-161(B)-P-A Supplement 1-P-A, "Improvements to Fuel Evaluation Model," January 1992.

33. CEN-372-P-A, “Fuel Rod Maximum Allowable Gas Pressure,” May 1990

34. CEN-386-P-A, "Verification of the Acceptability of a 1-Pin Burnup Limit of 60 MWD/Kg for Combustion Engineering 16 x 16 PWR Fuel," August 1992.

➔(EC-13881, R304)
35. WCAP-16072-P-A, “Implementation of Zirconium Diboride Burnable Absorber Coatings in CE Nuclear Power Fuel Assembly Designs,” August 2004.
←(EC-13881, R304)

➔(DRN 03-270, R12-B)
36. ENEAD-01-P, Revision 0, “Qualification of Reactor Physics Methods for the Pressurized Water Reactors of the Entergy System,” December 1993.
←(DRN 03-270, R12-B)

➔(EC-9533, R302)
37. WCAP-11596-P-A, “Qualification of the PHOENIX-P/ANC Nuclear Design System for Pressurized Water Reactor Cores,” June 1988

38. WCAP-10965-P-A, “ANC: A Westinghouse Advanced Nodal Computer Code,” September 1986

39. WCAP-10965-P-A Addendum 1, “ANC: A Westinghouse Advanced Nodal Computer Code: Enhancements to ANC Rod Power Recovery,” April 1989

40. WCAP-16045-P-A, “Qualification of the Two-Dimensional Transport Code PARAGON,” August 2004

41. WCAP-16523-P-A, Rev. 0. “Westinghouse Correlations WSSV and WSSV-T for Predicting Critical Heat Flux in Rod Bundles with Side-Supported Mixing Vanes”, August 2007.

42. CENPD-153-P, Revision 1-P-A, “Evaluation of Uncertainty in the Nuclear Power Peaking Measured by the Self-Powered, Fixed In-Core Detector System”, May 1980.
←(EC-9533, R302)
➔(EC-13881, R304, LBDCR 14-008, R038)
43. WCAP-16500-P-A, “CE 16x16 Next Generation Fuel Core Reference Report”, August 2007.

44. WCAP-12610-P-A and CENPD-404-P-A Addendum 1-A, “Optimized ZIRLO™”, July 2006.

45. CENPD-404-P-A, “Implementation of ZIRLO™ Material Cladding in CE Nuclear Power Fuel Assembly Designs,” November 2001.

46. CENPD-387-P-A, “ABB Critical Heat Flux Correlations for PWR Fuel,” May 2000.
←(EC-13881, R304, LBDCR 14-008, R308)

→(DRN 00-1820, R10; 02-1477, R12; 04-502, R13; 05-508, R14; 06-1059, R15; EC-9533, R302; EC-13881, R304; EC-30663, R307, LBDCR 14-008, R308, LBDCR 15-035, R309; LBDCR 17-015, R310)

Waterford - 3 Cycle 22 Core Loading Description

Sub-Batch ID	Number of Assemblies	Pattern ID	UO_2 Rods per Assembly	Nominal Enrichment (wt. %)	ZrB_2 Rods per Assembly	Shim Loading (ZrB_2)	Number of Fuel Rods (Including ZrB_2 Rods)	Number of ZrB_2 Rods
GA	16	PAT1632IFB	176	4.86	8	2.0 X	2944	128
		(48 IFBA)	12	4.46	40	2.0 X	832	640
GB	4	PAT1648IFB	124	4.86	60	2.0 X	736	240
		(88 IFBA)	24	4.46	28	2.0 X	208	112
GC	12	PAT1636IFB	112	4.86	72	2.0 X	2208	864
		(124 IFBA)	0	4.46	52	2.0 X	624	624
GD	60	PAT1650IFB	92	4.56	92	2.0 X	11040	5520
		(136 IFBA)	8	4.16	44	2.0 X	3120	2640
GU	8	PAT1636IFB	112	4.86	72	2.0 X	1472	576
		(124 IFBA)	0	4.46	52	2.0 X	416	416
Total	100						23600	11760
EA	20	PAT1633IFB	164	4.38	20	2.0 X	3680	400
		(60 IFBA)	12	3.98	40	2.0 X	1040	800
EB	8	PAT1649IFB	116	4.38	68	2.0 X	1472	544
		(112 IFBA)	8	3.98	44	2.0 X	416	352
EC	4	PAT1632IFB	176	3.98	8	2.0 X	736	32
		(48 IFBA)	12	3.58	40	2.0 X	208	160
ED	48	PAT1649IFB	116	3.98	68	2.0 X	8832	3264
		(112 IFBA)	8	3.58	44	2.0 X	2496	2112
EE	16	PAT1636IFB	112	3.98	72	2.0 X	2944	1152
		(124 IFBA)	0	3.58	52	2.0 X	832	832
Total	96						22656	9648
DA	4	PAT16432FB	176	4.53	8	2.0 X	736	32
		(48 IFBA)	12	4.23	40	2.0 X	208	160
DG	16	PAT1650IFB	92	3.83	92	2.0 X	2944	1472
		(136 IFBA)	8	3.53	44	2.0 X	832	704
Total	20						4720	2368
AD	1	PAT1635IFB	136	3.90	48	2.0 X	184	48
		(100 IFBA)	0	3.50	52	2.0 X	52	52
Total	1						236	100
Grand Total	217						51212	23876

←(DRN 00-1820, R10; 02-1477, R12; 04-502, R13; 05-508, R14; 06-1059, R15; EC-9533, R302; EC-13881, R304; EC-30663, R307, LBDCR 14-008, R308, LBDCR 15-035, R309; LBDCR 17-015, R310)

TABLE 4.3A-2 Revision 310 (12/17)

→(DRN 05-508, R14; 06-1059, R15; EC-9533, R302; EC-13881, R304; EC-30663, R307, LBDCR 14-008, R308, LBDCR 15-035, R309; LBDCR 17-015, R310)

NOMINAL PHYSICS CHARACTERISTICS

	Units	Reference Cycle**	Cycle 22*
Dissolved Boron			
Dissolved Boron Concentration for Criticality, CEAs Withdrawn, Hot Full Power, Equilibrium Xenon	PPM	583	713
Inverse Boron Worth			
Hot Full Power, Equilibrium Xenon			
BOC	PPM/%Δρ	130	139
EOC	PPM/%Δρ	104	108
Moderator Temperature Coefficients			
Hot Full Power, Equilibrium Xenon			
BOC	10^{-4}Δρ/°F	-1.4	-1.2
EOC	10^{-4}Δρ/°F	-2.9	-2.9
Doppler Coefficient			
Hot Zero Power, BOC	10^{-5}Δρ/°F	-1.7	-1.7
Hot Full Power, Equilibrium Xenon			
BOC	10^{-5}Δρ/°F	-1.6	-1.6
EOC	10^{-5}Δρ/°F	-1.8	-1.8
Total Delayed Neutron Fraction βeff			
BOC	----------	0.0061	0.0061
EOC	----------	0.0050	0.0050
Neutron Generation Time, τ*			
BOC	10^{-6} sec	18.0	15.8
EOC	10^{-6} sec	27.9	26.8

* values vary with cycle

** Reference cycle is Cycle 21

←(DRN 05-508, R14; 06-1059, R15; EC-9533, R302; EC-13881, R304; EC-30663, R307, LBDCR 14-008, R308, LBDCR 15-035, R309; LBDCR 17-015, R310)

TABLE 4.3A-3 Revision 310 (12/17)

LIMITING VALUES OF
REACTIVITY WORTHS AND ALLOWANCES FOR HOT
FULL POWER STEAM LINE BREAK, %Δρ, END-OF-CYCLE (EOC)

→(DRN 05-508, R14; 06-1059, R15; EC-9533, R302; EC-13881, R304; EC-30663, R307, LBDCR 14-008, R308, LBDCR 15-035, R309; LBDCR 17-015, R310)

	Reference Cycle**	Cycle 22*
Net Available Scram Worth (No LOAC)	7.9	7.9

* values vary with cycle
** Reference cycle is Cycle 21

←(DRN 05-508, R14; 06-1059, R15; EC-9533, R302; EC-13881, R304; EC-30663, R307, LBDCR 14-008, R308, LBDCR 15-035, R309; LBDCR 17-015, R310)

TABLE 4.3A-4 Revision 310 (12/17)

REACTIVITY WORTH OF CEA REGULATING GROUPS
AT HOT FULL POWER, %Δρ

→(DRN 05-508, R14; 06-1059, R15; EC-9533, R302; EC-13881, R304; EC-30663, R307, LBDCR 14-008, R308, LBDCR 15-035, R309; LBDCR 17-015, R310)

	Beginning of Cycle		End Of Cycle	
←(EC-13881, R304)	Reference Cycle**	Cycle 22*	Reference Cycle**	Cycle 22*
Group P @ 0"	0.4	0.4	0.4	0.4
Group 6 @ 0"	0.4	0.4	0.4	0.4
Group 5 @ 0"	0.3	0.4	0.4	0.4

Note: Values shown assume sequential group insertion

* Values vary with cycle
→(EC-13881, R304)
** Reference cycle is Cycle 21
←(DRN 05-508, R14; 06-1059, R15; EC-9533, R302; EC-13881, R304; EC-30663, R307, LBDCR 14-008, R308, LBDCR 15-035, 309; LBDCR 17-015, R310)

→(DRN 00-1820, R10; 02-523, R12; 02-1477, R12; 04-502, R13 ,03-2058, R14; 05-508, R14; 06-1059, R15; EC-9533, R302; EC-13881, R304; EC-30663, R307, LBDCR 14-008, R308, LBDCR 15-035, R309; LBDCR 17-015, R310)

Cycle 22
Thermal-Hydraulic Parameters at Full Power

General Characteristics	Units	Cycle 21	Cycle 22
Total Heat Output (Core Only)	(MW_{th})	3716	3716
	(10^6 Btu/hr)	12680	12680
Fraction of Heat Generated in Fuel Rod	---	0.975	0.975
Primary System Pressure (Nominal)	(psia)	2250	2250
Inlet Temperature (Maximum Indicated)	(°F)	543	543
Total Reactor Coolant Flow (Minimum Steady State)	(gpm)	390,220	390,220
	(10^6 lbm/hr)	148.0	148.0
Coolant Flow Through Core (Minimum)	(10^6 lbm/hr)	144.2	144.2
Hydraulic Diameter (Nominal Channel)	(ft)	0.041	0.041
Core Average Mass Velocity	(10^6 lbm/hr-ft^2)	2.55	2.55
Pressure Drop Across Core (at Minimum Steady State Core Flow Rate)	(psi)	20.7	20.7
Total Pressure Drop Across Vessel (Based on Nominal Dimensions and Minimum Steady State Flow)	(psi)	46.6	46.6
Core Average Heat Flux (Accounts for Fraction of Heat Generated in Fuel Rod and Axial Densification Factor)	(Btu/hr-ft^2)	198,016(1)	198,016(1)
Total Heat Transfer Area (Accounts for Axial Densification Factor)	(ft^2)	62,432(1)	62,432(1)
Film Coefficient at Average Conditions	(Btu/hr-ft^2-°F)	6092	6092
Average Film Temperature Difference	(°F)	32.50(1)	32.50(1)
Average Linear Heat Rate of Undensified Fuel Rod (Accounts for Fraction of Heat Generated In Fuel Rod)	(kw/ft)	5.67(1)	5.67(1)
Average Core Enthalpy Rise	(Btu/lbm)	88.0	88.0
Maximum Clad Surface Temperature	(°F)	656.76(1)	656.76(1)
Engineering Heat Flux Factor	---	1.03(2),(3)	1.03(2),(3)
Engineering Factor on Hot Channel Heat Input	---	1.03(2),(3)	1.03(2),(3)
Rod Pitch, Bowing and Clad Diameter Factor	---	1.05(2),(3)	1.05(2),(3)
Fuel Densification Factor (Axial)	---	1.002	1.002

(1) Based on 100 shims (non fuel rods) in the core and 217 NGF assemblies.
(2) These factors have been combined statistically with other uncertainty factors at 95/95 confidence/probability level and included in the design limit on ABB-NV minimum DNBR and WSSV-T minimum DNBR.
(3) These values are generic based on fuel design drawing tolerances and are also applicable to NGF.

←(DRN 00-1820, R10; 02-523, R12; 02-1477, R12; 04-502, R13 ,03-2058, R14; 05-508, R14; 06-1059, R15; EC-9533, R302; EC-13881, R304; EC-30663, R307, LBDCR 14-008, R308, LBDCR 15-035, R309; LBDCR 17-015, R310)

Region GA
PAT1632IFB 48 ZrB_2 Rods

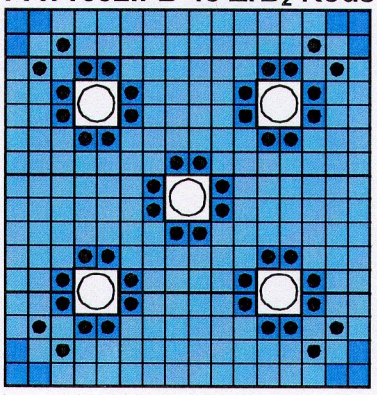

Region GB
PAT1648IFB 88 ZrB_2 Rods

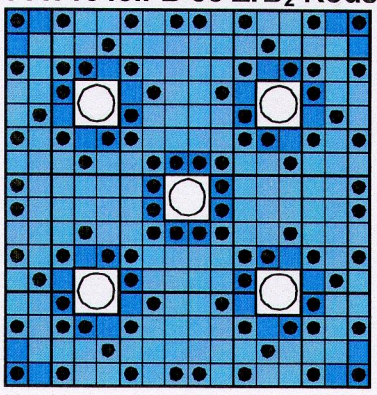

Region GC and GU
PAT1636IFB 124 ZrB_2 Rods

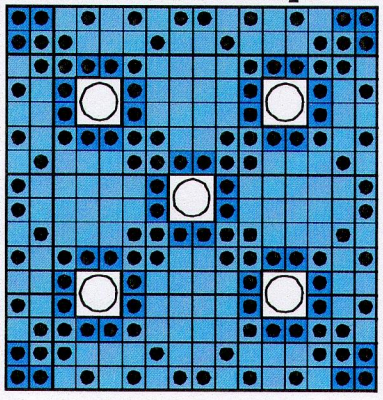

Region GD
PAT1650IFB 136 ZrB_2 Rods

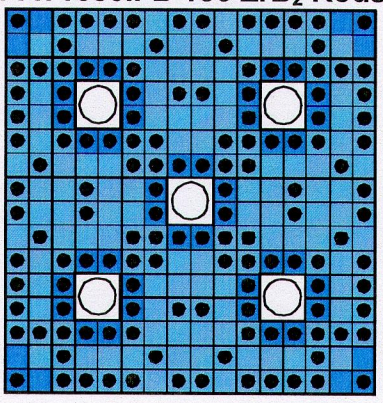

Low Enriched Fuel Rod with ZrB_2

Low Enriched Fuel Rod

High Enriched Fuel Rod with ZrB_2

High Enriched Fuel Rod

REV. 310 (12/17)

Waterford Steam Electric Station #3	WATERFORD-3 CYCLE 22 INTEGRAL BURNABLE POISON SHIM AND ENRICHMENT ZONING PATTERNS	Figure 4.3A-1

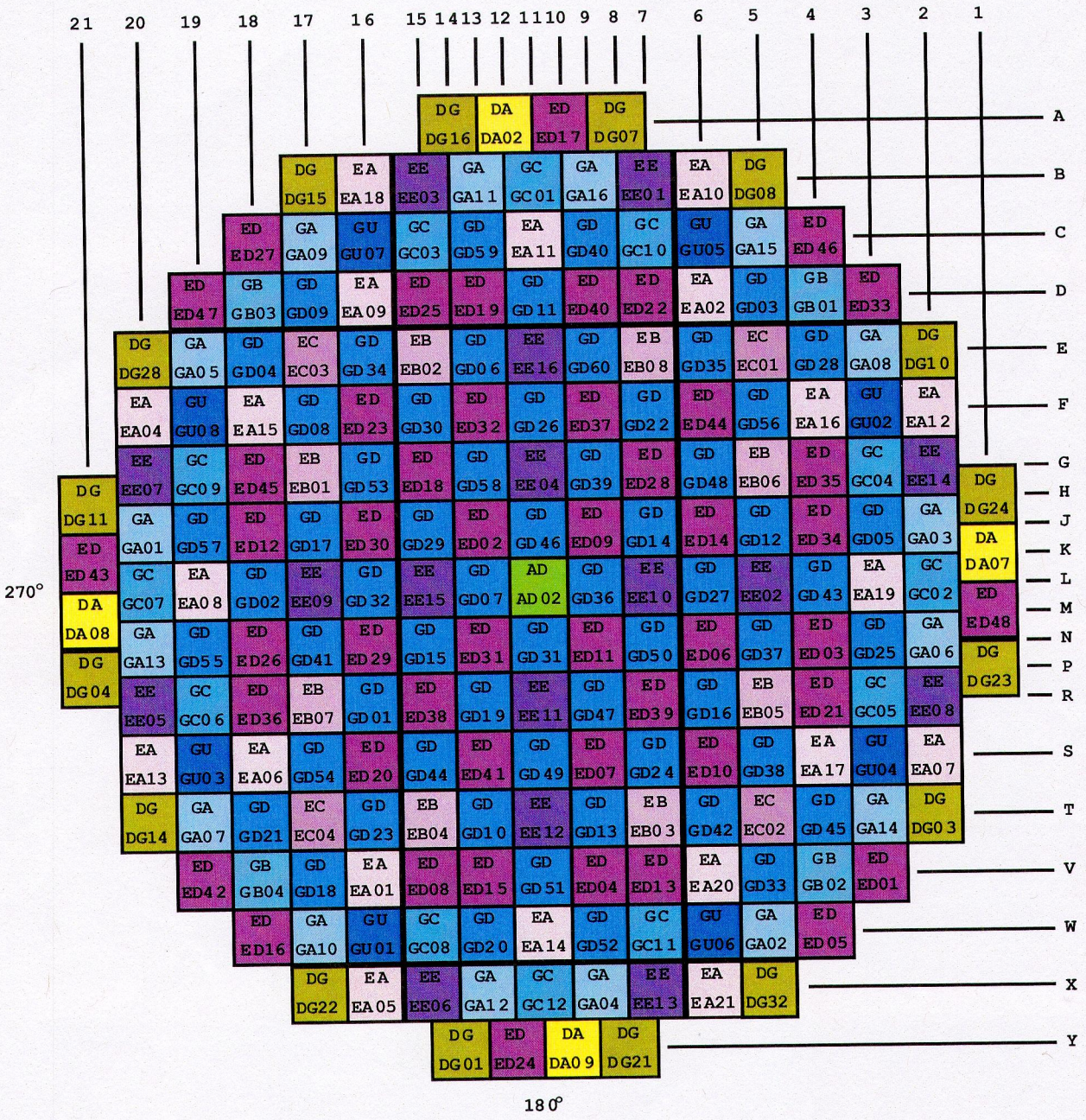

Note: 180° indicates plant South.

REV.310 (12/17)

Waterford Steam Electric Station #3	WATERFORD-3 CYCLE 22 FUEL MANAGEMENT SCHEME	Figure 4.3A-2

→(EC-9533, R302)

Figure 4.3A-3 has been intentionally deleted.

←(EC-9533, R302)

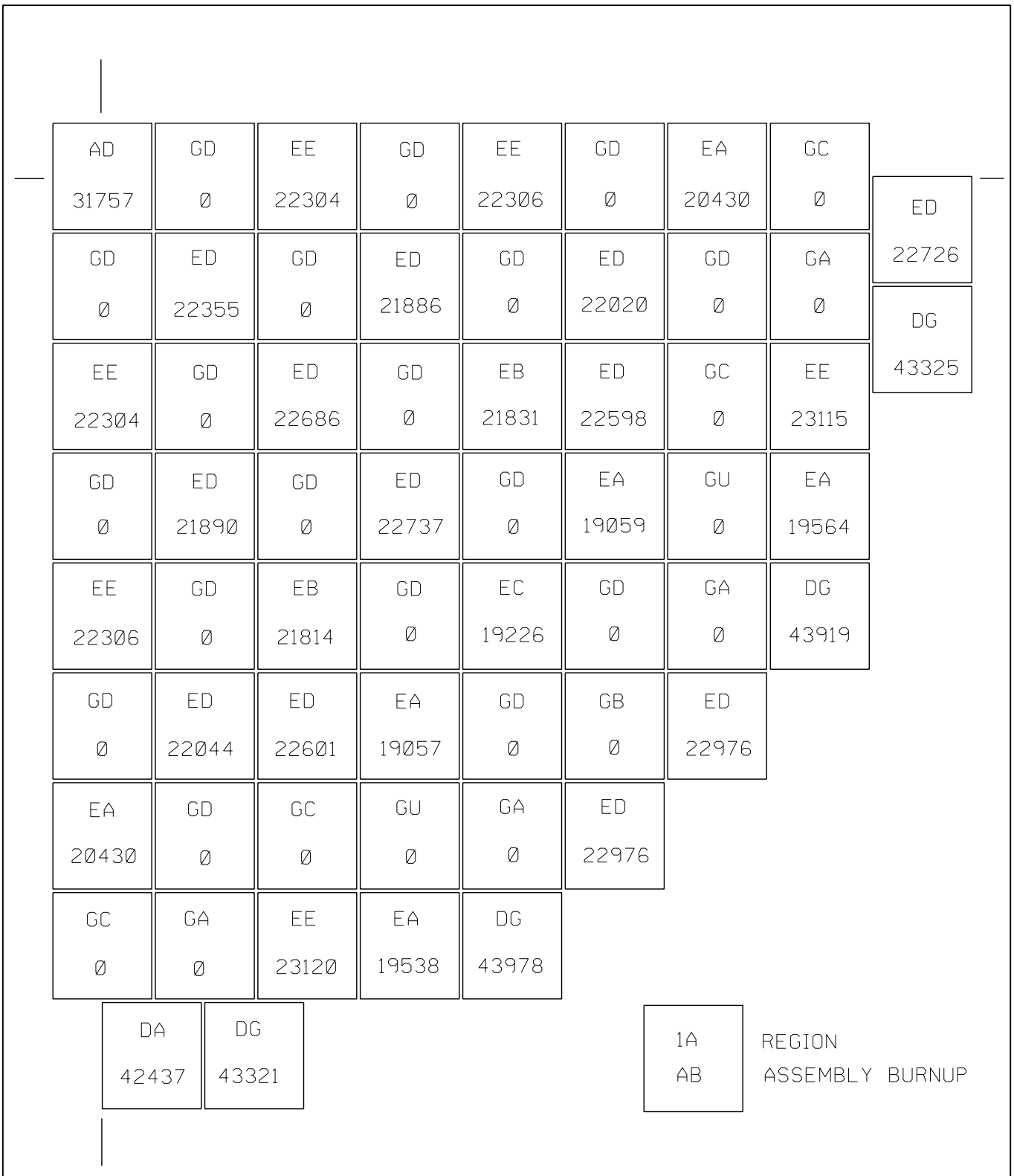

REVISION 310 (12/17)

Waterford Steam Electric Station #3	WATERFORD 3 - CYCLE 22 BEGINNING OF CYCLE FROM SHORT ENDPOINT OF PREVIOUS CYCLE (BOCS) ASSEMBLY AVERAGE BURNUP	Figure 4.3A-3a

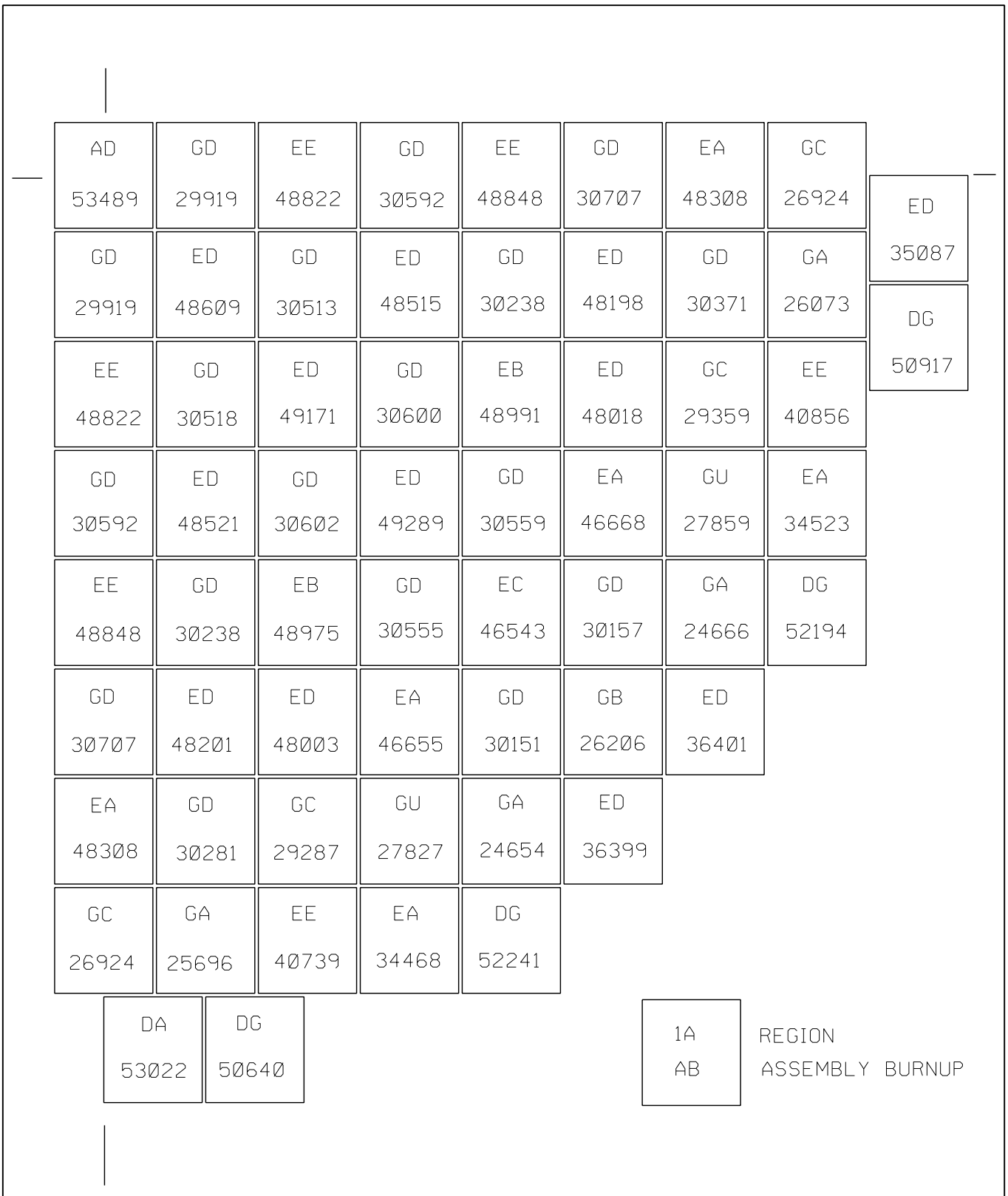

REVISION 310 (12/17)

Waterford Steam Electric Station #3	WATERFORD 3 - CYCLE 22 END OF CYCLE FROM LONG ENDPOINT OF PREVIOUS CYCLE (EOCL) ASSEMBLY AVERAGE BURNUP	Figure 4.3A-3b

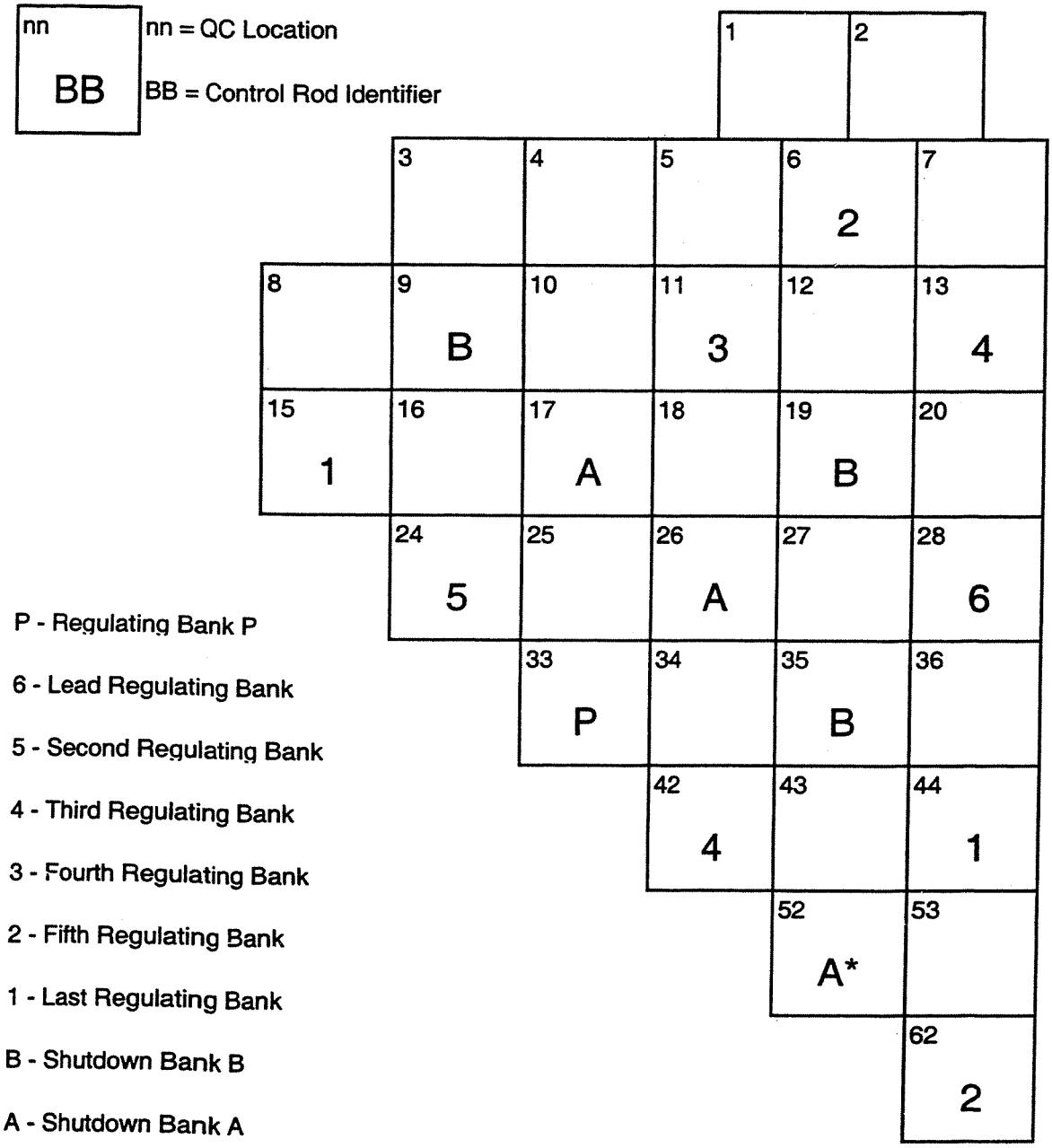

* Shutdown rod in position 52 is available for only two diagonally opposite core quadrants.

Revision 12 (10/02)

Waterford Steam Electric Station #3	Waterford 3 CEA Bank Identification	Figure 4.3A-4

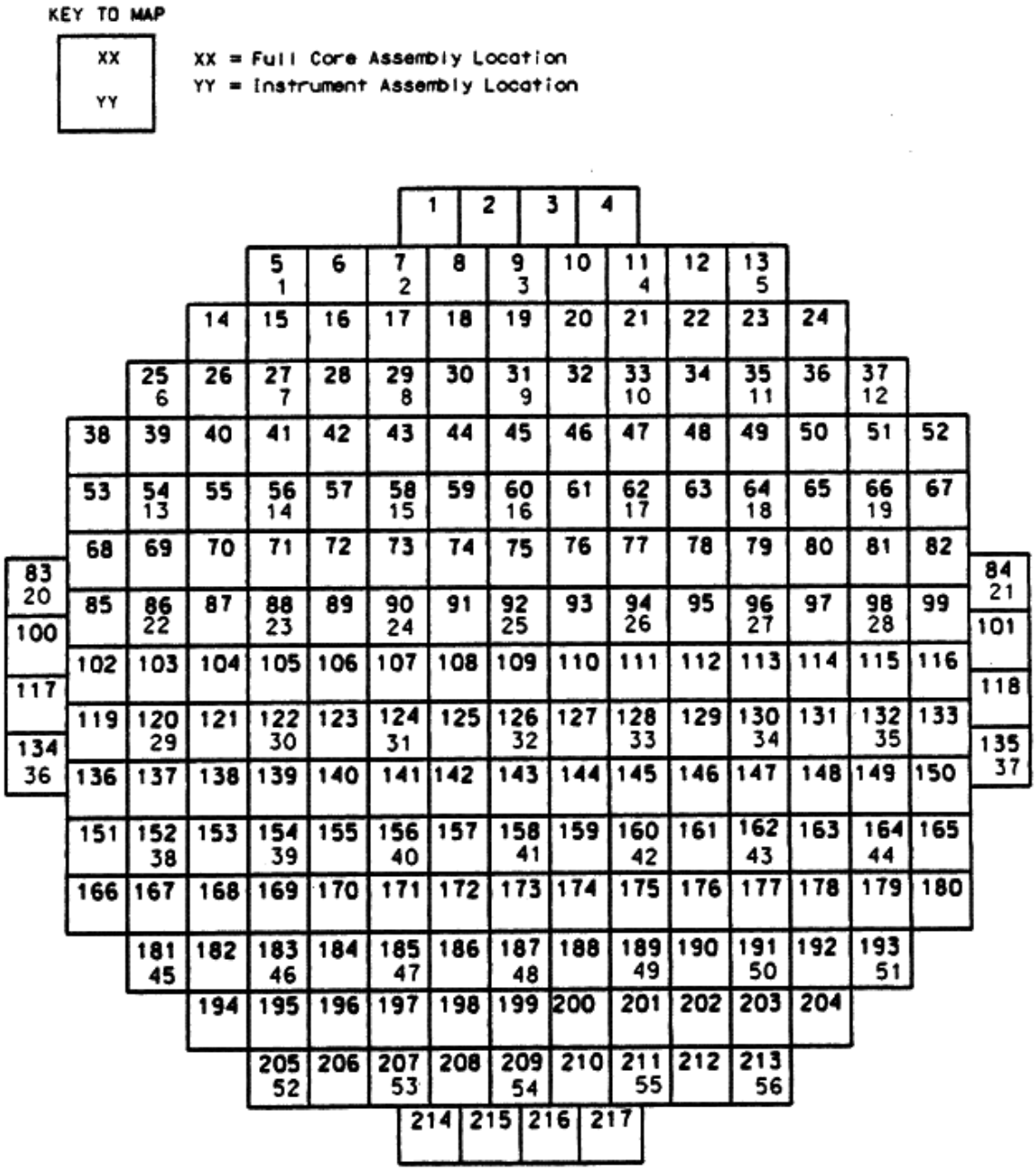

NOTE : THERE ARE NO INCORE INSTRUMENT ASSEMBLIES AT CORE LOCATIONS 9, 11, AND 30.

Revision 304 (06/10)

Waterford Steam Electric Station #3	WATERFORD 3 IN-CORE INSTRUMENT ASSEMBLIES CORE LOCATIONS	Figure 4.3A-5

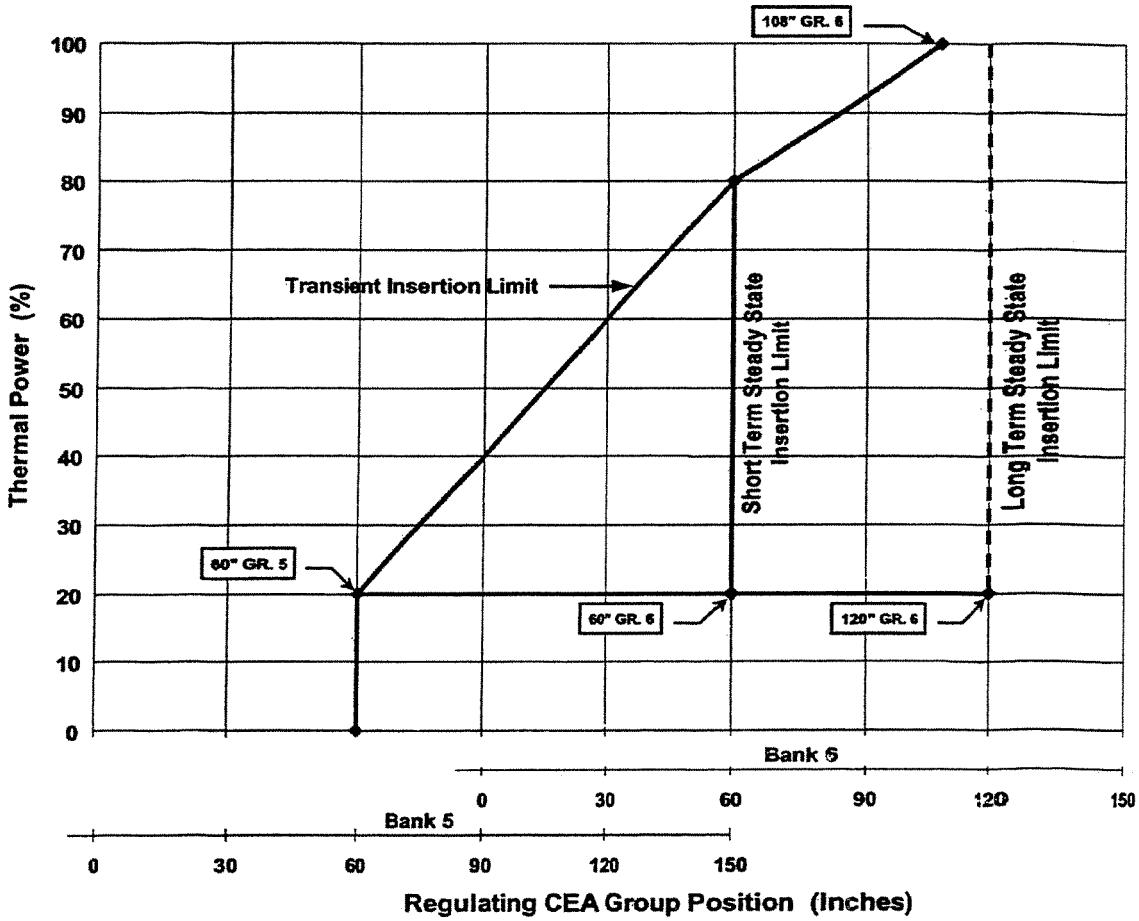

Revision 12 (10/02)

Waterford Steam Electric Station #3	WATERFORD 3 PDIL FOR REGULATING GROUPS	Figure 4.3A-6

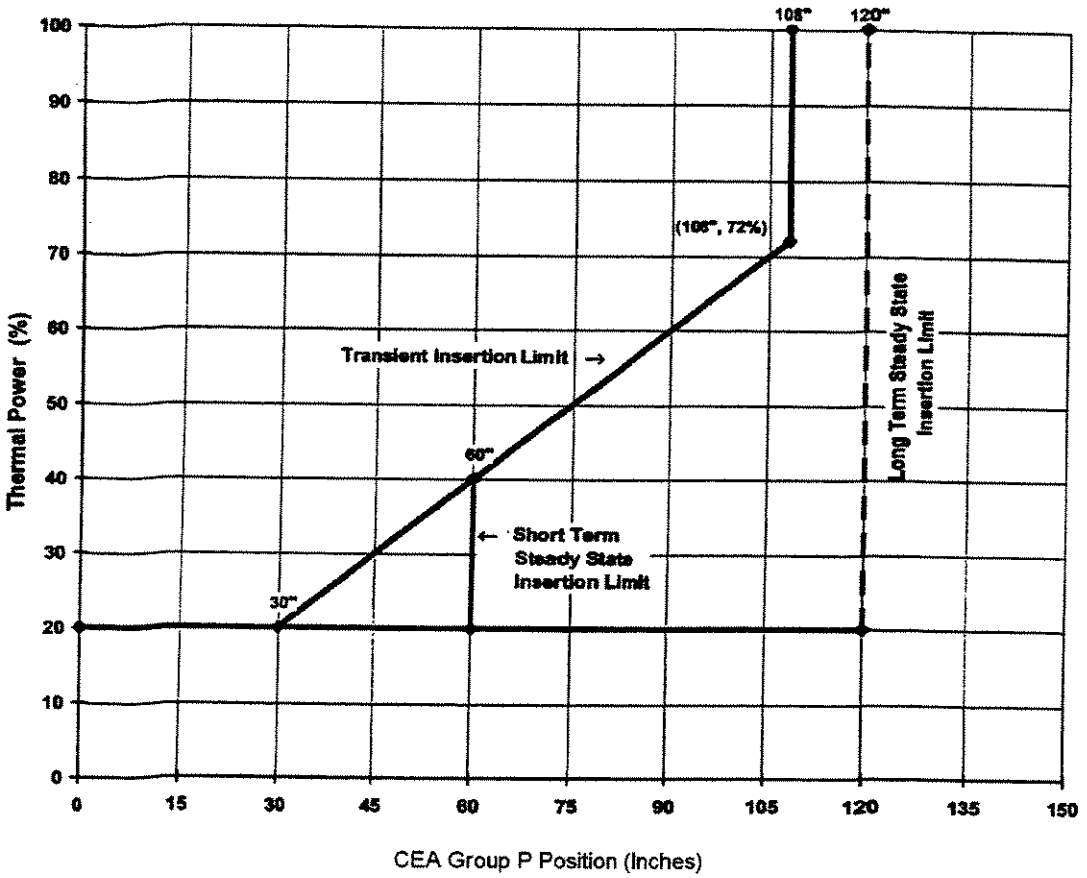

Revision 13 (04/04)

Waterford Steam Electric Station #3	WATERFORD 3 CEA GROUP P INSERTION LIMIT VS THERMAL POWER	Figure 4.3A-7

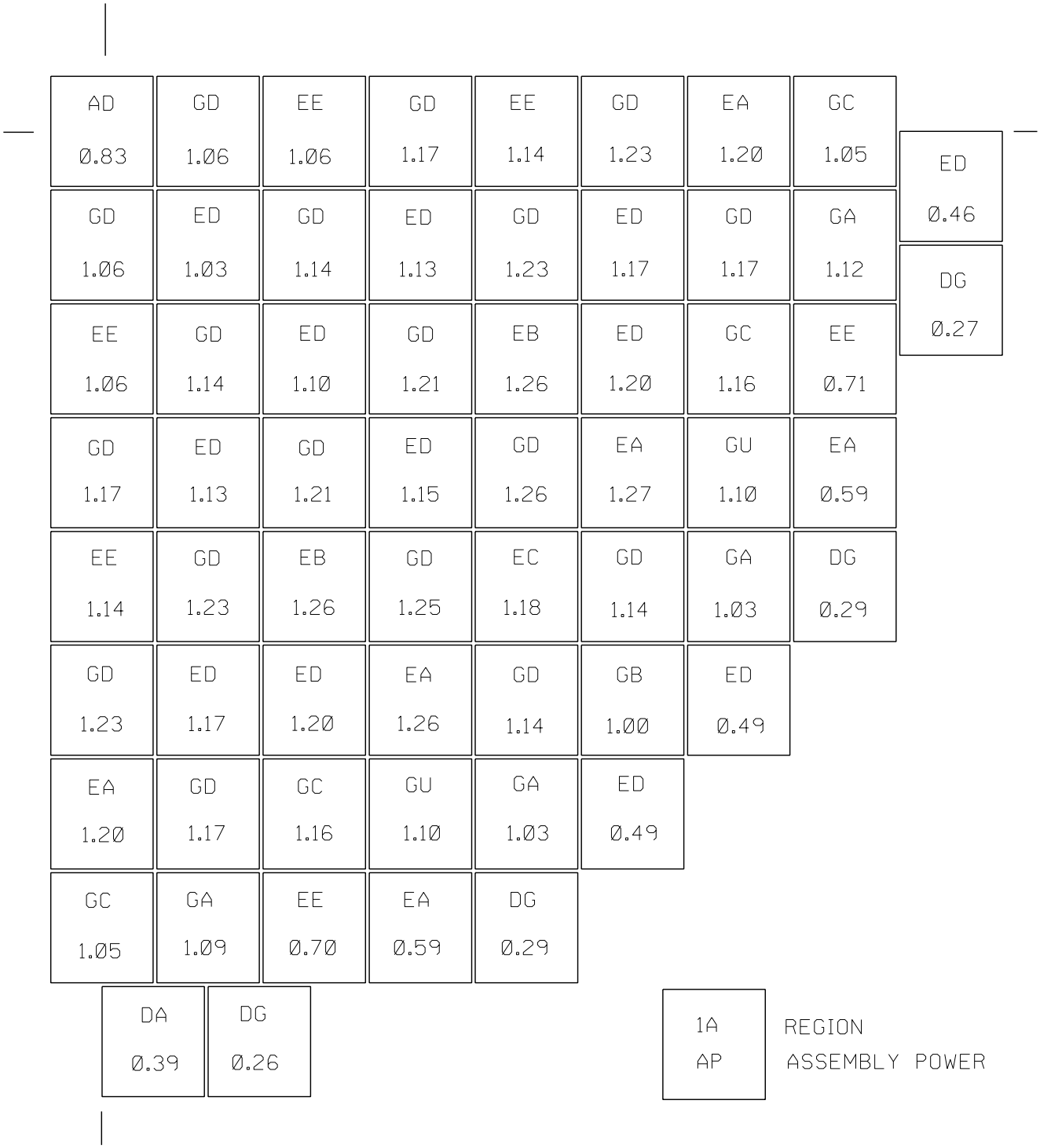

MAXIMUM 1-PIN PEAK (FXY) = 1.414 IN FULL CORE (FC) ASSEMBLY NUMBER 149

REVISION 310 (12/17)

Waterford Steam Electric Station #3	WATERFORD 3 - CYCLE 22 ASSEMBLY RELATIVE POWER DENSITY BOCS, HOT FULL POWER (HFP), EQUILIBRIUM XENON, ARO	Figure 4.3A-8

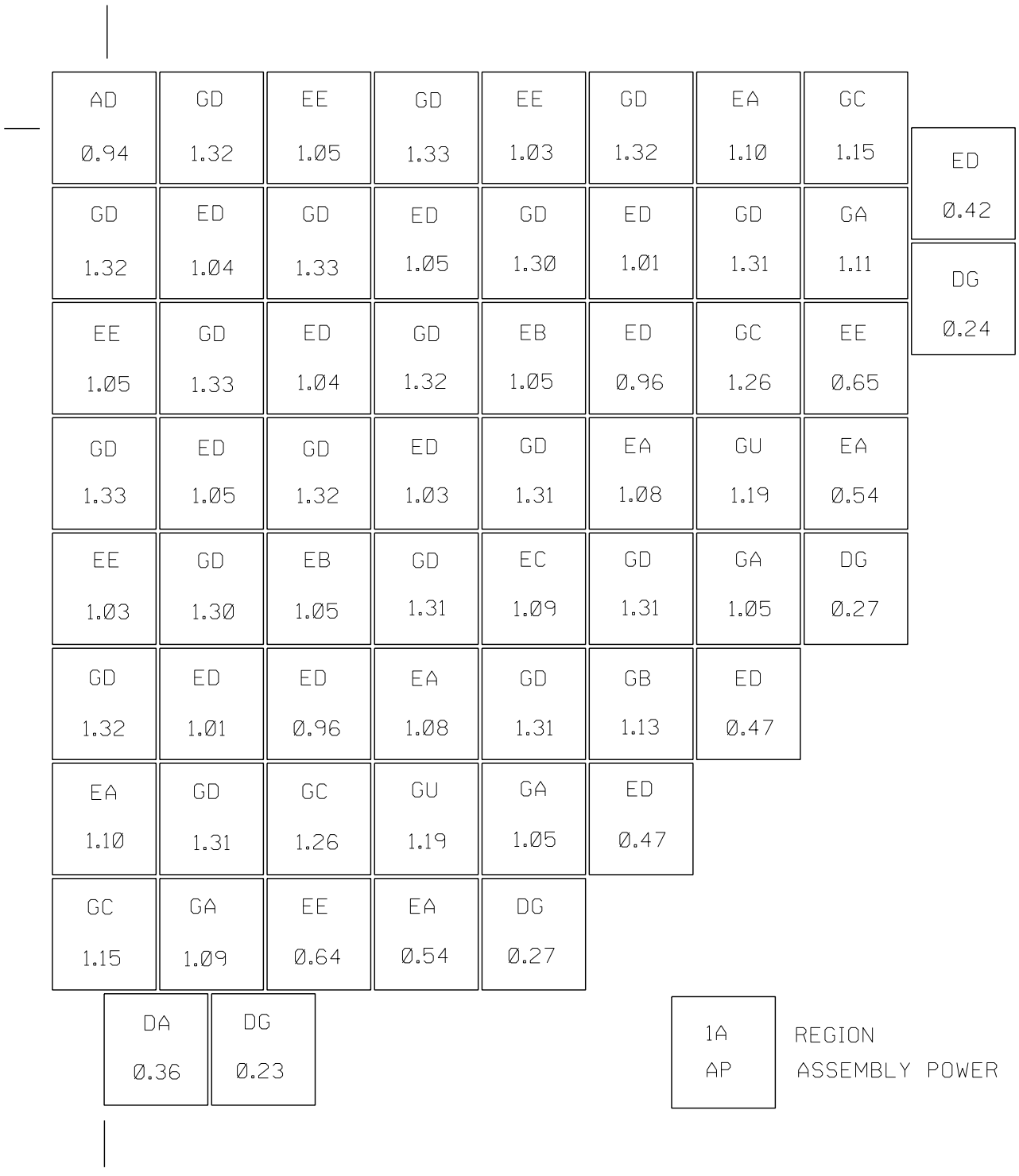

MAXIMUM 1-PIN PEAK (F_{xy}) = 1.451 IN FC ASSEMBLY NUMBER 192

REVISION 310 (12/17)

Waterford Steam Electric Station #3	WATERFORD 3 - CYCLE 22 ASSEMBLY RELATIVE POWER DENSITY MIDDLE OF CYCLE FROM LONG ENDPOINT OF PREVIOUS CYCLE (MOCL), HFP, EQUILIBRIUM XENON, ARO	Figure 4.3A-9

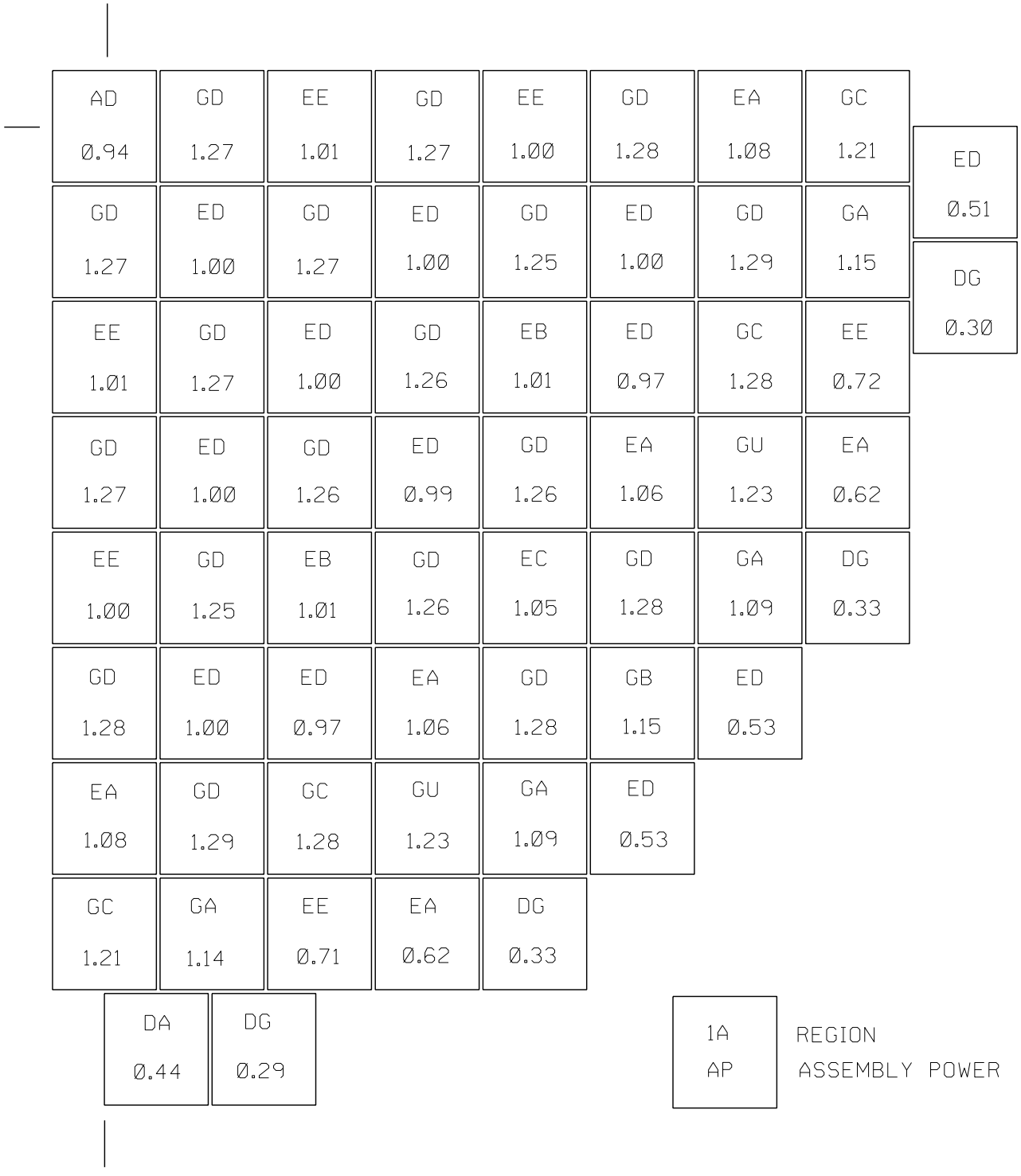

MAXIMUM 1-PIN PEAK (F_{xy}) = 1.378 IN FC ASSEMBLY NUMBER 201

REVISION 310 (12/17)

Waterford Steam Electric Station #3	WATERFORD 3 - CYCLE 22 ASSEMBLY RELATIVE POWER DENSITY EOCL, HFP, EQUILIBRIUM XENON, ARO	Figure 4.3A-10

FIGURE 4.3A-11
HAS BEEN INTENTIONALLY
DELETED

REVISION 6 (12/92)

Waterford Steam Electric Station •3	**WATERFORD 3 - CYCLE 6** ASSEMBLY RELATIVE POWER DENSITY HFP AT BOC. EQUILIBRIUM XENON, PLCEAS	Figure 4.3A-11

FIGURE 4.3A-12
HAS BEEN INTENT I ONALLY
DELETED

REVISION 6 (12/92)

Waterford Steam Electric Station *3	WATERFORD 3 - CYCLE 6 ASSEMBLY RELATIVE POWER DENSITY HFP AT BOC, EQUILIBRIUM XENON, WITH BANK 6	Figure 4.3A-12

FIGURE 4.3A-13
HAS BEEN INTENTIONALLY
DELETED

REVISION 6 (12/92)

Woterford Steam Electric Station *3	WATERFORD 3 - CYCLE 6 ASSEMBLY RELATIVE POWER DENSITY HFP AT BOC. EQUILIBRIUM XENON, WITH BANK 6 AND PLCEAS	Figure 4.3A-13

FIGURE 4.3A-14
HAS BEEN INTENTIONALLY
DELETED

REVISION 6 (12/92)

Woterford Steam Electric Station *3	WATERFORD 3 - CYCLE 6 ASSEMBLY RELATIVE POWER DENSITY HFP AT EOC. EQUILIBRIUM XENON, WITH PLCEAS	Figure 4.3A-14

FIGURE 4.3A-15
HAS BEEN INTENTIONALLY
DELETED

REVISION 6 (12/92)

Waterford Steam Electric Station ● 3	WATERFORD 3 - CYCLE 6 ASSEMBLY RELATIVE POWER DENSITY HFP AT EOC, EQUILIBRIUM XENON WITH BANK 6	Figure 4.3A-15

FIGURE 4.3A-16
HAS BEEN INTENTIONALLY
DELETED

REVISION 6 (12/92)

Waterford Steam Electric Station ● 3	WATERFORD 3 - CYCLE 6 ASSEMBLY RELATIVE POWER DENSITY HFP AT EOC, EQUILIBRIUM XENON, WITH BANK 6 AND PLCEAS	Figure 4.3A-16

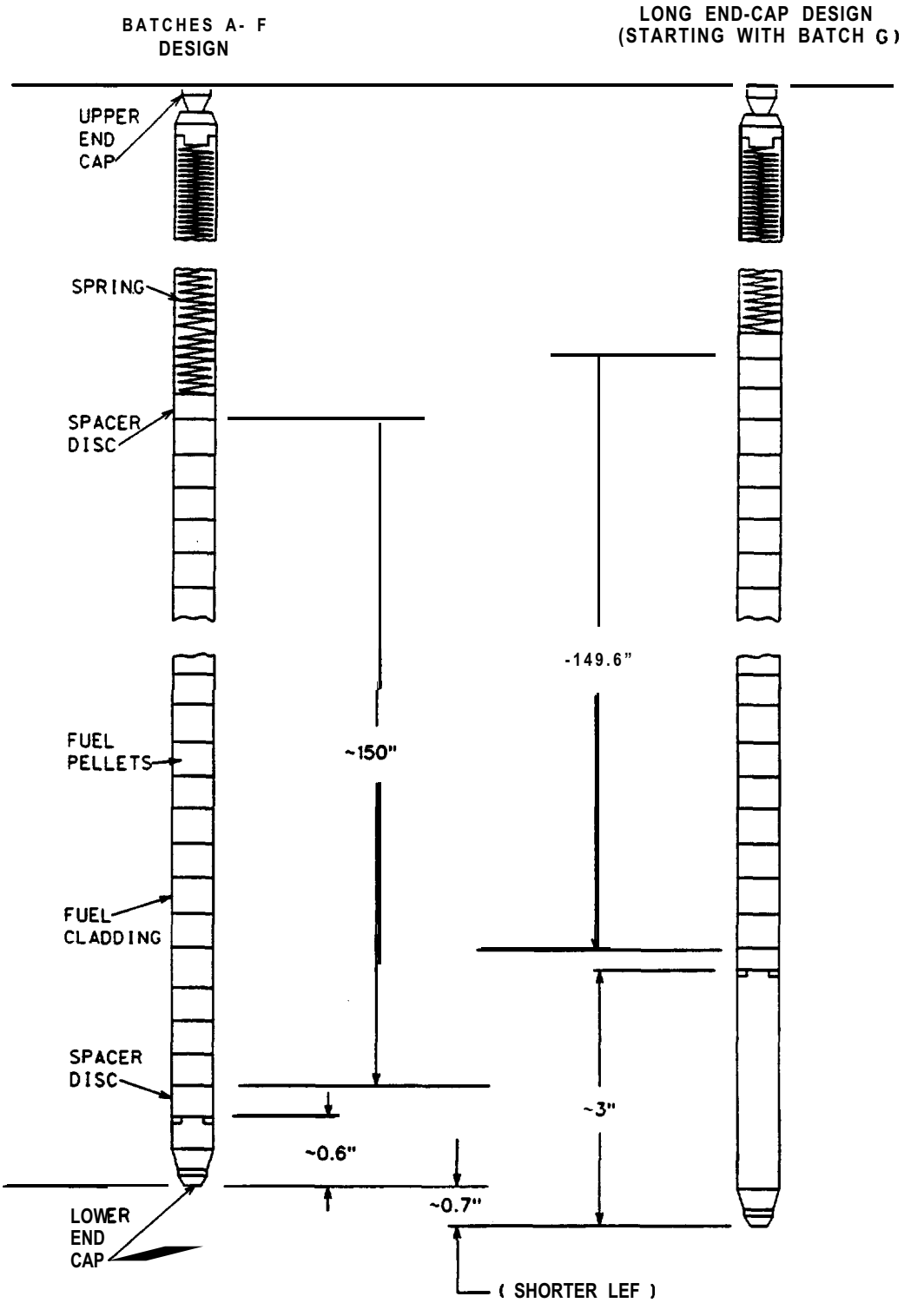

REVISION 6 (12/92)

Waterford Steam Electric Station •3	FUEL ROD AND LOWER END FITTING CHANGES	Figure 4.3A-17

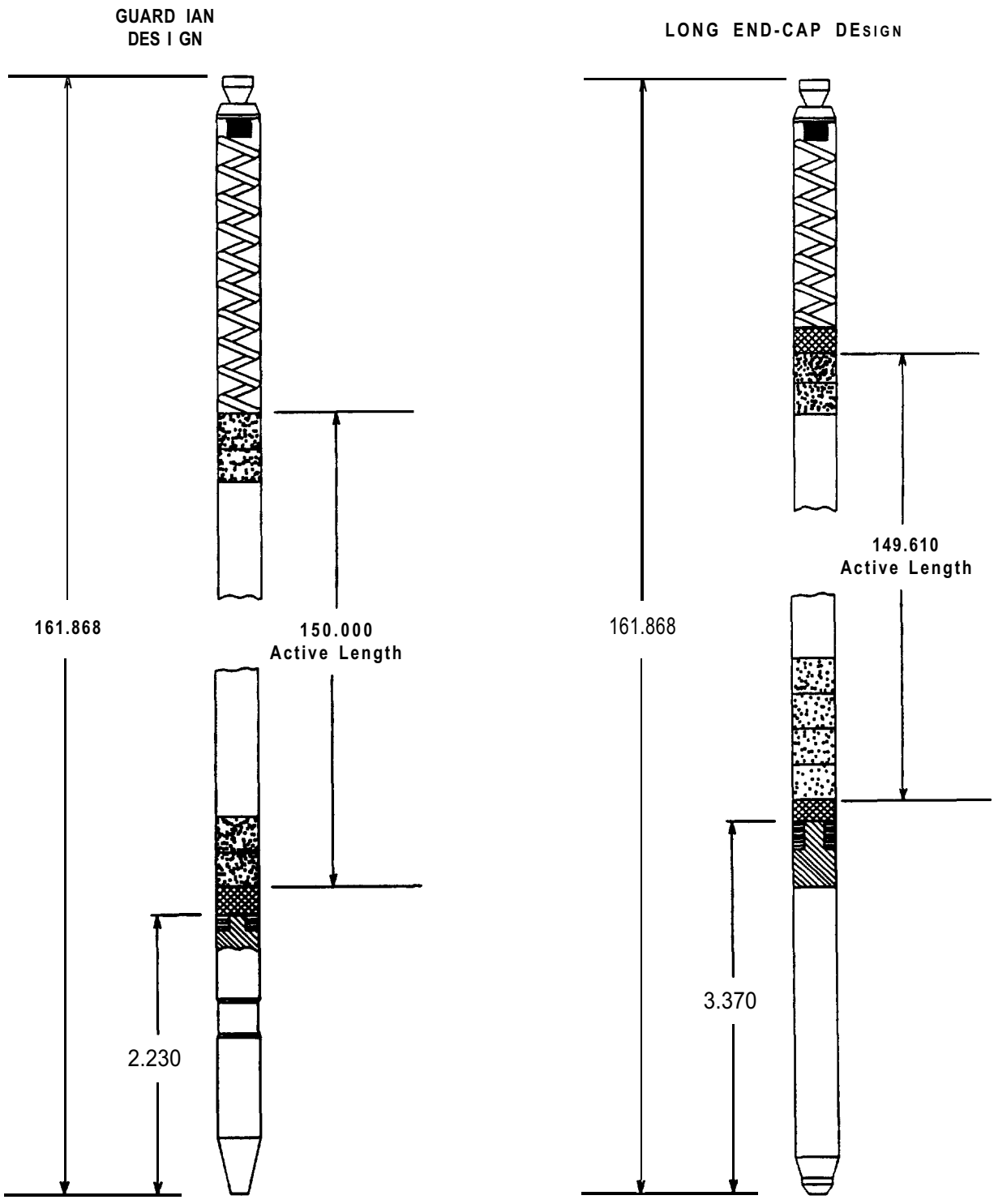

COMPARISON OF FUEL ROD DESIGNS

REVISION 8 (5/96)

Waterford Steam Electric Station ● 3	FUEL ROD DESIGNS	Figure 4.3A-18

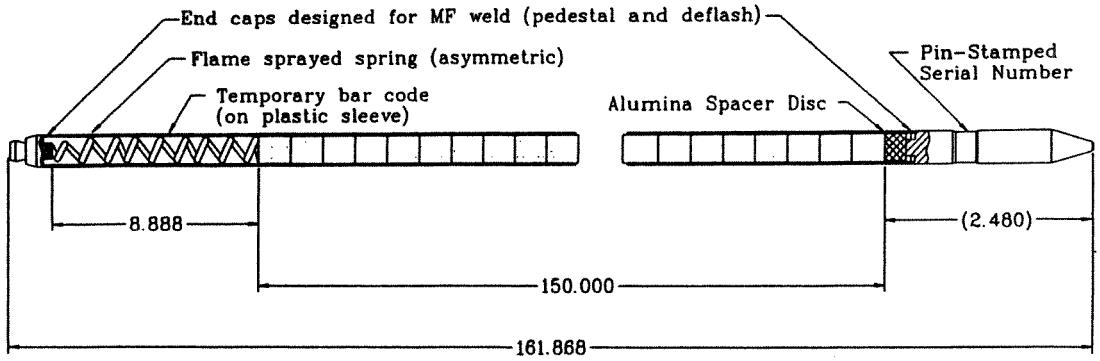

Batch T Rod Assembly with MF Welds (Hematite Production)

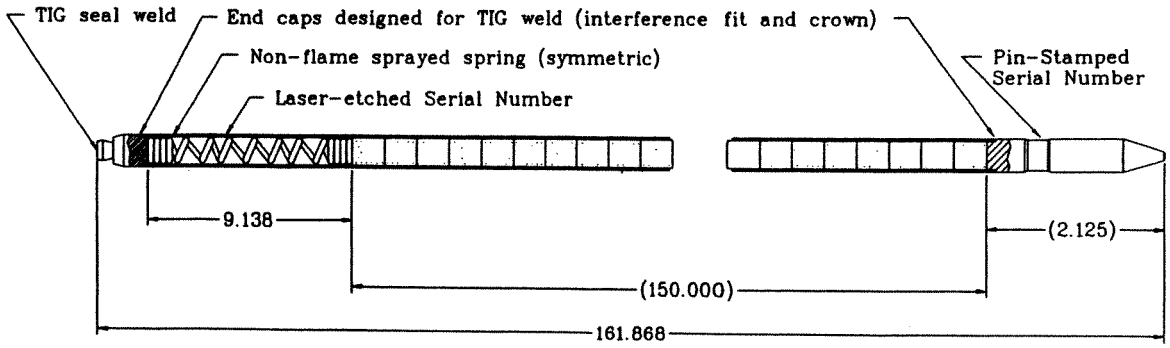

Batch U Rod Assembly with TIG Welds (Columbia Production)

Revision 12 (10/02)

Waterford Steam Electric Station #3	Comparison of Urania Rod Assembly Features	Figure 4.3A-18a

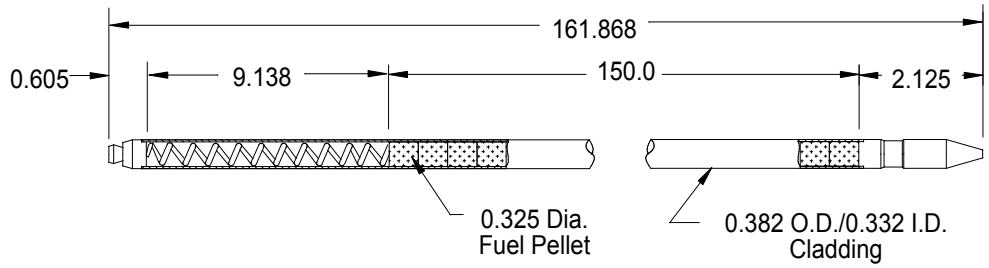

WSES Urania Rod Design
(Batches U, X, and Y)

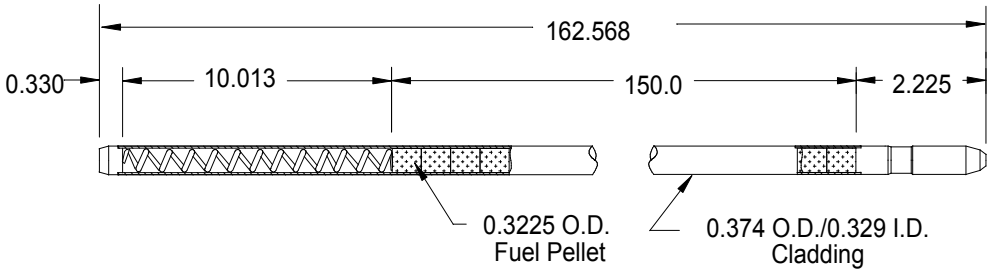

WSES NGF Urania Rod Design
(begins w/Batch Z)

Waterford Steam Electric Station #3	Comparison of Urania Rod Assembly Features	Figure 4.3A-18b

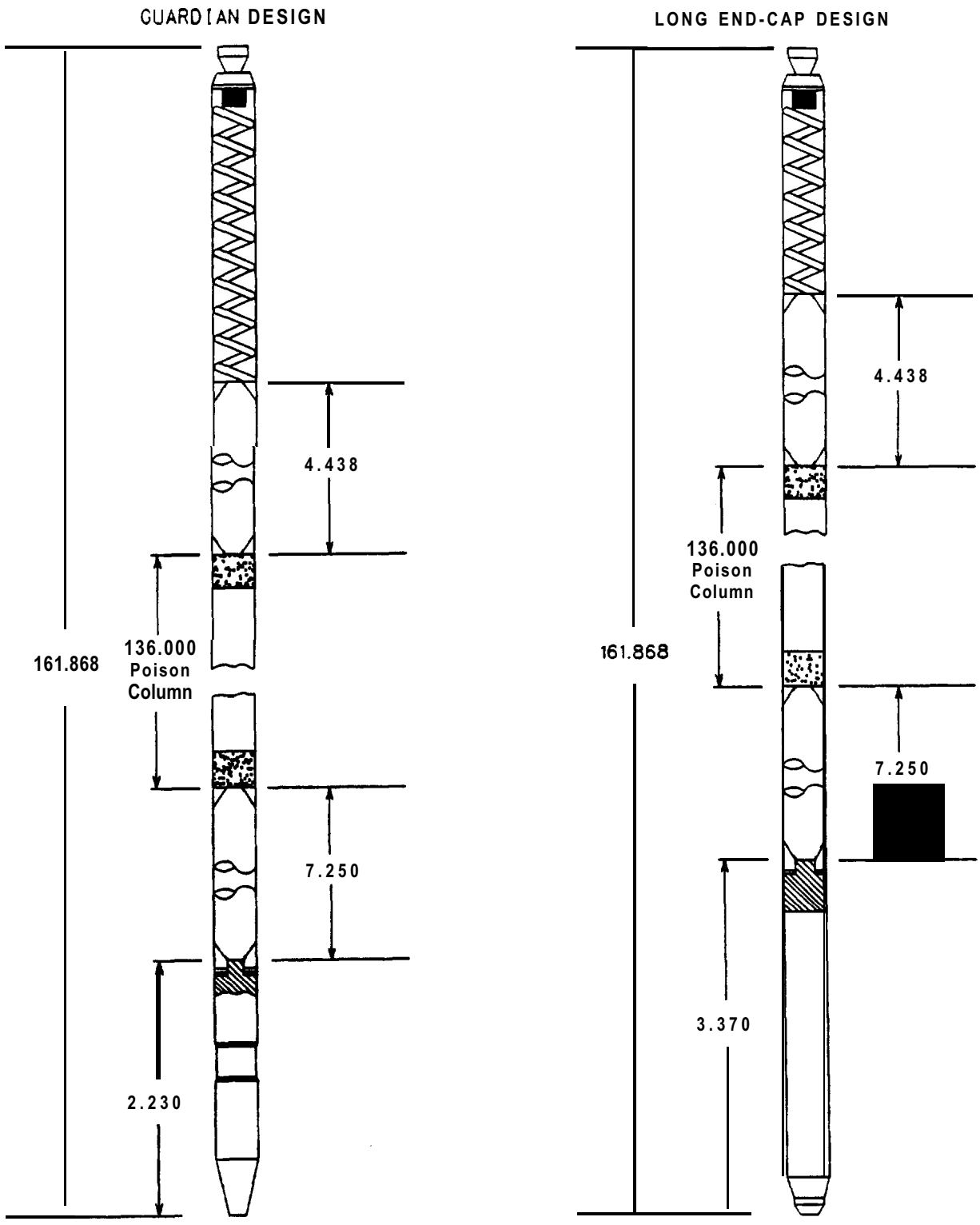

COMPARISON OF POISON ROD DESIGNS

REVISION 8 (5/96)

Waterford Steam Electric Station ● 3	POISON ROD DESIGNS	Figure 4.3A-19

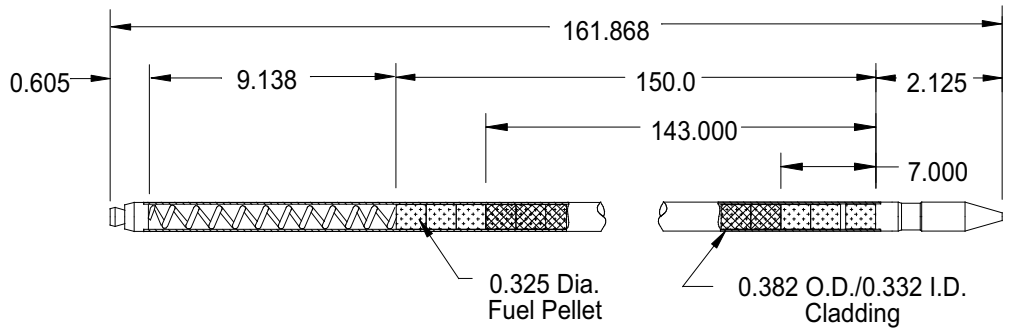

WSES IFBA Rod Design
(Batch Y)

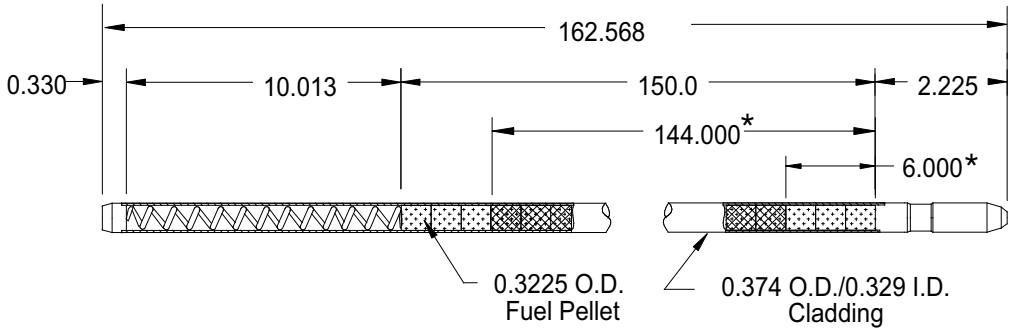

WSES NGF IFBA Rod Design
(begins w/Batch Z)

* These values may change from batch to batch.

4.4 THERMAL AND HYDRAULIC DESIGN

This section presents the steady-state thermal and hydraulic analysis of the reactor core, the analytical methods, and the experimental work done to support the analytical techniques during Cycle 1. Additional information for the current fuel cycle is discussed in Appendix 4.3A. Discussions of the analyses of anticipated operational occurrences and accidents are presented in Chapter 15. The prime objective of the thermal and hydraulic design of the reactor is to ensure that the core can meet steady-state and transient performance requirements without violating the design bases.

4.4.1 DESIGN BASES

Avoidance of thermally or hydraulically induced fuel damage during normal steady-state operation and during anticipated operational occurrences is the principal thermal hydraulic design basis. The design bases for accidents are specified in Chapter 15. In order to satisfy the design basis for steady-state operation and anticipated operational occurrences, the following design limits are established, but violation of these will not necessarily result in fuel damage. The reactor protective system (RPS) provides for automatic reactor trip or other corrective action before these design limits are violated.

4.4.1.1 Minimum Departure from Nucleate Boiling Ratio

→(DRN 03-2058, R14; EC-9533, R302; EC-30663, R307)
The minimum DNBR shall be such as to provide at least 95 percent probability with 95 percent confidence that departure from nucleate boiling (DNB) does not occur on a fuel rod having that minimum DNBR during steady-state operation and anticipated operational occurrences. A value of 1.19 using the CE-1 correlation, 1.12 using WSSV-T correlation, and 1.13 using ABB-NV correlation, coupled with the TORC code provides at least this probability and confidence. See Subsections 4.3A.4.1 and 4.3A.4.2 for current cycle critical heat flux correlations and DNBR limits.
←(DRN 03-2058, R14; EC-9533, R302; EC-30663, R307)

4.4.1.2 Hydraulic Stability

Operating conditions shall not lead to flow instability during steady-state operation and during anticipated operational occurrences.

4.4.1.3 Fuel Design Bases

→(DRN 04-1096, R14)
a) The peak temperature of the fuel shall be less than the melting point (5080 F unirradiated and reduced by 58 F per 10,000 MWd/MTU and adjusted for burnable poison per Reference 22) during steady-state operation and anticipated operation and anticipated operational occurrences.
←(DRN 04-1096, R14)

b) The fuel design bases for fuel clad integrity and fuel assembly integrity are given in Subsection 4.2.1. Thermal and hydraulic parameters that influence the fuel integrity include maximum linear heat rate, core coolant velocity, coolant temperature, clad temperature, fuel-to-clad gap conductance, fuel burnup and UO_2 temperature. Other than the design limits already specified, no limits need be applied to these parameters directly. No violation of the design limits specified here and no violation of the design bases specified in Subsection 4.2.1, are sufficient to ensure fuel clad integrity, fuel assembly integrity, and the avoidance of thermally or hydraulically induced fuel damage for steady-state operation and anticipated operational occurrences.

4.4.1.4 Coolant Flow, Velocity, and Void Fraction

➔(DRN 00-644)
The primary coolant flow with all four pumps in operation shall be greater than the design minimum. A percentage of the flow entering the reactor vessel is not effective for cooling the core. This percentage is called the core bypass flow. The calculated core bypass flow shall be less than the design maximum. The design minimum value for the calculated core flow is obtained by subtracting the design maximum value for the calculated core bypass flow from the design minimum primary coolant flow. For thermal margin analyses, the design minimum value for the calculated core flow is used. These design flows are listed in Table 4.4-1.
←(DRN 00-644)
Design of the reactor internals ensures that the coolant flow is distributed to the core such that the core is adequately cooled during steady-state operation and anticipated operational occurrences. Therefore, no specific orificing configuration is used.

Although the coolant velocity, its distribution, and the coolant voids affect the thermal margin, design limits need not be applied to these parameters because they are not in themselves limiting. These parameters are included in the thermal margin analyses and thus affect the thermal margin to the design limits.

4.4.2 DESCRIPTION OF THERMAL AND HYDRAULIC DESIGN OF THE REACTOR CORE

4.4.2.1 Summary Comparison

The thermal and hydraulic parameters for the reactor are listed in Table 4.4-1. A comparison of these parameters with the Boston Edison Pilgrim Station Unit 2 reactor (Amendment 20, 1975, Docket No. 50-471) is given in Table 4.4-1.
➔(EC-9533, R302; EC-13881, R304)
The principal differences between the two reactors are the total core heat output and the reactor inlet coolant temperature. With respect to the analysis of DNB, the Waterford 3 reactor was analyzed (through Cycle 16) using the CE-1 Correlation; [1][2] whereas, the Pilgrim reactor (Docket, No. 50-471) was analyzed using the original W3 Correlation.[3] The Waterford 3 Cycle 16 core was also analyzed using the WSSV-T correlation[23] and the ABB-NV correlation[24] due to the introduction of NGF assemblies in region quantities in that cycle. Beginning with Cycle 17, the core has consisted of only NGF assemblies; consequently, the Waterford 3 core is being analyzed using only the WSSV-T correlation[23] and the ABB-NV correlation[24].
←(EC-9533, R302; EC-13881, R304)

4.4.2.2 Critical Heat Flux Ratios

4.4.2.2.1 Departure from Nucleate Boiling Ratio

The margin of the DNB in the core is expressed in terms of the DNBR. The DNBR is defined as the ratio of the heat flux required to produce departure from nucleate boiling at the calculated local coolant conditions to the actual local heat flux.
➔(EC-9533, R302; EC-13881, R304; EC-30663, R307)
Starting with Cycle 17, the DNB correlations used for design of the core are the ABB-NV correlation[24] and the WSSV-T correlation[23] for NGF assemblies. Based on statistical evaluation of the ABB-NV and WSSV-T correlations and relevant data, it is concluded that the appropriate minimum DNBR values are 1.13 (ABB-NV) and 1.12 (WSSV-T).

NRC evaluation of the uniform axial power distribution data resulted in their concluding that the CE-1 critical heat flux correlation[1][2], when coupled with the TORC code, provides an acceptable correlation of uniform axial CHF data and that the minimum acceptable DNBR is 1.19.[4]
←(EC-9533, R302; EC-13881, R304; EC-30663, R307)

➔(DRN 00-644; EC-9533, R302; EC-13881, R304)
Therefore, the minimum DNBR used for design is 1.19. Table 4.4-1 gives the value of minimum DNBR for the coolant conditions and engineering factors in the table, for the radial power distributions in Figures 4.4-1 and 4.4-2, and for the 1.26 peaked axial power distribution in Figure 4.4-3. Values of minimum DNBR or maximum fuel temperature at the design overpower cannot be provided with any meaning. The concept of a design overpower is not applicable for Waterford 3 since the Reactor Protective System prevents the design limits from being exceeded.
←(DRN 00-644; EC-9533, R302; EC-13881, R304)

A comparison of the minimum DNBRs computed using different correlations for the same power, flow, coolant temperature and pressure, and power distribution is presented in Table 4.4-2. The minimum DNBR values in both the limiting matrix subchannel and the limiting subchannel next to the guide tube are presented. The correlations compared are the CE-1 correlation, the original W3 correlation,[3] the revised W3 correlation[5] and the B&W-2 correlation.[5] The differences between the original and revised W3 correlations as used here are in the C-factor and the cold wall correction factor.
➔(DRN 00-644)
Additional comparisons are contained in CENPD-162[1]. In general, the CE-1 correlation predicts lower values of CHF than the B&W-2 Correlation, with the differences increasing with increasing inlet subcooling. In comparison with the W3 Correlation, the CE-1 Correlation tends to predict lower values of Critical Heat Flux (CHF) with high inlet subcooling and higher values of CHF with low inlet subcooling.
←(DRN 00-644)
The TORC computer code[6] is used to compute the local coolant conditions in the core and thereby the minimum DNBR. A discussion of the CE-1 DNB correlation and the analytical methods is presented in Subsections 4.4.4.1 and 4.4.4.5.2, respectively.

4.4.2.2.2 Application of Power Distribution and Engineering Factors

Distribution of power in the core is expressed in terms of factors that define the local power per unit length produced by the fuel relative to the core average power per unit length produced by the fuel. The method to compute these factors, which describe the core power distribution, is discussed in Section 4.3. The energy produced in the fuel is deposited in the fuel pellets, fuel cladding, and the moderator and results in the generation of heat in those places. The fraction of energy deposited in the fuel pellet and cladding is called the fuel rod energy deposition fraction. Accordingly, the core average heat flux from the fuel rods is determined by multiplying the core power by the average fuel rod energy deposition fraction and then dividing by the total heat transfer area. The energy deposition fractions used for DNB analyses for the average and the hot fuel rods are given in Table 4.4-1.
➔(DRN 00-644)
The effects on the local heat flux and subchannel enthalpy rise of within tolerance deviation from nominal dimensions and specifications are included in thermal margin analyses by certain factors called engineering factors. These factors are applied to increase the local heat flux at the location of minimum DNBR and to increase the enthalpy rise in the subchannel adjacent to the rod with the minimum DNBR. Diversion crossflow and turbulent interchange mixing are not input as factors on subchannel enthalpy rise but are explicitly treated in the TORC code analytical model.

➔(EC-9533, R302; EC-13881, R304; EC-30663, R307)
Cycle 16 is a mixed core consisting of standard fuel assemblies and NGF assemblies. Since NGF assemblies are more resistant to flow because of mixing vane spacer grids as compared to standard fuel assemblies, the hydraulic characteristics of these two types of fuel assemblies are modeled explicitly in TORC thermal-hydraulic calculations of coolant pressure drop and cross-flow between assemblies. Uncertainties in the power distribution factors are discussed in Subsection 4.4.2.9.4. Starting with Cycle 17, the core consists of a full core of NGF assemblies as stated previously. The ABB-NV critical heat flux correlation is used in the non-mixing vane region and the WSSV-T correlation is used in the mixing vane region.
←(DRN 00-644; EC-9533, R302; EC-13881, R304; EC-30663, R307)

4.4.2.2.2.1 Power Distribution Factors

a) Rod Radial Power Factor

The rod radial power factor is the ratio of the average power per unit length produced by a particular fuel rod to the average power per unit length produced by the average powered fuel rod in the core. The maximum rod radial power factor is the ratio of the average power per unit length produced by the highest powered rod in the core to the average power per unit length produced by the average powered fuel rod in the core. Radial power distributions are dependent upon a variety of parameters (control rod insertion, power level, fuel exposure, etc.). The core wide and hot assembly radial power distributions used for this analysis are shown in Figures 4.4-1 and 4.4-2. The maximum rod radial power factor for those figures is selected as 1.55 for better comparisons with Pilgrim Station Unit 2. The actual maximum rod radial power factor in the core will normally be lower; but it is not limited to a maximum value of 1.55. The only limits are those specified in Subsection 4.4.1. The protective system in conjunction with the reactor operator utilizing the Core Operating Limit Supervisory System (COLSS) ensures that those design limits are not violated.

b) Axial Power Factor

The axial power factor is the ratio of the local power per unit length produced by a fuel rod to the average power per unit length produced by the same fuel rod. The maximum axial power factor is the ratio of the maximum local power per unit length produced by a rod to the average power per unit length produced by the same fuel rod. The axial power distribution directly affects DNBR.

Typically, the farther the peak heat flux is from the core inlet, the lower the value of the peak heat flux needed to reach the DNBR limit. On the other hand, fuel temperature is almost independent of the location of the peak heat flux and is principally dependent on the value of the peak heat flux or linear heat rate. The axial power distribution and the maximum rod dial power factor are continuously determined and processed through the COLSS and the RPS such that the design basis limits are not exceeded. Section 4.3 describes the power distributions and their control. Figure 4.4-3 shows several axial power distributions and their control. Figure 4.4-3 shows several axial power distributions used for this analysis. The minimum DNBR in Table 4.4-1 is determined using the 1.26 peaked axial power distribution whereas the maximum heat fluxes are determined using the 1.47 peaked axial power distribution.

c) Nuclear Power Factor

The nuclear power factor is the ratio of the maximum local power per unit length produced in the core to the average power per unit length produced by the average powered fuel rod in the core. It is identical to the product of the maximum axial and radial power factors. For better comparisons with Pilgrim Station Unit 2, a value of 2.28 is selected for computing maximum heat fluxes. The actual value of the nuclear power factor will normally be lower throughout the cycle; but it is not limited to a maximum value of 2.28. The design limits are those specified in Subsection 4.4.1. The protective and supervisory systems assure that those design limits are not violated.

d) Total Heat Flux Factor

The total heat flux factor is the ratio of the local fuel rod heat flux to the core average fuel rod heat flux. The effects of fuel densification are not included in this factor. To determine the maximum local heat flux including the effect of gaps occurring between the fuel rod pellets, the augmentation factor should be applied. From this definition the total heat flux factor is the product of the nuclear power factor, the engineering heat flux factor, and the ratio of the hot to the average rod energy deposition fractions. The total heat flux factor is given in Table 4.4-1.

e) Augmentation Factor

→(DRN 00-644)

The densification of the fuel may lead to axial gaps in the fuel pellet stacks and can cause increased localized power peaking. This effect is expressed in terms of the augmentation factor which is defined as the ratio of the local heat flux to the unperturbed heat flux. The axial length of the localized power perturbation is called the gap length. Maximum values of the augmentation factor and gap length are given in Table 4.4-1. The effect of this factor on DNBR is discussed in Subsection 4.4.2.2.3.

←(DRN 00-644)

4.4.2.2.2.2 Engineering Factors

a) Engineering Heat Flux Factor

The effect on local heat flux due to normal manufacturing deviations from nominal design dimensions and specifications is accounted for by the engineering heat flux factor. Design variables that contribute to this engineering factor are initial pellet density, pellet diameter, and clad outside diameter.

→(EC-13881, R304)

These variables are combined statistically to obtain the engineering heat flux factor. The design value used for the engineering heat flux factor is based on deviations obtained from fuel manufacturing inspection data for over 25 batches of fuel for previous reactor cores. Similar tolerances and quality control procedures are used for Waterford 3, and as built fuel manufacturing data have been used to confirm that the factor given in Table 4.4-1 is conservative. The engineering heat flux factor is applied to the rod with the minimum DNBR and increases the heat flux when calculating DNBR.

←(EC-13881, R304)

→(EC-13881, R304)

It does not affect the enthalpy rise in the subchannel; the effect on the enthalpy rise in the subchannel due to normal manufacturing deviations from normal design dimensions and specifications is accounted for by the engineering enthalpy rise factor.

←(EC-13881, R304)

b) Engineering Factor on Linear Heat Rate

The effect of local linear heat rate due to deviations from nominal design dimensions and specifications is accounted for by the engineering factor on linear heat rate. Except for the clad outside diameter, the design variable that contribute to this factor are the same as those for the engineering heat flux factor. A value of 1.03 is applicable for the engineering factor on linear heat rate for Waterford 3.

c) Engineering Enthalpy Rise Factor

→(DRN 00-644)

The engineering enthalpy rise factor accounts for the effects of normal manufacturing deviations in fuel fabrication from nominal dimensions or specifications on the enthalpy rise in the subchannel adjacent to the rod with the minimum DNBR. Tolerance deviations (averaged over the length of the fuel rods that adjoin the subchannel) for fuel pellet density, enrichment, and diameter contribute to this factor. As-built fuel manufacturing data have been used to confirm that the factor given Table 4.4-1 is conservative.

The engineering enthalpy rise factor is applied by multiplying by the factor, the rod radial power factor of each of the fuel rods adjacent to the subchannel adjoining the rod with the minimum DNBR (see Figure 4.4-2). This increases the enthalpy rise in the subchannels which adjoin the same fuel rods.

←(DRN 00-644)

d) Pitch and Bow Factor

The pitch and bow factor is an allowance for the effect on enthalpy rise of the possible decreased flow rate in the subchannel resulting from a smaller than nominal subchannel flow area.

The pitch and bow factor given in Table 4.4-1 is applied by multiplying by the factor, the incremental enthalpy rise in the subchannel adjacent to the rod with the minimum DNBR (see Figure 4.4-2). This increases the enthalpy rise in that subchannel in the same manner as does the engineering enthalpy rise factor, but does not directly affect the heat input into the surrounding subchannels. The combined effects of divergent crossflow and turbulent interchange resulting from the higher heat input and enthalpy rise are computed by the TORC code. Additional discussions of fuel and poison rod bowing are presented in CENPD-225.(20)

4.4.2.2.3 Fuel Densification Effect on DNBR

The perturbation in local heat flux due to fuel densification is given in Table 4.4-1.

As shown in CENPD-207 (See Subsection 4.4.4.1), even much larger local heat flux variations have no significant adverse effect on DNB in Waterford 3 fuel assembly. Therefore, no specific allowance is made or required for the effect on DNBR of local heat flux variations due to densification of the fuel.

4.4.2.3 Linear Heat Generation Rate

→(DRN 00-644)

The core average and maximum fuel rod linear heat generation rates are given in Table 4.4-1. The maximum fuel rod linear heat generation rate is determined by multiplying core average fuel rod linear heat generation rate by the product of the nuclear power factor, the engineering factor on linear heat rate, and the ratio of the hot to the average fuel rod energy deposition factors. The effects of fuel densification are not included in the maximum fuel rod linear heat generation rate presented in Table 4.4-1; although, to determine the maximum local linear heat generation rate including the effect of gaps occurring between the fuel pellets, the augmentation factor should be applied.

←(DRN 00-644)

4.4.2.4 Void Fraction Distribution

→(DRN 00-644; EC-13881, R304)

The core average void fraction and the maximum void fraction are calculated using the Maurer method.[7] The void fractions discussed below are value for the reactor operating conditions and engineering factors given in Table 4.4-1, for the radial power distributions in Figures 4.4-1 and 4.4-2, and for the 1.26 peaked axial power distribution in Figure 4.4-3. For these conditions, only subcooled boiling occurs in the core.

←(DRN 00-644; EC-13881, R304)

The core average void fraction is less than 0.1 percent. The local maximum void fraction is 1.3 percent and occurs at the exit of the subchannel adjacent to the rod with the minimum DNBR. The average exit void fractions and qualities in different regions of the core are shown in Figure 4.4-4 for the core radial power distribution shown in Figure 4.4-1. The axial distribution of void fraction and quality in the subchannel adjacent to the rod with the minimum DNBR is shown in Figure 4.4-5. The average void fraction in that subchannel is 0.2 percent.

4.4.2.5 Core Coolant Flow Distribution

The core inlet flow distribution is required as input to the TORC thermal margin core (refer to Subsection 4.4.4.5.2). The inlet flow distribution 4-loop operation was determined from a reactor flow model test. Descriptions of the model test and the resulting core inlet flow distribution are given in Subsection 4.4.4.2.1.

Intentional selective orificing is not used in the core design.

4.4.2.6 Core Pressure Drops and Hydraulic Loads

4.4.2.6.1 Reactor Vessel Flow Distribution

The design minimum coolant flow entering the four reactor vessel inlet nozzles is given in Table 4.4-1. The main coolant flow path in the reactor vessel and the core support barrel, through the flow skirt and lower support cylinder, up through the core support region and the reactor core, through the fuel alignment plate, and out through the two reactor vessel outlet nozzles. A portion of this flow leaves the main flow path as shown schematically in

Figure 4.4-6. Part of the bypass flow is used to cool the reactor internals in areas not in the main coolant flow path and to cool the CEAs. Table 4.4-3 lists the bypass flow paths and the percent of the total vessel flow that enters and leaves these paths.

The thermal margin calculations conservatively use the design maximum bypass flow of 2.6 percent of the total vessel flow as compared to the calculated bypass flow of 2.1 percent shown in Table 4.4-3.

4.4.2.6.2 Reactor Vessel and Core Pressure Drops

The irrecoverable pressure losses from the inlet to the outlet nozzles are calculated using standard loss coefficient methods which are verified by flow model tests (refer to Subsection 4.4.4.2.1).

Pressure losses at 100 percent power, the design minimum primary coolant flow, and an operating pressure of 2250 psia are listed in Table 4.4-4 together with the coolant temperature used to calculate each pressure loss. The calculated pressure losses include both geometric and Reynolds number dependent effects. The calculated nozzle-to-nozzle pressure loss, using the same methods as above, and the as-measured pressure loss on operating plants are in good agreement, (refer to Subsection 4.4.4.2.1).

4.4.2.6.3 Hydraulic Loads on Internal Components

The significant hydraulic loads which act on the reactor internals during steady state operation are listed in Table 4.4-5. These loads are derived from analyses which make use of reactor flow model and components test results (refer to Subsection 4.4.4.2.1 and 4.4.4.2.2, respectively). All hydraulic loads in Table 4.4-5 are based on 120 percent of the design minimum primary coolant flow and a coolant temperature of 500 F.

→(DRN 03-2058, R14; EC-13881, R304)
When other coolant conditions and core power levels result in more limiting loading for individual components, the loads in Table 4.4-5 are adjusted in the detailed design analysis. For the power uprate to 3716 MWt, adjustments of this nature have been made to the hydraulic loads for use as input to the component stress analyses. The detailed design considers the steady state drag and impingement loads and the fluctuating loads induced by pressure pulsations, turbulence, and vortex shedding.
←(DRN 03-2058, R14; EC-13881, R304)

Hydraulic loads for postulated accident conditions are discussed in Subsection 3.9.2.5.

4.4.2.7 Correlations and Physical Data

4.4.2.7.1 Heat Transfer Coefficients

The correlations used to determine cladding temperatures for non-boiling forced convection and nucleate boiling are discussed here. The surface temperature of the cladding is dependent on the axial and radial power distributions, the temperature of the coolant, and the surface heat transfer coefficient.

The surface heat transfer coefficient for non-boiling forced convection is obtained from the Dittus-Boelter correlation[8] where fluid properties are evaluated at the bulk condition.

$$h_{db} = \frac{0.023k}{De} (N_R)^{0.8} (N_{Pr})^{0.4}$$

where:

h_{db} = Heat transfer coefficient, Btu/hr-ft^2-F

k = Thermal conductivity, Btu/hr-ft-F

De = Equivalent diameter = $4A/P_w$, ft

N_R = Reynolds number, based on the equivalent diameter and coolant properties evaluated at the local bulk coolant temperature.

N_{Pr} = Prandt1 number, based on coolant properties evaluated at the local bulk coolant temperature.

A = Cross-sectional area of flow subchannel, ft^2.

P_w = Wetted perimeter flow subchannel, ft.

No specific allowance is made or considered necessary for the uncertainties associated with the Dittus-Boelter Correlation because the Dittus-Boelter Correlation is not used directly in computing thermal margin, but rather plays a part in determining pressure drop and cladding temperature. The validity of the overall scheme for predicting pressure drop is shown by the excellent agreement between predicted and experimental values obtained during the DNB test program and described in Subsection 4.4.4.1. The uncertainty associated with the cladding temperatures calculated for single phase heat transfer is not a major concern because the limiting fuel and cladding temperatures occur where the cladding-to-coolant heat transfer is by nucleate boiling.

The temperature drop across the surface film is calculated from:

$$\Delta T_{film} = q''/h_{db}$$

where:

q" = fuel rod surface heat flux, Btu/hr-ft^2

The maximum fuel rod heat flux is the product of the core average fuel rod heat flux and the total heat flux factor (refer to Table 4.4-1 and Subsection 4.4.2.2.2). At the location of maximum heat flux, nucleate boiling may occur on the clad surface. In the nucleate boiling regime, the surface temperature of the cladding is determined from the Jens and Lottes correlation: [9]

$$T_{wall} = T_{sat} + 60\ (q'' \times 10^{-6})^{0.25}\ [\exp\ (-P/900)]$$

where:

P = Pressure, psia

q" = Defined above

T_{sat} = Saturation temperature, F

Nucleate boiling is assumed to exist if T_{wall} is less than the sum of $T_{coolant}$ plus ΔT_{film}.

The cladding surface temperature is calculated by summing the temperature of the coolant at the particular location and the temperature drop across the surface film, or if nucleate boiling is occurring, it is calculated directly from the Jens and Lottes correlation.

4.4.2.7.2 Core Irrecoverable Pressure Drop Loss Coefficients

Irrecoverable pressure losses through the core result from friction and geometric changes. The pressure losses through the lower and upper end fittings are calculated using the standard loss coefficient method and are verified by test (refer to Subsection 4.4.4.2.2). The correlations used to determine frictional and geometric losses in the core are presented in Subsection 4.4.4.2.3.

4.4.2.7.3 Void Fraction Correlations

There are three separate void regions to be considered in flow boiling. Region 1 is highly subcooled in which a single layer of bubbles develops on the heated surface and remains attached to the surface. Region 2 is a transition region from highly subcooled to bulk boiling where the steam bubbles detach from the heated surface. Region 3 is the bulk boiling regime.

The void fraction in Regions 1 and 2 is predicted using the Maurer method.[7] The calculation of the void fraction in the bulk boiling regime is discussed in Subsection 4.4.4.2.3.

4.4.2.8 Thermal Effects of Operational Transients

→(EC-13881, R304)

Design basis limits on DNBR and fuel temperature are established to assure that thermally induced fuel damage will not occur during steady-state operation and during anticipated operational occurrences. The COLSS provides information to the operator so he can assure that proper steady-state conditions exist. The RPS ensures that the design limits are not violated. The COLSS provides the reactor operator with a comparison of the actual core operating power to the licensed power and to the limiting powers based on DNBR and local power density. If the operating power reaches one of the limiting powers, an alarm is sounded. These limits are calculated by COLSS to provide sufficient margin not to exceed the design basis limits in the event the most limiting anticipated operational occurrence occurs simultaneously with the operating power being at the limiting power in steady state.

←(EC-13881, R304)

→(EC-13881, R304)
The COLSS thermal margin algorithm is an analytical approximation to the standard thermal margin design methods described in Subsection 4.4.4.5.2.
←(EC-13881, R304)

Approximations take the form of tabular data replacing complex algebraic functions as are used in the design code (for instance, fluid property routines). As such, there exist small random and systematic differences in the computed results from the two methods when comparison is made for identical initial conditions. Any non-conservatisms in these differences are accommodated by the following procedure:

A large number of cases are evaluated by both the design code and the thermal margin algorithm. The cases simulate a wide range of initial conditions expected in plant operation as allowed by the COLSS. A penalty factor is applied to the COLSS algorithm computed core power limit. This penalty accounts for the difference in the computed core power limit between the design code results and that of the algorithm results as determined from the cases discussed above. In this manner, the COLSS thermal margin algorithm is biased to give acceptable values of overpower compared to results calculated by the design analytical method.

Measurement uncertainties and calculational uncertainties are applied in a conservative manner in the COLSS calculation of the core operating power and the COLSS calculation of the core power limits. These uncertainties are discussed further in Subsection 7.7.1.3.4.

For automatic protection of the core, the RPS is designed to effect a rapid shutdown in the event that the thermal-hydraulic design limits are approached.

The core minimum DNBR and maximum local power density are determined by a core protection calculator (CPC), which uses core parameters either measured or calculated as input.

For the protective system, a DNB algorithm provides a rapid online calculation of DNBR. This algorithm, like the standard core analytical technique, uses the following core parameters either measured or calculated as input: core inlet temperature, pressure, flow, power, and power distribution. The CPC assessment of minimum DNBR is biased, in a manner similar to that of the overpower calculation performed in the COLSS, to give acceptable DNBRs compared to results calculated by the design analytical method.

Additional information concerning the supervisory and protective systems is contained in Sections 7.7 and 7.2, respectively, and additional discussion on the effects of thermal transients on waterlogged fuel elements is contained in Subsection 4.2.3. Analysis of anticipated operational occurrences to demonstrate that fuel design bases are met is presented in Chapter 15.

4.4.2.9 Uncertainties in Estimates

4.4.2.9.1 Pressure Drop Uncertainties

The reactor vessel pressure losses in Table 4.4-4 are the best estimate values calculated for the design minimum flow with standard loss coefficient methods. The uncertainties in the correlations for the loss coefficients and the dimensional uncertainties on the reactor vessel and internals are accounted for when determining maximum and minimum vessel hydraulic resistance. The uncertainties are estimated to be equivalent to approximately ± 10 percent of the best estimate vessel pressure loss.

4.4.2.9.2 Hydraulic Loads Uncertainties

→(DRN 00-644)

The hydraulic loads for the design of the internals, Table 4.4-5, are based on 120 percent of the design minimum flowrate (see Subsections 4.4.1.4 and 4.4.4.5.1).

←(DRN 00-644)

4.4.2.9.3 Fuel and Clad Temperature Uncertainty

Uncertainty in the ability to predict the maximum fuel temperature is a function of gap conductance, thermal conductivities, peak linear heat rate, and heat generation distribution. Uncertainties in gap conductance and thermal conductivity are taken into account in the analytical model. Uncertainties in the peak linear heat rate are accounted for by including the uncertainty in estimating the total nuclear peak and by including the uncertainties in fuel pellet density, enrichment, and pellet diameter expresses by the engineering factor on linear heat rate (Subsection 4.4.2.2.2).

Uncertainty in predicting the cladding temperature at the location of maximum heat flux is the uncertainty in the film temperature drop, which is minimal at this location where nucleate boiling occurs.

4.4.2.9.4 DNBR Calculation Uncertainties

a) The uncertainty in the calculation of minimum DNBR is divided into:

   1) The uncertainty in the input to the core analytical model, the TORC code. This includes the core geometry, power distribution, inlet flow and temperature distribution, exit pressure distribution, single phase friction factor constants, spacer grid loss coefficients, divergent crossflow resistance and momentum parameters, turbulent interchange constants, and hot fuel rod energy deposition fraction.

   2) The uncertainty in the analytical model to compute the actual distribution of flow and the local subchannel coolant conditions.

→(EC-9533, R302; EC-13881, R304)

   3) The uncertainty in the CE-1 correlation for standard fuel assemblies and the WSSV-T and ABB-NV correlations for NGF assemblies to predict DNB.

←(EC-9533, R302; EC-13881, R304)

b) The following paragraphs discuss the above uncertainties and the allowances for them, if needed, in the thermal margin analysis of the core:

1) Uncertainty in the input to the core analytical model:

(a) Uncertainty in core geometry, as manifested by manufacturing variations within tolerances, is considered by the inclusion of engineering factors in the DNBR analyses; see Subsection 4.4.2.2.2 for a discussion of the method used to compute conservative values.

→ (DRN 00-644)

(b) Uncertainties on the power distribution factors are applied in the COLSS and RPS (see Subsection 7.7.1.3.4).

← (DRN 00-644)

(c) The non-uniformity of the core inlet flow distribution is obtained from flow model testing discussed in Subsection 4.4.4.2, and is included in the design method for TORC analyses - see Subsection 4.4.4.5.2.

(d) Non-uniformities in the core exit pressure distribution are included in the design method for TORC analyses - see Subsection 4.4.4.5.2.

(e) The Blasius single-phase friction factor equation for smooth rods is given and shown to be valid in Subsection 4.4.4.2.3. The spacer grid loss coefficient for the standard grid is obtained from pressure drop data discussed in Subsection 4.4.4.2.3.

(f) The value of minimum DNBR is relatively insensitive to crossflow resistance and momentum parameters.(6)

(g) Subsection 4.4.4.1 describes the testing to determine the inverse Peclet number which is indicative of the turbulent flow interchange between subchannels. The inverse Peclet number is input to the TORC code and is used to determine the effect of turbulent interchange on the enthalpy rise in adjacent subchannels. From the testing, a value of 0.0035 is justified.

(h) The same fuel rod energy deposition fraction is used for the hot rod as for the average rod. The hotter the rod, the lower is the actual value of energy deposition fraction with respect to that for the average rod. A lower energy deposition fraction reduces the hot rod heat flux and thereby increases its DNBR. The use of the average rod energy deposition fraction for the hot rod is therefore conservative. See Section 4.3 for a discussion of the calculation of the energy deposition fractions.

2) Uncertainty in the analytical model:

The ability of the TORC code to predict accurately subchannel local conditions in rod bundles is described in CENPD-161.(6) The ability of the code to predict accurately the core wide coolant conditions is described in CENPD-206.(10)

3) Uncertainty in the DNB correlation:

➔(EC-9533, R302; EC-13881, R304; EC-30663, R307)

The uncertainty in the DNB correlation is determined by a statistical analysis of DNB test data. A value of 1.19 for the CE-1 correlation, 1.12 for the WSSV-T correlation, and 1.13 for the ABB-NV correlation has been shown to provide a 95 percent probability with 95 confidence that DNB will not occur on a fuel rod having that minimum DNB.[1][2][23][24]

←(EC-9533, R302; EC-13881, R304; EC-30663, R307)

4.4.2.10 Flux Tilt Considerations

An allowance for degradation in the power distribution in the x-y plane (commonly referred to as flux tilt) is provided in the protection limit set points even though little, if any, tilt in the x-y plane is expected.

The tilt, along with other pertinent core parameters, are monitored during operation by the COLSS (described in Section 7.7). If the core margins are not maintained, the COLSS actuates an alarm, requiring the operator to take corrective action. The CPCs actuate a trip if limiting safety system settings are reached.

The thermal margin calculations used in designing the reactor core are performed using the TORC code. The TORC code, which is described in Subsection 4.4.4.5.2, is based on an open core analytical method for performing such calculations and treats the entire core on a three-dimensional basis. Thus, any asymmetry or tilt in the power distribution is analyzed by providing the corresponding power distribution in the TORC input.

4.4.3 DESCRIPTION OF THE THERMAL AND HYDRAULIC DESIGN OF THE REACTOR COOLANT SYSTEM (RCS)

A summary description of the RCS is given in Section 5.1.

4.4.3.1 Plant Configuration Data

4.4.3.1.1 Configuration of the RCS

An isometric view of the RCS is given in Figure 4.4-7.

Table 4.4-6 lists the valves and pipefittings which form part of the RCS.

Table 4.4-7 lists the design minimum flow through each flowpath in the RCS.

Table 4.4-8 provides the volume, minimum flow area, flowpath length, height and liquid level of each volume, and bottom elevation for each component within the RCS.

The line lengths and sizes of the safety injection lines are given in Table 4.4-9 and Figure 4.4-8 (for Figure 4.4-8, Sheet 3, refer to Drawing G167, Sheet 3).

Table 5.1-1 provides a steady-state pressure, temperature, and flow distribution throughout the RCS.

4.4.3.2 Operating Restrictions on Pumps

The minimum RCS pressure at any given temperature is limited by the required net positive suction head (NPSH) for the reactor coolant pumps during portions of plant heatup and cooldown. To ensure that the pump NPSH requirements are met under all possible operating conditions, an operating curve is used which gives permissible RCS pressure as a function of temperature.
→ (DRN 00-644)
The reactor coolant pump NPSH restriction on this curve is determined by using the NPSH requirement for one pump operation (maximum flow, hence, maximum required NPSH) and correcting it for pressure and temperature instrument errors and pressure measurement location. The NPSH required versus pump flow is supplied by the pump vendor. Plant operation below this curve is prohibited. At low reactor coolant temperatures and pressures, other considerations require that the minimum pressure versus temperature curve be above the NPSH curve.
← (DRN 00-644)

4.4.3.3 Power Flow Operating Map (BWR)

This subsection is not applicable.

4.4.3.4 Temperature - Power Operating Map (PWR)

Reactor operation at power with one, two, or three pumps operating, or while in natural circulation is not allowed. However, decay heat may be transferred to the steam generator in any of the above cases. A temperature-power operating map (temperature control program) is provided in Subsection 5.4.10.

The adequacy of natural circulation for decay heat removal after reactor shutdown has been verified analytically and by tests on the Palisades reactor (Docket No. 50-255). The core ΔT in the analysis has been shown to be lower than the normal full power ΔT; thus the thermal and mechanical loads on the core structure are less severe than normal design conditions.

To assess the margin available in a post-coastdown situation, a study was made assuming termination of pump coastdown 100 seconds after reactor trip, with immediate flow decay to the stable natural circulation condition. It should be recognized that pump rotation will continue for substantially longer than 100 seconds. With the maximum decay heat load 100 seconds after trip, the system will sustain stable natural circulation flow adequate to give a thermal power-to-flow ratio of less than 0.9. This power-to-flow ratio was verified by tests completed on the Palisades reactor (Docket No. 50-255), the Omaha reactor (Docket No. 50-285), the Maine Yankee reactor (Docket No. 50-265) and the Calvert Cliffs I reactor (Docket No. 50-317).

Heat removed from the core during natural circulation may be rejected either by dumping to the main condenser or to the atmosphere; the rate of heat removal may be controlled to maintain core ΔT within allowable limits.

The flowrate through the reactor vessel is calculated by use of a computer code called COAST.(11) COAST predicts flow in the RCS with any combination of active and inactive pumps in a two-loop, four-pump plant. Momentum balances are performed on all the flow paths. Frictional losses, shock losses, the operating pump(s) head-flow characteristic curve(s), and an experimentally derived reverse flow, locked rotor, loss coefficient for the nonoperating pump(s) are utilized in determining the unique flow distribution through the system.

4.4.3.5 Load Following Characteristic

The design features of the RCS influence its load following and transient response. The RCS is capable of following the normal condition transients identified in Subsection 3.9.1.1. These requirements are considered when sizing the pressurizer spray and heater capacities and control setpoints. The charging/letdown system control setpoint are selected through detailed computer simulation studies. The Reactor Regulating System (RRS) reactivity insertion rate is also based on these requirements. In addition, the feedwater regulating system control setpoints are selected through computer analysis of these transients. Finally, these transients are included in the equipment specification for each RCS component to ensure the structural integrity of the system.

Load changes are initiated by adjustment of the Turbine Control System load reference setpoint which positions the turbine admission valve. The RRS senses a change in the turbine first stage pressure and positions CEAs to attain the appropriate coolant average temperature. The feedwater regulating system employs a three-element controller which senses changes in steam flow, feed flow, and water level and acts to maintain steam generator level at the desired point.

The pressurizer pressure and level control systems respond to deviations from preselected setpoints caused by the expansion or contraction of the reactor coolant and actuate the spray or heaters and the charging or letdown systems as necessary to maintain pressure and coolant volume.

4.4.3.6 Thermal and Hydraulic Characteristics Table

Principal thermal hydraulic characteristics of the RCS components are listed in Table 4.4-10.

4.4.4 EVALUATION

4.4.4.1 Critical Heat Flux

The margin to critical heat flux (CHF) or DNB is expressed in terms of the DNBR. The DNBR is defined as the ratio of the heat flux required to produce DNB at the calculated local coolant conditions to the actual heat flux.

→(EC-9533, R302; EC-13881, R304; EC-30663, R307)
The CE-1 Correlation[1][2] for standard fuel assemblies and the WSSV-T and ABB-NV correlations[23][24] for NGF assemblies were used with the TORC computer code[6] to determine DNBR values for normal operation and anticipated operational occurrences. Topical Reports CENPD-162[1] and CENPD-207[2] provide detailed information on the CE-1 correlation and source data, and also provide comparisons with other data and correlations. Topical reports WCAP-16523-P-A[23] and CENPD-387-P-A[24] provides detailed information on the WSSV-T CHF correlation and the ABB-NV CHF correlation.

The CE-1 correlation was developed in conjunction with the TORC code specifically for DNB margin predictions for fuel assemblies with standard spacer grids similar to those previously deployed in Waterford 3.
←(EC-9533, R302; EC-13881, R304; EC-30663, R307)

➔(EC-9533, R302; EC-13881, R304; EC-30663, R307)
In brief, the CE-1 correlation is based on data from tests conducted for C-E at the Chemical Engineering Research Laboratories of Columbia University. Those tests used electrically-heated five x five array rod bundles corresponding dimensionally to a portion of a 16 x 16 or 14 x 14 assembly geometries each included tests to determine the effects on DNB of the CEA guide tube, bundle heated length, axial grid spacing, and lateral and axial power distributions.
←(EC-9533, R302; EC-13881, R304; EC-30663, R307)

The uniform axial power CE-1 Correlation[1] was developed from DNB data for six tests sections with the following characteristics:

Fuel Assembly Geometry	No. Heated Rods	Lateral Power Distr	Heated Length (ft.)	Axial Grid Spacing (in.)
16 x 16	25	Uniform	7	16.0
16 x 16	21	Nonuniform	7	18.3
16 x 16	21	Nonuniform	12.5	17.4
14 x 14	25	Uniform	7	14.3
14 x 14	21	Nonuniform	7	14.3
14 x 14	21	Nonuniform	12.5	14.3

Local coolant conditions at the DNB location were determined by using the TORC code in a manner consistent with the use of the code for reactor thermal margin calculations. The uniform axial power CE-1 correlation was developed from 731 DNB data for the following parameter ranges:

Pressure	1785 to 2415 psia
Inlet temperature	382 to 644F
Heat flux	0.213×10^6 to 0.952×10^6 Btu/hr-ft^2
Local coolant quality	-0.16 to 0.20
Local mass velocity	0.87×10^6 to 3.21×10^6 lb/hr-ft^2

The uniform axial power CE-1 correlation predicted the 731 source data with a mean and standard deviation of the ratio of measured and predicted DNB heat fluxes of 1.000 and 0.068, respectively. The validity of the CE-1 correlation for predicting DNB for 16 x 16 fuel assemblies was further verified by the analysis data obtained by repeating one of the tests for the 16 x 16 assembly geometry at the Winfrith Laboratory of the UKAEA.

For nonuniform axial power distributions the uniform axial power CE-1 correlation is modified by the F-factor[5]. The conservatism of that method of predicting DNB for 16 x 16 fuel assemblies with nonuniform axial flux shapes is demonstrated in CENPD-207[2]. CENPD-207[2] presents measured and predicted DNB heat fluxes for a series of tests using nonuniform axial power rod bundles representative of 16 x 16 or 14 x 14 fuel assemblies utilizing standard spacer grids. Those test sections had the following characteristics.

Fuel Assembly Geometry	No. Heater Rods	Lateral Power Distr	Axial Power Distr	Heated Length (ft.)	Axial Grid Spacing (in.)
16 x 16	21	Nonuniform	1.46 symmetric	12.5	14.2
16 x 16	21	Nonuniform	1.47 top peak	12.5	14.2
14 x 14	21	Uniform	1.68 top peak	12.5	17.4
14 x 14	21	Nonuniform	1.68 bottom peak	12.5	17.4

The DNB data from those tests were evaluated using the CE-1 correlation modified by the F-factor and the TORC code used in a manner consistent with the use of the code for reactor calculations. That evaluation included DNB data within the following parameter ranges:

Pressure	1745 to 2425 psia
Inlet temperatures	333 to 631F
Local coolant quality	-0.27 to 0.20
Local mass velocity	0.81 to 10^6 to 3.07 x 10^6 lb/hr-ft^2

It was found that the mean and standard deviation of the ratio of measured and predicted DNB heat fluxes were 1.229 and 0.125, respectively, for the 369 DNB data within the parameter ranges mentioned above.

Testing was also conducted with rod bundles representative of the 16 x 16 fuel assembly to determine the effect on DNB of local perturbations in heat flux. Results are presented in CENPD-207(2) for two nonuniform axial power rod bundles which were similar except that one test bundle had a heat flux spike (23 percent higher heat flux for a four in. length) at the location where DNB anticipated. The results show that there is no significant adverse effect on DNB due to that flux spike. Therefore, it is concluded that no allowance is required for the effect on DNB of local heat flux perturbations less severe than that tested.

One important factor in the prediction of DNB and local coolant conditions is the treatment of coolant mixing or turbulent interchange. The effect of turbulent interchange on enthalpy rise in the subchannels of 16 x 16 fuel assemblies with standard spacer grids is calculated in the TORC code by:

$$P_e^{\Lambda} = \frac{\omega'}{\overline{G}\ \overline{D}_e} = 0.0035$$

where:

P_e^{Λ} = inverse Peclet number

ω' = turbulent interchange between adjacent subchannels, lb/hr-ft

$\overline{D}_e$ = average equivalent diameter of the adjacent subchannels, ft

$\overline{G}$ = average mass velocity of the adjacent subchannel, lb/hr-ft^2

The value of 0.0035 for the inverse Peclet number for use with the 16 x 16 fuel assembly with standard spacer grids was originally chosen based on cold water dye mixing tests conducted for the 14 x 14 assembly and for a "prototype" of the Palisades reactor fuel assembly. The validity of the inverse Peclet number of 0.0035 for the 16 x 16 assembly with standards grids was verified with data obtained in the tests conducted at Columbia University(1).

The design basis requires that the minimum DNBR for normal operation and anticipated operational occurrences be chosen to provide a 95 percent probability at the 95 percent confidence level that DNB will not occur on a fuel rod having that minimum DNBR. Statistical evaluation of the CE-1 correlation and relevant data shows that appropriate minimum DNBR is 1.13.(1)(2) Based on review of CENPD-152(1), the NRC requires use of a minimum DNBR of 1.19. Therefore, the minimum DNBR used for design is 1.19.

4.4.4.2 Reactor Hydraulics

4.4.4.2.1 Reactor Flow Model Tests

Design values for the reactor hydraulic parameters are obtained or verified by means of flow model tests. These flow model tests involve the use of scale reactor models and are part of the C-E reactor development program. The test programs provide information on flow distribution in various regions of the reactor, pressure loss coefficients, hydraulic loads on vessel internal components, and turbulence-induced pressure and velocity fluctuations.

C-E's PWR designs fall into seven basic geometric configurations as shown below:

Configuration	Reactor(s)	Distinguishing Hydraulic Features
1	Palisades	Four inlets, two outlets, cruciform control rods, 204 fuel assemblies.
2	Fort Calhoun	Four inlets, two outlets, CEAS, 133 fuel assemblies
Configuration	Reactor(s)	Distinguishing Hydraulic Features
3	Maine Yankee	Three inlets, three outlets, CEAS, 217 fuel assemblies, 137-in. long core.
4	Calvert Cliffs 1 & 2 St. Lucie 1 & 2 Millstone (Unit 2)	Four inlets, two outlets, CEAS, 217 fuel assemblies, 137-in. long core.
5	Arkansas Nuclear One Unit 2 Blue Hills Station	Four inlets, two outlets, CEAS. 177 fuel assemblies, 150-in. long core.
6	San Onofre (Units 2 & 3) Forked River Waterford, Pilgrim	Four inlets, two outlets, CEAS, 217 fuel assemblies, 150-in. long core.

7	System 80	Four inlets, two outlets, 241 fuel assemblies, modified upper and lower plena design, 150-in. long core.

Flow model tests have been conducted on configurations one through four and six. The Palisades and Fort Calhoun flow tests were run under contract with Battelle Memorial Institute using air as the test medium. The Maine Yankee and the configuration four reactor flow model tests were performed in a 15,000 gal/min cold water facility in the C-E Nuclear Laboratories. The flow models for configuration one through four were 1/5 scale models that simulated the entire reactor, from inlet to outlet. These models had closed cores. Allow model test was also performed with a 115 scale water flow model of the configuration six geometry: This model has an open core.

The design hydraulic parameter for Waterford 3 were obtained from results of the configuration six model test and by extrapolating from the flow model tests on configurations one through four. Where interpolation was required, geometric differences between configuration six and the earlier reactor configurations were accounted for by analytical means and by utilizing the experience gained from the earlier tests, during which numerous investigations were made of the effect of various internal components on flow distribution and pressure drop.

The principal design hydraulic parameters include:

- The core inlet flow distribution
- Reactor pressure losses
- Hydraulic loads on reactor internal components

The approaches for deriving the design hydraulic parameters are described as follows:

a) Core Inlet Flow Distribution

→ (DRN 00-644)

The core inlet flow distribution is required as input to the TORC thermal margin computer code (refer to Subsection 4.4.4.5.2). A core inlet flow distribution was determined for four-loop operation from the 115 scale water flow model of the configuration six reactor. the resulting core inlet flow distribution shows quadrantal symmetry. Most centrally located fuel assemblies, located at least one row in from the core peripheral boundary, have higher than average flow rates. The peripheral fuel assemblies have lower than average flow rates. The flow distribution is described in CENPD-206 P([10]).

← (DRN 00-644)

b) Reactor Pressure Losses

Reactor vessel pressure losses are determined with a standard calculational model. This model was developed partly on the basis of pressure loss results from flow model tests on the earlier reactor configurations one through four.

The calculational model divides the flow path through the reactor into segments; the principal flow path segments are :

1) The inlet region

2) The downcomer region

3) The lower plenum region

4) The core support structure region

5) The core region

6) The upper plenum region.

→(DRN 00-644)

A combination of analytical or empirical relationships are used for each flow path segment in the standard pressure loss calculational method. When empirical relationships are used for a new reactor, the coefficient(s) from the originating model tests are modified by analytical means to account for geometry variations between the original reactor geometry and that for the new reactor geometry.

→(DRN 06-871, R15)

Agreement between predictions by the standard calculational method and experimental pressure losses is found to be good. For example, from flow model tests on configuration four, the agreement between predicted and measured values for the segmental losses was within 15 percent while the nozzle-to-nozzle pressure losses were found to be systematically high relative to the measured values. Comparisons have also been made between nozzle-to-nozzle pressure drops measured in two C-E reactors (configurations 1 and 3) and values predicted by the standard calculational method. These later comparisons show agreement within seven percent, again with the predicted values being higher than the measured values.

←(DRN 00-644; 06-871, R15)

The vessel pressure losses were estimated with the standard calculational method, taking into account the observed systematic differences between predicted and measured pressure losses.

The core pressure drop is increased by six psi in the calculation of design hydraulic loads to account for the possibility of core crudding. The six psi value was chosen on the basis that it provides a sufficient margin to accommodate core crudding effects. Experience with operating plants indicates that any increases in core pressure drop due to crudding effects are much smaller compared to the six psi design value.

c) Hydraulic Loads on Reactor Internal Components

Hydraulic loads were estimated on the basis of both experimental data from flow model tests on reactor configurations 1 through 4 and by analytical means. When experimental data are used, they are first reduced to dimensionless form in terms of a pressure difference coefficient.

$$E = \frac{P_{local} - P_{ref}}{\rho V_{ref}^{2} / 2g}$$

a force coefficient,

$$C_F = \frac{F}{\rho V_{ref}^{2} A_{ref} / 2g}$$

or a velocity ratio,

$$\frac{V_{local}}{V_{ref}}$$

The quantities with subscript "ref" represent appropriate reference values: for example, the average velocity or pressure at the particular flow path station of interest. These dimensionless quantities are then converted to absolute quantities by multiplying by the appropriate reference quantity (i.e., by $\rho V^2_{ref} / 2g$ or V_{ref}) for the reactor of interest.

Adjustment to the resulting absolute quantities are made by analytical means if there are substantial differences in geometry between the reactor configuration for which the test data were derived and the reactor configuration of interest.

Further discussion of the philosophy of flow model testing appears in CENPD-12.(12)

4.4.4.2.2 Components Testing

Components test programs have been conducted in support of all C-E reactors. The tests subject a full-scale reactor core module comprising one to four fuel assemblies, control rod assembly and extension shaft, control element drive mechanism, and reactor vessel internals to reactor conditions of water chemistry, flow velocity, temperature, and pressure under the most adverse operating conditions allowed by the design. Two objectives of the programs are to confirm the basis hydraulic characteristics of the components and to verify that fretting and wear will not be excessive during the components' lifetime. When the reactor design is revised, a new program embodying the important aspects of the latest design is conducted.

Thus, components tests have been run on the Palisades design, with cruciform control rods, on the Fort Calhoun design with CEAs and rack-and-pinion control element drive mechanisms (CEDM), and on the Maine Yankee design with a dual CEA and a magnetic jack CEDM. A components test program on a typical 16 x 16 fuel assembly, a CEA, and magnetic jack CEDM has been performed. The results apply to Waterford 3.

During the course of the tests, information is obtained on fuel rod fretting, on CEA/CEDM trip behavior, and on fuel assembly uplift and pressure drop. The first two subjects are discussed in Section 4.2. The third is discussed below.

As part of the assessment of fuel assembly margin to uplift in the reactor, measurements are made of the coolant velocity required to lift the fuel assembly for an isothermal temperature range of 150 to 600 F at a system pressure of 350 to 2100 psia. To obtain the desired information, a fuel assembly was mounted either on load beams or liftoff probes. These devices are used to indicate the liftoff of the fuel assembly. Data reduction involves the calculation of an uplift coefficient, describing the hydraulic uplift force acting on the assembly; the coefficient is defined as follows:

→ (DRN 00-644)

$$K_{up} = Wo/\gamma V^2 A/2g_c$$

← (DRN 00-644)

where:

Wo = Wet weight of assembly with no flow, lb

V = Flow velocity in assembly at the point of liftoff, ft/sec

A = Envelope area of assembly, ft^2

→ (DRN 00-644)

γ = Water density, lb/ft^3

← (DRN 00-644)

A plot of the K_{up} data shows that they can be fitted by the relation:

$$K_{up} = \alpha N_R^{-B}$$

where α and β are peculiar to the particular components test being run and where the standard error of estimate is typically about 4 percent, including replication and instrument error.

→ (DRN 00-644)

The uplift coefficient and its associated uncertainty are employed in the analysis of the uplift forces on the fuel assemblies in the reactor. The force is determined at the least favorable location hydraulically for startup and steady-state operating conditions. Additional input to the calculation includes analytical corrections to the coefficient for the absence of the CEA, for crud formation, and for small geometrical differences among the fuel assemblies for the different reactor designs all nominally describable by the same components tests.

← (DRN 00-644)

Pressure drop measurements are also made during the components test program to verify the accuracy of the calculated loss coefficients for various fuel assembly components. Direct reduction of the pressure drop data yields the loss coefficients for the lower and upper end fitting region, while the rod friction loss from the measured pressure drop across the fuel rod region.

Loss coefficients for the upper and lower end fittings and spacer grids on the Waterford 3 fuel have been obtained from flow testing of the 16 x 16 fuel. These data have been provided to the NRC in Reference 21.

4.4.4.2.3 Core Pressure Drop Correlations

The total pressure drop along the active fuel region of the core is computed as the sum of the individual losses resulting from friction, acceleration of the fluid and change in elevation of the fluid and spacer grids. The individual losses are computed using the momentum equation and the consistent set of empirical correlations presented in the TORC code(6).

In the following paragraphs, the correlations used are summarized and the validity of the scheme is demonstrated with a comparison of measured and predicted pressure drops for single-phase and two-phase flow in rod bundles with CEA-type geometry.

For isothermal, single-phase flow, the pressure drop due to friction for flow along the bare rods is based on the equivalent diameter of the bare rod assembly and the Blasius friction factor:

$$f = 0.184\ N_R^{-0.2}$$

The pressure drop associated with the spacer grids is computed using a grid loss coefficient (K_{SG}) given by a correlation which has the following form:

$$K_{SG} = D_1 + D_2 (N_R)^{D_3} \pm \text{Standard Error of Estimate}$$

→(DRN 00-644)

The constants, D_η, are determined from pressure drop data obtained for a wide range of Reynolds Number for isothermal flow through CEA-type rod bundles fitted with standard spacer grids. The data comes from the DNB program (Subsection 4.4.4.1) and from the components test program (Subsection 4.4.4.2.2). The standard error of estimate associated with the loss coefficient relation includes replication and instrument error.

←(DRN 00-644)

To compute pressure drop either for heating without boiling or for sub cooled boiling, the friction factor given above for isothemal flow is modified through the use of the multipliers given in Pyle.(13) It is important to recognize that the multipliers were developed in such a way as to incorporate the effects of subcooled voids on the acceleration and elevation components of the pressure drop as well as the effect on the friction losses. Consequently, it is not necessary to compute specifically either a void fraction for subcooled boiling or the individual effects of subcooled boiling on the friction, acceleration, or elevation components of the total pressure drop.

→(DRN 00-644; EC-13881, R304)

The effect of bulk boiling on the friction pressure drop is computed using a curve fit to the Martinelli-Nelson data(14) above 2000 psia or the Martinelli-Nelson correlation(14) with the modification given in Pyle(13) below 2000 psia. The acceleration component of the pressure drop for bulk boiling conditions is computed in the usual manner for the case of two-phase flow where there may be a nonunity slip ratio.(15) The elevation and spacer grid pressure drops for bulk boiling are computed as for single phase flow except that the bulk coolant density $(\bar{\rho})$ is used, where:

←(DRN 00-644; EC-13881, R304)

$$\bar{\rho} = \alpha \rho_V + (1 - \alpha)\rho_1$$

and

α = bulk boiling void fraction

ρ_V = density of saturated vapor, lb/ft^3

ρ_1 = density of saturated liquid, lb/ft^3

The bulk boiling void fraction used in computing the elevation, acceleration, and spacer grid losses is calculated by assuming a slip ratio of unity if the pressure is greater than 1850 psia or by using the Martinelli-Nelson void fraction correlation[14] with the modifications presented in Pyle[13] if the pressure is below 1850 psia.

To verify that the scheme described above accurately predicts pressure drop for single-phase and two-phase flow through the 16 x 16 assembly geometry comparisons have been made of measured pressure drop and the pressure drop predicted by TORC,[6] for the rod bundles used in the DNB test program at Columbia University (refer to Subsection 4.4.4.1). Figure 4.4-9 shows some typical results for a 21-rod bundle of the 16 x 16 fuel assembly geometry (five x five array with four rods replaced by a control rod guide tube). The excellent agreement demonstrates the validity of the methods described above.

4.4.4.3 Influence of Power Distributions

The reactor operator, utilizing the COLSS, will restrict operation of the plant such that power distributions which are permitted to occur will have adequate margin to satisfy the design bases during anticipated operational occurrences. A discussion of the methods of controlling the power distributions is given in Subsection 4.3.2.4.2. A discussion of the expected power distributions is given in Subsection 4.3.2.2.3, and typical planar rod radial power factors and axial shapes are given in Figures 4.3-2 through 4.3-18. The full-power maximum rod radial power factor is taken as 1.55 and is used in the calculations of the core thermal margins which are given here in Section 4.4. Comparison with expected power distributions, discussed in Section 4.3, shows that this integrated rod radial power factor is at least 10 percent higher than all the calculated values and, therefore, is a meaningful value for thermal margin analyses.

→(DRN 02-1477)

If CEAs are inserted in the core, the same planar radial power distribution does not exist at each axial elevation of the core, nor does the same axial power distribution exist at each radial location in the core. From the analysis of many three-dimensional power distributions, the important parameters which establish the thermal margin in the core the maximum rod power and its axial power distribution.[10] Examination of many axial power distributions shows the 1.26 peaked axial power distribution in Figure 4.4-3 to be among those giving the lowest DNBRs. The combination of that axial shape and the maximum rod radial power factor of 1.55 is therefore a meaningful combination for DNB analyses. The maximum linear heat rate at a given power is determined directly from the core average fuel rod linear heat rate and the nuclear power factor. The value of 2.28 for the nuclear

←(DRN 02-1477)

power factor is selected and corresponds to the 1.55 rod radial power factor combined with the 1.47 peaked axial shape shown in Figure 4.4-3. As stated before, the supervisory and protective systems measure the maximum rod radial power factor and the axial power distribution in the core and ensure that the design limits specified in Subsection 4.4.1 are not violated.

4.4.4.4 Core Thermal Response

Steady-state core parameters are summarized in Table 4.4-1 for normal four pump operation. Figure 4.4-10 shows the sensitivity of the minimum DNBR to small changes in pressure, inlet temperature, and flow from the conditions specified in Table 4.4-1. The same 1.26 peaked axial power distribution and 1.55 maximum rod radial power factor are used.

The response of the core to anticipated operational occurrences is discussed in Chapter 15. The response of the core at the design over power cannot be presented with any meaning. The concept of a design overpower is not applicable for Waterford 3 since the RPS prevents the design basis limits from being exceeded.

The supervisory and protective systems will ensure that the design bases in Subsection 4.4.1 are not violated for any steady state operating condition of inlet temperature, pressure, flow, power, and core power distribution and for the anticipated operational occurrences discussed in Chapter 15.

4.4.4.5 Analytical Methods

4.4.4.5.1 Reactor Coolant System Flow Determination

The design minimum flow to be provided by the reactor coolant pumps is established by the required mass flow to result in no violation of the design limits in Subsection 4.4.1 during steady state operation and anticipated operational occurrences. This design minimum flow is specified in Table 4.4-1.

The reactor coolant pumps are designed to produce a flow greater than or equal to the design minimum flow for the maximum expected system flow resistance. The maximum system flow resistance is determined by adding an allowance for uncertainty to the best estimate system flow resistance. From this maximum system flow resistance, the required minimum reactor coolant pump head is determined.

Upon completion of the manufacturing and testing of the pumps, the characteristic pump head or performance curve is established. The expected maximum, best estimate, and minimum reactor coolant system flow rates are determined as follows:

a) Best Estimate Expected Flow

The best estimate expected RCS flow is determined by equating the head loss around the reactor coolant flow path to the head rise supplied by the reactor coolant pumps (Subsection 5.4.1 has a description of the pumps).

b) Maximum Expected Flow

The maximum expected flow is determined in a manner analogous to the best estimate expected flow. A maximum pump performance curve for each pump is calculated from the uncertainty in flow measurement. This uncertainty is based on performance and acceptance testing done at the pump vendor's facility. The minimum pressure loss for the steam generator and piping is determined by subtracting 10 percent on best estimate friction losses and 20 percent on best estimate geometry losses. The minimum pressure loss for the reactor vessel is evaluated by considering the uncertainties in the correlations for the loss coefficients and the normal manufacturing deviations from nominal dimensions. The maximum expected flow results from the combination of the maximum pump curve and the minimum system resistance.

c) Minimum Expected Flow

The minimum expected flow is determined in a manner analogous to the maximum expected flow. The minimum expected flow results from the combination of the minimum pump curve and the maximum system resistance. The minimum expected flow will be equal to or greater than the design minimum flow.

→ (DRN 00-644)
Upon installation of the pumps in the Reactor Coolant System, the operating flow is determined from measurements of pressure differential across a pair of taps in each pump casing inlet and outlet. The individual loop flows are deduced from plots of pump flow vs pump Δp developed from calibration measurements made at the vendor's test facility. The total system flow is obtained by summing the loop flows. The uncertainties included in the calculation of the operating flow are the uncertainty associated with measurement of flow and pump differential pressure at the test facility, and the uncertainty in the measurement of pump differential pressure at the plant site. These uncertainties are statistically combined to give the overall uncertainty in primary coolant flow as determined from onsite tests. The best estimate flow reduced for uncertainties shall be greater than the design minimum flow.
← (DRN 00-644)
Any significant formation of crud buildup is detected by continuous monitoring of the Reactor Coolant System flow. A significant buildup of crud is not anticipated, however, because the water chemistry is designed to minimize crud buildup.

4.4.4.5.2 Thermal Margin Analysis

Thermal margin analyses of the reactor core are performed using the TORC code which is an open core analytical method based on the COBRA-IIIC code[16]. A complete description of the TORC code and its detailed application to core thermal margin analyses is contained in CENPD-161[6]. A brief description of the code and its use is given here.

The COBRA-IIIC code solves the conservation equations for mass, axial and lateral momentum, and energy for a collection of parallel flow channels that are hydraulically open to each other. Since the size of a channel in design varies from the size of a fuel assembly or more to the size of a subchannel within a fuel assembly, certain modifications were

necessary to enable a realistic analysis of thermal-hydraulic conditions in both geometries. The principal revisions to arrive at the TORC code, which leave the basis structure of COBRA-IIIC unaltered, are in the following areas:

a) Modification of the lateral momentum equation for core wide calculations where the smallest channel size is typically that of a fuel assembly.

b) Addition of the capability for handling non-zero lateral boundary conditions on the periphery of a collection of parallel flow channels. This capability is particularly important when analyzing the group of subchannels within the hot fuel assembly.

c) Insertion of standard C-E empirical correlations and the ASME fluid property relationships.

Details of the lateral momentum equations and the standard empirical relationships are given in CENPD-161(6). The application of the TORC code involves two or at most three stages where each stage is a separate TORC code computer run. The three stage approach is discussed below.

The first stage consists of calculating coolant conditions throughout the core on a coarse mesh basis. The core is modeled such that the smallest unit represented by a flow channel is a single fuel assembly. The three-dimensional power distribution in the core is superimposed on the core coolant inlet flow and temperature distributions. The core inlet flow distribution is obtained from flow model tests discussed in subsection 4.4.4.2, and the inlet temperature for normal four-loop operation is assumed uniform. The core exit static pressure distribution is obtained from flow model tests. The axial distributions of flow and enthalpy in each fuel assembly are then calculated on the basis that the fuel assemblies are hydraulically open to each other. Also determined during this stage are the transport quantities of mass, momentum, and energy which cross the lateral boundaries of each flow channel.

In the second stage, the hot assembly is analyzed with a coarse mesh in which the hot assembly and its adjoining fuel assemblies are modeled. The hot assembly is typically divided into four to five partial assembly regions. One of these regions is centered on the subchannels adjacent to the rod having the minimum DNBR. It need not be the highest powered rod in the fuel assembly. The three-dimensional power distribution is superimposed on the core coolant inlet flow and temperature distributions. The lateral transport of mass, momentum, and energy from the stage one calculations is imposed on the peripheral boundary enclosing the hot assembly and the neighboring assemblies. The axial distributions of flow and enthalpy in each channel are calculated as well as the transport quantities of mass, momentum, and energy which cross the lateral boundary of each flow channel.

→(EC-13881, R304)
The third stage involves a fine mesh modeling of the partial-assembly region which centers on the subchannels adjacent to the rod having the minimum DNBR. All of the flow channels used in this stage are hydraulically open to their neighbors. The output from the stage two calculations, in terms of the lateral transport of mass, momentum, and energy is imparted on the lateral boundaries of the stage three partial assembly region. Engineering factors are applied to the minimum DNBR rod and the hottest adjacent subchannel to account for uncertainties on the enthalpy rise and heat flow due to manufacturing tolerances. The local coolant conditions are calculated for each flow channel. These coolant conditions are then input to the DNB correlation and the minimum value of DNBR in the core is determined.
←(EC-13881, R304)

→(EC-13881, R304)
A more detailed description of this procedure with example is contained in CENPD-161[6]. This procedure is used to analyze any specific three-dimensional power distribution superimposed on an explicit core inlet flow distribution.
←(EC-13881, R304)

→(DRN 00-644)
The method used for design calculations is discussed in detail in CENPD-206[10]. In summary, the method is to use one limiting core radial power distribution for all analyses, to rise or lower the hot assembly power to provide the proper maximum rod radial power factor, and to use the core average mass velocity in all fuel assemblies except the hot assembly. The percent reduction for the hot assembly mass velocity is determined by comparison of results with the above detailed procedure. This methodology is used in the thermal margin analyses of the W3 reactor.
←(DRN 00-644)

4.4.4.5.3 Hydraulic Instability Analysis

Flow instabilities leading to flow excursions or flow oscillations have been observed in some boiling flow systems containing one or more closed, heated channels. Flow instabilities are a concern primarily because they may lead to a reduction in the DNB heat flux relative to that observed during a steady flow condition. Flow instabilities of several types have been observed or postulated for closed channel systems. Although the state of the art does not permit detailed theoretical analyses for each qW of flow instability, the available information on boiling systems indicates that flow instabilities will not adversely affect thermal margin of W3 during normal operation or anticipated operational occurrences.

→(DRN 00-644)
Flow instabilities which have been observed have occurred almost exclusively in closed channel systems operating at low pressures relative to PWR operating pressures. As shown by the tests discussed in Subsection 4.2.3, the resistance to coolant crossflow among subchannels of the 16 x 16 fuel assembly is extremely small. It would be expected that the low resistance to crossflow between adjacent subchannels would have a stabilizing effect, and that expectation is confirmed by the results of Veziroglu and Lee[17] who found that flow stability in parallel heated channels was enhanced by having cross connections between the channels. Increasing pressure has been found to have a stabilizing influence in many case where flow instabilities have been observed,[18] and the high operating pressure characteristic of PWRs tends to minimize the potential for flow instability. Kao, Morgan, and Parker,[19] who conducted flow stability experiments at pressures up to 2200 psia with closed parallel heated channels, found that no flow oscillations could be induced at pressure above 1200 psia for low power and power levels encountered in power reactors. Additional evidence that flow instabilities do not adversely affect thermal margin is provided by the data from the rod bundle DNB tests (see Subsection 4.4.4.1). Many rod bundles have been tested over wide ranges of operating conditions with no evidence of premature DNB or of inconsistent data which might be indicative of flow instabilities in the rod bundle.,
←(DRN 00-644)

→(DRN 00-644)
In summary, it is concluded that flow instabilities will not adversely affect thermal margin of Waterford 3 during normal operation and anticipated operational occurrences.
←(DRN 00-644; LBDCR 13-014, R309)

4.4.5 TESTING AND VERIFICATION

→(DRN 00-644; LBDCR 13-014, R309)
Data descriptive of thermal and hydraulic conditions within the reactor vessel will be obtained as part of the startup program described in Section 14.2. These will include hot and cold leg temperature, loop flowrates, and core power distributions. The data will be evaluated and compared with design calculations and parameters to assure that the reactor thermal and hydraulic behavior is as predicted.
←(DRN 00-644)

4.4.6 INSTRUMENTATION REQUIREMENTS

→(LBDCR 13-014, R309)
The in-core instrumentation system will be used to confirm core power distribution, perform periodic calibrations of the excore flux measurement system, and provide inputs to the COLSS. Further descriptions are contained in Section 7.7.
→(LBDCR 13-014, R309)

4.4.6.1 Valve and Loose Parts Monitoring System (V&LPMS)

The valve and loose parts monitoring equipment is provided to monitor the Reactor Coolant System (RCS) for loose parts in the reactor internals. In addition, the equipment is also used to detect primary safety valve position (see Section 1.9.23).

→(EC-26965, R305)
The V&LPMS meets the requirement of Regulatory Guide 1.133 as modified by NRC Technical Specification Amendment 104, and the Neutron Noise Monitoring system meets the requirements of ASME/ANSI OM-1987 Part OM-5.
←(EC-26965, R305)

→(DRN 00-644)
Loose parts become detectable when they are driven or waited against the inner walls of a pressure vessel or piping. A steady flow of coolant within the reactor vessels will wedge the loose part in a fixed position until flow is changed. When a loose part is driven from its position and hits the inner walls, the impact produces the sound waves radiating in the metal walls.

The Waterford 3 V&LPMS has been designed and manufactured by the Framatome and is included as part of the plant instrumentation for continuous monitoring of anomalous conditions due to a presence of loose parts in the RCS.

This system consists of sixteen high-temperature sensor assemblies; eight in Train A and eight in Train B, independent preamplifiers with shielded enclosures, all the hardware associated with mounting and wiring of the system and one signal processing and monitoring cabinet. Components installed inside containment are designed to comply with OBE requirements. The cabinet contains eight loose parts detector channels and four core internals channels (with signal conditioning and A/D conversion), system computer, mass storage, system, interface module, graphics printer, modem, back up cartridge tape drive, and software. Each detector module will monitor either channel A or B sensors via a toggle switch in the cabinet. Contact outputs which open on alarm for loose parts detected and pressurizer relief valve open are provided as interface to the main plant annunciator. Neutron noise monitoring consisting of the four core internal channels and neutron noise monitoring software is provided. A manual reset is provided to clear the alarm condition.
←(DRN 00-644)

The system includes an acoustic valve monitoring system consisting of four (4) acoustic Valve Monitoring System (VMS) detector modules, and acoustic monitoring system software. The system has the ability to provide monitoring and alarm functions without the system computer or hard disk in operation, and the ability to allow manual switching of the audio monitor through the channels with the computer or hard disk off line. Four (4) 0-10 VDC output channels are provided for the valve monitoring modules with two channels to the QSPDS and the remaining two channels to the PMC.

→(DRN 00-644)
The sensors are strategically located with two sensors at each collection region as shown in Figure 4.4-11. They are designed to detect the impact sound waves and transduce the detected unusual vibration signals to the main control room. The sensors and immediate sensor cable are tested and qualified for 10^{10} rad., 0-100 percent humidity, 100g vibration, and 650°F.
←(DRN 00-644)

Noise Rejection Capability is provided by the following:

a) Electrical isolation of the sensors from the plant structure.

b) Loose part detection is at a high (27 Khz) frequency which is above the plant background noise spectrum.

c) Double-shielding of sensor to preamp cable through use of coaxial cable in 3/4 in. iron conduit.

d) High-gain charge preamp placed as close as practical to the sensor.

→(DRN 00-644)
e) Twisted shielded pair cables are used from the charge preamp to the cabinet. These cables are laid low-level trays. These trays are to have no 60-hz control signals and switching transients.
←(DRN 00-644)

f) Shielded MS connectors (supplied by ESG) are used.

g) Cabinet power is low noise. A line filter is included.

h) EMI filters are included on every channel.

→(DRN 03-1689, R13-A; 04-1780, R14; 06-871, R15)
The preamplifiers are mechanically protected in junction boxes and are located outside the biological shield, close to the sensors. They are tested and qualified for 10^{7} rad., 0-100 percent humidity, 10g vibration, and 150°F temperature. Sensor to preamplifier cable runs are through rigid conduit inside the containment.
←(DRN 03-1689, R13-A; 04-1780, R14; 06-871, R15)

→(DRN 00-644)
The motion of the reactor core internals is detected by the core internals monitoring channel configuration using the Neutron Noise Monitor to detect the neutron noise signal from each channel and obtaining core motion information therefrom. The core internals channels use existing signals from the excore monitoring system through Class 1E buffers. Signals in the one to 25 Hz range can indicate the existence of fuel pin or core barrel motion.
←(DRN 00-644)

4.4.6.1.1 Sensor Location

The sensors and preamplifiers are located in the containment (as shown in Figure 4.4-11) at the following locations:

Channel No.	Location	Type of Accelerometer
1 (A&B)	Bottom of Reactor Vessel	Hi - Temp
2 (A&B)	Head of Reactor Vessel	Hi - Temp
3 (A&B)	RC Pump 1A	Hi - Temp
4 (A&B)	RC Pump 1B	Hi - Temp
5 (A&B)	RC Pump 2A	Hi - Temp
6 (A&B)	RC Pump 2B	Hi - Temp
7 (A&B)	Top of Steam Generator No. 1	Hi - Temp
8 (A&B)	Top of Steam Generator No. 2	Hi - Temp
9 (A&B)	Detector Module (Spare)	-
10 (A&B)	Detector Module (Spare)	-
13 (A&B)	Core Internals	Noise Channels
14 (A&B)	Core Internals	Noise Channels
15 (A&B)	Core Internals	Noise Channels
16 (A&B)	Core Internals	Noise Channels
17	Pressurizer Safety Relief Valve A	Hi - Temp
18	Pressurizer Safety Relief Valve B	Hi - Temp
19	Pressurizer Safety Relief Valve A	Hi - Temp
20	Pressurizer Safety Relief Valve B	Hi - Temp
21	Acoustic Valve Monitoring Module (Spare)	-
22	Acoustic Valve Monitoring Module (Spare)	-

All sensors with their signal processing loops have the capability of monitoring the signals emanating from the presence of loose parts within the system at the location where the sensors are installed.

4.4.6.1.2 Signal Processing and Monitoring Cabinet

This cabinet is located in the main control room and includes the system computer, mass storage, system interface module, graphics printer, modem, backup cartridge tape drive, software, and detector modules for the V&LPMS. The system has a test and reset capability for automatically testing the system. Alarm indication is provided for all the valve and loose parts sensing channels.

4.4.6.1.3 Training

A complete training program is provided. The training program includes the following, in either lecture or demonstration form:

- Theory of Operation
- System Description
- Hardware Description
- Installation
- Calibration
- Normal Operation
- Actions in the Event of an Alarm
- Trouble Shooting

SECTION 4.4: REFERENCES

1. "Critical Heat Flux Correlation for C-E Fuel Assemblies with Standard Spacer Grids, Part 1, Uniform Axial Power Distribution," September, 1976; CENPD-162-P-A (Proprietary), CENPD-162-A (Non-proprietary).

2. "Critical Heat Flux Correlation for C-E Fuel Assemblies with Standard Spacer Grids, Part 2, Non-Uniform Axial Power Distributions," June, 1976; CENPD-207-P (Proprietary), CENPD-207 (Non-Proprietary).

3. Tong, L.S., "An Evaluation of the Departure from Nucleate Boiling in Bundles of Reactor Fuel Rods", Nuclear Science and Engineering", Vol 33, pp 7 to 15, 1968.

4. Letter from Olan O. Parr of NRC to A.E. Schemer of C-E dated May 5, 1976 concerning NRC review of CENPD-162.

5. Tong, L.S., "Boiling Crisis and Critical Heat Flux," AEC Critical Review Series, 1972.

6. "TORC Code: A Computer Code for Determining the Thermal Margin of a Reactor Core," July, 1975; CENPD-161-P (Proprietary), CENPD-161 (Non-proprietary).

7. Maurer, G.W., "A Method of Predicting Steady-State Boiling Vapor Fractions in Reactor Coolant Channels," Bettis Technical Review, WAPD-BT-19, Reactor Technology, June, 1960.

8. Dittus, F.W. and Boelter, L.M.K., "Heat Transfer in Automobile Radiators of the Tubular Type," University of California Publication in Engineer Vol 2, No. 13, pp 443-461, 1930.

9. Jens, W.H. and Lottes, P.A., "Analysis of Heat Transfer, Burnout, Pressure Drop, and Density Data for High Pressure Water," ANL-4627, May 1, 1951.

10. "TORC Code Verification and Simplified Modeling Methods," CENPD-206-P (Proprietary), CENPD-206 (Non-Proprietary) January, 1977.

11. "Coast Code Description," approval letter from O. Parr (NRC) to F. Stern (C-E), December 4, 1974, C-E Topical Report, CENPD-98, April, 1973.

SECTION 4.4 REFERENCES (Cont'd)

12. "Additional Thermal Hydraulic Information on Combustion Engineering 3390 MWT Reactor Cores," C-E proprietary report, CENPD-12.

13. Pyle, R.S., "A Program for the Thermal Analysis of a Pressurized Water Nuclear Reactor During Steady-State Operation," STEADY-3, WAPD-TM-213, June, 1960.

14. Martinelli, R.C. and Nelson, D.B., "Prediction of Pressure Drop During Forced Circulation Boiling of Water," ASME Transactions, August, 1948.

15. Mendler, O.J., et al., "Natural Circulation Tests with Water at 800 to 2000 psia under Non-Boiling, Local Boiling, and Bulk Boiling Conditions," Journal of Heat Transfer, August, 1961.

16. Rowe, D.S., "COBRA-IIIC: A Digital Computer Program for Steady-State and Transient Thermal-Hydraulic Analysis of Rod Bundle Nuclear Fuel Elements," BNWL-1695, March 1973.

17. Veziroglu, T.N. and Lee, S.S., "Boiling-Flow Instabilities in a Cross-Connected Parallel-Channel or Flow System," ASME Paper 71-HT-12, August, 1971.

18. Boure, J.A., Bergles, A.E., and Tong, L.S., "Review of Two-Phase Flow Instability, ASME Paper 71-HT-42, August, 1971.

19. Kao, H.S., Morgan, C.D., and Parker, M.B., "Prediction of Flow Oscillation in Reactor Core Channel," ANS Transactions, Vol 16, p 212, 1973.

20. "Fuel and Poison Rod Bowing," Combustion Engineering Topical Report, CENPD-225, (Non-Proprietary and CENPD-225-P Proprietary) October, 1976.

21. Final Safety Analysis Report, Amendment 3, Section 4.4.4.2, San Onofre Nuclear Generating Station Units 2 and 3, NRC Docket Nos. 50-361 and 50-362, Response to NRC Question 221.5 (Proprietary), August, 1977.

→(DRN 04-1096, R14)

22. CEN-382-P-A, “Methodology for Core Designs Containing Erbium Burnable Absorbers,” ABB Combustion Engineering Nuclear Fuel, August 1993.

←(DRN 04-1096, R14)

→(EC-9533, R302)

23. WCAP-16523-P-A, Rev. 0, “Westinghouse Correlations WSSV and WSSV-T for Predicting Critical Heat Flux in Rod Bundles with Side-Supported Mixing Vanes”, August 2007.

←(EC-9533. R302)

→(EC-13881, R304)

24. CENPD-387-P-A, “ABB Critical Heat Flux Correlations for PWR Fuel,” May 2000.

←(EC-13881, R304)

-TABLE 4.4-1 (Sheet 1 of 2)

THERMAL AND HYDRAULIC PARAMETERS

Reactor Parameters	Waterford 3	Pilgrim Station Unit 2 (Docket 50-471)
Core Average Characteristics at Full Power:		
Total core heat output, MWt	3,390	3,456
Total core heat output, million Btu/hr	11,570	11,80
Average fuel rod energy deposition fraction	0.975	0.965
Hot fuel rod energy deposition fraction	0.975	0.960
Primary system pressure, psia	2,250	2,250
Reactor inlet coolant temperature, F	553	557.5
Reactor outlet coolant temperature, F	611	616
Core exit average coolant temperature, F	613	618
Average core enthalpy rise, Btu/lb_m	80.3	82.6
Design minimum primary coolant flow rate, gpm	396,000	396,000
Design maximum core bypass flow, % of primary	2.6	3.5
Design minimum core flow rate, gpm	385,700	382,140
Hydraulic diameter of nominal subchannel, in.	0.471	0.471
Core flow area, ft^2	54.7	54.8
Core avg mass velocity, million $lb_m/hr\text{-}ft^2$	2.64	2.60
Core avg coolant velocity, ft/sec	16.4	16.5
Core avg fuel rod heat flux, Btu/hr-ft^2	182,400	184,000
Total heat transfer area, ft^2	62,000	62,000
Average fuel rod linear heat rate, KW/ft	5.34	5.39
Power density, kW/liter	94.9	96.5

TABLE 4.4-1 (Sheet 2 of 2)

THERMAL AND HYDRAULIC PARAMETERS

Reactor Parameters	Waterford 3	Pilgrim Station Unit 2 (Docket 50-471)
No. of active fuel rods	49,580	49,476
Power Distribution Factors:		
Rod radial power factor	1.55	1.55
Nuclear power factor	2.28	2.28
Total heat flux factor	2.35	2.33
Maximum augmentation factor	1.041	1.076
Maximum gap length, in.	1.20	0.865
Engineering Factors:		
Engineering heat flux factor	1.03	1.03
Engineering enthalpy rise factor	1.03	1.03
Pitch and bow factor	1.05	1.05
Engineering factor on linear heat rate	1.03	1.03
Characteristics of Rod and Channel with Minimum DNBR:		
Maximum fuel rod heat flux, Btu/hr-ft^2	428,000	429,000
Maximum fuel rod linear heat rate, kW/ft	12.5	12.6
UO_2 maximum steady state temperature, F	3,180	3,420
Outlet temperature, F	642	651
Outlet enthalpy, Btu/lb_m	680	699
Minimum DNBR at nominal conditions	2.07(a)	2.26(b)

(a) Computed using the CE-1 CORRELATION
(b) Computed using the original W3 CORRELATION

TABLE 4.4-2

COMPARISON OF THE DEPARTURE FROM NUCLEATE BOILING RATIOS COMPUTED WITH DIFFERENT CORRELATIONS

	DNBRs for Nominal Reactor Conditions		DNBRs for Reactor Conditions Giving a 1.13 CE-1 Minimum DNBR	
Correlation	Matrix Subchannel	Subchannel Next to Guide Tube	Matrix Subchannel	Subchannel Next to Guide Tube
CE-1	2.29	2.07	1.13	1.14
Original W3[3]	2.36	2.50	1.03	1.13
Revised W3[5]	2.36	2.24	1.03	1.05
B&W-2[5]	2.76	3.01	1.35	1.63

TABLE 4.4-3

REACTOR COOLANT FLOWS IN BYPASS CHANNELS

Bypass Route	Percent of Total Vessel Flow
Outlet nozzle clearances	0.6
Alignment keyways	0.1
Support cylinder holes	0.3
Core shroud clearances	0.3
Guide tubes	0.8
Total bypass	2.1

TABLE 4.4-4

REACTOR VESSEL BEST ESTIMATE
PRESSURE LOSSES AND COOLANT TEMPERATURES

Component	Pressure Loss (psi)	Temperature (F)
Inlet nozzle and 90° turn	6.9	553
Downcomer, lower plenum, and support structure	11.1	553
Fuel assembly	15.7	583
Fuel assembly outlet to outlet nozzle	8.1	613
Total Pressure Loss	41.8	

TABLE 4.4-5

DESIGN STEADY STATE HYDRAULIC LOADS
ON VESSEL INTERNALS AND FUEL ASSEMBLIES (a)

	Component	Load Description	Load Value
1.	Core support barrel	Steady-state radial pressure differential directed inward opposite inlet duct.	84 psi
2.	Core support barrel and upper guide structure	Steady-state uplift load	1.2×10^6 lb
3.	Flow skirt	Steady-state radial drag load directed inward	3500 lb/ft of circumference, average; 7000 lb/ft maximum
4.	Bottom plate	Steady-state drag load directed upward	58,000 lb
5.	Core support plate	Steady-state drag load directed upward	69,000 lb
6.	Fuel assembly	Steady-state uplift load	2,300 lb
7.	Core Shroud	Steady-state radial pressure differential directed outward	34 psi at bottom zero psi at top
8.	Upper guide structure	Steady-state load directed upward	490,000 lb
9.	Fuel alignment plate	Steady-state drag load directed upward	138,000 lb
10.	Upper guide plate	Steady-state load directed downward	66,000 lb
11.	CEA shrouds	Steady-state lateral drag load	5,700 lb
12.	CEA shrouds	Steady-state radial pressure differential directed outward	17 psi

(a) Loads listed are at 500 F, 120 percent of design minimum flow, core in place.

TABLE 4.4-6 (Sheet 1 of 3)

RCS VALVES AND PIPE FITTINGS

Pressure Boundary Valves

Valve	Valve No.	Size (in)	Quantity
Pressurizer safety	RC-200, RC-201	6 x 8	2
Spray control	RC-100E, RC-100F	3	2
Bypass needle	RC-236 RC-237	3/4	2
Letdown Stop	CH-515	2	1
Safety injection tank isolation check valve	SI-215 SI-225 SI-235 SI-245	12	4
Safety injection check valve leakage drain valves	SI-618 SI-628 SI-638 SI-648	1	4
Hot leg injection isolation check valves	SI-510A SI-512A SI-510B SI-512B	3	4
Hot leg injection isolation check valve leakage drain valves	SI-301 SI-302	1	2
Safety injection line isolation check valves	SI-217 SI-227 SI-237 SI-247	12	4
Low pressure safety injection isolation check valve	SI-114 SI-124 SI-134 SI-144	8	4
High pressure safety injection isolation check valves	SI-113 SI-123 SI-133 SI-143	3	4

TABLE 4.4-6 (Sheet 2 of 3) Revision 305 (11/11)

Pressure Boundary Valves (Cont'd)

Valve	Valve No.	Size (in)	Quantity
Safety injection tank isolation valve	SI-614 SI-624 SI-634 SI-644	12	4
Hot leg sample line isolation valve	RC-213	3/4	1
Pressurizer vent isolation valve	RC-239	3/4	1
Pressurizer vapor space sample isolation valve	RC-238	3/4	1
Surge line sample line isolation valve	RC-210	3/4	1
Refueling level indicator connection isolation valves	RC-214 RC-216	3/4	2
Reactor vessel head vent isolation valve	RC-212	3/4	1
Hot leg drain line isolation valves	RC-215 RC-215A	2	2
→(EC-14765, R305) Shutdown cooling isolation valves	SI-651 SI-652 SI-665 SI-666 SI-4052A SI-4052B	14 3/4	6
←(EC-14765, R305)			
Shutdown cooling line thermal relief valves	SI-464 SI-469	1 x 1	2
Charging line Check valves	CH-423 CH-432	2	2
Refueling water level indicating system reference leg isolation valves	RC-217 RC-218	1/2	2
Auxiliary spray line check valve	CH-431	2	1
Charging isolation check	CH-432	2	1

TABLE 4.4-6 (Sheet 3 of 3)

Pressure Boundary Valves (Cont'd)

Valve	Valve No.	Size (in)	Quantity
Charging line bypass isolation valve	CH-434	2	1
Charging line bypass check valve	CH-435	2	1
Charging line isolation valves	CH-518 CH-519	2	2
Auxiliary spray line isolation valve	CH-517	2	1
Letdown line isolation valve	CH-516 CH-515	2	1
Cold leg drain isolation valves	RC-232 RC-332 RC-233 RC-333 RC-234 RC-334 RC-235 RC-335	2	8

RCS Pipe Fittings

Elbows	Size (in.)	Radius (in.)	Quantity
35°	42	63	2
45°	30	45	4
90°	30	45	8
34°	30	45	2
60°	30	45	2

TABLE 4.4-7

RCS DESIGN MINIMUM FLOWS

Flow Path	Flow (gal.min)
Total minimum RCS flow	396,000
Core bypass flow (design maximum)	10,300
Core flow	385,700
Hot leg flow	198,000
Cold leg flow	99,000

TABLE 4.4-8 (Sheet 1 of 2)

REACTOR COOLANT SYSTEM GEOMETRY

Component	Flow Path Length (ft)	Height and Liquid Level (ft) (e)	Bottom Elevation (ft) (d)	Minimum Flow Area (ft^2)	Volume (ft^3)
Hot leg	14.64	4.13	- 1.75	9.62	139.99
Suction leg	24.85	8.48	- 7.50	4.91	119.39
Discharge leg					
Parallel	16.16	2.50	- 1.25	4.91	79.01
Nonparallel	16.19	2.50	- 1.25	4.91	79.15
Pressurizer					
Liquid level (full power)	--	19.84	14.61	50.53(a)	1,500
Height	--	36.33	--	--	--
Surge line	66.11	12.33	2.38	0.57	36.97
Steam generator					
Inlet nozzle (ea.)	2.99	4.31	- 0.48	9.82	30.74
Outlet nozzle (ea.)	2.21	3.17	- 0.79	5.05	11.13
Inlet plenum	9.10(b)	6.01	0.13	9.82	249.22
Outlet plenum	9.10(b)	6.01	0.13	5.05	249.22
Tubes	60.51	33.66	6.13	0.002(c)	1,278.98
Reactor Vessel					
Inlet nozzle (ea.)	3.2	2.5	- 1.25	4.9	19.5
Downcomer	24.1	31.6	-25.5	33.3	1,111.0
Lower plenum	3.0	6.3	-28.6	43.7	519.0

a. For the cylinder.
b. Represents a geometrical rather than an actual flow path length.
c. Flow area per tube.
d. Reactor vessel nozzle center line is the reference elevation. It has an elevation of 0.0 ft.
e. Elevation difference between high and low point.

TABLE 4.4-8 (Sheet 2 of 2)

Component	Flow Path Length (ft)	Height and Liquid Level (ft) (e)	Bottom Elevation (ft) (d)	Minimum Flow Area (ft^2)	Volume (ft^3)
Lower support structure & lower inactive core	3.5	3.4	-22.3	28.0	300.0
Active core	12.5	12.5	-18.9	54.9	687.0
Upper inactive core	1.8	1.8	- 6.4	54.9	126.0
Outlet plenum	7.7	8.9	- 4.6	23.5	646.0
CEA shrouds	12.8	14.8	- 4.6	13.3	430.0
Upper head	4.2	8.9	4.3	0.5	652.0
Outlet nozzle (ea.)	3.7	4.0	- 2.0	9.6	52.5

TABLE 4.4-9 (Sheet 1 of 2) Revision 10 (10/99)

SAFETY INJECTION LINES LENGTHS

(X)* - (Y)*	LENGTH (FT)	LINE SIZE (IN)
(1) - (2)	56	24
(2) - (16)	55	20
(16) - (66)	10	8
(52) - (30)	30.5	8
(30) - (31)	103.5	10
(15) - (17)	54.5	20
(17) - (67)	10	8
(53) - (18)	27	8
(18) - (19)	161	10
(3) - (5)	9.5	10
(5) - (6)	32.5	10
(5) - (8)	87	10
(54) - (20)	63	4
(20) - (22)	155	4
(22) - (23)	4	4
(23) - (24)	4	4
(24) - (21)	0.5	4
(15) - (14)	7.5	24
(14) - (7)	9	10
(7) - (10)	89	10
(56) - (26)	58	4
(26) - (27)	13	4
(27) - (29)	2	4
(27) - (28)	2.5	4
(6) - (9)	119.5	10
(55) - (25)	86	4
(25) - (20)	21	4
(25) - (26)	26.5	4
(6) - (7)	38	10
(11) - (12)	20	24
(12) - (13)	54	24
(12) - (14)	28.5	24
(4) - (3)	142	24
(40) - (39)	102	12
(39) - (41)	39	12
(39) - (59)	2	12
(59) - (38)	49.5	8
(38) - (19)	201	8
(38) - (37)	143	3
(37) - (29)	142	2
(60) - (22)	32.5	2
(31) - (43)	130	8
(51) - (49)	24	12
(49) - (50)	97	12

→

* Indicating the sect's (1) - (2), (4) - (5) etc as shown in Figure 4.4-8 (for Figure 4.4-8, Sheet 3, refer to Drawing G167, Sheet 3)

←

TABLE 4.4-9 (Sheet 2 of 2) Revision 10 (10/99)

SAFETY INJECTION LINES LENGTHS

(X)* - (Y)*	LENGTH (FT)	LINE SIZE (IN)
(49) - (61)	1.5	12
(61) - (48)	28	8
(48) - (31)	179	8
(48) - (47)	97	3
(47) - (62)	12.5	2
(62) - (28)	38	2
(62) - (24)	86	2
(35) - (34)	24	12
(34) - (36)	75	12
(34) - (64)	1.5	12
(64) - (33)	52.5	8
(33) - (19)	120	8
(33) - (32)	99	3
(32) - (29)	104	2
(63) - (23)	24	2
(46) - (44)	35	12
(44) - (45)	94.5	12
(65) - (44)	2	12
(43) - (42)	92	3
(43) - (31)	160	8
(42) - (57)	59	2
(57) - (28)	29	2
(57) - (21)	94.5	2
(65) - (43)	45.5	8

→

* Indicating the sect's (1) - (2), (4) - (5) etc as shown in Figure 4.4-8 (for Figure 4.4-8, Sheet 3, refer to Drawing G167, Sheet 3)

←

TABLE 4.4-10 (Sheet 1 of 2)

REACTOR COOLANT SYSTEM COMPONENT
THERMAL AND HYDRAULIC DATA (a)

Component	Data
Reactor Vessel	
Rated core thermal power, MWt	3,390
Design pressure, psia	2,500
Operating pressure, psia	2,250
Coolant outlet temperature, F	611
Coolant inlet temperature, F	553
Coolant outlet state	Subcooled
Total coolant flow, 10^6 lbm/hr	148
Core average coolant enthalpy	
Inlet, Btu/lbm	551
Outlet, Btu/lbm	632
Average coolant density	
Inlet. lbm/ft^3	46.7
Outlet, lbm/ft^3	42.0
Steam Generators	
Number of units	2
Primary side (or tube sides)	
Design pressure/temperature, psia/F	2,500/650
Operating pressure, psia	2,250
Inlet temperature, F	611
Outlet temperature, F	553
Secondary (or shell side)	
Design pressure/temperature, psia/F	1,110/560
Full load steam pressure/temperature, psia/F	900/532
Zero load steam pressure, psia	1,000
Total steam flow per gen., lbm/hr	7.565×10^6
Full load steam quality, %	99.8
Feedwater temperature, full power, F	445
Pressurizer	
Design pressure, psia	2,500
Design temperature, F	700
Operating pressure, psia	2,250
Operating temperature, F	653
Internal volume, ft^3	1,500
Heaters	
Type and rating of heaters, kW	Immersion/50
Installed heater capacity, kW	1,500

(a) Full power conditions.

TABLE 4.4-10 (Sheet 2 of 2)

REACTOR COOLANT SYSTEM COMPONENT
THERMAL AND HYDRAULIC DATA [a]

Component	Data
Reactor Coolant Pumps	
Number of units	4
Type	Vert-Centfgl
Design capacity, gpm	99,000
Design pressure/temperature, psia F	2,250/650
Operating pressure, psia	2,250
Type drive	Squirrel cage induction motor
Total dynamic head, ft	310
Rating and power requirements, hp	7,200
Pump speed, rpm	1,180
Reactor Coolant Piping	
Flow per loop (106 lbm/hr)	
Hot leg	74
Cold leg	37
Pipe size (inside dia./wall thickness), in.	
Hot leg	42/4 1/8
Suction leg	30/2 7/8
Discharge leg	30/3 3/8
Elbow size (inside dia./wall thickness), in.	
Hot leg	42/4 3/4
Suction leg	30/3 5/8
Discharge leg	30/3 5/8
Pipe design press./temp, psia/F	
Pipe operating press./temp, psia/F	
Hot leg	2,250/611
Cold leg	2,250/553

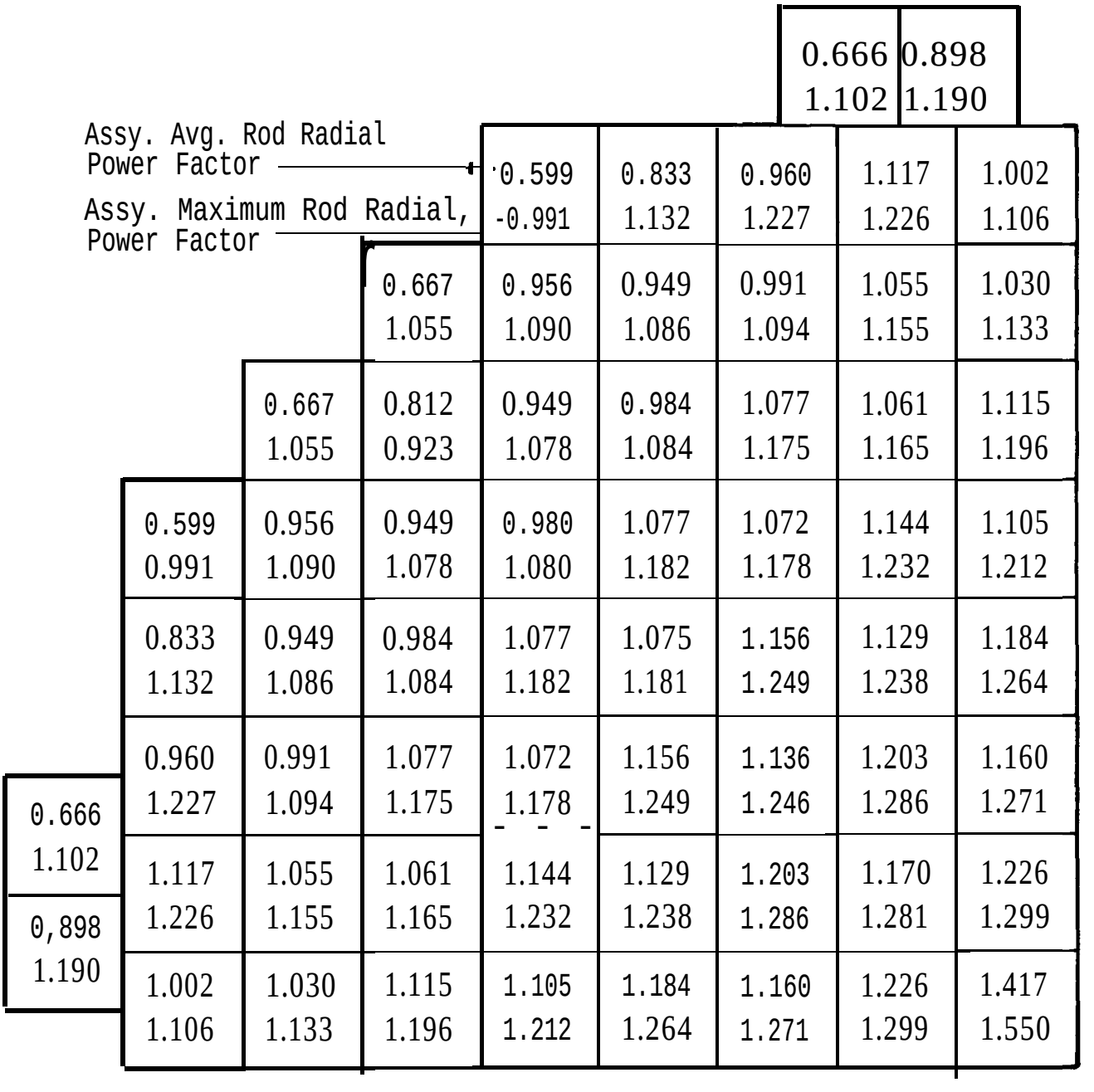

LOUISIANA POWER & LIGHT CO. Waterford Steam Electric Station	CORE WIDE PLANAR POWER DISTRIBUTION FOR SAMPLE DNB ANALYSIS	Figure 4.4-1

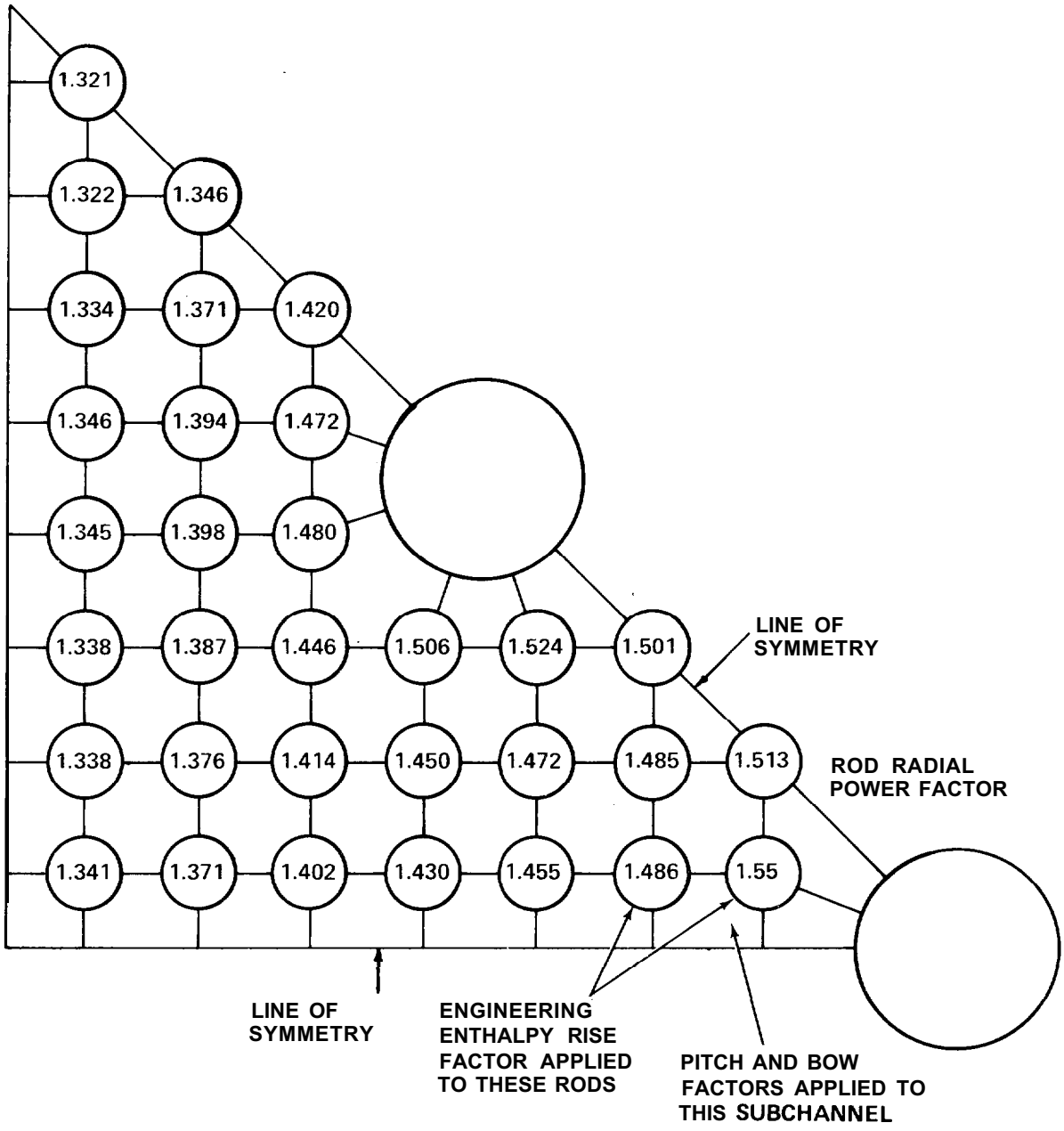

LOUISIANA POWER & LIGHT CO. Waterford Steam Electric Station	ROD RADIAL POWER FACTORS IN HOT ASSEMBLY FOR SAMPLE DNB ANALYSIS	Figure 4.4-2

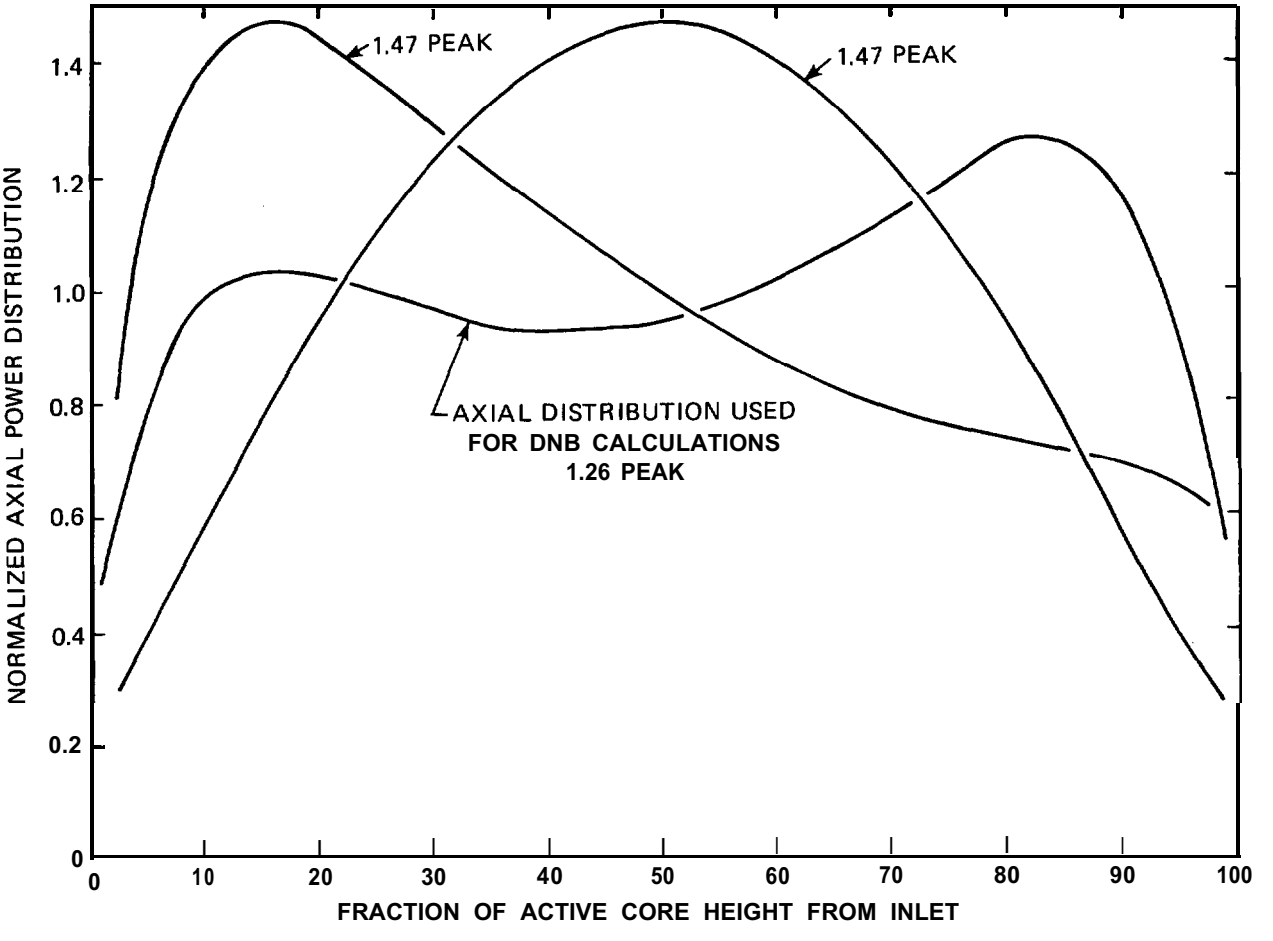

LOUISIANA POWER & LIGHT CO. Waterford Steam Electric Station	TYPICAL AXIAL POWER DISTRIBUTIONS	Figure 4.4-3

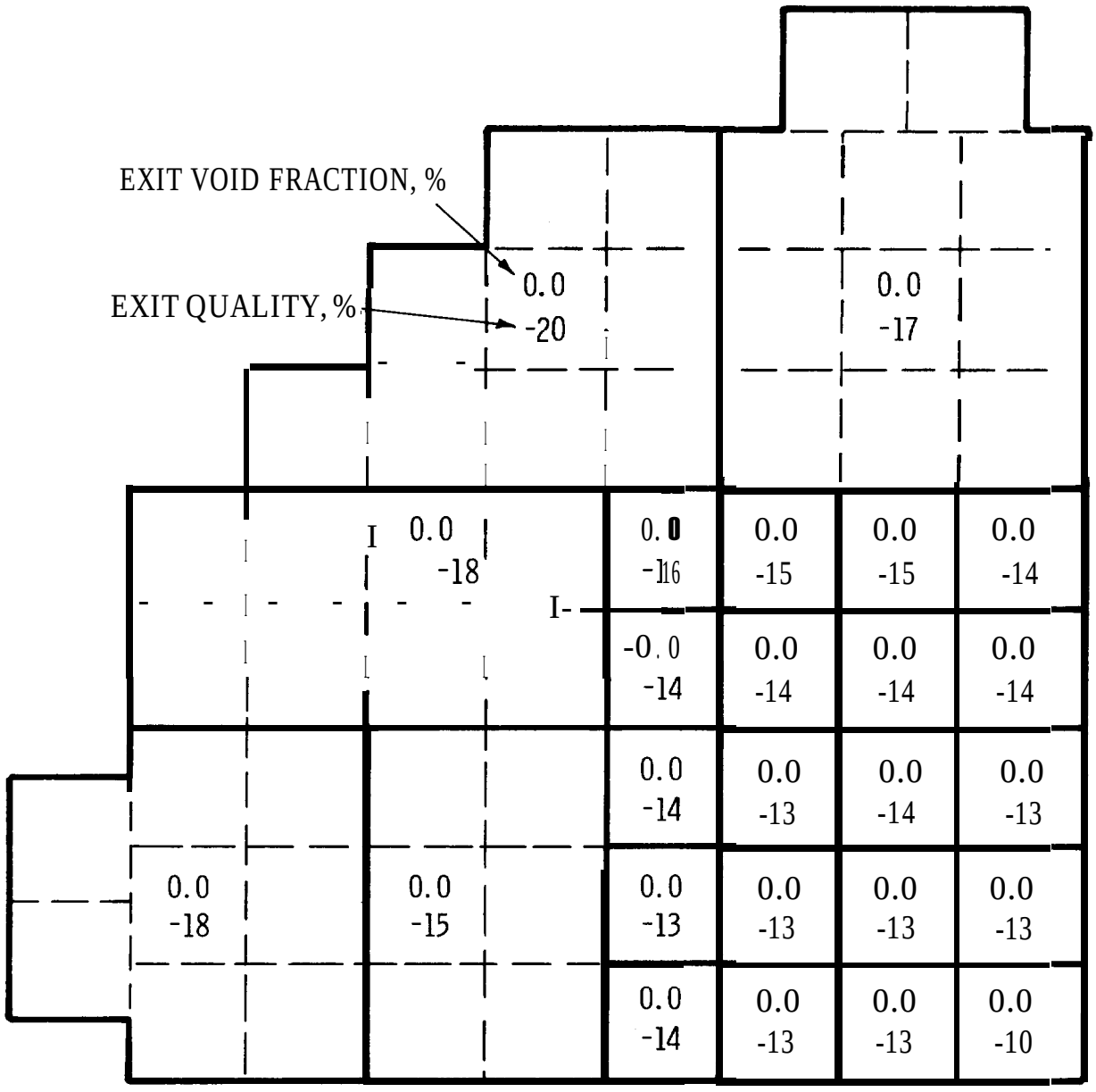

LOUISIANA POWER & LIGHT CO. Waterford Steam Electric Station	**AVERAGE VOID FRACTIONS AND QUALITIES AT THE EXIT OF DIFFERENT CORE REGIONS**	Figure 4.4-4

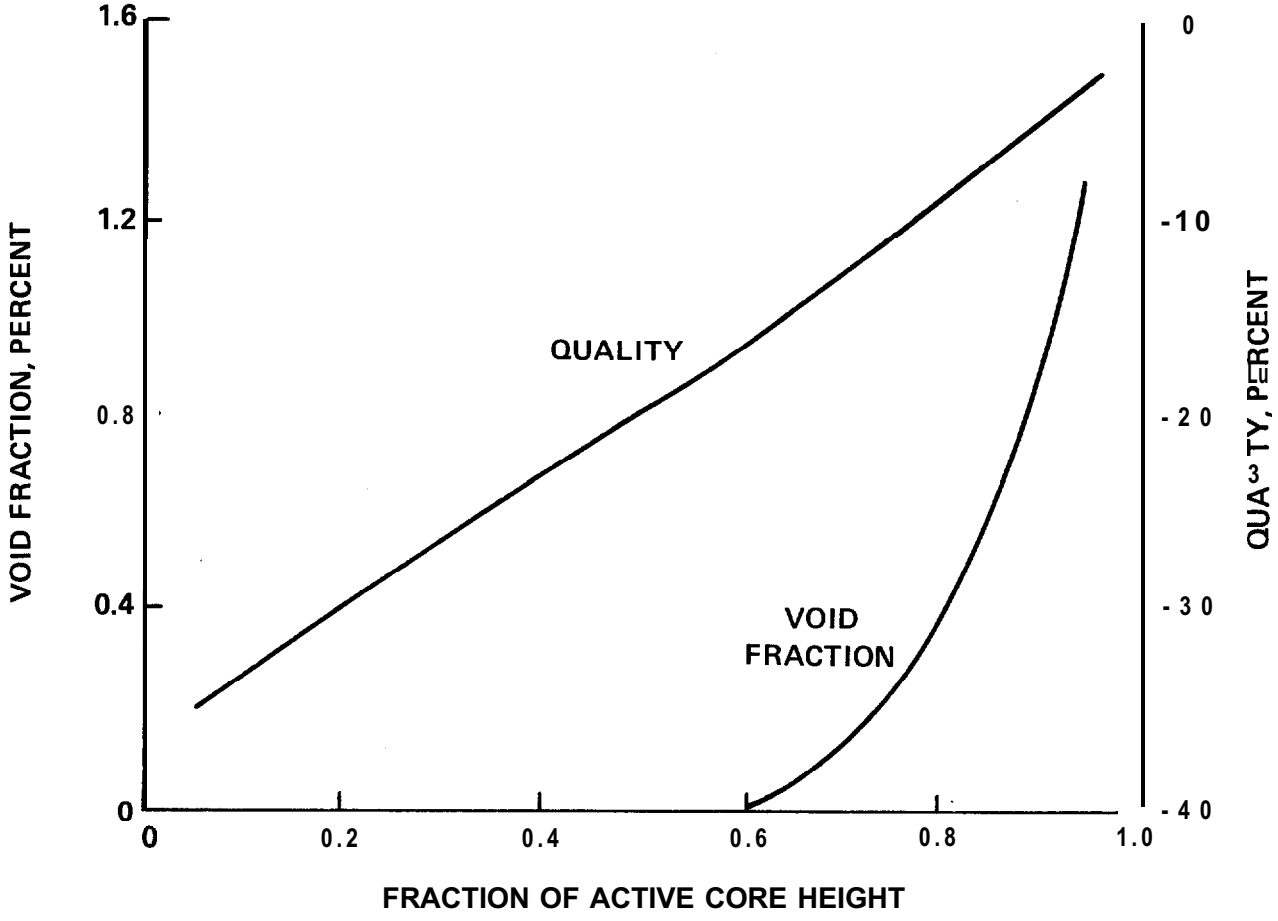

LOUISIANA POWER & LIGHT CO. Waterford Steam Electric Station	AXIAL DISTRIBUTION OF VOID FRACTION AND QUALITY IN THE SUBCHANNEL ADJACENT TO THE ROD WITH MINIMUM DNBR	Figure 4.4-5

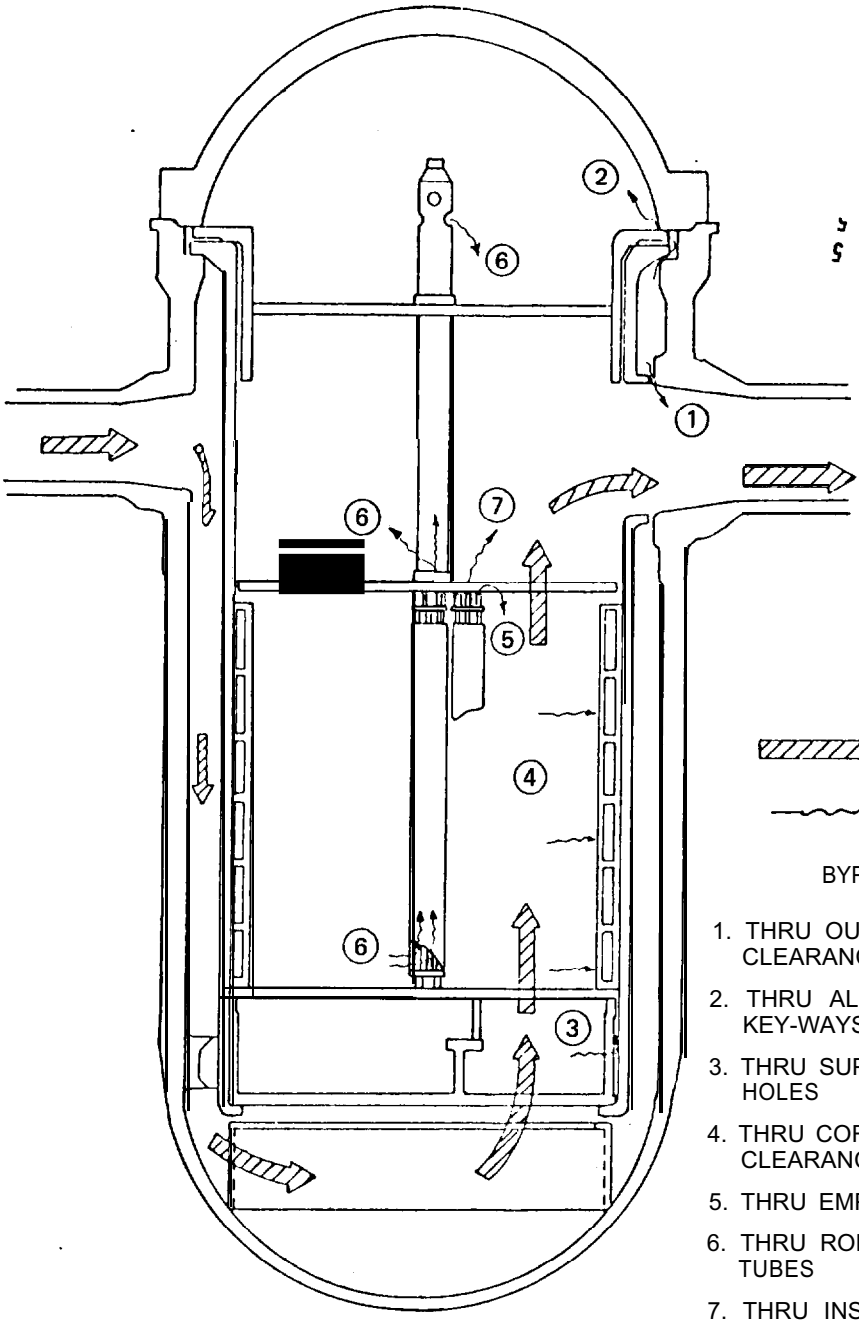

MAIN FLOW

BYPASS FLOW

BYPASS PATHS

1. THRU OUTLET NOZZLE CLEARANCES
2. THRU ALIGNMENT KEY-WAYS
3. THRU SUPPORT CYLINDER HOLES
4. THRU CORE SHROUD CLEARANCES
5. THRU EMPTY GUIDE TUBES
6. THRU RODDED GUIDE TUBES
7. THRU INSTRUMENTED CENTER GUIDE TUBES

LOUISIANA
POWER & LIGHT CO.
Waterford Steam
Electric Station

REACTOR VERTICAL ARRANGEMENT SHOWING BYPASS FLOW PATHS

Figure
4.4-6

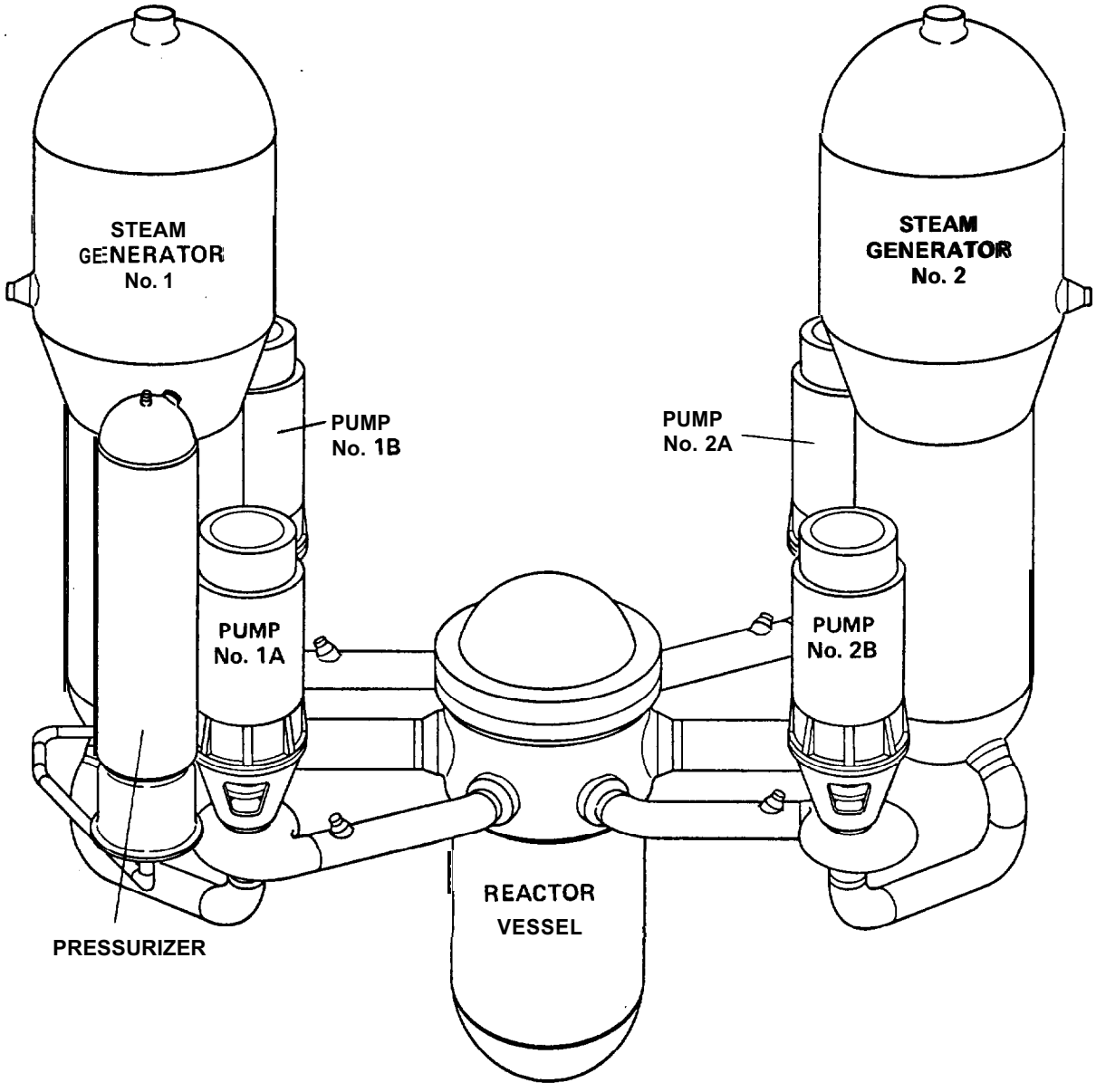

LOUISIANA
POWER & LIGHT CO.
Waterford Steam
Electric Station

ISOMETRIC VIEW OF THE REACTOR COOLANT SYSTEM

Figure
4.4-7

→ (DRN 01-416)

Figure 4.4-8, Sheet 1 has been incorporated by reference in accordance with NEI 98-03.

Figure information can be found in Drawing G167, Sheet 1.

← (DRN 01-416)

→(DRN 02-1016)

Figure 4.4-8, Sheet 2 has been incorporated by reference in accordance with NEI 98-03.

Figure information can be found in Drawing G167, Sheet 2.

←(DRN 02-1016)

→ (DRN 01-416)

Figure 4.4-8, Sheet 3 has been incorporated by reference in accordance with NEI 98-03.

Figure information can be found in Drawing G167, Sheet 3.

← (DRN 01-416)

→(DRN 02-1016)

Figure 4.4-8, Sheet 4 has been incorporated by reference in accordance with NEI 98-03.

Figure information can be found in Drawing G167, Sheet 4.

←(DRN 02-1016)

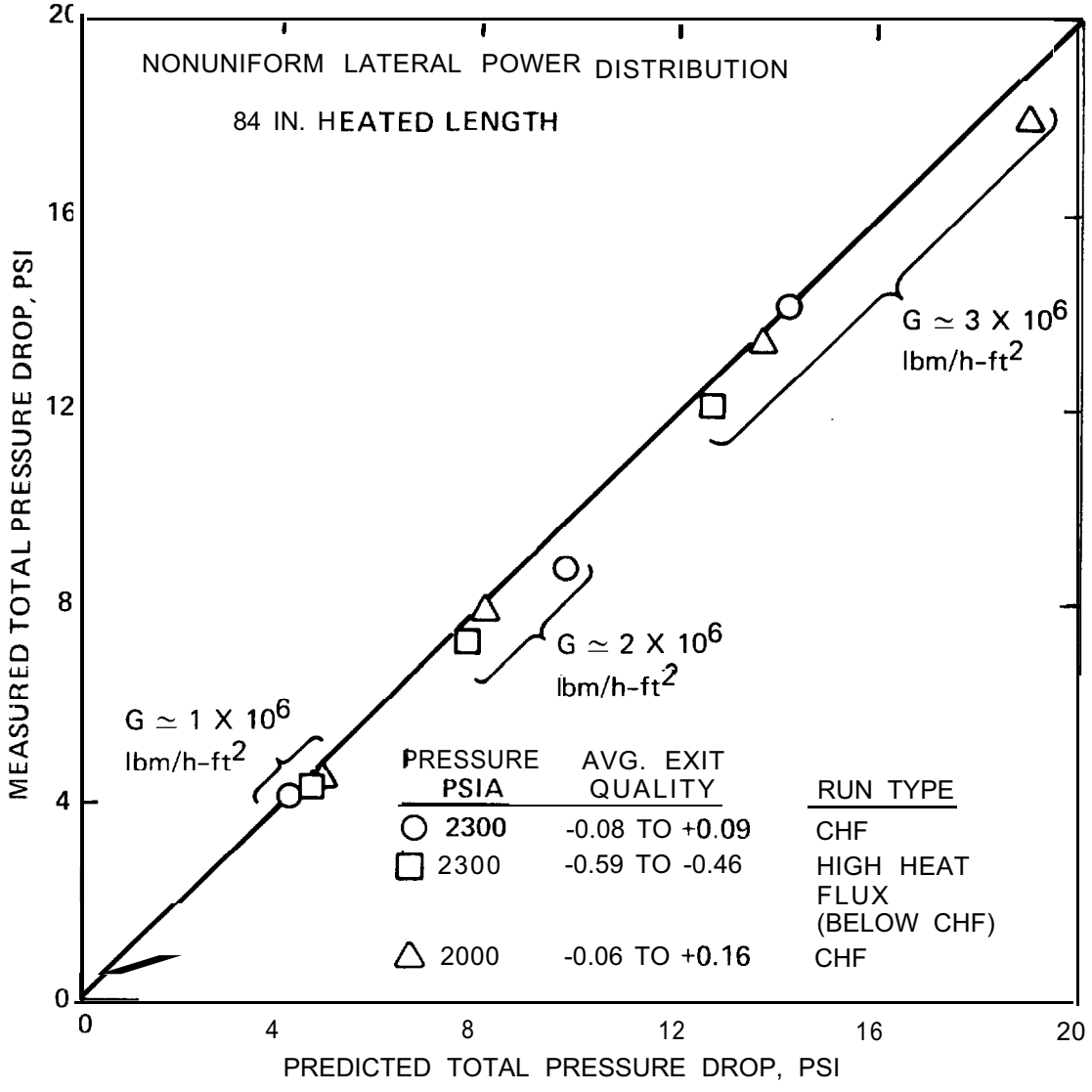

LOUISIANA POWER & LIGHT CO. Waterford Steam Electric Station	PRESSURE DROP PREDICTIONS FOR A 21-ROD BUNDLE	Figure 4.4-9

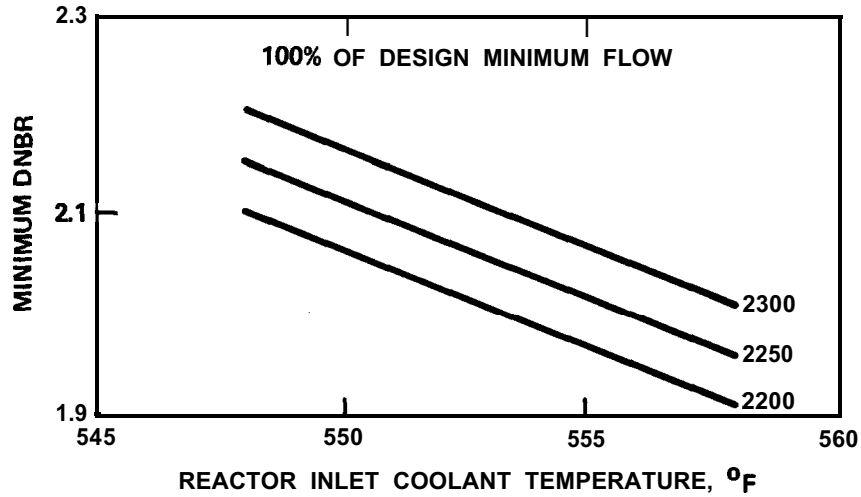

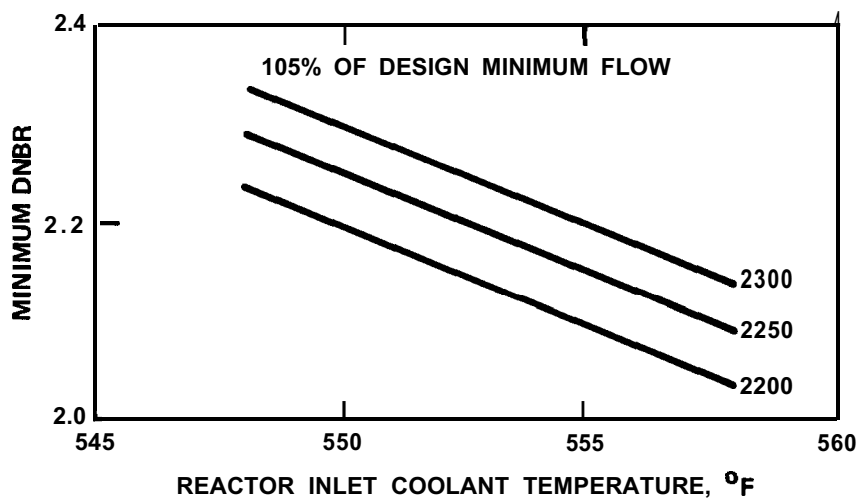

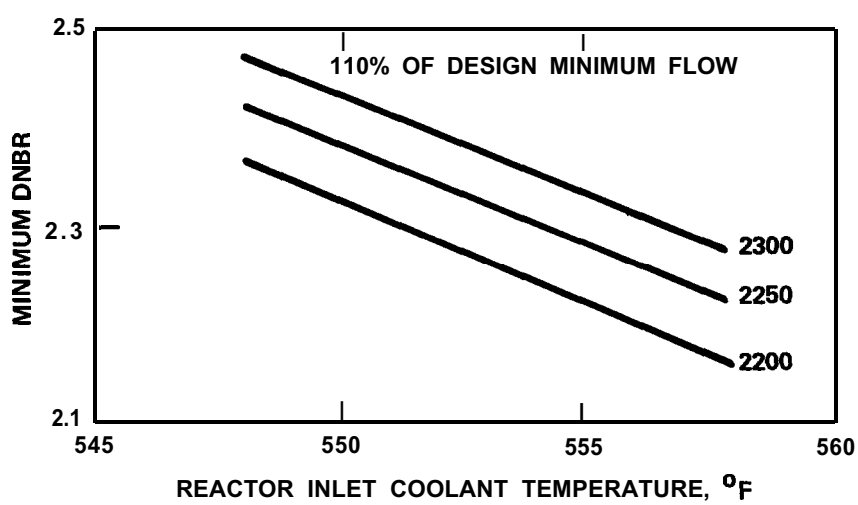

LOUISIANA POWER & LIGHT CO. Waterford Steam Electric Station	**SENSITIVITY OF MINIMUM DNBR TO SMALL CHANGES IN REACTOR COOLANT CONDITIONS**	Figure 4.4-1 0

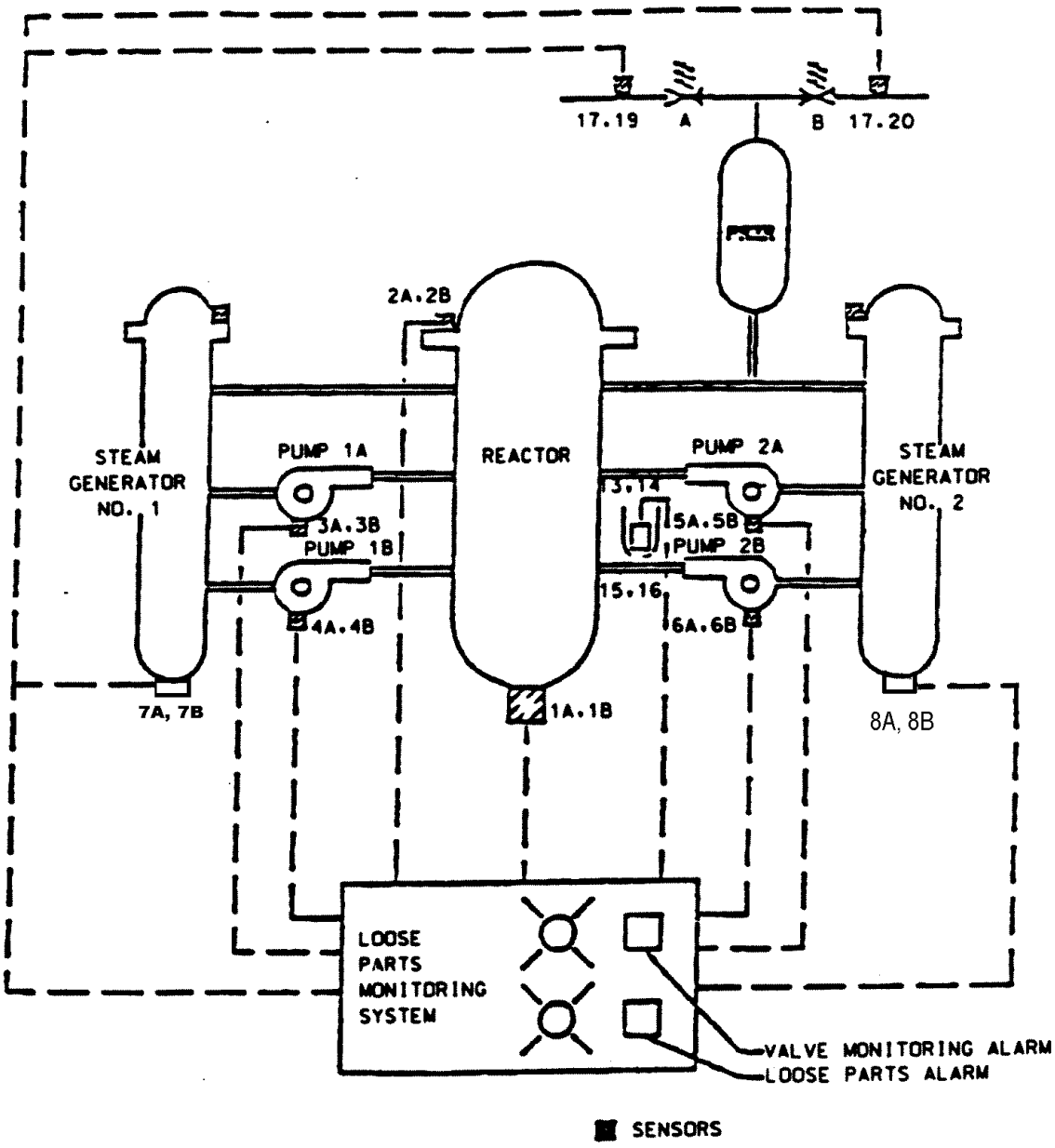

NOTE:

SENSORS & PREAMPLIFIERS LOCATION & CONNECTION ARE DESCRIPTIVE ONLY AND DO NOT REPRESENT ACTUAL CONNECTIONS.

Revision 11 (05/01)

Waterford Steam Electric Station #3	VALVE & LOOSE PARTS MONITORING SYSTEM SCHEMATIC	Figure 4.4-11

4.5 REACTOR MATERIALS

4.5.1 CONTROL ELEMENT DRIVE STRUCTURAL MATERIALS

4.5.1.1 Material Specifications

a) The materials used in the control element drive mechanism (CEDM) reactor coolant pressure boundary components are as follows:

1. Motor housing assembly

SA 182, Type 348 (austenitic stainless steel)

→(EC-2800, R307)

Modified, Type 403, Conforming to Code Case N-4-12 Condition 2 (martensitic stainless steel)

←(EC-2800, R307)

SB 166 (nickel-chromium-iron alloy)

2. Upper pressure housing

SA 213, Type 316 (austenitic stainless steel)

→(EC-2800, R307)

←(EC-2800, R307)

SA 479, Type 316 (austenitic stainless steel)

ASTM A276, Type 440 (martensitic stainless steel with yield strength greater than 90,000 psi)

→(EC-2800, R307)

The above listed materials with the exception of the ASTM A276, Type 440 material are also listed in Appendix I of the 1998 Edition of Section III of the ASME Boiler and Pressure Vessel Code, including the 2000 Addenda. In addition, the materials comply with the 1998 Edition of Sections II and IX of the ASME Boiler and Pressure Vessel Code including the 2000 Addenda.

←(EC-2800, R307)

The functions of the above listed components are described in Subsection 3.9.4.1.1.1.

b) The materials in contact with the reactor coolant used in the CEDM motor assembly components are as follows:

1. Latch guide tubes

ASTM A269, Type 316 (austenitic stainless steel)

Chrome Oxide (plasma spray treatment)

2. Magnet and spacer

ASTM A276, Type 410 (martensitic stainless steel)

→(EC-2800, R307)

ASTM A240 Type 304 (Austenitic Stainless Steel)

←(EC-2800, R307)

3. Latch and magnet housing

ASTM A276, Type 316 (austenitic stainless steel)

→(EC-2800, R307)

QQ-C320, Class 2 (chrome plating)

←(EC-2800, R307)

4. Spacer

ASTM A240, Type 304 (austenitic stainless steel)

5. Alignment Button

→(EC-2800, R307)

AMS 5643 (martensitic stainless steel)

←(EC-2800, R307)

6. Spring

→(EC-2800, R307)

AMS 5698 (nickel base alloy)

←(EC-2800, R307)

7. Pin

→(EC-2800, R307)

AMS 5894 (cobalt base alloy)

←(EC-2800, R307)

8. Dowel pin

→(EC-2800, R307)

ASTM A276, Type 304 (Austenitic stainless steel)
ASTM A276 Type 410 (Martensitic stainless steel)

←(EC-2800, R307)

9. Spacer and screw

ASTM A276, Type 304 (austenitic stainless steel)

10. Stop

ASTM A276, Type 304 (austenitic stainless steel)

11. Latch and pin

Haynes Stellite No. 36 (cobalt base alloy)

→(EC-2800, R307)

ASTM A240 Type 304 (Austenitic stainless steel)
ASTM A193 Grade B8 (Austenitic stainless steel)
ASTM A276 Type 304 (Austenitic stainless steel)

←(EC-2800, R307)

12. Locking cup and screws

300 Series austenitic stainless steel

The functions of the CEDM motor assembly components are described in Subsection 3.9.4.1.1.2.

c) The materials in contact with the reactor coolant used in the extension shafts are listed below:

1. Shafts, rod, and plunger

➔(EC-2800, R307)

ASTM A276 (austenitic stainless steel)

ASTM A269 (austenitic stainless steel)

←(EC-2800, R307)

2. Gripper

ASTM B446 (nickel-chromium-molybdenum-columbium alloy)

QQ-C-320a, Class 2B (chrome plating)

3. Spring

AMS 5699B, Inconel X-750 (nickel base alloy)

4. Pin

Type 304 austenitic stainless steel

The function of the extension shaft components are described in Subsection 3.9.4.1.1.5.

➔(EC-2800, R307)

d) The weld rod filler materials used with the above listed components are 308 stainless steel, Type 316 stainless steel and Alloy 52M.

←(EC-2800, R307)

All of the material listed in the above listings, a through d, were used in an extensively tested CEDM assembly that exceeded lifetime requirements, as described in Subsection 3.9.4.4.1. Also, all of the materials have performed satisfactorily in service in the Main Yankee (Docket 50-309), Millstone II (Docket 50-336), Calvert Cliffs (Docket 50-317), in addition to other designed reactors.

4.5.1.2 Control of the Use of 90 ksi Yield Strength Material

The only control element drive structural material identified in Subsection 4.5.1.1 which has a yield strength greater than 90 ksi is ASTM A276, Type 440, martensitic stainless steel. Its usage is limited to the steel ball in the vent valve on the top of the CEDM. The ball is used as a seal and is not a primary load bearing member of the pressure boundary. This material was tested and exceeded lifetime requirements. Also, this material is presently being used in operating reactors such as Maine Yankee (Docket 50-309), Millstone II (Docket 50-336) and Calvert Cliffs (Docket 50-317) and has performed satisfactorily for the same application.

4.5.1.3 Control of the Use of Sensitized Austenitic Stainless Steel

Control of the use of sensitized austenitic stainless steel is consistent with the recommendations of Regulatory Guide 1.44 as described in Subsections 4.5.1.3.1 through 4.5.1.3.32, except for the criteria used to demonstrate freedom from sensitization. The ASTM A393 Strauss Test was used in lieu of the ASTM A262 Method E Modified Strauss Test to demonstrate freedom from sensitization in fabricated unstabilized austenitic stainless steel. The former test has shown, through experimentation, excellent correlation with the type of corrosion observed in severely sensitized austenitic stainless steel NSSS components.
→(EC-2800, R307)
The replacement CEDM used the ASTM A262 Practice E test.
←(EC-2800, R307)

4.5.1.3.1 Solution Heat Treatment Requirements

All raw austenitic stainless steel, both wrought and cast, employed in the fabrication of the control element drive system structural components is supplied in the solution annealed condition as described in Subsection 4.5.2.4.2.1.

4.5.1.3.2 Material Inspection Program
→(DRN 00-644)
Extensive testing on stainless steel mockups, fabricated using production techniques, was conducted to determine the effect of various welding procedures on the susceptibility of unstabilized 300 series stainless steels to sensitization-induced intergranular corrosion. Only those procedures or practices demonstrated not to produce a sensitized structure were used in the fabrication of control element drive system structural components. The ASTM Standard A393 (Strauss Test) is the criterion used to determine susceptibility to intergranular corrosion. This test has shown excellent correlation with a form of localized corrosion peculiar to sensitized stainless steels. As such, ASTM A393 is utilized as a go/no-go standard of acceptability.
←(DRN 00-644)
→(EC-2800, R307)
The replacement CEDM used the ASTM A262 Practice E test.
←(EC-2800, R307)

4.5.1.3.3 Avoidance of Sensitization

Homogeneous or localized heat treatment of unstabilized austenitic stainless steel in the temperature range 800-1500 F is prohibited.

Weld heat affected zone sensitized austenitic stainless steel (which will fail the Strauss Test, ASTM A-393) is avoided in control element drive system structural components by careful control of

→(EC-2800, R307)
For replacement CEDMs, the ASTM A262 Practice E test was used.
←(EC-2800, R307)

a) Weld heat input to less than 60 kJ/in.

b) Interpass temperature to 350 F maximum.

4.5.1.4 Control of Delta Ferrite in Austenitic Stainless Steel Welds
→(EC-2800, R307)
The austenitic stainless steel, primary pressure retaining welds in the control element drive system structural components are consistent with the recommendations of the Interim Position of Regulatory Guide 1.31, MTEB 5-1, as described in Subsection 4.5.2.4.3.

Replacement CEDMs conform to Reg. Guide 1.31 Rev. 3. Revision 3 supersedes earlier revisions and BTP MTEB 5-1. See Section 1.8.
←(EC-2800, R307)

4.5.1.5 Cleaning and Contamination Protection Procedures

The procedure and practice followed for cleaning and contamination protection of the control element drive system structural components are as described in Subsection 4.5.2.4.1.

4.5.2 REACTOR INTERNALS MATERIALS

4.5.2.1 Material Specifications

The materials used in fabrication of the reactor internal structures are primarily Type 304 stainless steel. The flow skirt is fabricated from Inconel. Welded connections are used where feasible; however, in locations where mechanical connections are required, structural fasteners are used which are designed to remain captured in the event of a single failure. Structural fastener material is typically a high strength austenitic stainless steel; however, in less critical applications Type 316 stainless steel is employed. Hardfacing of Stellite material is used at wear points. The effect of irradiation on the properties of the materials is considered in the design of the reactor internal structures. Work hardening properties of austenitic stainless steels are not used.

The following is a list of the major component of the reactor internals together with their material specifications:

a) Core support barrel assembly

   1) Type 304 austenitic stainless steel to the following specifications:

      (a) ASTM-A-182

      (b) ASTM-A-240

      (c) ASTM-A-479

   2) Precipitation hardening stainless steel to the following specifications:

      (a) ASTM-A-453, Grade 660

      (b) ASTM-A-638, Grade 660

b) Upper guide structure assembly

   1) Type 304 austenitic stainless steel to the following specifications:

      (a) ASTM-A-182

      (b) ASTM-A-240

      (c) ASTM-A-269

      (d) ASTM-A-312

(e) ASTM-A-451

(f) ASTM-A-479

2) Precipitation hardening stainless steel to the following specifications:

(a) ASTM-A-453, Grade 660

c) Core shroud assembly

1) Type 304 austenitic stainless steel to the following specifications:

(a) ASTM-A-182

(b) ASTM-A-240

d) Holddown ring

ASTM-A-182, Grade F-6, modified to ASME Code Case 1337-6 with exception to the temper temperature which shall be 1150F for 4 hours.

The ASTM-A-182, Grade F-6 used for the holddown ring is heat treated to a minimum yield strength of 90,000 psia. Under reactor operating conditions of low oxygen and slightly alkaline pH, a slightly higher (than austenitic stainless steel) but acceptable general corrosion rate is anticipated to occur. No localized corrosion is anticipated under these conditions. When heat treated in hardness with Code Case 1337, i.e., BHN 226-277 (HRC 21-29), Type 403 can be expected to be resistant to stress corrosion in the primary coolant. Stress corrosion failures in PWR environments have occurred only where the material has been heat treated to hardness levels higher than specified.(1)

e) In-core instrument support system

1) Type 304 austenitic stainless steel to the following specifications:

(a) ASTM-A-193

(b) ASTM-A-194

(c) ASTM-A-240

(d) ASTM-A-249

(e) ASTM-A-269

(f) ASTM-A-276

(g) ASTM-A-312

(h) ASTM-A-473

(i) ASTM-A-479

(j) ASTM-B-353

(k) ASTM-B-446

2) Zircaloy -4

(a) ASTM-B-353

→(EC-10453, R304)

(b) ASTM-B-351

←(EC-10453, R304)

f) Bolt and pin material

ASTM-A-453 and ASTM-A-638, Grade 660 material (trade name A-286) is used for bolting and pin applications. This alloy is heat treated to a minimum yield strength of 85,000 psia. Its corrosion properties are similar to those of the 300 series austenitic stainless steels. It is austenitic in all conditions of fabrication and heat treatment. This alloy was used for bolting in previous reactor systems and test facilities in contact with primary coolant and has proven completely satisfactory.

g) Chrome plating and hardfacing

→(DRN 00-644)

Chrome plating or hardfacing are employed in the reactor internals components or portions thereof where required by function. Chrome plating complies with Federal Specification No. QQ-C-320a. The hardfacing material employed is Stellite 25.

←(DRN 00-644)

All of the materials employed in the reactor internals and in-core instrument support system have performed satisfactorily in operating reactors such as Palisades (Docket 50-255), Fort Calhoun (Docket 50-285), Maine Yankee (Docket 50-309).

4.5.2.2 Controls on Welding

Welds employed on reactor internals and core support structures meet the acceptance standards delineated in article NG-5000 Section III, Division I - 1974 Edition, and control of welding has been performed in accordance with Sections III Division 1, and IX of the applicable ASME Code. In addition, consistency with the recommendations for Regulatory Guides 1.31 and 1.44 is described in Subsection 4.5.2.4.

4.5.2.3 Nondestructive Examination of Wrought Seamless Tubular Products and Fittings

Quality Group A components in the reactor internals which are wrought seamless tubular products or fittings are consistent with the recommendations of Regulatory Guide 1.66.

4.5.2.4 Fabrication and Processing of Austenitic Stainless Steel Components

The following information applies to unstabilized austenitic stainless steel as used in the reactor internals.

4.5.2.4.1 Cleaning and Contamination Protection Procedures

Specific requirements for cleanliness and contamination protection are included in the equipment specifications for components fabricated with austenitic stainless steel. The provisions described below indicate the type of procedures utilized for components to provide contamination control during fabrication, shipment, and storage.

Contamination of austenitic stainless steels of the 300 type by compounds that can alter the physical or metallurgical structure and/or properties of the material are avoided during all stages of fabrication. Painting of 300 series stainless steels is prohibited. Grinding is accomplished with resin or rubber-boned aluminum oxide or silicon carbide wheels that have not previously been used on materials other than 300 series stainless alloys.

Internal surfaces of completed components are cleaned to the extent that grit, scale, corrosion products, grease, oil, wax gum, adhered or embedded dirt, or extraneous material are not visible to the unaided eye.

Cleaning is effected by either solvents (acetone or isopropyl alcohol) or inhibited water (30-200 ppm hydrazine). Water will conform to the following requirements:

Halides	0.60
Chloride, ppm	< 0.60
Fluoride, ppm	< 0.40
Conductivity, μmhos/cm	< 5.0
pH	6.0-8.0
Visual clarity	No turbidity, oil or sediment

→ (DRN 00-644)
To prevent halide-induced, intergranular corrosion that could occur in an aqueous environment with significant quantities of dissolved oxygen, flushing water is inhibited via additions of hydrazine. Experiments have proven this inhibitor to be efective(2). Operational chemistry specificatiopns preclude halides and oxygen, (both prerequisites of intergranular attacks), and are shown in Subsection 9.3.4 and 16.3/4.
← (DRN 00-644)

4.5.2.4.2 Control of the Use of Sensitized Austenitic Stainless Steel

→ (DRN 00-644)
The recommendations of Regulatory Guide 1.44, as desribed in Subsections 4.5.2.4.2.1 through 4.5.2.4.2.5, were followed except for the criteria used to demonstrate freedom from sensitization. The ASTM A393 Strauss Test was used in lieu of the ASTM A262 Method E Modified E Modified Strauss Test to demonstrate freedom from sensitization in fabricated unstabilized austenitic stainless steel, since the former test has shown, through experimentation, excellent correlation with the type of corrosion observed in severely sensitized austenitic stainless steel NSSS components. Either ASTM A262 Method E or A393 were used as the acceptance criteria for raw austenitic stainless steel material, with the exception of tubing for the in-core instrument support system. Tubing for this application
← (DRN 00-644)

conforms to the requirements of ASTM-A 269, which includes provisions for rapid cooling subsequent to solution heat treatment.

4.5.2.4.2.1 Solution Heat Treatment Requirements

➔(DRN 00-644)
All raw austenitic stainless steel material, both wrought and cast, employed in the fabrication of the reactor internals is supplied in the solution annealed condition as specified by the pertinent ASTM or ASME B&PV Code material specification; viz, 1900 to 2050 F for 1/2 to one hr per in. of thickness and rapidly cooled to below 700 F. The time at temperature is determined by the size and type of component.

Solution heat treatment is not performed on completed or partially fabricated components. Rather, the extent of chromium carbide precipitation is controlled during all stages of fabrication as described in Subsection 4.5.2.4.2.4.

4.5.2.4.2.2 Material Inspection Program

Extensive testing of stainless steel mockups, fabricated using production techniques, was conducted to determine the effect of various welding procedures on the susceptibility of unstabilized 300 series stainless steels to sensitization-induced intergranular corrosion. Only those procedures or practices demonstrated not to produce a sensitized structure were used in the fabrication of reactor internals components. The ASTM Standard A393 (Strauss Test) is the criterion used to determine susceptibility to intergranular corrosion. This test has shown excellent correlation with a form of localized corrosion peculiar to sensitized stainless steels. As such, ASTM A393 is utilized as a go/no-go standard for acceptability.
←(DRN 00-644)
As a result of the above tests, a relationship was established between the carbon content of Type 304 stainless steel and weld heat input. This relationship is used to avoid weld heat affected zone sensitization as described in Subsection 4.5.2.4.2.4.

➔(EC-2800, R307)
For replacement CEDMs, the ASTM A262 Practice E test was used.
←(EC-2800, R307)

4.5.2.4.2.3 Unstabilized Austenitic Stainless Steels

➔(DRN 03-2058, R14)
The unstabilized grade of austenitic stainless steel with a carbon content greater than 0.03 percent used for components of the reactor internals is Type 304. This material is furnished in the solution annealed condition. The acceptance criteria used for this material as furnished from the steel supplier is ASTM A262 Practice E or ASTM A393.

Exposure of completed or partially fabricated components to temperatures ranging from 800 to 1500F is prohibited except as described in Subsecvtion 4.5.2.4.2.5.

Duplex, austenitic stainless steels, containing >5 v/o delta ferrite (weld metal, cast metal, weld deposit overlay), are not considered unstabilized since these alloys do not sensitize; i.e., form a continuous network of chromium-iron carbides. Specifically, alloys in this category are:
←(DRN 03-2058, R14)

a) CF8M Cast stainless steels (delta ferrite controlled to 5-25 v/o

b) CF8

c) Type 308 Singly and combined

d) Type 309 Stainless steel weld filler metals. (Delta ferrite controlled to 5-18 v.o as deposited.)

e) Type 312

f) Type 316

In duplex austenitic/ferrite alloys, chromium-iron carbides are precipitated preferentially at the ferrite/austenitic interfaces during exposure to temperatures ranging from 1000-1500F. This precipitate morphology precludes intergranular penetrations associated with sensitized 300 series stainless steels exposed to oxygenated or otherwise faulted environments.

4.5.2.4.2.4 Avoidance of Sensitization

Exposure of unstabilized austenitic 300 stainless steels to temperatures ranging from 800 to 1600 F will result in carbide precipitation. The degree of carbide precipitation, or sensitization, depends on the temperature, the time at that temperature, and also the carbon content. Severe sensitization is defined as a continuous grain boundary chromium-iron carbide network. This condition induces susceptibility to intergranular corrosion in oxygenated aqueous environments, as well as those containing halides. Such a metallurgical structure will readily fail the Strauss Test, ASTM A393. Discontinuous precipitates (i.e., an intermittent grain foundary carbide network) are not susceptible to intergranular corrosion in a PWR environment.

→(EC-2800, R307)
For replacement CEDMs, the ASTM A262 Practice E test was used.
←(EC-2800, R307)

Weld heat affected zone sensitized austenitic stainless steels were avoided (which will fail the Strauss Test, ASTM A393) by careful control of:

a) Weld heat input

b) Interpass temperature

A weld heat input of less than 60kJ/in. is used during most fabrication stages of the Type 304 stainless steel core support structure. Higher heat inputs are used in some heavy section weld joints. Freedom from weld heat-affected zone sensitization in these higher heat input weldments is demonstrated with weld runoff samples produced at the time of component welding in material having a carbon content equal to or greater than the highest carbon content of those heats of steel being fabricated. Specimens so provided are subjected to the Strauss Test, ASTM A393.

4.5.2.4.2.5 Retesting Unstabilized Austenitic Stainless Steels Exposed to Sensitizing Temperature

Sensitization which may be susceptible to intergranular corrosion, is avoided during welding as described in Subsection 4.5.2.4.2.4. Homogeneous or localized heat treatment of unstabilized stainless steels in the temperature range 800 to 1500 F is prohibited except in the case of the core support structure. This complex substructure is thermally stabilized at 900 ±25 F for seven hours after fabrication and prior to final machining. Such treatment produces only minor, discontinuous precipitates. In addition to thermocouple records during this heat treatment, a sample of Type 304 stainless steel having a carbon content equal to or greater than the highest carbon heat of material present in the structure is included as a monitor sample. After heat treatment, the monitor sample is subject to the Strauss Test, ASTM A393, as well as a metallographic examination to verify freedom from sensitization.

4.5.2.4.3 Control of Delta Ferrite in Welds

The recommendations of the Interim Position on Regulatory Guide 1.31, MTEB 5-1 were followed in the following manner:

a) The delta ferrite content of A-7 austenitic stainless steel filler metal used in the fabrication of major components of the reactor internals, was controlled to 5-20 v/o (FN5-23). Delta ferrite content was predicted either by chemical analysis performed on undiluted weld deposits using the Schaeffler or McKay diagram or by a calibrated magnetic measuring instrument. In the case of metal used with a nonconsumable electrode process, the delta ferrite content may be predicted by chemical analysis of the rod, wire, or consumable insert in conjunction with the stainless steel constitution diagram. The ferrite recommendations are met for each heat, lot, or heat/lot combination of weld filler material.

b) The average minimum delta ferrite content of production welds is three percent (FN3) as measured on an audit the basis.

➔(EC-2800, R307)
For the replacement CEDMs, the recommendations of Reg. Guide 1.31 Revision 3 were followed. Revision 3 supersedes earlier revisions and BTP MTEB 5-1. See Section 1.8.
←(EC-2800, R307)

4.5.2.4.4 Control of Electroslag Weld Properties

The electroslag process was not utilized to fabricate reactor internal components.

4.5.2.4.5 Welder Qualification for Areas of Limited Accessibility

The specific recommendations of Regulatory Guide 1.71 were not followed. However, performance qualifications, for personnel welding under conditions of limited accessibility, are conducted and maintained in accordance with the requirements of ASME BPV Code Sections III an IX. A requalification is required when:

a) Any of the essential variables of Section IX are changed.

b) When authorized personnel have reason to question the ability of the welder to satisfactorily perform to the applicable requirements.

Production welding is monitored for compliance with the procedure parameters and welding qualification requirements are certified in accordance with Sections III and IX. Further

assurance of acceptable welds of limited accessibility is afforded by the welding supervisor assigning only the most highly skilled personnel to these tasks. Finally, weld quality, regardless of accessibility, is verified by the performance of the required nondestructive examination.

4.5.2.4.6 Non-Metallic Thermal Insulation

Non-metallic thermal insulation is not used on the reactor internals.

4.5.2.5 Contamination Protection and Cleaning of Austenitic Stainless Steel

→ (DRN 00-644)

Waterford 3 is consistent with the recommendations of Regulatory Guide 1.37. The QA program for safety-related items during onsite cleaning and layup of components, cleanliness control, and preoperational cleaning and layup of nuclear fluid systems was in accordance with ANSI-N-45.2.1-1973 as interpreted by Regulatory Guide 1.37.

← (DRN 00-644)

SECTION 4.5: REFERENCES

1. Bush, S.H. and Dillon, R.L., Stress Corrosion in Nuclear Systems, Pacific Northwest Laboratories, Battelle Memorial Institute, Richland, Washington, March 1973.

2. Habicht, P.R. and Bryant, P.E.C., Fluoride Induced Intergranular Corrosion of Sensitized Austenitic and Austenoferritic Stainless Steel, presented at the International Atomic Energy Authority Workshop on Stress Corrosion Cracking, San Francisco, California, March 1976.

4.6 FUNCTIONAL DESIGN OF REACTIVITY CONTROL SYSTEM

4.6.1 INFORMATION FOR CONTROL ELEMENT ASSEMBLY DRIVE SYSTEM

The CEADs is comprised of magnetic jack control element drive mechanisms (CEDM). Component diagrams, descriptions, and characteristics are presented in Subsection 3.9.4. Figure 4.6-1 shows the reactor vessel closure head plan view detailing the CEDM layout.

4.6.2 EVALUATION OF THE CEADS

The safety function of the CEADS is to insert control element assemblies (CEA) into the reactor core when electrical power is removed from the coils of the CEDMs by the Reactor Protection System (RPS). A failure modes and effects analysis is presented in Section 7.2 which demonstrates compliance with IEEE standard 279-1971 and shows that no single failure can prevent electrical power from being removed from the CDE coils, the armature springs automatically cause the driving and holding latches to be withdrawn from the CEDM coils, the armature springs automatically cause the driving and holding latches to be withdrawn from the CEDM drive shaft, allowing insertion of CEAs by gravity. Actuation of trip breaker is independent of any existing control signals.

For the trip function, all CEDMs are independent of one another. That is, the failure of one CEDM to trip would have no effect on the operability of other CEDMs. Sufficient shutdown margin is always provided to assure that the CEADs safety function can be performed assuming a failure of any CEDM.
→ (DRN 00-644)
The CEADS includes the CEDMs and extends to the coupling interface with the reactivity CEAs. Since there is no nonessential portion of the CEADS, no isolation is required between essential an nonessential portions of the CEADS.

The CEDMs are located where they are protected from common mode failure due to missiles and failure of moderate and high energy pipes. Sections 3.5 and 3.6 discuss protection of essential systems against missiles and pipe breaks. A potential source of common mode failure is loss of air cooling to the CEDM coils. Worse case analysis indicated that there would be adequate mechanical clearances to permit it to trip at temperatures well above normal operating of the reactor[(1)]. Testing was performed to determine the maximum CEDM temperature under conditions that simulated loss of air cooling. With the upper gripper coil energized, which is the normal operating mode, and with a reactor coolant loop temperature of 600°F, the maximum CEDM temperature was 535°F. An analysis of worst case tolerance stack-up within the CEDM indicated adequate clearances to assure scram at 650°F.
← (DRN 00-644)
For any single malfunction of the reactivity control systems, such as accidental withdrawal (not ejection or dropout) of CEAs, specified acceptable fuel design limits are not exceeded. Analyses of possible control malfunctions are discussed in Section 15.4.

4.6.3 TESTING AND VERIFICATION OF THE CEADS

➔(DRN 00-644)
The functional testing program for the CEADS is described in Subsections 3.9.4.4 (CEDMs) and 4.2.4.4 (CEAs).The preoperational and startup test program for the CEADS is presented in Section 14.2.
←(DRN 00-644)

As discussed in Subsection 4.6.2, upon reactor trip all CEDMs are independent of one another. Thus the worse single failure is one that prevents one CEDM from tripping. This failure mode was considered and included in the accident analysis presented in Chapter 15.

Under large break LOCA conditions where severe loads may be applied to CEAs, no credit is taken for CEDM functioning. Testing was performed on a prototype CEDM to verify insertion time, assuming worse case plant operating conditions. Insertion time was verified by dropping the minimum effective (dry) weight of 86 pounds. This weight was calculated to be the minimum effective dry weight, assuming maximum delta-P across the core due to crudding and high reactor coolant density due to operating at a loop temperature of 475° F.

4.6.4 INFORMATION FOR COMBINED PERFORMANCE OF REACTIVITY SYSTEMS

Figures 1.2-11 through 1.2-23, Drawing G134, Drawing G135 and Drawing G136, provide plant and elevation layout drawings. These figures and drawings show that the CEADS, SIS, and CVCS are located in the Reactor Building, and the Reactor Auxiliary Building. The physical arrangement insures that no single occurrence can affect two or more reactivity control systems concurrently.

Table 4.6-1 lists the postulated accidents evaluated in Chapter 15 that take credit for two or more reactivity control systems for preventing or mitigating each accident. The related reactivity systems are also tabulated.

The maximum rate of reactivity addition that may be produced by the CVCS is too low to induce any significant pressure forces that might rupture the reactor coolant pressure boundary or disturb the reactor vessel internals.

Inadvertent startup of the safety injection system during normal plant operation would have no effect since RCS pressure is higher than the shutoff head of the HPSI pumps.

4.6.5 EVALUATIONS OF COMBINED PERFORMANCE

➔(DRN 00-644; 06-871, R15; LBDCR 16-012, R310)
Since the CEADS and the CVCS/SIS are separate and totally diverse in design and operation, with no common link, and since the CEADS is protected from the effects of failure of high and moderate energy piping, there are no credible potential common mode failures that could cause the CEADS to fail in combination with CVCS or SIS. This is demonstrated by the evaluations provided in Sections 3.5 and 3.6.
←(DRN 00-644; 06-871, R15; LBDCR 16-012, R310)

SECTION 4.6: REFERENCES

1. "Review of Reactor Shutdown Systems (PPS Design) for Common Mode Failure Susceptibility," Combustion Engineering Topical Report, CENPD-148, November 1974.

TABLE 4.6-1 Revision 14 (12/05)

POSTULATED EVENTS REQUIRING OPERATING OF TWO OR MORE REACTIVITY CONTROL SYSTEMS

Subsection	Title	CEADS	CVCS	SIS
15.1.3.1	Steam System Piping Failures	X		X
→(DRN 03-2058, R14) ←(DRN 03-2058, R14)	Deleted			
15.4.1.5	CVCS Malfunction (Boron Dilution)	X	X	
15.6.3.1	Letdown Line Break Outside Containment	X		X
15.6.3.2	Steam Generator Tube Rupture	X		X
15.6.3.3	Small Break LOCA	X		X

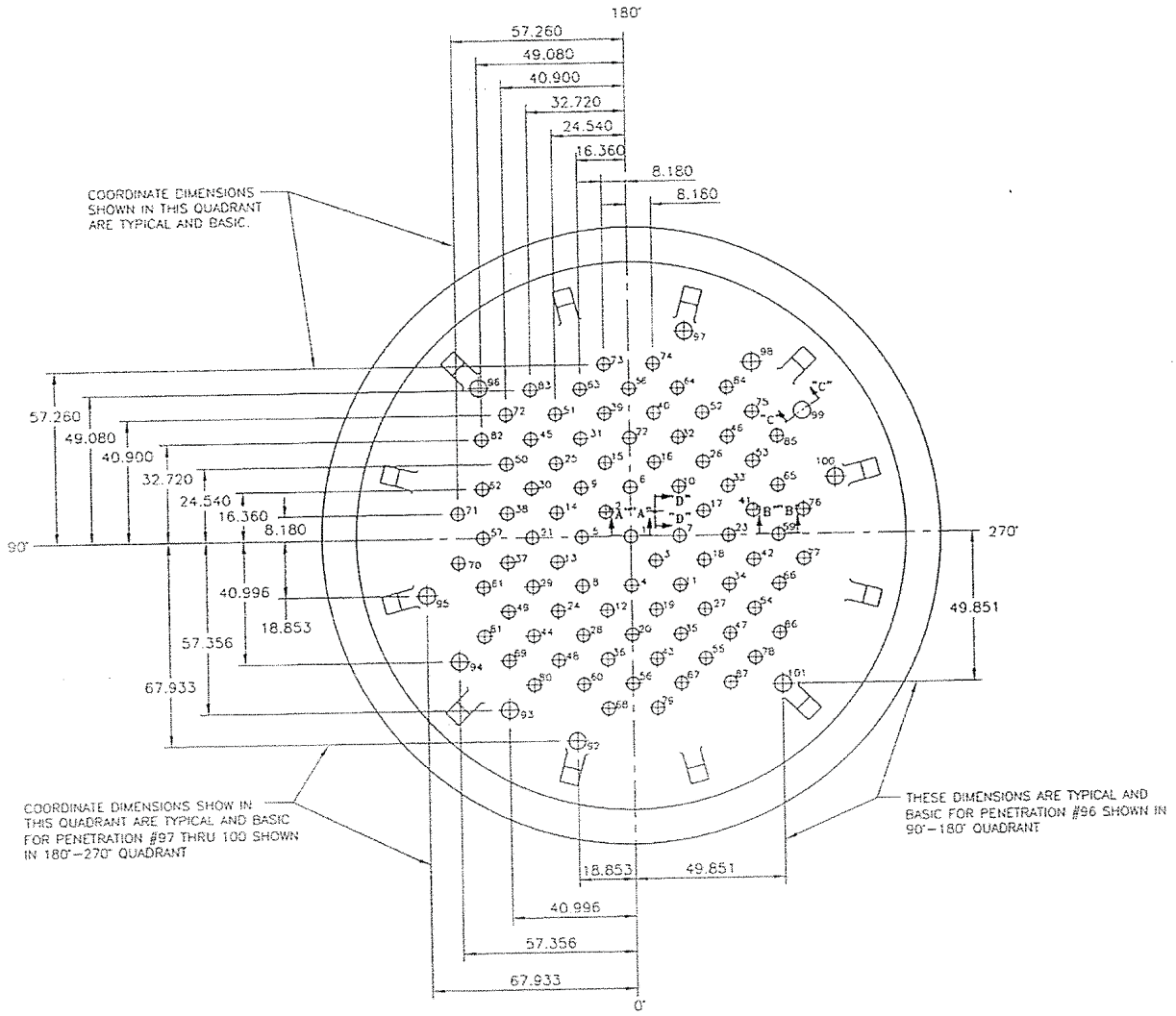

Revision 307 (07/13)

LOUISIANA POWER & LIGHT CO. Waterford Steam Electric Station	REACTOR VESSEL CLOSURE HEAD PLAN VIEW CEDM LAYOUT	Figure 4.6-1